Asok K. Sen
Kamal K. Bardhan
Bikas K. Chakrabarti
Editors

LECTURE NOTES IN PHYSICS 762

Quantum and Semi-classical Percolation and Breakdown in Disordered Solids

Springer

Lecture Notes in Physics

The Lecture Notes in Physics

The series Lecture Notes in Physics (LNP), founded in 1969, reports new developments in physics research and teaching – quickly and informally, but with a high quality and the explicit aim to summarize and communicate current knowledge in an accessible way. Books published in this series are conceived as bridging material between advanced graduate textbooks and the forefront of research and to serve three purposes:

- to be a compact and modern up-to-date source of reference on a well-defined topic
- to serve as an accessible introduction to the field to postgraduate students and nonspecialist researchers from related areas
- to be a source of advanced teaching material for specialized seminars, courses and schools

Both monographs and multi-author volumes will be considered for publication. Edited volumes should, however, consist of a very limited number of contributions only. Proceedings will not be considered for LNP.

Volumes published in LNP are disseminated both in print and in electronic formats, the electronic archive being available at springerlink.com. The series content is indexed, abstracted and referenced by many abstracting and information services, bibliographic networks, subscription agencies, library networks, and consortia.

Proposals should be sent to a member of the Editorial Board, or directly to the managing editor at Springer:

Christian Caron
Springer Heidelberg
Physics Editorial Department I
Tiergartenstrasse 17
69121 Heidelberg / Germany
christian.caron@springer.com

A. K. Sen
K. K. Bardhan
B. K. Chakrabarti (Eds.)

Quantum and Semi-classical Percolation and Breakdown in Disordered Solids

Asok K. Sen
Saha Institute of Nuclear Physics
Theoretical Condensed Matter
Physics (TCMP) Division
1/AF Bidhannagar
Kolkata-700064
India

Kamal K. Bardhan
Saha Institute of Nuclear Physics
1/AF Bidhannagar
Kolkata-700064
India

Bikas K. Chakrabarti
Saha Institute of Nuclear Physics
Centre for Applied Mathematics &
Computational Science
1/AF Bidhannagar
Kolkata-700064
India

Sen A.K. et al. (Eds.), *Quantum and Semi-classical Percolation and Breakdown in Disordered Solids*, Lect. Notes Phys. 762 (Springer, Berlin Heidelberg 2009), DOI 10.1007/978-3-540-85428-9

ISBN: 978-3-540-85427-2 e-ISBN: 978-3-540-85428-9

DOI 10.1007/978-3-540-85428-9

Lecture Notes in Physics ISSN: 0075-8450 e-ISSN: 1616-6361

Library of Congress Control Number: 2008934652

Cover design: eStudio Calamar S.L., F. Steinen-Broo, Pau/Girona, Spain

Printed on acid-free paper

9 8 7 6 5 4 3 2 1

springer.com

AKS dedicates this book to his two sons,
Aronyak and Arkopal

Preface

This lecture notes in physics volume mainly focuses on the semi classical and quantum aspects of percolation and breakdown in disordered, composite or granular systems. The main reason for this undertaking has been the fact that, of late, there have been a lot of (theoretical) work on quantum percolation, but there is not even a (single) published review on the topic (and, of course, no book). Also, there are many theoretical and experimental studies on the nonlinear current-voltage characteristics both away from, as well as one approaches, an electrical breakdown in composite materials. Some of the results are quite intriguing and may broadly be explained utilising a semi classical (if not, fully quantum mechanical) tunnelling between micron or nano-sized metallic islands dispersed separated by thin insulating layers, or in other words, between the dangling ends of small percolation clusters. There have also been several (theoretical) studies of Zener breakdown in Mott or Anderson insulators. Again, there is no review available, connecting them in any coherent fashion. A compendium volume connecting these experimental and theoretical studies should be unique and very timely, and hence this volume.

The book is organised as follows. For completeness, we have started with a short and concise introduction on classical percolation. In the first chapter, D. Stauffer reviews the scaling theory of classical percolation emphasizing (biased) diffusion, without any quantum effects.

The next chapter by A.K. Sen deals with the physics between the classical and the quantum effects. It gives a detailed, pedagogic description of the genesis and development of a semi classical (or, semi quantum) percolation model as a driven network, named as a Random Resistor cum Tunnelling-bond Network, or RRTN in short. The chapter deals with both the semi classical percolation transition and its breakdown characteristics. On the way, it covers nonlinear dc and ac response, low-temperature variable range hopping (VRH) conductance and some dynamical aspects such as two early-stage power-law relaxations, predictability of the breakthrough (breakdown process starting at one end and crossing to the other) time in terms of a relaxation time, etc. Each of the topics covered has been introduced with a variety of observations and the theoretical results have been contrasted with experiments. It has been emphasized that a large variety of *non-electrical* phenomena of Nature,

where the 'tunnelling' response may be replaced by some other *non-linear response with threshold* (e.g., capillary forces of fluids in porous media, frictional forces in mechanical systems, viscous drags in some fluids, forces due to random 'pinning' of vortices in sliding charge density wave type of systems, etc.), may be modelled using the RRTN or its variant.

A. Mookerjee, T. Saha-Dasgupta and I. Dasgupta start out the Chapter 3 with a concise review of the models and techniques to study quantum percolation and conclude from numerical studies that it belongs to the same universality class as the single electron (i.e. no e-e interaction) Anderson (impurity) model. Their numerical approach, using vector recursion method alongwith finite size scaling analysis, can not resolve the controversy whether quantum percolation exists in two dimensions, and seems to indicate that there is not localised to extended states transition (i.e. no q-percolation) in 2D. More precisely, they did not find any fool-proof answer to the question of whether, even for a very weak (non-zero) disorder in 2D, all the states are exponentially localised or some power-law-localised states exist in the vicinity of the band centre.

The chapter by H. Nakanishi and M.F. Islam describes the subject of quantum percolation in two dimensions, a topic still controversial with decades of studies regarding the nature of localisation and presence or absence of phase transitions in its transmission behaviour. They show that the results of some recent numerical studies of the transmission coefficient of a hopping Hamiltonian are most consistent with an interpretation that (a) there are two different localisation regimes, exponentially localised and algebraically localised, (b) there is a delocalised regime, and (c) characteristic power-laws in the algebraically localised regime vary with dilution and energy.

The chapter by G. Schubert and H. Fehske presents a large-scale numerical study of localisation effects in 2D and 3D quantum site percolation. Combining exact diagonalisation, Chebyshev expansion and local distribution approaches, the authors analyse the mean and typical densities of states, but also dynamical properties such as the time evolution and recurrence probability of a quantum particle on the spanning cluster. The results throw a new light on the existence of a quantum percolation threshold and may have implications for percolative transport scenarios in novel materials.

The next chapter by C. Sohrmann, J. Oswald and R.A. Römer, addresses the issue of quantum percolation in the presence of perpendicular electric and magnetic fields, especially when the system is in its (well-known) integral quantum Hall effect (IQHE) regime. The authors introduce the topics in a lucid, pedagogical style using single particle (electronic) wave functions and quantised Landau levels in a magnetic field. Then they review some of the most prominent network models for the IQHE. Screening effects due to the e-e exchange interaction are considered at the Hartree-Fock (HF) level. The IQHE phenomenon is finally described in terms of quantum transport (or, percolation) across the ensuing effective potentials.

P. Majumdar concisely reviews next the percolative quantum effects due to the coexistence of competing phases in the manganites. A summary of the key experiments in this area throwing light on spatial clustering and transport is followed by a

description of the two microscopic models carrying the essence of *correlated* quantum percolation involving both 'site' and 'bond' randomness. The distribution function involves the iterative solution of a Schrodinger equation. The microscopic results are compared with predictions from phenomenological resistor network theory and experimental results.

The chapter by D. Samanta, B.K. Chakrabarti and P. Ray reviews first the classical breakdown properties and their statistics for random fuse-conductor networks and random dielectric-conductor networks. The results are for both the dilute limit as well as near the percolation point and in lattice as well as continuum systems. It discusses next the Zener Breakdown problem in quantum percolation or in Anderson insulators (in particular in three dimension).

A microscopic quantum theory of nonequilibrium (open q-system) insulator to metal transition (quantum dielectric breakdown) in the presence of *strong e-e interaction* (correlation) is discussed in the next chapter by T. Oka and H. Aoki. The equilibrium version (closed q-system) of this is called the Mott transition. In the open q-system, the ground state is separated from the first excited state by the Mott gap, and *quantum breakdown* occurs through non-adiabatic, *Landau-Zener tunnelling* transitions, with *concommitant nonlinear transport*. In retrospect, it is interesting to note how some of these important elements had already been incorporated (at a minimal level) in some phenomenological models, for example, the semi-quantum RRTN model (see Asok K. Sen, *Nonlinear Response, Semi-classical Percolation and Breakdown in the RRTN Model*). Oka and Aoki next discuss the preservation of quantum coherence at sufficiently low temperatures, giving rise to dynamical localisation that saturates the creation process (of excitation pairs) and eventually leads to a nonequilibrium stable state.

The last chapter by K. Kieling and J. Eisert on *quantum computation and communication* is the sole representative of a very important and fast growing field of research. Here, one encounters a 'percolative type situation' originating from the statistical nature of quantum measurement or quantum state preparation processes. So, at a mental level, one is dealing with *engineered quantum systems* and the disorder is due to probabilistic *quantum gates*, or to Mott defects arising from the preparation of a cluster state. As such, the authors point out that the percolative disorder here is *statistically correlated* (not fully random). This general theme of correlated percolation is also of essence in the topics of two previous chapters: one on the RRTN model and the other on colossal magneto resistance in manganites. In the present chapter, methods of renormalisation are useful to overcome the probabilistic aspects of manipulating various quantum states. As the authors emphasize, one of the most important issues is to understand how far renormalisation over mixed quantum states could be of use to develop fault-tolerance, error correcting codes etc. for the use of quantum computation.

It gives us great pleasure to acknowledge all the contributors for their sincere support and patience while interacting with us on their individual chapters. Without the enthusiasm towards keeping their contributions up-to-date, this lecture notes volume would not be what it is today. We expect that all these combined bits of informations contained within its pages would have some usefulness to the relevant research

communities alongwith its overlapping areas, and to the newcomers who would like to be introduced to the topics covered here. Our efforts would be worthwhile and we would certainly hope so, if this book gives rise to further research in these and related areas. Finally, we must acknowledge the editors of Springer for their warm acceptance of this book project when it was proposed last year, and very helpful support throughout the process of publication.

Kolkata

Asok K. Sen
Kamal K. Bardhan
Bikas K. Chakrabarti

Contents

Classical Percolation
D. Stauffer 1
1 Introduction 1
2 Methods 3
3 Quantities and Exponents 6
4 Fractal Dimension: Incipient Infinite Cluster 9
5 Simple Renormalisation Group 12
6 Diffusion and Percolation 14
7 Summary 18
References 18

Nonlinear Response, Semi-classical Percolation and Breakdown in the RRTN Model
A.K. Sen 21
1 Introduction 21
2 The Origin of the RRTN Model and Its Percolative Aspects 27
3 Nonlinear Steady-State I-V Characteristics 35
4 Periodic Driving and AC-Response in the RRTN/CRC Model 46
5 VRH and Low Temperature Conduction in the RRTN 55
6 Slow Power-law Dynamics Far-from-Equilibrium 59
7 Aspects of Reversible Breakdown in the RRTN Model 65
8 Dynamical Characteristics of Breakdown 73
9 Summary and Further Works 77
References 78

Quantum Transmittance Through Random Media
A. Mookerjee, T. Saha-Dasgupta, and I. Dasgupta 83
1 Introduction 83
2 One Parameter Scaling Theory of Localization 84
3 Transport Mechanisms in Disordered Media 85
4 Some Models of Disordered Systems 87

5 Some Earlier Studies on the Quantum Percolation Model 89
6 The Vector Recursion Method and Its Applications 92
7 Conclusions 105
References 106

Quantum Percolation in Two Dimensions
H. Nakanishi, and Md. Fhokrul Islam 109
1 Introduction 109
2 Resonances and Phase Variations in Ordered Limit 116
3 Time-Independent Schrödinger Equation for Finite Disorder 120
4 Time-Dependent Schrödinger Equation: Sending a Wave Packet Through a 2D Cluster 125
5 Summary 132
References 133

Quantum Percolation in Disordered Structures
G. Schubert and H. Fehske 135
1 Introduction 135
2 Local Distribution Approach 137
3 Localization Effects in Quantum Percolation 144
4 Percolative Effects in Advanced Materials 154
5 Conclusions 159
References 160

Quantum Percolation in the Quantum Hall Regime
C. Sohrmann, J. Oswald and R.A. Römer 163
1 Introduction 163
2 The Quantized Hall Effect and Classical Percolation 165
3 Network Models at the IQHE 168
4 Hartree-Fock Approach to the IQHE 184
5 Conclusions 189
References 190

Percolative Quantum Transport in Manganites
P. Majumdar 195
1 Introduction 195
2 Standard Quantum Percolation 196
3 Manganites: Phenomenology and Model 198
4 Percolative Effects in a One Band Model of Phase Competition 205
5 Percolation in Two Band Models with Electron-Phonon Coupling 217
6 Connection with Quantum Percolation and Resistor Networks 221
7 Conclusions 225
References 225

Classical and Quantum Breakdown in Disordered Materials
D. Samanta, B.K. Chakrabarti and P. Ray 227
1 Introduction 227
2 Analysis of the Fuse Problem 229
3 Dielectric Breakdown Problem 238
4 Zener Breakdown in Anderson Insulators 247
5 Conclusions 249
References 249

Nonequilibrium Quantum Breakdown in a Strongly Correlated Electron System
T. Oka and H. Aoki 251
1 Introduction 251
2 Nonadiabatic Evolution and Pair Creation of Carriers 256
References 283

Percolation in Quantum Computation and Communication
K. Kieling and J. Eisert 287
1 Introduction 287
2 Percolation and Quantum Computing 290
3 Quantum Repeater Networks for Quantum Communication 307
4 Summary and Open Problems 315
References 317

Index 321

Classical Percolation

D. Stauffer

Institute for Theoretical Physics, Cologne University, D-50923 Köln, Euroland

1 Introduction

Percolation theory mostly deals with large lattices where every site is randomly either occupied or empty. In particular, it studies the resulting clusters that are sets of neighbouring occupied sites. It was three decades ago that Stauffer published his last research on quantum effects; he is, thus, eminently qualified to write this introductory chapter, where $\hbar = 0$. Mostly, this review combines in a shortened form two articles written for the *Encyclopedia of Complexity and Systems Science*, for the same publisher.

Paul Flory, who later got the Chemistry Nobel prize, published in 1941 the first percolation theory [1–6], to describe the vulcanisation of rubber [7]. Others later applied and generalised it, in particular by dealing with percolation theory on lattices and by studying it with computers. Most of the theory presented here was known around 1980, although it was in the case of computer simulation with less accuracy than today. But on the questions of universality of critical spanning probability and of the uniqueness of infinite clusters, the 1990s have shown some of our earlier opinions to be wrong, and biased diffusion also was clarified around the year 2000 only. Even today it is questioned by some that the critical exponents of percolation theory can be applied to real polymer gelation, the application which Flory had in mind in 1940s.

On a large lattice, we assume that each site independently and randomly is occupied with probability p and empty with probability $1 - p$. Depending on the applications, other words can also be used instead of occupied and empty, for example. Republican and Democrat for the majority party in an electoral district of the USA. A *cluster* is now defined as a set of occupied neighbouring sites. Percolation theory deals with the number and structure of these clusters, as a function of their size s, that is of the number s of occupied sites in the cluster. In particular, it asks whether an infinite cluster spans from one side of the lattice to the opposite side. Alternatively, and more naturally if one wants to describe chemical reactions for rubber vulcanisation, this site percolation can be replaced by bond percolation, where every site is occupied but the link between neighbouring sites is either present with probability p or absent with probability $1 - p$, again independently and randomly for each

Stauffer, D.: *Classical Percolation*. Lect. Notes Phys. **762**, 1–19 (2009)
DOI 10.1007/978-3-540-85428-9_1

link. A cluster is now a set of neighbouring sites connected by links, and the size s of the cluster can be counted as the number of links, or as the number of sites, in that cluster. Because of this ambiguity we discuss here mainly site percolation; bond percolation is similar in the sense that it belongs to the same universality class (same critical exponents). One may also combine both choices and study site-bond percolation, where each site is randomly occupied or empty, and where each bond between neighbouring occupied sites is randomly present or absent.

Neither temperature nor quantum effects enter this standard percolation model, which is purely geometrical probability theory. However, to understand why percolation works the way it does, it is helpful to understand thermal phase transitions such as the vapour-liquid critical point; and for magnetic applications it is useful to know that some spins (atomic magnetic moments) have only two states, up or down, according to quantum mechanics. We will explain these physics aspects later, in the Sect. 2.5.

For small p, most of the occupied sites are isolated, $s = 1$, coexisting with only few pairs, $s = 2$ and triplets, $s = 3$. For large p, most of the occupied sites form one 'infinite' cluster spanning the lattice from left to right, with a few small isolated holes in it. Thus, there exists one percolation threshold, p_c such that for $p < p_c$ we have no spanning cluster and for $p > p_c$ we have (at least) one spanning cluster. Inspite of decades of research on this seemingly simple problem, no exact solution for p_c is proven or guessed for site percolation on the square lattice with nearest-neighbour bonds; only numerically we know it to be about 0.5927460. For site percolation on the triangular lattice or bond percolation on the square lattice, $p_c = 1/2$ exactly. More thresholds are given in the Table 1[1–6]. They are valid in the limit of $L \to \infty$ for lattices with L^d sites in d dimensions. For small L instead of a sharp transition at p_c one has a rounded changeover: with a very low probability one chain of L occupied sites at $p = 1/L^{d-1}$ spans from left to right. In one dimension, a small chain

Table 1. Site and bond percolation thresholds for one dimension, 3 two-dimensional, 4 three-dimensional and 4 hypercubic lattices in higher dimensions [1–6, 8]

p_c	Site	Bond
$d = 1$ chain	1	1
Honeycomb	.697043	$1 - 2\sin(\pi/18)$
Square	.592746	1/2
Triangular	1/2	$2\sin(\pi/18)$
Diamond	.4301	.3893
SC	.311608	.248813
BCC	.245691	.180287
FCC	.199236	.120163
$d = 4$ Hypercubic	.196885	.160131
$d = 5$ Hypercubic	.140797	.118172
$d = 6$ Hypercubic	.109018	.094202
$d = 7$ Hypercubic	.088951	.078675

can easily be spanned if p is close to 1, but for $L \to \infty$ the threshold approaches $p_c = 1$ since at smaller p a hole will appear about every $1/(1-p)$ sites and prevent any cluster to span.

2 Methods

This section summarises some of the methods employed to find percolation properties, first by pencil and paper, and then with the help of computers for which Fortran programs are published, for example, in [9, 10].

2.1 Mean Field Limit

The Bethe lattice or Cayley tree neglects all cyclic links and allows a solution with paper and pencil. We start from one central site, and let z bonds emanate from that. At the end of each bond sits a neighbour. Then from each of these neighbours again z bonds emanate, one back to the central site and $z-1$ to new sites-outward. They in turn lead again each to $z-1$ new sites, and so on. None of the newly added sites agrees with one of the already existing sites, and so we can travel along the bonds only outwards or back, but never in a loop. It is quite plausible that an infinite cluster of bond percolation is formed if each site leads to at least one more outward site along an existing bond, which means if $(z-1)p > 1$. This condition also holds for site percolation. Thus,

$$p_c = 1/(z-1)\ . \tag{1}$$

In this way, Flory calculated the threshold and other percolation properties. Today we call this the 'mean field' universality class in analogy with thermal phase transitions. The critical exponents, to be discussed below, are integers or simple fractions. To this universality class also belong the Erdös-Rényi random graphs, where we connect in an assembly of N points each pair with a low probability $\propto 1/N$. And the same universality class is reached if we let the dimension d of the hypercubic lattice go to infinity (or at least take it above 6). A disadvantage of the Bethe lattice is its lack of realism: If the length of the bonds is constant, then the exponential increase of the number of sites and bonds with increasing radius leads to an infinite density.

2.2 Small Clusters

The probability of a site to be an isolated $s = 1$ cluster on the square lattice is $n_1 = p(1-p)^4$ since the site must be occupied and all its four neighbours be empty. The formula for pairs is $n_2 = 2p^2(1-p)^6$ since the pair can be oriented horizontally or vertically, resulting in the factor 2. Similar, only more difficult, is the evaluation of n_s with a maximum s usually 10 to 20; the general formula is

$$n_s = \sum_t g_{st}\, p^s\, (1-p)^t, \tag{2}$$

where the perimeter t is the number of empty neighbours and g_{st} is the number of configurations (or lattice animals, or polyominoes) of size s and perimeter t. The King's College group in London published these results decades ago. With techniques borrowed from series expansions near thermal critical phenomena, these polynomials allow to estimate not only p_c but also many other quantities (see below), diverging or vanishing near p_c.

2.3 Leath Cluster Growth

In the cluster growth method of Leath (1976), one starts with one occupied site in the centre of the lattice. Then a cluster is grown by letting each empty neighbour of an already occupied cluster site decide once and for all, whether it is occupied or empty. One needs to keep and to update a perimeter list of empty neighbours. If that list becomes empty, the cluster growth is finished, and no boundary effects of the lattice influence this cluster. If, on the other hand, the cluster reaches the lattice boundary, one has to stop the simulation and can regard this cluster as spanning (from the centre to one of the sides). Repeating many times this growth simulation one can estimate p_c as well as the cluster numbers. More precisely, the cluster statistics obtained in this way is not n_s but $n_s s$ since the original centre site belongs with higher probability to a larger than to a smaller cluster.

2.4 Hoshen-Kopelman Labelling

To go regularly through a large lattice, which may even be an experimentally observed structure to be analysed by computer, one could number consecutively each seemingly new cluster, and if no clusters merge later then one has a clear classification: All sites belonging to the first cluster have Label 1, all sites of the second cluster have Label 2, and so forth. Unfortunately, this does not work. In the later analysis, it may turn out that two clusters that at first seemed separate actually merge and form one cluster:

```
* *     * *        1 1     2 2
  *   * * *          1   3 ? 2
* * * * *          4 ? ? x ?     .
```

Already in the simple structure shown to the left we have several such label conflicts. The labels to the right come going though the lattice such as a typewriter, from left to right, and after each line to the lower line. When we come to the right neighbour of the 3, we see that 3 is really a part of the cluster with Label 2. And at the right neighbour of 4, we see that 4 belongs to Cluster 1. The stupid method is to go back and to relabel all 3 into 2, and all 4 into 1. If, then, we come to the site marked with x we see that the whole structure is really one single cluster, and thus all labels 2 have to be relabeled into a 1. This is inefficient for large lattices. Instead, Hoshen and Kopelman (1976) gave to each site label $m = 1, 2, 3, \ldots$ another index $n(m)$. This label $n(m)$ of labels equals its argument, $n(m) = m$, if it is still a good 'root label', and it equals another number k which is the cluster with initial label m that later

turned out to be a part of an earlier cluster k. By iterating the command `m = n(m)` until finally the new m equals $n(m)$ one finds this root label. For the above we make the following assignments and re-assignments to n: $n(1) = 1,\ n(2) = 2,\ n(3) = 3,\ n(3) = 2,\ n(4) = 4,\ n(4) = 1,\ n(2) = 1$. Clusters are now characterised by the same root label for all their labels.

An advantage of this method is that only one line of the square lattice, or one hyperplane of the d-dimensional lattice, needs to be stored at any time, besides the array $n(m)$. And that array can also be reduced in size (following Reynolds and Nakanishi) by regular recycling no longer used labels n, just as beer bottles can be recycled. Lattices with more than 10^{13} sites were simulated, using parallel computers. However, understanding the details of the algorithms and finding errors in them can be very frustrating.

Sometimes one wants to determine the cluster numbers for numerous different p's from 0 to 1. Instead of starting a new analysis for each different p one may also fill the lattice with new sites, and make the proper labelling of labels whenever a new site is added [11]. Similarly, one can determine the properties of various lattice sizes L by letting L grow one by one and relabelling the cluster after each growth step [12]. Unfortunately, these two methods came long after most of the percolation properties were already studied quite well by standard Hoshen-Kopelman analysis.

2.5 Relation to Ising and Potts Models

The relation between percolation and thermal physics was useful for both sides: Scaling theories for percolation could follow scaling theories for thermal physics about 10 years earlier, and computer simulations for thermal physics could use the Leath and Hoshen-Kopelman algorithms of cluster analysis, leading to the Wolff and Swendsen-Wang methods, respectively, a decade later. A mathematical foundation is given by the Kasteleyn-Fortuin theorem [13] for the partition function Z of the Q-state Potts model at temperature T:

$$Z(Q) = \langle Q^N \rangle \tag{3}$$

where N is the total number $\sum_s n_s$ of clusters for bond percolation at probability $1 = \exp(-2J/k_BT)$, $\langle \dots \rangle$ indicates an average over the configurations at this probability, k_B is Boltzmann's constant and $2J$ is the energy needed to break a bond between neighbouring spins. (Each site i of a Potts lattice carries a variable $S_i = 1, 2, \dots Q$; the energy of a neighbouring pair is $-2J$ if the two variables agree, and zero otherwise.)

Q values of 3 and larger are interesting, since for increasing Q a second-order phase transition with a continuous order parameter changes into a first-order phase transition with a jumping order parameter, when T increases. The special case $Q = 2$ is the spin of 1/2 Ising model (the model is pronounced EEsing, not EYEsing since Ernst Ising was born in Cologne, Germany, and became US citizen Ernest Ising only after publishing his theory in 1925 and surviving Nazi persecution.) The limit $Q \to 0$ corresponds to some tree structures (no cyclic links, as in Flory's percolation theory,

[14]). Percolation, on the other hand, correponds to the limit $Q \to 1$, in the following way: The 'free energy' in units of $k_B T$ is in this limit, $\ln Z = \ln\langle \exp(N \ln Q)\rangle \simeq \ln\langle \exp[(Q-1)N]\rangle \simeq \ln\langle 1 + (Q-1)N\rangle \simeq (Q-1)N$. Thus, for Q near unity this thermal free energy, divided by $Q-1$, is the number of percolation clusters.

In this way, thermal physics and percolation are related, and the cluster numbers N correspond to a free energy. In thermal physics, the negative derivative of the free energy with respect to a conjugate field gives the order parameter (e.g. magnetic field and magnetisation), and the field derivative of the order parameter is called the susceptibility. For liquid-gas equilibria, the order parameter is the volume (or the density), the field is the pressure (or chemical potential) and the analog of the susceptibility is the compressibility. We should keep in mind this result, not its derivation, if we now look at the percolation quantities of interest.

Formally, we may define for percolation a free energy F as a generating function of a ghost field h:

$$F(h) = \sum_s n_s \exp(-hs) \quad . \tag{4}$$

Then its first h-derivative is $-\sum_s n_s s$, and the second one is $\sum_s n_s s^2$, sums, which appear below in the percolation probability P_∞ (the order parameter) and the mean cluster size, $S = \sum_s n_s s^2 / \sum_s n_s s$ (the susceptibility).

3 Quantities and Exponents

The basic quantity is n_s, the number (per site) of clusters containing s sites each, and often is an average over several realisations for the same occupation probability p in the same lattice. Several moments

$$M_k = \sum_s n_s s^k \tag{5}$$

are used to define other quantities of interest; in these sums, the infinite (spanning) clusters are omitted. The following proportionalities are valid asymptotically in the limit of large lattice size L and for $p \to p_c$:

$$F = M_0 \propto |p - p_c|^{2-\alpha} + \ldots \; ; \tag{6a}$$

$$P_\infty = p - M_1 \propto (p - p_c)^\beta \; ; \tag{6b}$$

$$S = M_2/M_1 \propto |p - p_c|^{-\gamma} \; . \tag{6c}$$

Here, F is the analogue of the thermal free energy, where the three dots represent analytic background terms, whose derivatives are all finite. Since every occupied site must belong either to a finite or to an infinite cluster, $P_\infty = p - \sum_s n_s s$ is the fraction of sites belonging to the infinite cluster, and gives the probability that from a randomly selected site we can walk to a lattice boundary along a path of occupied sites. It is, thus, called the percolation probability but needs to be distinguished from

the probability p that a single site is occupied and from the probability R, with $R(p < p_c) = 0,\ R(p > p_c) = 1$, that there is a spanning cluster in the lattice.

The quantity S is usually called the mean cluster size, and we follow this tradition even though it is very bad. There are many ways to define a mean size, and polymer chemists have the much more precise notation of a number average M_1/M_0, a weight average M_2/M_1 and a z average M_3/M_2 for the cluster size ($=$ degree of polymerisation). Physicists arbitrarily call the weight-averaged s the mean cluster size S. Numerically, the exponent γ is determined more easily from the 'susceptibility' $\chi = M_2 \propto |p - p_c|^{-\gamma}$, since the denominator M_1 in Eq. (6c) approaches very slowly its asymptotic limit of 1.

The radius of a cluster R_s can be defined as the rms distance, $r_i,\ i = 1, 2, \ldots, s$, of cluster sites from the centre of mass r_c of the cluster (radius of gyration):

$$R_s^2 = \langle \sum_i (r_i - r_c)^2 / s \rangle, \tag{6d}$$

where the $\langle \ldots \rangle$ average is over all cluster configurations at probability p. Then the correlation length ξ is related to the z-average cluster radius through

$$\xi^2 = \sum_s R_s^2 n_s s^2 / \sum_s n_s s^2 \propto |p - p_c|^{-2\nu} \tag{6e}$$

with another critical exponent ν.

Finally, right at $p = p_c$, the cluster numbers decay as

$$n_s \propto 1/s^{2+1/\delta}, \tag{7}$$

where δ must be positive to allow a finite density, $\sum_s n_s s = p$.

These five critical exponents are not independent of each other, but are related in d dimensions through the scaling laws:

$$2 - \alpha = \gamma + 2\beta = (\delta + 1)\beta = d\nu \tag{8a}$$

as known from thermal phase transitions; the last equation involving d is not valid in mean field theory (large d) but only for $d \leq 6$. Table 2 gives the numerical estimates of the exponents in three dimensions as well as their mean field values for $d \geq 6$

Table 2. Critical exponents, Eqs. (6, 9), for percolation clusters. The mean field values are valid for six and more dimensions and also apply to Flory's Bethe approximation and to Erdös-Rényi random graphs. The exponents α, δ, σ, and τ can be derived from the scaling laws, Eq. (8)

d	β	γ	ν	μ
2	5/36	43/18	4/3	1.31
3	0.41	1.796	0.88	2.0
≥ 6	1	1	1/2	3

and their exact two-dimensional results [15, 16]. Thus, for six and less dimensions, if you know two exponents you know them all thus far.

These scaling laws (8a) can be derived by assuming

$$n_s = s^{-\tau} f[(p - p_c)s^{\sigma}] \quad (\tau = 2 + 1/\delta,\ 1/\sigma = \beta\delta), \tag{8b}$$

which was first postulated for the thermal Ising model, and then successfully applied to percolation. Here, f is a suitable scaling function, which only in the mean-field limit approaches a Gaussian.

For both thermal critical phenomena and percolation, 'universality' asserts that these critical exponents are independent of many details and (for the Potts model) depend only on the dimensionality d and the number Q of possible spin states. Since percolation corresponds to $Q \to 1$, this means that the exponents depend only on d. There are exceptions from this universality for thermal-phase transitions, but for random percolation thus far it worked. However, the numerical value of the percolation threshold p_c is not a critical exponent, depends on the lattice structure and is different for site and bond percolation.

This universality is one of the reasons why the investigation of exponents is important: They allow to classify models and materials. Similarly, in biology we have many birds of different colours, and many types of domestic animals. Biology became a systematic science only when it was found that all mammals share certain properties, which birds do not have. Thus, there is the universality class of mammals.

(The proportionality factors in Eq. (6) are not universal, but some of their combinations are, for example, the ratio of the proportionality factors for S above to below p_c is universal. In some sense also, the probability $R(p = p_c)$ of a lattice to contain one spanning cluster at the threshold is universal: same for bond and site percolation; however, this probability depends on the boundary conditions and the shape of the sample, and thus is far less universal that the mentioned ratio for S.)

Unfortunately, there is another exponent that does not follow from the cluster numbers and radii and for which no scaling law is accepted, which relates it to the other exponents above. This refers to the electrical conductivity

$$\Sigma \propto (p - p_c)^{\mu}, \tag{9a}$$

when each occupied site (or bond) conducts electrical current and each empty site (or deleted bond) is an insulator. The numerical values were given in Table 2. If bonds are realised by elastic springs with bending forces, the elastic exponent may be $\mu + 2\nu$ if entropy effects are negligible, or $2 - \alpha$, if entropy effects are dominant. Moreover, μ is less universal: the above lattice values do not hold on a continuum (conducting spheres that may overlap). Similarly, the kinetics of the Ising model determine a critical exponent, which differs in different variants of the kinetics and may not be related to the static Ising exponents such as β and γ. Even though μ seems not to be determined by the static percolation exponents, related quantities such as the minimum gap between clusters or the first passage time are determined by at [17, 18].

Instead of a mixture of conductors (p) and insulators ($1-p$) we may also investigate a mixture of superconductors (p) and conductors ($1-p$). Now for all $p > p_c$ the overall conductivity Σ is infinite, while slightly below p_c it diverges with the power law

$$\Sigma \propto (p - p_c)^{-\mu'} \tag{9b}$$

with $\mu = \mu'$ only in two dimensions; otherwise one has a new exponent μ' ($\simeq 0.73$ for $d = 3$) not related by scaling laws to the other exponents.

4 Fractal Dimension: Incipient Infinite Cluster

4.1 Fractal Dimension D

Typical objects of geometry classes in school are one-dimensional lines, two-dimensional squares or circles and three-dimensional cubes or spheres. They have a length (radius), L, and a mass (volume for unit density) M with $M \propto L^d$ for d dimensions. In reality, mother nature produces much more complex objects, such as trees, where the mass varies with the power of the tree height below 3:

$$M \propto L^D \quad (D < d,\ L \to \infty). \tag{10a}$$

Where D is the fractal dimension, and such objects are called fractals, particularly if they also are self-similar in that a small twig looks like a big branch, and so on. An exactly solved example are random walks (= polymer chains without interaction), where $D = 2$ if the length of the walk is identified with the mass M. For self-avoiding walks (= polymer chains with excluded volume interaction), the Flory approximation gives $D = (d+2)/3$ in $d \leq 4$ dimensions ($D(d \geq 4) = 2$ as for random walks), which is exact in one, two and four dimensions, and too small by only about 2% in three dimensions.

For percolation, finite-size scaling theory then relates D of the largest (spanning?) cluster at, $p = p_c$, to the above percolation exponents through

$$D = d - \beta/\nu = (\gamma + \beta)/\nu = 1/(\sigma\nu) = d/(1 + 1/\delta) \tag{10b}$$

for $d \leq 6$. Thus, the typical critical cluster is about 1.9-dimensional in 2 and 2.5-dimensional in three dimensions, while in the mean field regime for $d \geq 6$ we have $D = 4$.

Why is this so? Any quantity X which is supposed to vary near $p = p_c$ as $|p-p_c|^x$ does so only for infinitely large systems. For a finite lattice size L, the transition is rounded, and neither X nor any of its p-derivatives diverges or becomes exactly zero. In particular, the typical cluster radius or correlation length $\xi \propto |p - p_c|^{-\nu}$ cannot become infinite but becomes of order L. Then the relation $X \propto \xi^{-x/\nu}$ is replaced by

$$X(p = p_c) \propto L^{-x/\nu} \tag{11a}$$

them the threshold, and

$$X(p \simeq p_c) = L^{-x/\nu} g[(p - p_c)L^{1/\nu}] \tag{11b}$$

near the threshold, with a suitable scaling function g. In particular, the fraction P_∞ of sites belonging to the largest cluster at $p = p_c$ vanishes as $L^{-\beta/\nu}$, and the total number M of sites in this cluster as

$$M \propto L^{d-\beta/\nu} \quad \text{or} \quad D = d - \beta/\nu \tag{11c}$$

as asserted in Eq. (10b) for typical critical clusters.

Figure 1 shows the second moment $\chi = M_2 = \sum_s n_s s^2$ in small (curve) and large $(+)$ simple cubic lattices, differing only for $p \simeq p_c$. Simulations are shown in Fig. 2 for the number M of sites in the largest cluster as well as for susceptibility (related to the mean cluster size), both at $p = p_c$.

In a finite lattice, the probability $R(p)$ of a spanning cluster to exist goes from nearly zero to nearly unity in a p-interval proportional to $1/L^{1/\nu}$, according to Eq. (11a) with $x = 0$. The derivative dR/dp is the probability that spanning first occurred at probability p. It is plausible that this probability, peaked around p_c, is a Gaussian, that is, a normal distribution. Unfortunately, Ziff destroyed [10] this beautiful idea: Since for $p \simeq p_c$ and $\xi \sim L$ every part of the lattice is correlated with the rest of the lattice, the central limit theorem does not hold.

(If for $p \ll p_c$ we let the cluster size s go to infinity, which requires a special algorithm, we get into the universality class of lattice animals, Sect. (2.2). Most simply, in the limit $p \to 0$, Eq. (2) simplifies to $n_s/p^s = g_{st}$, which means we look at the distribution of configurations with s sites and perimeter t, where all configurations of a given s are weighted equally, whatever their perimeter t is. An important

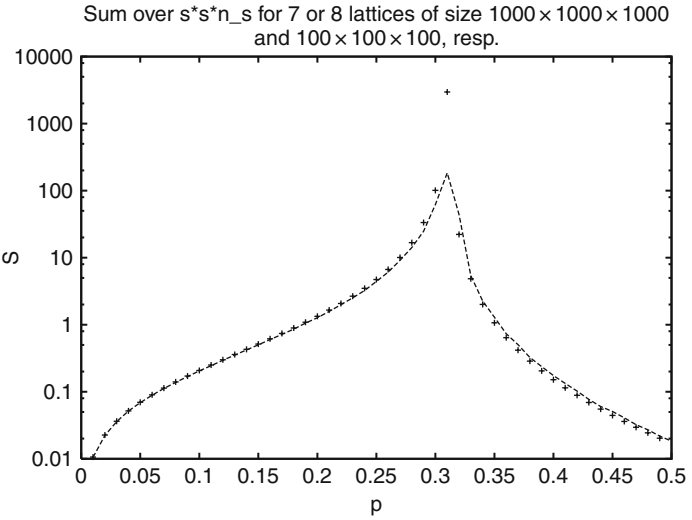

Fig. 1. "Susceptibility" M_2 in simple-cubic lattice. For the smaller size the maximum is reduced appreciably

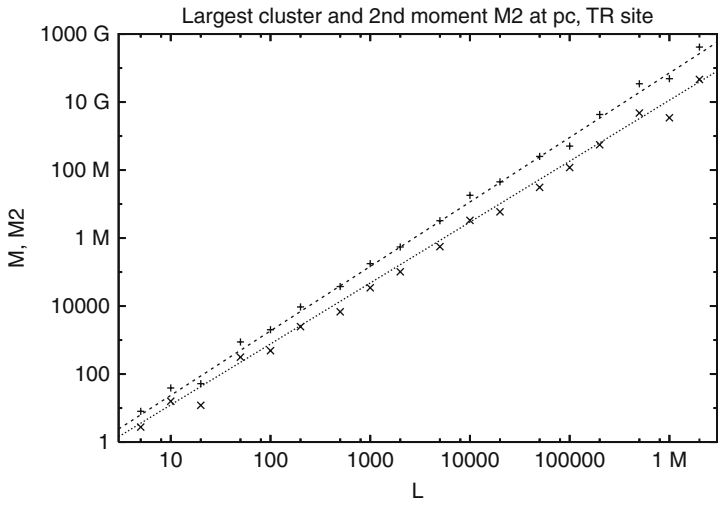

Fig. 2. Number M of sites in largest cluster $(+)$ and susceptibility M_2 (x) at $p = p_c = 1/2$ for triangular site percolation. The two straight lines have the exact slopes $D = 91/48$ and $\gamma/\nu = 43/24$ predicted by finite-size scaling. The largest lattice took about 36 hours on a workstation with 2 gigabytes memory. Tiggemann [12] simulated $L = 7 \times 10^6$, 25024, 1305, 225 for $d = 2$, 3, 4, 5 on a large parallel computer

result for these animals is that in three dimensions their radius R_s varies as $\sqrt{s}$, that is, their fractal dimension is exactly 2. In two dimensions, only numerical estimates exist with $D \simeq 1.56$. It is highly unusual that a problem has an exact solution in three but not in two dimensions.)

4.2 Incipient Infinite Cluster

Right at $p = p_c$, the largest cluster spans the lattice with a pseudo-universal probability $0 < R(p_c) < 1$, and then has a density P_∞ going to zero for L going to infinity. It is also called the incipient infinite cluster IIC. Most of the IIC consists of dangling ends that carry no current, if the cluster is interpreted as a random resistor network with conductivity Σ, see Eq. (9) above. The remaining current carrying 'backbone' has a fractal dimension 1.643 in two dimensions, 1.7 in three and 2 in at least six dimensions, and mostly consists of blobs where current flows along several parallel though connected paths. The few 'articulation' sites or bonds, the removal of which cuts the network into two or more parts, are also called 'red' since all the current flows through them; they have a fractal dimension of only $1/\nu = 0.75$, 1.14 and 2 in two, three and $\geq$ six dimensions.

How many infinite clusters do we have? The easy answer is: none below, perhaps one at and always one above p_c in an infinite network. Indeed, this is what was claimed mathematically in the 1980s [20]: The number of infinite clusters is zero, one or infinite. Later mathematics excluded the last choice of infinitely many clusters, even though in seven dimensions scaling arguments, confirmed by numerical

studies [21], indicated the number of IIC to go to infinity for increasing L in seven dimensions. Only in 1995 and later Aizenman [22] predicted that in all dimensions one may have several spanning clusters at $p = p_c$, in agreement with simulations [23]. In the presence of several spanning clusters their fractality has been questioned [24].

Why were the earlier uniqueness theorems irreproducible at p_c and for very elongated rectangles even above p_c [25]? A clear definition of 'infinite' is missing in some of the mathematics, although [20] defined a cluster as infinite if its cardinality (= number of sites in it) is infinite for $L \to \infty$ in a hypercubic lattice of L^d sites. Clear definitions of infinity are, of course, needed for reliable proofs [26]. Measure theory as applied in some theorems may be based on some axioms which are not applicable for a fractal IIC. Very simply, imagine each line of an $L \times L$ square lattice to have one randomly selected site occupied and all others empty. The set of occupied site then has cardinality L which is infinite for infinite lattices, but its density becomes zero. Does your measure theory agree with this? More relevant for percolation, even for $p < p_c$ the largest cluster has a size increasing logarithmically with lattice size and thus can be described as infinite, invalidating the percolation threshold as the onset of infinite clusters. Thus, infinite might be defined as increasing with a positive power of L, that is, having a positive fractal dimension. Then, we have infinitely many infinite clusters only at $p = p_c$, although in most cases only the largest of them is a spanning cluster. Using 'spanning' as a definition of an infinite cluster seems to cause the smallest problems.

Thus, one should not regard a question as settled if some mathematical theorem claims to have answered it. The mathematics may not apply to the same problem one is interested in, or [27] may apply only for unrealistically large lattices. On the other hand, computer simulations should also be relied upon only if confirmed independently. And in the interpretation of simulation results, one should be objective and not try to agree with prevailing theories. For example, de Arcangelis [21] might already have seen the multiplicity of infinite clusters in five dimensions, not only in seven, had she not followed her obviously incompetent postdoctoral mentor.

(On a more positive side, mathematicians [28] solved biased diffusion on percolating clusters above p_c only a few years after physicists had controversies about their simulations.)

5 Simple Renormalisation Group

Why are scaling laws and finite-size scaling so simple? Why is universality valid for the exponents? These questions arose for thermal critical phenomena as well as for percolation. The main reason is that the correlation length ξ goes to infinity at the critical point. Thus, all approximations that restrict the correlations to some finite lengths eventually become wrong, and instead the scaling ideas become correct. They were explained by Ken Wilson through what he called renormalisation group, around 1970, and he got the physics Nobel prize for it in 1982. Basically, since correlations extend over long distances, the single atom or lattice point becomes irrelevant and can be averaged over. In politics, we have a similar effect: Many democracies are

based on electoral districts, and the candidate winning most votes within this district represents this district in the national parliament. It is the cooperation of many people within the electoral district, not the single vote, which is decisive.

Returning to an $L \times L$ lattice, we can divide it into many blocks of linear dimension b, and treat a block analogously to an electoral district. Thus, in an Ising model, if the majority of block spins point upward, the whole block is represented by a superspin pointing up, analogous to the single representative in politics. These block spins then act like the original spins, one can put $b \times b$ superspins into one superblock, and can have just one super-representative following the majority opinion of the representatives within the superblock. This process can be continued: at each stage $b \times b$ lower representatives are renormalised into a single higher representative.

Such a renormalisation by majority rule works fine with Ising spins, but percolation deals with connections, not with up and down spins. Thus, for percolation a $b \times b$ block is renormalised into an occupied supersite if and only if there is a spanning cluster within the block; otherwise, the superblock is defined empty. In this way, whole blocks are renormalised into singe sites via connectedness. And the renormalisation is reduced to the standard question which was asked already before Wilson's invention: Does a $b \times b$ lattice have a spanning cluster? The supersite is thus occupied if and only if the block spans, which happens with probability $R_b(p)$. If we call p' the probability of the supersite to be occupied, we thus have

$$p' = R_b(p) \; . \tag{12a}$$

If we are at $p = p_c$, then the renormalisation should not change anything drastic since ξ is larger than any b; thus, if the renormalisation would be exact we would have

$$p_c = R_b(p_c) \; . \tag{12b}$$

Practically we determine a fixed point $p = p^*$, such that

$$p^* = R_b(p^*) \; . \tag{12c}$$

and then find p_c as the limit of p^* for $b \to \infty$, which again is similar to what percolation experts did before this renormalisation theory.

A particularly simple example is the triangular site percolation problem with $p_c = 1/2$, if we do not divide the lattice into large $b \times b$ blocks, but into small triangles of three sites which are nearest neighbours, as shown on the left:

```
   *            x            x
 *   *        x   x        x   .
```

The triangle contains a spanning cluster if either all three sites are occupied (x, central diagram) or two sites are occupied (x) and one site is empty (. , right diagram). The first choice appears with probability p^3, the second with probability $p^2(1-p)$. However, this second choice has three possible orientations since each of the three sites can be the single empty site. Thus, the total probability of the triangle to have a spanning cluster is

$$p' = p^3 + 3(1-p)p^2 \tag{13a}$$

with three fixed points p^*, where $p' = p$:

$$p^* = 0, \quad p^* = 1/2, \quad p^* = 1\ . \tag{13b}$$

The second of these fixed points is the percolation threshold, while the first corresponds to lattice animals (Sect. 2.2 and end of Sect. 4.1) and the third to compact non-fractal clusters. With somewhat more effort, one can derive also a good approximation for ν.

This agreement of the fixed point p^* with the true threshold $p_c = 1/2$ is not valid for other lattices or block choices. Nevertheless, there was a widespread fixed-point consensus that $R_b(p_c) = p_c$ for sufficiently large b. Regrettably, Ziff [29] again destroyed this beauty and found $R_b(p_c) = 1/2$ for square site percolation, where $p_c \simeq 0.593$. In general, $R(p_c)$ is a pseudo-universal quantity depending on boundary conditions and sample shape, while p_c for large samples is independent of these details but is different for site and bond percolation and depends on the size of the neighbourhood. Life was much nicer before. Fortunately, if a fixed point is determined by Eq. (12c) and the block size goes to infinity, then the fixed point still approaches p_c.

6 Diffusion and Percolation

6.1 Unbiased Diffusion

The most thoroughly investigated dynamics for percolation are presumably random walkers on percolation clusters [30, 31], particularly at $p = p_c$. This research was started by Brandt [32], but it was the later Nobel laureate, de Gennes [33] who gave it the catchy name 'ant in the labyrinth'. The anomalous diffusion [34–36] then made it famous a few years later and may also have biological applications [37].

We put an ant onto a randomly selected occupied site in the middle of a large lattice, where each site is permanently occupied (randomly with probability p) or empty $(1-p)$. At each time step, the ant selects randomly a neighbour direction and moves one lattice unit in this direction if and only if that neighbour site is occupied. We measure the mean distance

$$R(t) = \langle r(t)^2 \rangle^{1/2} \quad \text{or} \quad = \langle r(t) \rangle, \tag{14}$$

where, $\mathbf{r}$, is the vector from the starting point of the walk and the present position, and $r = |\mathbf{r}|$ its length. The average $\langle \dots \rangle$ goes over many such walking ants and disordered lattices. These ants are blind, which means they do not see from their old place whether or not the selected neighbour site is accessible (occupied) or prohibited (empty). (Also myopic ants were grown, which select randomly always an occupied neighbour, since they can see over a distance of one lattice unit.) The squared distance r^2 is measured by counting how often the ant moved to the left, to the right, to the top, to the bottom, to the front, or to the back on a simple cubic lattice.

The problem is simple enough to be given to students as a programming project. They then should find out by their simulations that for $p < p_c$ the above R remains finite, while for $p > p_c$ it goes to infinity as $\sqrt{t}$, for sufficiently long times t. But even for $p > p_c$ it may happen that for a single ant the distance remains finite: If the starting point happened to fall on a finite cluster, then $R(t \to \infty)$ measures the radius of that cluster. Right at $p = p_c$, instead of a constant or a square-root law, we have anomalous diffusion:

$$R \propto t^k, \quad k = (\nu - \beta/2)/(2\nu + \mu - \beta) \tag{15}$$

for sufficiently long times. This exponent k is close to but not exactly 1/3 in two and 1/5 in three dimensions. β and ν are the already mentioned percolation exponents, and μ is the exponent for the conductivity if percolation is interpreted as a mixture of electrically conducting and insulating sites. If we always start the ant walk on the largest cluster at $p = p_c$ instead of on any cluster, the formula for the exponent k simplifies to $\nu/(2\nu + \mu - \beta)$. The theory is explained in detail in the standard books and reviews [1–6, 30, 31]. We see here how the percolative-phase transition influences the random walk and introduces there a transition between diffusion for $p > p_c$ and finite motion for $p < p_c$, with the intermediate 'anomalous' diffusion (exponent below 1/2) at $p = p_c$. Figure 3 shows this transition on a large cubic lattice.

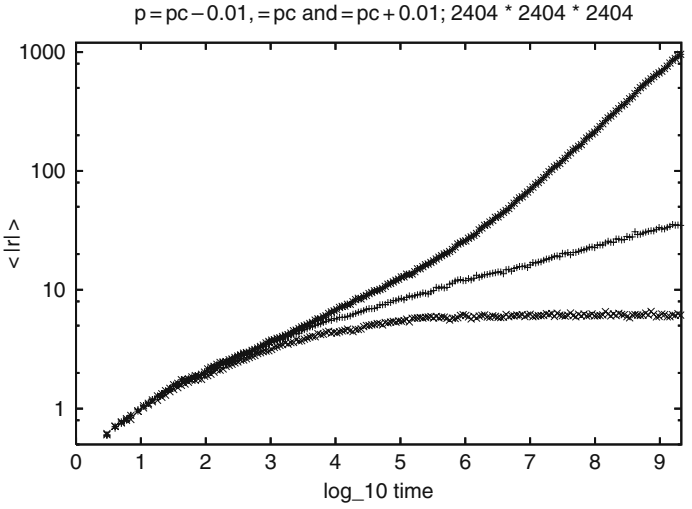

Fig. 3. Log-log plot for unbiased diffusion at (*middle curve*), above (*upper data*) and below (*lower data*) the percolation threshold p_c. We see the phase transition from limited growth at $p_c - 0.01$ to diffusion at $p_c + 0.01$, separated by anomalous diffusion at p_c. Average over 80 lattices with 10 walks each

6.2 Biased Diffusion

Another type of transition is seen in biased diffusion, also for $p > p_c$. Instead of selecting all neighbours randomly, we do that only with probability $1 - B$, while with probability B the ant tries to move in the positive x-direction. One may think of an electron moving through a disordered lattice in an external electric field. For a long time, experts discussed whether for $p > p_c$ one has a drift behaviour (distance proportional to time) for small B, and a slower motion for larger B, with a sharp transition at some p-dependent B_c. In the drift regime one may see log-periodic oscillations $\propto \sin(\text{const} \log t)$ in the approach towards the long-time limit, Fig. 4. Such oscillations have been predicted for stock markets [38], where they could have made us rich, but for diffusion they hamper the analysis. They come presumably from sections of occupied sites that allow motion in the biased direction and then end in prohibited sites [39].

Even in a region without such oscillations, Fig. 5 shows no clear transition from drift to no drift; this transition could only be seen by a more sophisticated analysis that showed for the p of Fig. 5 that the reciprocal velocity, plotted versus log(time), switches from concave to convex shape at $B_c \simeq 0.53$. Fortunately, only a few years after these simulations [40], the transition was shown to exist mathematically [28].

These simulations were made for $p > p_c$; at $p = p_c$ with a fractal largest cluster, drift seems impossible, and for a fixed B the distance varies logarithmically, with a stronger increase slightly above p_c and a limited distance slightly below p_c, Fig. 6.

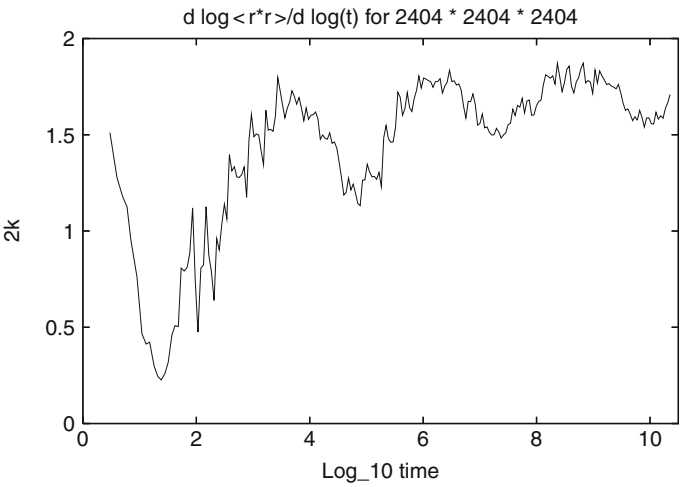

Fig. 4. Log-periodic oscillation in the effective exponent k for biased diffusion; $p = 0.725,\ B = 0.98$. The limit $k = 1$ corresponds to drift; 80 lattices with 10 walks each

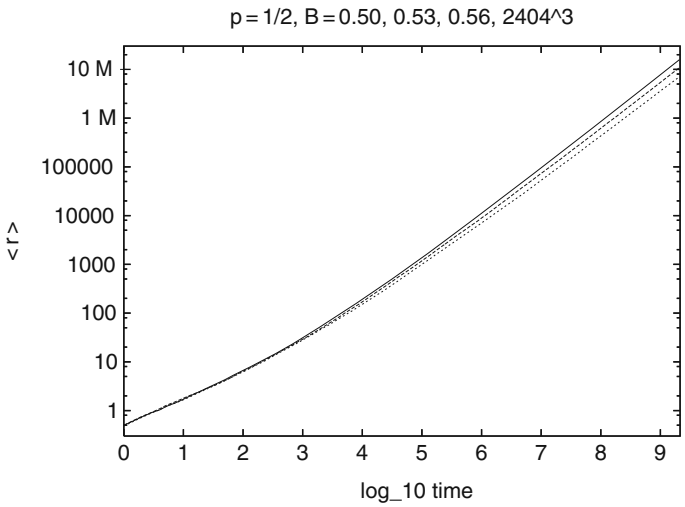

Fig. 5. Difficulties at transition from drift (small bias, *upper data*) to slower motion (large bias, *lower data*); 80 lattices with 10 walks each

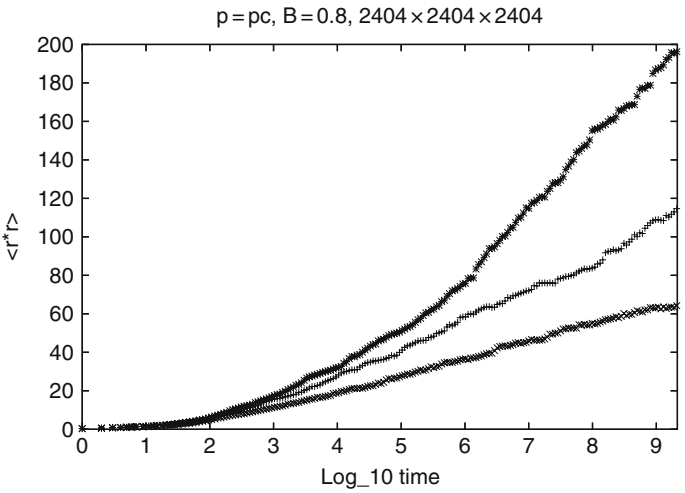

Fig. 6. Biased diffusion at $p = pc$ (*middle curve*) and $p = p_c \pm 0.01$ (*upper* and *lower data*) for bias $B = 0.8$; 80 lattices with 10 walks each

7 Summary

This review summarised the basic theory, particularly when it was not yet contained in the earlier books [1–6]. Applications were left to the Sahimi book [4]; even for the very first application [7] there is not yet a complete consensus that the three-dimensional percolation exponents apply to polymer gelation. More recent applications are social percolation [41] for marketing by word-of-mouth, and stock market fluctuations due to herding among traders [42].

Classical percolation theory, similar to Fortran programming or capitalism, was thought to be finished but seems to be alive and kicking [43]. Nevertheless, I think the future is more in its applications.

References

1. D. Stauffer, Phys. Rep. **54**, 1 (1979) 1, 2, 15, 18
2. J.W. Essam, Rep. Prog. Phys. **43**, 843 (1980) 1, 2, 15, 18
3. D. Stauffer and A. Aharony, *Introduction to Percolation Theory*, 2nd ed. (Taylor and Francis, London, 1994) 1, 2, 15, 18
4. M. Sahimi, *Applications of Percolation Theory* (Taylor and Francis, London, 1994) 1, 2, 15, 18
5. A. Bunde and S. Havlin, *Fractals and Disordered Systems* (Springer, Berlin, 1996) 1, 2, 15, 18
6. G. Grimmett, *Percolation*, 2nd ed. (Springer, Berlin, 1999) 1, 2, 15, 18
7. P.J. Flory, J. Am. Chem. Soc. **63**, 3083 (1941) 1, 18
8. P. Grassberger, Phys. Rev. E **67**, 036101 (2003) 2
9. S. Redner, J. Stat. Phys. **29**, 309 (1982) 3
10. D. Stauffer and N. Jan. In: *Annual Reviews of Computational Physics*, vol. VIII, Zanjan School (World Scientific, Singapore, 2000) 3, 10
11. M.E.J. Newman and R.M. Ziff, Phys. Rev. Lett. **85**, 4104 (2000) 5
12. D. Tiggemann, Int. J. Mod. Phys. C **17**, 1141 (2006), and PhD thesis, Cologne University (unpublished) 5, 11
13. P.W. Kasteleyn and C.M. Fortuin, J. Phys. Soc. Jpn. Suppl. S **26**, 11 (1969) 5
14. V.J. Deng, T.M. Garoni, and A.D. Sokal, Phys. Rev. Lett. **98**, 030602 (2007) 6
15. B. Nienhuis, J. Phys. A **15**, 199 (1982) 8
16. S. Smirnov and W. Werner, Math. Res. Lett. **8**, 729 (2001) 8
17. S.S. Manna and B.K. Chakrabarti, Phys. Rev. B **36**, 4078 (1986) 8
18. J.L. Chayes, L. Chayes, and R. Durrett, J. Stat. Phys. **45**, 933 (1986) 8
19. R.M. Ziff, Phys. Rev. Lett. **72**, 1942 (1994)
20. C.M. Newman and L.S. Schulman, J. Stat. Phys. **26**, 613 (1981) 11, 12
21. L. de Arcangelis, J. Phys. A **20**, 3057 (1987) 12
22. M. Aizenman, Nucl. Phys. (FS) B **485**, 551 (1997) 12
23. L.N. Shchur and T. Rostunov, JETP Lett. **76**, 475 (2002) 12
24. Y. Yakubo and M. Mitobe, J. Phys. Soc. Jpn. **76**, 034004 (2007) 12
25. D. Stauffer, J. Irreproducible Results, **44**, 57 (1999) 12

26. A.A. Jarai, Ann. Prob. **31**, 444 (2003) 12
27. P. de Gregorio, A. Lawlor, P. Bradley, and K.A. Dawson, Proc. Natl. Acad. Sci. (USA) **102**, 5669 (2005) 12
28. N. Berger, N. Ganten, and Y. Peres, Probab. Theory Relat. Fields, **126**, 221 (2003) 12, 16
29. R.M. Ziff, Phys. Rev. Lett. **69**, 2670 (1992) 14
30. S. Havlin and D. Ben-Avraham, Adv. Phys. **36**, 395 (1987) 14, 15
31. S. Havlin and D. Ben-Avraham, Adv. Phys. **51**, 187 (2002) 14, 15
32. W.W. Brandt, J. Chem. Phys. **63**, 5162 (1975) 14
33. P.G. de Gennes, La Recherche **7**, 916 (1976) 14
34. D. Ben-Avraham and S. Havlin, J. Phys. A **15**, L691 (1982) 14
35. Y. Gefen, A. Aharony, and S. Alexander, Phys. Rev. Lett. **50**, 77 (1983) 14
36. R. Kutner and K. Kehr, Phil. Mag. A **48**, 199 (1983) 14
37. E. Frey, and K. Kroy, Ann. Physik **14**, 20 (2005) 14
38. A. Johansen and D. Sornette, Int. J. Mod. Phys. C **10**, 563 (1999) 16
39. A. Kirsch, Int. J. Mod. Phys. C **10**, 753 (1999) 16
40. D. Dhar and D. Stauffer, Int. J. Mod. Phys. C **9**, 349 (1998) 16
41. G. Weisbuch and S. Solomon. In: *Handbook of Graphs and Networks*, ed by S. Bornholdt and H.G. Schuster, p. 113 (Wiley-VCH, Weinheim, 2002) 18
42. R. Cont and J.-P. Bouchaud, Macroecon. Dyn. **4**, 170 (2000) 18
43. J.J.H. Simmons, P. Kleban, and R.M. Ziff, J.Phys.A **40**, F 771 (2007) 18

Nonlinear Response, Semi-classical Percolation and Breakdown in the RRTN Model

A.K. Sen

TCMP Division, Saha Institute of Nuclear Physics, 1/AF, Bidhan Nagar,
Kolkata 700 064, India
asokk.sen@saha.ac.in

1 Introduction

In this chapter, we address the issue of nonlinearity of response functions of disordered, granular composite materials and more specifically, an extension of the classical percolation (a classical insulator to metal phase transition; concisely reviewed by the author of the first chapter) problem to a situation where the contributions of non-classical or non-diffusive processes cannot be neglected. In the paradigm of charge transport in electrical composites, this implies that the charge carriers travel not only inside metallic phases or grains but also outside of it; e.g., in the microscopic gap between two such grains using some externally assisted hopping over the barrier potential due to the gap. The assistance may be due to the phonons (ambient thermal bath), impressed electrical and/or chemical potential differences, etc. As such, these processes are known to bring forth nonlinearity in the response functions of the macroscopic system.

Further, if the imminent phase transition as a function of the external driving field gives rise to a hazardous failure of some sort (usually irreversible), we are faced with a generalised breakdown phenomenon. In the paradigm of electrical phenomena, if it is the failure of a dielectric/insulator to stop charges from flowing, one observes a spark discharge (e.g. lightning in nature) and the phenomenon is called a dielectric breakdown. If, on the other hand, the failure is due to the transformation of a good metal into an insulator due to a very high current, then it is called a fuse or simply electrical breakdown. Classical (or, Zener) breakdown has been concisely reviewed and a fully microscopic theory of quantum (or, Landau-Zener) breakdown have been presented in the later two chapters of this book. We discuss some aspects of reversible, semi-classical breakdown as well, later in this chapter.

1.1 General Scenario of Nonlinear Processes in Nature

Interest in nonlinear response phenomena in many diverse types of systems (magnetic, electrical, thermal, mechanical, fluid-dynamical, geological, biological etc.),

Sen, A.K.: *Nonlinear Response, Semi-classical Percolation and Breakdown in the RRTN Model*. Lect. Notes Phys. **762**, 21–82 (2009)
DOI 10.1007/978-3-540-85428-9_2

has had a history of extensive research, particularly during the last four to five decades, by physical scientists and engineers. Yet, many experiments on such systems remain intriguing and mostly unexplained. The generalized susceptibility, being a measure of the *response* of a system to an appropriate external perturbation or a *driving* field, is typically assumed to be *linear* under a vanishingly small external field (perturbation) that does not appreciably change the basic nature of the system or the modes characterising the response under study.

But in practice, for an appropriately large perturbation (a non-destructive one), the physical system may acquire newer modes of response and hence the response characteristic of the system could change with the external field. This is the basic reason for the response growing faster than linearly beyond some finite, system-dependent value of the field. If the number of available modes or channels of response becomes smaller on increasing the external perturbation (e.g. Type-I superconductors in a magnetic field), the response function decays nonlinearly as in the case of a fuse breakdown. In either case, the nonlinear macroscopic response of the system is typically *reversible* if the increment or decrement of the participating channels takes place reversibly. Percolative picture comes into play if this change in the number of channels, as a function of the relevant driving field, is due to the change in the coverage of the physical space of the system with more of one phase (e.g. conducting) than another (e.g. insulating). Most of our discussions in this review would focus on this mechanism of nonlinearity. One of the intriguing observations on many such systems has been that the appropriate generalized response is observable and nonlinear at relatively small values of the external field. Akin to soft mechanical systems with high compressibility, they evoke a sense of softness even when the response is non-mechanical. Thus, such *driven systems* have variously been called *soft-condensed* or *complex* systems.

Another interesting fact has been that many natural systems/phenomena do not show any measurable response until an appropriate driving force exceeds a measurable *threshold*. For example, a rigid body on a rough surface does not move until the driving force exceeds a finite frictional force. More intriguingly, there seems to exist an almost general law of nature that if there is a finite threshold for a non-zero response in a driven macroscopic system, the response characteristics is nonlinear [1–4] with a concommitant *dynamic criticality* at this threshold. In the example of mechanical systems near the verge of motion, it is well-known that the co-efficient of static friction is larger than the co-efficient of dynamic friction and is thus indicative of a clear nonlinearity.

In this context, it may be noted that disorder in many quantum systems such as charge-density-wave (CDW) systems or flux-vortex lattices of Type-II superconductors can give rise to 'pinning' or inhibition to transport upto a critical or threshold value of the applied field above which a current appears. As an example, we cite a case of highly disordered granular superconductors [5]. In a quantum two-dimensional electron gas system made of micron-sized Si-MOSFET's (Metal Oxide Semiconductor Field Effect Transistor) [6] at several hundred milli-Kelvins, one observes a metal insulator transition at a critical electron density, and a strongly nonlinear current-voltage response on both sides of the transition. Among other examples

of nonlinear electrical response with a low threshold voltage, we just mention one on electrical transport through single walled carbon nanotube (SWNT) intramolecular junctions [7] and another through DNA molecules [8].

There exists a wide variety of disordered composite materials with various generalized nonlinear response properties (besides the electrical ones). Many attempts have been devoted towards finding out if any unified description exists for these varieties of systems. An obvious case in point would be nonlinear thermal conductivity if the electrical conductivity is nonlinear (due to the Wiedemann-Franz law). There is an interesting example of super elastic percolation networks (viscosity of gels) giving rise to nonlinear elastic response. These networks consist of inclusions of a perfectly rigid material (with infinite elastic constants) inside an isotropic elastic host material, e.g., alumina or zirconia powders inside a soft gel [9, 10], and the elastic constants of such a composite tend to diverge near its percolation threshold.

In some problems of fluid flow, one may use an analogy between laminar flow in tubes and electrical currents, and use the language of electrical network for convenience. Then the volumetric flow rate q is identified to the current I and the pressure drop ΔP across a tube or a pore to the voltage difference V across a bond. Thus, e.g., the flow of polymers is modelled (see e.g. [11] and references therein) considering a power law $I = GV^{\alpha}$ for each bond (tube or pore), where G is a generalized susceptibility (mobility). For a Bingham fluid, there is a critical shear stress, τ_c, above which it has a finite viscosity and below which it is so enormously viscous that it almost ceases to flow. Considering the percolating network model of porous media one may employ an effective medium approximation (a mean field approximation) or some numerical method to calculate the rheological properties of a power-law fluid inside porous media. Next we give an example where surface (or, interface) tension is important. Foam is a non-Newtonian fluid that is used in the displacement and the enhancement of oil recovery from the porous rocks. However, to move the foams through the pores, external pressure has to exceed a certain critical value of capillary (surface tension mediated) forces.

In the studies of fracture type of failures also, it has been observed that no microcrack nucleation process takes place unless the applied shear strain exceeds a system size-dependent critical value. It may be noted here that in such rupture type of breakdown phenomena, the system crosses over from a higher elastic modulus (implying a very stable mechanical system) to a lower one where the system cannot hold itself anymore. The basic physics of such processes has been studied using the analogue of electrical fuse [12].

1.2 Electrical Systems: Experimental Facts

Nonlinear electrical transport characteristics have been revealed in an early (1964) work by van Beek and van Pul [13] on carbon-black loaded rubbers and in many different types of materials [4, 12]. In another series of early experiments on ZnO [14–16] varistors, very strong nonlinear response had been reported; see Mahan et al. [17] for a short review, further experiments and a proposed theory. The observed I-V characteristics in the ZnO varistors are often empirically described by a

power-law: $I = kV^{\alpha}$. The theory developed by Mahan et al. predicted the nonlinearity exponent (α) to be as high as 50 or even 100. The works regarding nonlinear electrical response, mentioned so far above and in our discussions below, are meant to be representative and not exhaustive. We point out here some interesting and common features of composite materials, specially those which are highly structured and give rise to well-known universal behaviours. As an example we may here refer to the carbon-black-polyvinylchloride (PVC) composites [18, 19]. Carbon blacks composed of small but complicated shaped particles usually exist in the form of 'high-structure' aggregates, whereas smaller and geometrically simpler particle aggregates are also possible in the form of 'intermediate-structure' and 'low-structure' blacks [18, 19]). Only the high-structure composite (with a conductivity exponent of $t = 2$) was found to be in the universality class of ordinary percolation problems. Similarly, we have the example of camphor sulphonic acid (CSA) treated polyaniline (PANI-CSA) with percolative characteristics [20]. In fact, the following features pertain to a wide variety of available disordered electrical composites.

- **Very low semi-classical (-quantum) percolation threshold:** Usually these composites exhibit an unusually low percolation threshold. For example, in an experiment on carbon-wax system [21], there is a percolation transition at $p_c = 0.0076$. Very low thresholds are also reported for other systems, e.g., $p_c = 0.002$ for carbon-black-polymer composites [22, 23] and $p_c = 0.003$ for sulphonated (doped) polyaniline networks [20]. In the Fig. 1, one may look at the transmission electron micrographs (TEM) of a percolating and a non-percolating sample of PANI-CSA to appreciate how ultra-tenuous (thus very difficult to prepare) such structures are.
- **Qualitatively identical nonlinear response, both below and above the classical threshold:** As an example, one may note the experiment on Ag particles

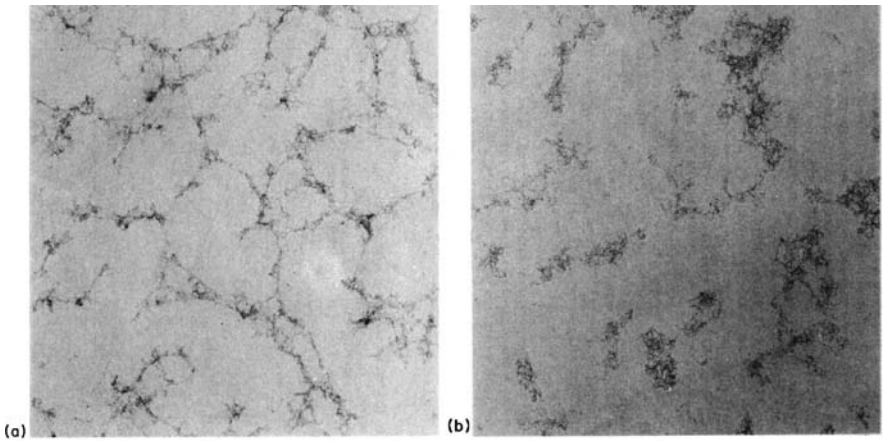

Fig. 1. TEM pictures of (**a**) a percolating, and (**b**) a non-percolating sample of PANI-CSA around sulphur-doping concentrations of $p = 0.003$, an ultra-low percolation threshold (adapted from [20])

in KCl matrix by Chen and Johnson [24], where similar nonlinear transport was reported both below and above $p_c = 0.213$ (thus, *tunnelling/hopping between disconnected conducting regions* seems to be responsible for the nonlinearity).

- **Power-law growth of conductance:** The nonlinearity in the I-V curves (above a constant ohmic part) and an associated *non-integer power-law* behaviour (for low field), $I \sim (V - V_g)^{\alpha}$, V_g being the system's threshold/breakdown voltage, have been observed in a variety of experiments (for conductance G, the nonlinearity exponent, $\delta = \alpha - 1$. Many theoretical works take δ to be an integer equal to 2 (voltage inversion symmetry), but for many complex systems the exponent is clearly a non-integer. For example, for arrays of normal metal islands connected by small tunnel junctions , $\alpha = 1.36 \pm 0.16$ in 1D and 1.80 ± 0.16 in 2D [25]. Near breakdown the carbon-wax system in 3D seems to give $\delta = 1.36$ [21], and ZnO varistors show a very strong nonlinearity $\alpha \geq 50$. Further, both the Chen-Johnson experiment [24] and the experiment on Si-MOSFET [6] near metal-insulator transition suggest that $\alpha = \alpha\ (p)$ is a function of dopant concentration, p or of the carrier electron density.
- **Saturation of conductance:** For disordered composite systems and for many other materials, the G-V curve is seen to saturate for an appropriately high enough voltage below the Joule-heating regime, i.e., it looks like a nonlinear sigmoidal type function interpolating two linear regimes (see [21, 24]). For microemulsions of water in oil under an external electric field, a similar curve is also presented by Aertsens and Naudts [26].
- **Crossover current for nonlinearity:** The current I_c (voltage V_c), at which the conductance G differs from the zero-voltage conductance G_0 (if non-zero) by some arbitrarily chosen small fraction ϵ ($\sim 1\%$), is called the crossover current (voltage). It is seen to scale as $I_c \propto G_0^x$, where x is called the crossover exponent for nonlinearity. For 3D carbon-wax composites, $x \cong 1.4$ [21, 27], and for discontinuous thick gold films, $x \cong 1.5$ [4]. One can easily check that this exponent is related to δ above by $\delta = 1/(x - 1)$.
- **Frequency-dependent conduction:** Experiments on the complex ac conductance $G(\omega)$ in various composite systems, dispersed metals etc., as well as many disordered/ amorphous systems [27–39], report a non-integer power-law behaviour of the modulus, $|G(\omega)| = [(Re\ G)^2 + (Im\ G)^2]^{1/2}$. At a fixed voltage amplitude and at a moderately low-ω, $[|G(\omega)| - G(0)] \propto \omega^{\alpha'}$, where the exponent $\alpha' \cong 0.7$; and for a vast majority of disordered solids, $0.6 \leq \alpha' \leq 1.0$ (the case of very low ω's is different, see Sect. 4).
- **Low-temperature hopping-dominated conduction:** Disordered insulators display a very interesting temperature-dependent conduction properties particularly in the low-temperature regime where the conduction is mainly due to phonon-assisted hopping of the electrons between randomly spaced localized states. One then needs to consider Mott's variable range hopping (VRH) conductance [40, 41], or some of its variations, namely $G(T) \sim \exp[-(T_0/T)^{\gamma}]$ at low temperatures, T, with an anomalous nature of the VRH-exponent being dependent upon the concentration p, i.e., $\gamma = \gamma(p)$ [20]. Further, the conductance of the

sample goes through a maximum as the temperature is increased towards a metallic behaviour. Details are discussed in the Sect. 5.

- **Early power-law dynamics far-from-equilibrium:** This ubiquitous phenomenon, as amply described by its name, occurs in many different classes of systems, not just electrical in nature and indicates the failure of the classical Boltzmann kinetics (or, Debye relaxation) with exponential relaxation. The subject is vast in its scope and we give a fascinating but brief description of this ill-understood arena in the Sect. 6.
- **Breakdown as a critical phenomenon:** One of the characteristics of a breakdown phenomenon is the breakdown field and its measure close to criticality in terms of an exponent. Another could be a characteristic time as the system approaches this singularity, reversibly or irreversibly. In the electrical analogue, reversible dielectric breakdown (and the related exponent) has been studied by laboratory simulation [42]. We address them in terms of a reversible, semi-classical dielectric breakdown in the RRTN in Sects. 7 and 8.

1.3 Some Passing Remarks

Disordered, composite or granular systems, the main objects of our study here, are composed of many microscopic elements or grains (much larger than atomic dimensions) having different physical properties. In the electrical case, it means that some of them may be conducting (a metal or superconductor), some insulating and yet some others semi conducting. For example, a Schottky potential barrier (v) arising at the interface of a semiconductor in intimate contact with a metal, gives rise to a tunneling current, $i \propto \exp(v/E_0)$, where the energy-scale E_0 is some function of temperature. In the case of a p-n junction heavily doped with Sb donors, the current seems to go from one linear region to another in steps, or the conductance smoothly connects two plateaus. Qualitatively similar curves[1] are observed for InP tunnel diode, Au doped Ge tunnel diode, a Zener diode etc. These processes thus provide extra paths or channels for current flow (thus, increasing the conductance), and hence one may observe breaks in the i-v curves joining two piece-wise linear (ohmic) regions. In the conventional circuit analyses to obtain the *dc* response, one treats these elements semi-classically in the sense that one does not solve for the wave function, but takes the quantum mechanical effects indirectly by including only the tunnelling currents through barriers.[2]

[1] For quite high voltages, other complicated phenomena, e.g., negative differential conductance) may arise, but we do not address them here.

[2] Even in this semi-classical sense, these tunnelling barriers are still fundamentally different from the Ohmic resistors, since they contribute to the resistance but not to heat dissipation. It may be noted that heat dissipation due to these barriers does take place, but it requires non-equilibrium processes which, in an idealised setup, take place in the electrochemical reservoirs attached to the perfect leads (and, hence outside of the sample).

2 The Origin of the RRTN Model and Its Percolative Aspects

In many of the works mentioned above, dilution plays an important role. These are situations where the percolation theory has been the underlying framework and many of the interesting properties may be related to the cluster statistics and geometric connectivity. The first thing to note from the facts listed above is the ultra-low percolation threshold even when the included conducting phases are isotropic. This along with the fact that many of these nonlinear systems carry current at a dilution (p) below the classical percolation threshold (p_c) indicates strongly that tunnelling through disconnected (dispersed) metallic regions must give some extra virtually connected percolating clusters. From the nonlinear I-V characteristic (e.g., see the experiment by Chen and Johnson [24]) it is observed that the response behaviour is reversible with respect to the applied field in the sense that the response curve (current or voltage) does almost trace back as the field is decreased. This fact also indicates that reversible tunnelling is responsible for such a behaviour. Also the temperature-dependent conductance with a maximum at some characteristic temperature (dependent on the amount of disorder present) and the Mott VRH type behaviour at very low temperatures give further credence to tunnelling assisted percolation. In the following section, we recall our proposal of a semi-classical (or, semi-quantum) model of percolation [43] which works on the borderline between a classical and a quantum picture. The semi-classical physics enters our discussion through the possibility of tunnelling of a charge carrier through a barrier (non-existent in classical electricity).

To mimic charge transport in composite systems or dispersed metals, we assume the grains (metallic or metal-like) to be much larger than atoms but much smaller than laboratory-scale macroscopic objects. These grains are randomly placed in the host material that are insulators. Further, we assume semi-classical *tunnelling* between such grains across some potential barriers. Clearly, these barriers would depend on the local geometry of the insulating and the metallic grains. Since in practice, the tunnelling conductance should fall off exponentially, the tunnelling should have some length scale designating an upper cut-off (for tunnelling to occur) in the separation between two metallic grains. Further, the separation between two grains or the potential barrier can vary continuously between zero and some upper cut-off.

Thus, our approach would be to solve for an appropriate electrical network based on a semi-classical (or semi-quantum) percolation model. For simplicity and to capture the basic physics, we construct a bond (lattice) percolation model for this problem, such that (i) tunnelling may take place only between two ohmic conductors (or, o-bonds) separated by a nearest neighbour gap and no further,[3] and that (ii) the potential barrier in such a nearest neighbour insulating gap between two metallic grains is constant. Thus, one may imagine a virtual bond sitting at each such gap that conducts current nonlinearly due to tunnelling phenomenon. We call these tunnelling conductors as tunnelling bonds (or t-bonds). Made of both random resistive and tunnelling

[3] It may be noted that if we include tunnelling between next nearest neighbours also, the effective percolation threshold would go down even further. For simplicity, in this work we restrict ourselves to nearest neighbour gaps only.

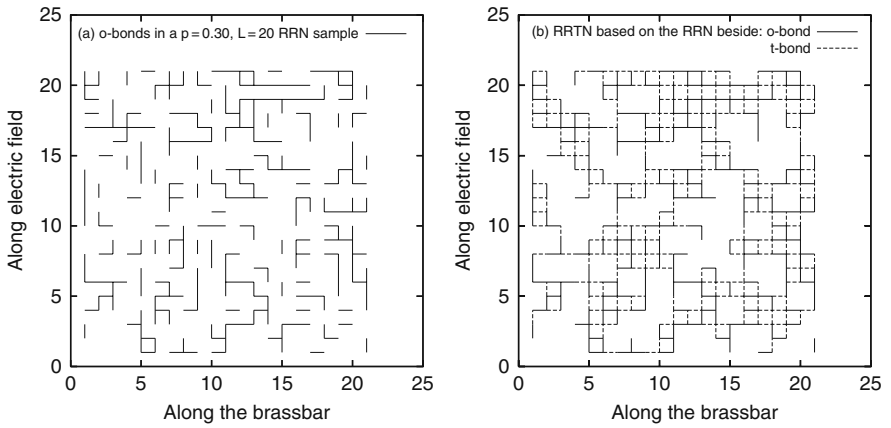

Fig. 2. (**a**) A typical Random Resistor Network (RRN) configuration embedded on a 2D 20×20 square lattice with a randomly placed ohmic bond (*solid line*) concentration of $p = 0.3$. The insulating bonds have been suppressed from view. (**b**) The realisation of a 2D Random Resistor cum Tunnelling-bond Network (RRTN) in its maximal state (one where all the possible nearest neighbour tunnelling bonds, shown in dashed lines, are active) built upon the same RRN sample at $p = 0.3$. It is clear that while the RRN does not percolate, the RRTN does. More important, once a RRN configuration is chosen, the maximal RRTN (where all the perfectly correlated t-bonds are active) is fully determined

elements,[4] this network was named by us as a Random Resistor cum Tunnelling-bond Network (RRTN). An illustration is given in the Fig. 2. Now tunnelling may take place through the tunnelling bonds in various ways, so that the functional form of the tunnelling current as a *nonlinear* function of the potential difference across them may look quite complicated. For simplicity, we address the aspects of nonlinearity in a macroscopic system which arises due to two piecewise linear regions of the i-v characteristic of the t-bonds. The piecewise linear response is actually a highly nonlinear response with a cusp-singularity at the threshold of the nonlinear regime.

The transport due to tunnelling which is the source of nonlinearity in the experimental systems [24, 27] we focus on, can be well approximated in this way and, thus, the nonlinearity of the macroscopic systems may be understood at a qualitative (and, sometimes even at a quantitative) level. In the RRTN model, we work with t-bonds,

[4] There exists a similar model in the literature called a dynamic random resistor network (DRRN) as applied by Gefen et al. [4] to explain the crossover exponent in the experiment on Au-films reported in the same reference. The difference between these two models lies in the fact that the tunnelling elements (or the *nonlinear* conductors) in the DRRN could be anywhere in the non-metallic domain of the system, whereas in the RRTN these elements exist only in the proximity gap between two metallic domains (one can imagine that the charge transfer by tunneling should be most effective only in such gaps). It may also be noted that traditionally the dielectric breakdown problem has been treated in the DRRN type models.

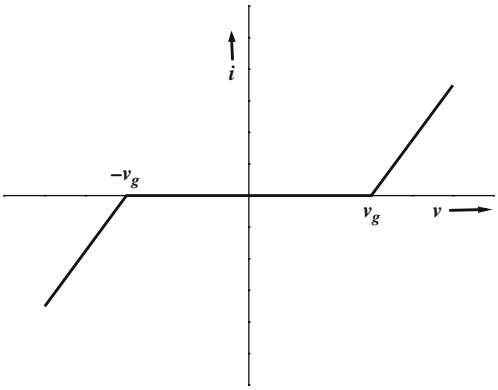

Fig. 3. The current-voltage (i-v) characteristic of a t-bond with a threshold (v_g)

which have zero conductance below a threshold voltage, v_g; see Fig. 3. The calculation of the new percolation threshold (p_{ct}) was carried out for the class of *maximal* RRTN's, i.e., for RRTN configurations where all the possible t-bonds are active [e.g., see Fig. 2(b)].

The high-field saturation of the macroscopic conductance (upper ohmic regime) does clearly take place if the microscopic 'nonlinear' elements become linear beyond some characteristic microscopic voltage. But even if the conductance of these microscopic elements tend to infinity (e.g. a Schottky barrier) at a high voltage or frequency, the macroscopic circuit still saturates to an upper linear (or, ohmic) region if the nonlinear elements do not form a continuous system-spanning path.[5]

We do again point out that the word *tunnelling* in the naming of the model (RRTN, [43], 1994) bears only the historical fact that it was initially proposed by us to study nonlinear electrical response where tunnelling of charges may be of essence. But, the very simple and basic sense, in which it is introduced, makes it amenable to many other non-electrical systems with quenched disorder. To reiterate, the word 'tunnelling' may be replaced by 'nonlinearity' in the form of microscopic threshold/s for response. Thus, while the name continues because of historical reasons, it remains applicable to very many different classes of systems.

2.1 Effective Medium Approximation (EMA) for d-Dimensional Maximal RRTN's

An effective medium approximation gives reasonable result for any p away from the threshold (here p_{ct}). The EMA has been used to calculate accurately the conductivity

[5] Actually, one may envisage some configurations in the RRTN where only the t-bonds may span the system even in 2D (in higher dimensions, such possibilities increase). But, for an infinite-size system, the probability of such configurations seem to be very small, particularly at low dilution of disorder. So such RRTN samples are atypical and not considered for dc properties. Their role in the ac properties is discussed in Sect. 4.

of general binary mixtures except in the vicinity of the critical regions. This approach is old and had been devised for the transport properties of inhomogeneous materials first by Bruggeman [44] and then independently by Landauer [45]. Its successful application to the percolation theory by Kirkpatrick [46] has drawn the attention of many others in this field. It has then been applied for a wide variety of inhomogeneous materials. The development has some similarity with the well known coherent potential approximation (CPA) for treating the electronic properties of the binary alloy problem.

The composite systems have seen a series of attempts in this direction while dealing with the nonlinearity in the response involved (see [47] and references therein). Here we follow the method as described in [46]. The method is as follows. Consider a random electrical network on a hyper cubic lattice of dimension $d > 1$. The basic idea is to replace a random network by a homogeneous effective network or an effective medium where each bond has the same *average* or *effective* conductivity G_e. The value of the unknown G_e is calculated in a self-consistent manner. To accomplish this, one bond embedded in the effective medium is assigned the conductivity distribution of the actual random network. The value of G_e is then determined with the condition that the voltage fluctuation across the special bond within the effective medium, when averaged over the proper conductivity distribution, is zero. The voltage (v) developed across such a special bond can be calculated [46] for a discrete lattice of z ($= 2d$ for a hyper cubic lattice) nearest neighbours as

$$v \propto (G_e - g)/[g + (d-1)G_e]. \tag{1}$$

The requirement is that the average of v be zero when the conductance for the special bond may take any of the ohmic, the tunnelling or the insulating bond value with appropriate probabilities for the actual network.

If the probabilities of a bond to be ohmic, tunnelling and purely insulating are p_o, p_t and p_i, respectively, then the probability density for a distribution of these three types of resistors, is

$$f(g) = p_o\delta(g - g_o) + p_t\delta(g - g_t) + p_i\delta(g - g_i), \tag{2}$$

where g_o, g_t and g_i are the conductances of ohmic, tunnelling and the insulating resistors, respectively. The EMA condition stated above, i.e., $< v >= 0$ now reads

$$\int dg\ f(g)(G_e - g)/[g + (d-1)G_e] = 0. \tag{3}$$

Putting Eq. (2) into the above Eq. (3), we get

$$\frac{p_o(G_e - g_o)}{[g_o + (d-1)G_e]} + \frac{p_t(G_e - g_t)}{[g_t + (d-1)G_e]} + \frac{p_i(G_e - g_i)}{[g_i + (d-1)G_e]} = 0. \tag{4}$$

The above equation reduces to the EMA equation (quadratic in G_e)

$$AG_e^2 + BG_e + C = 0, \tag{5}$$

where $A = (d-1)^2$, $B = (d-1)[(1-dp_o)g_o + (1-dp_t)g_t]$ and $C = -[(d-1) - dp_i]g_o g_t$, considering the conductance of the insulating bonds to be $g_i = 0$. The valid solution of Eq. (5) is

$$G_e = \frac{-B + (B^2 - 4AC)^{1/2}}{2A}. \tag{6}$$

The other solution with the $-$ sign in front of the square-root is an unphysical one as one can show that it makes G_e negative. Now one can obtain the linear conductance of the macroscopic model composite system in 2D and 3D, putting $d = 2$ and 3, respectively, given some specific values or functional forms for the conductances of the elementary components such as the ohmic and the tunnelling bonds.

For calculating the percolative properties, we assume that the conductance of a tunnelling bond, when it overcomes its voltage threshold, is the same as that of an ohmic bond. We believe that this equality ansatz does not change the phase transition characteristics. Thus, putting $g_t = g_o = 1$ and $g_i = 0$ in the Eq. (6), we obtain

$$G_e = \frac{d(p_o + p_t) - 1}{(d-1)}. \tag{7}$$

To calculate the percolation threshold, p_{ct}, the effective conductance (G_e) in the above equation is set to zero. As an example, in the limit when all the possible t-bonds are active (the maximal RRTN) in a 2D square lattice, we have

$$p_o = p, \tag{8}$$

$$p_t = (p^3 + 3p^2q + 3pq^2)^2 q, \tag{9}$$

$$p_i = 1 - p_o - p_t = [1 - (p^3 + 3p^2q + 3pq^2)^2]q, \tag{10}$$

where $q = 1 - p$. Thus, using $d = 2$ in the Eq. (7) along with the above expressions for p_o and p_t, one obtains the EMA equation for p_{ct} for the square lattice maximal RRTN:

$$2(p_o + p_t) = 1. \tag{11}$$

Solution of this equation gives $p = p_{ct} \cong 0.2497$. This may be compared with our numerical result [48] that gives $p_{ct} \cong 0.181$. The EMA is basically a mean field calculation that overestimates the percolation threshold value in lower dimensions. However, for pure/classical bond percolation in 2D, this gives the exact result $p_c = 1/2$. This is so because the square lattice in 2D is self-dual in the case of purely random bond percolation problem.

We may also find the value of p_{ct} for 3D (simple cubic lattice) maximal RRTN, where the probability of a tunnelling bond is

$$p_t = (p^5 + 5p^4q + 10p^3q^2 + 10p^2q^3 + 5pq^4)^2 q \tag{12}$$

Using $d = 3$ in Eq. (7) and the expression for p_t, an equation similar to Eq. (11) is obtained, which when solved gives $p_{ct} \cong 0.1252$.

2.2 Small Cell Renormalization Result for 2D Maximal RRTN's

Just for its effectiveness as a good starting point, we present here a small-cell renormalisation calculation for RRTN's in 2D. The idea here is to add the probabilities of all the percolating configurations of a few small cells and call it the probability of a single coarse-grained or renormalized bond [49]. For this purpose, we consider the recombination of two original cells with all the seven bonds. We use the criterion that any such combination gives rise to percolation (i.e. a renormalized o-bond exists) whenever the left and the right edges of the combination are in contact through two o- and/or t-bonds. The necessity of the two extra vertical bonds at the left and the right edges become clear by considering, e.g., Fig. 4 (*Left*). It is obvious that without the leftmost and rightmost vertical bonds, the two horizontal t-bonds cannot be placed in either of these two diagrams, and hence these configurations will not percolate just as in the uncorrelated bond percolation problem. But, these are a couple of typical diagrams that make this problem different from the RRN bond percolation, and, thus, their contributions should not be neglected.

Summing the probability (p') of all such contributions, one obtains [48]

$$p' = p^7 - 4p^6 + 4p^5 + 5p^4 - 13p^3 + 8p^2 = R(p). \tag{13}$$

The fixed point of the equation $p^* = R(p^*)$ is calculated numerically and we obtain, $p^* \cong 0.167$. This may be considered as the nonlinear percolation threshold p_{ct} for this finite-size system. We may also calculate the correlation length exponent (ν) defined by $\xi \sim (p - p_{ct})^{-\nu}$. Derivative of $R(p)$ at the fixed point is $\lambda = (dp'/dp)|_{p=p^*} \cong 1.68$. Then the exponent ν may be calculated as [49]

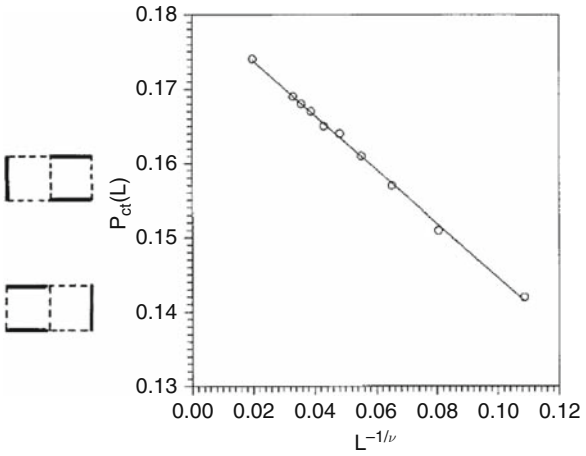

Fig. 4. *Left*: Example of two typical graphs contributing to the small cell renormalization calculation for the smallest cell with size $b = 2$ (solid bonds are o-bonds). *Right*: Plot of $p_{ct}(L)$ against $L^{-1/\nu}$ for maximal RRTN's in two dimensions. A choice of $\nu = 1.35$, gives the best fitted line with the result of $p_{ct} \cong 0.181$ [48]

$\nu = \ln b \,/\, \ln \lambda \cong 1.34$, which unexpectedly happens to be very close to that from a much more elaborate calculation removing the effects of finite-size of a system (described next). It is also close to $\nu = 4/3$, the exponent for uncorrelated bond percolation.

2.3 Real Space Renormalization and Finite-Size Scaling for 2D Maximal RRTN's

To investigate the effect of the finite size of the system on the percolation threshold and the related critical exponents, we did basically Monte Carlo renormalization, along the lines of [49] on 2D square lattices of various sizes ($L = 20 - 200$) and carried out a Finite-size Scaling Analysis (FSA) for the percolation threshold.

Suppose $R(p, L)$ is the probability of a square lattice of dilution p to percolate (note that $b \equiv L$ is implicit in this implicit in this statement). We evaluate the function $R(p, L)$ for a fixed L and a range of p (0.05–0.2) taking some 10,000 configurations each time. Using the set of data for a given L, numerical solution of the fixed point equation: $p^* = R(p^*, L)$ gives the $p_{ct}(L)$ as above. This is calculated for different discrete values of L in the range mentioned above, and then the asysmptotically infinite size value p_{ct} is obtained from the following finite size scaling form [50]:

$$p_{ct} = p_{ct}(L) + AL^{-1/\nu}. \tag{14}$$

The best-fitted straight line in the plot of $p_{ct}(L)$ versus $L^{-1/\nu}$, with the trial value of $\nu = 1.35$, is shown in the Fig. 4 (*Right*) and it gives the result of $p_{ct} = 0.181 \pm 0.001$.

To calculate the exponent, ν as well as p_{ct}, independently, we use the FSA somewhat differently [50]. The average concentration at which a cluster connects the top and the bottom of the lattice for the first time, i.e., barely percolates, is defined as

$$< p >= \int_{p=0}^{1} p(dR/dp)dp. \tag{15}$$

To determine $< p >$ from many Monte Carlo runs for the same L, one starts from a reasonable, p and checks whether the system percolates for a certain configuration. If it does, then one lowers the value of p by $p/2$, or else increases it by $p/2$. In the next step, one checks again whether the system percolates or not and increases or decreases accordingly, and so on. After performing a few such steps, one can get a sufficiently accurate value of the threshold for one's purpose. Instead, we fix the accuracy to a value of 10^{-5} to obtain the threshold for each configuration. This process is repeated for a large number of configurations (10,000 for each L) and then calculate $< p >$ as well as $< p^2 >$ for a number of system sizes from $L = 20$ to 300. The finite size scaling relationships for $< p >$ and its mean square deviation $\Delta^2 \equiv < p^2 > - < p >^2$ have the forms $p_{ct} - < p > \sim L^{-1/\nu}$ and $\Delta \sim L^{-1/\nu}$. We have plotted ln Δ versus ln L in the Fig. 5 (*Left*). From the slope of the best fitted line for this plot, we find that $\nu = 1.35 \pm 0.06$. Further, it is apparent from the above relations that $p_{ct} - < p > \sim \Delta$.

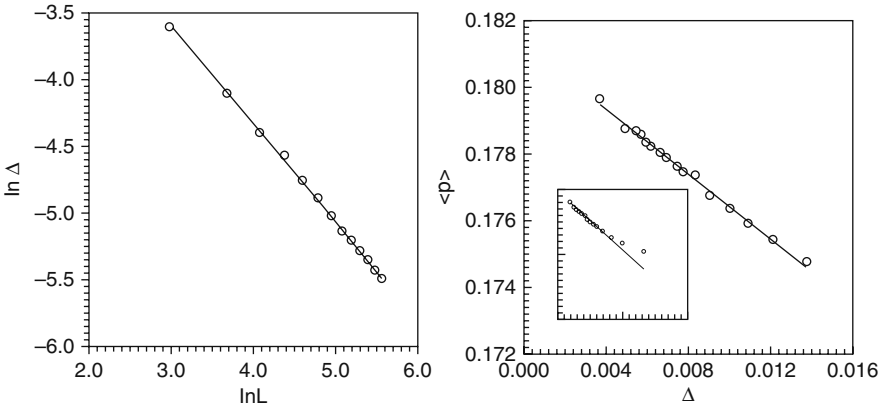

Fig. 5. *Left*: Plot of ln Δ against ln L where Δ is as described in the text. The best-fit line gives $\nu \cong 1.35$ in $2D$ [48]. *Right*: The best-fit line on the plot of $< p >$ against Δ shown above, for $L = 50$ to 300, gives the intercept, $p_{ct} \cong 0.181$ in $2D$ [48]. The inset shows a plot of all data from $L = 20$ to 300

We plot the graph of $< p >$ against Δ in Fig. 5 (*Right*). The intercept on the y-axis for the best fit line for $L = 50$ to 300, gives $p_{ct} \cong 0.181$, which agrees with the value obtained by using the previous method. The size, $S_\infty(L)$ of the spanning cluster at $p = p_{ct}(L)$ has a finite size behaviour $S_\infty \sim L^{d_f}$, where d_f is the fractal dimension of the incipient 'infinite' cluster at the threshold, p_{ct}. We calculate, $S_\infty(L)$ for different system sizes $L = 50$ to 300, taking 5000 configurations each, and find from the best fitted line of Fig. 6 (*Left*) that $d_f \cong 1.87$ [48] which is very close to $91/48$, the fractal dimension for $2D$ random (classical) percolation.

We did also calculate the conductivity exponent t defined through $\sigma(p) \sim (p - p_{ct}(L))^t$, for p at the threshold. For a system of size, L, at or above the threshold, the correlation length ξ is nothing but L, and hence $\sigma(p_{ct}) \sim L^{-t/\nu}$. From the best fitted line [see Fig. 6 (*Right*)] for a plot of ln σ against ln L (averages over 1000 configurations at each $p_{ct}(L)$ for L between 4 and 40) gives $t/\nu \cong 0.90$ [48] for the RRTN, with a rough estimate of error involved being less than 10%. So it is apparent that this exponent is also reasonably close to the value of 0.97 in [50] for uncorrelated random percolation in $2D$.

Thus, our computations above on a fully correlated bond percolation (identical to *maximal* RRTN's, if the statistically correlated bridge bonds appear at all the places where the nonlinear t-bonds could appear), clearly demonstrate that the new percolation threshold p_{ct} in 2D is well below the classical percolation threshold p_c (even in the mean field EMA). Further, we find that the values of two independent exponents near p_{ct} (namely, t and ν) as well as the fractal dimension d_f of the spanning cluster on a 2D square lattice based correlated percolation, are indeed very close to those of its uncorrelated version. Consequently, this fully correlated model for bond percolation (in maximal RRTN) seems to belong to the same universality class as that for uncorrelated bond percolation (RRN).

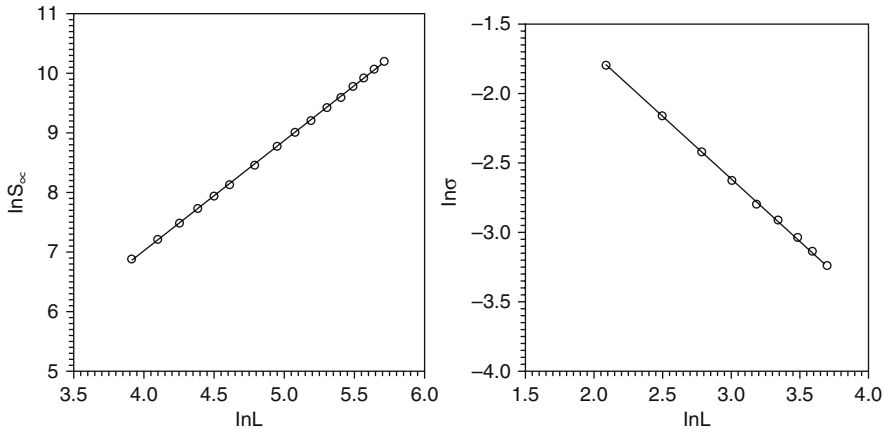

Fig. 6. *Left*: Plot of ln S_∞ against ln L. The slope of the best-fit line gives the fractal dimension $d_f \cong 1.87$ [48]. *Right*: Double-log plot of the conductivity (σ) against L. The slope of the best-fit line gives $t/\nu = 0.90$ in $2D$ RRTN [48]

3 Nonlinear Steady-State I-V Characteristics

For the work presented below, we make the simplifying assumption that all the tunnelling bonds (t-bonds) in our RRTN model have an identical voltage threshold (v_g) below which they are perfect insulators and above which they behave as the ohmic bonds. One could certainly introduce disorder by making v_g random as in [51]. In our case, disorder is already introduced through random positioning of the bonds, and we believe that our assumption should not affect the dilution-induced nonlinearity exponents. Indeed, as shown in the sequel, our model gives richer possibilities (dilution dependence) for the nonlinearity exponent and the VRH exponent (temperature dependence of conductance at very low T) in a composite system (see Sect. 5).

As the steady (*dc*) external field is increased beyond some macroscopic threshold, some of the t-bonds overcome their microscopic thresholds and may thus increase the overall conductance of the system, if the process leads to newer parallel connectivities for the whole macroscopic composite. Our numerical work to study these effects [57, 112] involves the solution of Kirchhoff's law of current conservation at the nodes of the RRTN with the linear and the nonlinear (assumed piecewise linear) resistors and the standard Gauss-Seidel relaxation. The current response was averaged over 50 configurations in all the cases mentioned here.[6]

We obtain current (I) against voltage, V and there from the differential conductance ($G = dI/dV$) for the whole network at a given volume fraction p of the ohmic bonds. Some numerical solutions for steady state, nonlinear I-V curves for a square lattice of size $L = 40$ are plotted in Fig. 7 for $p = 0.3$ to 0.9. For $p > p_c$, one

[6] It may be noted that the experimentalists prefer to work with a current bias and the theorists, with a voltage bias. But, whatever is the chosen bias, the response functions must behave identically for them.

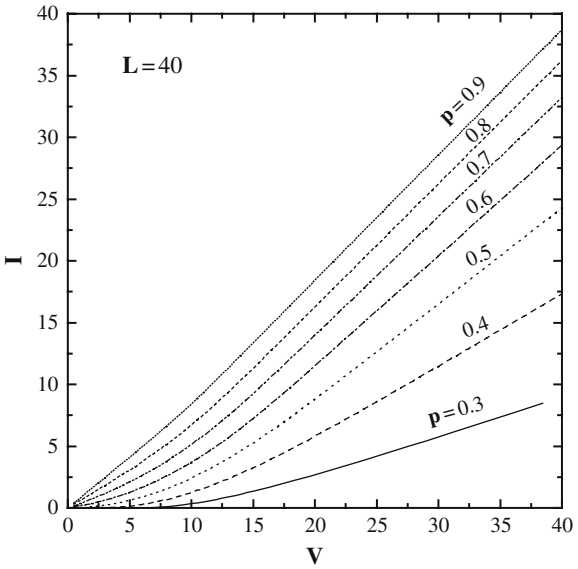

Fig. 7. A set of nonlinear I-V curves for $p = 0.3$ to 0.9 for the RRTN network of size 40×40. The current response is averaged over 50 configurations each

may note that the I-V curve is linear up to a certain voltage (V_g), beyond which the nonlinearity shows up. For $p < p_c$, there is no current (zero conductance) below a threshold voltage (V_g), beyond which the nonlinear conduction starts. Nonlinearity is always there in the I-V response for any value of p in the interval, $p_{ct} < p < 1$. However, for $p_{ct} < p < p_c$, there is no system-spanning path with the ohmic bonds (in an average sense) and the response (average current) is zero for small voltages. The response in this case starts out nonlinearly from a non-zero average threshold voltage. On the other hand, for $p > p_c$, the system always has a conducting path through the ohmic bonds (again on an average), and so up to a certain voltage (V_g) there is a constant non-zero conductance and the average response is linear. As V is increased beyond V_g, more and more t-bonds become active, thereby increasing the current carrying paths and hence the conductance.

We find that the entire nonlinear regime of a I-V curve cannot be fitted by a simple power-law that in general may be fitted by a polynomial function. Even after doing that, the *exponent of nonlinearity* from the fitting of the various I-V curves remained somewhat ambiguous since the fitting was not very robust. Thus, to have a better idea, we obtain the differential conductance ($G = dI/dV$) by taking the numerical derivative of the the I-V data. In these derived G-V curves, one can identify the *onset of nonlinearity* (hence, the threshold voltage V_g) and the onset of the *asymptotic upper linear* or ohmic conductance G_f, much more clearly than in the I-V curves.

The G-V curves corresponding to $p = 0.7$ and 0.3 in the Fig. 7 are shown in the twin plots of Fig. 8. As expected for the two different cases, in the Fig. 8 (*Left*)

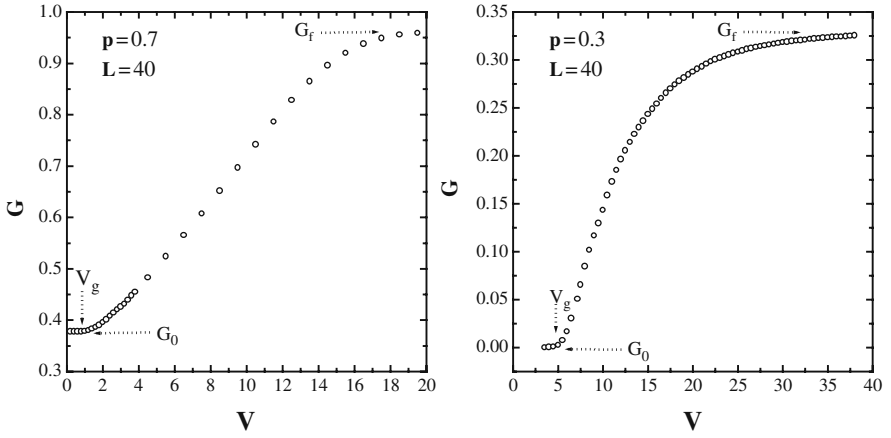

Fig. 8. *Left*: The G-V curve of a RRTN based on a percolating RRN (i.e. lower linear conductance $G_0 > 0$) at $p = 0.7$ of Fig. 7 ($p > p_c$). The low threshold voltage (V_g) and the asymptotic upper linear conductance (G_f) of the *maximal* RRTN are as indicated. *Right*: A similar response curve for another RRTN of Fig. 7, based on a non-percolating RRN at $p = 0.3$ (i.e. $p < p_c$ with a conductance $G_0 = 0$). The threshold voltage (V_g) is typically larger with a qualitatively similar sigmoidal region and a $G_f > G_0 = 0$ trivially

($p > p_c$) the lower linear conductance has a finite non-zero value ($G_0 \neq 0$), while in the Fig. 8 (*Right*) ($p < p_c$) the lower linear conductance is zero ($G_0 = 0$). The general nature of the G-V characteristics is that eventually all of them become flat, i.e., assume a configuration- and p-dependent constant conductance beyond some very large voltage V_s. The reason is that for a *finite-sized* system there is always a very large but *finite voltage* V_s at which the conductance of the whole system saturates to an upper maximum conductance G_f (upper linear regime) since all the possible t-bonds become activated and no more channel parallel to the backbone come into play for a further increment of V. Below we concentrate on the analysis of the nonlinear conductance behaviour of the model system in an effort to first find a general functional form to describe all these different G-V curves and then to find the exponent of nonlinearity at different volume fractions.

3.1 Analysis of the Behaviour of Conductance

Guided by the conductance behaviour of a complex system made out of many simple prototype circuits [43] and by the fact that the initial power-law law type growth of G beyond G_0 finally saturates to G_f, we try to fit the whole region in our numerical work by a function of the form:

$$G = G_0 \qquad (V < V_g) \tag{16}$$

$$= G_f - G_d[1 + \lambda \Delta V^{\mu}]^{-\gamma}, \qquad (V \geq V_g), \tag{17}$$

where $\Delta V = V - V_g$ is the driving voltage measured from the onset (V_g) of nonlinear response, and $G_d = G_f - G_0$. For concreteness, we discuss here the fitting of a

sample data set for $L = 40$, $p = 0.6$. For this sample, $G_0 \cong 0.154$, $G_f \cong 0.881$. The parameter for the best fit in this case as obtained by a simplex search procedure are $\lambda \cong 3.27 \times 10^{-4}$, $\mu \cong 1.408$, and $\gamma = 125$. Such large values of γ are obtained for all the cases studied and yet the approach to G_f was slower than in actual data. This obviously indicates that the approach to saturation is *not a power-law function* and probably an exponential function is involved.

For this we refer to the Fig. 9 (*Left*), where we have shown a G-V curve for $p = 0.8$ and $L = 40$ for which the conductance (G) seems to saturate (to the naked eye) at a voltage above $V = 20$ and one can see a practically flat regime in between $V = 20$ to 40. However, by zooming in on the y-axis in the inset of the same figure we have demonstrated that the actual saturation is yet to come and that the conductance (G) in this regime increases very slowly with V. The reason is that there are some tunnelling bonds (typically in the transverse direction to the electric field) that do not become active even with the application of a very large voltage implying that the conductance for the whole system is yet to reach the complete saturation. This pathology supports the fact that the final saturation occurs at an extremely large voltage, and that the approach to the saturation is indeed very slow.

We tried the following four plausible functions involving exponentials for the entire nonlinear regime replacing the above Eq. (17).

$$G = G_0 + G_d \exp(-\lambda/\Delta V) \tag{18}$$

$$= G_0 + G_d \tanh(\lambda \Delta V^{\alpha}) \tag{19}$$

$$= G_f - G_d \exp[1 - \exp(\lambda \Delta V^{\alpha})] \tag{20}$$

$$= G_0 + G_d [1 - \exp(-\lambda \Delta V^{\mu})]^{\gamma} \tag{21}$$

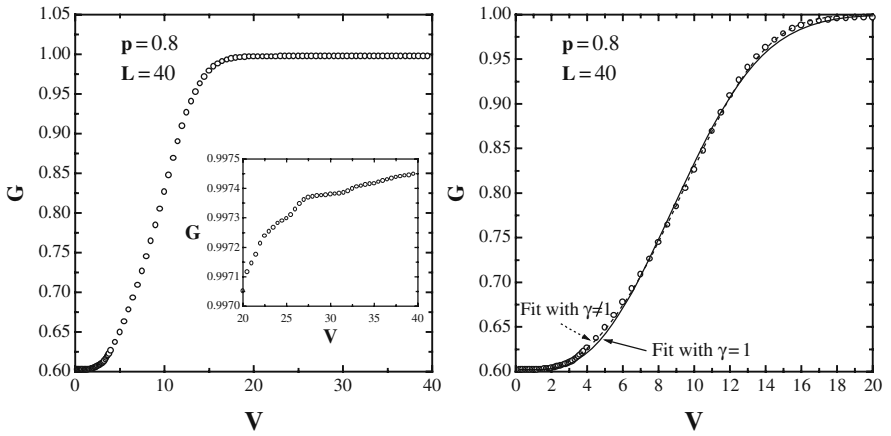

Fig. 9. *Left*: A typical G-V curve for $L = 40$ and $p = 0.8$ with an apparent onset of the saturation regime beyond $V \approx 20$. The inset shows that the G does not yet saturate in the true sense and instead ever increases in the regime $20 < V < 40$. *Right*: The demonstration of the fitting of a G-V curve by the proposed function, Eq. (22), shown for $L = 40$ and $p = 0.8$. The fitting is better with $\gamma \neq 1$ (shown in *dashed line*) for the entire data set than that with $\gamma = 1$ (shown in *full line*)

Out of all the optimally fitted functions as described above, the last Eq. (21) is the best in the sense that it gives the least mean square deviation (MSD) in fitting the G-V data. It may be noted that a special case of Eq. (21) with $\gamma = 1$ was the form of nonlinearity used by Chen and Johnson [24] in fitting their experimental conductance against voltage data for a composite system of Ag-KCl. But for all p and L's considered by us, $\gamma = 1$ was found inadequate for fitting the typical sigmoidal curves. For example, we have shown in the Fig. 9 (*Right*), the fitting with the function in Eq. (21) for $p = 0.8$, $L = 40$: the restricted case of $\gamma = 1$ shown by full line, and an unrestricted, optimally fit $\gamma \neq 1$ by dashed line. Clearly, the unrestricted case fits the data extremely well and gives an MSD which is much smaller than that of the restricted case as mentioned above.

3.2 The Nonlinearity Exponent

The conductance (G) for metal-insulator composite systems starts growing nonlinearly with the applied voltage V from a lower bound (G_0) and finally saturates to an upper linear value G_f (as indicated in the two cases of Fig. 8). As such, G_0 is the conductance when none of the t-bonds is active and this happens in the traditional percolation model without tunnelling (i.e., a RRN). Likewise, G_f is the conductance of a maximal RRTN where all the so-called tunnelling bonds (t-bonds) are actually taking part in the conduction. There are three distinct regimes that, in general, can be more precisely located from the G-V characteristics than from the I-V characteristics:

- (i) Upto some voltage V_g the initial conductance (G_0) of the system is either zero or a fixed finite value depending on whether the system has initially conducting path through the ohmic (or metallic) bonds or not (see Fig. 8).
- (ii) Beyond V_g, the nonlinearity starts showing up. The conductance, (G) is nonlinear in the regime $V_g < V < V_s$.
- (iii) Beyond the voltage V_s, G saturates to a voltage G_f (see Fig. 8).

The data obtained through our model system in 2D were fitted through the following general formula as discussed above:

$$G = G_0 + G_d[1 - \exp(-\lambda \Delta V^{\mu})]^{\gamma}, \tag{22}$$

Clearly, irrespective of the value of V_g, G_0 is the conductance in the limit $\Delta V \to 0$. Experimentally, G_f may be obtained by applying a large enough voltage such that the Joule heating is negligible or dispersed out with a thermostat. In our numerical works on finite sized systems, we find V_s to be a large but finite voltage (in arbitrary units). For example, for squares with $L = 40$, V_s is found to be typically of the order of 10^4–10^6.

In an experiment by Chen and Johnson [24] on Ag-KCl composite (silver particles in KCl matrix), very similar G-V curves were obtained and the non-ohmic effect was postulated to arise from a localized reversible dielectric breakdown between narrowly separated metal clusters in the metal-insulator composite. The intercluster or

interparticle spacing may have some distribution that is related to the fractal dimension d_f of the network at the threshold. Chen and Johnson [24] used the following conductance behaviour for their data:

$$G = G_0 + (G_f - G_0)[1 - \exp(-V/V_g)^{n(d_f)}], \tag{23}$$

which is a special form of the function (22) we propose. We find Eq. (23) to be inadequate for the representation of our experimental data (see above). The exponent $n(d_f)$ is in fact the same as δ and is, hence, related to the *nonlinearity exponent* α (see Sect. 1.2) by $\alpha = n(d_f) + 1$. It has been further shown in the above work that $n(d_f)$ increases as the silver volume fraction is decreased and it shows a sharp change at the threshold. We shall discuss in this section how our model captures this dilution-dependent nonlinearity exponent.

For a meaningful comparison of all the G-V data with different G_0, G_f, V_g etc., we look at the scaled conductance $\tilde{G} = (G - G_0)/G_d$ against the scaled voltage $\tilde{V} = (V - V_g)/V_g$. To see if the G-V data for various values of p both below and above p_c scale, we first looked within the range $0.48 \leq p \leq 0.52$ (i.e., very close to p_c), and found that all the data do reasonably collapse. In the Fig. 10 (*Left*), we show such a plot for a 20×20 system. This suggests the following general form for the functional behaviour;

$$\tilde{G} = f(\tilde{V}), \tag{24}$$

where $f(x)$ is a function such that $f(0) = 0$, and $f(\infty) = 1$ and is, otherwise, quite general as long as it represents the behaviour of $\tilde{G}$ very well. Clearly, the scaled function in Eq. (22) satisfy these properties very well.

Here we point out that the threshold voltage V_g is the only relevant variable that enters into the scaling function. The other voltage scale V_s which is the onset voltage for saturation, is seen to have no role in the above scaling Eq. (24). For small

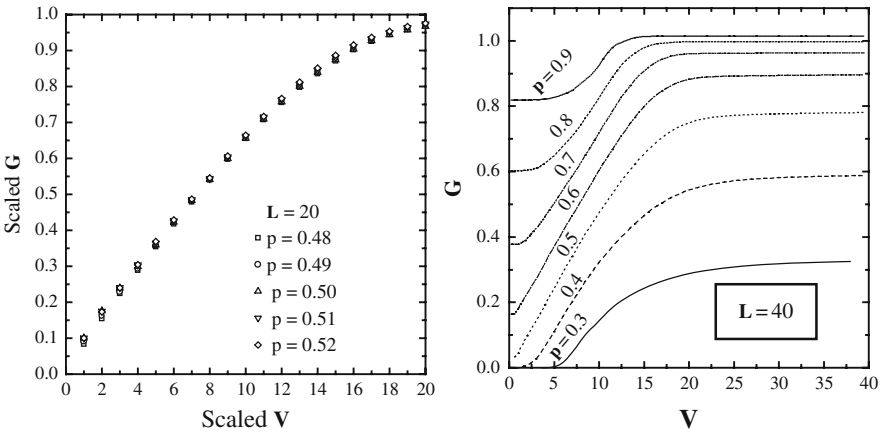

Fig. 10. *Left*: The plot of scaled conductance against scaled voltage for various p around p_c. *Right*: The family of G-V curves corresponding to the Fig. 7

$\Delta V = V - V_g$, i.e., near the onset of nonlinearity, the excess conductance $\Delta G = G - G_0$ varies with the voltage difference (ΔV) as a power-law as one may easily check by expanding Eq. (22) in the limit ($\Delta V \to 0$):

$$\Delta G \sim \Delta V^{\mu\gamma} = \Delta V^{\delta}. \tag{25}$$

Thus, the nonlinearity exponent, δ is related to the fitting parameters, μ and γ, by $\delta = \mu\gamma$. In our earlier work [43], with our preliminary observations we had reported the nonlinearity exponent δ to be close to 1 and to be independent of p near the geometrical percolation point $p_c = 0.5$. Indeed, in most of the experiments an average value of the above exponent is reported for the data for samples close to p_c.

Further careful analysis of the results at widely different volume fractions indicate that the nonlinearity exponent δ increases significantly, as we go sufficiently away from the percolation threshold (both below and above). This becomes apparent from the shape of the G-V curves for different volume fractions in a wide range of p (from 0.3 to 0.9) in the Fig. 10 (*Right*) corresponding to the I-V curves shown in Fig. 7. In the Fig. 11 (*Left*), we plot the scaled conductance ($\tilde{G}$) against scaled voltage ($\tilde{V}$) corresponding to all the G-V curves in the Fig. 10 (*Right*). The scaled data for all the curves now do not fall on top of each other indicating that all of them cannot be described by the same fitting parameters μ and γ, even though the form of the best-fitting function $f(x)$ remains the same. Hence, the nonlinearity exponent in the power-law regime ($\Delta V \to 0^+$) for these curves of different p are *not identical.* These are like corrections to scaling away from a critical point (p_c).

The fitting of the individual G-V curves for squares of sizes $L = 20$ and 40 and some data for $L = 60$ and 80 for different p in the range of $p = 0.2$ to 0.9 were done by using Eq. (22). The Fig. 11 (*Right*) demonstrates that the exponent δ

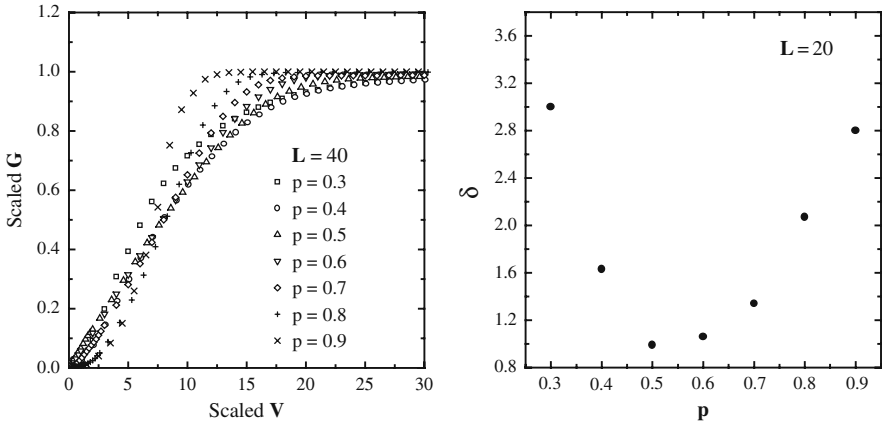

Fig. 11. *Left*: The scaled conductance against the scaled voltage for different p (both below and above p_c) corresponding to the curves in Fig. 10. The data do not collapse at all, indicating different exponents for different p's. *Right*: The variation of nonlinearity exponent (δ) for the G-V curves with p for a system of size 40×40

for $L = 40$ increases from a value close to 1 at $p = p_c$ to values close to 3 and above on either side ($0.3 \leq p \leq 0.9$). We found that the value of δ at p_c lies in the range 0.97 to 1.04 for system sizes $L = 10$ to 60. There is no systematic variation with L and this indicates the absence of any finite size dependence for the above exponent at p_c. Thus, within our numerical accuracy we find that $\delta(p_c) \cong 1.0$. It is, thus, clear from the Fig. 11 (*Right*) that $\delta(p_c)$ is the minimum of the p-dependent exponent $\delta(p)$. Note that the nonlinearity exponent α for the I-V curves would be just $\alpha = \delta + 1 \cong 2.0$ (in this case), where $I \sim (V - V_g)^{\alpha}$, and for p sufficiently far from p_c, α would also show the same concentration dependence. In comparison, we observe that in an experiment on 2D arrays of normal metal islands connected by small tunnel junctions, Rimberg et al. [25] found the nonlinearity exponent α to be 1.80 ± 0.16. It may also be noted that Roux and Herrmann [51] had also found from their numerical work that the nonlinearity exponent $\alpha = 2$ in their model 2D network with resistors having random thresholds (no positional disorder). Clearly, thus, our bond-diluted RRTN model is richer than the random threshold model at least as far as the nonlinearity exponent is concerned.

3.3 The Crossover Exponent

Now we discuss the *crossover exponent* that is an alternative way of accounting for the strength of nonlinearity. The crossover exponent (x) is defined from the power-law relationship $I_c \sim G_0^x$, where I_c is the crossover current at which the conductance of the system has increased from a non-zero initial value G_0 by a small but arbitrarily fixed fraction ϵ. The relation between the nonlinearity exponent δ and the crossover exponent x is simple to derive. The crossover voltage V_c is related to the initial non-zero conductance G_0 by $V_c \sim G_0^{x-1}$. But from Eq. (25) we know that the excess conductance $\Delta G(V) \cong \Delta V^{\delta}$ for small, ΔV. If one chooses $\Delta G \cong \epsilon G_0$ for an arbitrary but small ϵ and if one is close to the percolation threshold, one has $V_c \sim G_0^{1/\delta}$, which implies that $\delta = 1/(x-1)$. Clearly, x is defined only above p_c.

The value of x was calculated by Gefen et al. [4] from the experimental nonlinear response data of discontinuous thick gold films near and above the percolation threshold (in 3D). Their experimental measurement gives $x = 1.47 \pm 0.10$, and they argue through a model of dynamical random resistor network (DRRN) that the value of x should be 3/2 (in 3D). The argument is based on the assumption of a power law dependence of conductance (G), which interpolates between its initial value G_0 (at $V = V_g$) and the saturation value G_f ($V = V_s$). Note that the crossover exponent for the carbon-wax experiment in 3D is also close to this value. Gefen et al. [4] found that near the threshold $\delta = t/\nu$. Thus, one expects that close to p_c, $\delta = 1.3/1.33 \cong 0.97$ and the nonlinearity exponent for I-V characteristic is thus $\alpha = \delta + 1 \cong 1.97$ in 2D. It will be noted that close to p_c, the nonlinearity exponent for our model in 2D is very close to it. Further, since the exponent δ lies between about 3 and 1 for p between 0.3 and 0.9, the crossover exponent in our model can vary between 1.3 and 2 in the same dilution range in 2D.

3.4 Non-self-averaging Behaviour at Low Dilution or Field

We have seen that the nonlinearity exponent, α ($= \delta + 1$) varies significantly with the volume fraction (p) of the conducting component, the minimum value of the exponent being around 2.0 at $p = p_c$. Chen and Johnson, in their experiment on Ag-KCl [24], found the above nonlinearity exponent to vary with p. In particular, they found that for a sample very close to percolation threshold, the nonlinearity exponent is as large as 20. It was also noted in the experiments on ZnO varistors that the nonlinearity exponent (α) could have any value between 50 and 100 (such a high value of α tends to indicate an exponential relationship rather than a power-law)!

Intrigued by these results we ran some test for a square lattice with ($L = 20$ and 40) $p = 0.2$, very close to our p_{ct}. We obtained in our preliminary analysis by fitting G with voltage V that $\alpha > 20$ for $L = 20$ and $\alpha \gg 1$ (diverging for ever) for $L = 40$. This was very suspicious and by zooming into the fitting close to the threshold (V_g), we found the fitting to be extremely bad. The other functions listed before (including the double exponential) did not give any better fitting either. But this is the region that gives the initial power-law exponent. To get the fit better in this region, we fitted the logarithmic conductance (ln ΔG), keeping our fitting function the same Eq. (22) as before. Then we found the exponent δ to be of the order of 3 (the exponents in the Fig. 11 (*Right*) were calculated by taking care of this fitting problem). Thus, power-law description still seems to hold but there seems to be a different problem close to p_{ct}. Since the fitting was still not as good as at higher $p \geq 0.4$, we wanted to check if the averaging process itself is at flaw at very low-volume fractions. Hence, we look at the distribution of the current (I) for different realizations of the sample of size $L = 20$ and $p = 0.2$ for two different voltages.

In the Fig. 12 (*Left*), the histogram is shown for $V = 5$, and in the Fig. 12 (*Right*), the same is shown for $V = 10$. The distribution for $V = 10$ is reasonably well behaved, but the one for $V = 5$ has an isolated delta-function-like peak at zero conductance apart from two other broader peaks at higher conductances. We did also look at the relative value of the variance (relative to the mean squared) defined as

$$var = \frac{(< I^2 > - < I >^2)}{< I >^2} \tag{26}$$

If this value is less than 1, averaging is alright, but if it is much larger than 1, the self-averaging property of the distribution does not work. We have tested that var is about 3.3 for the set of data for $V = 5$ and it is about 0.3 for $V = 10$. Thus, the low p samples are non-self-averaging at low voltages but tend to be more self-averaging at higher voltages. This property was also reported for quantum systems by Lenstra and Smokers [52], and, thus, our semi-classical model of percolation indeed seems to capture the quantum, non-self-averaging behaviour at low p (and low field) as expected.

3.5 Further Comments on the RRTN and the DC Response

So far, we have been concerned with the semi-classical percolation threshold and the nonlinear dc response characteristics in composites and granular metallic systems

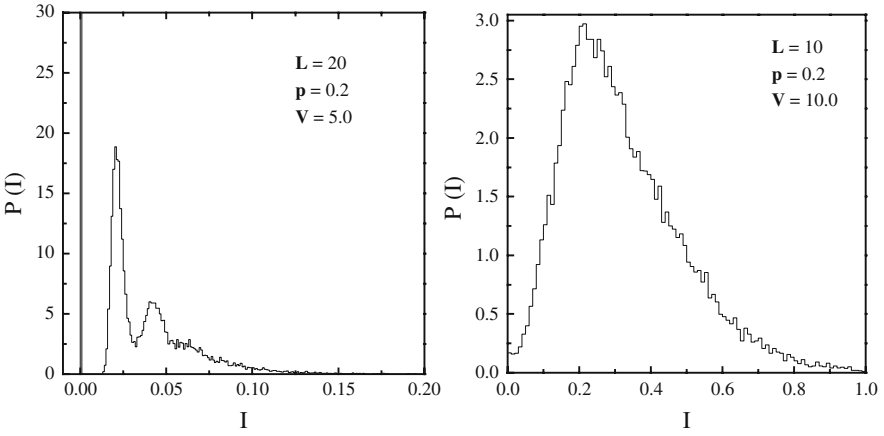

Fig. 12. *Left*: The distribution of current (I) in the 2D square network of size $L = 20$ for $p = 0.2$ and an applied voltage, $V = 5.0$. This distribution is non-self-averaging. 6×10^4 configurations were used for this purpose. *Right*: The distribution of current (I) in the 2D square network of size, $L = 20$ for $p = 0.2$ and an applied voltage, $V = 10.0$. This distribution is self-averaging. 2×10^4 configurations were used for this purpose

where transport due to charge 'tunnelling' (any other nonlinear effect with a threshold) plays an important role. The existence of a well-defined voltage threshold (V_g) close to which a power-law regime appears, indicates that this threshold (breakdown) voltage is a *critical point*. Similar threshold behaviour has been observed in pinned charge-density-wave (CDW) conductors, superconductors with pinned vortices (Type-II), etc. Indeed, it has been demonstrated long ago that wherever there exists some sort of threshold of force for motion to occur, the threshold actually corresponds to a *dynamic critical point* [1–4] for the driven dynamical system. Disorder in such systems is known to give rise to 'pinning' or inhibition to transport upto a critical value of the force. Clearly, in our percolation model, the threshold V_g acts as a dynamical critical point for the systems with volume fractions in the range $p_{ct} < p < p_c$. For such systems the field corresponding to the threshold voltage V_g may be called the *breakdown field* and is pretty well studied in the DRRN type models. We have focussed on the threshold as a dynamical critical point and calculated the relevant breakdown exponent in the RRTN model (in 2D) in the Sect. 7 [53].

As we pointed out above (see also [43, 57]), the mechanism of nonlinearity is essentially the same both below and above the system threshold. Below the system threshold, there is no system-spanning cluster. So the transport is identified as *intercluster* tunnelling or hopping across dangling bonds or gaps. Above the threshold there are both intercluster and intracluster tunnelling. But *intracluster* tunnelling mechanism certainly dominates. The nearest neighbour gaps are everywhere: both inside the smaller isolated clusters as well as in the system spanning cluster. So the tunnelling mechanism is operative both below and above p_c (in the interval $p_{ct} < p < 1$), giving rise to nonlinear regime in the response. As we would see

in the discussions of Sect. 6.1, these two types of cluster mechanisms have important roles in the early dynamics towards a steady state.

Next, we would like to emphasize that characterization of the nonlinear response by fitting of a derived G-V data (if available, on a wide range) is always more dependable than that of the I-V data. From our analysis of current-voltage (I-V) data we understand that one does not do justice by fitting only the I-V curve and finding out the nonlinearity exponent there from, since that fitting is not robust. One may easily be tempted to fit the nonlinear regime of a I-V curve in general through an n-th degree polynomial function. For example, a reasonable choice [47] for many experimental systems, would be to fit with a series expansion: $I = G_1V + G_2V^3$, assuming that the leading (dominant) nonlinear term is cubic (and, ignoring other higher order terms). On the contrary, a typical I-V curve, for the kind of systems we address, may in general be fitted by a simple power-law: $I \sim (V - V_g)^\alpha$, at least close to the threshold voltage, V_g. One may note that if the response approaches a diffusive (linear, or ohmic in the electrical case) or any non-power law behaviour in the large field limit, then the exponent for such power-law fittings change continuously as the applied voltage, V is increased from V_g. Arbitrary selection of sections of I-V data, particularly the upper cut-off voltage, for this purpose and the fitting of that could lead to unreasonable values of the pre-factors or the exponents. This type of fitting had been at the root of some confusing results found in the literature. Instead, our prescription of fitting of the G-V data for the (almost) entire nonlinear regime, is found to be very satisfactory because the approach to linearity is better detected in this derived data. From such a fitting of the G-V data using Eq. (22), one can obtain the desired power-law and find the exponent. The G-V curves for the type of composites we focus our attention on, may all be generically fitted by a function such as $G(V) = G_0 + G_d f(\Delta V)$, where $f(\Delta V)$ is a function that behaves as ΔV^δ for small ΔV, where $\Delta V = V - V_g$. $f(\Delta V) \to 0$ as $\Delta V \to 0$ and $f(\Delta V) \to 1$ as $\Delta V \to \infty$ (or an appropriately large value for a given finite system).

As the value of nonlinearity exponent is dependent on p, the crossover exponent (x) should also be dependent on p. The values of the crossover exponent, x, so far reported in the literature are for the experimental data for the samples close to but above the threshold. But we may conclude that this exponent should also show change with p if p is away from p_c. In fact, such an example may be mentioned here. The crossover exponent was found to be widely different in measurements[7] on a set of samples. The reason for this is not clear. But if the samples taken for measurements have widely different volume fractions (p) of conducting components, then the nonlinearity exponent and, thus, the crossover exponents for them could be very different.

Finally, it may be noted that if $\delta > 1$ or in other words $\mu\gamma > 1$ in the Eq. (22), the first derivative of G with respect to V, i.e., dG/dV would attain a maximum value at the inflexion point (at some voltage in the nonlinear regime). We fitted a set of G-V and the corresponding dG/dV-V data [57, 112], taken from the experimental observations on a carbon-wax composite system [21] to show the appearance of a

[7] U.N. Nandy and K.K. Bardhan, private communication.

peak in the dG/dV-V curve. To indicate how good or bad our fitting equation is, we fit the above data set for G-V characteristics by the Eq. (22). The fitted line is seen to match the experimental data very well with the above function. As a further test of the fitting, we took the parameters of the G-V-fit, and used them (the functional form) to obtain dG/dV as a function of V. The agreement with the experimental values for dG/dV should be considered rather good given that G and dG/dV are independent measurements and that higher the harmonic more error-prone is its value. Incidentally, the nonlinearity exponent δ for this 3D experimental data fitted by our method comes out to be 1.74 [54], where the crossover exponent measurement on the same sample would give a δ-value of about 2.

4 Periodic Driving and AC-Response in the RRTN/CRC Model

The results and the discussions of this section are basically taken from [55]. In the presence of an alternating field of frequency $f = \omega/(2\pi)$ across a random binary composite (modelled as a RRN), the elementary conductances g_1 and g_2 ($= 0$, for insulators) do in general become complex admittances (inverse of impedances), because of the presence of inductances and/or capacitances in some parts of the circuit. In this section, we are concerned with the modelling of the generic ac response of a whole variety of experimental systems within the RRTN framework In the traditional RC network models used to study the ac response of composites, the conducting bonds are pure (real) resistors and all the insulating bonds may behave as capacitors in the presence of an ac-field. A fairly complete review and references (from the percolative aspect) on the linear response may be found in [28]. Two more relatively recent reviews are found in [31, 35].

If one applies an sinusoidal electric field across our RRTN model, a t-bond between two nearby metallic bonds are expected to behave as a capacitor. Note that *perfect* capacitors at all the t-bonds correspond to a situation where all the t-bonds have zero dc conductance at low voltages, and hence the RRTN is in its *lower linear dc (or, ohmic) regime*. Similarly, *leaky* capacitors with a very low constant conductance for all the t-bonds, implies that the RRTN is in its *upper linear dc regime*. To obtain the nonlinear ac response in the truly nonlinear dc regime, one has to let the t-bonds be active or passive according to the voltage differences across them. In this work, we study the nonlinear ac response in either the upper or the lower linear dc regimes only. Further, we make a simplifying assumption that all the capacitances across insulators farther than the nearest neighbour distance are zero. Based on the RRTN model, this model for studying ac response may, thus, be called a *correlated* RC (or, CRC) model. We believe that the simplicity of our model is physically appealing and realistic enough. Since the capacitors placed in this way create relatively few configurations where the capacitors percolate by themselves, the $|G(\omega)|$ of almost all the samples is expected to connect nonlinearly between its own lower and upper ac saturation regimes of $\omega \to 0^+$ and $\omega \to \infty$, respectively. Even if one gets a configuration, where the capacitors make a connecting path, the high-frequency response may still be flat because of the inability of the system to respond within a cycle.

In this respect, we note that in most of the early experiments, the steady frequency required to approach the upper ac saturation regime were probably too high to be accessible. Further, we find at least one experiment on Li-doped NiO sample [56], where the upper saturation is clearly observed. We do also show a typical numerical result for the real part of the ac conductance for $p = 0.52$ in a 20×20 size sample with leaky capacitors, in the Fig. 13 (*Left*).

As a pedagogical example, one may calculate the complex $G(\omega)$ for two elementary circuits using the capacitive conductance $g_t = j\omega c$ where c is the microscopic capacitance and $j = \sqrt{-1}$. For the elementary conducting circuit (a) of Fig. 13:

$$G(\omega) = \frac{(r_1 + r_2 + \omega^2 r_1 r_2^2 c^2) + j\omega r_2^2 c}{(r_1 + r_2)^2 + \omega^2 r_1^2 r_2^2 c^2}. \tag{27}$$

On the other hand, for the case of the elementary insulating circuit (b) of Fig. 13:

$$G(\omega) = \frac{\omega[\omega(r_1 + r_2)c^2 + jc]}{1 + \omega^2 (r_1 + r_2)^2 c^2}. \tag{28}$$

It may be noted that the dc conductance $G(\omega = 0)$ of the circuit (a) is $1/(r_1 + r_2) > 0$ (thus, it is a conductor), whereas the dc conductance of the circuit (b) is zero (an insulator). The extremely low frequency ($\omega \to 0^+$) behaviours for both the circuits

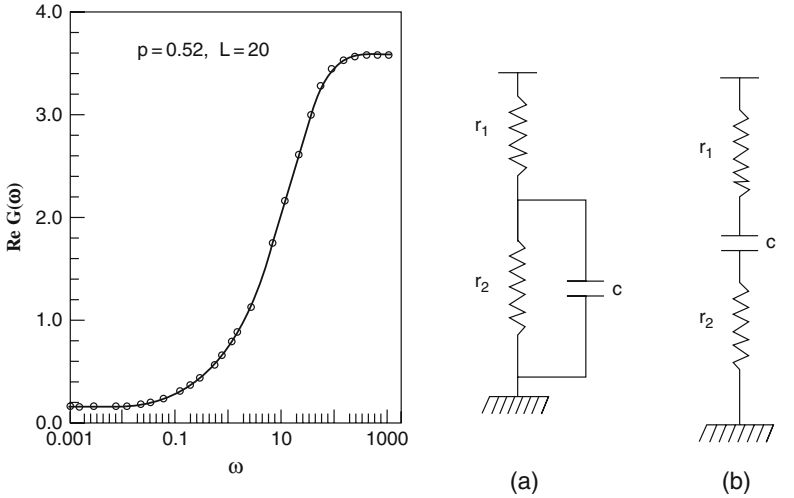

Fig. 13. *Left*: Real part of the complex $G(\omega)$ for a typical 20×20 sample of our correlated RC (CRC) network at $p = 0.52$, with leaky capacitors placed at the tunnel junctions. An equation akin to the Eq. (29) gives the best-fitting *solid line*. *Right*: Two prototypical elementary circuits each with two ohmic resistors and one capacitor. Note that the circuit (**a**) corresponds to a metal-like zero-frequency behaviour (i.e. $G_e(\omega = 0) > 0$), whereas the circuit (**b**) corresponds to an insulator (i.e. $G_e(\omega = 0) = 0$). Another elementary circuit with two t-bonds is possible, but the probability of such bonds connecting to give a percolative backbone of only t-bonds in a macroscopic ($L \to \infty$) RRTN seems negligible

is [Re $G(\omega) - G(\omega = 0)$] $\propto \omega^2$ and Im $G(\omega) \propto \omega$. Thus, Re $G(\omega)$ or Im $G(\omega)$ at very low, ω, cannot distinguish between the two types of circuits. But in the same limit, $[|G(\omega)| - G(\omega = 0)] \propto \omega^2$ for the elementary conducting circuit (a) of Fig. 13, while $|G(\omega)| \propto \omega$ for the elementary insulating circuit (b) of Fig. 13. As $\omega \to \infty$, the upper ac saturation value for the circuit (a) is $1/r_1$ and that for the circuit (b) it is $1/(r_1 + r_2)$, both of which are finite because one or more capacitors, c, do *not geometrically extend* from one electrode to the other.

Note that on adding together many such elementary circuits (i.e. on increasing L), the rational algebraic function type behaviour of Re $G(\omega)$ obtained from Eq. (27) and Eq. (28) changes over to a sigmoidal type function as shown in the Fig. 13 (*Left*) and looks qualitatively very similar to the nonlinear dc conductance as a function of V [43, 57]. Here, Im $G(\omega)$ is zero for both $\omega = 0$ and ∞, with a broad peak in-between. In case, a percolative backbone of only t-bonds (purely capacitive, finite-sized RRTN) exists, then the $G(\omega)$ of such a sample should have an extra term proportional to ω to accommodate the $\omega \to \infty$ behaviour. But, the probability of such a macroscopic ($L \to \infty$) RRTN sample seems to be very small, and patently atypical. Further, for very large ω ($> 1/\tau$, τ being an asymptotic relaxation time), the system fails to respond physically to the ac field. Hence, we do not consider such linear terms in the response. An identical fitting function as the one for $G(V)$ [57], fits (solid line) the numerical results very well, as shown in this figure for six decades [55]. In the same spirit, $|G(\omega)|$ in the ac case is written as:

$$|G(\omega)| = G(\omega = 0) + G_d(p)[1 - \exp(-\lambda\omega^{\mu})]^{\gamma}. \tag{29}$$

To obtain the power-law behaviour, one linearizes the exponential function in Eq. (29) for small ω (much below the upper ac saturation regime) and one gets: $[G|(\omega)| - G(0)] \propto \omega^{\alpha'}$, where $\alpha' = \mu\gamma$. Now, for considering the ac response in our CRC model, we have virtually a three-component mixture of the ohmic bonds (conductance $g_o = g$), the t-bonds (in general leaky with a complex $g_t = g_c + j\omega c$), and the insulating bonds ($g_i = 0$). A sinusoidal voltage $V = V_0 \exp(j\omega t)$, such that $V_0 < V_g$, is applied across the network. We set $V_0 = 1$, $c = 1$ and $g_o = 1$ for convenience, thereby setting the scales for the voltage, the frequency and the conductance, respectively. We focus on either the Re G and Im G, or the $|G|$ as a function of ω. We do also study the phase-angle of the complex G relative to the phase of the voltage source at any time t, and compare the numerical results with the EMA (for the CRC) and some basic experimental results.

4.1 The EMA Result for the CRC Model

For studying the ac conductance of the correlated RC model within the EMA, we assume for simplicity that the t-bonds behave as *perfect* capacitors with $g_t = j\omega c$. Since all the microscopic elements are now linear, the whole system is linear/ohmic at any dc, V. But, the ac effective conductance G_e, as given by the EMA Eq. (6), is now complex and so are the terms B and C appearing in the solution. So, we show again that only the $+$ sign in front of the square root in the Eq. (6) is the physical one. Separating the real and the imaginary parts of $G_e(\omega)$, one gets

$$\text{Re } G_e(\omega) = \frac{(2p_o - 1)}{2} + \frac{1}{2\sqrt{2}} \left[X + (X^2 + Y^2)^{1/2} \right]^{1/2}, \tag{30}$$

and,

$$\text{Im } G_e(\omega) = \frac{\omega(2p_t - 1)}{2} + \frac{1}{2\sqrt{2}} \left[-X + (X^2 + Y^2)^{1/2} \right]^{1/2}, \tag{31}$$

where $X = (2p_o - 1)^2 - \omega^2(2p_t - 1)^2$ and $Y = 2\omega[(2p_o - 1)(2p_t - 1) - 2(2p_i - 1)]$. It may be noted here that $p_t(p)$ has a single broad peak structure with a maximum value of about 0.3840 at a $p = 0.4800$. Thus, the quantity $\omega(2p_t - 1)$ is always negative. Further, X is also negative for $\omega > |(2p_o - 1)/(2p_t - 1)|$ and approaches $-\infty$ quadratically as $\omega \to \infty$. We will take only the absolute value of the square-rooted expression for two reasons; (i) Re $G_e(\omega)$ in Fig. 14 (*Left*) achieves the necessary upper ac saturation since the built-in square-root function in the computer uses exactly that, and (ii) this procedure keeps Im $G_e(\omega) > 0$ for all $\omega > 0$ (needed since Im $g_t > 0$).

Let us first check the $\omega \to \infty$ limit. The dissipative part of the complex conductance, Re $G_e(\omega)$, should be positive, finite and greater than $G_e(\omega = 0)$ in this limit. Further, the reactive part Im $G_e(\omega)$ of the CRC network must become zero (i.e., show no response) when the driving field oscillates much faster than the network's relaxation time (or, the *time-constant*). Now, in this limit,

$$\text{Re } G_e(\omega) = \frac{(2p_o - 1)}{2} + \frac{1}{2} \left| \frac{2(2p_i - 1)}{(2p_t - 1)} - (2p_o - 1) \right|, \tag{32}$$

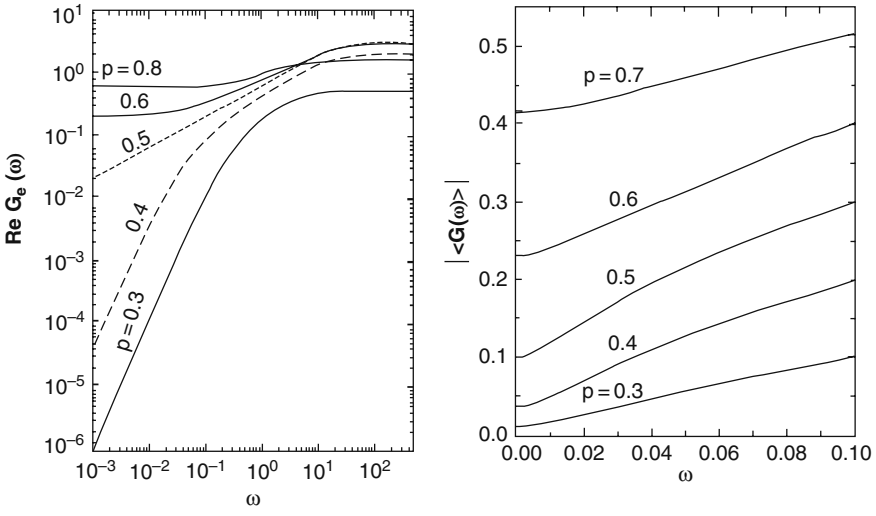

Fig. 14. *Left*: Real part of the effective conductance Re $G_e(\omega)$ against ω for a set of values of p; the EMA results on 2D square lattice for the CRC model. *Right*: The numerical results in 2D for the CRC model with leaky capacitors with a finite real conductance, $g_c = 0.001 g_o$: the average $| < G(\omega) > |$ against ω for a set of values of p. For each p and ω, the average over 20 different configurations were taken

and,

$$\text{Im}\, G_e(\omega) = \frac{\omega(2p_t - 1)}{2} + \frac{1}{2}\ |\omega(2p_t - 1)|\,, \tag{33}$$

and, thus, for all $p > p_{ct}$, $G_e(0) <$ Re $G_e(\omega = \infty) < \infty$. Also, clearly, Im $G_e(\omega)$ in this limit is zero. Thus, both the conditions hold in the $\omega \to \infty$ limit.

Next, we check the asymptotic expansion as $\omega \to 0^+$. In this limit, [Re $G_e(\omega) - G_e(0)] \sim \omega^2$ and Im $G_e(\omega) \sim \omega$. We find that this extremely low-ω behaviour of the complex G_e in the EMA is generic for all $p_{ct} < p < 1$ (*except* at $p = p_c$, see below), and $[|G_e(\omega)| - G_e(\omega = 0)] \sim \omega^2$. Hence, the EMA cannot recognise a non-percolating configuration from a percolating one (as anticipated) from their low-ω behaviour.

Now, in the special case when $p = p_c$ (= 1/2 for a square lattice), we find that in the limit $\omega \to 0^+$, both the Re $G_e(\omega)$ and Im $G_e(\omega)$ varies as $\omega^{\alpha'}$, where $\alpha' = 0.5$. Obviously, $|G_e(\omega)| \sim \omega^{0.5}$ in this limit. In passing, we would like to quote the extremely low-frequency EMA exponent in the case of 3D. By looking at the EMA expressions for $G_e(\omega)$, which are the analogues of Eq. (30) and Eq. (31) for a simple cubic lattice at its EMA percolation threshold ($p_c = 1/3$ in 3D), one finds again that $\alpha' = 0.5$ (in 3D).

We show in Fig. 14 (*Left*) a log-log plot of Re $G_e(\omega)$ against ω in 2D [Eq. (30)]. In conformity with the asymptotic expansions obtained above, analytically for very small ω's, the EMA results shown in this figure give $\alpha'(p) = 2.0$ for all $p_{ct} < p < 1.0$ except for the special case of $p = p_c$. We have $\alpha'(p_c) = 0.5$ both in the very low and in the moderately low-ω regimes much below the upper saturation of Re $G_e(\omega = \infty)$. Further, for each fixed $p \neq p_c$, there is a characteristic $\omega_0(p)$ around which $\alpha'(p)$ starts crossing over from 2.0 to the moderately low-ω exponent of about 0.5. The jump of $\alpha'(p)$ at an extremely low-ω from 2.0 to 0.5 is the hallmark of the inadequacy of EMA. One does also note that for a fixed $p \neq p_c$, this crossover region becomes smaller for smaller p's. Indeed, the crossover region finally tends to vanish as $p \to p_{ct}$ ($\simeq 0.18$ in 2D square lattice). Thus, we observe that there are no low to moderate, ω, crossovers for $p = p_c$ with $\alpha' = 0.5$ and, similarly, for $p = p_{ct}$ where $\alpha' = 2.0$.

We do also calculate the EMA results with leaky capacitors at each t-bond ($g_t = g_c + j\omega c$), i.e., in the upper linear dc regime. The only change here compared to the case of perfect capacitors above is that even at $p = p_c$, $|G_e(\omega)| = G_e(\omega = 0) + k\omega^2$ ($k = \text{constant}$) for very low-ω. Also for all $p > p_{ct}$, $G_e(\omega = 0) > 0$, as expected.

4.2 Numerical Results for the Conductance in the CRC Model

We now solve Kirchoff's laws (equation of continuity) in our 2D complex network at each node of our correlated RC model. We obtain the complex conductance of the macroscopic samples, their real and imaginary parts, the $modulus$ values and the phase-angle through iterative numerical solution using the Gauss-Seidel relaxation method. In the Fig. 14 (*Right*), we have plotted the modulus of the average complex conductance, $| < G(\omega) > |$ against ω for $0.3 \leq p \leq 0.7$ and for an external

sinusoidal voltage $V = \cos(\omega t)$. We let the t-bonds be *leaky* capacitors with a conductance $g_c = 0.001 g_o$ and averaged over the same 20 configurations for each ω. So, we are virtually in the upper dc saturation regime. For clarity, we have shown the graphs in the Fig. 14 (*Right*) from zero to a moderately low ω $(= 0.1)$ much below the upper ac saturation regime.

Now, it is quite well-known that since the actual experimental data become flat only at very large ω's, the computed power-law exponent α' (for small values of ω) may depend crucially on the arbitrarily chosen (may also be dictated by experimental data) upper cut-off in ω for fitting purposes. Consequently, the possibility of an unique function should be explored (as we do here) that fits all the way from the lower to the upper saturation range (if sufficient data are available), and then the power-law behaviour in the moderately low-ω range should be extracted from that function. We find that for $p \simeq p_c$, the respective graphs in the Fig. 13 (*Left*) and the Fig. 14 (*Right*) are fitted very well with the Eq. (29) such that $\alpha' = \mu\gamma \simeq 0.7$. Thus, in the moderately low-ω regime, α obtained experimentally in varieties of systems [27, 35–39, 58] and in an *Extended Pair Approximation* (EPA) theory [59] is close to what we obtain here (i.e. 0.7). We remark here that for a 2D system exactly at p_c , $\alpha' = 0.5$ both in the simple RC model (see e.g., [28]) and the EMA of our CRC model. Indeed, both of them fall short of the realistic value of α' not only at $p = p_c$, but also at any $p \neq p_c$.

As mentioned before, there are experiments, e.g., [38, 39, 56], where the upper saturation of the Re $G_e(\omega)$ may be clearly observed.We discuss here the one by Pollak et al. [56] on Li-doped NiO single crystals at sufficiently low temperatures. The frequency range used in that work is from about 10^7 Hz to about 10^{10} Hz. We did not try to fit them by our method since no data below 10^7 Hz was available. In any case, we note that the upper saturation is also consistent with the fact that the measured relaxation time for this sample is about 2.2×10^{-10} s. In passing, we do also note that in this system the concentration of the Li-dopant is extremely low as well: from about 13×10^{-6} to about 136×10^{-6}, and that the pristine NiO is an insulator. We observe that the upper saturation value of the conductivity for this experiment [56] is about 0.1 S/m, and that the data for all the three concentrations used for Li, fall closely enough to their fitting function in the high-frequency range, but not so well in the low-/moderate-frequency range. The power-law exponent α' (around $10^7 Hz$) seems to be close to 2.0.

Next, we would like to emphasize that the apparently excellent fitting shown in the Fig. 13 (*Left*) with Eq. (29) may be misleading to the eye in the very low-ω regime. A careful analysis of the data in a more revealing log-log plot show that for very low ω, the fittings may be actually quite bad. We observed that for the two elementary circuits [Fig. 13 (a) and (b)] for very low ω, $|G(\omega)| \sim \omega^2$ or ω depending upon whether the circuit is conducting or insulating. Similarly, we anticipate that for extremely low ω and in the lower dc regime, the CRC network would also show such simple behaviours (instead of a more complicated percolative behaviour in the moderately low-ω regime as described above). Further this simple behaviour is expected to persist (as seen in our EMA results) generically for each p up to some scaled crossover frequency, ω_0 depending on p, g_o, g_c and c. For $\omega > \omega_0$, we expect

macroscopic percolative effects to gain control and instead of Eq. (29), $|G(\omega)|$ should follow a more general equation closer in form to that used for the dc-conductance, Eq. (22),

$$|G(\omega)| = G(\omega_0) + G_d(p)[1 - \exp(-\lambda[\omega - \omega_0]^{\mu})]^{\gamma}. \tag{34}$$

A typical fit by the above equation is shown in Fig. 15 for a system size, $L = 20$ and $p = 0.3$ for about seven decades in ω using leaky capacitors. In the inset of Fig. 15, we show the log-log plot for the $modulus$ value of G and observe a very convincing quadratic behaviour with $| < G(\omega) > | = 0.01219 + 55\omega^2$ for $\omega_0 \leq 0.01$. This observation is totally matching with our analyses for the elementary circuit (a) of Fig. 13. For $\omega > \omega_0$, we get a very good fit for the intermediate frequency range with the general Eq. (34) where $\alpha' = \mu\gamma \simeq 3.0$ (which is much larger than 0.7). Similarly large second power-law exponent, has also been observed in some experiments, e.g., in a very recent one on impedance spectroscopy in multiferroic thin films [109].

Next in the Fig. 16, we show another fit for a single configuration (at $p = 0.45 < p_c$) with perfect capacitors at the t-bonds ($g_c = 0$, non-percolating) of the CRC network with $L = 20$. In this case, one can easily observe that in the very low-ω range up to a crossover frequency $\omega_0 \simeq 0.01$, $|G(\omega)| \simeq 6\omega$. This behaviour is akin to that of the elementary insulating circuit (b) of Fig. 13. Further, beyond ω_0, we do again have an excellent fit with the Eq. (34) with $\alpha' = \mu\gamma \simeq 0.5$. So we have

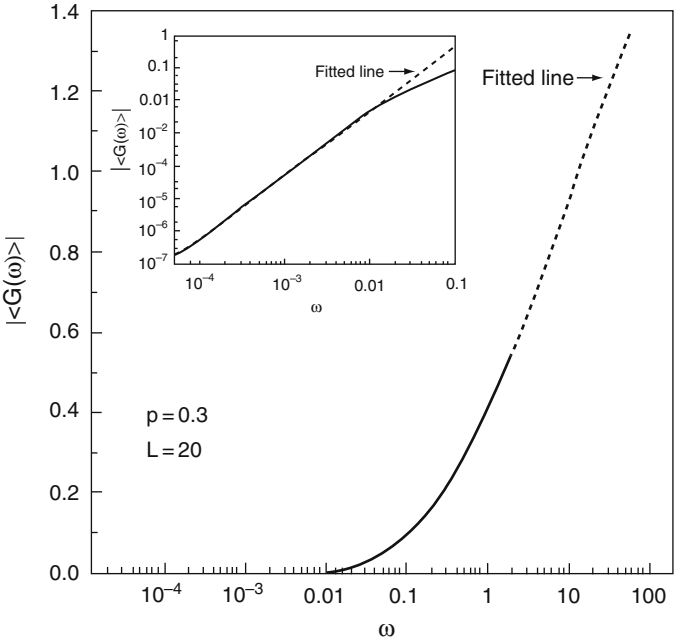

Fig. 15. The $| < G(\omega) > |$ for $p = 0.3$ and a square lattice of size $L = 20$. Just as in right Fig. 14, each t-bond represented a leaky capacitor and an average over 20 configurations were taken. The inset shows an ω^2-dependence upto a crossover frequency of $\omega_0 \simeq 0.01$. Above ω_0, the Eq. (34) gives a very good fit as shown

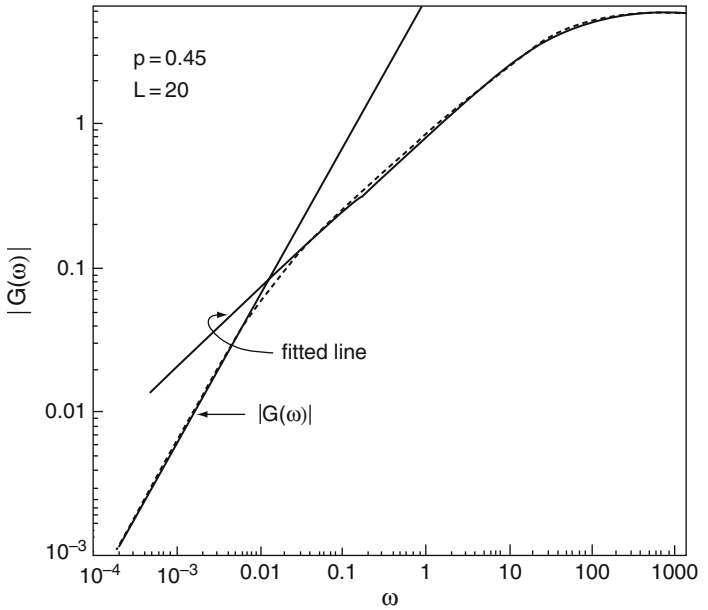

Fig. 16. Another example of $|G(\omega)|$ against ω for $p = 0.45$ and for a typical configuration on a square lattice of size $L = 20$. The very low-ω part shows a purely linear behaviour. But for $\omega > \omega_0 \simeq 0.01$, Eq. (34) gives the optimum fit

two things to note here for non-percolating configurations (with perfect capacitors, i.e. in the lower dc regime): (i) the very low-ω behaviour is linear in ω, and (ii) the intermediate frequency behaviour seems to give a lower value for the exponent compared to that for percolating configurations (e.g., as in the upper dc regimes of the Fig. 13 (*Left*) and the Fig. 15 where $\delta = 0.7$ near p_c). Note that for the non-percolating configurations (only at p_c) in the lower linear dc regime, $\alpha' = 0.5$ in the case of EMA as well.

For many practical situations, this intermediate frequency range (away from both the lower and the upper ac saturation regimes) is of prime interest. For t-bonds with leaky capacitors at any $p > p_{ct}$ (i.e., in the upper dc regime), we find that α' has a minimum value of about 0.7 near p_c, and increases on both sides of it with a value of about 3.0 at $p = 0.3$ (as shown above) and of about 1.35 (not explicitly shown here) at $p = 0.7$. Clearly, this result has a qualitative similarity with the dc nonlinearity exponent $\delta(p)$ as a function of p as shown in the Fig. 11 (*Right*) [57]. Finally, we reiterate that a couple of power-law behaviours in the low and intermediate range of ω's (as observed in the RRTN model and supported, for example, by a recent experimental study [109]) seem to be generic.

4.3 Phase Angle of the AC Response Versus the Driving Frequency

We do now describe the behaviour of phase-angle of the complex conductance, $G_e(\omega)$ with respect to the frequency (ω). The phase-angle (ϕ) is defined through

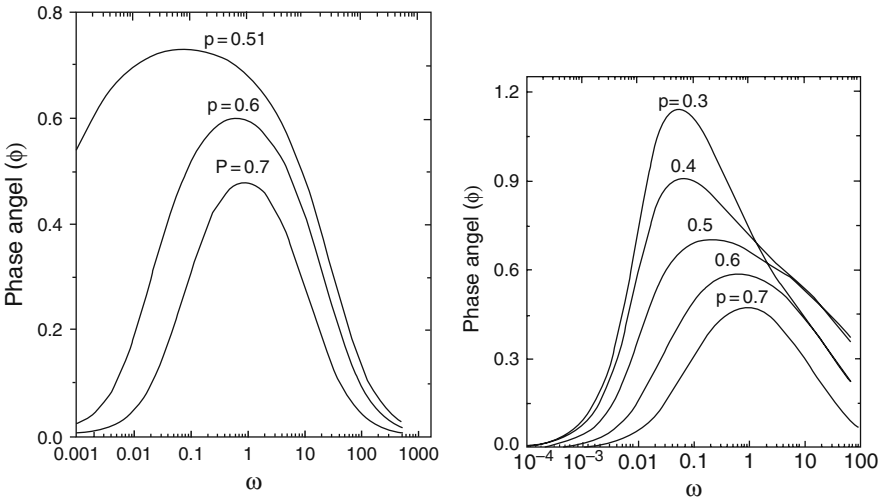

Fig. 17. *Left*: The EMA results for the phase-angle (ϕ) in the CRC model against the frequency ω for different values of p (2D square lattices). *Right*: Phase-angle (ϕ) as a function of ω from the numerical solutions of our CRC model on square lattices

$$\tan\phi = \frac{\text{Im } G_e(\omega)}{\text{Re } G_e(\omega)}. \tag{35}$$

In the Fig. 17 (*Left*), we plot the phase-angle (ϕ) of the complex conductance against frequency (ω) for the EMA. As expected, this angle is zero [just like the Im $G_e(\omega)$] both at very small and at very large ω's. Further the phase has a peak value $\phi = \phi_m$ which increases as p is decreased and the ω at which the peak occurs is p-dependent. We find from this figure that the positions of the peaks tend towards zero and that ϕ_m becomes progressively larger as p approaches p_c from higher values. It may be noted that we cannot calculate the phase angle, ϕ for $p < p_c$ in the EMA with confidence because the quantity $G_e(\omega = 0) = 2p_o - 1$ takes on *unphysical negative* values. Hence, we have not shown any curve for $p < p_c$ in the Fig. 17 (*Left*).

The variation of the phase-angle (ϕ) with frequency (ω) obtained by numerical (Kirchoff's laws) solution of our CRC network has been shown in the Fig. 17 (*Right*) for $0.3 \leq p \leq 0.7$. One can easily observe from this figure that in the CRC model, for configurations with p around p_c for a 2D square lattice, the peak value of the phase, $\phi_m \cong 0.7$ (radian). This is close to the *universal phase-angle value* of $\pi/4$ radian obtained in the simple RC model in 2D at p_c as predicted by Clerc et al. [28]. As noted before, the EMA calculations (i.e. mean-field approach) of the phase $\phi(\omega)$ for our CRC model also obtains $\phi_m \cong 0.7$ rad when $p \cong p_c$. The main problem with the EMA, in this case, is that the peak occurs at an ω of about 0.1 rad/s (instead of at around 0.2 rad/s as for the CRC in the Fig. 17 (*Right*)) and that it is too broad. Further, as shown in this figure, ϕ_m increases as p decreases: from a value of $\phi_m \simeq 1.1$ rad

for $p = 0.3$ to a value of $\phi_m \simeq 0.4$ rad for $p = 0.7$. Everything considered, the results and the arguments above indicate that exact solutions of the CRC network is much more effective than its mean-field theory (EMA) or the uncorrelated RC network, for modelling the ac response of real systems.

5 VRH and Low Temperature Conduction in the RRTN

In this section, we discuss some results of our studies on temperature dependent conduction based mostly on our short report in [60]. The low-temperature *dc* electrical conductance $G(T)$ is being studied for many decades now, in the regime where the thermal energy k_BT (k_B = Boltzmann constant) is of the order of or smaller than the disorder or the Coulomb interaction energy between the charge carrying fermions. During 1960s, Mott [40, 41] had put forward an analytical expression for the *phonon-assisted hopping* conduction of *spinless fermions*, taking *only the lattice disorder* effect into account and his *Variable Range Hopping* (VRH) formula is written as,

$$G(T) = G_0 \exp\left[-\left(\frac{T_0}{T}\right)^{\gamma}\right], \tag{36}$$

where G_0 is a material parameter, $\gamma = 1/(d+1)$ for a d-dimensional sample (e.g., $\gamma = 1/4$ in 3D), and T_0 is a sample-specific temperature scale, below which *quantum mechanical tunnelling* between nearby fermionic states (electron or hole), *localized* around a finite number of *lattice sites*, starts contributing significantly to the $G(T)$ with the help of *hopping* due to phonons. Classically, these regions behave as *finite-size clusters*. For a quantum insulator, as T tends to T_0, the *coherent tunnelling* process (or, hopping conduction) keeps increasing, while the *incoherent scattering* due to the phonons (or, the ohmic resistance) keeps decreasing. After Mott's seminal work, Efros and Shklovskii [61] considered the localization due *only* to the *repulsive Coulomb interaction* between the charge carriers in a pure system, and achieved the complementary result that $\gamma = 1/2$ for an insulating sample in any d. Musing over both the types of VRH, one may take k_BT_0 as the energy-scale that determines the domain above which incoherent (dephasing) scattering among the localized electron/hole states *completely takes over*, and transforms an Anderson or a Mott insulator into an Ohmic (diffusive) metal. Thus, for a complete description, the VRH formula should take the following *general* form:

$$G(T) = G_0 \left(\frac{T_0}{T}\right)^{s} \exp\left[-\left(\frac{T_0}{T}\right)^{\gamma}\right], \tag{37}$$

as argued by Aharony et al. [62].

But, relatively recently, there have been a few theoretical works (e.g. [63]) and some experiments (e.g. [20, 22, 64]), which do not seem to fall into any of the above schemes, in the sense that the exponent γ is different from the above predictions. While the theory of [63] predicts $\gamma > 1/4$ in 3D disordered systems on fractal media

(due to hopping between *superlocalized states*), the experiment of [22] on carbon black-PVC composites seem to confirm such hoppings in the presence of both disorder and interaction. Here, superlocalized states are those whose wave-functions decay with the distance R as exp $[-(R/\xi)^{\zeta}]$, with $\zeta > 1$; ξ being the localization length. If hopping takes place between superlocalized states, then the Mott VRH was shown to modify the exponent γ in Eq. (36) to $\gamma = d_f/(d_f + \zeta)$, where d_f is the fractal dimension of the medium [63]. Experimental [22] evidence of the above has been reported in carbon-black-polymer composites, where it is claimed that $\zeta = 1.94 \pm 0.06$. However, doubt has been cast by Aharony et al. [62] whether the superlocalization was really observed in such composites.

As a matter of fact, several experiments (e.g. [20, 64]) in the past, reported qualitative deviations from the above-mentioned results. Indeed, the more serious deviation has been the continuous variation of the exponent γ with the dopant (or, disorder) concentration, p, in some *granular* or *composite* materials.

5.1 A Temperature-Dependent RRTN Model

To capture the basic physics of this intriguing behaviour, we undertook a thorough study of the low-temperature conductance in our semi-classical percolative RRTN model. But the temperature T does not appear explicitly in any percolation model. Hence, to study the VRH phenomenon in the RRTN (in a 2D square lattice), we use some *empirical parameters* for the T-dependence of the *microscopic* conductance of the various types of bonds. For simplicity, we use, $g_o = a/T$ (i.e. a pure metallic bond) and $g_t = u \exp(-b/T)$, where a, u and b are phenomenological constants. Here, a behaves like the temperature coefficient of resistance for the pure o-bonds (disorder effect comes through their random positions), b is a measure of the threshold potential v_g of a t-bond due to the gap between the valence and the conduction bands of a semi-conductor or due to the Coulomb blockade in an interacting system.

First, we describe the mean field results using the EMA. Putting the above forms of g_o and g_t in the Eq. (6), one obtains for $d = 2$ square lattice based maximal RRTN's (i.e. in the upper ohmic regime):

$$G_e = \frac{1}{2}\left[-B \pm \sqrt{B^2 - 4C}\right], \tag{38}$$

where

$$(1-2p)\frac{a}{T} + (1-2p_t)u \exp\left(-\frac{b}{T}\right) \tag{39}$$

and

$$C = \frac{au(2p_i - 1)}{T} \exp\left(-\frac{b}{T}\right). \tag{40}$$

In the Fig. 18 (*Left*), we present graphically the T-dependence of the effective conductance $G_e(T)$ for five different $p > p_{ct}^{EMA} \cong 0.25$ (square lattice), as given by the EMA Eq. (38) above. For this purpose, we have considered the parameter values as $a = 100$, $b = 100$ and $u = 10$, and plotted the T-dependent curves for five o-bond concentrations in the range, $p = 0.30 - 0.70$. All the graphs have a non-trivial

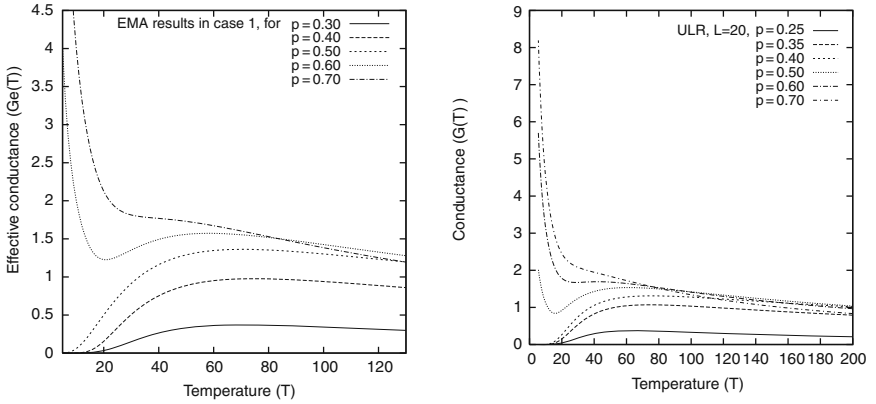

Fig. 18. A simple basic temperature T-dependent RRTN with material parameters $a = 100, b = 100$ and $u = 10$. *Left*: Effective mean field (EMA) conductances, G_e versus T given by Eq. (38), for various p's in the dc upper linear regime (ULR). *Right*: Beyond mean field, numerically exact conductance $G(T)$ vs. T in six 20×20 RRTN *square-lattice* configurations of various p's in the ULR

conductance maximum (resistance minimum) as in a disordered quantum system. Further, for the graphs $p > p_c = 0.5$, there is a sharp rise in $G_e(T)$ at very low T's with an infinite peak at $T = 0$ (see also [65]) since the dominating ohmic bonds (droplet type regions in a real sample) are *pure metallic* and diverge as $1/T$ in the model T-dependence considered here. The case where the metallic phases/bonds are also dirty (i.e. disordered with a zero-T residual resistance) is considered elsewhere.

As $T \to 0$, we find that $G_e(T)$ behaves as $T^{-1/2}\exp(-b/T)$. Hence, the EMA values for the exponents shown in the Eq. (37) come out to be $s = 1/2$ and $\gamma = 1$, when the macroscopic sample is a maximal RRTN, or it is in its upper ohmic regime (ULR). For $T \to \infty$ (indeed for $T >> b$), one can make an asymptotic expansion $\exp(-b/T) \simeq (1 - b/T)$. Then, one finds from Eq. (38) that the macroscopic EMA $G_e(T) \simeq 1/T$, i.e., the ohmic metal-like behaviour dominates for $T >> T_0 = b$ (a material parameter dependent scaled temperature). So, from the *mean-field level* EMA calculations, there is p-dependence and a temperature maximum (as expected) in $G_e(T)$, but no p-dependence in the VRH exponent γ (or, s).

To go beyond the EMA, i.e., to study the effects of both the thermal and the (semi)-quantum fluctuations, we do again take recourse to an exact numerical solution of the local current conservation equations in the RRTN iteratively until a steady state at a temperature T is reached. To get the results in the ULR (maximal RRTN), we use the trick of applying a very high voltage (10^6 V or more). In the Fig. 18 (*Right*), we present the T-dependence of the numerical results for differential conductance $G(T) = (dI/dV)_T$ in finite-sized ($L = 20$) RRTN samples for six different p's ($p > p_{ct} = 0.18$ for square lattices). Qualitatively, these $G(T)$'s and the $G_e(T)$'s in the EMA [see Fig. 18 (*Left*)] look very similar. In a classically percolating situation, where the ohmic backbone is already percolating, we find a *non-monotonic* sharp rise in the conductance as $T \to 0$. As T is increased slowly, one first notes a

conductance minimum followed by a relatively slower increase to a conductance maximum G_m at $T = T_m$ (due to a competition between the decoherent diffusive processes in the randomly positioned o-bonds and the coherent tunnelling processes across the positionally correlated t-bonds). These findings have, at least a qualitative matching, with some experimental results on composite/granular materials, as well as some theoretical works on *fully quantum* disordered systems (e.g. see [65]).

To treat both the percolating and the non-percolating RRTN samples on the same footing (for studying the VRH phenomenon), we work with the excess RRTN conductance over the RRN conductance at the same temperature: $G(T, RRTN) - G(T, RRN)$. The Fig. 19 (*Left*) shows this excess differential conductance for the same samples as in the Fig. 18 (*Right*). Clearly, now the samples for all p's look very similar. We calculated the VRH-exponents first by using the finite-size scaling analysis. In our previous study [60] in this regime, the finite-size effects had seemed vanishing. More precise analyses with four ranges of T's (for $T < T_m$) indicate that γ has a fine size dependence in the asymptotic upper linear regime (ULR). In the Fig. 19 (*Right*), we show some finite-size corrected VRH exponents [$\gamma(p, T)$'s] for the 2D RRTN square lattices in the ULR. We observed from our numerical analyses that the VRH exponent γ depends quite sensitively on p, but s is quite robust ($2.0 < s < 3.0$) as $T \to 0$. In passing, we would like to mention that this size-effect is stronger in the strongly nonlinear sigmoidal regime of the *dc* current-voltage response. The details are discussed elsewhere.

Thus, we find that our RRTN model is quite successful for describing the VRH and that the *generalised* VRH formula, Eq. (37), works better than the restricted one, i.e., Eq. (36). As such, the exponents vary continuously with the concentration p of the o-bonds, as shown in the Table 1. So, it is capable of reproducing, at least qualitatively, the intriguing results of some recent experiments on (Carbon-black)-

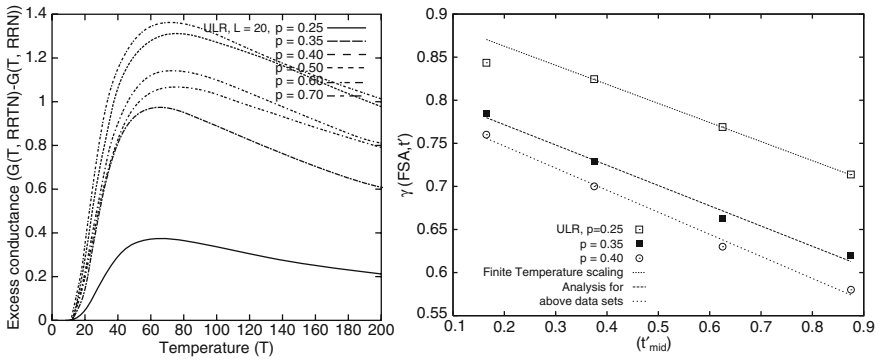

Fig. 19. *Left*: Excess $G(T)$ for the same RRTN samples as in the Fig. 18 (*Right*). The word *excess* means that the ohmic (RRN) part of the $G(T)$ for the RRTN samples at each T is subtracted out (to treat percolating and non-percolating samples under the same footing). Each sample has a characteristic temperature (T_m) maximum of conductance. *Right*: The finite-size corrected VRH exponents (γ) in the upper ohmic regime of 2D square lattice RRTN's at four representative reduced temperatures ($t' = T/T_m$), for $p = 0.25$, 0.35 and 0.40

Table 1. Numerical study of the VRH-exponent $\gamma(p)$ in a square lattice RRTN at different p's

o-bond conc. p	VRH-exponent $\gamma(p)$
0.25	0.91
0.35	0.82
0.40	0.80

(PVC) mixtures [22], sulfonated polyaniline (called PANI-CSA) composites [20], some doped Langmuir-Blodgett films [64] etc.

6 Slow Power-law Dynamics Far-from-Equilibrium

Slow relaxation phenomena in random composite materials made of components having widely different generalized susceptibilities (e.g. permeability, dielectric constant, electrical/ thermal conductivity, viscosity, elastic module etc.), continue to remain intriguing and hence a topic of intense research. In studying the dynamical behaviour of a material, one usually measures its appropriate response property, say, $\phi(t)$, as a function of time t, from a non-equilibrium to an equilibrium (for a closed system) or to a steady (for an open system) state. In general, this relaxation may be classified into two groups.

(i) A purely Debye type where the response function relaxes exponentially, i.e., $\phi(t) = \exp(-t/\tau)$, τ being the only characteristic time-scale, called the *relaxation time*. This *Debye relaxation*[66], also called Boltzmann's *relaxation time approximation*[67], takes place typically when the deviations from the equilibrium statistics due to perturbing external forces are rather small and the temporal rate of change of response towards a steady/equilibrium state, is proportional to the response itself; i.e., $d\phi(t)/dt \propto \pm\phi(t)$.

(ii) A non-Debye type where $\phi(t)$ could be a sub-exponential function (as in some glassy systems), or a linear superposition of exponential functions, etc. with *multiple* relaxation times. If the distribution of τ's may be expressed in terms of a probability density function or, an weighting function, $w(\tau)$, then the weighted response may be expressed as

$$\phi(t) = \int \exp(-t/\tau) w(\tau) d\tau. \tag{41}$$

The response function may thus be considered as the Laplace transform of the weighting function of relaxation times $w(\tau)$ from the τ-space to the space of real times, t. Obviously, in the limit of large observation times, the response is dominated by the smallest one of the set of relaxation times.

In the rather intriguing cases of complex systems or a system very far from any steady state (if there exists any), this non-Debye relaxation may behave as a power-law or a logarithmic function or one with $\tau \to \infty$. Clearly, in all such cases, either

a time scale (even in the very large time limit) does not exist or it is ill-defined. The appearence of such a *scale-free, slow* dynamics with one or more power-laws in the early stages of evolution, is what concerns us here because of the fundamental issue of the failure of Boltzmann's relaxation time approximation in driven systems far-from-equilibrium (actually, from a steady state).

6.1 Experiments and Some Related Models

In a lucidly written review, Scher et al. [68, 69] focus on experimental observations (1970s onwards) and the origin of two power-law kinetics. For a few examples, we cite some transient photocurrent measurements [70, 71] on a-Si:H, a-As_2Se_3 etc. and a couple of whole transport [72, 73] data on PVK and Si-MOS devices, where two consecutive power-law decays, of the forms $t^{-\alpha}$ and $t^{-\beta}$ ($\alpha, \beta > 0$), covering one or more decades in time each (with a crossover in-between) were observed. Based on the *continuous time random walk* with a long-tailed power-law probability density function for the *random waiting times* (release time of trapped carriers by tunnelling), Scher et al.[68, 69] formulated a theory regarding the above results. The latter long-tailed power-law function violates the *Central Limit Theorem*[74], since all of its moments including the first (mean waiting-time) diverge. The unifying feature of the above random walk is the *scale-invariance* of the *shape of the relaxation* current $I(t)$, if one *rescales the time* by a *transit time*, t_r, which is a sample dependent parameter. This stochastic theory by Scher et al. [68, 69] explains the results of many early experiments, following the relation $\alpha + \beta = 2$.

But, there is a huge variety of relatively recent, more intriguing experiments on *soft-condensed* or *complex* systems, where the couple of exponents α and β do not seem to follow any simple algebraic relation. We start off with the relaxation in a metal-insulator composite, the main object of our study. Weron and Jurlewicz noted that the dielectric relaxation in a system of dipoles [75] involves the crossover between different forms of self-similarity. They argue that [76] a couple of power-law decays appear due to the coupling of micro-clusters of dipoles with a distribution of τ's (i.e. multiple time-scales). Next, an experiment on the *intermittency* (i.e. the *blinking* characteristics) in the visible spectrum fluorescence of *single* CdSe quantum dots [77], reported that the distribution of the *on* and *off* times of the blinking kinetics follows a single power-law.[8] In a biological system of photo-dissociated hemeproteins, the rebinding of the ligands of iron (i.e. the CO and the O_2 molecules) is observed to follow an inverse power-law dynamics [78, 79]. In a theoretical study of the same work, Tsallis et al. [80] claim two inverse power-law regimes and demonstrated its possible connection with *non-extensive thermo-statistics* (entropy). Naudts and Czachor [81, 82] analyzed the data of many experiments including those above [75, 77–79], and maintain that these two power-law decays result from some choice of parameters of their probability density function $w(\tau)$. All of the above theories lead to the result that $\alpha < \beta$, if two power-law relaxations exist. In another biological system, the dynamics of Ca^{2+} channels in living cells [83], the distribution of

[8] Our analysis suggests that two inverse power-law kinetics are present in this experiment [77], as well.

the survival-times of the channels has been studied. A stochastic dynamical model, with one dimensional (1D) geometry, was proposed to explain specifically the latter (second) power-law[84] dynamics.[9] In this case, one finds that the system relaxes faster in the first power-law regime than in the second, i.e., $\alpha > \beta$.

In a computer-experiment on the growth of large single DLA (diffusion limited aggregation) clusters of upto 10^8 particles, two power-laws seem to dictate the growth as a function [86] of a time-like entity. A similar theme has been reflected in various methods of *synthesis* of synthesizing nanomaterials [85]. For example, depending on the size (micron, sub-micron, nano-sized etc.) and shape of the microscopic primary particles or powders to be compacted, one may use chemical forces as in a sol-gel/polymerization process, hydrostatic (capillary) forces between nearby nano-clusters with large curvature, or mechanical and thermal forces as in sintering or compaction without external forces. Two power-law growths are also claimed to have been found, using atomic force microscopy (AFM), in the early dynamics of sputtered Ag particles on Si(0 0 1) substrate [87]. These authors relate the two different growth-dynamics to two competing structural rearrangements at two different length-scales. In all these processes, the approach to a steady/equilibrium state involves a local relaxation by forming or restructuring many local clusters by crossing the local barriers due to a *caging effect* (typical of liquid-like, amorphous or dense granular materials). This is followed by (or, may be co-existent with) another slow relaxation of global restructuring of the local clusters themselves. In the dynamics of nano-cluster formation, one finds the average grain size (diameter) growth as a power-law in timcluster formation, one finds the average grain size (diameter) to grow as a power-law in time. A schematic picture of a pair of underlying scales of restructuring (due to appropriate *unbalanced* internal forces) is shown in the Fig. 20.

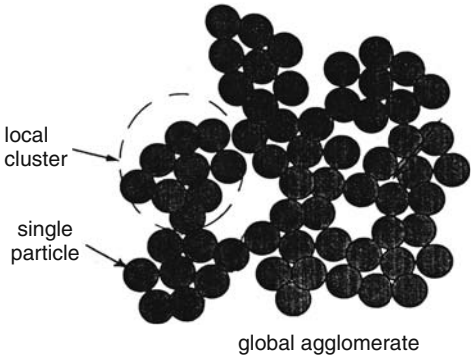

Fig. 20. Schematic diagram of a 'stable' cluster with two different length scales (adapted from [85]) as the origin of two different domains of restructuring times

[9] Two inverse power-law kinetics are clearly present in their Fig. 2 [84], a typical result of this 1D model.

Finally, we cite one of the most spectacular occurrences of this early, far-from-equlibrium, two-power law dynamics in one of the most highly devastating of natural phenomena called *earthquake* [88, 89]. Data collected over a long time and from various regions of the earth have been condensed by geophysicists in the form of *Omori law*, which says that the intensity of small localized quakes, called the *aftershocks* which are the aftermath of a much more extensive *main event*, follow a power-law in time. Interestingly, more recent and accurate data analyses, as discussed in an advanced textbook on the nonlinear dynamics of the lithosphere [88, 89], indicate that the intensity of the cooperative build-up prior to the main event, called the *foreshocks*, also follow a power law in time. The reason for the late revelation of the power-law dynamics of foreshocks is that reasonably well-identified data on them are available only for rather large quakes. As far as a simple theoretical modelling of quake dynamics is concerned, a relatively recent study of a cellular automata model of earthquakes[90], indicate that one power-law dynamics seems to result under certain choice of parameters.

Thus, even though, time enters in an implicit fashion in some of the above studies, an explicit characterization of the relaxation dynamics in the RRTN model in the perspective of various experiments and models (as described above) was considered to be worthwhile. It may be mentioned here that this phenomenological, microscopic model (RRTN with no temperature, or at $T = 0$) has a minimal number of adjustable parameters for nonlinear, steady state properties; and none at all for the non-equilibrium dynamics, e.g., no assumption of multiple relaxation times or any power-law type probability density function thereof, or any underlying stochastic fractal/multi-fractal geometry (p is not constrained to be close to p_c or p_{ct}), etc.

6.2 Far-from-Equilibrium Slow Dynamics in the RRTN

We review here the current relaxation dynamics towards a steady state in the RRTN model. Away from equilibrium, a t-bond with a microscopic $v < v_g$ behaves like a dielectric material between two metals (o-bonds), and the resulting charging effect gives rise to a *displacement current* ($c\frac{dv(t)}{dt}$, where c is the capacitance). Thus, a t-bond gives rise to a displacement current if $v(t) < v_g$, and an 'ohmic' current if $v(t) \geq v_g$ [91, 108]. For our calculations, we use the values of the microscopic conductance $g_o = 1.0$ (o-bonds), $g_t = 10^{-2}$ (t-bonds), $v_g = 0.5$ and $c = 10^{-5}$ for the t-bonds (in some arbitrary units).

In our numerical study, we apply an uniform electric field across RRTN's of different system sizes (L) and ohmic bond concentrations (p). We study the evolution of the current in a RRTN starting from the switching-on-state until it approaches its *asymptotic* steady state. To do this, we follow basically the current conservation (Kirchhoff's laws) locally at each node of the lattice. The aim is to study the achievement of a *global current conservation* as an outcome of the *local current conservation* (hence, the dynamics). A discrete, *scaled* time unit has been chosen as one complete scan through each site of the lattice. The local conservation or the equation of continuity reads as.

$$\sum i_{nn}(t) = 0, \qquad \forall t. \tag{42}$$

Here, the *sum* has been taken over currents $i_{nn}(t)$ through various types of nearest neighbour (nn) microscopic bonds around any node/site of the lattice. For the case of a square lattice, one considers the four nn's around a node inside the bulk (three and two nn's, respectively, at any boundary or a corner). If Eq. (42) were true simultaneously for each site of the lattice, then the global conservation (the steady state) for the entire network would automatically be achieved. As we need to start with an initial (arbitrary) microscopic voltage distribution, the Eq. (42) would not hold for all the sites of the lattice. Some correction term would be required at each site and this requirement leads to the following time evolution algorithm, which we call as the *lattice Kirchhoff's dynamics* [108]:

$$v(j,k,t+1) = v(j,k,t) + \frac{\sum i_{nn}(t)}{\sum g_{nn}}, \tag{43}$$

where g_{nn} are the various microscopic conductances of the nn bonds around the node (j,k). Then, we numerically solve a set of coupled *difference* equations on the lattice. The move towards a macroscopic steady state implies that the difference of currents through the first and the last layers tends to zero as a function of time. In practice, the system is considered to have reached its steady state when this difference decreases to a pre-assigned smallness.

As shown in the Figs. 21(a,b), we observe [108] a non-Debye type current relaxation with two consecutive initial power-laws (and a crossover in-between), each of them spanning at least a decade. This asymptotic steady-state current (whether insulating or conducting) for any randomly chosen RRTN is found to be very robust against any initially chosen voltage distribution on the lattice. To analyse the current evolution of an insulating or a conducting sample on the same footing, we subtract the corresponding steady current, $I(t \rightarrow \infty)$, from the evolving current $I(t)$ at the time t. Our observation on the transient current response, indicates clearly the existence of a couple of initial power-laws, whose exponents differ significantly for systems with different configurations, p, L and external voltage, V. So, we choose to work with one sample at a time and analyze its results within our numerical accuracy.

For example, in the Fig. 21(a), we show the dynamics for a sample with $L = 60$, $p = 0.55, V = 2.0$ and in the Fig. 21(b) another with $L = 80, p = 0.35, V = 20.0$. The first figure [i.e., Fig. 21(a)] represents the class of relaxation, where the second exponent (0.72) is larger than the first (0.44) (the only class reported in our previous work at a particular $p > p_c$ [91]). There are quite a few theoretical works [68, 69, 76, 80] in this regard. Some other experiments [83, 84, 87] find a second exponent smaller than the first. Since our earlier report [91], we have been able to reproduce this other class of relaxation [e.g., Fig. 21(b) with the exponents 0.78 and 0.57, respectively], as well, within the context of our RRTN [108]. In special cases, we do find only one power-law relaxation, which may be considered to be the borderline between the above two, or as the merging of the two power-law exponents. Further, we do not find any particular relation between the exponents. Next, the existence or the lack of any asymptotic exponential kinetics is not explicitly stated in

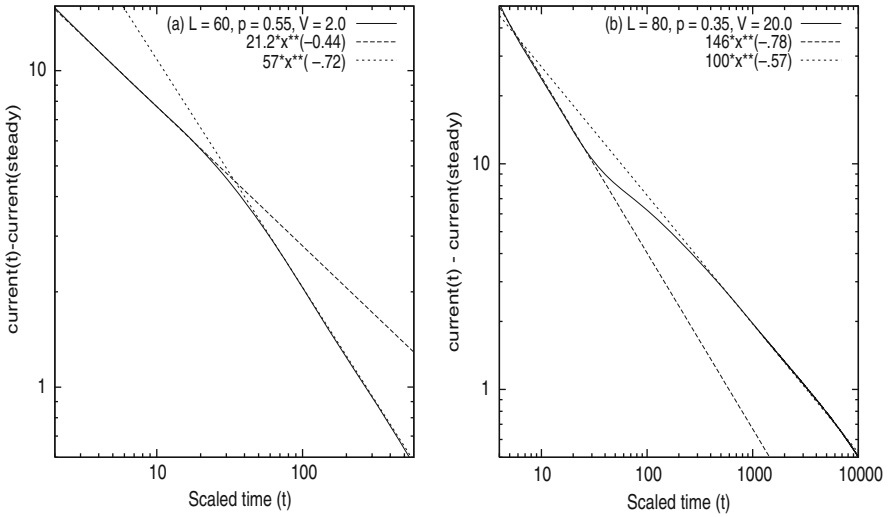

Fig. 21. (**a**) Non-equilibrium dynamics in terms of a *scaled time* shows two initial power-law decays (with intermediate crossover) in the current relaxation for (**a**) one RRTN sample ($p = 0.55, L = 60$) with the exponents of 0.44 and 0.72; and (**b**) another sample ($p = 0.35, L = 80$) where the exponents are 0.78 and 0.57, respectively. The dynamics in the RRTN is always followed by an *exponentially* decaying tail (not shown in the figures here) towards its steady state

most of them. Indeed, in some of the theoretical studies (e.g. in [68, 69, 76, 86]), the second power-law persists upto asymptotically infinite times. This trend cannot describe the possibility for these systems to reach an appropriate steady state. In contrast, beyond the power-law relaxations (whether one or two), our model acquires a relaxation time, τ and the system evolves with a *fast* exponential dynamics to a final steady state (diffusive/ ohmic). The power-law relaxations at times, $t < \tau$, imply a strong deviation from the Boltzmann's *relaxation time approximation*, i.e., a strongly non-Debye relaxation.

As far as the origin of the two power-law dynamics are concerned, we have already outlined the main content of some of them [68, 69, 76, 80–82, 84, 90] in the section on experiments. In most of them, they occur due to local structural rearrangements preceding the final global structural rearrangements. In our case, the basic structure in a particular sample is created once for all, and it is the fields across the bonds that keep changing in such a fashion that the local conservation (Kirchhoff's laws at each node) dominates the first power-law regime and the global current conservation dominates the latter power-law regime (of course, there are the required structural rearrangements of the active t-bonds). So, it is interesting that these two very different mechanisms give rise to a qualitatively identical outcome. Another origin could be that the free energy of such *athermal* systems depend on the random internal voltage fluctuations, partly correlated due to a scale-invariant (deterministic) placement of the t-bonds. This may give rise to non-extensive entropic energy

[92, 93] and failure of the standard fluctuation-dissipation theorem (regular diffusive motion). Further, since the power-law dynamics occurs even for p's away from p_c or p_{ct}, it clearly demonstrates that they are not organized by any type of criticality. Finally, as discussed above, while most of the other theoretical works, are destined to get only one class of two-power-law relaxation behaviour (namely, $\alpha < \beta$), the RRTN dynamics has the ability to capture both of the classes for different sets of parameters.

7 Aspects of Reversible Breakdown in the RRTN Model

Material breakdown is an ubiquitous phenomenon of Nature observed in widely different varieties of *driven systems*, starting from failures of mechanical systems (such as fractures of materials, avalanches, earthquakes etc.) to biological systems (like denatured proteins etc.). In electrical systems, this run-away phenomenon relates to the abrupt change of the electrical properties from one kind to another. Electrical breakdown itself can be of two different types. One is the fuse-type breakdown due to the Joule heating through the ohmic conductors, and, hence, it is an irreversible phenomenon. The other is a dielectric breakdown. If an insulating material (made of microscopic disordered metallic and dielectric, i.e. insulating, phases) is placed between two electrodes and a voltage V is applied across them, such that the electric field $E = V/L$ (L being the length of the sample in the direction of the field) has a low value, no current flows through the solid. The islands of conducting phase without the external force cannot provide for a continuous path for a current to flow through the macroscopic sample. However, if the field is higher than some sample-dependent critical value $E_c = V_c/L$, then some dielectric regions may break under their local field (electrical stress) thereby making extra pathways for current to flow through, and the solid becomes a conductor. If E is brought below E_c from higher values, the solid becomes insulating again. Hence, this type of breakdown is *reversible*. At a low enough temperature and in the presence of disorder (or, other scattering mechanisms, not considered here), quantum mechanical tunnelling (or hopping) between the sites or bonds, may become important, and thus contribute to a breakdown (dielectric) of the system.

To understand the dynamics of a reversible dielectric breakdown or fracture, we use a bond percolation model. As is customary in a statistical physics approach of studying breakdown, it is believed that some of our results may have some relevance for varieties of generalized breakdown/fracture processes, and in particular, for an (earth)-quake, where mechanical fracture is involved. A preliminary report of our present study has already appeared in [94]. If a field above E_c is applied to a macroscopically insulating sample, which is a composite made of microscopic insulating and conducting domains, the breakdown of some dielectric/insulating regions into conducting zones in such a system, propagates in time through the sample until the whole sample acquires a geometrical connectivity of conducting regions, and starts conducting. In other words, the dynamics of the system leading to such a phase transition, is extremely important to understand.

Statistical physics of the breakdown of an insulating dielectric into a conducting state (or of a conductor into a *fused* insulating state) has been the subject of intense research [95, 110, 111] for more than a decade now. The general discussions and the numerical results described below closely follow our work [53, 94] on this topic. Suppose one considers a random binary, two-phase mixture of metallic and non-metallic components. If the volume fraction of the metallic phase is large enough, the metal phase forms at least one [96] sample-spanning cluster in which the non-metallic phase is dispersed in the form of isolated islands. In this regime, the electrical conductivity of the sample is large. The system is *metallic*. On the other hand, for a small volume fraction of the metallic components, the non-metallic phase forms at least one [96] sample-spanning cluster in the presence of small and isolated metallic islands. The system is then in the *dielectric* or insulating regime. The electrical conductivity of the sample in this regime is ideally zero and extremely small in practice. Now, if one increases the electric field across the sample in this regime, the voltage across the non-metallic bonds keeps increasing and it is not unlikely that some of them may give in to let some current through them or turn metallic. Clearly, in this case the breakdown problem is set up with an underlying percolation model.

In the usual dielectric breakdown model [97–99] of a random mixture of conductors and insulators, it is assumed that each insulating bond can withstand a fixed potential difference across it and becomes a conductor if the local potential difference exceeds its threshold. Therefore, the whole lattice is subjected to breakdown at any volume fraction ($p < p_c$) of conducting components when an appropriately large external voltage, called the *dielectric breakdown voltage*, V_B, is applied. Its value depends on the specific configuration of the sample, and usually one talks about the configuration-averaged value of V_B at any particular p. For $p = 0$, i.e., when all the bonds are insulators, the breakdown voltage (V_B) scales as the linear size (L) of the lattice: $V_B/L = v_g$, where v_g is the voltage threshold for an individual tunnelling bond. For $p \geq p_c$, such a lattice is conducting for any small-applied voltage and the question of dielectric breakdown does not apply: $V_B/L = 0$. To remove the trivial system size (L) dependence, we talk about the external breakdown field ($E_B = V_B/L$) instead of the breakdown voltage from now on. The interesting thing happens as one approaches $p \to p_c$ from below. One obtains a criticality and a power law

$$E_B \sim (p_c - p)^{t_B}, \tag{44}$$

where t_B is called the breakdown exponent. A similar scaling is also known for the mechanical fracture process [95, 100, 101]: $\sigma_{min} \sim (p - p_c)^b$, where σ_{min} is the minimum stress needed to break the system apart.

In general, in a breakdown process, one defines two critical voltages: one is the breakdown initiation voltage V_I at which the nucleation of the breakdown process (akin to an avalanche) is initiated and the other is the final breakdown voltage V_F which is the minimum voltage at which the system as a whole breaks apart. In some cases V_I is no different from V_F [97–99]. In other cases, the system needs some more voltage beyond V_I to reach the final breakdown state. It is commented in some earlier works [102, 103] that V_I and V_F are essentially the same. So the authors of many

previous works had actually treated the average value of V_I as the average breakdown voltage (V_B). The statistics of V_I and V_F are also claimed to be the same, i.e., they are described by the same critical exponent near the threshold (p_c). There has been a number of works (e.g., see the references [95, 97–103]) in the literature for estimating the *breakdown exponent*. A closely related quantity of interest is the *mimium gap path*, $g(p)$, of a non-percolating lattice configuration. It is the minimum number of insulating bonds that are to overcome their thresholds to give a connecting path between two opposite sides of a lattice across which the external voltage is applied. The breakdown voltage (V_B) and the minimum gap (g) are actually two different quantities [102] except at $p = 0$ and at $p = p_c$, although both the quantities near p_c seem to behave in the same way and the numerical results [102] claim that their scaling exponents are the same near p_c. It was claimed through an analytical calculation on a hierarchical lattice and through a numerical study on a square lattice [104, 105] that the breakdown voltage ($V_B(p)$) behaves like $g(p)$ in a random lattice. The average of $g(p)$ is supposed to vary as $(p_c - p)^{t_g}$, where t_g (the minimum gap exponent) is identified with the breakdown exponent t_B. Later, it was rigorously established by Chayes et al. [106] in an invasion (or, under an external force) percolation type situation, that $t_g = \nu$ in 2D, where ν is correlation length exponent. This indicates that $t_B = t_g = \nu$. However, in such RRN models without any threshold, there is a *finite size logarithmic* term involved in the scaling relationship of breakdown field (E_B) near the percolation threshold (p_c), and $E_B \sim \frac{(p_c-p)^{\zeta}}{lnL}$ [103].

7.1 Semi-classical Breakdown in the RRTN Model

Here we discuss on our study of a semi-classical (or, semi-quantum) model of dielectric breakdown [43], i.e., one which works on the borderline between a classical and a quantum picture. As before, our approach involves the semi-classical RRTN model. Semi-classical nature enters our discussion only through the possibility of a charge carrier *breaking* or tunnelling through a barrier. Disorder in such systems gives rise to inhibition to transport upto a critical (or, threshold, Sect. 3) value of the applied field, above which a charge can pass through. As discussed in Sect. 2, onset of nonlinear response and dielectric breakdown has been discussed on a similar dynamic random resistor network (DRRN) (Gefen et al. [4]), where the tunnelling elements (or the *imperfect* insulators) could be anywhere in the non-metallic domain of the system. In the RRTN, such charge transfers may be possible only in the proximity gap between two metallic domains, and one can imagine that breakthrough by the charge carriers (reversible tunnelling) should be most effective in the vicinity of such gaps. This also highlights the fact that the macroscopic breakdown discussed below is reversible.

Our percolative RRTN is not just a random mixture of two phases. As we have seen before, in the presence of an external field, the dynamics of this model mimics an effectively three-phase (driven) system. For our convenience, we take a square lattice in 2D. The basic physics should remain the same if we go over to 3D. Since the nonlinear bonds (t-bonds) are allowed only across the nearest-neighbour (nn) gaps of two conducting bonds (and no further), the RRTN acts as a perfectly (statistically)

correlated bond percolation model. Our interest is to examine this correlated percolation model in the spirit of dielectric breakdown phenomenon. The mechanism operating here is clearly not traditional dielectric breakdown because the piecewise linear response considered here in the tunnelling bonds is *reversible* in the sense that if the local voltage difference is lowered below the threshold, a tunnelling bond becomes insulating again. This is an important point because if we would assume the process to be irreversible, then the irreversible conversion of one insulating element to a conducting one may trigger a sharp/runaway macroscopic *avalanche* effect. Since a local current redistribution takes place in the reversible RRTN model also whenever an inactive t-bond turns metallic, avalanches may take place in this model as well. But, they may be more restricted in the RRTN than in the traditional reversible models.

Similarly in the random fuse network [12], one has the *irreversibility* with respect to conductor $\rightarrow$ insulator transition with the increase of applied field. Breaking (fusing) of one bond in a certain path permanently (because of too much stress) may lead to an increase of current density in the other paths and, thus, it may trigger an 'reverse' *avalanche* effect, i.e., a macroscopic destruction of conductors in the network. In practice the 'reversibility' situation is achieved when the *charge transport by tunnelling* gives the most important contribution to the breakdown process than the irreversible thermal (fuse) breakdown of the microscopic conductors/insulators inside the system. One example of reversible breakdown is the experiment on dielectric breakdown by Benguigui and Ron [42], using a network of tunnelling diodes. This network and many other real systems (nonlinear composites), where the macroscopic response characteristic is reversible (no appreciable static hysteresis effect, e.g., in carbon-wax mixture [21] etc.), demonstrate this reversibility of dielectric breakdown.

Next we comment on the procedure for obtaining the breakdown voltage (V_B) for the usual dielectric breakdown problem as understood from the references above. The usual procedure to obtain the electrostatic voltage distribution at the nodes of the networks in the non-percolating situation is to solve for the Laplace's equation ($\nabla^2 V = 0$). This procedure, when discretised on a square lattice and in the situation where the dielectric constant for all the bonds are assumed to be the same (pure dielectric), reduces to $v_0 = \sum v_i/4$, where v_0 is the voltage at any node and v_i's are the voltages at the four nearest-neighbour (nn) nodes on a square lattice.

In our case, we approach the breakdown point from the conducting side and apply Kirchhoff's law for our problem that takes the form: $v_0 = \sum v_i g_i / \sum g_i$, where g_i's are the conductances of the nn bonds. Clearly, this may be reduced to the discrete Laplace's equation above, had the g_i's for all the bonds been essentially the same. Further, in the usual models, as soon as the voltage difference ($v_i - v_0$) across an insulating bond exceeds its threshold value v_g, this bond is turned into a 'perfect' conductor for all later time (iterations) to come, and v_i is made equal to v_0. On the other hand, in our model, even when a t-bond has been broken (turned metallic), neither does it become a perfect conductor (unable to sustain any voltage difference across it) nor does it carry any current if the voltage difference across it becomes less

than v_g, at any later time (iteration). We believe that this is a crucial difference and should be more akin to reality.

As far as our model is concerned, we assume that the tunnelling bonds (the bonds which break) may be placed only in the nn gaps of two conducting bonds and nowhere else. It may be noted that because of the reversible nature of the t-bonds and their finite thresholds v_g, rarely would V_I be equal to V_F in our model. Indeed we *do not* work with V_I and actually identify V_B as the average of the final breakdown voltages, V_F. Hence, a typical breakdown path in the RRTN model consists of an actual number of the so-called 'broken' bonds and does not quite, correspond to the minimum gap path except when p is very close to p_c. If there are n number of active tunnelling (or broken) bonds in the minimum gap path having a threshold voltage v_g for each of them, the overall breakdown voltage $V_B = nv_g$. It may be noted that this is also the case with the dielectric breakdown experiment by Benguigui and Ron [42] on an artificially constructed electrical network of resistors and light emitting diodes (LED). The initial breakdown voltage V_I (at which just one tunnelling bond breaks) is just v_g. Very rarely (except for p near p_c) one has $n = 1$, and $V_B = V_I$ in our model or in the above-mentioned experiment by Benguigui and Ron. As a demonstration, we show in the Fig. 22 (*Left*), a typical configuration of the lattice of size $L = 10$ at a volume fraction $p = 0.30$, where just one breakdown path has been formed. Indicated by the dotted lines are the number of broken t-bonds. The path is explicitly seen to *not* be the minimum gap path.

One may notice another difference of our model from the usual models of dielectric breakdown problems so far studied (where the dielectric bonds can break at any place in the network) from the above demonstration. There may be a series of broken bonds at more than nn gaps of two conducting bonds in the breakdown path in the usual model (see, e.g. the figures in [103]) but not in ours. It is worth commenting here that the breakdown paths generated by Benguigui and Ron [42] are more akin

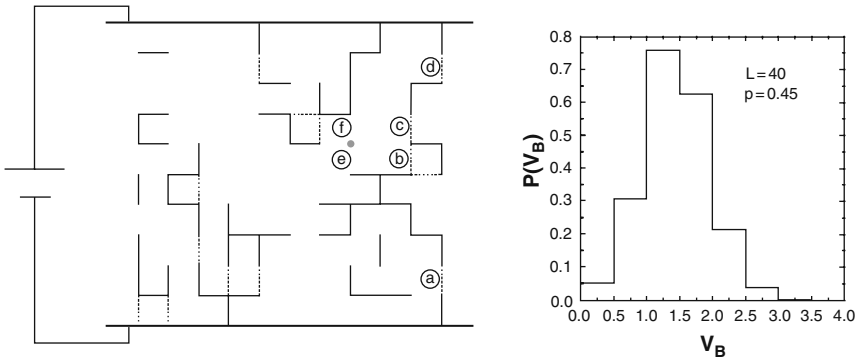

Fig. 22. *Left*: A typical configuration of the lattice for a square of size 10×10 with $p = 0.3$ (below p_c). The breakdown path is indicated by 'abcd' with $n = 4$, which is seen to be different from the minimum gap path 'aef' of an usual dielectric breakdown model with $g(p) = 3$. *Right*: A typical distribution (histogram) of the breakdown voltage V_B for various samples of fixed $L = 40$, $p = 0.45$ and $v_g = 0.5$

to our model than the usual model. This is because even though many more than one LED's seem to be broken in series, in practice two consecutive LED's are connected by metallic wires and hence do not correspond to breakdown over two or more near neighbour distances (or lattice constants). The breakdown exponent (t_B) in this experiment was reported to be $\cong 1.1$, which is smaller than expected (i.e., 4/3, the exact value of ν in 2D), and the difference was attributed to the finite-size effect since a system of size 20×20 was used in the experiment.

7.2 Calculation of the Breakdown Exponent in the RRTN

Here, we examine the dielectric breakdown phenomenon in our model as the onset of nonlinear conduction against applied field for $p \leq p_c$. Below the percolation threshold (p_c) there exists a number of metallic clusters, isolated from each other, but closely spaced. The conductivity is a sensitive function of the configuration and the applied electric field [43] as new conducting paths are created when the electric field increases above the dielectric breakdown field ($E_B = V_B/L$) of the insulator. In the Fig. 22 (*Right*), a typical distribution (quite asymmetric) of breakdown voltages is shown for a system size $L = 40$ and $p = 0.45$. Clearly, for the RRTN's with $p < p_{ct}$, there is no infinite size percolating cluster of combined o- and all possible t-bonds (maximal RRTN), and hence, there is no conduction (on an average) at any finite electric field, according to the criteria set for the model.

Thus, three types of configurations arise in the regime $p_{ct} < p < p_c$:

- Some configurations that are already percolating with the ohmic bonds only: they have *zero* voltage threshold macroscopically,
- Some configurations that do not percolate with the ohmic bonds but only do so in conjunction with the tunnelling bonds: they have a *finite* voltage threshold,
- Some other configurations are there that never percolate even with the assistance of all the available tunnelling bonds: they *do not take part* in the breakdown process.

This third possibility does not arise in the usual class of breakdown problems where any insulating bond may break, given enough voltage, and hence, eventually renders the system conducting.

Clearly, to find the average breakdown voltage (V_B) we have to disregard those configurations that do not take part in the breakdown phenomenon. Below we talk only about configuration averaged fields by averaging over distributions such as the one shown in the Fig. 22 (*Right*). A typical phase diagram (finite size) is shown in the Fig. 23 (*Left*) as the average of breakdown field (E_B) plotted against the volume fraction (p) of conducting bonds. This typical figure is shown for a system of size $L = 30$ and average is taken over 500 configurations. Our interest would be to know how does the average breakdown field ($E_B = V_B/L$) scale against $(p_c - p)$ as in Eq. (44). One usually plots the quantity V_B or E_B for a finite-sized system against $(p_c - p)$ around p_c in log-log scale and find out the breakdown exponent $t_B(L)$ from the least square fit.

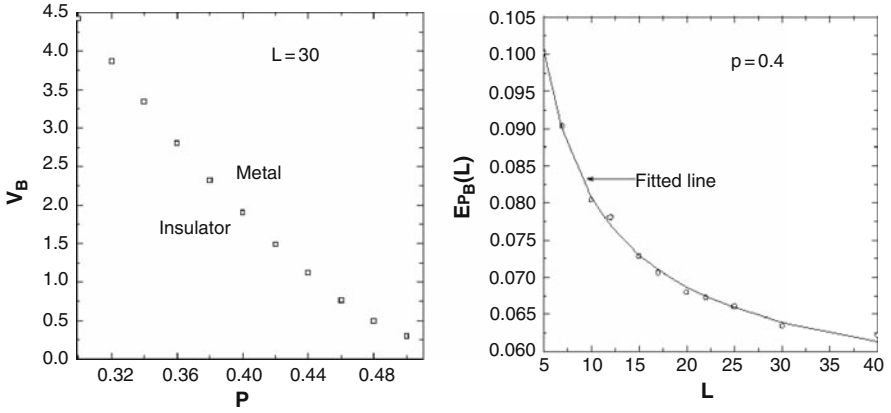

Fig. 23. *Left*: The phase diagram for dielectric breakdown in 30×30 RRTN; configuration-averaged V_B as a function of p. *Right*: The finite-size scaling of breakdown field E_B for $p = 0.4$

To remove the finite-size effects, however, we follow a slightly different way of finding the above exponent. We first obtain the finite size scaling of the breakdown field, E_B. One such scaling plot is shown in the Fig. 23 (*Right*) for $p = 0.4$. In this way, we obtain the asymptotic values $E_B(L = \infty)$ of the breakdown field for all p ranging from 0.3 to 0.5 through finite-size scaling, which seems to follow

$$E_B^p(L) = E_B^p(\infty) + a(p)L^{-\mu(p)}, \tag{45}$$

where $\mu(p_c) \simeq 1$; but $\mu(p)$ is quite different (0.4–0.75) at other $p < p_c$. Further, $E_B^{p_c}(\infty)$ has a very small but positive value, which for the accuracy of our calculation implies that $E_B^{p_c}(\infty) = 0$. But as p becomes smaller and smaller than p_c, $E_B^p(\infty)$ increases systematically as the graph in Fig. 24 (*Left*) indicates. We point out that forcing $E_B^p(\infty) = 0$ at $p < p_c$ gives significantly worse fitting. Equation (45) strongly demonstrates the fact that the breakdown model we are considering is somewhat different in nature from the usual models available in the literature where one observes a $1/lnL$ scaling of E_B^p demonstrated clearly in the work of Beale and Duxbury [103]. This scaling, which makes the E_B^p's vanish irrespective of the p in a truly infinite size system, is non-existent in our model. Since the breakdown field in the previous models vanishes to zero irrespective of any p ($p < p_c$), it is worth noting that the above $1/lnL$ scaling and the consequent vanishing of E_B^p is also non-existent in another model that has no dilution but has reversible tunnelling conductors with random thresholds at each and every bond in the lattice. In such a network, Roux and Herrmann [51] found that $V_B = (0.22 \pm 0.02)L$.

The scaling of the asymptotic breakdown field $E_B^p(\infty)$ can be written as

$$E_B^p(\infty) \sim (p_c - p)^{t_B}. \tag{46}$$

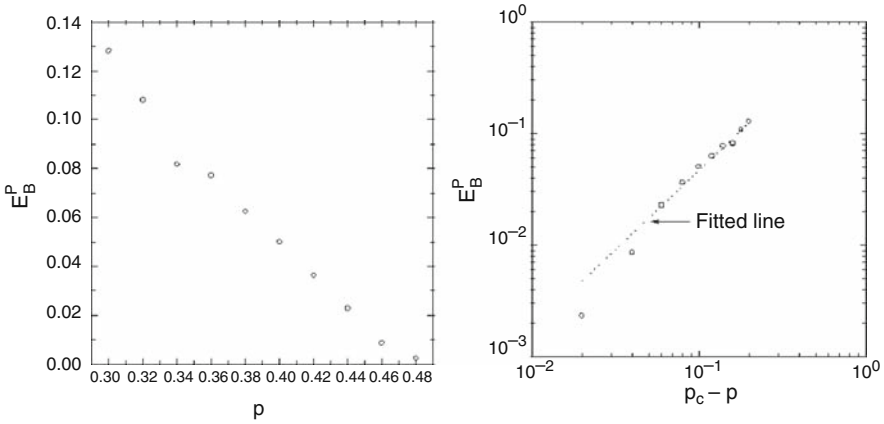

Fig. 24. *Left*: The behaviour of asymptotic breakdown field $E_B^p(\infty)$ with p. *Right*: The log-log plot of $E_B^p(\infty)$ against $(p_c - p)$ and the best-fit line to find the breakdown exponent. The fitted line gives $t_B = 1.42$

The double logarithmic plot of Eq. (46) is shown in Fig. 24 (*Right*) and the least square fit of the data is also shown. We find from this fitting that the breakdown exponent $t_B \cong 1.42$ for the RRTN model.

7.3 Comments on the Reversible Breakdown

It seems that the above exponent t_B is not very different from that of the usual breakdown exponent $t_B = \nu = 1.33$ as discussed above. But it is not unlikely either that we do indeed have a different result in our hands. If different, it could be because of the nature of the electric field in increasing the effective volume fraction of the conductors. As may be understood, the electric field adds on new bridge bonds (active t-bonds) at well-determined positions (according to the *deterministic* laws of *electrodynamics*). The statistically correlated bridge bonds increase the connectivity of the o-bonds, and increase the effective volume fraction ($p' > p$) of the o-bonds. One may create some other configuration with the same effective volume fraction p' by adding on bridge bonds following *electrostatic*, i.e., Laplace's equation (Sect. 7.1). Intuitively, the correlations obtained by these two different means should be qualitatively similar (being both anisotropic), but quantitatively quite different. Indeed, as seen in the experiment of [42] and in numerical studies [48, 103] [also Fig. 22 (*Left*)], an electric field tends to make somewhat elongated clusters directed towards the direction of the external field.

But, our results in [107] do also show that while the anisotropy of the clusters increases with an increasing field upto a maximum, it does finally start to decay (i.e. grows more and more isotropic) at still larger fields and the RRTN at an infinite field, which becomes our fully correlated bond percolation model [48], does not fall in the category of directed percolation (rather it falls in the same universality class as the ordinary random bond percolation). Thus, at a small but finite field, we may observe

the percolation statistics to be directed only a little bit. Now, it is well known from the results on directed percolation that the correlation length exponent in a direction parallel to the electric field is $\nu_{\|} \cong 1.7$. So, it is *not unlikely* that the correlation length exponent near the breakdown field (which is quite small) takes some value between 1.3 and 1.7. If true, this may very well explain why our $t_B = 1.42$. In this respect, it may be noted that Beale and Duxbury [103] also found the average $t_B = 1.46$. Thus, the exponent $t_B = 1.42$ for our model may actually be a result different from the standard quoted result of 4/3 for this exponent.

8 Dynamical Characteristics of Breakdown

As one can envisage, not a single t-bond would 'fire' (i.e. become active), if the external potential $V < v_g$. Now, if the RRN is insulating (i.e. non-percolating), then it may require some minimum number of t-bonds to fire, to make the corresponding RRTN conducting (or to make the breakdown occur). Clearly, this gives rise to a macroscopic threshold voltage (V_g), or equivalently, a breakdown voltage ($V_B = V_g$) for that particular RRTN configuration. Thus, the RRTN shows a reversible breakdown if the underlying RRN is an insulator and if the external electric field $E > E_B = V_B/L$ [53], the breakdown field. For example, with $p = 0.4$, $L = 20$, we find from the Fig. 23 (*Right*) that E_B is around 0.068 on average [53]. In 2D square lattices, we found that $E_B \sim (p_c - p)^{t_B}$, where the breakdown exponent $t_B = 1.42$ [53], not very different from the value of $t_B = 1.33$ for the RRN.

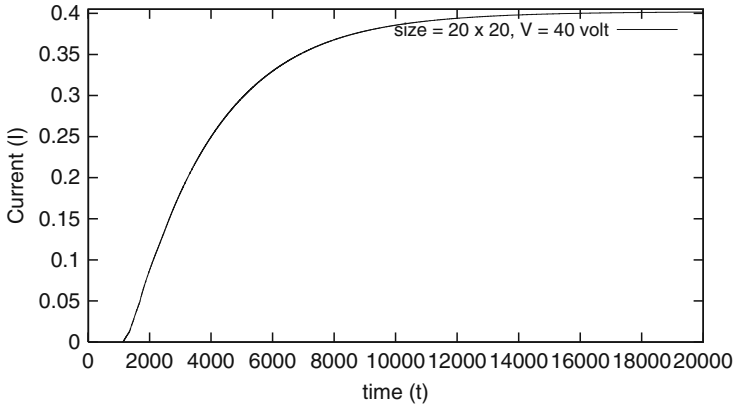

Fig. 25. A typical growth of response (current) as a possible measure of the growth of breakdown (dielectric here) with time in a 20×20 square lattice RRTN at a fixed driving voltage

8.1 Finite-size Statistics of Two Time-Scales

Here, we present the results on the dynamics of breakdown in square lattice RRTN's of $p = 0.35$ ($p_{ct} < p < p_c$), $v_g = 0.5$ and a $E = 2.0$ (above E_B). The Fig. 25 shows the growth dynamics of current *I*(*t*) for a typical RRTN sample. In contrast

with our earlier studies (e.g., in [108]), we start from a qualitatively different initial condition, as dictated by the definition of the present problem [94]. In earlier studies, the initial voltages at all the nodes of the lattice were taken to be non-zero (typically, totally random) within the bounds of the external voltage. In the present study, the initial voltages, at all the layers except the first one, are taken to be zero. The initial voltages at all the nodes of the first layer, which is in contact with the external source, are kept at the full external voltage V. Clearly, with such a choice, the breakdown time is equivalent to the first passage time of the moving charges through the bulk system. So, we look for the first passage of an *observable non-zero* current through the last layer of the system which is always kept grounded (neutral).

For numerical calculations, the conductance of the inactive t-bonds is chosen to be zero (and capacitance $c = 10^{-5}$), for $v < v_g$ and to be the fixed non-zero value $g_t = 10^{-2}$ mho, for $v > v_g$. The initial condition is chosen as discussed above. To be able to observe the progress of the dielectric breakdown, analogous to the ductile failure phenomenon in the RRTN, the voltage at each node is updated using the time evolution algorithm, we called the lattice Kirchhoff's dynamics, as described by Eq. (43). The time taken to update the voltages of all the nodes once, is taken as unity. This *scaled* unit of time clearly varies as the size of the sample increases [108]. After each unit time, the current through the last layer (kept grounded) is computed.

8.2 Time-Scale for Reversible Breakdown

Obviously, a typical dynamics, under an external electric potential in the first layer, shows no current through the last layer for quite some time, if the sample (underlying RRN) is insulating. We demonstrate through the snapshots of Fig. 26 how and where a charge carrier breaks open some crucial insulating bonds (or, activates some inactive t-bonds) with the help of the external field, in an effort to spread through the insulating sample. Thus, more and more disconnected, active t-bonds in the form of dashed lines, start appearing (analogous to ductile failure lines/regions building up) reversibly with time in the form of ever larger local clusters all across the sample. Thus, the 'fracture front', as if, *cracks through* further layers away from the first as shown in the Fig. 26(a–d), but no complete breakthrough has as yet taken place, and one does not observe any current through the whole system. Finally as shown in the Fig. 26(e), with the help of only a few t-bonds at some critical positions, several big clusters connect to span the whole system. This corresponds to the breakthrough of the charge carrier by opening up a system-spanning cluster for the first time, and the system has suffered a dielectric breakdown. We denote this time by τ_B, and call it the *breakthrough time* or the first passage time. Now, the system has barely succumbed to the flow of charge through it and with further passage of time, some of the other local clusters continue to grow either to join the main cluster that spans the system or to form separate paths for percolation. A few clusters may still remain local and cannot grow to contribute to the path of percolation under the given field. If one looks at the evolution of the current through the first layer, one finds that it decays/relaxes during $t < \tau_B$, with two inverse power-law functions in time [108].

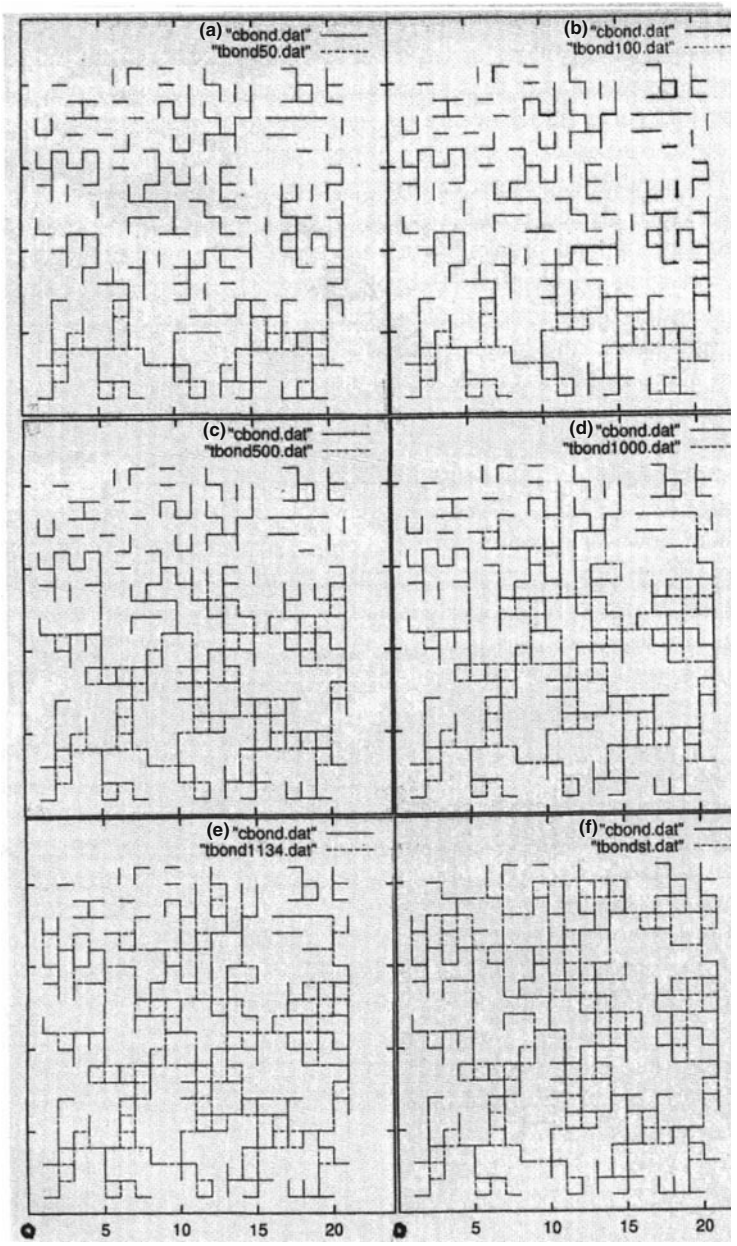

Fig. 26. A sequence of snapshots of an electrically 'fracturing' 20×20 square lattice at times (**a**) $t = 50$, (**b**) $t = 100$, (**c**) $t = 500$, (**d**) $t = 1000$, (**e**) $t = 1134$, and (**f**) the time to reach the steady state with a given accuracy. Here the time is already scaled in units of one updating scan through all the nodes of the lattice. The dielectric breakdown or the macroscopic system spanning 'fracture' of t-bonds appears for the first time at $t = 1134$ units. So, the breakthrough time, $\tau_B = 1134$, for this sample

Once all the possible paths of percolation at that voltage have formed (no more t-bond breaks down), the system approaches an asymptotic steady state (complete breakdown/fully grown fracture for the given external field) following exponential (Debye) relaxation, with the relaxation time τ for the upper linear (ohmic) regime of a fully reversible dielectric breakdown. To achieve the steady state, we monitor the relative difference of currents through the first and the last layers and check out when it goes below a pre-decided tolerance factor (here, less than 10^{-8}) as a function of time. The time scale τ is computed from the exponential regime of the dynamics for $t >> \tau_B$. The values of τ_B and τ vary from sample to sample with the same p. Both of them however increase with the size of the system. The values of τ_B and τ were found for many samples of each different sizes $L : 20 - 120$. The dispersion of the ratio of the two times scales, that is, $\kappa = \tau/\tau_B$ is plotted in the form of a histogram. The Fig. 27 (*Left*) shows such a histogram for $L = 40$, as a normalized probability density, and Fig. 27 (*Right*) shows the same for $L = 80$.

One observes that there is a rapid decrease of the width, a concomitant increase of the peak value (becoming δ-function-like), and a slow but steady decrease in the position (median) of the peak of the distribution of κ, as L increases. We need to compute these quantities for a large number of configurations (of each L), to get a good statistic for the process. Our current study gives a strong hint that the width of the distribution vanishes. The times τ_B and τ are two important time-scales in any breakdown process. In the RRTN model, the ratio $\kappa = \tau/\tau_B$ approaches a near-constant value of about 1.6 (see Fig. 28) for a given disorder ($p = 0.35$) and an external field ($E = 2.0$). This trend prompts us to conclude that only one independent time-scale exists, in the class of ductile failure-like phenomena (akin to the appearance of broken or activated nonlinear t-bonds, scattered across the whole system, under force).

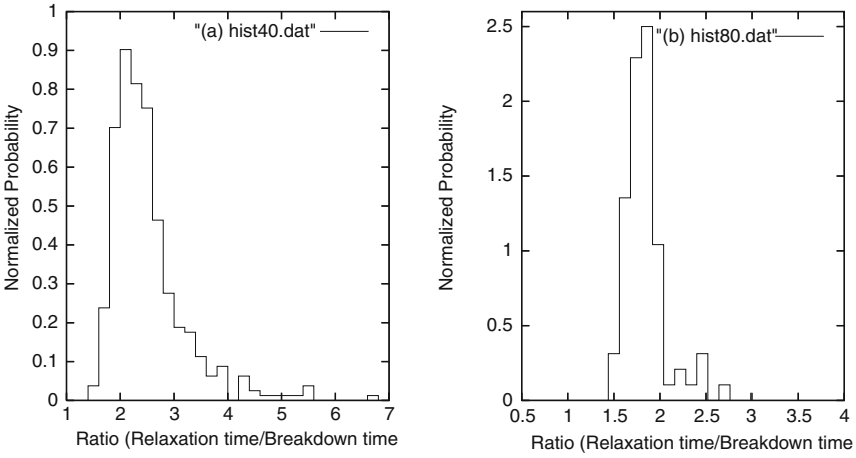

Fig. 27. *Left*: The histogram of the ratio of two time scales, $\kappa = \tau/\tau_B$, for an external field of $E = 2.0$, $p = 0.35$ and square lattice RRTN's of $L = 40$; and *Right*: the same for $L = 80$

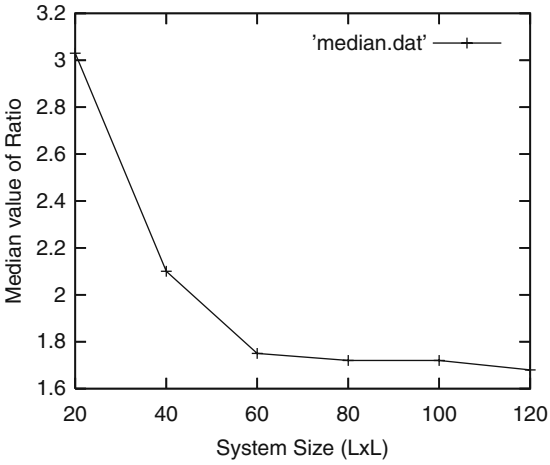

Fig. 28. The median value of $\kappa = \tau/\tau_B$ as a function of the size L of square lattices. With a strong finite-size effect κ attains its asymptotic value very fast. It indicates that τ_B of a large system may be predicted, if steady state τ is known

9 Summary and Further Works

We have presented above the details of the genesis and development of a semi-classical percolation (insulator-metal) transition model as a driven system. We stress that though we had named it as the Random Resistor cum Tunnelling-bond Network (RRTN) model for historical reasons, the word *tunnelling* is not restrictive as far as its application to various natural systems are concerned. The 'tunnelling' elements are simplified here basically as two-level systems with a threshold force for the appearance of an appropriate response (or, its absence), electrical or otherwise, of some of its microscopic constituents. Just like Zener diodes in electrical composites or granular systems, frictional surfaces in rigid mechanical systems, viscous forces in high viscosity fluid systems, or capillary forces in non-viscous fluid flow through (microscopic) porous media may serve as examples. Clearly, the microscopic threshold of activity is at the heart of a macroscopic threshold or, *breakdown* field, if it exists, for the whole system from one phase into another. If the threshold response pattern of the microscopic constituents is reversible, then the macroscopic system also has an onset threshold field for (reversible) breakdown or of nonlinear response.

The origin of ultra-low percolation threshold in semi-classical electrical composites has been studied using the maximal RRTN network with only nearest neighbour hopping. We have also studied the nonlinear response characteristics and some aspects of the statics and the dynamics of (reversible) breakdown phenomenon in the RRTN model. Further, the fully statistically correlated (i.e. deterministic) positioning of the nonlinear t-bonds in an underlying random resistor network (RRN) gives rise to quantum coherence type effects in the RRTN at low concentration or at low external fields (electrical or thermal). We observe the failure of self-averaging of conductance at low electric fields (zero temperature), or anomalous variable range

hopping (VRH) conductance at low temperatures as the manifestations of this coherence. For the same reason, the system shows very strong memory effects. They give rise to the ubiquitous two initial (inverse) power-law relaxations, as observed in many natural phenomena, driven far-away from equilibrium or steady state and allowed to relax. Such a strong memory and recognition of quite random configurations could be very useful in the field of cognitive processes and fault-tolerant coding [113]. Obviously, this effect should be visible in the dynamical hysteresis phenomenon as well in the RRTN, under the action of an external alternating field with a time-period less than the relaxation time of the system. Indeed, some intriguing (unconventional) dynamic hysteresis loops have been observed in the RRTN and further studies continue [114].

Acknowledgements

The author gratefully acknowledges the extended support of the AS-ICTP, in particular through a Senior Associateship, with which much of the ideas and detailed presentations were sorted out through one and a half decades of association. This review is based on collaborations with A. Kar Gupta, P.P. Ray, S. Bhattacharya and S. Mozumdar. The author is especially thankful to D. Bergman, L.G. Benguigui, B.K. Chakrabarti, M. Barma, A. Hansen, K.K. Bardhan, S. Shenoy, H.J. Herrmann, and A. Das among many others, for useful discussions.

References

1. S.A. Wolf, D.U. Gubser, and Y. Imry, Phys. Rev. Lett. **42**, 324 (1979) 22, 44
2. D.S. Fisher, Phys. Rev. Lett. **68**, 670 (1983) 22, 44
3. M. Kardar. In: *Dynamics of Fluctuating Interfaces and Related Phenomena*, ed by D. Kim, H. Park, and B. Kahng, p. 30 (World Scientific, Singapore, 1997) 22, 44
4. Y. Gefen, W.-H. Shih, R.B. Laibowitz, and J.M. Viggiano, Phys. Rev. Lett. **57**, 3097 (1986) 22, 23, 25, 28, 42, 44, 67
5. R.M. Bradley, D. Kung, P.N. Strenski, and S. Doniach, Physica B **152**, 282–287 (1988) 22
6. R. Heemskerk and T.M. Klapwijk, Phys. Rev. B **58**, R1754–R1757 (1998) 22, 25
7. Z. Yao, H.W. Ch. Postma, L. Balents, and C. Dekker, Nature **402**, 273–276 (1999) 23
8. D. Porath, A. Bezryadin, S. de Vries, and C. Dekker, Nature **403**, 635–638 (2000) 23
9. M. Sahimi and J.D. Goddard, Phys. Rev. B **32**, 1869–1871 (1985) 23
10. L. Benguigui and P. Ron, Phys. Rev. Lett. **70**, 2423–2426 (1993) 23
11. M. Sahimi. In. *Annual Reviews of Computational Physics II*, ed by D. Stauffer, p. 175 (World Scientific, Singapore, 1995) 23
12. L. de Arcangelis, S. Redner and H.J. Herrmann, J. Physique Lett. **46**, L585–L590 (1985) 23, 68

13. L.K.H. van Beek and B.I.C.F. van Pul, Carbon **2**, 121 (1964) 23
14. G.E. Pike and C.H. Seager, J. Appl. Phys. **48**, 5152 (1977) 23
15. E.K. Sichel, J.I. Gittelman, and P. Sheng, Phys. Rev. B **18**, 5712 (1978) 23
16. M. Prester, E. Babić, M. Stubičar, and P. Nozar, Phys. Rev. B **49**, 6967 (1994) 23
17. G.D. Mahan, Lionel M. Levinson, and H.R. Philipp, J. Appl. Phys. **50**, 2799 (1979) 23
18. I. Balberg, Phys. Rev. Lett. **59**, 1305 (1987) 24
19. J. Robertson, Adv. Phys. **35**, 318–374 (1986) for filamented structure of a-C 24
20. M. Reghu, C.O. Yoon, C.Y. Yang, D. Moses, P. Smith, and A.J. Heeger, Phys. Rev. B **50**, 13931 (1994) 24, 25, 55, 56, 59
21. K.K. Bardhan and R.K. Chakrabarty, Phys. Rev. Lett. **69**, 2559 (1992) 24, 25, 45, 68
22. D. van der Putten, J.T. Moonen, H.B. Brom, J.C.M. Brokken-Zijp, and M.A.J. Michels, Phys. Rev. Lett. **69**, 494 (1992) 24, 55, 56, 59
23. P. Mandal, A. Neumann, A.G.M. Jansen, P. Wyder, and R. Deltour, Phys. Rev. B, **55**, 452 (1997) 24
24. I-G. Chen and W.B. Johnson, J. Mat. Sc. **27**, 5497 (1992) 25, 27, 28, 39, 40, 43
25. A.J. Rimberg, T.R. Ho, and J. Clarke, Phys. Rev. Lett. **74**, 4714 (1995) 25, 42
26. M. Aertsens and J. Naudts. In: *Phase Transitions in Soft Condensed Matter*, ed by T. Riste and D. Sherrington, NATO ASI Series B: Physics, **211** (Plenum, New York, 1990) 25
27. R.K. Chakrabarty, K.K. Bardhan, and A. Basu, J. Phys.: Condens. Matt. **5**, 2377 (1993) 25, 28, 51
28. J.P. Clerc, G. Giraud, J.M. Laugier, and J.M. Luck. In: *The Electrical Conductivity of Binary Disordered Systems, Percolation Clusters, Fractals and Related Models*, Adv. Phys. **39**, 191–309 (1990) 25, 46, 51, 54
29. See the articles in *Percolation Structures and Processes*, ed by G. Deutscher, R. Zallen, and J. Adler, Annals of the Israel Physical Society, **5** (1983) 25
30. D.J. Bergman and D. Stroud. In: *Solid State Physics: Advances in Research and Applications*, ed by H. Ehrenreich and D. Turnbull, pp. 148–269 (Academic Press, New York, 1992) 25
31. See the articles in *Proceedings of the Fourth International Conference on Electrical Transport and Optical Properties of Inhomogeneous Media*, ed by A.M. Dykhne, A.N. Lagar'kov, and A.K. Sarychev, Physica A **241**, 1–452 (1997) 25, 46
32. *Hopping and Related Phenomena*, ed by H. Fritzsche and M. Pollak (World Scientific, Singapore, 1990) 25
33. *Hopping Transport in Solids*, ed by M. Pollak and B. Shklovskii (Elsevier, North Holland, 1991) 25
34. *Fourth International Conference on Hopping and Related Phenomena*, Marburg 1991, ed by H. Bottger, Phil. Mag. B **65**, 593–894 (1992) 25
35. J.C. Dyre and T.B. Schroder, Rev. Mod. Phys. **72**, 873–892 (2000) 25, 46, 51
36. V.M. Shalaev, Phys. Rep. **272**, 61 (1996) 25, 51
37. A. Ghosh and M. Sural, Europhys. Lett. **47**, 688–693 (1999) 25, 51
38. A. Dutta, T.P. Sinha, and S. Shannigrahi. Dielectric relaxation and electronic structure of CaFeSbO3. Phys. Rev. B **76**, 155113 (2007) 25, 51

39. A. Dutta, C. Bharti and T.P. Sinha. AC conductivity and dielectric relaxation in CaMgNbO3. Mater. Res. Bull., doi:10.1016/j.materresbull.2007.05.023 (2007) 25, 51
40. N.F. Mott, J. Non-Cryst. Solids **1**, 1 (1968) 25, 55
41. V. Ambegaokar, B.L. Halperin, and J.S. Langer, Phys. Rev. B **4**, 2612 (1971) 25, 55
42. L. Benguigui and P. Ron. In: *Non-linearity and Breakdown in Soft Condensed Matter*, ed by K.K. Bardhan, B.K. Chakrabarti, and Alex Hansen, Lecture Notes in Physics, **437**, 221–234 (Springer, Berlin, 1994) 26, 68, 69, 72
43. A.K. Sen and A. Kar Gupta. In: *Non-linearity and Breakdown in Soft Condensed Matter*, ed by K.K. Bardhan, B.K. Chakrabarti, and A. Hansen, Lecture Notes in Physics, **437**, 271–287 (Springer, Berlin, 1994) 27, 29, 37, 41, 44, 48, 67, 70
44. D.A.G. Bruggeman, Ann. Phys. (Leipz.) **24**, 636 (1935) 30
45. R. Landauer, J. Appl. Phys. **23**, 779 (1952) 30
46. S. Kirkpatrick, Rev. Mod. Phys. **45**, 574 (1973) 30
47. P.M. Hui. In: *Non-linearity and Breakdown in Soft Condensed Matter*, ed by K.K. Bardhan, B.K. Chakrabarti, and A. Hansen, Lecture Notes in Physics, **437**, 261–270 (Springer, Berlin, 1994) 30, 45
48. A. Kar Gupta and A.K. Sen, Physica A **215**, 1–9 (1995) 31, 32, 34, 35, 72
49. H.E. Stanley, P.J. Reynolds, S. Redner, and F. Family. In: *Real-Space Renormalization*, ed by T.W. Burkhardt and J.M.J. van Leeuwen, pp. 169–206 (Springer, Berlin, 1982) 32, 33
50. D. Stauffer and A. Aharony. *Introduction to Percolation Theory*, 2nd revised ed. (Taylor and Francis, London, 1994) 33, 34
51. S. Roux and H.J. Herrmann, Europhys. Lett. **4**, 1227 (1987) 35, 42, 71
52. D. Lenstra and R.T.M. Smokers, Phys. Rev. B **38**, 6452 (1988) 43
53. A. Kar Gupta and A.K. Sen, Physica A **247**, 30–40 (1997) 44, 66, 73
54. A.K. Sen, Phys. Rev. Lett. **74**, 1693 (1995) 46
55. A.K. Sen and A. Kar Gupta, Phys Rev B **59**, 9167–9173 (1999) 46, 48
56. M. Pollak. In *Proc. Int. Conf. Semiconductor Physics*, p. 86 (Exeter, 1962) 47, 51
57. A. Kar Gupta and A.K. Sen, Phys Rev B **57**, 3375–3388 (1998) 44, 45, 48, 53
58. A.R. Long. In: *Hopping Transport in Solids*, ed by M. Pollak and B. Shklovskii, pp. 207–231 (Elsevier, North Holland, 1991) 51
59. S. Summerfield and P.N. Butcher, J. Phys. C **15**, 7003 (1982) 51
60. A.K. Sen and S. Bhattacharya. In: *Continuum Models and Discrete Systems*, NATO Sci. Ser. II. Math. Phys. Chem., ed by D. Bergman and E. Inan, **158**, 367–373 (Kluwer Acad. Publ., Dordrecht, 2004); A preliminary study of the VRH in the RRTN was published by: A. Kar Gupta, D. Dan and A.K. Sen. Ind. J. Phys. A **71**, 357 (1997) 55, 58
61. A.L. Efros and B.I. Shklovskii, J. Phys. C **8**, 249 (1975) 55
62. A. Aharony, A.B. Harris, and O. Entin-Wohlman, Phys. Rev. Lett. **70**, 4160 (1993) 55, 56
63. G. Deutscher, Y.-E. Lévy, and B. Souillard, Europhys. Lett. **4**, 577 (1987) 55, 56
64. K. Ogasawara, T. Ishiguro, S. Horiuchi, H. Yamochi, G. Saito, and Y. Nogami, J. Phys. Chem. Solids **58**, 39 (1997) 55, 56, 59
65. Y. Meir, Phys. Rev. B **61**, 16470 (2000) 57, 58

66. P. Debye. Z. Phys. **13**, 97 (1912) 59
67. J.M. Ziman. *Principles of the Theory of Solids*, 2nd. ed., p. 213 (Cambridge Univ. Press, London, 1972) 59
68. H. Scher, M.F. Shlesinger, and J.T. Bendler. Physics Today **44** (1), 26 (1991) 60, 63, 64
69. H. Scher and E.W. Montroll, Phys. Rev. B **12**, 2455 (1975) 60, 63, 64
70. T. Tiedje. In: *Semiconductors and Semimetals* **21C**, ed by J. Pankove p. 207 (Academic, New York 1984) 60
71. G. Pfister, Phys. Rev. Lett. **33**, 1474 (1974) 60
72. F.C. Bos and D.M. Burland, Phys. Rev. Lett. **58**, 152 (1987) 60
73. H.E. Boesch Jr. et al., IEEE Trans. Nucl. Sci. **25**, 1239 (1978) 60
74. W. Feller. *An Introduction to Probability Theory and its Applications*, 2nd ed., p. 258 (John Wiley and Sons, London, 2000) 60
75. R.M. Hill, J. Mater. Sci. **17**, 3630 (1982) 60
76. K. Weron and A. Jurlewicz, J. Phys. A **26**, 395 (1993) 60, 63, 64
77. M. Kuno, D.P. Fromm, H.F. Hamann, A. Gallagher, and D.J. Nesbitt. J. Chem. Phys **112**, 3117 (2000) 60
78. F. Parak and H. Frauenfelder, Physica A **201**, 332 (1993) 60
79. R.H. Austin, K. Beeson, L. Eisenstein, H. Frauenfelder, I.C. Gunsalus, and V.P. Marshall, Phys. Rev. Lett. **32**, 403 (1974) 60
80. C. Tsallis, G. Bemski, and R.S. Mendes. Phys. Lett. A **257**, 93 (1999) 60, 63, 64
81. J. Naudts, Rev. Math. Phys. **12**, 1305 (2000) 60, 64
82. J. Naudts and M. Czachor. In: *Nonextensive Statistical Mechanics and its Applications*, ed by S. Abe and Y. Okamoto, Lecture Notes in Physics **560**, 333–340 (Springer, Berlin, 2001); also available as *arXiv:cond-mat/0108354* (2001)
83. I. Bezprozvanny, J. Watras, and B.E. Ehrlich. Nature (London) **351**, 751 (1991) 60, 64
84. M. Bar, M. Falcke, H. Levine, and L.S. Tsimring, Phys. Rev. Lett **84**, 5664 (2000) 60, 63
85. *Nanomaterials: Synthesis, Properties and Applications*, ed. by A.S. Edelstein and R.C. Cammarata, 1st. paperback ed. (Inst. of Phys. Publ., Bristol, 1998) 61, 63, 64
86. B.B. Mandelbrot, B. Kol, and A. Aharony, Phys. Rev. Lett. **88**, 055501 (2002) 61
87. S. Banerjee and S. Kundu, Surf. Science **537**, 153 (2001) 61, 64
88. F. Omori, J. Coll. Sci. Imp. Univ. Tokyo **7**, 111 (1894) 61, 63
89. M. Shnirman and E. Blanter. In: *Nonlinear Dynamics of the Lithosphere and Earthquake Prediction*, ed by V.I. Kellis-Borok and A.A. Soloviev, p. 67 (Springer Series in Synergetics, Berlin-Heidelberg, 2003) 62
90. H. Nakanishi, Phys. Rev. A **43**, 6613 (1991) 62
91. S. Bhattacharya, P.P. Roy, and A.K. Sen. In: *Proceedings of an Internationl Conference on Applied Mathematics and Mathematical Physics, 2002*, ed by M.A. Hossain and G.D. Roy p. 205 (SUST, Sylhet, Bangladesh 2004) it also appears as: *arXiv cond-mat/0310374* (2003) 62, 64
92. C. Tsallis, M. Gell-Mann and Y. Sato, Proc. Natl. Acad. Sci. **102**, 15377 (2005); also available as *arXiv:cond-mat/0502274v3* (2005) 62, 63
93. C. Beck, Phys. Rev. Lett. **87**, 180601 (2001) 65

94. A.K. Sen and S. Mozumdar. In: *Modelling Critical and Catastrophic Phenomena in Geoscience: A Statistical Physics Approach*, ed by P. Bhattacharya and B.K. Chakrabarti, Lecture Notes in Physics **705**, 507–513 (Springer, Berlin, 2006); for a more detailed and revised version see A.K. Sen and S. Mozumdar. In: Proc. International Symposium on *Continuum Models and Discrete Systems* (CMDS11), Paris, 30 July–3 August, 2007, ed by D. Jeulin and S. Forest, pp. 251–256 (Ecoles des mines de Paris, 2008) 65
95. For example, see the articles in *Statistical Models for the Fracture of Disordered Media*, ed by H.J. Herrmann and S. Roux (North-Holland, Amsterdam 1990); for a more recent and pedagogical review one may consult an advanced text-book: *Heterogeneous Materials II: Nonlinear and Breakdown Properties and Atomistic Modeling*, M. Sahimi (Springer, New York 2003) 65, 66, 74
96. D. Stauffer, Physica A **242**, 1 (1997) 66, 67
97. D.R. Bowman and D. Stroud, Bull. Am. Phys. Soc. **30**, 563 (1985) 66
98. D.R. Bowman and D. Stroud, Phys. Rev. B **40**, 4641 (1989) 66, 67
99. P.M. Duxbury, P.D. Beale, and P.L. Leath, Phys. Rev. Lett. **57**, 1052 (1986) 66, 67
100. P. Ray and B.K. Chakrabarti, J. Phys. C **18**, L185 (1985) 66, 67
101. P. Ray and B.K. Chakrabarti, Solid State Commn. **53**, 477 (1985) 66, 67
102. S.S. Manna and B.K. Chakrabarti, Phys. Rev. B **36**, 4078 (1987) 66, 67
103. P.D. Beale, and P.M. Duxbury, Phys. Rev. B, **37**, 2785 (1988) 66, 67
104. R.B. Stinchcombe, P.M. Duxbury, and P. Shukla, J. Phys. A **19**, 3903 (1986) 66, 67, 69, 71
105. B.K. Chakrabarti, K.K. Bardhan, and P. Ray, J. Phys. C **20**, L57 (1987) 67
106. J.T. Chayes, L. Chayes, and R. Durret, J. Stat. Phys. **45**, 933 (1986) 67
107. A. Kar Gupta and A.K. Sen, J. Stat. Phys. **80**, 1425 (1995) 67
108. S. Bhattacharya and A.K. Sen. Europhys. Lett. **71**, 797–803 (2005) 72
109. N. Ortega, A. Kumar, P. Bhattacharya, S.B. Majumder, and R.S. Katiyar, Phys. Rev. B **77**, 014111 (2008) 62, 63, 74
110. B. Kahng, G.G. Batrouni, S.Redner, L. deArcangelis, and H.J. Herrmann. Phys. Rev. B **37**, 7625–7637 (1988)
111. E.L. Hinrichsen, S.Roux, and A. Hansen, Physica C **167**, 433–455 (1990) 66
112. A. Kar Gupta, PhD thesis, Jadavpur University, Kolkata (1997) 66
113. A.K. Sen. In: *Proceedings of the Fourth International Conference on Natural Computation, Jinan, China, 18–20 October 2008,* ed by M. Guo, L. Zhao, L. Wong, ICNC2008, **3**, 339–343 (Conference Publishing Services, IEEE Computer Society, Los Alamitos, California, 2008) 45
114. S. Bhattacharya, PhD thesis, University of Calcutta, Kolkata (2008)

Quantum Transmittance Through Random Media

A. Mookerjee[1], T. Saha-Dasgupta[1], and I. Dasgupta[2]

[1] S.N. Bose National Center for Basic Sciences, JD-III, Salt Lake City, Kolkata 700098, India
[2] Indian Association for the Cultivation of Science, Raja Subodh Mullick Road, Kolkata 700032, India
abhijit@bose.res.in

1 Introduction

In one electron picture, the electronic states in a crystalline solid are extended Bloch states. This is a direct consequence of the Bloch-Floquet's theorem. These quantum states are labelled by the wave-vector, $\boldsymbol{k}$, and the band index, n. For Bloch states these are good quantum numbers. In a disordered solid, on the other hand, with the breakdown of long-ranged order, the wave-vector, $\boldsymbol{k}$, is no longer a good quantum number. Of course, the states may still be extended, but cannot be characterized by $\boldsymbol{k}$. The seminal paper by Anderson [1] stated that if the disorder is strong enough, all the electronic states become localized and at $T = 0^o$ leads to a metal-insulator transition. He considered a tight-binding Hamiltonian with only on-site disorder characterized by a probability density of width W and a crystalline band-width of, B. Anderson showed that when the dimensionless parameter W/B is greater than a critical value $(W/B)_c$ *all* states in the band of the electron in the disordered lattice are localized.

The presence of these localized states manifests itself in transport properties leading to a vanishing *d.c.*-conductivity at $T = 0^{\rm o}$. When disorder is not strong enough the scattering due to disorder fluctuations is weak and in this limit one expects Boltzmann transport. Calculations in the framework of Boltzmann transport has the important assumption that disorder creates phase incoherence characterized by a mean-free path, ℓ_e (or relaxation time τ_e), while the amplitude of the eigenstates are relatively unaffected. This assumption seems to break down when disorder scattering becomes strong. Now quantum interference effects dominate transport properties and affects both the phase and the amplitude of the wave-functions, eventually, leading to localization. Classically, it is easy to see that disorder on a macroscopic scale can lead to localization by providing enclosed regions with barriers too high for the electrons to surmount. However, quantum mechanical tunnelling should enable the electrons to tunnel through barriers on an atomic scale. This Anderson localization is thought to arise not from failure to cross particular barriers, but rather from the interference of electronic waves scattered by many barriers. This superposition of random phases leads, at some energies, to localized wave-functions. The amplitudes

Mookerjee, A. et al.: *Quantum Transmittance Through Random Media*. Lect. Notes Phys. **762**, 83–107 (2009)
DOI 10.1007/978-3-540-85428-9_3

of these wave-functions are large on just a few atoms and negligible on atoms away from the localization centre. This notion of localization was later extended by Mott [2] and others. They argued that when the parameter $W/B < (W/B)_c$ the states at the tails of the bands are localized. The sharp energy dividing the localized from the extended states was called the *mobility edge* and when changes in pressure, degree of disorder or applied electric field push the Fermi level across these mobility edges, we have a metal-insulator transition.

Disorder leads to scattering, so a disordered metal has a non-zero residual resistivity, ρ_0 at $T = 0^o$ and with increasing disorder ρ_0 also increases. An obvious question is whether ρ_0 increases without limit as the system parameters tend towards the critical disorder (Anderson transition) or whether there is an upper limit (i.e. a minimum metallic conductivity, σ_{min}). Ioffe and Regel [3] and Mott [4] argued that there should indeed be a minimum metallic conductivity when the mean-free path becomes of the order of the lattice spacing or less. In this case, the residual conductivity vanishes discontinuously as some physical parameter attains a critical value. From the localized side however, the localization length is expected to diverge continuously so that the inverse static dielectric constant goes smoothly to zero. Thus, the Anderson transition seems rather strange. Discontinuous when we go from the extended to the localized side, but continuous when we go in the reverse direction.

The one parameter scaling theory of localization [5] questions this idea of a minimum metallic conductivity. This theory argues that near, σ_{min}, quantum interference effects such as coherent back-scattering, produces a negative correction to the diffusion coefficient. This results in depressing σ_{min} to zero and making the transition continuous. The one-parameter scaling theory provides a detailed picture of localization based on the ideas of universal scale dependent conductance in a disordered system and singular back-scattering as a basic mechanism for localization.

2 One Parameter Scaling Theory of Localization

The scaling theory of localization was based on an idea proposed by Thouless [6], regarding the sensitivity of the electronic spectrum in a disordered sample on the boundary conditions on its free surfaces. If δE be the average energy separation between the eigenstates and ΔE the average shift in the energy levels as a result of changing the boundary conditions from periodic to anti-periodic, then the Thouless ratio $\mathcal{T} = \delta E/\Delta E$ can be shown to be the dimensionless conductance of the disordered sample.

$$\mathcal{T} = \frac{\pi\hbar}{e^2} G = g \tag{1}$$

Here G is the conductance and g the dimensionless conductance. In an attempt to define a suitable scaling function, Abrahams et al. [5] tried to relate the energy level sensitivity or the Thouless ratio of a disordered sample of size $[L(1+b)]^d$ to a smaller system with size L^d. Here $L(1+b)$ or L are the lengths of the sides of hyper cube sample in dimension, d and $(1+b)$ is the scaling ratio. They assumed that $\mathcal{T}(L\{1+b\}) = F[\mathcal{T}(L)]$. Finally using the association of this ratio with the dimensionless

conductance: $g(\mathcal{T}[L\{1+b\}]) = g[\mathcal{T}(L)]$. Expressing this in terms of logarithmic derivatives:

$$\beta(g) = -\frac{d\ln(g)}{d\ln(L)} \tag{2}$$

The basic assumption is that the relevant scaling function $\beta(g)$ is a function of conductance g *alone*.

The form of the scaling function indicates that if $\beta > 0$, then as $L \to \infty$, $g \to \infty$. In other words, the problem of the infinite system is one in which the average difference between energy eigenvalues $\delta E \to 0$. The spectrum is then *absolutely continuous* and, therefore, consists of extended states.

On the the hand, if $\beta < 0$, then $g \to 0$ as $L \to \infty$. For such infinite systems, the sensitivity of the spectrum to boundary perturbations measured by $\Delta E \to 0$. This is characteristic of localized states. The relationships between the various criteria for localization have been discussed by Chaudhry and Mookerjee [7].

Assuming that the scaling function is a smooth and monotonic function, together with its known asymptotic behaviour as the main preconditions, the prediction of the scaling theory may be summarized as follows:

(i) For $d \leq 2$ all eigenstates are localized no matter how weak the disorder is.
(ii) For $d > 2$ in, weak disorder the spectrum consists of regions of extended and localized states sharply separated by *mobility edges*. As the strength of disorder increases the mobility edges merge and the entire spectrum becomes localized leading to the Anderson transition.
(iii) Then $d = 2$ is a critical dimension of the problem, below which there is no transition across mobility edges.

The one-parameter scaling hypothesis for the continuous metal-insulator transition across mobility edges seems to be consistent with experiments on the temperature, frequency and magnetic field dependent resistances of disordered systems. Further, the scaling theory was also supported by numerical experiments [8, 9]. However, the microscopic basis of the one-parameter scaling theory and critical behaviour is a matter of continuing debate. The experimental results are complicated by the fact that electron-electron correlation effects are difficult to disentangle from disorder driven localization aspects. However, it is universally accepted that in one-dimensional disordered systems, provided that the hopping term in the Hamiltonian is sufficiently short-ranged, no matter how weak the disorder, all states are exponentially localized. This has been formally proved by Borland in an early work [10]. In three dimensional system, the Mott-CFO picture with extended states near the band centre and localized band tails is generally accepted. The situation at the critical dimensionality of two is not settled to everyone's satisfaction.

3 Transport Mechanisms in Disordered Media

Transport by localized states in disordered systems is dominated by two possible mechanisms:

(i) Thermally assisted tunnelling from one localized state to another by a mechanism known as variable range hopping.
(ii) Resonant tunnelling through localized states [11, 12].

Variable range hopping manifests itself in the temperature variation of the conductivity at low temperatures:

$$g(T) \;=\; \exp\{-(T_0/T)^{\alpha}\}$$

Hopping is characterized by the exponent, α. For Anderson localized states, Mott showed that $\alpha \;=\; 1/(d+1)$. Such behaviour was observed in amorphous Si. However, if the sample length L is smaller than the most probable hopping length R_0, then the contribution from variable range hopping becomes negligible and transport is dominated by resonant tunnelling through localized states. Such resonant tunnelling has been confirmed by experiments [13, 14].

Theoretical interpretation of resonant tunnelling was first put forward by Azbel [11]. He argued that in the strongly localized regime the wave-functions decay exponentially a way from the region of localization. The overlap of such states with the metallic contacts at the two ends of the sample, having length L, are $\exp(-R/\xi)$ and $\exp(-(L-R)/\xi$, where R is the centre of localization and ξ is the localization length. It is now easy to see that unless the localization centre R is near the centre of the sample, one or the other of these overlaps is small. If R is near the centre of the sample, then the two overlaps are almost the same and since transmittance is the ratio of the wave amplitude at the two contacts, it is almost 1 in this case and a resonance sets in.

Pendry [12] suggested a different mechanism by which resonances can take place. He argued that in an otherwise localized regime there may be some probabilistically exceptional *necklace* states with more than one local maxima spanning the material. These necklace states are made out of linear combinations of almost degenerate localized states, but localized in different regions of the sample. These system-spanning states may result in transparent resonances. Pendry has explicitly shown that the line width of the necklace states are much larger than those of Azbel resonances and have argued that they are easier to locate in the spectrum.

Conductivity measurements by Popovich et al. [15] at very low temperatures ($T \;\leq\; 0.1^{\circ}K$) on rectangular metal-oxide field effect transistors show decrease of resistance with length in the resonant tunneling regime (i.e. when the sample length is less than the most probable hopping range). This effect can only be understood on ideas based on Pendry's conjecture about necklace states. Similar resonant states were numerically observed by Basu et al. in one- and Dasgupta et al. in two-dimensional systems.

Although the predictions of the one parameter scaling theory of localization explains the gross features of quantum transport in disordered media, there are several finer points that are not taken into account by the configuration averaging inherent in that theory. There are indications that although the one-parameter hypothesis seems to be correct, the analytic approximations used for the scaling functions have been questioned. Kumar [16] has raised questions regarding the correct choice of the

scaling variable. Analytic work in one-dimension based on the invariant imbedding method by Kumar and Jayannavar [17] and random matrix theory by Muttalib et al. [18] predicted new features arising out of the non-self-averaging aspect of conductance. This is obviously not captured by the one-parameter scaling theory.

The scenario in two and three dimensions is more interesting. Since in these higher dimensions analytic work becomes increasingly difficult, one has to rely on numerical methods. Most of the analysis of existing numerical methods either suffer from the fact that explicit assumptions are made regarding the nature of electronic states or the methods suffer from numerical instabilities. Over the years several numerical investigations have thrown up indications of a transition in $d = 2$ in contradiction to the one-parameter scaling theory. One of the most reliable of these are the work of Haydock and co-workers [19, 20] which indicate a transition from exponentially localized states to algebraically decaying ones. This transition from strongly to weakly localized states is across a pseudo-mobility edge. The work of Kirkpatrick and Eggarter [21] on the Quantum Percolation model, which is a variant of the Anderson model where disorder arises because of the geometry of the lattice, has received much attention. Several recent works have suggested evidence of a transition, which heralds the breakdown of exponential localization.

In $d = 3$, the physics at and close to the mobility edge E_c appears to be interesting. The narrowness of the critical regime and the presence of electron–electron interaction make the comparison with experiment not clear cut. It has been anticipated by Tit and co-workers [22] that as $E \rightarrow E_c$ coherent back-scattering develops into a new kind of states, resonances, before fully developed localized states appear below the mobility edge.

Here we shall review some numerical works to investigate the above probabilities.

4 Some Models of Disordered Systems

4.1 The Anderson Model

The simplest model of a disordered system is the one-band tight-binding model with diagonal disorder. This is the Anderson model introduced in [1]. The Hamiltonian is given by:

$$H \;=\; \sum_i \; \epsilon_i \; a_i^\dagger \; a_i \;+\; \sum_i \sum_j \; t_{ij} \; a_i^\dagger \; a_j . \tag{3}$$

Here, $t_{ij} = t$ if the sites labelled by i and j are nearest neighbours and 0 otherwise. *t* is not random, but the probability density of the diagonal terms is given by:

$$P(\epsilon_i) = \begin{cases} 1/W & -W/2 \leq \epsilon_i \leq W/2 \\ 0 & \text{otherwise.} \end{cases}$$

The simple model incorporates the essential competition between the transfer or hopping term, t and the energy mismatch characterized by W.

4.2 Anderson Model in the Presence of a Magnetic Field

In the presence of an external magnetic field described by a vector potential $\boldsymbol{A}$, Peierls substitution [23] leads to the hopping term gaining a position-dependent phase:

$$H = \sum_i \epsilon_i a_i^\dagger a_i + \sum_i \sum_j t_{ij} \exp\left(-\frac{2\pi i}{\phi_0} \int_i^j \boldsymbol{A} \cdot d\boldsymbol{s}\right) a_i^\dagger a_j. \tag{4}$$

Although the matrix elements of the Hamiltonian are complex, the Hamiltonian is still Hermitian and eigenvalues real.

4.3 The Quantum Percolation Model

In order to study quantum transmittance in a percolating network, one has to set up a Hamiltonian incorporating all the features of a dilute lattice. Let us first consider where both the diagonal and the hopping terms of an Anderson model have binary distributions:

$$P(\epsilon_i) = (1-q)\delta(\epsilon_i - \epsilon_A) + q\delta(\epsilon_i - \epsilon_B)$$
$$P(t_{ij}) = (1-q)\delta(t_{ij} - t_A) + q\delta(t_{ij} - t_B)$$

The probability distributions are characterized by two parameters: the site (or bond) occupation probabilities q and the disorder strength $|\epsilon_A - \epsilon_B|/B$ or $|t_A - t_B|/B$, where B is the band width in the absence of disorder. The special cases with either $\epsilon_A \to \infty$ or $t_A \to 0$ correspond to the site or bond percolation models. In the case of site percolation, an electron that starts off at a B site can percolate through the lattice by hopping only to other B sites. Similarly, for the bond percolation model, an electron starting from any site can percolate through the lattice hopping across t_B bonds alone. The model was first proposed by Kirkpatrick and Eggarter [21] to study quantum transmittance through percolating networks.

The quantum percolation model differs from the standard Anderson model in a number of ways. In the latter, disorder is incorporated by assuming that the diagonal terms of the Hamiltonian have a continuous distribution with a finite variance. The former model, on the other hand, has binary type of disorder, which essentially removes the A sites or A bonds effectively from the lattice as far as percolation goes. The disorder then manifests itself in both the geometrical and the quantum aspects of the model. One expects an interplay between classical percolation and the Anderson transition.

The density of states for the quantum percolation model consists of split bands, with a central spike and a dip around it, where the states are localized [21]. The Anderson transition can only occur through the merging of at least two pairs of mobility edges, as distinct from the standard Anderson model. Pimental and Queiroz [24] have argued that for the site percolation model, all moments of order ≥ 1 of $P(\epsilon_i)$ diverge. For the bond percolation model, all moments of $\ln(t)$ diverge. Now,

there is a theorem which suggests that if moments of the distributions of the Hamiltonian matrix elements diverge then all states are localized in any dimension. This contradicts the conclusion of the one-parameter scaling theory and suggests that the quantum percolation model may belong to a different universality class. On the other hand, numerical work on the model in $d = 3$ indicates transition from extended to localized states. In $d = 2$, there is still controversy about the type of states in the quantum percolation model. This provides a motivation of further study of the quantum percolation model.

In the following section, we shall describe some of the earlier works on the two-dimensional quantum percolation model and discuss the origin of the controversy.

5 Some Earlier Studies on the Quantum Percolation Model

5.1 Real Space Renormalization

The real space renormalization method has been used to study the classical percolation problem extensively. The idea was extended to the quantum problem by Odagaki and Chang [25] and Root et al. [26]. The method of renormalization is based on the fact that near the critical point only the long-ranged fluctuations are important and one can coarse-grain the system by summing up the degrees of freedom in the partition function over small length scales until one reaches the length scale of the correlation length ξ. In this process of coarse graining, the parameters of the Hamiltonian get renormalized and they are related to the old parameters by a transformation $\mathcal{R}$. At the critical point, the system becomes self-similar under renormalization, and $\mathcal{R}$ acting on the Hamiltonian leaves the parameters unchanged. In a classical percolation problem H there is no underlying Hamiltonian. Summing up, the degrees of freedom is obtained by applying the *decimation procedure* directly on the site or bond probabilities on a rescaled lattice, consistent with classical percolation. Finally, assuming the same singular structure for the connectedness length ξ in the renormalized lattice, one can extract the percolation threshold (q_c) and the relevant critical exponents.

For the corresponding quantum problem, the relevant length scale is the localization length. Here the electron percolates when an extended state is formed and the transition is then characterized by the divergence of he localization length. Odagaki and Chang [25] modified the classical transformation rule, relating the renormalized site or bond occupation probability with that of a new concept, namely the *wetting probability*, which is defined as the probability of the state starting at a site i evolves onto a site j quantum mechanically. Using the above methodology they obtained a percolation threshold $q_c = 0.133$ or a site diluted square lattice and 0.235 for the bond diluted square lattice.

Odagaki and Chang's calculations assumed the independent call approximation. They assumed that we start from site and bond occupations probabilities to be independent, even after renormalization, the renormalized sites and bonds are still occupied randomly. This is certainly not true, as correlations tend to build up on

renormalization. The results also suffered from small-cell renormalization. Later the same authors [27] employed large-cell Monte-Carlo renormalization and the percolation probability went down to 0.06. These results were dominated by large fluctuations. This approach could not really establish the existence of a transition in two-dimensions.

5.2 The Scalar Recursion Method

The standard recursion or Lancos tri-diagonalization method has been used by Stein and Krey [28] to study the localization phenomenon. It was later adopted by Raghavan and Mattis [29] for the quantum percolation model. They concluded that in a two-dimensional lattice *all* states are localized. Later, Raghavan [30] looked at the statistical distribution of the recursion coefficients and concluded that $q_c \leq 0.05$.

5.3 The Thouless-Edwards-Licciardello Criterion

The idea of sensitivity to boundary perturbation, which was first introduced by Edwards and Thouless [31] and Licciardello and Thouless [32], has been used by Koslowski and von Neissen [33] for studying the two- and three-dimensional disordered lattices. In the quantum percolation model, in two-dimensions they concluded that there is a signature of weakly (algebraic) localized to strongly (exponential) localized states at $q_c = 0.3$.

5.4 The Slice Recursion Method

McKinnon and Kramer [8, 9] has used the slice recursion method that partitions the system into slices and connects the first to the n-th slice recursively, to study the quantum percolation model. The idea is very similar to vector recursion, the difference is in the partitioning of the system. Here, the lattice is partitioned into slices perpendicular to the direction of the flow of the current. The method then evaluates the Lyapunov exponent and all conclusions about localization or otherwise is drawn from the behaviour of its scaling function.

In practice, the localization length $\lambda(M, q)$ is calculated for a strip of cross-section M and, in analogy to critical phenomena, we assume a scaling form:

$$\frac{\lambda(M,q)}{M} \;=\; f_d\left(\frac{\lambda(\infty,q)}{q}\right).$$

This $\lambda(\infty, q)$ is the characteristic length of a lattice with infinite cross-section, which can be identified with the localization length.

Further calculations by Taylor and MacKinnon [34] confirmed the predictions of the scaling theory of localization. Soukoulis and Grest [35] obtained a form of this scaling function and found this to be in agreement with that of the scaling theory.

The great advantage of this technique is that $\lambda(M, q)$ can be efficiently with arbitrary accuracy. The statistical error can be controlled much better than the direct calculation of conductance. The numerical process is stable and does not require any detailed information of the wave-function to be stored.

However, if we carefully analyze the basic assumptions underlying the slice recursion, we come across several pints that require further discussion. First of all, in order that the relationship between the Green function and the localization length to hold, the lengths of the slices have to be very large. The extrapolation to larger widths was done assuming that the localization length obeys a specific scaling law. However, even the widest slices have narrow strip geometry (256 by 10^4). The possibility of an in-built one-dimensional geometry imposed cannot be ruled out. A more careful analysis by Pastawsky et al. [36] has shown that although on the average all states appear to be exponentially localized in two-dimensions, as we go to larger and larger widths, the proportion of states that decay algebraically also increases. Until more extensive and careful work is done with a full two-dimensional geometry, there will always be room for doubt about the existence of a weak to strong localization transition in two-dimensions.

A second point has been raised by Godin and Haydock [19]. Within the slice recursion the Green function or transfer matrices contain ratios of polynomials, whose orders are comparable to the number of basis sets. A slice recursion for an isolated, but, large slice is a sensitive function of energy with zeroes and poles close to the real-energy axis. Since in the slice recursion very many numbers of greatly differing magnitude are added together, the errors accumulate rapidly as the width of he slices increase.

5.5 The Series Analysis Method

The series analysis method of Harris, Aharony and co-workers [37–39] was based on the fact that the transition between localized and extended states in a percolating cluster is signalled by the divergence of some physical quantities as a function of the occupation probability q. The point of divergence and the exponents related to it were obtained by Padé analysis [40]. Meir et al. [39] obtained what they called the 'quantum mechanical transmittance' $T_{ij}(E, q)$ between two sites, i and j, connected by bonds on a lattice. They ingeniously obtained transmittances of various shapes and sizes of clusters through a recurrence relation between that of a given cluster and those of smaller sizes. They eventually expressed the quantity, $T(E, q) = \sum_{ij} T_{ij}(E, q)$ as a series in q. If the states are exponentially localized, then they argued that

$$T(E, q) \sim \int_a^\infty dr\, r^x\, \exp(-r/\xi) \sim \xi^{x+1}(E, q),$$

where a is the lattice constant. They carried out a Padé analysis of the series for $T(E, q)$ and concluded that around $q_c = 0.4$–0.2 for the square lattice, this factor diverges.

However, we first notice that $T(E,q)$ is certainly not the transmittance, which by definition is the proportion of information (energy or charge) that is transmitted by a scattering object. It has to satisfy $0 \leq T(E,q) \leq 1$ for all, q and E. For a exponentially localized state, it is a measure of the localization length. For power law localized states behaving like $r^{-\alpha}$

$$T(E,q) \sim \int_a^\infty dr\, r^{1-\alpha} \to \infty \text{ if } \alpha < 2.$$

Thus the divergence of $T(E,q)$ could just as well herald the breakdown of exponentially decaying states or even that of states decaying faster than r^{-2}.

5.6 Comments

We have shown that although in one and three-dimensions there is no controversy, the body of earlier numerical works cannot completely determine if two is indeed the critical dimensionality with absence of any transition. Some works suggest that all states in two-dimensions are localized, as proposed by the single parameter scaling theory of localization. Others indicate some sort of transition may be from exponentially to algebraically localized states. Conclusive evidence is still missing.

The Table 1 summarizes the main results.

Table 1. Earlier estimates of q_c for the two-dimensional quantum percolation model

Authors	Method	q_c
Odagaki & Chang (1984) [25]	Real space renormalization	0.13
Chang & Odagaki (1987) [27]	Real space renormalization	≤ 0.06
Raghavan (1984) [30]	Scalar recursion	0.0–0.3
Koslowski & von Neissen (1990) [33]	Thouless-Edwards	0.3
Taylor & McKinnon (1989) [34]	Slice recursion	0.0
Soukoulis & Grest (1991) [35]	Slice recursion	0.0
Pastawski et al. (1983) [36]	Slice recursion	< 0.9

This encourages further study, perhaps using different techniques. One such study will be the subject of the following section.

6 The Vector Recursion Method and Its Applications

6.1 The Method

The vector recursion method was introduced by Godin and Haydock [19], although a version of this had been briefly described by Haydock earlier [41]. The system under study consists of a two- or three-dimensional lattice with $2N$ sites on which a quantum percolation Hamiltonian is described. We attach $2M$ perfectly conducting

leads to two opposing ends of the system. The system is then arranged in a circuit so that M of the leads act as incoming leads for electronic current and M of them act as outgoing leads. The quantum circuit is shown in Fig. 1.

If the basis $\{|m\rangle\}$ spans the sample, and $\{|m'\}$ spans the leads, then:

$$H_{sample} = \sum_{m=1}^{2N} \epsilon_m |m\rangle\langle m| + \sum_{<m,n>} t_S |m\rangle\langle n|$$

$$H_{leads} = \sum_{<m',n'>} t_L |m'\rangle\langle n'|.$$

Here, $< m, n >$ refer to nearest neighbour sites only. If we substitute the form, $\Psi_L = \sum_{m'} A \exp(\pm im\phi)$ into the Schrödinger equation for the leads we get (after a simple manipulation):

$$2t_L \cos\phi = E \quad \Rightarrow \quad \phi = \cos^{-1}\left(\frac{E}{2t_L}\right).$$

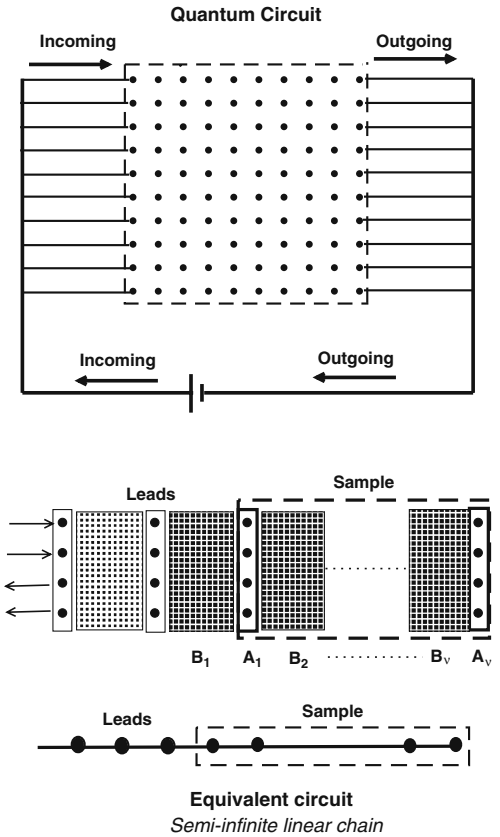

Fig. 1. *Top*: The quantum circuit with $2N$ sites and M-incoming and M-outgoing leads; *Bottom*: the equivalent circuit after vector recursion

Thus, ϕ will be real or there will be propagating waves in the leads, if $-2t_L < E < 2t_L$. Similarly, for the site percolation model, these states will propagate through the sample and reach the other lead only if $\epsilon_{min} - 2t_S < E < \epsilon_{max} + 2t_S$. The parameter t_L in the leads is so chosen that we have propagating waves both in the leads and in the sample. Note that the diagonal terms in the leads are taken to be zero, thus setting the zero of the energy scale. We may set the hopping element t_S of the sample to be 1, thus setting the scale of energy. For the bond percolation model there will be propagating waves if: $\epsilon - 2(t_S)_{max} < E < \epsilon + (t_S)_{max}$. Here we cannot set t_S to be 1.

When the electronic wave enters through the incoming leads and travels through the sample, it is scattered by its random potentials. Part of it is reflected back into the incoming leads and part of it gets transmitted away into the outgoing leads. Let us denote the reflection coefficient of the wave entering through the *n-th* incoming lead and reflected into the *m-th* incoming lead by $r_{nm}(E)$, and the transmission coefficient of the wave entering through the *n-th* incoming lead and transmitted into the *m-th* outgoing lead by $t_{nm}(E)$.

The first step is to change to a new basis of representation in which the Hamiltonian is block tri-diagonal. Representations in the old basis are column vectors of length $2N$. In the new basis, representations are matrices of size $2N \times 2M$ and the Hamiltonian becomes a $\nu \times \nu$ array of $2M \times 2M$ matrices. Here $\nu = 2N/2M$. The new basis is constructed as follows:

To start with we fix:

$$|\Phi_1\} = (|i_1\rangle, |i_2\rangle, \ldots |i_M\rangle, |o_1\rangle, |o_2\rangle \ldots |o_M\rangle)$$

where $|_k\rangle$ and $|o_k\rangle$ are the positions at which the M-incoming and M-outgoing leads are attached to the sample. The representation of each of these kets is a column vector of length $2N$.

The subsequent basis members are generated recursively as:

$$|\Phi_2\} = |\Phi_1\}(H - \mathbf{A}_1)$$

and for $n > 1$

$$|\Phi_{n+1}\}\mathbf{B}_{n+1} = |\Phi_n\}(H - \mathbf{A}_n) - |\Phi_{n-1}\}\mathbf{B}_n^{\dagger}.$$

The matrix inner product is a $2M \times 2M$ matrix defined as:

$$\{\Psi|\Phi\}_{nm} \; = \; \sum_{i=1}^{2M} \Psi_{mi}^{*} \Phi_{ni}$$

and orthonormality as $\{\Psi|\Phi\} = I$. It can easily be shown that if we, demand orthonormality of the new basis we get: $\mathbf{A}_n = \{\Phi_n|H|\Phi_n\}$. $\mathbf{B}_{n+1}$ and $|\Phi_{n+1}\}$ are disentangled by using Gram-Schmidt procedure to make sure that the column vectors of the matrix $|\Phi_{n+1}\}\mathbf{B}_{n+1}$ are themselves orthonormal to one another.

In this new basis, the matrix representation of the Hamiltonian H is block tri-diagonal. The $\mathbf{A}_n$ are the diagonal blocks, while $\mathbf{B}_n$ and $\mathbf{B}_n^\dagger$ are the sub- and super-diagonal blocks, each of dimension $2M \times 2M$. All other elements are zero matrices. We may block tri-diagonalize the leads as well, with the the same starting state $|\Phi_1\}$. The two block matrices may now be joined at the starting state to form the equivalent circuit, which has the same transmittance as the original circuit (see Fig. 1).

In this new basis, we may expand the wave-function within the sample:

$$|\Psi\} \;=\; \sum_n \Psi_n \, |\Phi_n\},$$

where $\Psi_n \;=\; \{\Psi|\Phi_n\}$ is the projection of the wave-function onto the basis $|\Phi_n\}$. The boundary conditions on the wave-function at the junctions, where the leads meet the sample are:

$$\Psi_0 = \begin{pmatrix} 1 + r_{11} + r_{21} + \ldots + r_{M1} \\ 1 + r_{12} + r_{22} + \ldots + r_{M2} \\ \cdots\cdots \\ t_{M+1,1} + t_{M+2,1} + \ldots + t_{2M,1} \\ \cdots\cdots \\ t_{M+1,2M} + t_{M+2,2M} + \ldots + t_{2M,2M} \end{pmatrix}$$

$$\Psi_1 = \begin{pmatrix} \mathrm{e}^{-i\phi} + \mathrm{e}^{-i\phi} r_{11} + \mathrm{e}^{-i\phi} r_{21} + \ldots + \mathrm{e}^{-i\phi} r_{M1} \\ 1 + \mathrm{e}^{-i\phi} r_{12} + \mathrm{e}^{-i\phi} r_{22} + \ldots + \mathrm{e}^{-i\phi} r_{M2} \\ \cdots\cdots \\ \mathrm{e}^{-i\phi} t_{M+1,1} + \mathrm{e}^{-i\phi} t_{M+2,1} + \ldots + \mathrm{e}^{-i\phi} t_{2M,1} \\ \cdots\cdots \\ \mathrm{e}^{-i\phi} t_{M+1,2M} + \mathrm{e}^{-i\phi} t_{M+2,2M} + \ldots + \mathrm{e}^{-i\phi} t_{2M,2M} \end{pmatrix}. \tag{5}$$

Let us now generate a sequence of matrices $\{\mathbf{X}_n\}$ and $\{\mathbf{Y}_n\}$ that are the two linearly independent solutions of the second order difference equation:

$$\mathbf{Z}_{n+1}\mathbf{B}_{n+1} \;=\; \mathbf{Z}_n(H - \mathbf{A}_n) - \mathbf{Z}_{n-1} \tag{6}$$

with independent boundary conditions:

$$\begin{aligned} \mathbf{X}_0 &= \mathbf{I} \quad \text{and} \quad \mathbf{X}_1 = \mathbf{0} \\ \mathbf{Y}_0 &= \mathbf{0} \quad \text{and} \quad \mathbf{Y}_1 = \mathbf{I}. \end{aligned}$$

This new basis terminates after ν steps, where $\nu = 2N/2M$ since the rank of the space spanned by the two bases remains unchanged. In the absence of disorder, symmetry of the starting state may indeed restrict the new basis to a subspace of the original vector space spanned by $\{|i\rangle\}$. So, ν may be $\leq \; 2N/2M$. However, in the presence of disorder such symmetry is usually violated. This gives another boundary condition:

$$\mathbf{X}_\nu \Psi_0 \;+\; \mathbf{Y}_\nu \Psi_1 \;=\; 0. \tag{7}$$

We now carry out the same analysis interchanging the incoming and outgoing leads. We get another set of reflection and transmission coefficients $r'_{nm}(E)$ and $t'_{nm}(E)$. We club them together into an scattering **S**- matrix:

$$\mathbf{S} = \begin{pmatrix} r_{11} & r_{21} & \dots & r_{M1} & t'_{1,2M} & \dots & t'_{M,2M} \\ \vdots & \vdots & & \vdots & \vdots & & \vdots \\ r_{1M} & r_{2M} & \dots & r_{M,M} & t'_{1,M+1} & \dots & t'_{M,M+1} \\ t_{1,M+1} & t_{2,M+1} & \dots & t_{M,M+1} & r'_{1,M} & \dots & r'_{M,M} \\ \vdots & \vdots & & \vdots & \vdots & & \vdots \\ t_{1,2M} & t_{2,2M} & \dots & t_{M,2M} & r'_{11} & \dots & r'_{M,1} \end{pmatrix}.$$

This scattering matrix is given by:

$$\mathbf{S} = \left(\mathbf{X}_{\nu+1} + \mathbf{Y}_{\nu+1}\mathrm{e}^{-i\phi}\right)^{-1}\left(\mathbf{X}_{\nu+1} + \mathbf{Y}_{\nu+1}\mathrm{e}^{i\phi}\right). \tag{8}$$

The reflectance and transmittance, which measure the proportion of charges that are reflected and transmitted because of scattering by the sample, are given by:

$$\begin{aligned} R(E) &= \frac{1}{M}\sum_{n\in I}\sum_{m\in I}|r_{nm}(E)|^2 \\ T(E) &= \frac{1}{M}\sum_{n\in I}\sum_{m\in O}|t_{nm}(E)|^2, \end{aligned} \tag{9}$$

I and O are the set of incoming and outgoing leads. We should note that if we calculate reflection and transmission coefficients for the case when the incoming and outgoing leads are interchanged, they differ from the original case only by phases. This means that the reflectance and transmittances remain the same. Moreover, because the scattering is elastic we have the sum rule:

$$R(E) + T(E) \;=\; 1.$$

The stability of the recursion method has been described in some detail by Haydock and coworkers [42]. The gradual loss of orthogonality as recursion proceeds can be compensated by orthogonalizing at intermediate steps. This slows down the programme considerably. Haydock has suggested that we may just as well work with non-orthogonal bases, where loss of orthogonality is not a problem. Gradual loss of weight onto groups of basis functions is another problem. This has been tackled by the so called *dynamic recursion* by Haydock [43, 44]. In summary, the vector recursion technique is a fast and accurate numerical technique to obtain transmittance with great numerical precision.

6.2 Finite Size Scaling Studies

Finite size scaling attempts to answer the question of how various physical quantities of interest behave near the percolation threshold in a large but finite lattice. In classical percolation, for example, we study the way in which the probability $R(q, L)$ that

a lattice of linear dimensions L percolates at a concentration q. Classically, a lattice percolates if there is a connected cluster connecting two surface points. In an infinite lattice, R changes from 0 to 1 across the percolation concentration q_c. Aharony and Stauffer [45] suggested an ansatz for a suitable scaling function Φ such that:

$$R(q, L) \;=\; \Phi\left((q - q_c)L^{1/\nu}\right)$$

for large L and q close to q_c. This function is a step function for the infinite system and for a finite system it increases from 0 to 1 asymptotically. Similarly,

$$\frac{dR}{dq} \;=\; L^{1/\nu}\Phi'\left((q - q_c)L^{1/\nu}\right).$$

This function becomes a delta function at q_c as the size of the system becomes infinite. Figure 2 shows these functions as functions of q.

The average concentration, q_{av} at which, for the first time, a percolating cluster connects two surface sites of the lattice is defined as:

$$q_{av} \;=\; \int_0^1 dq\, q\frac{dR}{dq}.$$

It is easy to see from the above that with the substitution $z = (q - q_c)L^{1/\nu}$ that the effective threshold q_{av} for a system of size L approaches the asymptotic q_c as:

$$q_{av} - q_c \propto L^{-1/\nu}.$$

This suggests that the variation of q_{av} with system size L is one method of determining the critical exponent ν. We plot $q_{av}\ vs\ L^{-1/\nu}$ for various trial values of ν and select that value of ν, which gives the best straight line fit for large L.

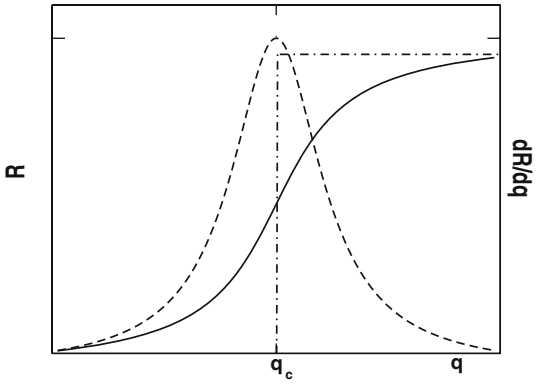

Fig. 2. Variation of the connectedness probability $R(q, L)$ and its derivative with respect to q. The width of the derivative varies as $L^{-1/\nu}$ [45]

The width of the transition function is given by:

$$\Delta^2 = \int_0^1 dq\,(q - q_{av})^2\,\frac{dR}{dq}$$

It is easy to note that $\Delta \propto L^{-1/\nu}$ and finally we note that $\Delta \propto (q_{av} - q_c)$, so that the intercept of the plot of Δ vs q_{av} gives q_c.

The existence of a system-spanning cluster is a necessary and sufficient condition for classical percolation. On the contrary, simple classical connectivity does not assure non-zero quantum transmittance. An infinite system-spanning cluster is characterized by backbone and dangling bonds with dead ends. Classical transport can take place only in the backbone and the dangling bonds play no role in the percolation process. For quantum transport, however, both the backbone and the dangling bonds are equally important. Whenever a particle percolating through the backbone enters a dangling bond and meets a dead end, it suffers scattering. An important fallout of this disorder induced scattering is the phenomenon of coherent back-scattering [46]. As long as the scatterings are elastic and time-reversal invariant, the scattered waves in the backward direction are coherent in time and constructively interfere. For large enough scattering strengths, this back-scattering corrections may reduce the diffusion constant to zero in an infinite lattice. It is not difficult to anticipate that the quantum threshold q_c^Q may be different from the classical one q_c. For a quantum system, the criterion for percolation is not the existence of a system-spanning cluster but a finite quantum transmittance across the sample. All the arguments of finite size scaling discussed earlier have to be translated in terms of quantum transmittance $T(E, q, L)$ rather than $R(q, L)$.

We shall calculate the quantum transmittance using the vector recursion method described in the preceding section. We shall attach semi-infinite, perfectly conducting leads on either side of the sample, described by the Hamiltonian of a quantum percolation model. Our systems will be square blocks of the size L^2 and we shall restrict ourselves to square geometry alone, avoiding any strip geometry. We shall consider the system to be percolating if we register a finite transmittance within our error bars.

Figure 3 (Top) shows the configuration averaged transmittance as a function of bond dilution q for three different size 3×3, 5×5 and 9×9 squares. We choose an energy for the incoming electrons suitably such that progressive waves travel through the perfect leads ($E = 0.5$). We vary q from 1 to 0 in small steps 0.01 until we obtain the first $q(L)$ at which the transmittance $T(E, q, L) >$ a tolerance level (chosen by us to be 10^{-3} consistent with our accuracy limits). We repeat this for at least 100 random configurations and calculate the averaged $q_{av}^Q(L)$ and the deviation Δq^Q for each size.

We note that for a finite size (L) the transmittance $T(E, L) > 0$ whenever the characteristic length $\xi \simeq L$. Assuming the $\xi \simeq (q - q_c)^\nu$ we get an effective percolation threshold $q_{av}^Q(L)$ when $\xi = L$. Invoking the finite size scaling ansatz:

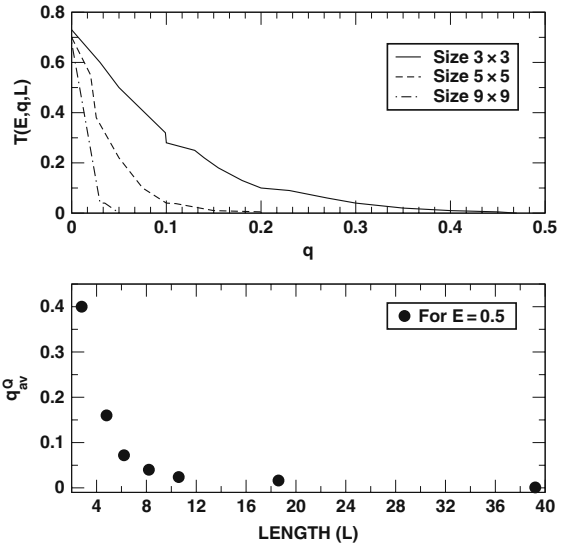

Fig. 3. *Top*: Averaged transmittance $T(E, q, L)$ vs q for three different sizes characterized by L and for the energy of the incoming electron $E = 0.5$ (in units of the hopping t). *Bottom*: Variation of the quantum threshold q_c^Q as a function of size L

$$L = A(E)\left[q_{av}^Q(L,E) - q_c^Q\right]^{-\nu}$$
$$\lim_{L\to\infty} q_{av}^Q(L) = q_c^Q$$
$$\Delta q^Q = B(E)L^{-1/\nu} \qquad .$$

So we eliminate L from the above and obtain q_c^Q as the y-intercept of the plot of q_{av}^Q vs Δq^Q. This is shown in Fig. 4. The intercept should have been at 0.4 had the

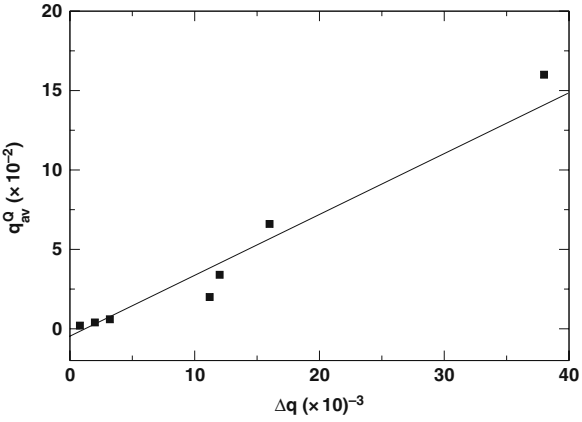

Fig. 4. The plot of q_{av}^Q vs Δq^Q

estimates of Meir et al. [38] been correct and heralded a true delocalization transition. Our estimate of the quantum percolation threshold, consistent with our accuracy threshold is 0, consistent with the one parameter scaling predictions.

In all cases, the transmittance increases as bond dilution probability decreases and becomes almost 1 at zero bond dilution. It is not exactly 1 since even in this case there is some scattering at the junction of the perfect leads and the lattice. For large sizes $T(E, q, L) \rightarrow T_0\delta(q)$, which is the asymptotic limit, indicating that probability $q_c = 0$ for this model.

The Fig. 5 shows the log-log plot of $q_{av}^Q(L)\ vs\ L$.The least square fit line yields an index $\nu \sim 0.48$.To get a more accurate estimate, we plot $q_{av}^Q\ vs\ L^{-1/\nu}$ for varying ν until the intercept passes through the origin. This gives an index $\nu = 0.5$. We have carried out similar calculations for a series of different incoming energies, $E = 0, 0.75, 1\ and\ 1.5$. Our results are qualitatively the same. The percolation threshold remains at $q_c^Q = 0$ and the index $\nu \sim 0.5$.

The conclusion from the finite size scaling indicates that $d = 2$ is indeed the critical dimensionality. Even the smallest of disorders completely localizes the entire spectrum for the quantum percolation model in this dimension. Our conclusion is that the quantum percolation model belongs to the same universality class as the Anderson model and the predictions of the one parameter scaling theory seems to hold good for this model as well. A look at the percolating cluster near the classical percolation threshold shows that in addition to the backbone there are also a large

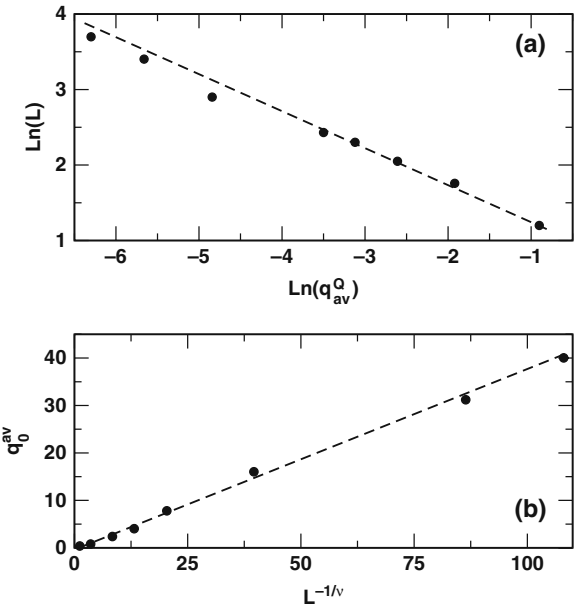

Fig. 5. *Top*: The log-log plot of $q_{av}^Q(L)\ vs\ L$. The line is a least square fit. *Bottom*: Plot of $q_{av}^Q\ vs\ L^{-1/\nu}$

number of dangling site chains with dead ends. These side chains scatter a wave propagating through the backbone and the consequent coherent back-scattering localizes the wave.

6.3 Block Renormalization of Transmittance in Quantum Percolation Model

Let us introduce ideas of scaling very similar to the Kadanoff block spin formalism. We shall divide up the lattice into rectangular blocks of size $M_1 \times M_2$. An isolated block is shown in the lower line of Fig. 6. The bonds attaching this isolated block to the lattice now act as input and output leads into and out of the block. This is shown in the top line of Fig. 6. The input leads bring in an electronic wave from the rest of the lattice into the block, which then scatters it. The output leads take away the transmitted wave into the rest of the lattice. We shall use the vector recursion technique to calculate the scattering S-matrix of this block. Our output will be the transmittance and reflectance of the scattering block. The next crucial step is to obtain a single scatterer that will yield the same transmittance and reflectance as the block. This is shown schematically in the bottom line of Fig. 6. Since we are interested only in the scattering characteristics of the system and not in the detailed wave-function characteristics of the lattice, the replacement of the block by a single equivalent scatterer is justified. Both the block and the single scatterer yield the same transmittance and reflectance. This single scatterer is characterized by a Hamiltonian $\hat{\epsilon} a_I^\dagger a_I$ and attached to the leads with Hamiltonian $\sum_J \; t\, a_I^\dagger a_J$. Note that the idea is very similar to Kadanoff block spin scaling. There we replace a block of spins by a single spin in such a way that the free energy remains unchanged. Here, we replace a block of scatterers by a single scatterer in such a way that the transmittance or reflectance remains unchanged.

To obtain $\hat{\epsilon}$, we carry out vector recursion on the system shown at the right-hand end of the top line of Fig. 6. This can be done by hand:

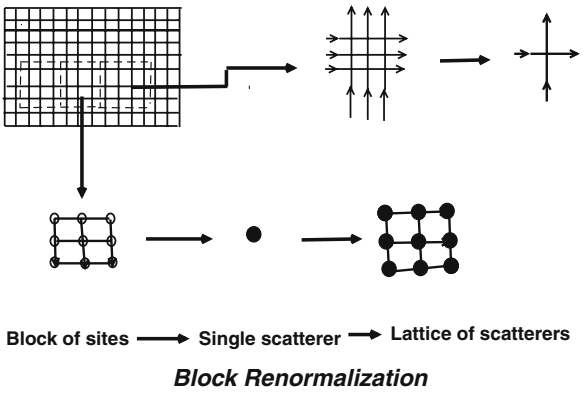

Fig. 6. Block scaling applied to a square lattice

$$A_1 = \begin{pmatrix} \hat{\epsilon} & t \\ t & 0 \end{pmatrix} \qquad B_1 = \begin{pmatrix} t & 0 \\ 0 & t \end{pmatrix}$$
$$B_2^\dagger X_2 = \begin{pmatrix} -t & 0 \\ 0 & -t \end{pmatrix} \qquad B_2^\dagger Y_2 = \begin{pmatrix} E - \hat{\epsilon} & -t \\ -t & E \end{pmatrix}.$$

The S-matrix is given by:

$$S = -\left[B_2^\dagger X_2 + B_2^\dagger Y_2 \exp(-i\theta)\right]^{-1} \left[B_2^\dagger X_2 + B_2^\dagger Y_2 \exp(i\theta)\right].$$

Thus, the reflection and transmission coefficients are given by:

$$r(E) = S_{11} = \frac{(E - \hat{\epsilon} + tE)\exp(-i\theta) - (E - \hat{\epsilon})E}{\Delta}$$
$$t(E) = S_{12} = \frac{2it^2 \sin(\theta)}{\Delta}$$
$$\Delta = \det\left[B_2^\dagger X_2 + B_2^\dagger Y_2 \exp(-i\theta)\right].$$

Finally we get,

$$\hat{\epsilon}_I = \sqrt{\rho(4t^2 - E^2)},$$

where $\rho = r(E)/t(E)$ calculated from the vector recursion of the $M_1 \times M_2$ block.

Since the different blocks involve different and interdependently random Hamiltonian matrix elements, these effective $\hat{\epsilon}$ are also random and independent. We now connect them back by leads into a self-similar square lattice as shown in the rightmost figure on the bottom row of Fig. 6. We go on repeating the procedure. At each stage of this renormalization the vector recursion simply involves a square scatter of the size $M_1 \times M_2$, but will give information about the scattering characteristics of increasingly larger systems of sizes $(M_1 \times M_2)^n$.

The Fig. 7 shows how the distribution of scattering elements evolves under renormalization. The distribution is obtained by running the vector recursion for up to 500

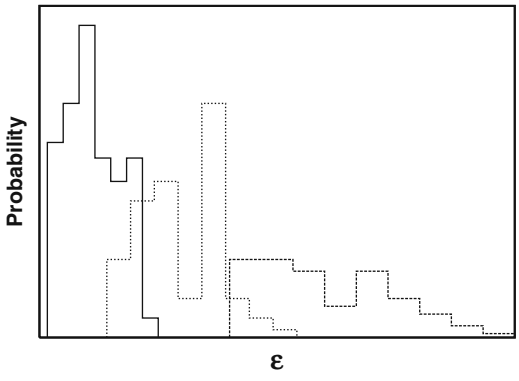

Fig. 7. Distribution of the single scattering elements after the first three renormalization steps

configurations of the block and then obtaining the histograms. In the next step of renormalization this distribution is used to generate the next set of scatterers $\{\hat{\epsilon}_I\}$ for the renormalized Hamiltonians. Several features of the distributions may be commented upon. First, even if we start with binary like discrete distribution as in the quantum percolation model, with renormalization the distribution becomes smooth. Second, as the renormalization proceeds a hole appears around the origin of the distribution. The existence of this *hole* in the distribution has been commented upon, specially in the related problem of spin-glasses. The mean of the distribution diverges as the renormalization proceeds. Simultaneously, the width of the distribution also increases. The asymptotic distribution is long tailed. Such long-tailed distributions usually have divergent moments. Kumar and Jayannavar [17] had commented upon these long-tailed distributions of scattering matrix elements earlier. It is a signature of non-self-averaging and non-ohmic behaviour of the resistance. We have used the basic blocks of sizes 48, 120 and 224. Very small blocks are not used since the effect of quantum coherence in them may not be effectively demonstrated. On the other hand, too large blocks have resistances too large for numerical stability.

The strength of disorder is measured by the quantity $\delta = W/B$, where B is the band width of the ordered case and W is the width of the distribution. We first study a moderate disorder $\delta = 0.5$. Since the resistance $\rho = r(E_F)/t(E_F)$ is not self-averaging, we average the logarithm of the resistance. Figure 8 shows the graph of $\langle \ln(\rho) \rangle$ versus ln(size) for $E_F = 0.5$, that is, not far from the band centre. The data are for sizes 48, 48^2, 48^4, 112, 112^2, 224 and 224^2. The line shown is the least square fit.

If we define $\ln(\tilde{\rho}) = \langle \ln(\rho) \rangle$, then the Fig. 8 indicates a scaling behaviour of the form:

$$\tilde{\rho} \simeq \rho_0 N^{\alpha},$$

N being the size of the system. We have carried out a similar set of calculations for varying disorders: δ = 6.25×10^{-4}, 0.25, 5.0 and 12.5; all for E_F = 0.5. The results

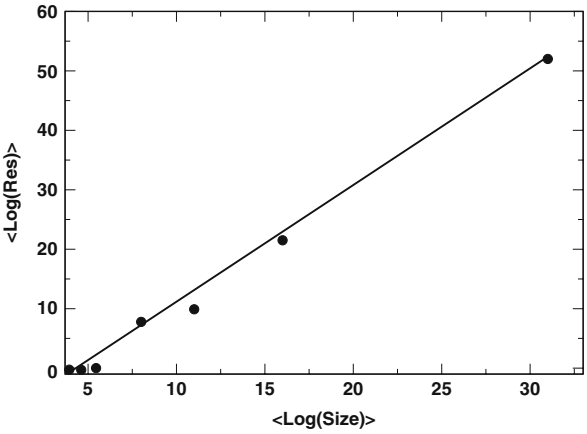

Fig. 8. The average of the logarithm of resistance versus logarithm of size for the case $\delta = 0.5$ and $E_F = 0.5$

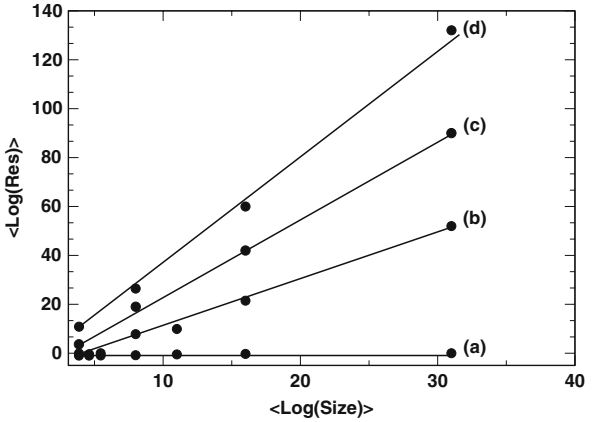

Fig. 9. The average of the logarithm of resistance versus logarithm of size for the cases δ = (a) 6.25×10^{-4}, (b) 0.25, (c) 5.0, (d) 12.5

are shown in Fig. 9. We note that the index α is dependent on the disorder strength, δ and increases with disorder strength. The best-fit curve for this behavior is

$$\ln(\delta) \;=\; -3.889 + 0.579\,\ln(\alpha).$$

The extrapolation of this function for weak disorders is shown in the Fig. 10.

The Fig. 11 shows that for extremely weak disorder, the states near the band centre show logarithmic scaling consistent with the power-law behaviour index $\alpha \to 0$. Whereas, for states near the band edges, there is a deviation from logarithmic scaling. The above study indicates that for states near the centre of the band, the nature of localization appears to be of a power law type that extrapolating to a logarithmic scaling consistent with the power (index) $\alpha \to 0$. This is because it is numerically impossible to distinguish between power law scaling with very low power and logarithmic scaling.

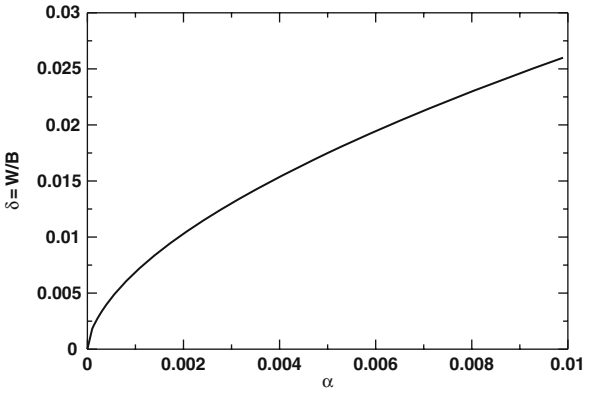

Fig. 10. Variation of the disorder strength, δ with the index α

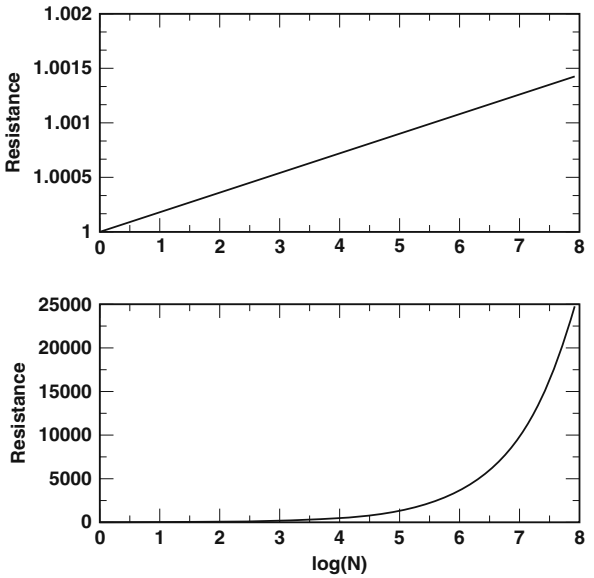

Fig. 11. Variation of $\tilde{\rho}$ vs ln(Size) for (*top*) very weak disorder $\delta = 5 \times 10^{-4}$ and (*bottom*) moderate disorder $\delta = 0.03$

The above study indicates that in two-dimensional lattices, for states near the centre of the band, the nature of localization appears to be of the the power law type, which extrapolates to logarithmic behaviour at ultra-weak-disorders. Such a power law behaviour is not in conformity with the single parameter scaling theory. Analytic works [42, 47] based on perturbative calculations on the scalar recursion method suggest different regimes of exponential and power law localization. This indicates a transition from weakly to strongly insulating states. Recent numerical work of Godin and Haydock [19] also reports weakly localized states near the band centre of the disordered square lattice and exponentially localized states near the band edges. This agrees with the earlier work of Picard and Sharma [48] and Pastawski et al. [36].

7 Conclusions

We have reviewed the models set up to study the phenomenon of quantum percolation and theoretical and numerical techniques used to analyze the models. Our general conclusion is that the quantum percolation model belongs to the same universality class as the Anderson model. Whether the single parameter scaling theory of localization describes all aspects of localization is still a matter of debate. We could not resolve the controversy of the behaviour in the critical dimensionality of two. While from our numerical approaches it is clear there seems to be no localization to extended states transition in two dimensions, our numerical studies using different methods do not give an unambiguous answer to the question of whether *all*

states in two-dimensions are exponentially localized, or there exists weakly power law localized states in the centre of the band. We have to leave the answer for future works.

References

1. P.W. Anderson, Phys. Rev. **109**, 1492 (1958) 83, 87
2. N.F. Mott, Adv. Phys. **16**, 49 (1967) 84
3. A.F. Ioffe and A.R. Regel, Prog. Semicond. **4**, 237 (1960) 84
4. N.F. Mott, Phil. Mag. **19**, 835 (1969) 84
5. E. Abrahams, P.W. Anderson, D.C. Licciardello, and T.V. Ramakrishnan, Phys. Rev. Lett. **42**, 673 (1979) 84
6. D.J. Thouless, Phys. Rep. **13**, 93 (1974) 84
7. V. Chaudhry and A. Mookerjee, Pramana **22**, 107 (1975) 85
8. A. McKinnon and B. Kramer, Phys. Rev. Lett. **147**, 1546 (1981) 85, 90
9. A. McKinnon and B. Kramer, Z. Phys. B **53**, 1 (1985) 85, 90
10. R.E. Borland, Proc. Roy. Soc. A **274**, 529 (1963) 85
11. M. Azbel Ya., Phys. Rev. B **28**, 4106 (1983) 86
12. J.B. Pendry, J. Phys. C: Solid State Phys. **20**, 733 (1987) 86
13. S.J. Bending and M.R. Beasley, Phys. Rev. B **35**, 2548 (1987) 86
14. M. Vaito and M.R. Beasley, Phys. Rev. B **35**, 9926 (1987) 86
15. D. Popovic, A.B. Fowler, and S. Washburn, Phys. Rev. Lett. **67**, 2870 (1991) 86
16. N. Kumar, J. Phys. C: Solid State Phys. **16**, L745 (1983) 86
17. N. Kumar and A.M. Jayannavar, Phys. Rev. B **32**, 3345 (1985) 87, 103
18. K.A. Muttalib, J. Picard and A.D. Stone, Phys. Rev. Lett. **59**, 2473 (1987) 87
19. T.J. Godin and R. Haydock, Phys. Rev. B **38**, 5237 (1988) 87, 91, 92, 105
20. T.J. Godin and R. Haydock, Europhys. Lett. **14**(2), 137 (1991) 87
21. S. Kirkpatrick and T.P. Eggarter, Phys. Rev. B **6**, 3598 (1972) 87, 88
22. N. Tit, N. Kumar, J.W. Halley, and H. Shore, Phys. Rev. B **47**, 15988 (1993) 87
23. R.E. Peierls, Z. Phys. **80**, 763 (1933) 88
24. J. Pimental and S.L.A. de Queiroz, J. Phys. A: Math. Phys. **22**, L345 (1983) 88
25. T. Odagaki and K.C. Chang, Phys. Rev. B **30**, 1612 (1984) 89, 92
26. L.J. Root, J.D. Bauer, and J.L. Skinner, Phys. Rev. B **37**, 5518 (1988) 89
27. K.C. Chang and T. Odagaki, J. Phys. A: Math. Phys. **20**, L1027 (1987) 90, 92
28. J. Stein and U. Krey, Z. Phys. B **37**, 13 (1980) 90
29. R. Raghavan and D.C. Mattis, Phys. Rev. B **23**, 4791 (1981) 90
30. R. Raghavan, Phys. Rev. **29**, 748 (1984) 90, 92
31. J.T. Edwards and D.J. Thouless, J. Phys. C: Solid State Phys. **5**, 807 90
32. D.C. Licciardelo and D.J. Thouless, J. Phys. C: Solid State Phys. **8**, 4157 (1975) 90
33. Th. Koslowski and W. von Neissen, Phys. Rev. B **42**, 10342 (1990) 90, 92
34. J.P.G. Taylor and A. McKinnon, J. Phys. C: Solid State Phys. **1**, 9963 (1989) 90, 92
35. C.M. Soukoulis and G.S. Grest, Phys. Rev. B **44**, 4685 (1991) 90, 92
36. H.M. Pastawski, J.F. Weisz, and S. Albornoz, Phys. Rev. B **28**, 6896 (1983) 91, 92, 105
37. Y. Shapir, A. Aharony and A.B. Harris, Phys. Rev. Lett., **49** 486 (1982) 91

38. Y. Meir, A. Aharony and A.B. Harris, Phys. Rev. Lett., **56** 976 (1986) 91, 100
39. Y. Meir, A. Aharony and A.B. Harris, Europhys. Lett., **10** 275 (1989) 91
40. J.L. Gammel *Padé Approximants and their Applications* (Acadmeic Press, New York, 1973) 91
41. R. Haydock, *Solid State Physics* (Aacdemic Press, New York, **35**, 216, 1980) 92
42. R. Haydock, Philos. Mag. B **43**, 203 (1981) 96, 105
43. R. Haydock and R. Te, Phys. Rev. B **49**, 10845 (1994) 96
44. R. Haydock and R. Te, Phys. Rev. B **57** 296 (1997) 96
45. A. Aharony and D. Stauffer, *Inroduction to Percolation Theory* (Taylor and Francis, London, 1991) 97
46. D.E. Khmelnitskii, Physica **126** B + C 235 (1984) 98
47. R. Haydock, Philos. Mag. **53**, 554 (1986) 105
48. J.L. Picard and G. Sharma, J. Phys. C: Solid State Phys. **14**, L127, L617 (1981) 105

Quantum Percolation in Two Dimensions

H. Nakanishi[1], and Md. Fhokrul Islam[2]

[1] Department of Physics, Purdue University, West Lafayette, Indiana 47907 USA, hisao@physics.purdue.edu
[2] Department of Physics, University of Texas, Arlington, TX 76019 USA

1 Introduction

The transmission of a classical particle through a disordered system such as a percolation network is determined by the availability of a spanning path in the system, whereas the transmission of a quantum particle depends in addition on the quantum effects such as interference and tunneling. These effects are expected to be particularly important in mesoscopic systems such as the hopping transport of an electron through an array of quantum dots. In this chapter, we consider a particularly simple case of a single quantum mechanical particle of no spin or other internal degrees of freedom that is traversing a quenched, disordered lattice by hopping from an available site to another available nearest neighbor site. This is the model we call quantum percolation in this chapter. In this case, a diluted (or unavailable) nearest neighbor site presents an infinite barrier, and thus the only quantum effect included here will be the interference effect due to the many different paths of different lengths that may be available to the particle. Therefore, the existence of a spanning path through the system is a prerequisite for transmission but does not by itself guarantee. In general, we expect a higher geometrical connectivity among the sites to be required for transmission to occur, if at all, than for a classical particle. In fact, even for a completely ordered system, a quantum particle may exhibit zero transmission (reflection resonance) depending on the details such as the energy of the particle and boundary conditions [1].

We are motivated to study such a system at least in part because the existence or absence of a localized-to-delocalized transition in a two-dimensional (2D) quantum percolation system has been debated hotly in recent years. Initially, it had been widely assumed that the universal scaling theory of Abrahams et al. [2], which provided fundamental understanding of the Anderson model, also applied to quantum percolation. According to this theory, there can be no such transition in 2D for any finite amount of disorder in the absence of additional factors such as a magnetic field or interactions (but see [3]). Rather, all disordered systems in 2D are localized in thermodynamic limit according to the universal one-parameter scaling theory. While the literature on the theoretical and numerical calculations performed on

Nakanishi, H., Islam, Md. F.: *Quantum Percolation in Two Dimensions*. Lect. Notes Phys. **762**, 109–134 (2009)
DOI 10.1007/978-3-540-85428-9_4

both models agreed on the existence of such a transition in three dimensions [4–6], the same question for quantum percolation in two dimensions has remained a subject of controversy for over two decades with various works coming down on opposing sides.

On the one hand, the scaling studies based on numerical calculation of the conductance [7], the investigation using vibration-diffusion analogy [8], finite-size scaling analysis and transfer matrix methods [9] and vector recursion technique [10] found no evidence of a transition. A study by Inui et al. [11] found all states to be localized except for those with particle energies at the middle of the band and when the underlying lattice is bipartite, such as the square lattice.

On the other hand, some studies such as those made using the exact series expansion method applied to the moments of distances weighted by the transmission coefficient between pairs of lattice sites [12], real space renormalization method [13], and the inverse participation ratio [14] found a transition from exponentially localized states to more weakly localized states at some point within a range of site occupation (availability) probabilities between $0.73 \leq p_c \leq 0.87$ on the square lattice (where the classical site percolation threshold is about 0.59). A study based on energy level statistics [15], one using how a wave packet initially localized at a site spreads through the lattice [16] and one that calculates a transfer matrix [17] also found a transition, but the nature of the state on the delocalized side of the transition remained not fully understood. More recently, Cuansing and Nakanishi [18] and Islam and Nakanishi [19] used an approach that was first suggested by Daboul et al. [12] to calculate the conductance of finite percolation clusters of varying sizes with one-dimensional (1D) leads attached and extrapolated those results toward infinite system sizes, interpreting them in the spirit of finite-size scaling. They suggested that delocalized states exist and thus a transition would have to exist as well. The latter work also showed some evidence that both algebraically localized state and extended state exist in addition to the more common exponentially localized state and thus two successive transitions may exist as well.

1.1 Quantum Percolation Model

Our quantum percolation model is described by the Schrödinger equation $H\psi = E\psi$ with the following tight-binding Hamiltonian [20, 21]

$$H = \sum_{<ij>} V_{ij}|i\rangle\langle j| + (h.c.), \tag{1}$$

where $|i>$ and $|j>$ are localized basic functions at sites i and j, respectively, and V_{ij} is the hopping matrix element that is equal to a constant $V_0 \neq 0$ if i and j are available nearest neighbors, otherwise zero. The value of V_0 sets the overall energy scale and we will use $V_0 = 1$ as the nominal standard value. In particular, we take the diagonal terms to be $V_{ii} = 0$, corresponding to no on-site energy

(and thus no diagonal disorder). All disorder in this model is off-diagonal and is binary. Whether the sites are available or not is determined by a classical percolation algorithm, that is, by an independent occupation probability p either at each site (site percolation) or for each nearest-neighbor bond (bond percolation) [22]. In either case, the disorder is a quenched, geometrical one, where the absence of a site (or a bond) is equivalent to an infinite barrier. This is in contrast to the standard Anderson model, where we take the off-diagonal terms V_{ij} ($i \neq j$) to be fixed and uniform, and consider diagonal (or on-site) terms V_{ii}, which are distributed randomly with a certain probability distribution within some finite limits (such as uniformly within $|V_{ii}| \leq W$).

1.2 Quantum Percolation versus Ideal Chain

Before proceeding further, we note that the matrix $\mathbf{V}$ of Eq. (1) is identical up to a factor to the matrix that describes the evolution of a Markov process called the ideal chain that is constrained to the same percolation network [23–25]. An ideal chain is a Gaussian random walk (no excluded volume effect), which dies when it attempts to step into an unavailable site. Thus, the ideal chain probability density of the random walker $P_i(t+1)$ at site i at time step $t+1$ is related to $P_j(t)$ by

$$P_i(t+1) = \sum_j W_{ij} P_j(t) \ , \tag{2}$$

where the matrix $\mathbf{W}$ has only non-zero elements corresponding to the bonds connecting a nearest-neighbor pair of available sites i and j, and those elements have a uniform value. These are exactly the same properties as our matrix $\mathbf{V}$. So the classical problem of the ideal chain is formally and mathematically identical to our quantum percolation problem. The ideal chain problem is in turn equivalent to the problem of the classical vibration of the network with boundary tethering [26, 27] as well. Thus, quantum percolation belongs mathematically to a wide class of problems that are related to each other via diffusion-vibration type analogies.

However, the main difference between quantum percolation and ideal chain lies rather in the spectral regions of our interest; while in the ideal chain problem, we are normally interested in the asymptotically long-time (or long-chain) limit and thus the behavior at the very edges of the eigenspectrum of $\mathbf{W}$ (absolute values close to the maximum possible value of 1), while the main interest of the quantum percolation problem has been nearer the band center in energy E (certainly not locally around the spectral edges), that is, in the region of the eigenspectrum not far from zero. This is because we are usually looking for states with higher transmission probability (less localized) and the common wisdom is that those states tend to be found near the band center. As it turns out, this common wisdom is not entirely correct (as seen below) and we need to investigate a broad region throughout the spectrum, but it remains true that interesting behavior does occur near the band center. This means that methods developed to study the long-chain limit of the ideal

chain, which concentrate on the far edges of the spectrum of $\mathbf{W}$ [28] is unfortunately not suitable to study quantum percolation even if they deal with the same matrix.

1.3 Eigenspectrum of Quantum Percolation

A typical eigenvalue spectrum of quantum percolation on a (bond) percolation network on the square lattice is shown in Fig. 1 and a measure of the mean size $\langle s \rangle$ of an eigenstate is shown in Fig. 2. The sharp isolated peak right at the center of the band in Fig. 1 is due to a large number of extremely local states that reside on a small number of sites and they do not affect the global transmission characteristics; this peak is seen to be present essentially for all p. In contrast, the overall shape of the spectrum is seen to change dramatically from a depressed density of states at the band center for the smaller values of p (more dilution) to a monotonically increasing density of states toward the center for the larger values of p (less dilution). This may be a hint of the significant changes taking place as p is varied. Note that this change is taking place primarily near the center of the band. On the other hand, as we have stated above, the decreasing trend of the density toward the edges of the spectrum is what is important in the study of the ideal chain problem where it is expected to be a stretched exponential decay as a function of the reciprocal of the distance from the spectral edge (with a special stretch power at the classical percolation threshold) [24, 25]. Though not shown here, the corresponding spectrum of the classical random walk problem (*ants*) actually exhibits a power-law divergence towards the spectral edge with the power related to the critical exponent known as the spectral dimension

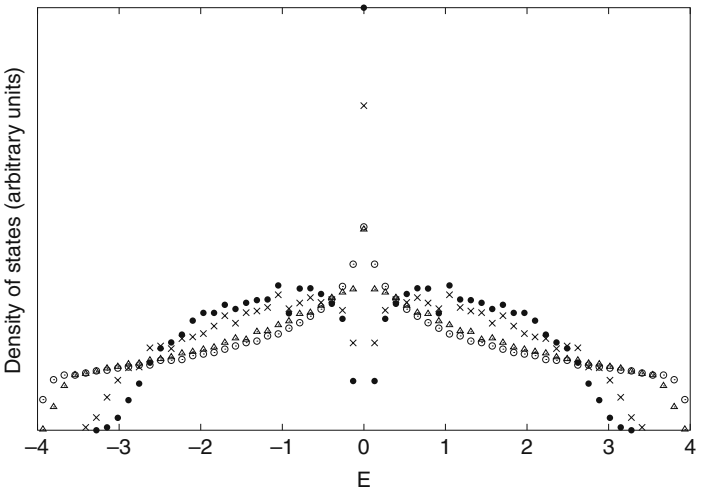

Fig. 1. Typical eigenvalue spectrum of the quantum percolation problem realized on bond percolation networks containing 5000 occupied sites on the square lattice at various bond occupation probabilities: $p = 0.5$ (•), 0.65 (×), 0.91 (△), 0.98 (◯)

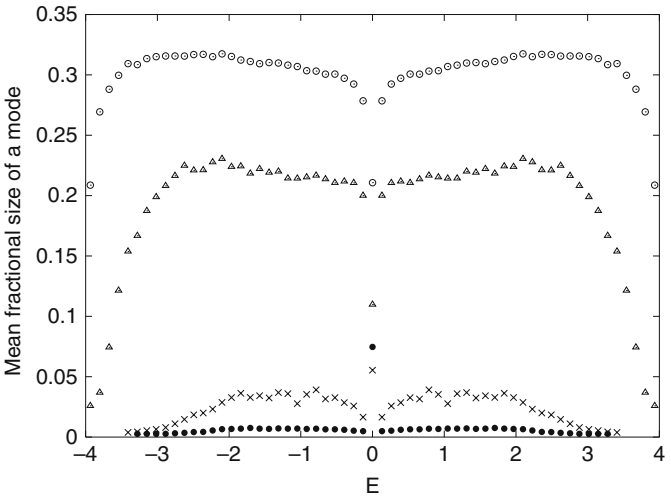

Fig. 2. The mean fractional size $\langle s \rangle$ of the eigenstates (as defined in the text) is shown from the same data as in the eigenvalue spectra of Fig. 1; $p = 0.5$ (•), 0.65 (×), 0.91 (△), 0.98 (◯)

[28]. Thus, the latter problem, which is associated with an analogous but somewhat different matrix, in fact has an entirely different spectral density.

The mean fractional mode size $\langle s \rangle$ shown in Fig. 2 is defined as the average of

$$s \;=\; \left(\sum_i |\psi_i|^4 \right)^{-1} \Big/ S \;, \tag{3}$$

for the eigenstates in the corresponding region of the spectrum where ψ_i is the amplitude of the eigenstate at site i and S is the total size of the cluster (number of available, connected sites in the network). The numerator in Eq. (3) is often called the inverse participation ratio and is a measure of the size of the eigenstate. To see this, just consider the extreme cases of a state that is concentrated at just one site versus a state that is uniformly spread out over the entire network. The former will have the numerator equal to 1, while the latter will have it equal to S. Thus, s amounts to a crude estimate of a factional size of the corresponding state. Of course, such a measure does not distinguish how $|\psi_i|^2$ is distributed geometrically; it only cares about what values $|\psi_i|^2$ occur on the cluster. Thus, it is at best one crude measure of the overall mode size, lacking the information on the geometrical shape of the probability density, and certainly not to speak of the distribution of the phases of ψ_i. We will see later that the latter information actually plays a key role in determining transmission.

From Fig. 2 we see that obvious changes again occur from a smooth dipping trend at the center of the band at low p to nearly constant density at higher p, disregarding the isolated, very small $\langle s \rangle$ right at the center. So as p increases, the size of the modes near the band center is catching up to the rest of the spectrum at the same time as their density is sharply increasing.

1.4 Approach

These observations give us additional motivation to study this problem in more detail to see whether such trends indeed lead to a phase transition. In the remaining part of this chapter, we will present an overview of the quantum percolation studies performed in our group over the last several years rather than attempting to describe a huge number and variety of work that exists in literature (we have already made references to a fair number of them above). Most of the results shown here are obtained using the following approach. To study the transmission of a quantum particle we connect two semi-infinite 1D leads to the 2D network (that we call *cluster*, borrowing the terminology from classical percolation), one as the input and the other as the output lead. We study this problem, for the most part, using two different types of connection of the leads. In the point-to-point contact, the input lead is connected to only one lattice site on the input side edge of the cluster and the output lead is connected also to only one lattice site on the opposite edge of the cluster (usually at diagonally opposite corners of the cluster). In the busbar type contact, all the lattice points on the input side edge of the cluster are connected to the input lead by single bonds, while all the lattice points on the output side of the cluster are similarly connected to the output lead. Figure 3 illustrates the two types of connection of the leads for the square lattice.

The wave function of the entire cluster-lead system can be calculated by solving the time-independent Schrödinger equation:

$$H\psi \;=\; E\psi, \tag{4}$$

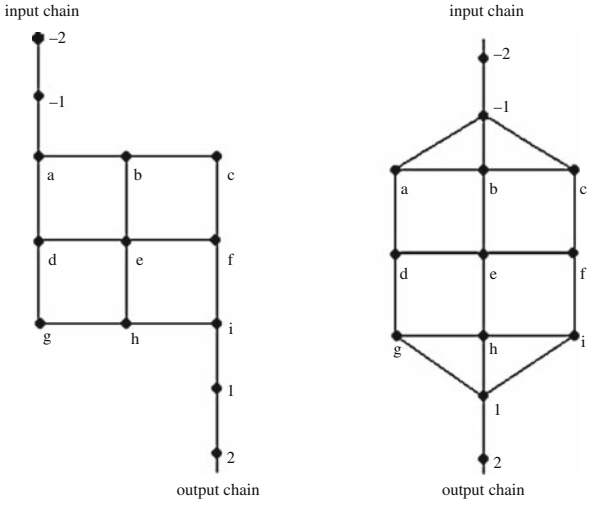

Fig. 3. 3×3 Square Lattice: On the *left*, the diagonal point-to-point connection and on the *right*, the busbar type connection. The letters label the lattice points of the cluster part of the Hamiltonian, while numbers label those of the leads

where

$$\psi = \begin{pmatrix} \psi_{in} \\ \psi_{cluster} \\ \psi_{out} \end{pmatrix} \tag{5}$$

and $\psi_{in} = \{\psi_{-(n+1)}\}$ and $\psi_{out} = \{\psi_{+(n+1)}\}$, $n = 0, 1, 2 \ldots$, are the input and output chain parts of the wave function, respectively.

Since the leads are of infinite lengths, the matrix form of the Schrödinger equation Eq. (4) becomes an infinite size problem. We can deal with this problem in two ways. One is to effectively reduce it to a numerically finite problem by using an ansatz proposed by Daboul et al. [12]. The other is to simply attach 1D chains of finite, but increasing lengths and try to extrapolate the results to the point where the dependence on the lead length essentially vanishes. Both approaches have been pursued. In the Daboul ansatz approach, one assumes that the input and output part of the wave function are of the form of discrete plane waves:

$$\begin{aligned} \psi_{in} \rightarrow \psi_{-(n+1)} &= e^{-in\kappa} + re^{in\kappa} \\ \psi_{out} \rightarrow \psi_{+(n+1)} &= te^{in\kappa}, \end{aligned} \tag{6}$$

where r is the amplitude of reflected wave and t is the amplitude of the transmitted wave. This ansatz is consistent with the Schrödinger equation only for the wave vector κ, which is related to the energy E by

$$E = e^{-i\kappa} + e^{i\kappa}. \tag{7}$$

As an example of using this ansatz along with the energy restriction Eq. (7), the matrix equation for a 3×3 cluster connected to the semi-infinite chains (Fig. 3) reduces to (for details see [12])

$$\begin{pmatrix} -E+e^{i\kappa} & c & 0 & 0 & 0 & 0 & 0 & 0 & 0 & 0 & 0 \\ c & -E & 1 & 0 & 1 & 0 & 0 & 0 & 0 & 0 & 0 \\ 0 & 1 & -E & 1 & 1 & 1 & 0 & 0 & 0 & 0 & 0 \\ 0 & 0 & 1 & -E & 0 & 0 & 1 & 0 & 0 & 0 & 0 \\ 0 & 1 & 0 & 0 & -E & 1 & 0 & 1 & 0 & 0 & 0 \\ 0 & 0 & 1 & 0 & 1 & -E & 1 & 0 & 1 & 0 & 0 \\ 0 & 0 & 0 & 1 & 0 & 1 & -E & 0 & 0 & 1 & 0 \\ 0 & 0 & 0 & 0 & 1 & 0 & 0 & -E & 1 & 0 & 0 \\ 0 & 0 & 0 & 0 & 0 & 1 & 0 & 1 & -E & 1 & 0 \\ 0 & 0 & 0 & 0 & 0 & 0 & 1 & 0 & 1 & -E & c \\ 0 & 0 & 0 & 0 & 0 & 0 & 0 & 0 & 0 & c & -E+e^{i\kappa} \end{pmatrix} \begin{pmatrix} 1+r \\ \psi_a \\ \psi_b \\ \psi_c \\ \psi_d \\ \psi_e \\ \psi_f \\ \psi_g \\ \psi_h \\ \psi_i \\ t \end{pmatrix} = \begin{pmatrix} e^{i\kappa} - e^{-i\kappa} \\ 0 \\ 0 \\ 0 \\ 0 \\ 0 \\ 0 \\ 0 \\ 0 \\ 0 \\ 0 \end{pmatrix} \tag{8}$$

Here c is the coupling of the leads with the cluster, which is usually also taken to be equal to 1, but can be varied to see interesting effects. The busbar configuration of Fig. 3(b) has a similar expression. Equation (8) is the exact expression for a 2D system connected to the semi-infinite chains by the Daboul ansatz and it leads to continuous eigenvalues ranging between -2 and $+2$. The spectrum is continuous because it is still effectively infinite and it is non-degenerate except for the reversal of left and right.

The main advantage of using this ansatz is that it not only allows us to calculate the wave function but also helps us to study the transmission characteristics of

the corresponding state directly. The transmission and the reflection coefficients are obtained by taking the absolute square of *t* and *r*, respectively, that is $T = |t|^2$ and $R = |r|^2$. Following the Landauer-Büttiker formalism [29], the conductance of the system can then be determined from the resulting T and R. A disadvantage on the other hand is that Eq. (7) that relates the wave vector of the incident particle with the energy, restricts the energy of the particle to between -2 and $+2$. This restricts our ability to study the system in the whole possible energy range since for the 2D cluster the energy could in principle range more widely (between -4 and $+4$ for the square lattice where the coordination number is 4). This is due, of course, to the effectively one-dimensional nature of the system forced by attaching 1D semi-infinite leads and by looking at the plane waves spreading over the entire leads. Although the restriction only allows us to study a subset of the two-dimensional part of the transmission that occurs within the 2D cluster portion, it still provides us with a large window to observe the behavior of transmission as a function of the main variables of the problem, that is, the energy E, the site occupation probability p (the remainder of this work uses the site percolation model for the underlying cluster), system size (i.e., the edge length L), and the way input and output leads are connected to the cluster.

2 Resonances and Phase Variations in Ordered Limit

We begin by considering the ordered limit of $p = 1$, that is, all sites (bonds) of the percolation network are occupied and thus available to host the hopping particle. As we will illustrate below, even in this limit, the transport through the lattice is very sensitive to the incident particle's energy, varying from complete transmission to complete reflection, and also to the type of coupling between the lattice and the input and output chains. Moreover, we will illustrate a surprising degree of connection between certain types of phase variations of ψ over the cluster and the transmission coefficient T.

2.1 Transmission and Reflection Resonances

Shown in Fig. 4 is the transmission coefficient against the particle energy E for a 10×10 lattice with two different boundary conditions, namely, the point-to-point and busbar type contacts of the input and output chains. Common to both types of connections is the presence of peaks and valleys in T with sharp edges, which we call resonances. Clearly, even with no disorder there are states that are almost completely reflecting ($T = 0$); in fact, these highly reflecting states dominate for the busbar boundary case.

The immediate proximity of transmission ($T = 1$) and reflection ($T = 0$) resonances suggest their common origin, and indeed, [1] found that many (if not all) of them arise mathematically as the degenerate eigenvalues of an isolated cluster portion are split when the 1D leads are attached. The diamonds ($\diamond$) in these figures indicate the location of those degenerate eigenvalues. This phenomenon is analogous

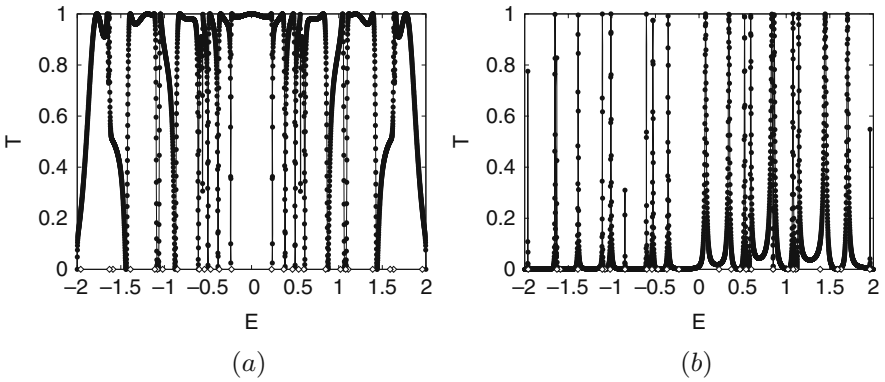

Fig. 4. The transmission coefficient T as a function of energy E for a 10×10 square lattice calculated using the Daboul ansatz. (**a**) is for the point-to-point contacts to the input and output chains, and (**b**) is for the busbar contacts. Also shown by the diamonds ($\diamond$) are the locations of the doubly degenerate eigenvalues of the submatrix that only contains the cluster sites. From [1]

to resonant tunneling [30] of an incident particle through, for example, a double-barrier system. In such a system, a peak in particle transmission occurs whenever the incident particle's energy is the same as the energy of one of the well's bound states. In this work, however, although there is no tunneling involved, we do see resonant transmission and reflection when the energy of the incident particle falls near an eigenvalue of the isolated cluster.

On the other hand, the two boundary conditions also differ in that the point-to-point contact case is largely transmitting while the busbar case is the opposite. This difference arises from the additional interference effects at the much larger contact region (edges) of the latter where large cancellations occur as an edge effect. We also note the loss of symmetry about $E = 0$ for the busbar case as it is no longer a bipartite geometry.

As the size of the central cluster is increased, the number of its associated eigenvalues also increases. The example from the ordered 50×50 square cluster with point-to-point chain contacts is shown in Fig. 5. It is clear that there are correspondingly much larger number of transmission and reflection resonances that are also located near the doubly degenerate eigenvalues of the corresponding isolated square cluster. Also highly transmitting states cluster near the band center as in the smaller networks.

2.2 Effects of Wave Function Phases

One obvious question is whether one can judge immediately by looking at the probability density $|\psi(\mathbf{r})|^2$ whether a state is highly transmitting or more reflecting. This question is relevant since some common approaches to study the transmission (or localization) characteristic of the quantum percolation problem focus on the geometric

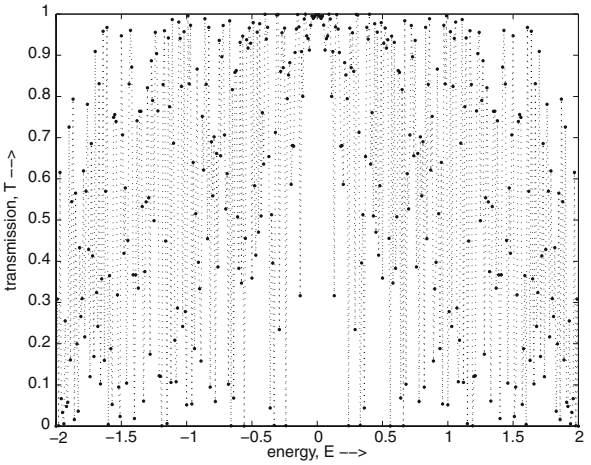

Fig. 5. The transmission coefficient T as function of energy E for a 50×50 square lattice calculated using the Daboul ansatz for the point-to-point contacts. From [31]

distribution of the probability density [10, 32–35]. This includes all studies that rely solely on the participation ratios.

Shown in Fig. 6(a) is the probability density $|\psi|^2$ for the state of $E = 1.19$ on a 50×50 ordered network with point-to-point contacts. Although we show only that portion of the wave function that resides on the square cluster, the problem was actually solved for the entire system including the effectively infinite 1D leads using the Daboul ansatz, and thus $\psi(\mathbf{r})$ is not an eigenstate of an isolated cluster. Therefore, the values of $|\psi|^2$ right at the sites where the leads connect to the cluster do not predispose the calculation of the transmission coefficient in the way such values might determine the overlap integrals based on the wave function solution over the isolated cluster and the leads separately. As seen from the figure, the probability density is extended throughout the cluster, and yet the transmission happens to be very low at $T \approx 0.0007$. This may appear puzzling at first, but if we look at the phase distribution shown in Fig. 6(b) and (c), we observe an interesting pattern. The phases consist of many small plateaus of essentially just two values that differ by $\sim \pi$, creating an appearance of a rectangular parallelopiped. The ubiquitous phase difference of $\sim \pi$ gives rise to destructive interference and hence the very low transmission. A calculation purely based on $|\psi|^2$ (such as participation ratio analyses) would never have picked up this state as one of almost zero transmission.

The state corresponding to energy $E = 0.99$, on the other hand, has a very high transmission at $T \approx 0.996$. The probability density and corresponding phase pattern of the state are shown in Fig. 7. Clearly, the probability density alone does not differentiate this state very well from that of Fig. 6. However, in this case the phase difference between the neighboring sites (or plateaus) is $\sim 2\pi$ (zero modulo 2π) and therefore ubiquitous constructive interference leads to very high transmission.

The two cases described above suggest that any state with a phase distribution such that the phases between the neighboring sites differ by $\sim \pi$ or $\sim 2\pi$ will give

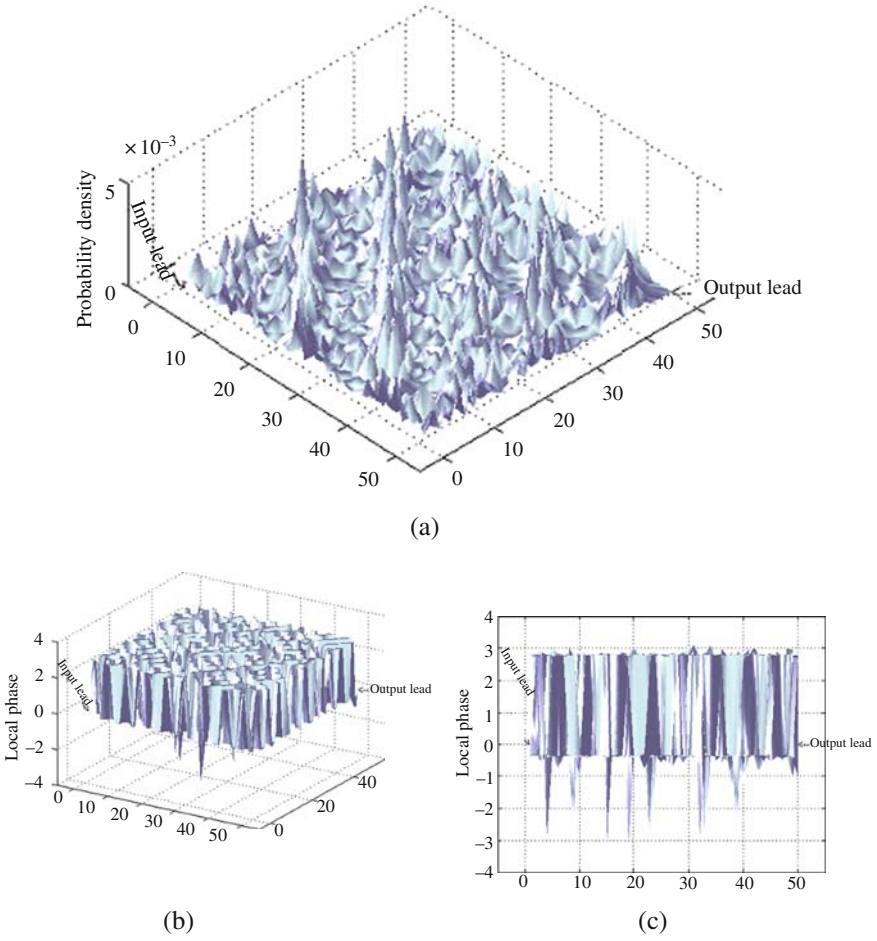

Fig. 6. (**a**) The probability density of the system of size 50×50 corresponding to energy $\mathrm{E} = 1.19$ with the transmission coefficient T of about 0.0007. (**b**) *Top view* of the local phases of the wave function and (c) *Side view*. From [31]

rise to especially low or high transmission, respectively. Any value of the prevalent phase differences between these two extremes will give rise to an intermediate transmission. Even though we only illustrated with two examples from the ordered cluster here, there appears to be a surprising degree of universality to the observation across the energy and even boundary conditions and lattice types. For example, the transmission under busbar type connection also turns out to follow the same simple criteria for high- and low-transmitting states as does transmission through a cluster on the triangular lattice. Thus, higher local connectivity and the lack of bipartiteness of the triangular lattice does not seem to lead to markedly different transmission characteristics at least in this regard. Moreover, the same correlation between the

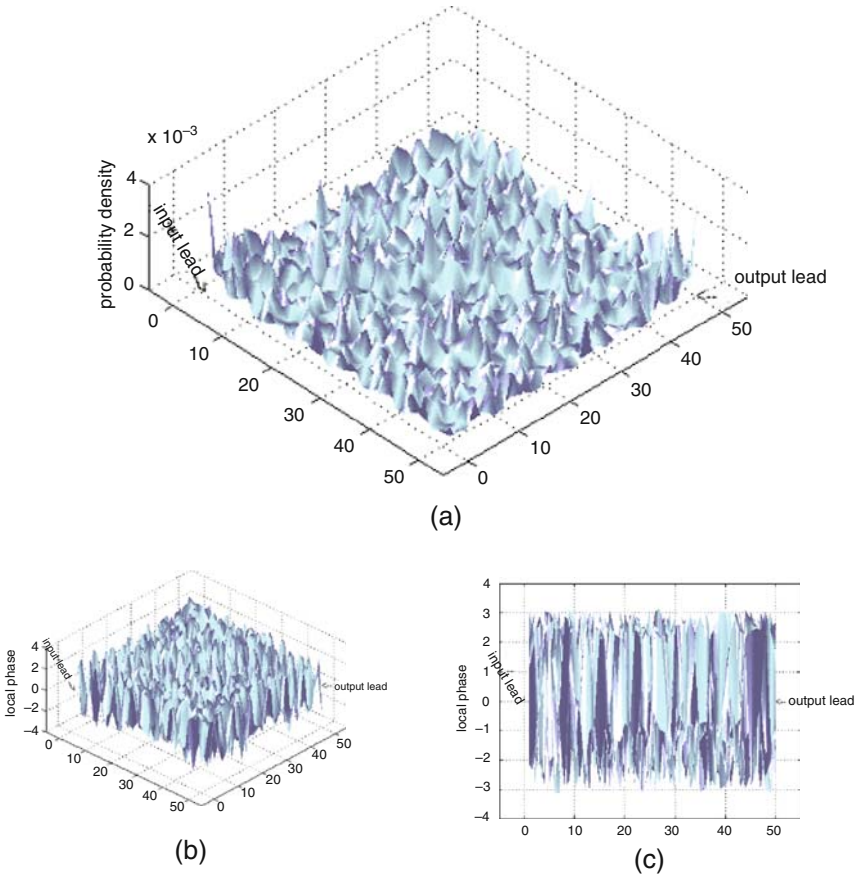

Fig. 7. (**a**) The probability density of the system of size 50×50 corresponding to energy $\mathrm{E} = 0.99$ with the transmission coefficient T of about 0.996. (**b**) *Top view* of the phase distribution of the wave function and (**c**) *Side view*. From [31]

transmission and phase variations of ψ is observed for disordered clusters [31] as well. These discussions illustrate the universal importance of the phase variations for the transmission of a quantum particle. The probability amplitudes alone do not determine the transmission characteristics, and in particular, studying quantities such as the participation ratio alone is not likely to reflect true transport properties of a quantum particle.

3 Time-Independent Schrödinger Equation for Finite Disorder

In our quantum percolation model, disorder is introduced by randomly diluting (or removing) a fraction of the lattice sites as unavailable to the hopping particle as in the classical percolation algorithm. As the latter geometrical problem is not exactly

solved, neither is the quantum problem at hand. We describe here the numerical approach that uses the Daboul ansatz as discussed before, but even then, we are faced with formidable challenges. First is that a meaningful result requires averages over a large number of quenched, disordered configurations at each amount of dilution. Second is that the determination of the localization status requires the investigation of the states of the system in thermodynamic limit. These challenges are on top of the fact that not all states at a given dilution will share the same localization characteristics; some may be well localized while others (say, at different E) on exactly the same diluted network may be nearly extended. That there are many possible boundary conditions adds an additional hurdle to a comprehensive understanding.

In view of these difficulties, Ref. [19] focused on the point-to-point contact geometry on the square lattice where transmission T is generally higher than for other boundary conditions such as the busbar contacts. This is because the 2D system is predominantly exponentially localized (with zero transmission in the thermodynamic limit) and we are mainly interested in searching for an extended (or less localized) state if any exists. In order to minimize the local effects of the immediate vicinity of the point contacts, they also made a certain number (usually 9) of sites at the corners of the cluster around the diagonal contact points to be always occupied (available). They then solved the time-independent Schrödinger equation using the Daboul ansatz on each of the many realizations of a disorder configuration of a given size cluster ($L \times L$) and a given value of disorder ($p < 1$), for strategically selected values of the energy E, calculated the transmission coefficient T, and averaged those to obtain the mean T for the size L and dilution $q \equiv 1 - p$. This is repeated for gradually increasing disorder (or q). The final step is to consider increasing cluster sizes L, and they interpreted the results in the spirit of finite size scaling.

3.1 Energies Away from the Band Center

Reference [19] found similar trends at all values of E except for the immediate vicinity of the band center $E = 0$. Thus, here we review their result from just one value of energy $E = 1.6$ to illustrate their findings away from the band center. For each level of disorder, the size of the clusters they studied varies from 10×10 to a maximum size of 180×180. The disorder average was performed over 1,000 clusters for each cluster size and dilution level. From the corresponding results on the Anderson model, the distribution of T over disorder realizations is expected to be non-Gaussian. Indeed, various calculations [18, 19] found this to be true for the quantum percolation as well. Thus, it is critical to study the statistics of T carefully in order to make meaningful statements about its trend. The results quoted here, as averaged over the 1,000 realizations per data point (given L, q, and E), have been subjected to such analyses and the averages shown here are believed to be meaningful.

The log-log plot of the mean transmission T against the size L of the clusters is shown at $E = 1.6$ for various disorder levels in the Fig. 8. Up to 28% dilution, linear fits of the form of $\ln T = -b \ln L + c$ are also shown, while for higher dilution, exponential fits of the form of $\ln T = -bL + c$ are also shown on the log-log plot.

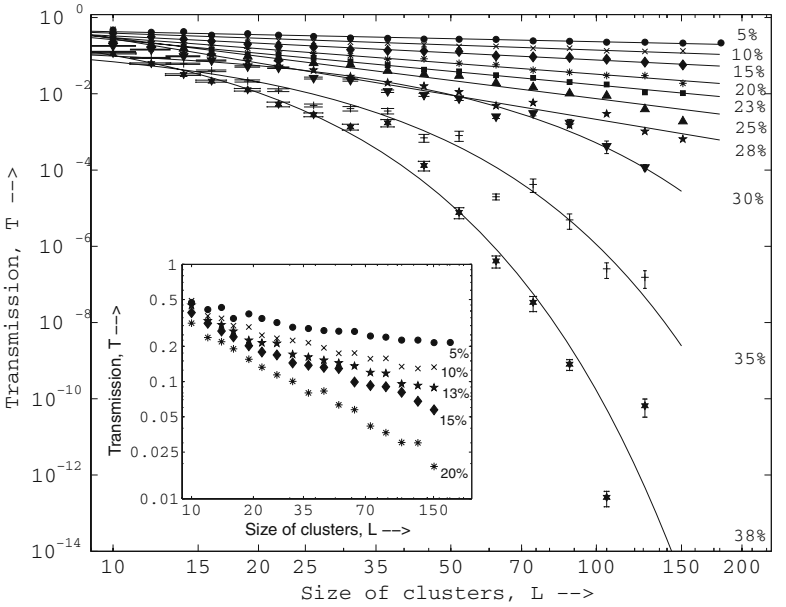

Fig. 8. The log-log plot of transmission through disordered clusters at $E = 1.6$. Each data point is the average over 1,000 independent realizations. The transmission curves for $q = 5\%$, 10%, 13%, 15% and 20% dilution are separately shown in the inset. *Error bars* shown are the standard errors of the mean. From [19]

At first sight, Fig. 8 appears to show that for lower dilution of up to about 25% or 28%, the transmission decreases almost linearly in the log-log plot as the size of the clusters increases, which translates to a power-law behavior of transmission in the linear scale $T = aL^{-b}$. However, the power-law exponent seems to gradually increase with dilution. Eventually, for dilution higher than about 28%, the transmission evidently begins to fall exponentially as a function of L (i.e., $T = a\exp(-bL)$), as is evident from the lowest three curves in Fig. 8. If we interpret the dependence on the cluster size as reflecting the corresponding distance scale dependence of T on a hypothetically infinite 2D cluster, then these observations would translate to an algebraic localization at lower dilution versus exponential localization at higher dilution.

These fits are of fair quality both by inspection and according to the usual measures such as the coefficients of regression ($|R_\sigma|^2 \geq 0.94$ in all cases) at first glance. However, the logarithmic scale conceals finer details particularly at lower dilutions. For example, though the main plot of Fig. 8 appears to suggest an excellent linear fit at dilution below 15%, the vertically expanded inset of the figure for the lower values of disorder clearly suggests that the decreasing trend of $\ln T$ against $\ln L$ is in fact much slower than linear.

Thus, Ref. [19] investigated the lower dilution regime more carefully, fitting the data for T from the larger clusters on the linear scale to both the power-law and exponential with a possibly nonzero offset

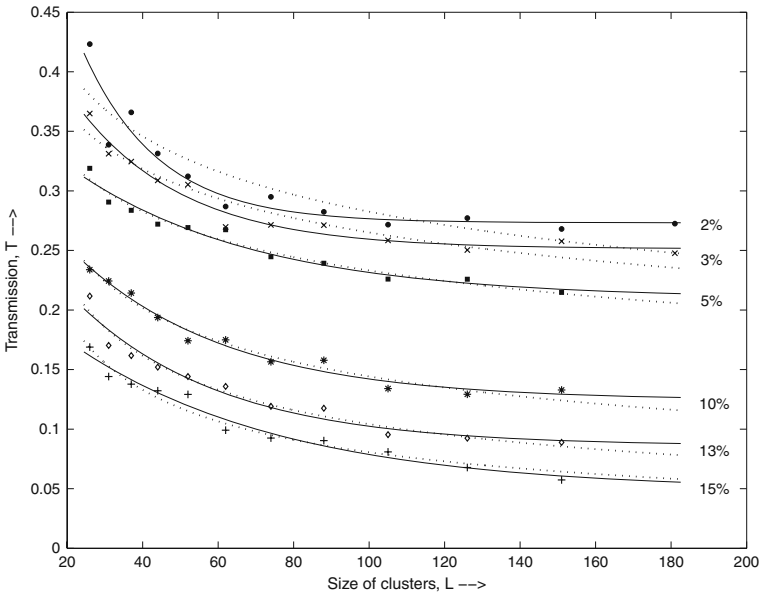

Fig. 9. The linear plot of average transmission T through clusters with 2%, 3%, 5%, 10%, 13% and 15% disorders at $E = 1.6$ for larger sizes of the clusters ($L > 26$). The *dotted lines* represent power-law fits and the *solid lines* represent the exponential fits with possibly a non-zero offset. From [19]

$$T = a\, \mathrm{e}^{-bL} + c \tag{9}$$

in Fig. 9. The dotted and solid lines represent the power-law fits and the exponential fits with the possibility of nonzero offsets, respectively. As we can see from Fig. 9, the exponential with offset begins to give a significantly better visual fit for small dilutions such as for 2% and 3% disorder, while the goodness of fits for higher disorders appear to be a toss-up between the two forms. This is corroborated by the measures such as the regression coefficient $|R_\sigma|^2$ and the cumulative square deviations between the data and the fits as well. For 2% and 3% dilution, the corresponding offsets are 0.27 ± 0.02 and 0.25 ± 0.01, respectively. Since a nonzero offset implies a residual conductance even in the thermodynamic limit of $L \to \infty$, the above observation suggests that the states at these low disorder are in fact extended, rather than simply weakly localized. We note that this is the first direct numerical evidence on the nonzero bulk transmission in quantum percolation (direct in the sense of the actual calculation of T).

The study of [19] thus suggests the existence of three regimes of transmission. At higher disorders, the transmission drops exponentially as the size of clusters increases. At intermediate disorders, the transmission follows power-laws of varying exponent, whereas at low disorders, its behavior approaches a constant non-zero offset, c, suggesting possible delocalization of the states.

3.2 Energies Near the Band Center

The transmission near the band center differs in some important ways compared to that at other energies. At $E \sim 0$, although the transmission is universally very high for zero disorder as seen in Sect. 2, as soon as even a small amount of disorder is introduced, the transmission quickly falls to very low values. Though it is difficult to locate the delocalization transition, if any, because of the generally low transmission, the analysis of [19] does show a behavior much weaker than power-law localization. The width of the power-law localization regime appears to be very small and exponentially localized states are present for a disorder as low as 9% dilution for the energy of $E = 0.001$.

Shown in Fig. 10 from [19] is a plot of T versus L, comparing the goodness of power-law fits versus exponential fits with possibly non-zero offsets for $E = 0.001$ near the band center, analogous to Fig. 9, which was for $E = 1.6$, far from the band center. The goodness of fits are not vastly different for the two kinds of fits except for the 2% dilution, but it is still clear that generally the exponential fits with an offset fits the data better than the power-laws for the dilution amounts shown in the figure. The best fit estimates of the offsets at 2% and 3% dilution are 0.15 ± 0.06 and 0.11 ± 0.02, respectively, still excluding zero offset within the errors and suggesting a non-zero, bulk conductance in the thermodynamic limit.

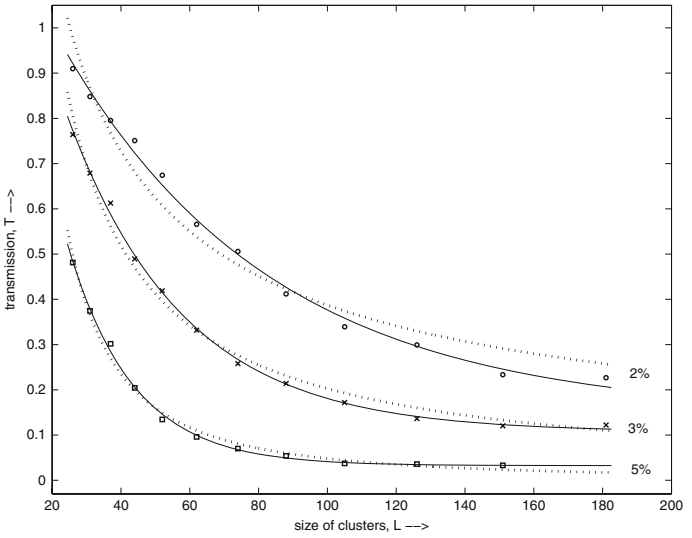

Fig. 10. Transmission coefficient T through the clusters with 2%, 3% and 5% disorders at $E = 0.001$ for clusters of $L > 26$, Where each data point is the average over 1,000 independent realizations. The *dotted lines* represent the power-law fits and the *solid lines* show the exponential fits with offsets. From [19]

3.3 Localization Length

The issue of the localization length L_l need to be discussed since even when the system happens to be exponentially localized in the thermodynamic limit, in order to observe it as such, the localization length of the state must be substantively smaller than the system size. Otherwise, one may observe what appears to be a weaker form of localization (such as power-law) or even an apparently extended state. So it would obviously be useful if we have an estimate of L_l to compare with the system size.

With the finite size scaling type of approach taken by [19], this is possible by using the data for T themselves self-consistently, at least in the regime clearly recognized as exponentially localized by the method. In such a regime, $T \sim a\ \mathrm{e}^{-bL}$ and thus $1/b$ gives the length scale over which T decays, which can then be interpreted as the localization length. Near the band center at $E = 0.001$, the value of L_l estimated in this manner ranges from about 3 lattice spacings for 20% disorder to 16 lattice spacings at 9% disorder, well within the cluster sizes used (which was up to 150×150 at the higher dilution levels) to obtain these estimates. At the other extreme of $E = 1.6$, the estimate of L_l ranged from about 4 lattice spacings for 38% disorder to 17 lattice spacings for 30% disorder, still well within the cluster sizes used. For dilutions smaller than these values, the power-law fits take over as the best numerical fits and thus the situation is again consistent with the expectation that the localization length would diverge both in an algebraically localized and extended regimes.

3.4 Suggested Localization Phase Diagram

Summarizing the study of [19], we have learned that there is a strong likelihood that three different regimes of localization exist for quantum percolation depending on the strength of disorder. The dilution range of these regimes, however, depends on the energy of the particle. Using their estimates, the delocalized states appear to emerge for a dilution of less than about 15%, except at the very center of the band. At the center of the band, it seems to be much narrower and restricted to a significantly less then 10%. Then, there is the power-law or algebraically localized regime upto about 30% dilution (again except at the band centre where it is much narrower), and finally an exponentially localized regime for higher dilution. A crude sketch showing the suggested phase diagram is shown in Fig. 11.

The exponent of the power-law in the intermediate power-law regime, however, depends on the disorder strength. As the disorder is varied continuously, the exponent of the power-law also varies continuously, a characteristic that is reminiscent of the Kosterlitz-Thouless (KT) transition in the 2D XY model [36].

4 Time-Dependent Schrödinger Equation: Sending a Wave Packet Through a 2D Cluster

It is also possible to study the actual propagation of a quantum particle through the 2D network. Reference [37] does this by constructing a Gaussian wave packet in the

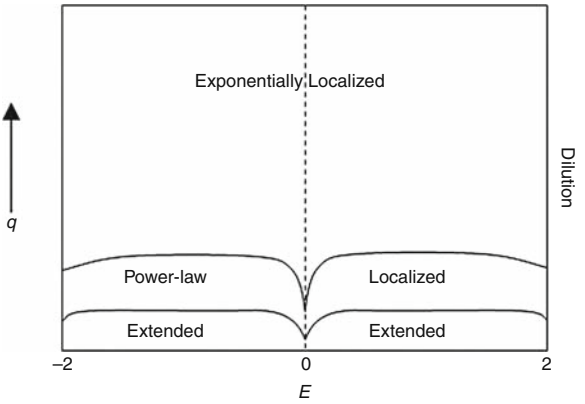

Fig. 11. A sketch (not to scale) of the three localization regimes in the space of energy E and dilution q based on the results of [19]

input chain that represents the incident particle and sending it into the 2D cluster and observing the time evolution of the wave packet by numerically solving the time dependent Schrödinger equation,

$$i\frac{\partial\psi(r,t)}{\partial t} = H\psi. \tag{10}$$

Here,

$$\psi(r,t=0) = (const.)\ \mathrm{e}^{-(r-r_0)^2/(4s^2)}\ \mathrm{e}^{-ik_0 r} \tag{11}$$

(on the input chain only) s is the width of the wave packet, k_0 is its central wave vector and r_0 is the location of the centre of the wave packet in the input chain. They typically chose $s = 4$ lattice spacings and the initial position to be at the middle of the input chain in their numerical calculations. The choices of these parameters have to be made judiciously so that k_0 is a well-defined mean wave number of the incoming particle.

It is also clear that there is no easy way out to reduce an infinite size problem (with infinite 1D chains) to an effectively finite one as we did for the time-independent Schrödinger equation using the Daboul ansatz, and thus one is forced to attach chains of finite length and solve the problem numerically for the entire cluster plus the chains. Since the chains must be finite in this approach, there are a few challenges not present in the approach of the previous section. First, one must minimise the effect of the finite length of the chains by, for example, solving the problem for gradually increasing chain lengths and ascertaining that the results obtained become insensitive to further increases. Second, one must establish a suitable method to determine the transmission coefficient T, since it is not explicitly contained in the time evolution of the wave function but rather need to be derived or estimated from it.

Reference [37] tracks the time evolution of the wave packet by using a leap-frog type method (described in detail, e.g. in [38]). According to this method, Eq. (10) is first written in terms of the real and imaginary parts of the wave function $\psi(\mathbf{r},t) = R(\mathbf{r},t) + i\,I(\mathbf{r},t)$ as

$$\frac{\partial R(r,t)}{\partial t} = H\ I(r,t) \tag{12}$$

$$\frac{\partial I(r,t)}{\partial t} = -H\ R(r,t)\ , \tag{13}$$

and then a leap-frog discretization for time t is applied to arrive at

$$I(r,t+\frac{1}{2}) \approx I(r,t-\frac{1}{2}) - \triangle t\ H\ R(r,t) \tag{14}$$

$$R(r,t+1) \approx R(r,t) + \triangle t\ H\ I(r,t+\frac{1}{2}) \tag{15}$$

These last equations are then used to update and evolve the wave packet numerically.

4.1 Propagation Through an Ordered System

It is instructive to first graphically see the evolution of the wave packet through a fully ordered ($p = 1$) cluster. Though we already know a great deal about the transmission properties of the ordered cluster (see Sect. 2), we can learn a number of things by actually visualizing the propagating wave packet as we will see below.

Shown in Fig. 12 are the snapshots when a wave packet propagates through the diagonally connected leads. Initially prepared as a Gaussian wave form at the middle of the input lead as in (a), its leading edge reaches the point of contact with the cluster in (b) and splits into a reflecting wave plus one that propagates through the cluster predominantly in the diagonal direction. As the wave packet spreads and propagates through the cluster, it interferes with itself in many ways. This interference effect is particularly large when the leading edge of the wave packet reaches the contact point with the output lead in (c). Finally in (d) some portion of the wave exits the cluster, largely keeping the Gaussian shape intact (though with a smaller amplitude), and its leading edge touches the end of the output lead. This also leaves behind a second wave of reflecting pattern slushing within the cluster.

As in this illustration, it is often obvious how to approximate the transmission coefficient T in this approach. Reference [37] estimates T by summing the probability density for the portion of the wave packet that is on the output lead when the leading edge of the wave packet has first reached the end of the output lead. They verified the validity of this approximation by first employing increasing lead lengths and thereby locating an optimal length where the approximation starts to yield stable values of T. Then they used this optimal length in subsequent work.

The particle transmission depends very sensitively on the details of the boundary connections for the ordered cluster, and this becomes visually obvious by looking at the wave packet evolution with different boundary connection types. For example, when the leads are connected in a point-to-point connection but to the edge sites other than the diagonal corners, transmission is generally reduced significantly. This is because, as the wave packet enters the cluster, it spreads out more broadly

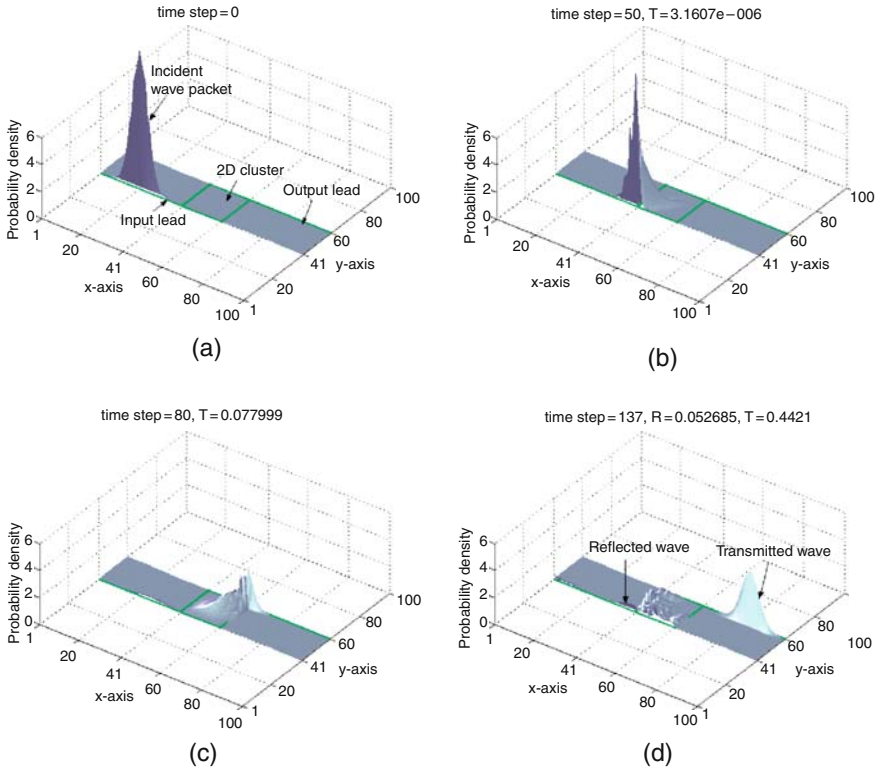

Fig. 12. A typical time evolution of a wave packet through a cluster of size 20×20 with leads connected diagonally at the lower left and upper right corners of the cluster. The time step for each snapshot and corresponding reflection and transmission coefficients R and T are shown at the *top* of each snapshot. From [37]

and generally in less well-defined directions, causing more widespread interference. Similarly, the propagation of the wave packet under the busbar connection is dominated by the destructive interference of the packet on the edge of the cluster at the input contact and very little transmission through the cluster will be observed. We refer the interested reader to the extensive illustrations in [37].

4.2 Wave Packet Propagation Through a Disordered Cluster

As a first step towards understanding the interference effects affecting the wave packet's transmission when the cluster is disordered, Ref. [37] investigated the effects of diluting (or removing) certain selected, fixed sites. The diluted sites act as infinite potential barriers for the particle.

With a single site near the body diagonal diluted in the diagonal, point-to-point connection, the time evolution of the wave packet is immensely affected as seen in Fig. 13. As the wave packet encounters the diluted site, it gets scattered by the infinite

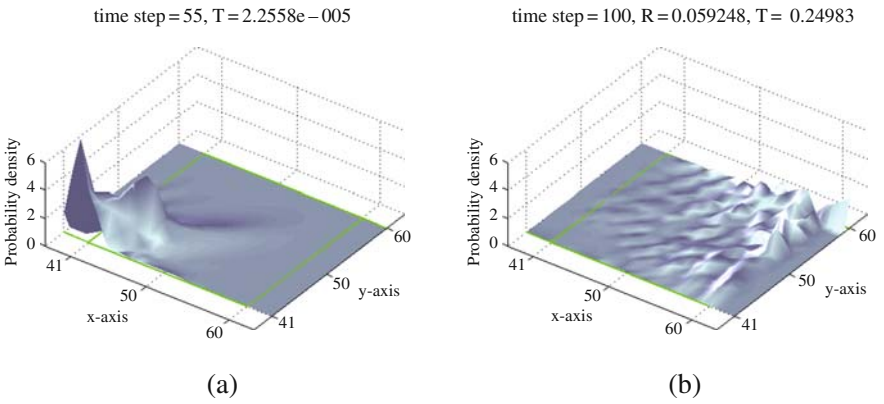

Fig. 13. Time evolution of a wave packet in the presence of a single diluted site near the body diagonal in the diagonal point-to-point connection. Compare with Fig. 12(b) and (c) with no dilution. After [37]

barrier and transmission is reduced. The much broader spreading of the wave packet is clearly observed in Fig. 13 as well as in the corresponding depressed values of T.

Effects of diluting selected sites is, however, in general complicated. For the diagonal connection, diluting any site tends to reduce transmission. For other boundary connections, for example, off-diagonal point-to-point connections, a judicious choice of the sites to remove can in fact lead to enhanced transmission. This is of course just a reflection of the fact that interference could be either destructive or constructive, and detailed geometry, particularly the symmetry or lack thereof, plays an important role in determining the net effect of interference. However, the extreme destructive and extreme constructive interferences that are needed to achieve near complete reflection or transmission, respectively, will require very special arrangements of disorder. In fact, what we mentioned in Sect. 2 about the correlation between transmission and the predominance of local phase variations of ψ of $\sim \pi$ or $\sim 2\pi$ appears to be true for the cases where the cluster is disordered as well. See [31] for the details.

We now turn to the random dilution of the quantum percolation problem, the same problem that we focused on in Sect. 3 where the stationary state solutions of the Schrödinger equation were investigated. Here, we track the time evolution of the wave packets, originally prepared as Gaussian, through the percolation network at some $q = 1 - p > 0$.

The Fig. 14 shows the time evolution of a wave packet through a particular realization of a disordered cluster of size 30×30 with 10% dilution, with diagonally connected leads. Comparing with Fig. 12 for the ordered cluster, the much broader spreading of $|\psi|^2$ is obvious, as is the much lower T. In addition, a large part of the wave packet is now trapped inside the disordered cluster at these time scales. While these features are common to all disorder realizations, closer analysis reveals that they can be quantitatively very different. In fact, the values of T can differ by many orders of magnitude from realization to realization, being very sensitive to the exact

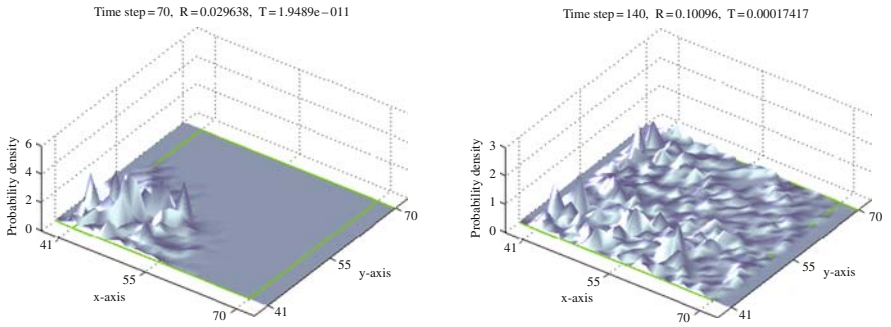

(a) (b)

Fig. 14. Propagation of a wave packet is illustrated through a particular realization of a 30×30 cluster with 10% dilution with diagonally connected input and output leads. (**a**) and (**b**) are two snapshots at $t = 70$ and 140, respectively. From [37]

locations of the diluted sites. For example, if the concentration of diluted sites near the input lead is large then the reflection coefficient is observed to be large. These subtleties become clear through visualizations such as the current method.

4.3 Localization Regimes from the Wave Packet Transmission

This method can also be used to study (and confirm) the nature of localization in 2D quantum percolation just in the same manner as the stationary state solution discussed in Sect. 3. For this purpose, one first prepares a particular incoming wave packet (with a selected central wave number k_0 which is analogous to a given value of the energy E in the static problem, etc.). Then on a set of disorder realizations at a particular level of disorder constructed on a given size of a cluster, the wave packet is released from the input lead and its evolution is tracked until the leading edge of the packet reaches the end of the output lead. At that point, one uses the probability fraction residing on the output lead as the approximate estimate of T. For each dilution level and cluster size, the disorder average is taken, and then the calculation is repeated for different dilution levels and cluster sizes. Clearly, the additional need to track the evolution of ψ leads to higher computational requirements than for the stationary state calculations particularly for larger cluster sizes, and thus limits the size of the cluster and the extent of disorder averages that can be taken. The results of such a calculation by [37] are shown in Fig. 15 where each data point is the average of 100 disorder realizations. In this work, the maximum size of the cluster was 70×70 and $k_0 = 4.7$ in units of reciprocal lattice spacings was used.

We note the similarities between Fig. 15 above and Fig. 8 from Sect. 3, particularly in the apparently good fits to a straight line for the lower dilution levels (of up to about 20% here) and to an exponential decrease for greater dilution. Again, a closer inspection of these the log-log scale fits reveals considerable, systematic deviations just as in the stationary state case. Thus, Ref. [37] further investigated the

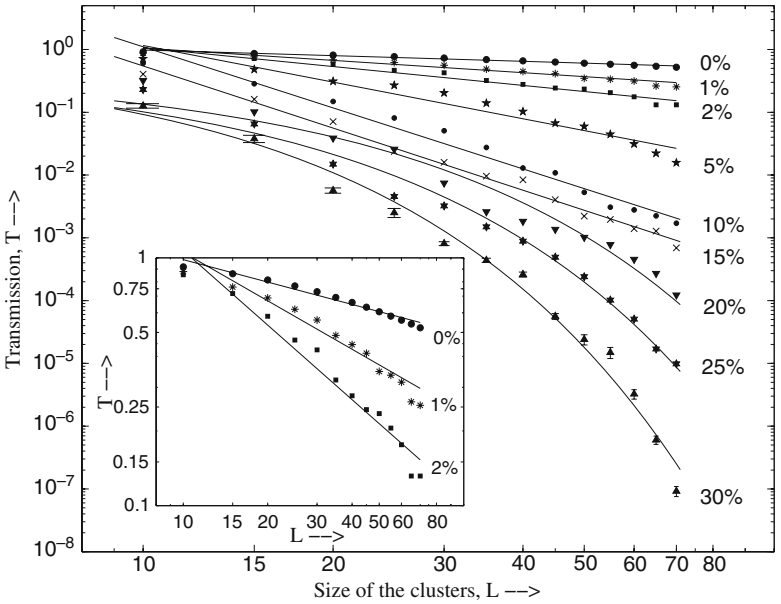

Fig. 15. The transmission of wave packets through disordered clusters with diagonally connected leads. In the main panel a log-log plot of T versus L is shown for various amounts of disorder. The *solid lines* are from the fits made on the log-log scale in the same manner as in Fig. 8 for the stationary state solutions. The inset shows the the transmission data only for lower disorders (up to 2%) with an expanded vertical scale. From [37]

matter by fitting the data on the linear scale for the larger cluster sizes ($L > 26$), just as we showed in Sect. 3 for the stationary state solutions. The latter fitting results are shown in Fig. 16.

Both by inspection of the fits and also more quantitative measures such as the regression coefficients $|R_\sigma|^2$ and residual square errors, Ref. [37] concluded that in all these counts an exponential with offsets gives significantly better fits than a power-law for the values of dilution shown in Fig. 16. Except for the 5% dilution case, the 95% confidence range of the offsets clearly excludes zero according to these fits, consistent with a nonzero T even in thermodynamic limit for these cases. Thus, the lower disorder portion of the data that was fitted to a power-law in Fig. 15 in fact splits into those that actually fit better to an exponential with a nonzero offset (i.e., extended; up to $\sim$5% disorder) and those that fit to a power-law better (power-law localized; between about $\sim$5% and $\sim$15% disorder) for the particular wave packets used.

Thus, the study of the propagation of the wave packet yields the same conclusion as that of the static solutions, leading to the existence of three distinct regimes, that is, exponentially localized states for about 20% or greater dilution (for these wave packets), power-law localized states down to about 5% dilution, and extended states with finite bulk conductance below that. This of course means that there must also

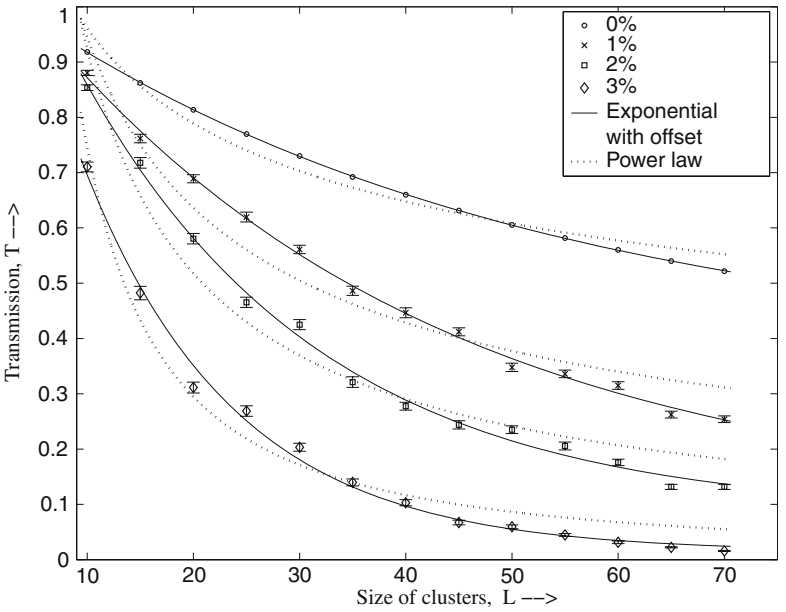

Fig. 16. The linear fits of the transmission coefficient T versus L obtained from the propagation of a Gaussian wave packet through the cluster of size $L \times L$. Data from lower dilution levels are shown and also those from ordered state (0% dilution) are included for comparison. The *dotted lines* represent power-law fits and the *solid lines* represent exponential fits with a possibly finite offset. For this range of disorder, an exponential with a finite offset seems to fit clearly better than a power-law, suggesting a nonzero transmission T even in the thermodynamic limit. After [37]

be phase transitions between these qualitatively distinct states of the wave function, confirming the static results at least for these particular wave packets.

5 Summary

In this chapter, we summarized the long-standing controversies related to the localization nature of the quantum percolation problem in two dimensions and gave an overview of the more recent numerical work that provides some evidence for the existence of three distinct localization regimes in such a system. According to this suggestion, in addition to the commonly found exponentially localized regime and more elusive power-law localized regime, there is also a fully delocalized regime with nonzero transmission in the thermodynamic limit. In addition, in the power-law regime, the exponent that describes the power-law dependence of the transmission on the system size (length scale) varies continuously with the strength of disorder, a situation somewhat reminiscent of the Kosterlitz-Thouless transition in the 2D XY model [36].

Acknowledgments

We would like to thank E. Cuansing, A. Overhauser, Y. Lyanda-Geller, L. Rokhinson, G. Giuliani and N. Giordano for fruitful discussions.

References

1. E. Cuansing and H. Nakanishi, Phys. Rev. E **70**, 066142 (2004) 109, 116, 117
2. E. Abrahams, P.W. Anderson, D.C. Licciardello, and T.V. Ramakrishnan, Phys. Rev. Lett. **42**, 673 (1979) 109
3. N. Goldenfeld and R. Haydock, Phys. Rev. B **73**, 045118 (2006). 109
4. C.M. Soukoulis, E.N. Economou, and G.S. Grest, Phys. Rev. B **36**, 8649 (1987) 110
5. Th. Koslowski and W. von Niessen, Phys. Rev. B **44**, 9926 (1991) 110
6. R. Berkovits and Y. Avishai Phys. Rev. B **53**, R16125 (1996) 110
7. G. Hałdaś, A. Kolek, and A.W. Stadler, Phys. Status Solidi B **230**, 249 (2002) 110
8. A. Bunde, J.W. Kantelhardt, and L. Schweitzer, Ann. Phys. (Leipzig) **7**, 372 (1998) 110
9. C.M. Soukoulis and G.S. Grest, Phys. Rev. B **44**, 4685 (1991) 110
10. A. Mookerje, I. Dasgupta, and T. Saha, Int. J. Mod. Phy. B **9** (23), 2989 (1995) 110, 118
11. M. Inui, S.A. Trugman, and E. Abrahams, Phys. Rev. B **49**, 3190 (1994) 110
12. D. Daboul, I. Chang, and A. Aharony, Eur. Phys. J B **16**, 303 (2000) 110, 115
13. T. Odagaki and K.C. Chang, Phys. Rev. B **30**, 1612 (1984) 110
14. V. Srivastava and M. Chaturvedi, Phys. Rev. B **30**, 2238 (1984) 110
15. M. Letz and K. Ziegler, Phil. Mag. B **79**, 491 (1999) 110
16. H.N. Nazareno, P.E. de Brito, and E.S. Rodrigues, Phys. Rev. B **66**, 012205 (2002) 110
17. A. Eilmes, R.A. Römer, and M. Schreiber, Physica B **296**, 46 (2001) 110
18. E. Cuansing and H. Nakanishi, Physica A **387**, 806 (2008) 110, 121
19. Md.F. Islam and H. Nakanishi, Phys. Rev. E 77, 061109 (2008). 110, 121, 122, 123, 124
20. S. Kirkpatrick and T.P. Eggarter, Phys. Rev. B **6**, 3598, (1972). 110
21. P.G. de Gennes, P. Lafore, J. Millot, J. Phys. Chem. Sol. **11**, 105 (1959) 110
22. D. Stauffer and A. Aharony. *Introduction to Percolation Theory* (Taylor and Francis, Bristol, Pennsylvania, 1994) 111
23. A. Giacometti, H. Nakanishi, A. Maritan, and N.H. Fuchs, J. Phys. A **25**, L461 (1992) 111
24. A. Giacometti and H. Nakanishi, Phys. Rev. E **50**, 1093 (1994) 111, 112
25. A. Giacometti and H. Nakanishi, Phys. Rev. E **51**, 6328E (1995) 111, 112
26. S. Mukherjee and H. Nakanishi, Fractals, **4**, 273 (1996) 111
27. S. Mukherjee and H. Nakanishi, Physica A, **294**, 123 (2001) 111
28. S. Mukherjee, H. Nakanishi, and N.H. Fuchs, Phys. Rev. E **49**, 5032 (1994) 112, 113
29. M. Büttiker, Y. Imry, R. Landauer, and S. Pinhas, Phys. Rev. B **31**, 6207 (1985) 116
30. S. Datta. *Electronic Transport in Mesoscopic Systems* (Cambridge Univ. Press, Cambridge, UK, 1992) 117

31. Md.F. Islam and H. Nakanishi, Euro. Phys. J. B., DOI: 10.1140/epjb/e2008-00363-x (2008). 118, 119, 120, 129
32. J.W. Kantelhardt and A. Bunde, Phys. Rev. E **56**, 6693 (1997) 118
33. J.W. Kantelhardt and A. Bunde, Ann. Phys. (Leipzig) **7**, 5–6, 400–405 (1998) 118
34. J. Drager and O. Halfpap, Ann. Phys. (Leipzig) **7**, 539 (1998) 118
35. K. Yakubo and T. Nakayama, Phys. Rev. B **40**, 517 (1989) 118
36. J.M. Kosterlitz and D.J. Thouless, J. Phys. C **6**, 1181 (1973) 125, 132
37. Md.F. Islam and H. Nakanishi, Euro. Phys. J. B. (submitted). 125, 126, 127, 128, 129, 130
38. N.J. Giordano and H. Nakanishi. *Computational Physics*, 2nd ed. (Prentice-Hall, New Jersy, USA, 2006) 126

Quantum Percolation in Disordered Structures

G. Schubert and H. Fehske

Ernst-Moritz-Arndt-Universität Greifswald, Institut für Physik, Felix-Hausdorff-Str. 6, D-17489 Greifswald, Germany
{schubert,fehske}@physik.uni-greifswald.de

1 Introduction

Many solids, such as alloys or doped semiconductors, form crystals consisting of two or more chemical species. In contrast to amorphous systems, they show a regular, periodic arrangement of sites but the different species are statistically distributed over the available lattice sites. This type of disorder is often called compositional. Likewise crystal imperfections present in any real material give rise to substitutional disordered structures. The presence of disorder has drastic effects on various characteristics of physical systems, most notably on their electronic structure and transport properties.

A particularly interesting case is a lattice composed of accessible and inaccessible sites (bonds). Dilution of the accessible sites defines a percolation problem for the lattice that can undergo a geometric phase transition between a connected and a disconnected phase. Since "absent" sites (bonds) act as infinite barriers such a model can be used to describe percolative particle transport through random resistor networks (see Fig. 1). Another example is the destruction of magnetic order in diluted classical magnets. The central question of classical percolation theory is whether the diluted lattice contains a cluster of accessible sites that spans the entire sample in the thermodynamic limit or whether it decomposes into small disconnected pieces.

The corresponding problem of percolation of a quantum particle through a random medium is much more involved. Here the famous concept of Anderson localization comes into play [1]. Anderson argued that the one-particle wave functions in macroscopic, disordered quantum systems at zero temperature can be exponentially localized. This happens if the disorder is sufficiently strong or in energy regions where the density of states is sufficiently small [2]. The transition from extended to localized states is a result of quantum interference arising from elastic scattering of the particle at the randomly varying site energies. Particles that occupy exponentially localized states are restricted to finite regions of space. On the other hand, particles in extended states can escape to infinity and therefore contribute to transport (see Fig. 2).

Schubert, G., Fehske, H.: *Quantum Percolation in Disordered Structures*. Lect. Notes Phys. **762**, 135–162 (2009)
DOI 10.1007/978-3-540-85428-9_5

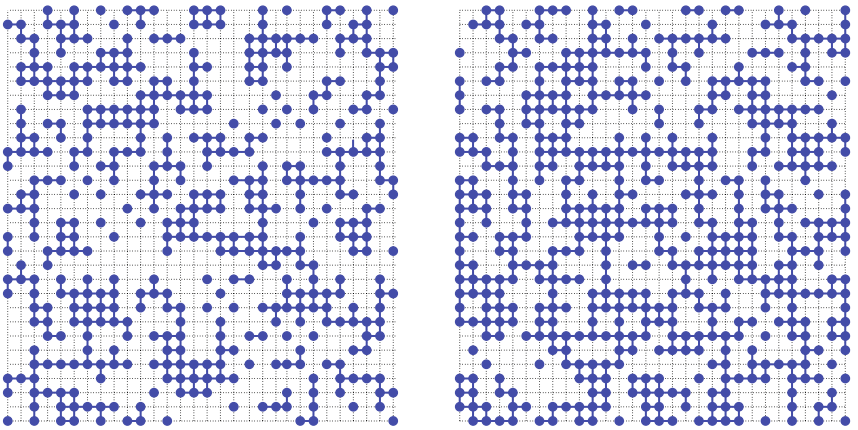

Fig. 1. $2D$ site percolation. Shown are lattice realizations below (*left*) and above (*right*) the classical percolation threshold $p_c = 0.592746$

For the quantum percolation problem all one-particle states are localized below the classical percolation threshold p_c. Furthermore, for arbitrary concentrations of conducting sites $p > p_c$ there always exist localized states on the infinite spanning cluster [3]. Since for a completely ordered system ($p = 1$) all states are extended and no states are extended for $p < p_c$, one might expect a disorder-induced Anderson transition at some critical concentration p_q, with $p_c \leq p_q \leq 1$. The reason is that the quantum nature of particles makes it harder for them to pass through narrow channels, despite the fact that quantum particles may tunnel through classically forbidden regions [4]. As yet the existence of a quantum percolation threshold, different from the classical one, is discussed controversial, in particular for the two-dimensional ($2D$) case where also weak localization effects might become important [5].

Localization and quantum percolation have been the subject of much recent research; for a review of the more back-dated work see for example, [6, 7]. The

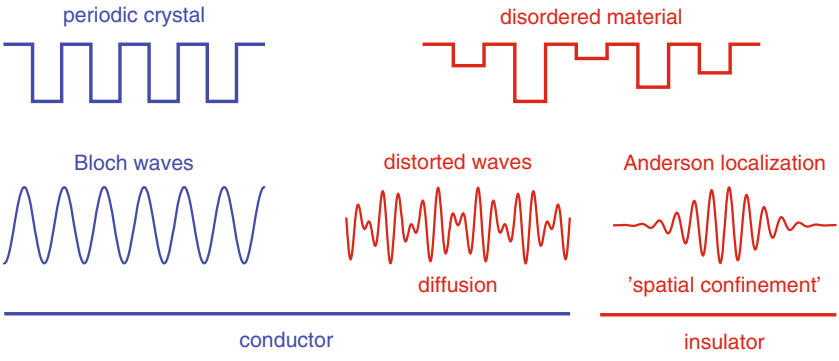

Fig. 2. Anderson transition in disordered systems

underlying Anderson model (with uniformly distributed local potentials) and site percolation or binary alloy models (with a bimodal distribution of the on-site energies) are the two standard models for disordered solids. Although, both problems have much in common, they differ in the type of disorder, and the localization phenomena of electrons in substitutional alloys are found to be much richer than previously claimed. For instance, the binary alloy model exhibits not one, as the $3D$ Anderson model, but several pairs of mobility edges, separating localized from extended states [3, 8, 9]. Moreover it appears that "forbidden energies" exist, in the sense that near the band center the density of states continuously goes to zero. These effects might be observed in actual experiments.

Understanding these issues is an important task, which we will address in this tutorial-style review by a stochastic approach that allows for a comprehensive description of disorder on a microscopic scale. This approach, which we call the local distribution (LD) approach [9, 10], considers the local density of states (LDOS), which is a quantity of primary importance in systems with prominent local interactions or scattering. What makes the LD approach "nonstandard" is that it directly deals with the distribution of the LDOS in the spirit that Anderson introduced in his pioneering work [1]. While the LDOS is just related to the amplitude of the electron's wave function on a certain lattice site, its distribution captures the fluctuations of the wave function through the system.

The present chapter will be organized as follows. After introducing the basic concepts of the LD approach in Sect. 2 and explaining how to calculate the LDOS via the highly efficient Kernel Polynomial Method (KPM), we exemplify the LD concept by a study of localization within the Anderson model. Then, having all necessary tools at hand, we proceed in Sect. 3 to the problem of quantum percolation. Refining previous studies of localization effects in quantum percolation, we will demonstrate the 'fragmentation' of the spectrum into extended and localized states. The existence of a quantum percolation threshold is critically examined. To this end, we investigate the dynamical properties of an initially localized wave packet on the spanning cluster, using Chebyshev expansion in the time domain. In Sect. 4 we apply the findings to several classes of advanced materials, where transport is related to percolating current patterns. Here prominent examples are $2D$ undoped graphene and the $3D$ colossal magnetoresistive manganites. Finally, in Sect. 5 we conclude with a short summary of the topic.

2 Local Distribution Approach

2.1 Conceptional Background

In the theoretical investigation of disordered systems, it turned out that the distribution of random quantities takes the center stage [1, 11]. Starting from a standard tight-binding Hamiltonian of non-interacting electrons on a D-dimensional hypercubic lattice with $N = L^D$ sites, the effect of compositional disorder in a solid may be described by site-dependent local potentials ϵ_j.

$$H = -t \sum_{\langle ij \rangle} \left(c_i^\dagger c_j + \text{H.c.} \right) + \sum_{j=1}^{N} \epsilon_j c_j^\dagger c_j \; . \tag{1}$$

The operators $c_j^\dagger$ (c_j) create (annihilate) an electron in a Wannier state centered at site j, the on-site potentials ϵ_j are drawn from some probability distribution $p[\epsilon_j]$, and t denotes the nearest-neighbor hopping element. While all characteristics of a certain material are determined by the corresponding distribution $p[\epsilon_j]$, we have to keep in mind, that each actual sample of this material constitutes only one particular realization $\{\epsilon_j\}$. The disorder in the potential landscape breaks translational invariance, which normally can be exploited for the description of ordered systems. Hence, we have to focus on site-dependent quantities such as the LDOS at lattice site i,

$$\rho_i(E) = \sum_{n=1}^{N} |\langle i|n\rangle|^2 \, \delta(E - E_n) \; , \tag{2}$$

where $|n\rangle$ is an eigenstate of H with energy E_n and $|i\rangle = c_i^\dagger |0\rangle$. Probing different sites in the crystal, $\rho_i(E)$ will strongly fluctuate, and recording the values of the LDOS we may accumulate the distribution $f[\rho_i(E)]$. In the thermodynamic limit, taking into account infinitely many lattice sites, the shape of $f[\rho_i(E)]$ will be independent of the actual realization of the on-site potentials $\{\epsilon_j\}$ and the chosen sites, but depend solely on the underlying distribution $p[\epsilon_j]$. Thus, in the sense of distributions, we have restored translational invariance, and the study of $f[\rho_i(E)]$ allows us to discuss the complete properties of the Hamiltonian (1). The probability density $f[\rho_i(E)]$ was found to have essentially different properties for extended and localized states [12]. For an extended state, the amplitude of the wave function is more or less uniform. Accordingly, $f[\rho_i(E)]$ is sharply peaked and symmetric about the (arithmetically averaged) mean value $\rho_{\rm me}(E)$. On the other hand, if states become localized, the wave function has considerable weight only on a few sites. In this case, the LDOS strongly fluctuates throughout the lattice and the corresponding LDOS distribution is mainly concentrated at $\rho_i = 0$, very asymmetric and has a long tail. The rare but large LDOS-values dominate the mean value $\rho_{\rm me}(E)$, which therefore cannot be taken as a good approximation of the most probable value of the LDOS. Such systems are referred to as "non-self-averaging". In numerical calculations, this different behavior may be used to discriminate localized from extended states in the following manner: Using the KPM with a variable number of moments for different interval sections (see Sect. 2.2) we calculate the LDOS for a large number of samples, K_r, and sites, K_s. Note that from a conceptual point of view, it makes no difference if we calculate $f[\rho_i(E)]$ for one large sample and many sites or consider smaller (but not too small) systems and more realizations of disorder. As the latter procedure is numerically more favorable, we will revert to this. Next, we sort the LDOS values for all energies within a small window around the desired energy E into a histogram. As the LDOS values vary over several orders of magnitude, a logarithmic partition of the histogram presents itself. Although this procedure allows for the most intuitive determination of the localization properties in the sense of Anderson [1], there

are two drawbacks. First, to achieve a reasonable statistics, in particular for the slots at small LDOS values, a huge number of realizations is necessary. To alleviate the problems of statistical noise, it is advantageous to look at integral quantities such as the distribution function

$$F[\rho_i(E)] = \int_0^{\rho_i(E)} f[\rho_i'(E)]\,\mathrm{d}\rho_i'(E)\ , \tag{3}$$

which also allows for the determination of the localization properties. While for extended states the more or less uniform amplitudes lead to a steep rise of $F[\rho_i]$, for localized states the increase extends over several orders of magnitude. Second, for practical calculations the recording of the whole distribution (or distribution function) is a bit inconvenient, especially if we want to discuss the localization properties of the whole band. Therefore, we try to capture the main features of the distribution by comparing two of its characteristic quantities, the (arithmetically averaged) mean DOS,

$$\rho_{\mathrm{me}}(E) = \frac{1}{K_r K_s}\sum_{k=1}^{K_r}\sum_{i=1}^{K_s}\rho_i(E)\ , \tag{4}$$

and the (geometrically averaged) so called typical DOS ,

$$\rho_{\mathrm{ty}}(E) = \exp\left(\frac{1}{K_r K_s}\sum_{k=1}^{K_r}\sum_{i=1}^{K_s}\ln\bigl(\rho_i(E)\bigr)\right). \tag{5}$$

The typical DOS puts sufficient weight on small values of ρ_i. Therefore, comparing $\rho_{\mathrm{ty}}(E)$ and $\rho_{\mathrm{me}}(E)$ allows to detect the localization transition. We classify a state at energy E with $\rho_{\mathrm{me}}(E) \neq 0$ as localized if $\rho_{\mathrm{ty}}(E) = 0$ and as extended if $\rho_{\mathrm{ty}}(E) \neq 0$. This method has been applied successfully to the pure Anderson model [13–15] and even to more complex situations, where the effects of correlated disorder [16], electron-electron interaction [17, 18] or electron-phonon coupling [19, 20] were taken into account.

2.2 Calculation of the Local Density of States by the Variable Moment Kernel Polynomial Method

At first glance, Ref. (2) suggests that the calculation of the LDOS could require a complete diagonalization of H. It turns out, however, that an expansion of ρ_i in terms of a finite series of Chebyshev polynomials $T_n(x) = \cos(n \arccos x)$ allows for an incredibly precise approximation [21]. Since the Chebyshev polynomials form an orthogonal set on $[-1, 1]$, prior to an expansion the Hamiltonian H needs to be rescaled, $\tilde{H} = (H - b)/a$. For reasons of numerical stability, we choose the parameters a and b such that the extreme eigenvalues of $\tilde{H}$ are ± 0.99. In this way, the outer parts of the interval, where the strong oscillations of $T_n(x)$ can amplify numerical errors, contain no physical information and may be discarded. In terms of the coefficients, the so called Chebyshev moments,

$$\mu_m = \int_{-1}^{1} \rho_i(x) T_m(x)\,\mathrm{d}x = \sum_{n=1}^{N} \langle i|n\rangle\langle n|T_m(x_n)|i\rangle = \langle i|T_m(\tilde{H})|i\rangle\ , \tag{6}$$

the approximate LDOS reads

$$\rho_i(x) = \frac{1}{\pi\sqrt{1-x^2}} \left(g_0\mu_0 + 2\sum_{m=1}^{M-1} g_m \mu_m T_m(x) \right)\ . \tag{7}$$

The Gibbs damping factors

$$g_m = \left(1 - \frac{m\phi}{\pi}\right)\cos(m\phi) + \frac{\phi}{\pi}\sin(m\phi)\cot(\phi) \tag{8}$$

with $\phi = \pi/(M+1)$, are introduced to damp out the Gibbs oscillations resulting from finite-order polynomial approximations. The introduction of these factors corresponds to convoluting the finite series with the so called Jackson kernel [22]. In essence, a δ-peak at position x_0 is approximated by an almost Gaussian of width [21]

$$\sigma = \sqrt{\frac{M - x_0^2(M-1)}{2(M+1)}\,(1-\cos(2\phi))} \approx \frac{\pi}{M}\sqrt{1 - x_0^2 + \frac{4x_0^2 - 3}{M}}\ . \tag{9}$$

Thus, for a fixed number of moments, M, the resolution of the expansion gets better toward the interval boundaries. While in most applications this feature is harmless or even useful, here a uniform resolution throughout the whole band is mandatory to discriminate resolution effects from localization. This gets clear, if we respect that a small value of ρ_i at a certain energy may either be due to a true low amplitude of the wave function, or to the absence of any energy level for the current disorder realization within one kernel width. Depending on which part of the interval we want to reconstruct, we need to restrict the used number of moments in (7) accordingly to ensure a constant σ. We call this procedure the Variable Moment KPM (VMKPM). The resulting approximations of a series of δ-peaks using the standard KPM and the VMKPM, respectively, are compared in Fig. 3.

For practical calculation of the moments, we may profit from the recursion relations of the Chebyshev polynomials,

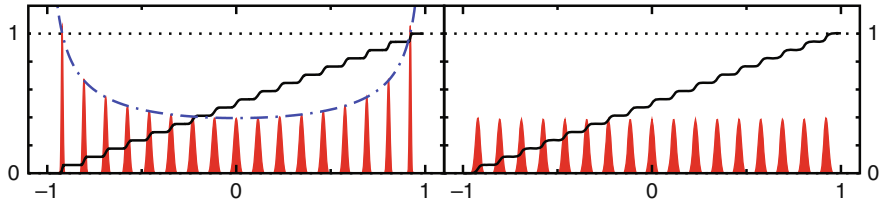

Fig. 3. Approximation of a series of equally weighted δ-peaks using the standard KPM (*left*) and the VMKPM (*right*). While both methods reproduce the correct spectral weight (*solid line*), only in the latter case a uniform resolution is obtained, reflected by the equal height of the peaks. The *dashed-dotted line* in the *left panel* is a guide to the eye being proportional to the inverse of the resolution (9)

$$T_{m+1}(x) = 2xT_m(x) - T_{m-1}(x) \ , \tag{10}$$

starting from $T_0(x) = 1$ and $T_1(x) = x$, and calculate the μ_m iteratively. Additionally, we may reduce the numerical effort by another factor $1/2$ by generating two moments with each matrix vector multiplication by $\tilde{H}$,

$$\begin{aligned} \mu_{2m-1} &= 2\langle i|T_m(\tilde{H})T_{m-1}(\tilde{H})|i\rangle - \mu_1 \ , \\ \mu_{2m} &= 2\langle i|T_m(\tilde{H})T_m(\tilde{H})|i\rangle - \mu_0 \ . \end{aligned} \tag{11}$$

Note that the algorithm requires storage only for the sparse matrix $\tilde{H}$ and two vectors of the corresponding dimension. Having calculated the desired number of moments, we calculate several reconstructions (7) for different M. We obtain the final result with uniform resolution by smoothly joining the corresponding results for the different subintervals. As the calculation of the μ_m dominates the computational effort, the additional overhead for performing several reconstructions is negligible as they can be done using a Fast Fourier Transform (FFT) routine.

2.3 Illustration of the Method: Anderson Localization in $3D$

To clarify the power of the method, let us briefly apply it to the Anderson model of localization [1], for which the principal results are well known and can be found in the literature [2, 7]. The Anderson model is described by the Hamiltonian (1), using local potentials ϵ_j, which are assumed to be independent, uniformly distributed random variables,

$$p[\epsilon_j] = \frac{1}{\gamma} \, \theta\left(\frac{\gamma}{2} - |\epsilon_j|\right) , \tag{12}$$

where the parameter γ is a measure for the strength of disorder. The spectral properties of the Anderson model have been carefully analyzed (see e.g. [23]). For sufficiently large disorder or near the band tails, the spectrum consists exclusively of discrete eigenvalues, and the corresponding eigenfunctions are exponentially localized. Since localized electrons do not contribute to the transport of charge or energy, the energy that separates localized and extended eigenstates is called the mobility edge. For any finite amount of disorder $\gamma > 0$, on a $1D$ lattice, all eigenstates of the Anderson Hamiltonian are localized [24, 25]. This is believed to hold also in $2D$, where the existence of a transition from localized to extended states at finite γ would contradict the one parameter scaling theory [26, 27]. In three dimensions, the disorder strength has a more distinctive effect on the spectrum. Only above a critical value γ_c all states are localized, whereas for $\gamma < \gamma_c$ a pair of mobility edges separates the extended states in the band center from the localized ones near the band edges [28]. For this reason, the $3D$ case serves as a prime example on which we demonstrate how to discriminate localized from extended states within the local distribution approach. In the upper panel of Fig. 4, we show the resulting distribution of $\rho_i(E = 0)$, normalized by its mean value $\rho_{\rm me}$, for two characteristic values of disorder. As $\rho_{\rm me}$ is a function of disorder, this normalization ensures $\langle \rho_i/\rho_{\rm me}\rangle = 1$ independent of γ, allowing for an appropriate comparison. In the delocalized phase, $\gamma = 3t$, the distribution is rather symmetric and peaked close to its mean value. Note

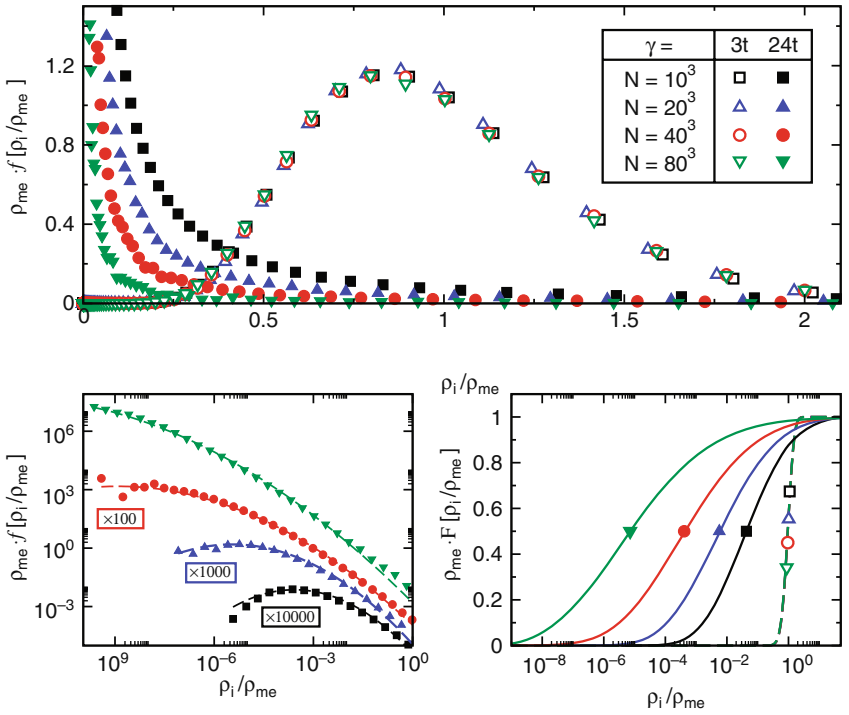

Fig. 4. *Upper panel*: Finite-size scaling of the normalized LDOS distribution $f[\rho_i/\rho_{\rm me}]$ at the band center ($|E| \leq 0.01t$) for the Anderson model. For the different system sizes N we adapted the resolution σ such that $N\sigma \approx 6.14$ is constant and calculated $10^6, 10^4, 1024, 400$ realizations of ρ_i for $N = 10^3, 20^3, 40^3, 80^3$. *Lower left panel*: Double-logarithmic plot of $f[\rho_i/\rho_{\rm me}]$ for the localized case together with lognormal fits (13) to the data. Note that for better visibility the data for $N = 40^3, 20^3, 10^3$ were shifted vertically by 2, 3, and 4 orders of magnitude towards smaller values. *Right lower panel*: Distribution function $F[\rho_i/\rho_{\rm me}]$ of the above data

that increasing both the system size and VMKPM resolution, such that the ratio of mean level spacing to the width of the Jackson kernel is fixed, does not change the distribution. This is in strong contrast to the localized phase, $\gamma = 24t$, where the distribution of $\rho_i(E)$ is extremely asymmetric. Although most of the weight is now concentrated close to zero, the distribution extends to very large values of ρ_i, causing the mean value to be much larger than the most probable value. Performing a similar finite-size scaling underlines both the asymmetry and the singular behavior, which we expect for infinite resolution in the thermodynamic limit. Note also, that for the localized case, the distribution of the LDOS is extremely well approximated by a lognormal distribution [29],

$$\Phi_{\log}(x) = \frac{1}{\sqrt{2\pi\sigma_0^2}} \frac{1}{x} \exp\left(-\frac{\left(\ln\left(x/x_0\right)\right)^2}{2\sigma_0^2}\right), \tag{13}$$

as illustrated in the lower-left panel of Fig. 4. The shifting of the distribution towards zero for localized states is most obvious in the distribution function $F[\rho_i]$, which is depicted in the lower-right panel of Fig. 4. While for extended states the more or less uniform amplitudes lead to a steep rise of $F[\rho_i]$, for localized states the increase extends over several orders of magnitude. Capturing the essential features of the LDOS distribution by concentrating on the mean (ρ_{me}) and typical (ρ_{ty}) density of states, we determine the localization properties for the whole energy band depending on the disorder. As can be seen from Fig. 5, $\rho_{\mathrm{me}}(E)$ and $\rho_{\mathrm{ty}}(E)$ are almost equal for extended states, whereas for localized states $\rho_{\mathrm{ty}}(E)$ vanishes while $\rho_{\mathrm{me}}(E)$ remains finite. Using the well-established value $\gamma_c(E = 0) \simeq 16.5\ t$ as a calibration for the critical ratio $\rho_{\mathrm{ty}}/\rho_{\mathrm{me}}$, required to distinguish localized from extended states for the used system size and resolution, we reproduce the mobility edge in the energy-disorder plane [2, 30, 31] (see lower-right panel of Fig. 5). We also find the well-known re-entrant behavior near the unperturbed band edges [32, 33]: Varying γ for some fixed values of E ($6\ t < E \leq 7.6\ t$) a region of extended states separates two regions of localized states. The Lifshitz boundaries, shown as dashed lines, indicate the energy range, where eigenstates are in principle allowed. As the probability of reaching the Lifshitz boundaries is exponentially small, we cannot expect to find states near these boundaries for the finite ensembles considered in any numerical calculation.

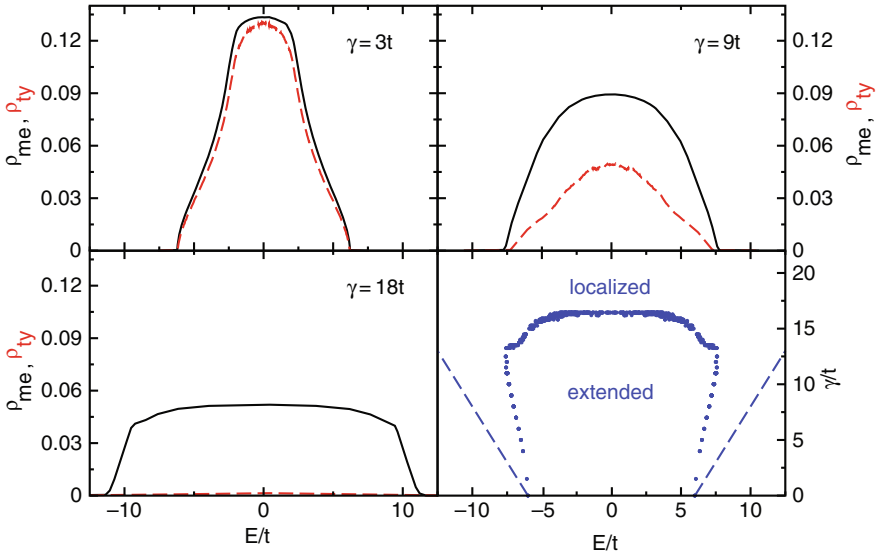

Fig. 5. Mean (*solid*) and typical (*dashed*) density of states of the $3D$ Anderson model on a lattice with $N = 60^3$ sites and periodic boundary conditions (PBC) for different values of disorder γ. We used $N\sigma = 45$ and the shown curves result from an ensemble of 2000 individual LDOS spectra obtained for different sites and realizations of disorder. *Lower right panel*: Mobility edge (*dots*) as obtained for $(\rho_{\mathrm{ty}}/\rho_{\mathrm{me}})_c = 0.05$ and Lifshitz boundaries (*dashed line*)

3 Localization Effects in Quantum Percolation

In disordered solids, the percolation problem is characterized by the interplay of pure classical and quantum effects. Besides the question of finding a percolating path of "accessible" sites through a given lattice, the quantum nature of the electrons imposes further restrictions on the existence of extended states and, consequently, of a finite DC-conductivity.

As a particularly simple model we start again from the basic Hamiltonian (1) drawing the $\{\epsilon_j\}$ from the bimodal distribution

$$p[\epsilon_j] = p\,\delta(\epsilon_j - \epsilon_A) + (1-p)\,\delta(\epsilon_j - \epsilon_B)\ . \tag{14}$$

The two energies ϵ_A and ϵ_B could, for instance, represent the potential landscape of a binary alloy $\mathrm{A}_p\mathrm{B}_{1-p}$, where each site is occupied by an A or B atom with probability p or $1-p$, respectively. Therefore we call (1) together with the distribution (14) the *binary alloy model*. In the limit $\Delta = (\epsilon_B - \epsilon_A) \to \infty$ the wave function of the A sub-band vanishes identically on the B-sites, making them completely inaccessible for the quantum particles. We then arrive at a situation where noninteracting electrons move on a random ensemble of $\tilde{N}$ lattice points, which, depending on p, may span the entire lattice or not. The corresponding *quantum site percolation model* reads

$$H = -t \sum_{\langle ij\rangle \in A} (c_i^\dagger c_j + \text{H.c.})\ , \tag{15}$$

where the summation extends over nearest-neighbor A-sites only and, without loss of generality, ϵ_A is chosen to be zero.

Within the classical percolation scenario the percolation threshold p_c is defined by the occurrence of an infinite cluster A_∞ of connected A sites. For the simple cubic lattice this site-percolation threshold is $p_c^{3D} = 0.311609$ [34] for the $3D$ case and $p_c^{2D} = 0.592746$ [35] in $2D$. In the quantum case, the multiple scattering of the particles at the irregular boundaries of the cluster can suppress the wave function, in particular within narrow channels or close to dead-ends of the cluster. Hence, this type of disorder can lead to absence of diffusion due to localization, even if there is a classical percolating path through the crystal. On the other hand, for finite Δ the tunneling between A and B sites may cause a finite DC-conductivity although the A sites are not percolating. Naturally, the question arises whether the quantum percolation threshold p_q, given by the probability above which an extended wave function exists within the A sub-band, is larger or smaller than p_c. Previous results [36, 37] for finite values of Δ indicate that the tunneling effect has a marginal influence on the percolation threshold as soon as $\Delta \gg 4tD$.

3.1 $3D$ Site Percolation

Before discussing possible localization phenomena let us investigate the behavior of the mean DOS for the binary alloy and quantum percolation model in $3D$. Figure 6 shows that as long as ϵ_A and ϵ_B do not differ too much, there exists a single and if

$p \neq 0.5$ asymmetric electronic band [36]. At about $\Delta \simeq 4tD$ this band separates into two sub-bands centered at ϵ_A and ϵ_B, respectively. The most prominent feature in the split-band regime is the series of spikes at discrete energies within the band. As an obvious guess, we might attribute these spikes to eigenstates on islands of A or B sites being isolated from the main cluster [3, 38]. It turns out, however, that some of the spikes persist, even if we neglect all finite clusters and restrict the calculation to the $\bar{N}$ sites of A-type on the spanning cluster, A_∞. This is illustrated in the upper panels of Fig. 7, where we compare the DOS of the binary alloy model at $\Delta \to \infty$ and the quantum percolation model. Increasing the concentration of accessible sites, the mean DOS of the spanning cluster is evocative of the DOS of the simple cubic lattice, but even at large values of p a sharp peak structure remains at $E = 0$ (see Fig. 7, lower panels).

To elucidate this effect, which for a long time was partially not accounted for in the literature [3, 36, 39, 40], in more detail, in Fig. 8 we fix p at 0.337, shortly above the classical percolation threshold. In addition to the most dominant peaks at $E/t = 0, \pm 1, \pm\sqrt{2}$, we can resolve distinct spikes at $E/t = \frac{1}{2}\left(\pm 1 \pm \sqrt{5}\right), \pm\sqrt{3}, \pm\sqrt{2 \pm \sqrt{2}}, \ldots$. These special energies coincide with the

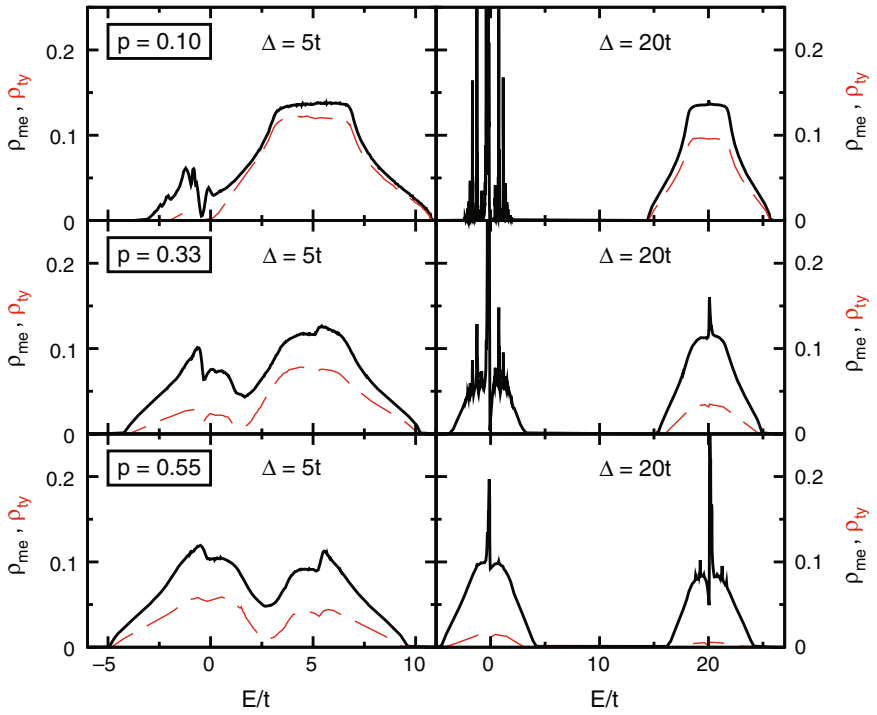

Fig. 6. Mean (*upper solid line*) and typical (*lower dashed line*) DOS of the binary alloy model on a $N = 64^3$ lattice with PBC for different concentrations of A-sites p and local potential differences Δ. Taking all sites into account, we chose the resolution such that $N\sigma = 45$ and calculated 1000 individual LDOS spectra for different probe realizations and sites

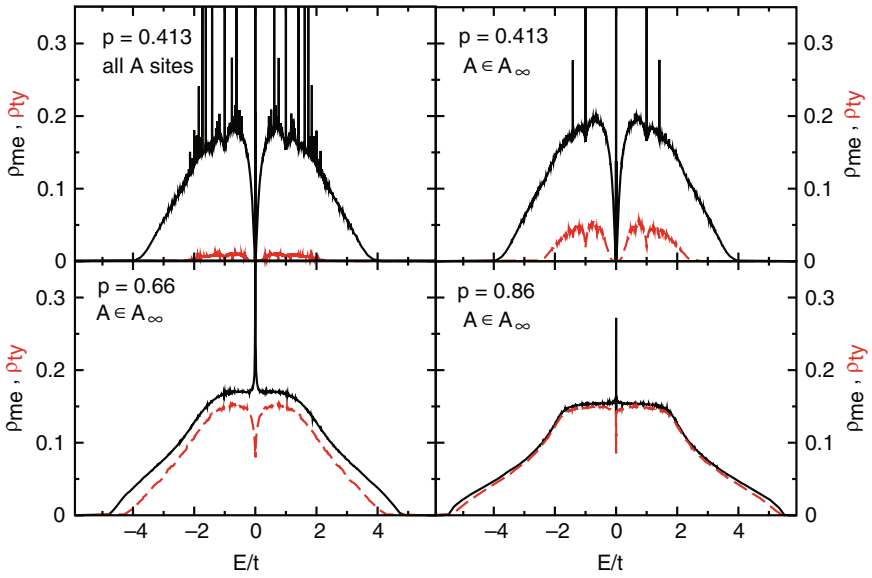

Fig. 7. Mean (*solid line*) and typical (*dashed line*) DOS for the quantum percolation model in the limit $\Delta \to \infty$. While in the upper left panel all A-sites are taken into account, the other three panels show data for the restricted model on the spanning cluster A_∞ only (note that $\rho_{\rm ty}$ is smaller in the former case because there are more sites with vanishing amplitude of the wave function). Using $\sigma = 0.0002$, we adapt the system sizes to ensure $\bar{N}\sigma = 45$ for the A_∞ case, i.e. , $N = 64^3, 70^3, 84^3$ for $p = 0.86, 0.66, 0.413$. For the case of all A sites at $p = 0.413$, $N = 82^3$ guarantees $\tilde{N}\sigma = 45$. For each system, we consider 512 individual LDOS spectra for different sites and realizations of disorder

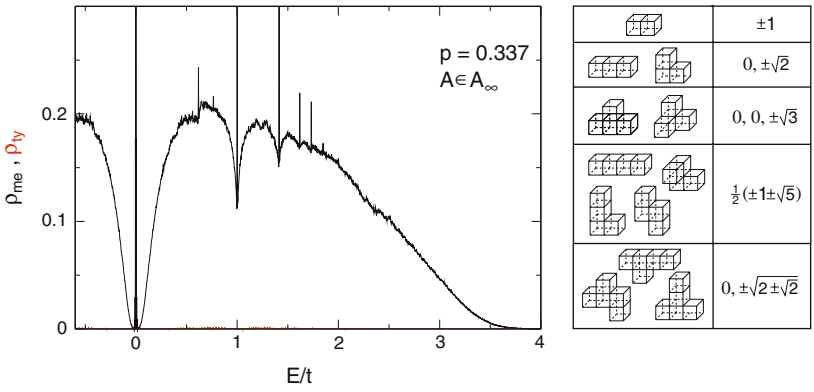

Fig. 8. *Left*: Mean (*solid line*) and typical (*dashed line*) DOS for the quantum percolation model with $p = 0.337$ on a $N = 100^3$ lattice (restriction to A_∞, PBC, $\bar{N}\sigma = 45$). The data are an ensemble average over 1000 realizations of disorder and different sites. Note that $\rho_{\rm ty} < 10^{-3}$ holds in the whole band. Right: Some cluster configurations related to the special energies at which the peaks in $\rho_{\rm me}$ occur

eigenvalues of the tight-binding model on small clusters of the geometries shown in the right part of Fig. 8. In accordance with [3] and [41] we can thus argue that the wave functions, which correspond to these special energies, are localized on some "dead ends" of the spanning cluster.

The assumption that the distinct peaks correspond to localized wave functions is corroborated by the fact that the typical DOS vanishes or, at least, shows a dip at these energies. Occurring also for finite Δ (Fig. 6), this effect becomes more pronounced as $\Delta \to \infty$ and in the vicinity of the classical percolation threshold p_c. From the study of the Anderson model we know that localization leads at first to a narrowing of the energy window containing extended states. For the percolation problem, in contrast, with decreasing p the typical DOS indicates both localization from the band edges and localization at particular energies within the band. Since finite cluster wave functions such as those shown in Fig. 8 can be constructed for numerous other, less probable geometries [42], an infinite discrete series of such spikes might exist within the spectrum, as proposed in [41]. The picture of localization in the quantum percolation model is then quite remarkable. If we generalize our numerical data for the peaks at $E = 0$ and $E = \pm t$, it seems as if there is an infinite discrete set of energies with localized wave functions, which is dense within the entire spectrum. In between there are many extended states, but to avoid mixing, their density goes to zero close to the localized states. Facilitated by its large special weight (up to 11% close to p_c) this is clearly observable for the peak at $E = 0$, and we suspect similar behavior at $E = \pm t$. For the other discrete spikes the resolution of our numerical data is still too poor and the system size might be even too small to draw a definite conclusion.

In order to understand the internal structure of the extended and localized states we calculate the probability density of specific eigenstates of (15) restricted to A_∞ for a fixed realization of disorder. Figure 9 visualizes the spatial variation of $|\langle i|n\rangle|^2$ for an occupation probability well above the classical percolation threshold. The figure clearly indicates that the state with $E = 0.649t$ is extended, that is, the spanning cluster is quantum mechanically "transparent". On the contrary, at $E = 3.501t$, the wave function is completely localized on a finite region of the spanning cluster. This is caused by the scattering of the particle at the random surface of the spanning cluster.

A particularly interesting behavior is observed at $E = 0$. Here, the eigenstates are highly degenerate and we can form wave functions that span the entire lattice in a checkerboard structure with zero and nonzero amplitudes (see Fig. 9). Although these states are extended in the sense that they are not confined to some region of the cluster, they are localized in the sense that they do not contribute to the DC-conductivity. This is caused by the alternating structure that suppresses the nearest-neighbor hopping, and in spite of the high degeneracy, the current matrix element between different $E = 0$ states is zero. Hence, having properties of both the classes of states, these states are called anomalously localized [43, 44]. Another indication for the robustness of this feature is its persistence for mismatching boundary conditions, for example, periodic (antiperiodic) boundary conditions for odd (even)

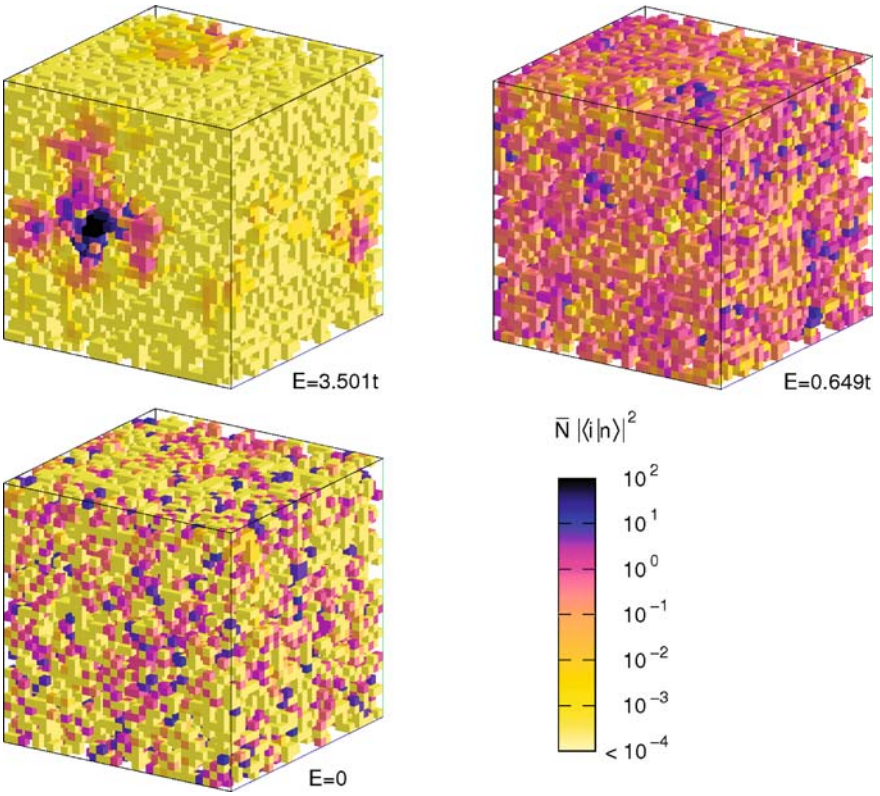

Fig. 9. Normalized probability density $\bar{N}|\langle i|n\rangle|^2$ for three eigenstates of the quantum percolation model. The chosen energies are representative for a localized ($E = 3.501t$), extended ($E = 0.649t$) and anomalous localized ($E = 0$) state. We performed an exact diagonalization for A_∞ for one realization of disorder on a $N = 32^3$ lattice with PBC and $p = 0.458$

values of the linear extension L. In these cases, the checkerboard is matched to itself by a manifold of sites with vanishing amplitude.

Furthermore, for the previously mentioned special energies, the wave function vanishes identically except for some finite domains on loose ends (such as those shown in the right panel of Fig. 8), where it takes, except for normalization, the values $(\pm 1, \mp 1)$, $(1, \pm\sqrt{2}, 1)$, $(-1, 0, 1)$, ... Note that these regions are part of the spanning cluster, connected to the rest of A_∞ by sites with wave function amplitude zero [41].

In the past, most of the methods used in numerical studies of Anderson localization have also been applied to the binary alloy model and the quantum percolation model in order to determine the quantum percolation threshold p_q, defined as the probability p below which all states are localized (see, e.g. [45, 46] and references therein). The existence of p_q is still disputed. As yet, the results for p_q are far less precise than, for example, the values of the critical disorder reported for the Anderson model. For the simple cubic lattice numerical estimates of quantum site-percolation thresholds range from 0.4 to 0.5 (see [46] and references therein). In Figs. 6–8 we

present data for $\rho_{\rm ty}$, which shows that $p_q > p_c$. In fact, within numerical accuracy, we found $\rho_{\rm ty} = 0$ for $p = 0.337 > p_c$.

To get a more detailed picture we calculate the normalized typical DOS, $\rho_{\rm ty}/\rho_{\rm me}$, in the whole concentration-energy plane. The left panel of Fig. 10 presents such a kind of phase diagram of the quantum percolation model. This data also support a finite quantum percolation threshold $p_q \gtrsim 0.4 > p_c$ (see also [36, 46–48]), but as the discussion above indicated, for $E = 0$ and $E = \pm t$ the critical value $p_q(E) = 1$, and the same may hold for the set of other "special" energies. The transition line between localized and extended states, $p_q(E)$, might thus be a rather irregular (fractal?) function. On the basis of our LDOS distribution approach, however, we are not in the position to answer this question with full rigor.

Finally, let us come back to the characterization of extended and localized states in terms of distribution functions. The right panel of Fig. 10 displays the distribution function, $F[\rho_i(E)]$, for four typical points in the energy-concentration plane, corresponding to localized, extended and anomalously localized states, respectively. The differences in $F[\rho_i(E)]$ are significant. The slow increase of $F[\rho_i(E)]$ observed for localized states corresponds to an extremely broad LDOS-distribution, with a very small most probable (or typical) value of $\rho_i(E)$. This is in agreement with the findings for the Anderson model. Accordingly, the jump-like increase found for extended states is related to an extremely narrow distribution of the LDOS centered around the mean DOS, where $\rho_{\rm me}$ coincides with the most probable value. At $E = 0$ and low p, the distribution function exhibits two steps, leading to a bimodal distribution density. Here the first (second) maximum is related to sites with a small (large) amplitude of the wave function–a feature that substantiates the checkerboard structure discussed above. For higher p, where we already found a reduced spectral weight of the central peak in $\rho_{\rm me}$, also the two-step shape of the distribution function is less pronounced.

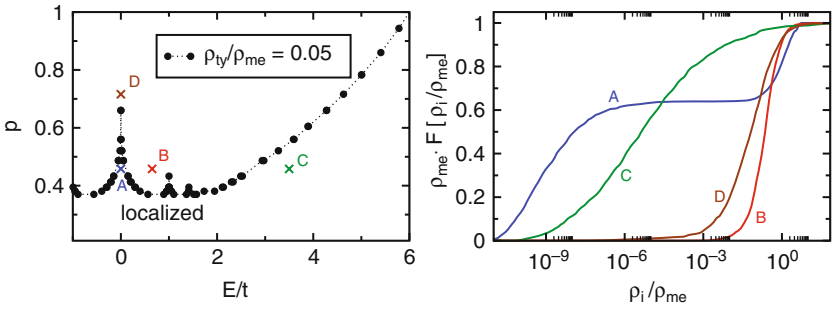

Fig. 10. *Left panel*: Normalized typical DOS $\rho_{\rm ty}/\rho_{\rm me}$ in the concentration-energy plane for the quantum percolation model restricted to A_∞. For a fixed resolution of $\sigma = 0.0002$ we adapted the system sizes to keep $\bar{N}\sigma = 45$ constant, that is, $N = 62^3, \ldots, 120^3$ for $p = 0.944, \ldots, 0.318$. The results based on the calculation of 1000 individual LDOS spectra for different cluster realizations and sites. *Right panel*: Distribution function of the LDOS for four characteristic states, for which the parameters (p, E) are indicated by crosses in the left panel. The parameters for the curves A, B and C are the same for which we showed the characteristic states in Fig. 9

Therefore we may argue that the increase in weight of the central peak for lower p is substantially due to the checkerboard states.

Having a rather complete perception of the physics in $3D$, let us now come to the $2D$ case, for which the findings in literature are more controversial.

3.2 $2D$ Site Percolation

Although the main characteristics of the $3D$ site-percolation problem, for example, the fragmentation of the spectrum, persist in $2D$, there exist some particularities and additional difficulties. In particular, the existence of a quantum percolation threshold $1 > p_q > p_c = 0.592746$ is even less settled than in $3D$. Published estimates range from $p_q = p_c$ to $p_q = 1$ (see [46, 49] and references therein). This uncertainty is due to the extremely large length scales, on which localization phenomena take place in $2D$, a fact well known for the standard Anderson model. Furthermore, the special characteristics of the band center states seem to be of particular importance [44, 50].

Local Density of States

Figure 11 shows the mean and typical DOS of the $2D$ quantum percolation model, calculated by the LD approach. For large p, ρ_{me} clearly resembles the $2D$ DOS shape for the ordered case. For these parameters ρ_{ty} nearly coincides with ρ_{me} except for the band center, where ρ_{ty} shows a strong dip. If we reduce the occupation probability, the spikes at special energies appear again (see Sect. 3.1), with most spectral weight at $E = 0$. The weight of the central peak (9% close to p_c) is reduced as compared with the $3D$ case.

In order to obtain reliable results for the infinite system, we examine the dependency of ρ_{ty} on the system size, for fixed $\bar{N}\sigma$. Here, we find a characteristic difference between large and small p. Whereas for large p, above a certain system size, ρ_{ty} is independent of N, it continuously decreases for low-occupation probabilities. This behavior is evocative of extended and localized states, respectively. Taking a look at the underlying distribution functions, we find a similar situation as in the $3D$ case. At $E = 0$, the two level distribution evolves, indicating the checkerboard structure of the state. Away from the special energies, the distribution function exhibits the shape characteristic for extended and localized states. This behavior exposes when we compare $F[\rho_i(E)]$ for different system sizes. Whereas for extended states the distribution function is insensitive against this scaling, it shifts towards smaller values for localized ones.

Although these results are quite encouraging, one aspect deserves further attention. If we try to calculate the LDOS distribution at a given energy E, due to the finite resolution of the KPM, it will also contain contributions from states in the vicinity of E. Thus, taking the fragmentation of the spectrum into localized and extended states seriously, the LDOS distribution within this artificial interval will contain contributions of each class of states.

For practical calculations, this causes no problems, as except for the most pronounced peaks, the probability of finding a state which is localized on one of the geometries as in the right panel of Fig. 8 drops very fast with its complexity.

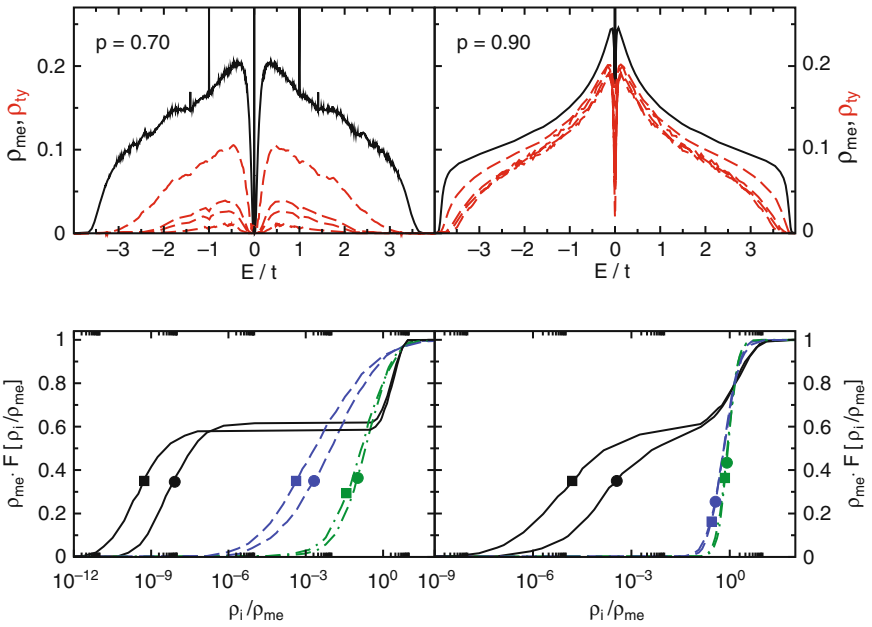

Fig. 11. *Upper panels*: Mean (*solid line*) and typical (*dashed lines*) DOS for the $2D$ percolation model for $p = 0.7$ (*left*) and $p = 0.9$ (*right*). The *dashed lines* correspond to the typical DOS for different system sizes (from *top* to *bottom*) $N = 114^2, 400^2, 572^2, 1144^2$ for $p = 0.7$ and $N = 100^2, 350^2, 500^2, 1000^2$ for $p = 0.9$. Again, we adapt σ, such that $\bar{N}\sigma = 45$. The curves are ensemble averages over 1000 (500 for the largest systems) individual LDOS spectra for different cluster realizations and sites. *Lower panel*: Distribution function of the LDOS for three characteristic energies: $E = 0$ (solid lines), $E = 0.5t$ (*dashed-dotted lines*), and $E = 2.5t$ (*dashed lines*). To underline the finite size scaling, we show the results for two system sizes, 350^2 (400^2) marked with circles, and 500^2 (572^2) with *squares*

Time Evolution

The expansion of the time evolution operator $U(\tau) = \mathrm{e}^{-\mathrm{i}H\tau}$ in Chebyshev polynomials allows for a very efficient method to calculate the dynamics of a quantum system. We may profit from this fact by calculating the recurrence probability of a particle to a given site, $P_R(\tau)$, which for $\tau \to \infty$ may serve as a criterion for localization [2, 27]. While for extended states on the spanning cluster $P_R(\tau \to \infty) = 1/\bar{N}$, which scales to zero in the thermodynamic limit, a localized state will have a finite value of $P_R(\tau)$ as $\bar{N} \to \infty$. The advantage of considering the time evolution is that in general the initial state is not an eigenstate of the system and therefore contains contributions of the whole spectrum. This allows for a global search for extended states and a detection of p_q.

Let us briefly outline how to calculate the time evolution of the system by means of Chebyshev expansion [51, 52]. Of course, as a first step, the Hamiltonian has to be rescaled to the definition interval of the Chebyshev polynomials, leading to

$$U(\tau) = \mathrm{e}^{-\mathrm{i}(a\tilde{H}+b)\tau} = \mathrm{e}^{-\mathrm{i}b\tau}\left[c_0 + 2\sum_{k=1}^{M} c_k T_k(\tilde{H})\right]. \tag{16}$$

The expansion coefficients c_k are given by

$$c_k = \int_{-1}^{1} \frac{T_k(x)e^{-\mathrm{i}ax\tau}}{\pi\sqrt{1-x^2}}\mathrm{d}x = (-\mathrm{i})^k J_k(a\tau)\ , \tag{17}$$

where J_k denotes the Bessel function of the first kind. Due to the fast asymptotic decay of the Bessel functions

$$J_k(a\tau) \sim \frac{1}{k!}\left(\frac{a\tau}{2}\right)^k \sim \frac{1}{\sqrt{2\pi k}}\left(\frac{\mathrm{e}a\tau}{2k}\right)^k \quad \text{for} \quad k \to \infty\ , \tag{18}$$

the higher-order expansion terms vanish rapidly. Thus, we do not need additional damping factors as in the Chebyshev expansion of the LDOS, but may truncate the series at some order without having to expect Gibbs oscillations. Note that the expansion order necessary to obtain precise results will surely depend on the time step used, normally $M \sim 2at$ will be sufficient. Thus, for optimum performance of the algorithm, we have to find a suitable compromise between time step $\Delta\tau$ and expansion order M. Anyhow, for reasonable M, the method permits the use of larger time steps compared to the standard Crank-Nicolson algorithm.

Having this powerful tool at hand, we are now in the position to calculate how $\psi(\mathbf{r}_i, \tau)$ evolves on A_∞ in time. The 'natural' time scales of the system are given by the energy of the nearest-neighbor hopping element $\tau_0 = 1/t$, describing one hopping event, and the time a particle needs (in a completely ordered system) to visit each site once, $T_0 = N\tau_0$. As initial state, we prepare a completely localized state, whose amplitude vanishes exactly, except for two neighboring sites, where it has amplitudes a and $\sqrt{1-a^2}$, respectively. For this state we can calculate the energy $E = 2ta\sqrt{1-a^2}$ and, choosing a appropriately, we may continuously tune $E \in [-t, t]$. Taking into account more complicated initial configurations of occupied sites (see right panel in Fig. 8) we may also adjust higher energies. For each starting position, however, the local structure of A_∞ limits the possible configurations.

In Fig. 12 we compare the time evolution of a state for high and low occupation probabilities *p*, for which qualitatively different behaviors emerge. For $p = 0.65$, the wave function is localized on a finite region of the cluster. Following the time evolution up to very long times ($> 100T_0$) we demonstrate that this is not just a transitional state during the spreading process of the wave function, but true 'dynamical' localization. This behavior is in strong contrast to $p = 0.90$, where the state spreads over the whole cluster within a short fraction of this time ($0.1T_0$). For any fixed time there are some sites with slightly larger amplitudes (see the darker dots in the last image of the time series). Those are due to contributions from localized states, which are also present in the initial state. However, as the wave function extends over the whole cluster, for large p not all states in the spectrum may be localized. Since the time evolution of initial states at $p = 0.65$ and $p = 0.90$ behaves in such a different manner, we conclude that there exists a quantum percolation threshold in between.

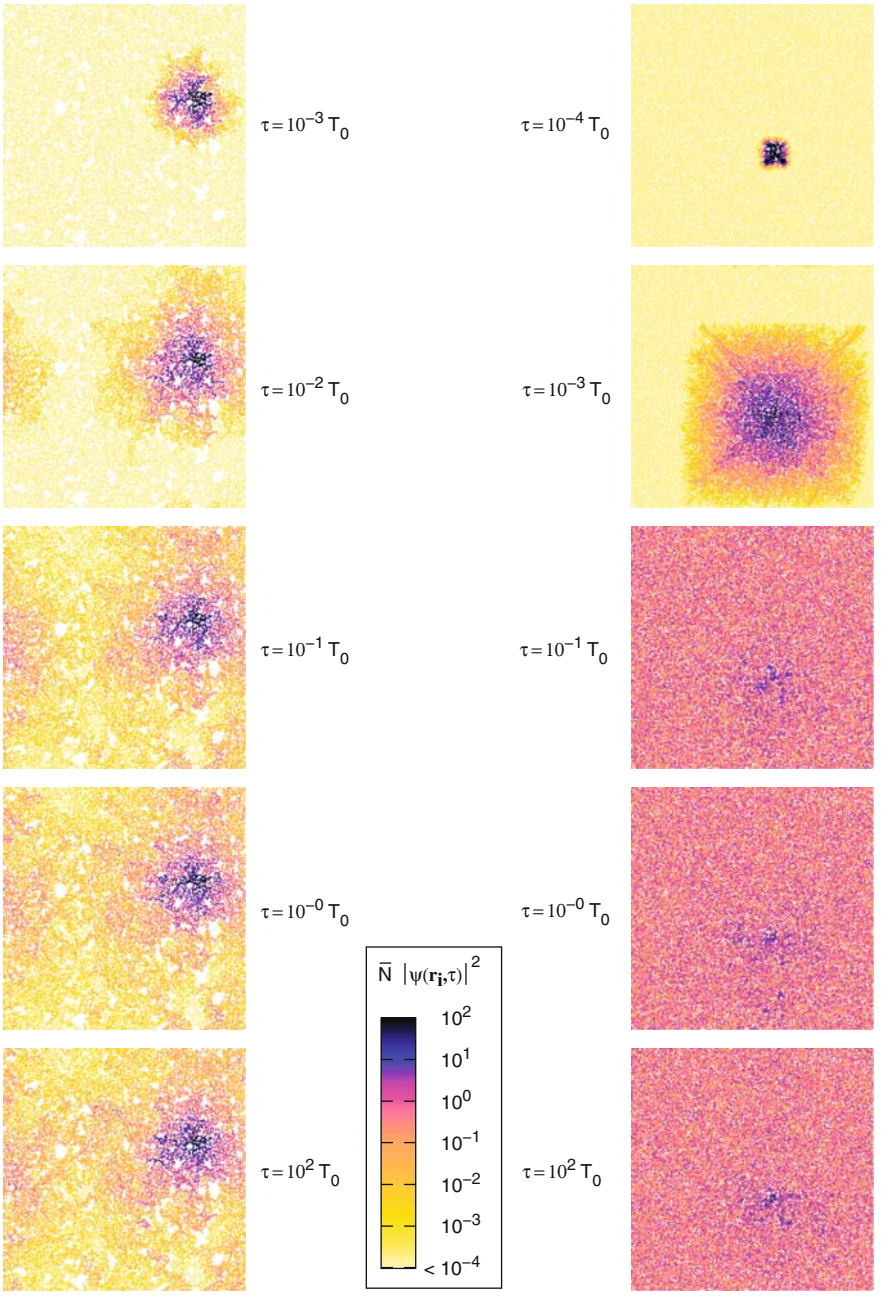

Fig. 12. Time evolution of a state at $E = 0.5t$ on the spanning cluster of a $N = 200^2$ lattice for $p = 0.65$ (*left*) and $p = 0.90$ (*right*). We show the normalized square of the wave function amplitude at the different sites $\bar{N}|\psi(\mathbf{r}_i, \tau)|^2$. Due to this normalization, for an extended state which is evenly spread over all sites of A_∞ this quantity is equal to unity

Consequently, we have a method at hand, capable to visualize the dynamical properties of localization in quantum percolation [53].

4 Percolative Effects in Advanced Materials

Current applications of quantum percolation concern, for example, transport properties of doped semiconductors [44] and granular metals [54], metal-insulator transition in 2D n-GaAs heterostructures [55], wave propagation through binary inhomogeneous media [56], superconductor-insulator and (integer) quantum Hall transitions [57, 58], or the dynamics of atomic Fermi-Bose mixtures [59]. Another important example is the metal-insulator transition in perovskite manganite films and the related colossal magnetoresistance (CMR) effect, which in the mean time is believed to be inherently percolative [60]. Quite recently (quantum), percolation models have been proposed to mimic the minimal conductivity in undoped graphene [61]. In doped graphene, in the split-band regime, an internal mobility edge might appear around the Fermi energy by introducing impurities [62]. Moreover, geometric disorder is shown to strongly affect electronic transport in graphene nanoribbons [63]. In the remaining part of this chapter we exemplarily investigate two specific random resistor network models to describe qualitatively charged transport in graphene sheets and bulk manganites.

4.1 Graphene

Due to its remarkable electronic properties, recently a lot of activity has been devoted to graphene, the atomic mono/bi-layer modification of graphite [64–66]. Especially the gapless spectrum with linear dispersion near the Fermi energy and the possibility of continuously varying the charge carrier density (from n- to p- type) by means of applying a gate voltage are of technological interest. In view of possible applications, such as graphene-based field effect transistors, it is highly desirable to know how these characteristics change in the presence of disorder, inherent in any prepared probe. Therefore, much work has been dedicated to study possible localization effects due to the presence of disorder (see [67] and references therein).

The extraordinary electronic structure of graphene results in unusual transport properties. In this material a finite minimal conductivity is observed, which might be attributed to a mesoscopically inhomogeneous density of charge carriers [68–70], caused by spatially varying charge trapping on the substrate. To describe the influence of these charge inhomogeneities on the transport properties, percolative random resistor networks (RRN) have been proposed [61]. Following this line, we apply the LD approach to a minimal model [71] that can be constructed in generalization of the $2D$ percolation model described in Sect. 3.2.

Let us consider a $2D$ lattice on which two sublattices represent regions of different charge carrier concentrations. These regions (sites) are randomly connected with each other (left panel of Fig. 13). The hopping probability for such links (to some next nearest neighbors) is assumed to be much higher than for direct nearest neighbor

hopping events. The later ones are reduced by the leakage, λ, as compared with the others. To examine the influence of anisotropic hopping, we model the corresponding RRN by the Hamiltonian

$$H = -t\Big[\lambda \sum_{m} \left(c_m^\dagger c_n + c_m^\dagger c_e\right) + \sum_{m \text{ even}} \left(\eta_m c_m^\dagger c_{ne} + (1-\eta_m) c_e^\dagger c_n\right) + \sum_{m \text{ odd}} \left(\eta_m c_e^\dagger c_n + (1-\eta_m) c_m^\dagger c_{ne}\right)\Big] + \text{H.c.}\,, \tag{19}$$

where e(ast) and n(orth) denote the nearest neighbors of site m in x- and y-direction and ne is the next-nearest neighbor in "north-east" direction. We assume PBC. The random variable $\eta_m \in \{0, 1\}$ determines which diagonal in a square is connected (right panel in Fig. 13). Shifting the expectation value of the $\{\eta_m\}$, we may adjust the anisotropy of the system $p = \langle \eta_m \rangle$. While the link directions are isotropically distributed for $p = 0.5$, increasing (decreasing) p generates a preferred direction of hopping, favoring stipe-like structures. Note that in the limit of vanishing leakage this model is equivalent to the $2D$ percolation model discussed in Sect. 3.

First representative results for the RRN model are presented in Fig. 14. In particular it shows the influence of finite leakage and anisotropy. In contrast to the $2D$ percolation model, where the DOS spectra are completely symmetric, the inclusion of next-nearest neighbor hopping causes an asymmetry that grows with increasing λ. For large p, the mean DOS is evocative of the $1D$ DOS, except for the multitude of spikes, which we can attribute again to localized states on isolated islands. In the isotropic, low-leakage case, a vanishing ρ_{ty} suggests that all states are localized. Either increasing p or λ leads to a finite value of ρ_{ty}. But even at $p = 0.90$ this effect is marginal for small λ, thus presumably no extended states exist. Increasing the leakage results in a finite ρ_{ty} for $E > 0$ also at $p = 0.5$. This feature becomes

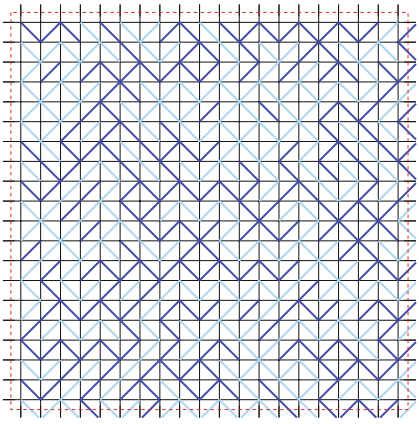

Fig. 13. *Left panel*: One particular cluster realization of the RRN model at $p = 0.5$. *Right panel*: Visualization of the generation rule for the RRN model

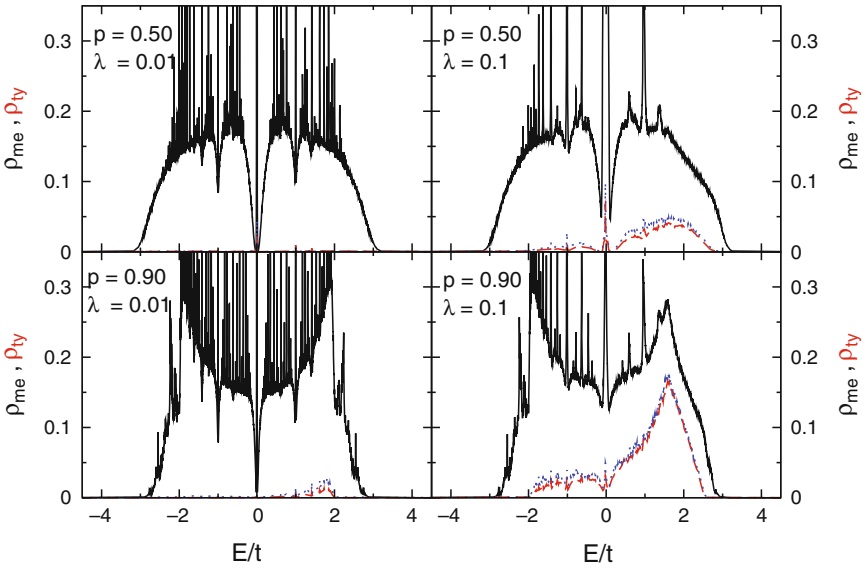

Fig. 14. Mean (*solid line*) and typical (*dashed line*) DOS for the RRN model. Results are shown for $N = 500^2$ and $N\sigma = 45$ for different anisotropy p and leakage λ. For illustration of the finite size dependence, ρ_{ty} for a $N = 350^2$ sites system is also included (*dotted lines*). The results base on the calculation of 1000 individual LDOS spectra for different cluster realizations and sites

even more pronounced at high anisotropy, which indicates the existence of extended states for these parameters.

In Fig. 15 we present some characteristic eigenstates of this model for a fixed realization of disorder. These results support the conclusions drawn from the typical DOS. For the isotropic, low-leakage case we find a clearly localized state with internal checkerboard structure. Increasing the anisotropy, many states are extended in one direction (see also the $1D$-like shape of ρ_{me}), while localized in the other one. The leakage has a more drastic effect on the nature of the states, as they are extended in some sense for both values of p. The amplitudes on different lattice sites fluctuate over several orders of magnitude, however, explaining the reduced value of ρ_{ty} as compared to ρ_{me} (cf. Fig. 14).

Due to the simplicity of the model, these results are surely not suitable to be compared to real experimental transport data, but can be seen as a first step towards an at least qualitative understanding of the extraordinary transport properties in graphene. In any case, also here the LD approach may serve as a reliable tool to discuss localization effects.

4.2 Doped CMR Manganites

The transition from a metallic ferromagnetic (FM) low-temperature phase to an insulating paramagnetic high-temperature phase observed in some hole-doped manganese

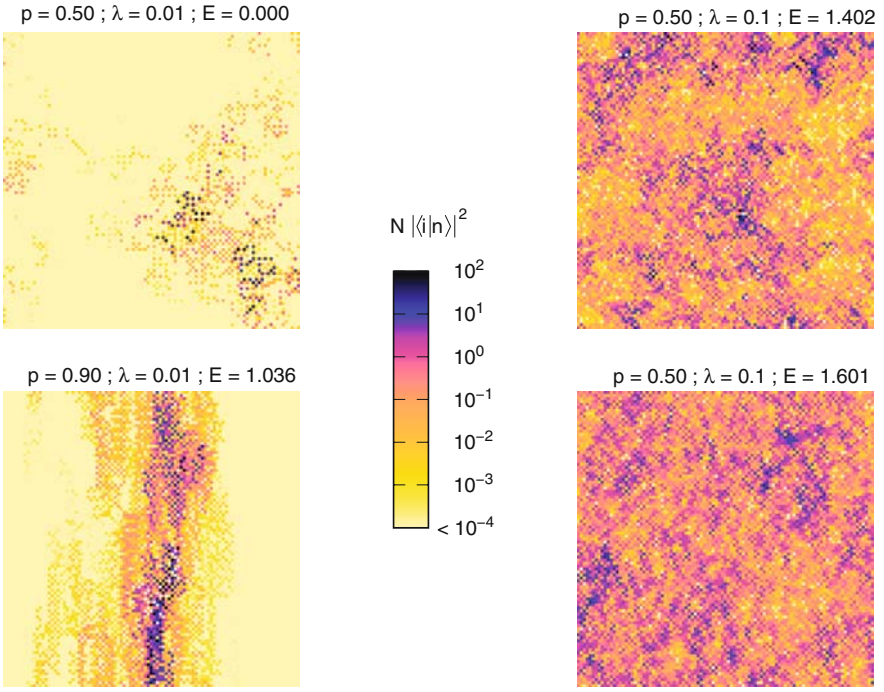

Fig. 15. Characteristic eigenstates of the RRN model on a $N = 100^2$ lattice at different anisotropies p, leakage rates λ, and energies E. Shown is the normalized occupation probability $N|\langle i|n\rangle|^2$

oxides (such as the perovskite family $\mathrm{La}_{1-\mathrm{x}}[\mathrm{Sr},\mathrm{Ca}]_{\mathrm{x}}\mathrm{MnO}_3$) is associated with an unusual dramatic change in their electronic and magnetic properties. This includes a spectacularly large negative magnetoresistive response to an applied magnetic field (see Fig. 16, Left panel), which might have important technological applications [72].

Recent experiments indicate the coexistence of localized and itinerant charge carriers close to the metal-insulator transition in the FM phase of CMR manganites. Above T_c the activated behaviour of the conductivity [73] as well as the structure of the pair distribution function (PDF) [74] indicate the formation of small polarons, that is, of almost localized carriers within a surrounding lattice distortion. Interestingly these polarons continue to exist in the metallic phase below T_c, merely their volume fraction is noticeably reduced. For the coexistence of conducting and insulating regions within the metallic phase different scenarios were discussed, which relate the metal-insulator transition to phase separation [75] and percolative phenomena [76, 77]. In particular microscopic imaging techniques, such as scanning tunnelling spectroscopy [78, 79] or dark-field imaging [80], seem to support the latter idea.

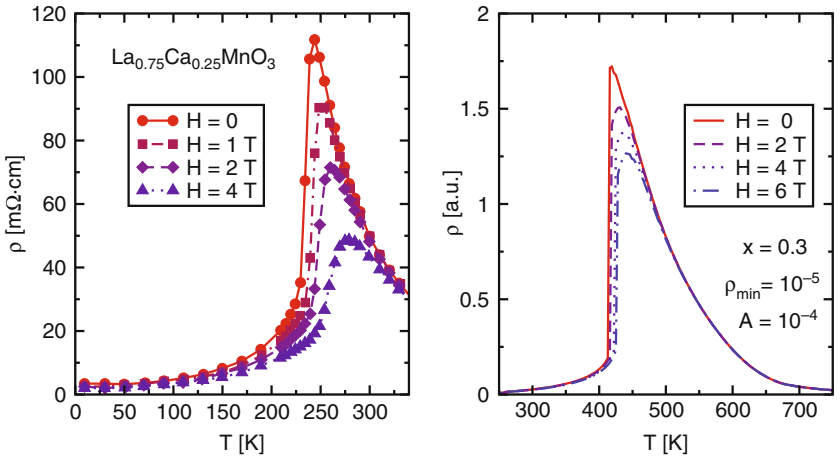

Fig. 16. Experimental (*left*) and theoretical (*right*) results for the temperature- and magnetic field-dependence of the resistivity in doped CMR manganites. Experimental data are taken from Ref. [83]. For a more detailed discussion see also [81]

In a previous work [81], we addressed this problem theoretically. We proposed a phenomenological mixed-phase description that is based on the competition of a polaronic insulating phase and a metallic, double-exchange driven ferromagnetic phase, whose volume fractions and carrier concentrations are determined self-consistently by requiring equal pressure and chemical potential. In more detail, we assume that the resistivity of the metallic component is proportional to the expression

$$\rho_S[z] = \frac{g_S[z] - \gamma_S[z]^2}{\gamma_S[z]^2} \,, \tag{20}$$

derived by Kubo and Ohata [82], which associates ρ with the fluctuation of the double-exchange matrix element caused by the thermal spin disorder. Here $S = 3/2$ is the localized spin formed by the t_{2g} electrons of the manganese. Both,

$$g_S[z] = \frac{S B_S[z]}{(2S+1)^2} \left((2S+2) \coth \frac{(S+1)z}{S} - \coth \frac{z}{2S} \right) + \frac{S+1}{2S+1} \tag{21}$$

$$\gamma_S[z] = \frac{S+1}{2S+1} + \frac{S}{2S+1} \coth \left(\frac{S+1}{S} z \right) B_S[z] \,, \tag{22}$$

exhibit a magnetic field dependence, where $B_S[z] = \frac{1}{2S} \left[(2S+1) \coth \frac{(2S+1)z}{2S} - \coth \frac{z}{2S} \right]$. The resistivity of the insulating component is assumed to match the resistivity of the high-temperature phase, which in experiment is well fit by the activated hopping of small-polarons [73]. Hence, the resistivities of the two components are given by,

$$\rho^{(f)} = \frac{B}{x^{(f)}} \left(\rho_S[S(\lambda + \lambda^{\text{ext}})] + \rho_{\text{min}} \right) \quad \text{and} \quad \rho^{(p)} = \frac{A}{\beta x^{(p)}} \, \rho_S[S\lambda^{\text{ext}}] \, \mathrm{e}^{-\beta \epsilon_p} \,, \tag{23}$$

where ϵ_p is the polaron binding energy, $\beta = 1/k_B T$ the inverse temperature, λ is the inner Weiss field, λ^{ext} is the external magnetic field and the prefactors A and B as well as the cut-off ρ_{min} are free model parameters which could be estimated from experimental data. Then, at a given doping level x, that is chemical potential μ, the resulting carrier concentrations $x^{(f)}$ and $x^{(p)}$ in the coexisting regions define the two volume fractions by the equations

$$x = p^{(f)} x^{(f)} + p^{(p)} x^{(p)} \quad \text{and} \quad p^{(f)} + p^{(p)} = 1\,, \tag{24}$$

(see [81]). The resistivity of the whole sample, which may consist of an inhomogeneous mixture of both components, is calculated on the basis of a RRN. More precisely, we choose nodes from a cubic lattice that belong to the metallic component with probability $p^{(f)}$ and to the polaronic component with probability $p^{(p)}$. Each of these nodes, which represent macroscopic regions of the sample, is connected to its neighbours with resistors of magnitude $\rho^{(f)}$ or $\rho^{(p)}$, respectively.

Inserting the volume fractions and carrier concentrations from the mixed-phase model we obtain the resistivities shown in Fig. 16 (Right panel). The jump-like behaviour of the resistivity originates to a large degree from the changing volume fraction of the metallic component, which can cross the percolation threshold. However, the conductivity of the component itself as well as its carrier concentration strongly affect ρ for $T < T_c$. An external magnetic field causes a reasonable suppression of ρ, that is, a noticeable negative magnetoresistance. Compared to the real compounds the calculated effect is a bit weaker. Nevertheless, in view of the rather simple model for the conductivity the agreement is quite satisfactory. More involved assumptions, for example, an affinity to the formation of larger regions of the same type in the sense of correlated percolation [84] would naturally affect the resistivity of the system and its response to an external field.

5 Conclusions

In this tutorial we demonstrated the capability of the local distribution approach to the problem of quantum percolation. In disordered systems the local density of states (LDOS) emerges as a stochastic, random quantity. It makes sense to take this stochastic character seriously and to incorporate the distribution of the LDOS in a description of disorder. Employing the Kernel Polynomial Method we can resolve with very moderate computational costs the rich structures in the density of states originating from the irregular boundary of the spanning cluster.

As for the standard Anderson localization and binary alloy problems the geometrically averaged (typical) density of states characterizes the LDOS distribution and may serve as a kind of order parameter differentiating between extended and localized states. For both $2D$ and $3D$ quantum site percolation, our numerical data corroborate previous results in favor of a quantum percolation threshold $p_q > p_c$ and a fragmentation of the electronic spectrum into extended and localized states. At the band center, so called anomalous localization is observed, which manifests itself

in a checkerboard-like structure of the wave function. Most notably, monitoring the spatial evolution of a wave packet in time for the $2D$ case, we find direct evidence for 'dynamical' localization of an incident quantum particle at $p = 0.65 > p_c$, while its wave function is spread over the percolated cluster for $p = 0.9$. This finding additionally supports the existence of a quantum percolation threshold.

Without doubt quantum percolation plays an important role in the transport of several contemporary materials, such as $2D$ graphene or $3D$ manganese oxides. To close the gap between the study of simple percolation models and a realistic treatment of percolative transport in these rather complicated materials will certainly be a challenge of future research.

We thank A. Alvermann, F. X. Bronold, J. W. Kantelhardt, S. A. Trugman, A. Weiße, and G. Wellein for valuable discussions. This work was supported by the DFG through the research program TR 24, the Competence Network for Technical/Scientific High-Performance Computing in Bavaria (KONWIHR), and the Leibniz Computing Center (LRZ) Munich.

References

1. P.W. Anderson, Phys. Rev. **109**, 1492 (1958) 135, 137, 138, 141
2. B. Kramer and A. Mac Kinnon, Rep. Prog. Phys. **56**, 1469 (1993) 135, 141, 143, 151
3. S. Kirkpatrick, T.P. Eggarter, Phys. Rev. B **6**, 3598 (1972) 136, 137, 145, 147
4. D. Vollhardt and P. Wölfle. In: *Electronic Phase Transitions*, ed by W. Hanke and Y.V. Kopaev, p. 1 (North Holland, Amsterdam, 1992) 136
5. T. Li, and P. Sheng, Phys. Rev. B **53**, R13268 (1996) 136
6. T. Odagaki. In: *Transport and Relaxation in Random Materials*, ed by J. Klafter, R.J. Rubin, and M.F. Shlesinger (World Scientific, Singapore, 1986) 136
7. P.A. Lee and T.V. Ramakrishnan, Rev. Mod. Phys. **57**, 287 (1985) 136, 141
8. G. Schubert, A. Weiße, and H. Fehske, Phys. Rev. B **71**, 045126 (2005) 137
9. A. Alvermann and H. Fehske, Eur. Phys. J. B **48**, 295 (2005) 137
10. A. Alvermann and H. Fehske, J. Phys.: Conf. Ser. **35**, 145 (2006) 137
11. R. Abou-Chacra, D.J. Thouless, and P.W. Anderson, J. Phys. C **6**, 1734 (1973) 137
12. A.D. Mirlin and Y.V. Fyodorov, J. Phys. I (France) **4**, 655 (1994) 138
13. V. Dobrosavljević, A.A. Pastor, and B.K. Nikolić, Europhys. Lett. **62**, 76 (2003) 139
14. G. Schubert, A. Weiße, G. Wellein, and H. Fehske. In: *High Performance Computing in Science and Engineering, Garching 2004*, ed by A. Bode and F. Durst, pp. 237–250 (Springer-Verlag, Heidelberg, 2005) 139
15. A. Alvermann, G. Schubert, A. Weiße, F.X. Bronold, and H. Fehske, Physica B **359–361**, 789 (2005) 139
16. G. Schubert, A. Weiße, and H. Fehske, Physica B **359–361**, 801 (2005) 139
17. V. Dobrosavljević and G. Kotliar, Phys. Rev. Lett. **78**, 3943 (1997) 139
18. K. Byczuk, W. Hofstetter, and D. Vollhardt, Phys. Rev. Lett. **94**, 056404 (2005) 139
19. F.X. Bronold and H. Fehske, Phys. Rev. B **66**, 073102 (2002) 139
20. F.X. Bronold, A. Alvermann, H. Fehske, Philos. Mag. **84**, 673 (2004) 139

21. A. Weiße, G. Wellein, A. Alvermann, and H. Fehske, Rev. Mod. Phys. **78**, 275 (2006) 139, 140
22. R.N. Silver, H. Röder, A.F. Voter, and D.J. Kress, J. Comp. Phys. **124**, 115 (1996) 140
23. J. Fröhlich, F. Martinelli, E. Scoppola, and T. Spencer, Commun. Math. Phys. **101**, 21 (1985) 141
24. R.E. Borland, Proc. Roy. Soc. London, Ser. A **274**, 529 (1963) 141
25. N.F. Mott and W.D. Twose, Adv. Phys. **10**, 107 (1961) 141
26. E. Abrahams, P.W. Anderson, D.C. Licciardello, and T.V. Ramakrishnan, Phys. Rev. Lett. **42**, 673 (1979) 141
27. M. Janssen, Phy. Rep. **295**, 1 (1998) 141, 151
28. N.F. Mott, Adv. Phys. **16**, 49 (1967) 141
29. E.W. Montroll and M.F. Shlesinger, J. Stat. Phys. **32**, 209 (1983) 142
30. A. Mac Kinnon and B. Kramer, Z. Phys. B **53**, 1 (1983) 143
31. H. Grussbach and M. Schreiber, Phys. Rev. B **51**, 663 (1995) 143
32. B. Bulka, M. Schreiber, and B. Kramer, Z. Phys. B **66**, 21 (1987) 143
33. S.L.A. de Queiroz, Phys. Rev. B **653**, 214202 (2001) 143
34. H.G. Ballesteros, L.A. Fernández, V. Martín-Mayor, G.P.A. Muiñoz Sudupe, and J.J. Ruiz-Lorenzo, J. Phys. A **32**, 1 (1999) 144
35. M.E.J. Newman and R.M. Ziff, Phys. Rev. Lett. **85**, 4104 (2000) 144
36. C.M. Soukoulis, Q. Li, and G.S. Grest, Phys. Rev. B **45**, 7724 (1992) 144, 145, 149
37. H.N. Nazareno, P.E. de Brito, and E.S. Rodrigues, Phys. Rev. B **66**, 012205 (2002) 144
38. R. Berkovits and Y. Avishai, Phys. Rev. B **53**, R16125 (1996) 145
39. T. Odagaki, N. Ogita, and H. Matsuda, J. Phys. C **13**, 189 (1980) 145
40. C.M. Soukoulis, E.N. Economou, and G.S. Grest, Phys. Rev. B **36**, 8649 (1987) 145
41. J.T. Chayes, L. Chayes, J.R. Franz, J.P. Sethna, and S.A. Trugman, J. Phys. A **19**, L1173 (1986) 147, 148
42. G. Schubert, Numerische Untersuchung ungeordneter Elektronensysteme. Diploma thesis, Universität Bayreuth (2003) 147
43. Y. Shapir, A. Aharony, and A.B. Harris, Phys. Rev. Lett. **49**, 486 (1982) 147
44. M. Inui, S.A. Trugman, and E. Abrahans, Phys. Rev. B **49**, 3190 (1994) 147, 150, 154
45. A. Mookerjee, I. Dasgupta, and T. Saha, Int. J. Mod. Phys. B **9**, 2989 (1995) 148
46. T. Koslowski and W. von Niessen, Phys. Rev. B **42**, 10342 (1990) 148, 149, 150
47. A. Kusy, A.W. Stadler, G. Hałdaś, and R. Sikora, Physica A **241**, 403 (1997) 149
48. A. Kaneko and T. Ohtsuki, J. Phys. Soc. Jpn. **68**, 1488 (1999) 149
49. M.F. Islam and H. Nakanishi, Phys. Rev. E **77**, 061109 (2008) 150
50. A. Eilmes, R.A. Römer, and M. Schreiber, Physica status solidi b **205**, 229 (1998) 150
51. H. Tal-Ezer and R. Kosloff, J. Chem. Phys. **81**, 3967 (1984) 151
52. R. Chen and H. Guo, Comp. Phys. Comm. **119**, 19 (1999) 151
53. G. Schubert and H. Fehske, Phys. Rev. B **77**, 245130 (2008) 154
54. M.V. Feigel'mann, A. Ioselevich, and M. Skvortsov, Phys. Rev. Lett. **93**, 136403 (2004) 154
55. S. Das Sarma, M.P. Lilly, E.H. Hwang, L.N. Pfeiffer, K.W. West, and J.L. Reno, Phys. Rev. Lett. **94**, 136401 (2005) 154

56. Y. Avishai and J. Luck, Phys. Rev. B **45**, 1974 (1992) 154
57. Y. Dubi, Y. Meir, and Y. Avishai, Phys. Rev. B **71**, 125311 (2005) 154
58. N. Sandler, H. Maei, and J. Kondev, Phys. Rev. B **70**, 045309 (2004) 154
59. A. Sanpera, A. Kantian, L. Sanchez-Palencia, J. Zakrzewski, and M. Lewenstein, Phys. Rev. Lett. **93**, 040401 (2004) 154
60. T. Becker, C. Streng, Y. Luo, V. Moshnyaga, B. Damaschke, N. Shannon, and K. Samwer, Phys. Rev. Lett. **89**, 237203 (2002) 154
61. V.V. Cheianov, V.I. Fal'ko, B.L. Altshuler, and I.L. Aleiner, Phys. Rev. Lett. 99, 176801 (2007) 154
62. G.G. Naumis, Phys. Rev. B **76**, 153403 (2007) 154
63. I. Martin and Y.M. Blanter, URL `arXiv:0705.0532v2` (2007) 154
64. K.S. Novoselov, A.K. Geim, S.V. Morozov, D. Jiang, Y. Zhang, S.V. Dubonos, I.V. Grigorieva, and A.A. Firsov, Science **306**, 666 (2004) 154
65. K.S. Novoselov, E. McCann, S.V. Morozov, V.I. Fal'ko, M.I. Katsnelson, U. Zeitler, D. Jiang, F. Schedin, and A.K. Geim, Nature Phys. **2**, 177 (2006) 154
66. A.K. Geim and K.S. Novoselov, Nature Mat. **6**, 183 (2007) 154
67. V.M. Pereira, F. Guimea, J.M.B. Lopes dos Santos, N.M.R. Peres, and A.H. Castro Neto, Phys. Rev. Lett. **96**, 036801 (2006) 154
68. A.K. Geim, Nature Phys. **2**, 620 (2006) 154
69. J. Martin, N. Akerman, G. Ulbricht, T. Lohmann, J.H. Smet, K. von Klitzing, and A. Yacoby, Nature Phys 4, 144 (2008) 154
70. S. Cho and M.S. Fuhrer, Phys. Rev. B **77**, 081402R (2008) 154
71. G. Schubert and H. Fehske, Phys. Rev. B **77**, 155115 (2008) 154
72. S. Jin, T.H. Tiefel, M. McCormack, R.A. Fastnach, R. Ramesh, and L.H. Chen, Science **264**, 413 (1994) 157
73. D.C. Worledge, L. Miéville, and T.H. Geballe, Phys. Rev. B **57**, 15267 (1998) 157, 158
74. S.J.L. Billinge, R.G. DiFrancesco, G.H. Kwei, J.J. Neumeier, and J.D. Thompson, Phys. Rev. Lett. **77**, 715 (1996) 157
75. E. Dagotto, T. Hotta, and A. Moreo, Phy. Rep. **344**, 1 (2001) 157
76. L.P. Gor'kov and V.Z. Kresin, JETP Lett. **67**, 985 (1998) 157
77. A. Moreo, M. Mayr, A. Feiguin, S. Yunoki, and E. Dagotto, Phys. Rev. Lett. **84**, 5568 (2000) 157
78. M. Fäth, S. Freisem, A.A. Menovsky, Y. Tomioka, J. Aarts, and J.A. Mydosh, Science **285**, 1540 (1999) 157
79. T. Becker, C. Streng, Y. Luo, V. Moshnyaga, B. Damaschke, N. Shannon, and K. Samwer, Phys. Rev. Lett. **89**, 237203 (2002) 157
80. M. Uehara, S. Mori, C.H. Chen, and S.W. Cheong, Nature **399**, 560 (1999) 157
81. A. Weiße, J. Loos, and H. Fehske, Phys. Rev. B **68**, 024402 (2003) 158, 159
82. K. Kubo and N. Ohata, J. Phys. Soc. Jpn. **33**, 21 (1972) 158
83. P. Schiffer, A.P. Ramirez, W. Bao, and S.W. Cheong, Phys. Rev. Lett. **75**, 3336 (1995) 158
84. D. Khomskii and L. Khomskii, Phys. Rev. B **67**, 052406 (2003) 159

Quantum Percolation in the Quantum Hall Regime

C. Sohrmann[1], J. Oswald[2] and R.A. Römer[1]

[1] Physics Department and Centre for Scientific Computing, University of Warwick, Coventry CV4 7AL, United Kingdom,
r.roemer@warwick.ac.uk
[2] Institute of Physics, University of Leoben, Franz Josef Str. 18, Leoben, A-8700, Austria,
josef.oswald@unileoben.ac.at

1 Introduction

In 1980, an altogether unexpected discovery was made by Klaus von Klitzing and coworkers [1] when carrying out Hall measurements on a metal-oxide-semiconductor field-effect transistor (MOSFET) . They discovered that for a system of electrons confined to two dimensions and subject to a strong, perpendicular magnetic field, B, the resistivity tensor, $\boldsymbol{\rho}$, and the conductivity tensor, $\boldsymbol{\sigma}$, can freeze to the form

$$\boldsymbol{\rho} \begin{pmatrix} 0 & h/e^2 j \\ -h/e^2 j & 0 \end{pmatrix} \quad \text{and} \quad \boldsymbol{\sigma} \begin{pmatrix} 0 & -je^2/h \\ je^2/h & 0 \end{pmatrix} , \tag{1}$$

with j being an integer.[3] Astonishingly, it turned out that this quantization holds over a wide range of B or the applied voltage, forming quantized plateaus, and is independent of the sample geometry and choice of material. A commonly adopted geometry is, for instance, the Hall bar, as sketched in Fig. 1(a). In between those plateaus, the Hall conductivity, σ_{xy}, performs a transition and the longitudinal conductivity, σ_{xx}, assumes a finite value of close to e^2/h, as shown schematically in Fig. 1(b). This was the fruitful discovery of the *integer quantum Hall effect* (IQHE). Contrary to the classically expected linear relation between ρ_{xy} and B, this quantization of transport sets in at very low temperatures and high-sample quality. The importance of the discovery lies in the precision and resilience of the quantization and allowed for a high-precision determination of the fine-structure constant, defined as $\alpha = e^2/(2\epsilon_0 hc)$, where c is the vacuum speed of light and ϵ_0 the vacuum permittivity. Ultimately, the IQHE was adopted as a metrological standard, defining the international reference resistance as

$$R_{\mathrm{K}-90} = h/e^2 = 25812.807\Omega , \tag{2}$$

[3] We note that in 2D, the resistivities (ρ_{xx}, ρ_{xy}) and conductivities (σ_{xx}, σ_{xy}) are equivalent to the resistances (R_{xx}, R_{xy}) and conductances (G_{xx}, G_{xy}), respectively.

Sohrmann, C. et al.: *Quantum Percolation in the Quantum Hall Regime*. Lect. Notes Phys. **762**, 163–193 (2009)
DOI 10.1007/978-3-540-85428-9_6

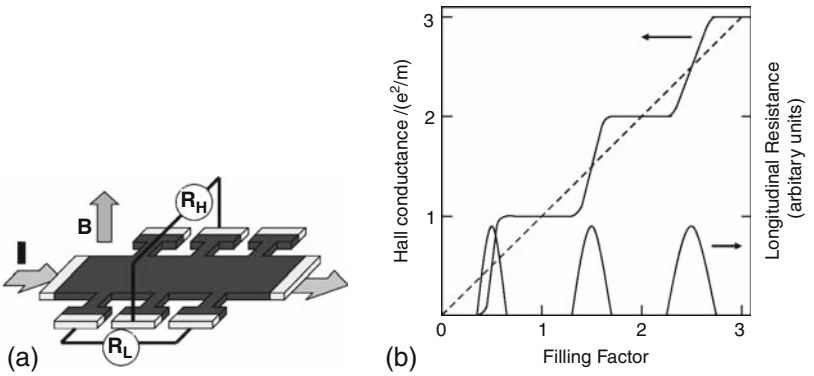

Fig. 1. Schematic sketch of (**a**) a Hall bar geometry for the measurement of the longitudinal and the Hall resistance, (**b**) the plateau structure of the Hall conductance as well as the finite longitudinal resistance at the plateau transitions in the IQHE. The current in the Hall bar flows from the so-called source to the drain, indicated by the arrow on the *left* and on the *right*, respectively

with an absolute error of $\pm 5 \cdot 10^{-3} \Omega$ [2]. The IQHE was soon followed by another unexpected, arguably even more surprising finding. When carrying out Hall measurements on even cleaner samples, higher fields, and lower temperatures, Tsui, Störmer and Gossard discovered in 1982 [3] that the Hall conductivity becomes quantized also at intermediate magnetic fields or voltages and acquires certain fractional values of e^2/h, such as $1/3$, $2/3$, $2/5$, and so on. Owing to the logic, this effect was called *fractional quantum Hall effect* (FQHE). Whereas the IQHE was soon motivated with a gauge argument in a noninteracting system of electrons [4], the FQHE turned out to be far more complicated and could only be described with correlated many-body states [5] or collective excitations with fractional charge [6, 7], although still lacking a firm, microscopic derivation.

The scope of this chapter will be limited to the IQHE for which single-particle and network-type models [4, 8–16] inspired by arguments of classical percolation and extensions thereof have successfully been able to reproduce general features such as the position and height of the plateaus. Furthermore, interactions become an essential part when trying to interpret experimental results such as recently observed patterns in the compressibility [17, 18] or the conductance [19, 20], enhancement of the g-factor [21], negative compressibility [22], filling factor dependence of the Landau level (LL) width [23], or the Hall insulator [24]. Hence, we also outline numerical investigations of such electron-electron interaction related effects using a mean-field Hartree-Fock (HF) approach and thereby neglecting higher correlations among the electrons. Since HF accounts for Thomas-Fermi screening effects while at the same time leading to a critical exponent $\tilde{\nu}$ whose value is found to be consistent with results of noninteracting approaches [25, 26], this appears to be a reasonable starting point.

2 The Quantized Hall Effect and Classical Percolation

2.1 The Clean 2D System in a Magnetic Field

For the classical picture of a two-dimensional system with perpendicular magnetic field $\mathbf{B} = (0, 0, B)$, one readily finds the classical Hall resistance

$$R_{\mathrm{xy}} = \frac{B}{en_{\mathrm{e}}} \,. \tag{3}$$

Thus, for a fixed carrier density, in the classical picture one expects a linear relation between the Hall resistance and the magnetic field as shown in Fig. 1.

Let's now turn to a quantum mechanical description of a 2D perfectly periodic system of electrons. Ignoring edge effects, we study the bulk Hamiltonian for a single electron

$$h_0 = \frac{1}{2m^*}(\mathbf{p} - e\mathbf{A})^2, \tag{4}$$

where $\mathbf{p}$ is the momentum and $\mathbf{A} = B(0, x)^{\mathrm{T}}$ the vector potential of the magnetic field in Landau gauge. Introducing the *cyclotron coordinate* $\boldsymbol{\zeta} = \binom{\xi}{\eta}$ and the *guiding center* coordinates $\mathbf{R} = \binom{X}{Y}$, we find

$$h_0 = \frac{\hbar\omega_c}{2l_c}\boldsymbol{\zeta}^2 = \frac{\hbar\omega_c}{2l_c}(\eta^2 + \xi^2) \,. \tag{5}$$

Then the Schrödinger equation with the magnetic Hamiltonian (4) is solved by the degenerate Landau functions [27]

$$\varphi_{n,k}(\mathbf{r}) = \langle \mathbf{r} | \varphi_{n,k} \rangle \frac{1}{\sqrt{2^n n! \sqrt{\pi} l_{\mathrm{c}} L}} \exp\left[iky - \frac{(x - kl_{\mathrm{c}}^2)^2}{2l_{\mathrm{c}}^2} \right] H_n\left(\frac{x - kl_{\mathrm{c}}^2}{l_{\mathrm{c}}} \right) \,, \tag{6}$$

with the eigenenergies $E_n = (n + 1/2)\hbar\omega_c$, where n labels the Landau level index and $k = 2\pi j/L$ with $j = 1, \ldots, N_\phi$ the momentum. $H_n(x)$ is the nth Hermite polynomial, and $l_{\mathrm{c}} = \sqrt{\hbar/eB}$, the magnetic length. We can determine the number of states per LL as $N_\phi = L^2 B/\Phi_0 = L^2/(2\pi l_c^2)$, which is also the number of magnetic flux quanta, $\Phi_0 = h/e$, which penetrate the area L^2. It proves very useful to define a quantity that characterizes the filling of the system, called the filling factor ν, by $\nu = N_{\mathrm{e}}/N_\phi$, where N_{e} is the number of electrons in the system. The spectrum of h_0 consists of a sequence of δ-peaks at energies E_n, where each energy corresponds to an N_ϕ-fold degenerate state.

2.2 Landau Level Broadening due to Disorder

Real systems will inevitably contain a certain amount of disorder due to, for instance, impurities, imperfections, or surface contamination. Having disorder in the system will lift the degeneracy by broadening the δ-peaked LLs into bands. For a smooth disorder potential compared to the magnetic length, especially in the

limit $B \to \infty$, it can be shown [28] that the eigenstates will follow equipotential lines of the disorder potential at the corresponding eigenenergies and the average density of states will then equal the overall distribution of energies in the potential, that is, $\rho(E) = P[V]$. We use N_I Gaussian-type "impurities", randomly distributed at $\mathbf{r}_s$, with random strengths $w_s \in [-W, W]$, and a fixed width d, such that $V_\mathrm{I}(\mathbf{r}) = \sum_{s=1}^{N_\mathrm{I}} \left(w_s/\pi d^2\right) \exp[-(\mathbf{r} - \mathbf{r}_s)^2/d^2] = \sum_\mathbf{q} V_\mathrm{I}(\mathbf{q}) \exp(i\mathbf{q} \cdot \mathbf{r})$ with

$$V_\mathrm{I}(\mathbf{q}) = \sum_{s=1}^{N_\mathrm{I}} \frac{w_s}{L^2} \exp\left(-\frac{d^2|\mathbf{q}|^2}{4} - i\mathbf{q} \cdot \mathbf{r}_s\right), \tag{7}$$

where $q_{x,y} = 2\pi j/L$ and $j = -N_\phi, -N_\phi - 1, \ldots, N_\phi$. The aerial density of impurities, therefore, is given by $n_\mathrm{I} = N_\mathrm{I}/L^2$ (cf. Fig. 2). The problem of whether a state is localized or extended in the presence of disorder can be captured conveniently with the localization length, $\xi(E)$, a quantity that characterizes the spatial spread of the wave function [28]. It has been show [29] that at the transition, the localization length diverges as a power,

$$\xi(E) = |E - E_c|^{-\tilde{\nu}}\,, \tag{8}$$

where $\tilde{\nu}$ is the critical exponent [29]. This exponent characterizes the transition and is believed to be independent of microscopic details of the impurity potential.

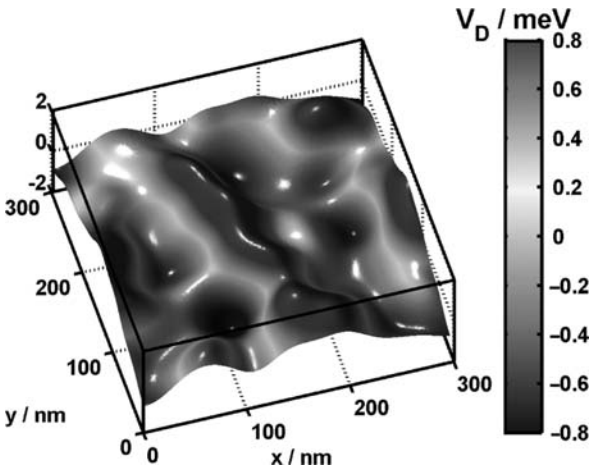

Fig. 2. Example for a smooth disorder potential constructed on a 300×300 nm sample from $N_\mathrm{I} = 288$ impurities with a Gaussian profile [30] as described in Sect. 4.1

2.3 Mapping Onto a Percolation Problem

The idea to map the IQHE onto a classical percolation problem can be visualized most easily in the high-field limit, $B \to \infty$, i.e. $l_c \to 0$. In this limit the cyclotron radius of the electrons vanishes and the center coordinates take the role of the ordinary

spatial coordinates. We assume a Hamiltonian of the form $H = h_0 + V(\mathbf{r})$, where $V(\mathbf{r})$ is a disorder potential due to the electron-impurity interaction. Furthermore, we assume the eigenstates of this Hamiltonian, $\phi_\alpha(\mathbf{r})$, are linear combinations of Landau states, that is, $\phi_\alpha(\mathbf{r}) = \sum_{n,k} C^\alpha_{n,k}\varphi_{n,k}(\mathbf{r})$. The coefficients can be found from the Schrödinger equation, $H|\phi\rangle = E|\phi\rangle$, which reads in matrix form

$$\sum_{n'k'} \langle\varphi_{nk}|V|\varphi_{n'k'}\rangle C^\alpha_{n',k'} = E'_\alpha C^\alpha_{n,k} \,, \tag{9}$$

and which by virtue of the form of the matrix elements,

$$\langle\varphi_{nk}|V|\varphi_{n'k'}\rangle = \int d^2\mathbf{r}\chi_n\left(x - kl_c^2\right) V(\mathbf{r})\chi_{n'}\left(x - k'l_c^2\right)\exp\left[-iy(k-k')\right], \tag{10}$$

is given in short as $\sum_{n'k'}\langle\varphi_{nk}|V|\varphi_{n'k'}\rangle C^\alpha_{n',k'} = E'_\alpha C^\alpha_{n,k}$. With the high-field approximation, the coupling between different LLs may be neglected and the problem can be solved for each level individually, that is, the n-index can be left out of the discussion. For easier analytical treatment, the sum will be replaced by an integral, that is, $\sum_{k'} = (L/2\pi)\int dk'$, and the coefficient is substituted by its Taylor expansion as $C(k') = \exp[(k-k')d/dq]C(q)|_{q=k}$. With some algebra [16, 31] and the limit $l_c \to 0$, one can state the problem as a differential equation. The solution yields parameterized orbits, $V(X, Y(X)) = E'$ along the equipotential lines of the disorder potential at the respective eigenenergies E'. In this approximation, it becomes apparent that only states along percolating equipotential lines will be extended. For a smooth potential in 2D, this is possible for a singular energy in the center of each LL and thus only a single state will be extended in the limit $L \to \infty$ [16]. Thus, the problem of the IQHE can be mapped approximately to a classical percolation problem [14] for each LL.

In Fig. 3, we show the charge density of a single state at the bottom and in the middle of the band, respectively. Evidentally, the states align along equipotentials

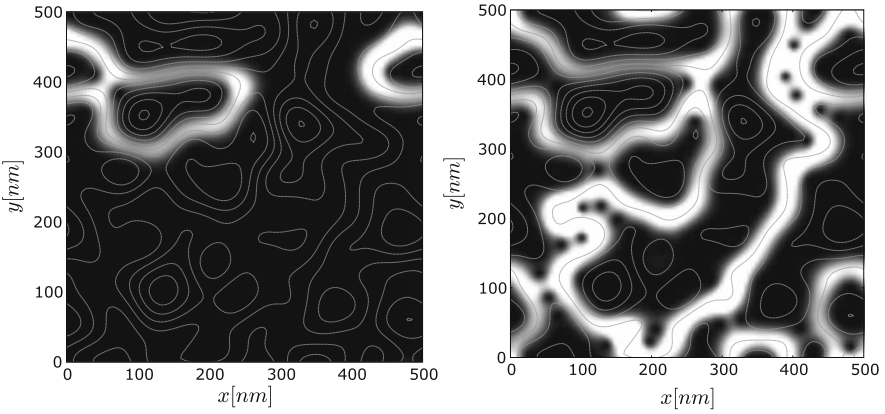

Fig. 3. Noninteracting charge density of a single localized (*left figure*) and delocalized (*right figure*) state for a system of size $L = 500$ nm at $B = 6$T. States are located at around $\nu = 0.1$ and $\nu = 0.5$, respectively. The disorder potential is indicated by the equipotential lines

of the disorder potential and thus the guiding center approximation gives a good account of the situation.

However, the IQHE is more complex than this simple, classical percolation picture suggest. Even ignoring many-body interactions, there are two quantum effects that may alter the scenario. The first is quantum mechanical tunneling, which may allow transmission through the system even away from the classically critical point. Clearly, tunneling will occur wherever different contour lines come very close. These points are the saddle points (SPs) in the potential landscape. The second effect is the possibility of quantum mechanical self-interference along the equipotential lines, leading to localization and hence a reduction in transmission. The modeling and investigation of these two counter-acting quantum effects is what gave rise to the network models to be considered next.

3 Network Models at the IQHE

3.1 The Chalker-Coddington Model

The original goal of the Chalker-Coddington (CC) concept was to calculate the localization length of the electronic states in the high magnetic field limit as a function of energy. In this context, the CC-model is a powerful method to circumvent a direct solution of Schrödingers equation by considering mainly the following facts: (a) the electronic states exhibit unidirectional transmission (directed channels) and (b) the extension of the wave function follows almost exactly the equipotential lines of the random potential, while it is localized on the length scale of the magnetic length perpendicular to the equipotential lines, which is schematically shown in Fig. 4(a). One has to demand current conservation all along the channels between the nodes, which are formed by the saddles of the random potential (encircled regions in Fig. 4(a)). Another important ingredient is current conservation at the nodes itself, which requests a unitary matrix between the transmitted amplitudes of incoming and outgoing channels. Figure 4(b) shows schematically the trajectories of the channels while passing a SP or being reflected at the SP of the potential. The transmitted amplitudes of the wave functions across the saddles are associated with currents and the current conservation of incoming and outgoing channels demands [14, 16]:

$$|\psi_1|^2 + |\psi_3|^2 = |\psi_2|^2 + |\psi_4|^2 \,. \tag{11}$$

This is maintained by the unitary scattering matrix S,

$$\begin{pmatrix} \psi_2 \\ \psi_4 \end{pmatrix} = S \cdot \begin{pmatrix} \psi_1 \\ \psi_3 \end{pmatrix} \,. \tag{12}$$

S has the general form

$$S = \begin{pmatrix} e^{-i\varphi_2} & 0 \\ 0 & e^{i\varphi_4} \end{pmatrix} \begin{pmatrix} -r & t \\ t & r \end{pmatrix} \begin{pmatrix} e^{i\varphi_1} & 0 \\ 0 & e^{-i\varphi_3} \end{pmatrix} \,, \tag{13}$$

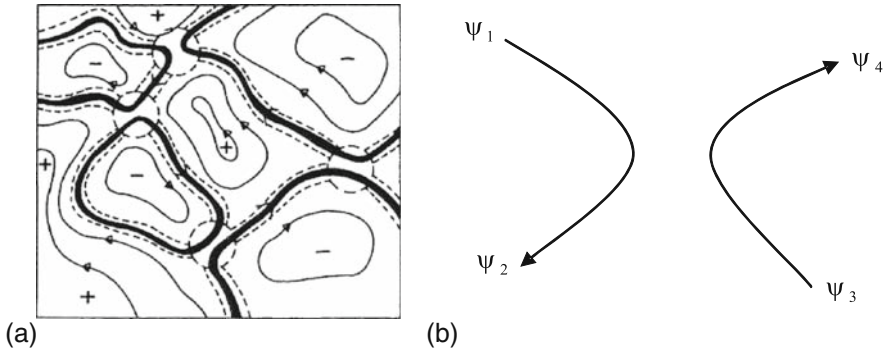

Fig. 4. (**a**) Schematic lateral potential distribution after [14]. The full curves represent equipotentials and the arrows give the direction of transmission. The + and - denotes maxima and minima. The bold line represents the contour along which the electronic state is extend. The perpendicular extension is indicated by the broken curves. The broken circles mark the coupling regions, which become the nodes of the network (**b**) Node of the network with two incoming and two outgoing channels. The channels in the CC network are treated according to the transfer matrix, which relates transmitted amplitudes and phases of the wave functions on the left (ψ_1, ψ_2) to the transmitted amplitudes and phases of the wave functions on the right (ψ_3, ψ_4)

with r the reflection and t the transmission coefficient for the amplitudes. An equivalent representation is the usage of the so-called transfer matrix T

$$\begin{pmatrix} \psi_4 \\ \psi_3 \end{pmatrix} = T \cdot \begin{pmatrix} \psi_1 \\ \psi_2 \end{pmatrix} , \tag{14}$$

with

$$T = \begin{pmatrix} e^{i\varphi_4} & 0 \\ 0 & e^{i\varphi_3} \end{pmatrix} \begin{pmatrix} 1/t & r/t \\ r/t & 1/t \end{pmatrix} \begin{pmatrix} e^{i\varphi_1} & 0 \\ 0 & e^{i\varphi_2} \end{pmatrix} . \tag{15}$$

Due to current conservation ($t = \sqrt{1 - r^2}$), the transfer matrix T can be described by a single parameter Θ, with Θ and φ real [14]:

$$T = \begin{pmatrix} e^{i\varphi_4} & 0 \\ 0 & e^{i\varphi_3} \end{pmatrix} \begin{pmatrix} \cosh\Theta & \sinh\Theta \\ \sinh\Theta & \cosh\Theta \end{pmatrix} \begin{pmatrix} e^{i\varphi_1} & 0 \\ 0 & e^{i\varphi_2} \end{pmatrix} . \tag{16}$$

Here $E \gg E_C$, E_C being a critical energy near the center of the LL and E the energy of the transmitting state, corresponds to $\Theta \ll 1$, whereas $E \ll E_C$ corresponds to $\Theta \gg 1$ [14]. Hence Θ is a monotonous function of the energy with respect to the critical energy near the LL center and is considered to depend linearly on the energy close to the LL center. A change between the cases $\Theta \ll 1$ and $\Theta \gg 1$ corresponds to switching from either full transmission to full reflection or vice versa, which at the same time acts like a rotation of the node by $90°$. Realistically, one should study a network that is topologically disordered. Instead, it has been supposed that randomness in the link phases of the channels that connect the nodes is

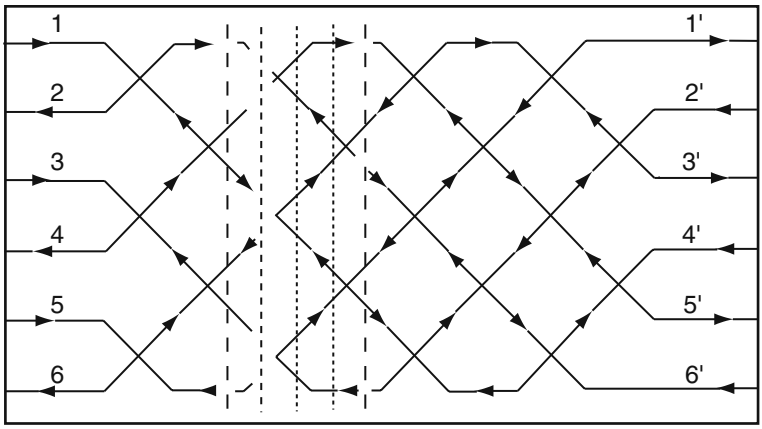

Fig. 5. The CC network of [14] with strip boundary conditions, connected to semi-infinite ideal conductors. A "slice" of the network is defined between dashed vertical lines and each slice is divided in to 4 different subslices, divided by the dotted lines. Each subslice is represented by a transfer matrix and their product gives the transfer matrix of a whole slice. The transmission through the whole system then is the product of all slices

sufficient while using a square lattice. For calculating the localization length, long narrow samples have been build on the basis of this network, which are connected to infinitely long ideal conductors on both sides. Periodic boundary conditions have been applied across the width of the sample, which thus represents a cylinder geometry. Figure 5 shows the network layout as used in [14]. The main purpose has been to calculate the transfer matrix of the whole network, which relates the amplitudes on the left to those on the right. The network has been cut into slices and the total transfer matrix being the product of the transfer matrix of each of the slices. Without going into further details, CC have been able to show, that except for one value of $\Theta_c = 0.8814$ all states tend to be localized. CC finally managed to fit the power law dependence of the localization length versus $\Theta - \Theta_c$ and obtained a slope of $\gamma = 2.5$. Quite a number of variations and extensions of the CC model have been made by different authors. A recent review of random network models is given by Kramer et al. [16].

3.2 The Nonequilibrium Network Model

One of the major features of the CC network model is the fact, that it attributes currents to the single directed channels. In this way, it does not distinguish between persistent currents, which can also exist without external current supply, and experimentally excited nonequilibrium currents. Furthermore, the CC model does not provide a handle to the excitation potentials, which are introduced by the contacts of real samples. Another important aspect is the fact that the CC model is unexceptionally a coherent network. Altogether this makes it impossible to extend the CC model in order to include the presence of dissipation. Strictly speaking, the CC model is well

able to map out the different QH transport regimes, as demonstrated in context with the scaling theory of the QHE, but it does not describe the current transport itself.

During the past couple of years a Landauer-Büttiker-type network representation, which aims directly at the current transport, has been developed. It can be used for the numerical simulation of the current transport of two-dimensional electron systems in the high-magnetic field regime [32, 33]. This approach allows to build up a network, which describes the effect of nonequilibrium currents injected via metallic contacts such as in real experiments. The handling of the nodes as well as the association of the channels with currents and potentials is substantially different from the CC model [33]. Figure 6(a) shows a single node of the network, which transmits the potentials u_1 and u_3 from the incoming channels to the outgoing channels with the potentials u_2 and u_4. Figure 6(b) demonstrates, how a network can be composed by combining several nodes. In contrast to the CC model, the currents are attributed to channel pairs. The longitudinal current I from the right to the left (see Fig. 6(a)) is described by

$$I = (e^2/h) \cdot (u_1 - u_4) = (e^2/h) \cdot (u_2 - u_3) \; . \tag{17}$$

Also the other possibility to build a pair of channels describes a current

$$I_R = (e^2/h) \cdot (u_1 - u_2) = (e^2/h) \cdot (u_4 - u_3) \; . \tag{18}$$

I_R is a transverse current between the channel pairs (indicated by the arrow in Fig. 6a). The ratio of I_R/I corresponds to the relation between reflection and transmission coefficients R/T of the Landauer-Büttiker (LB) formalism and has been given the symbol P. P allows to derive the potentials of the outgoing channels in terms of the potentials of the incoming channels [32, 33]

$$u_2 = (u_1 + P \cdot u_3)/(1 + P) \; , \tag{19}$$

$$u_4 = (u_3 + P \cdot u_1)/(1 + P) \; . \tag{20}$$

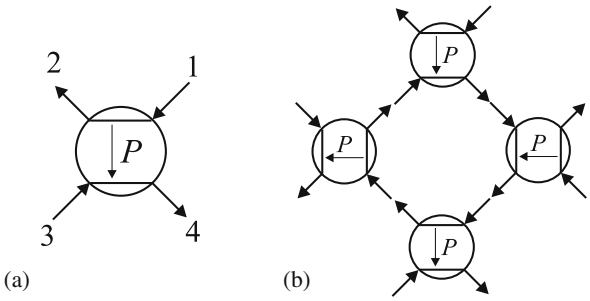

Fig. 6. (**a**) Node of the network with two incoming and two outgoing channels. The channels $1 \rightarrow 2$ and $3 \rightarrow 4$ are treated like edge channels (ECs) with backscattering, where P represents the backscattering (see text). (**b**) Arrangement of the nodes for building the minimal physical element of a network, which is a closed loop of a so called magnetic bound state. The complete network is composed by putting together a sufficient number of such adjacent loops

It is important to realize that in this way the nodes of the network provide a handle to both, the excitation potentials and the nonequilibrium currents. By substituting P by R/T, the above equations can be transformed also into the following matrix equation:

$$\begin{pmatrix} u_2 \\ u_4 \end{pmatrix} \begin{pmatrix} T & R \\ R & T \end{pmatrix} \cdot \begin{pmatrix} u_1 \\ u_3 \end{pmatrix}. \tag{21}$$

This matrix must not be confused with the scattering matrix (S) in Eq. (13) as used by the CC model. It might be somewhat confusing, that the S-Matrix of the CC model considers the transmission from $1 \rightarrow 2$ and $3 \rightarrow 4$ as a reflection, while in accordance with the EC-picture in this model the current transported by the channel pair ($1 \rightarrow 2$ and $3 \rightarrow 4$) is considered as a transmission process. This inconsistency results from the CC model, which assigns currents to single channels which then appear as being repelled at the saddle. Therefore we have to interchange $r \leftrightarrow t$ before comparing this model with the CC model. In this way, we obtain a matrix that seems almost identical with the S-matrix, except the fundamental difference that $T = t^2$ and $R = r^2$. Therefore there exists formally no way for deriving Eq. (21) from the S-matrix of the CC model.

The theoretical basis of P is transmission across SPs of long rage potential fluctuations in the bulk [33],

$$P = \exp\left[-\frac{L^2(E_{\mathrm{F}} - E_{\mathrm{LL}})}{e\tilde{V}} \frac{eB}{h}\right]. \tag{22}$$

The saddle energy corresponds to the LL center E_{LL}, eB/h is the number of states of a LL, L and $\tilde{V}$ are connected to the Taylor expansion of the involved SP: L is the period and $\tilde{V}$ the amplitude of a 2D cosine-potential, which has the same 2nd order Taylor expansion like the actual saddle potential. Representing the encircled saddle in Fig. 7 by an appropriate two-dimensional Cosine potential, which matches the saddle curvature, we get the dashed plotted Cosine function. However, the real potential modulation results from a random potential. It is easily seen, that, therefore, the overall LL broadening Γ will be larger than $\tilde{V}$.

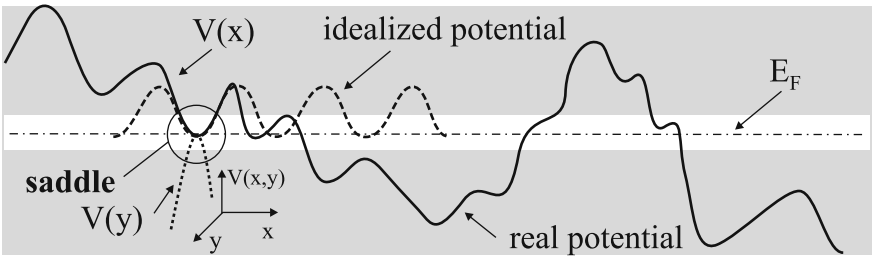

Fig. 7. Schematic one-dimensional representation (x - profile) of a fluctuating potential together with the idealized 2D-Cosine potential with the right Taylor coefficients for representing the encircled saddle

The geometry of the sample is defined by shaping the lateral density profile of the carriers, which are distributed over the network grid. The local carriers' density enters the nodes via the function P, which depends locally on $E_{\mathrm{F}} - E_{\mathrm{LL}}$, with E_{F} the Fermi energy and E_{LL} the LL center. Therefore P is in general different for different nodes and each involved Landau band is represented by a complete network [32]. In this way, contact leads, gate electrodes and the effect of inhomogeneities can be modeled. In order to fill up the network with P-values for the numerical calculation of the resulting current and potential distribution, we have two options that will be discussed in the next sections.

3.3 Periodic Grid

We use a periodic grid of reduced lateral resolution without explicitly including potential fluctuations. In this case, L corresponds to a much larger length than the real mean fluctuation period and therefore also the corresponding potential modulation $\tilde{V}$ appears much larger than the real mean fluctuation amplitude. Consequently, neither L nor $\tilde{V}$ have a physical meaning independently from each other. Only the prefactor of $(E_{\mathrm{F}} - E_{\mathrm{LL}})$ in the exponent of Eq. (22) as a whole is relevant. It defines an energy interval for the Fermi level, in which bulk conduction is possible. The overall LL broadening, which we assume to be Gaussian, in this case is only used for calculating the magnetic field dependent Fermi level E_{F}. Therefore different parameters have to be used for describing the density of states $(\mathrm{DOS})E_{\mathrm{F}}$ and the bulk conductance $G_{xx}(E_{\mathrm{F}})$. This is demonstrated for the most simple case of representing the whole sample by a single node and deriving $G_{xx}(E_{\mathrm{F}})$ for a single LL [34, 35]: Since $R_{xx} = P \cdot h/e^2$ and $G_{xx} = R_{xx}/(R_{xx}^2 + R_{xy}^2)$, we get $G_{xx} = (e^2/h) \cdot P/(1+P^2)$, which forms a peak, while $P = 0 \longrightarrow \infty$. If we plot now $\mathrm{DOS}(E_{\mathrm{F}})$ and $G_{xx}(E_{\mathrm{F}})$ normalized to each other within the same diagram, we get a situation as shown in Fig. 8. While the localization picture maps out localized and de-localized states as a function of energy [29], this model considers current transport across localized magnetic bound states by tunneling. The associated conductance decays exponentially as a function of the energy as indicated in Fig. 8. Such a smearing-out of the sharp boundaries between localized and de-localized states in the observed conductance variation is evident from experimental results [36] and already successfully reproduced by this model [37].

3.4 Realistic Fluctuating Potential Modulation

The second option for the numerical calculation is that we introduce a realistic fluctuating potential modulation, which also can be discretized on the network grid. At the first glance, the regular network appears as a model of a periodic potential modulation, while the native random potential of a real sample suggests that a random network should be used instead. However, as will be demonstrated in the following, this network model can be understood also as a concept for effective discretization of a random network. Obviously, lateral long-range potential fluctuations will lead to a corresponding lateral fluctuation of the local filling factor, which, in turn, will

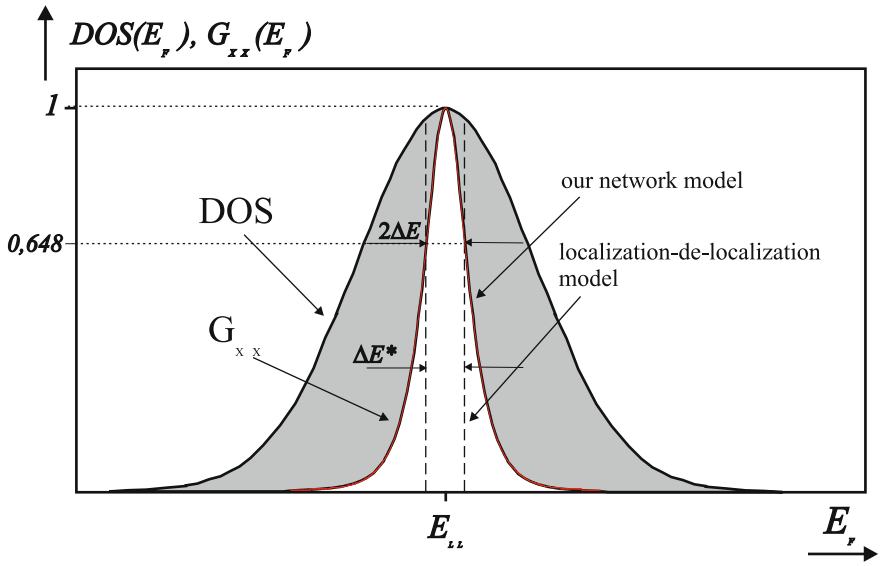

Fig. 8. DOS and conductance G_{xx} versus Fermi energy. The model suggests a smooth change of the bulk conductance at the boundaries between localized and de-localized states mapped out by the localization model (indicated by the two *vertical dashed lines*). The light colored G_{xx}-peak can be understood to correspond with the light colored region around the saddle energy in Fig. 7

lead to a lateral variation of the coupling function P of the nodes in the network. Suppose we wish to model a random potential on the basis of the regular network, then we need to choose the grid period to be much less than the typical length scale of the potential fluctuations. This is qualitatively shown in Fig. 9, where the system is supposed to be close to half filling, which means the possibility of bulk current flow. However, half filling only means $\nu = 0.5$ on average and, due to the potential fluctuations, there will exist regions with locally $\nu > 0.5$ and regions with locally $\nu < 0.5$. In Fig. 9 the shaded regions represent $\nu > 0.5$ and the nonshaded regions $\nu < 0.5$. Most effective coupling at the nodes appears at $P = 1$, which corresponds to exact half filling $\nu = 0.5$. Due to the randomization of the potential, only few of all nodes will remain close to half filling and most of them will depart from half filling, which leads to a coupling function of $P \ll 1$ in the shaded regions and $P \gg 1$ outside. However, $P \ll 1$ or $P \gg 1$ means mainly that an incoming channel is almost completely transmitted either to the one or the other outgoing channel of the node. This appears as a rotation of a node by $90°$ upon changing from one case to the other. As can be seen in Fig. 9, in this way the network guides the transmitted channels all around the boundaries between $\nu > 0.5$ and $\nu < 0.5$. Therefore, in this case, most of the nodes are physically inactive, but just switching the whole transmitted channel to either the one or the other outgoing channel. Only the nodes near the saddles of the real potential, where $\nu \approx 0.5$, and where also the real loops of the magnetic bound states get close to each other, become physically active by coupling different real loops. However, for modeling realistically shaped macroscopic sample

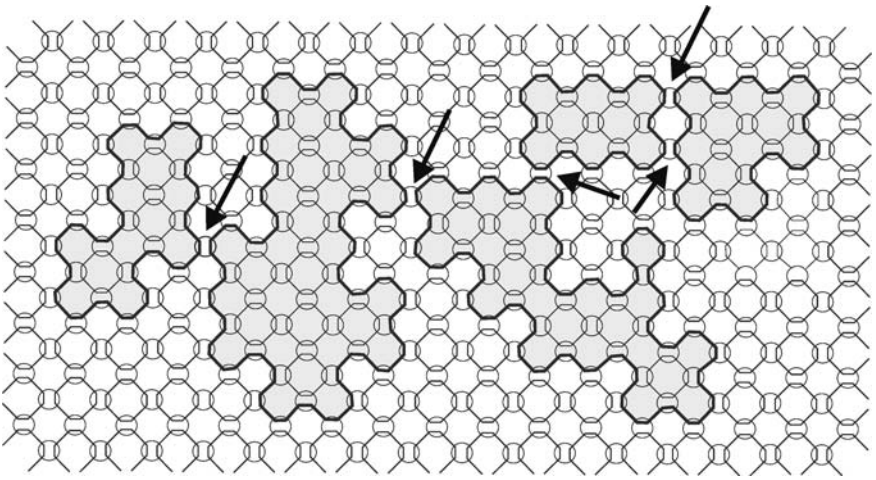

Fig. 9. Cutout of the bulk region showing the scheme of discretization of a random potential on the basis of the network model. The average filling factor of the associated LL is assumed to be close to $\nu = 0.5$. The shaded regions represent $\nu > 0.5$, which corresponds to a value of the coupling function $P \ll 1$ and the nonshaded regions represent $\nu < 0.5$, which corresponds to $P \gg 1$. The basic grid consists of alternating rows and lines of nodes in same orientation. Therefore, a change from $P \ll 1$ to $P \gg 1$ appears graphically as a rotation of the nodes by 90° within a line and a row and as can be seen in the figure, the corresponding nodes inside and outside the shaded area appear rotated against each other. Following now the inter connections in the network, one can see that in this way a channel at the boundary between $\nu > 0.5$ and $\nu < 0.5$ is automatically guided to follow these boundaries (bold line). In real samples, this corresponds to a arbitrarily shaped magnetic bound state following the contour lines of the random potential. Most of the nodes with $P \ll 1$ or $P \gg 1$ serve as some sort of switching device in the network and are therefore not physically active. Only those near the saddle of the real potential, where also the real magnetic bound states get close together (marked by the *arrows*), act physically as tunneling junctions within the framework of the Landauer-Büttiker formalism

structures together with realistic potential fluctuations, the numerical effort at present is beyond our capabilities.

It should be pointed out that this network concept for handling experimentally excited nonequilibrium currents and potentials is in principle not restricted to the above presented two options for generating the input data for the network. This network model can be more generally understood as an independent transport module, which can be merged with any microscopic model, that delivers the tunneling coefficients R and T at the designated nodes of the network.

3.5 An Application of the Nonequilibrium Network Model: The Standard Hall Bar

In the following, we present two examples for the application of this network model. The first one is the modeling of a standard Hall bar sample structure at a bulk carrier

density of $n = 4 \times 10^{11}\mathrm{cm}^{-2}$. The transport data in terms of R_{xx} as well as the lateral distribution of the excitation potential and the excess current density are calculated as a function of the magnetic field (Figs. 10, 11). The local current density is represented by the absolute value of the transmitted excess current at the individual nodes by using Eqs. (17) and (18). The distribution of the excitation potential, which is transmitted by the directed channels between the nodes, is shown gray scale coded in a 2D plot. The grid size of the network for this simulation is 255×39 nodes. For this special demonstration only very short voltage probes located close to the current contacts at the ends of the Hall bar have been used in order to get the maximum of an undisturbed bulk region without needing a too large network. The placement of the contacts and voltage probes can be designed freely and the distances are larger for comparison with real experiments. Also extended current contacts can be realized instead of point contacts as used in this case. The resulting longitudinal resistance R_{xx} is shown in Fig. 10 as a function of the magnetic field. Figure 11(a) shows the situation in the plateau regime at $B = 6.3\mathrm{T}$ close to the beginning of the plateau transition ($3 \rightarrow 2$). The excitation potential resembles edge stripes without longitudinal voltage drop, just as expected from the edge channel picture in the plateau regime of the IQHE. The edge stripe in dark gray at the lower edge corresponds to the high excitation potential, which is supplied to the current contact on the left, the upper edge stripe, which is slightly less dark, corresponds to the low-excitation potential, which is supplied to the current contact on the right. The intermediate potentials appear in light gray to allow the visualization of the existence of edge stripes. In contrast, the current is not pushed towards the edges but appears distributed homogeneously all over the bulk region instead. While this fact is in agreement with the bulk current picture of the IQHE, it seems in contradiction with the original idea of the EC picture. The peak in the current density at the far end of the 3D plot results from the usage of point contacts for the current supply.

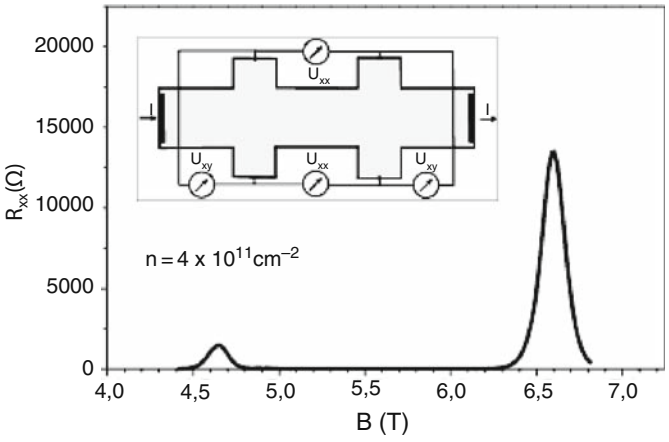

Fig. 10. Longitudinal resistance R_{xx} versus magnetic field. The R_{xx} peaks appear at the transitions between filling factors 4 and 3 as well as 3 and 2

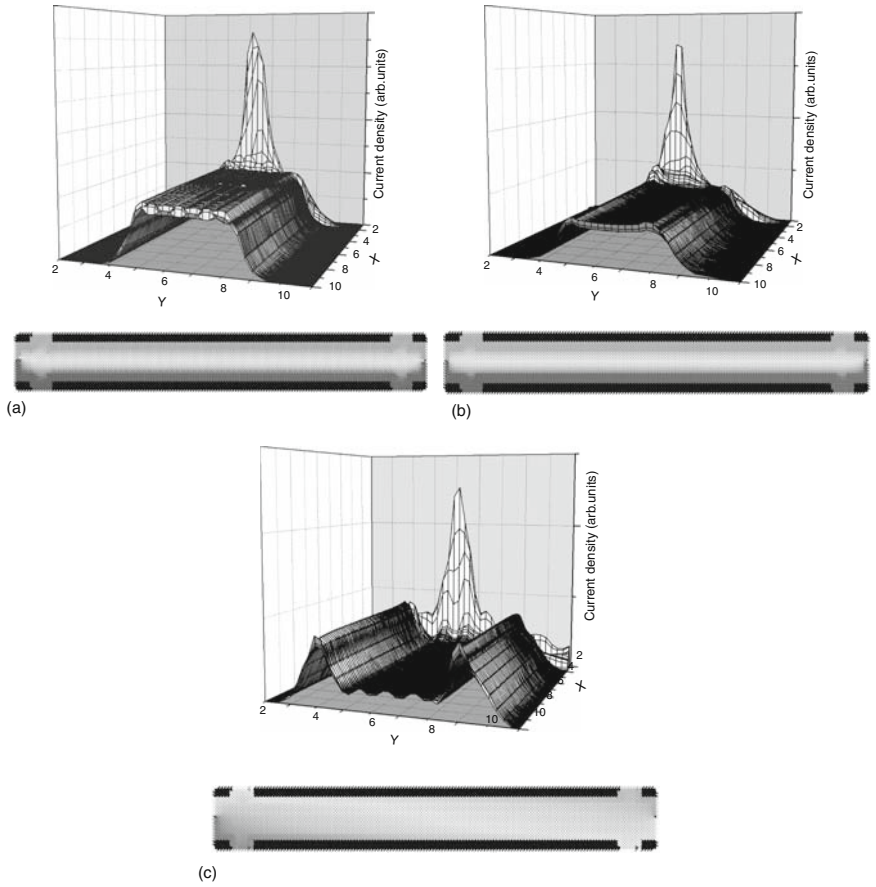

Fig. 11. Lateral distribution of the excess current (*upper* 3D plot) and the excitation potential (*lower gray scale* coded 2D plot, see text) (**a**) at the $\nu = 3$ plateau close to the beginning of the plateau transition from 3 to 2, (**b**) at the $\nu = 2$ plateau right after the plateau transition from 3 to 2 and (**c**) right at the plateau transition from 3 to 2

For a better visibility of the transverse current density profile in the middle of the sample, the second current point contact at the front end has been cut away in the 3D plot. Figure 11(c) shows the situation exactly at the position of the R_{xx} peak. As expected from an ohmic conductor the lateral distribution of the excitation potential exhibits now a smooth potential drop also in longitudinal direction of the sample. In contrast to Fig. 11(a) the edge stripes disappeared, leaving only slightly dark areas near the current contacts, which quickly dissolve into the bulk region. However, the lateral distribution of the excitation current now gets inhomogeneous and forms peaks near the edges of the sample. Figure 11(b) shows the situation again in the plateau regime, but now at $B = 6.9$T right after completing the transition to the $\nu = 2$ plateau. In this case, the situation is similar to Fig. 11(a) and the current is again distributed homogeneously all across the bulk. This puzzling behavior, which

at the first glance seems to contradict the edge channel picture, can be explained in the following way: Dissipation-less excess current is flowing in the so-called incompressible regions between edge stripes while the edge stripes themselves are current-less [38, 39]. In the plateau regime, all of the bulk region represents an incompressible stripe, while in the transition regime the bulk gets compressible. Therefore, in the plateau transition regime the bulk screens out most of the transverse excitation potential gradient and leaves only narrow incompressible stripes between the bulk and the inner most edge stripe, which now takes the screened part of the transverse potential gradient. Although we have a mixture of dissipation-less and dissipative current in the transition regime, the dissipation-less part of the current gets squeezed to those narrow incompressible stripes close to the edges, which consequently leads to an enhancement of the current density near the edges. At this point, it should be emphasized that the frequently appearing conflict in the discussion of edge versus bulk current picture comes mainly from a misinterpretation of the EC picture, by attributing the excess currents directly to the individual ECs. This is the same problem, which does not allow for the CC model to handle excess currents, because it also attributes currents to the individual channels, which is only correct for the equilibrium case.

3.6 Another Application: Complex Sample Structures

The second example demonstrates the complexity of sample structures that can be handled by this network model. The sample structure is a so-called 'anti-Hall bar within Hall bar' geometry. It consists of an outer boundary forming a standard Hall bar and a hole in the bulk region of this Hall bar, where the inner boundary also forms a Hall bar. Figure 12 shows the schematic outline of this structure, which is driven as a doubly connected specimen with independent floating current sources attached to the outer and inner boundary. This geometry was developed and experimentally investigated for the first time by R.G. Mani [40] and the first successful numerical

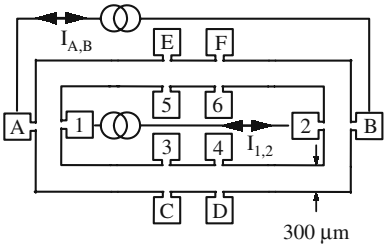

Fig. 12. The "anti-Hall bar within a Hall bar" experimental configuration utilized by Mani. [40] Here, the exterior boundary, associated contacts, and current source $I_{A,B}$ constitute the Hall bar, while the interior boundary, interior contacts, and the current supply $I_{1,2}$ make up the "anti-Hall bar" configuration. In the typical experiment, each of the floating current sources are set to a constant value, and the voltages on the Hall bar and/or the 'anti-Hall bar' are probed as a function of the ramped transverse magnetic field

simulation of this setup was achieved with this network model [41, 42]. The main motivation for this investigations was to pickup the question about the role of edge versus bulk in the IQHE. In the following only the main results will be summarized. It is most striking, that in full agreement between experimental (see Fig. 14) and simulation data (see Fig. 13) the Hall voltages of the inner (anti Hall bar) and outer (Hall bar) boundaries appear edge specific. This means that the Hall voltages depend exclusively on the current supplied to the associated edge. In contrast, the longitudinal voltages of the Hall bar and the anti-Hall bar are identical and depend exactly on the sum of both currents. This behavior is the same as in the high-magnetic field regime as well as in the low-magnetic field regime, where plateaus are not yet established [42]. This strongly indicates that edge and bulk related effects might be important at the same time and that, therefore, a clear distinction between those may even not be possible. Already in context with the investigation of the current distribution in a standard Hall bar above we got a strong indication that the results of this network model may cover both, the edge and bulk related aspects of the IQHE. In fact, it does not distinguish between bulk end edge effects in the first place and thus suggests an equivalence between the edge and bulk current picture. Such an equivalence in the plateau regime is nicely demonstrated for the current compensated situation of the anti-Hall bar within the Hall bar structure ($I_{12} = -I_{AB}$). Reconsidering

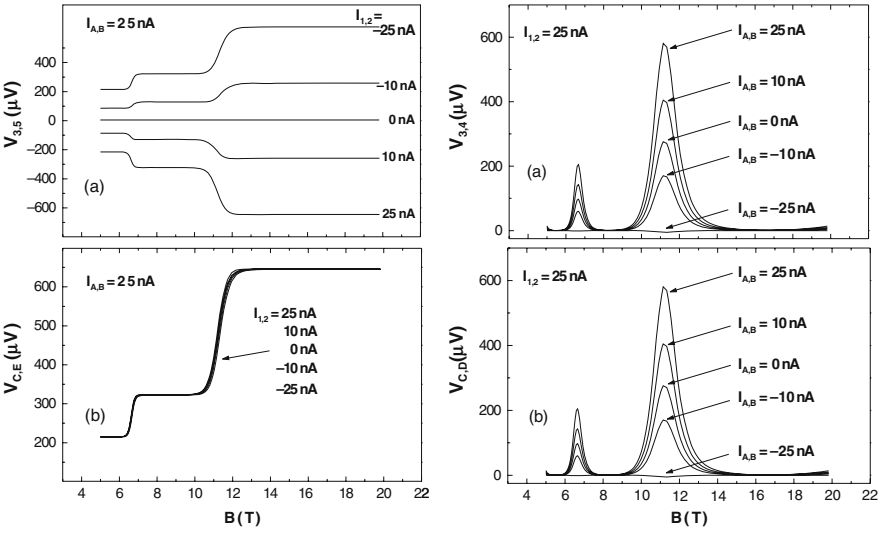

Fig. 13. *Left*: A network model simulation of (**a**) Hall voltage, $V_{3,5}$, at different $I_{1,2}$ and constant exterior current $I_{A,B} = 25\,\mathrm{nA}$. The interior Hall voltage $V_{3,5}$ is proportional to the interior current $I_{1,2}$. (**b**) Simulation of the exterior (Hall bar) Hall voltage, $V_{C,E}$, at different currents $I_{1,2}$ and constant exterior current $I_{A,B} = 25\,\mathbf{nA}$. The exterior Hall voltage $V_{C,E}$ is insensitive to the interior current $I_{1,2}$. *Right*: (a) the longitudinal voltage $V_{3,4}$ at the "anti-Hall bar" and (**b**) the longitudinal voltage $V_{C,D}$ at the Hall bar. Panel (**a**) and (**b**) are identical because the longitudinal voltages are insensitive to the boundary of origin of the current, unlike the Hall voltages. Note that the diagonal voltages vanish at current compensation, $I_{A,B} - I_{1,2}$

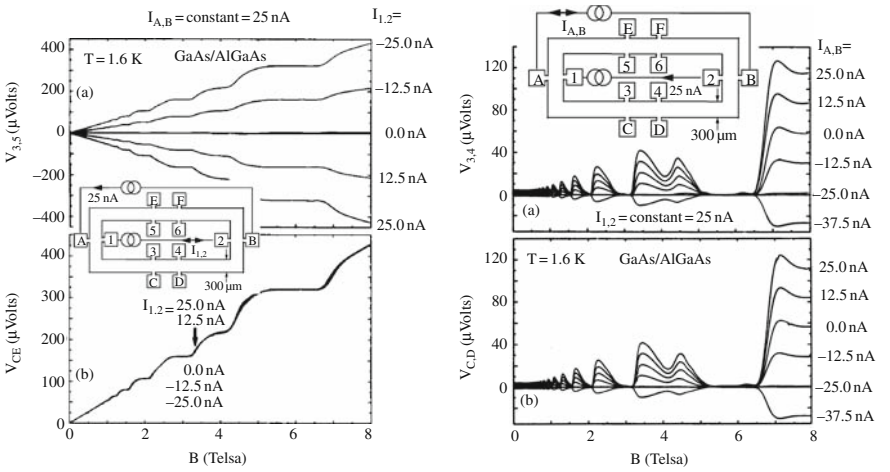

Fig. 14. Experimental data of Mani [40]. Insets: The "anti-Hall bar within a Hall bar" configuration. The voltage probes and current contacts are labeled as in the simulation of Fig. 13. *Left*: (**a**) The interior Hall voltage, $V_{3,5}$, with -25 nA $\leq I_{1,2} \leq +25$ nA and fixed current $I_{A,B} = 25$ nA. (**b**) The exterior Hall voltage $V_{C,E}$ under the same conditions remains unchanged. *Right*: (**a**) The longitudinal voltage $V_{3,4}$. (**b**) The longitudinal voltage $V_{C,D}$. The longitudinal voltages observed on either boundary of the left branch of the sample are identical because the longitudinal voltages are insensitive to the boundary of origin of the current. At current compensation, $I_{A,B} = -I_{1,2}$, the diagonal voltages vanish

Fig. 12 such a current compensation appears as if we would have a single circuit loop, including both current sources in series, while closing the current loop across the bulk region between contacts A and 1 as well as B and 2. Now we have two options for an interpretation: (i) Using the EC picture, the inner and outer edge appear

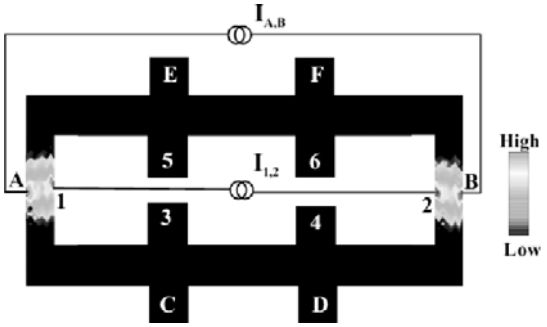

Fig. 15. The calculated current density distribution, which suggests bulk flow, is illustrated for the case of current compensation ($I_{A,B} = -I_{1,2}$) at a magnetic field of $B = 8$T according to Fig. 13. The logarithm of the current density is gray scale coded as indicated on the right side. Black indicates zero current density, while the current density increases toward the light gray regions, but finally gets dark again at highest-current density, thus allowing to visualize the "hot spots" of highest-current density at the point contacts A,B,1,2

decoupled and produce independent Hall voltages that have the same value and the same polarity. (ii) Using the bulk current picture, a bulk current flow should appear between inner and outer contacts (between A and 1 as well as B and 2), even in the plateau regime, while there should be no bulk current flow in the upper and lower branch of the sample. This is nicely demonstrated by Fig. 15, which shows the calculated bulk current density in the plateau regime of the structure for the case of current compensation. The upper and lower branch in this consideration serve as Hall voltage probes for the bulk current between A and 1 as well as B and 2, giving a Hall voltage between, for example, C and E but also between 3 and 5, which is the same.

The chosen examples for the application of the presented nonequilibrium network demonstrate that the model addresses edge and bulk aspects of current flow in the IQHE regime on an equal basis, and thus it may be able to handle most of the complex configurations investigated in experimental setups.

3.7 The Real-Space Renormalization Approach

The real-space RG approach [43, 44] is yet another way of numerically exploiting the successful percolation picture for describing a 2D electron systems and can, for instance, be applied to the CC network analogously to the case of 2D bond percolation [45–47]. The nonequilibrium network model presented in Sect. 3.2 might also be a potential candidate for renormalization. An RG unit is constructed containing several SPs from a CC network [48, 49]. For these SPs the RG transformation has to relate their S matrices with the S matrix of the super-SP. The RG unit used here is extracted from a CC network on a regular 2D square lattice. The super-SP consists of five original SPs connected according to Fig. 16. Circles correspond to SPs and lines to links in the network. Using this intuitive picture one can identify the loss of connectivity in comparison with the original CC network, namely, the four edge nodes within a 3×3 SP pattern are fully neglected as are their outer bonds. Thus, the super-SP has the same number of incoming and outgoing channels as an original SP. In analogy to bond percolation the size of the RG unit in terms of lattice spacing equals 2 [48].

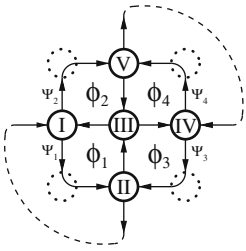

Fig. 16. CC network on a square lattice consisting of nodes (*circles*) and links (*arrows*). The RG unit combines five nodes (*full circles*) by neglecting some connectivity (*dashed circles*). $\Phi_1, \ldots, \Phi_4$ are the phases acquired by an electron along the loops as indicated by the arrows. $\Psi_1, \ldots, \Psi_4$ represent wave function amplitudes, and the thin dashed lines illustrate the boundary conditions used for the computation of level statistics

Between the SPs of the RG unit an electron travels along equipotential lines, and accumulates a certain Aharonov-Bohm phase as in the original network. Different phases are uncorrelated, which reflects the randomness of the original potential landscape. As shown in Sect. 3.2, each SP is described by an S matrix, which contributes two equations relating the wave-function amplitudes of incoming, I_i, I_i^* and outgoing, O_i, O_i^* channels. All amplitudes I_i, I_i^* besides the external I_1 and I_4^* can then be expressed by O_i, O_i^* using the phases, for example, $I_5 = e^{i\Phi_{15}} O_1$, where Φ_{15} is the phase shift along the link between SPs I and V. The resulting 10 modified scattering equations form a linear system that has to be solved in order to obtain the transmission properties of the corresponding super-SP:

$$A\mathbf{x} = \mathbf{b}\,, \tag{23}$$

with

$$A = \begin{pmatrix}
1 & 0 & 0 & 0 & 0 \\
0 & 1 & 0 & 0 & 0 \\
0 & -t_2 e^{i\Phi_{12}} & 1 & 0 & 0 \\
0 & -r_2 e^{i\Phi_{12}} & 0 & 1 & 0 \\
0 & 0 & -r_3 e^{i\Phi_{23}} & 0 & 1 \\
0 & 0 & t_3 e^{i\Phi_{23}} & 0 & 0 \\
0 & 0 & 0 & 0 & t_4 e^{i\Phi_{34}} \\
0 & 0 & 0 & 0 & -r_4 e^{i\Phi_{34}} \\
-t_5 e^{i\Phi_{15}} & 0 & 0 & 0 & 0 \\
-r_5 e^{i\Phi_{15}} & 0 & 0 & 0 & 0
\end{pmatrix} \Rightarrow$$

$$\Rightarrow \begin{pmatrix}
-r_1 e^{i\Phi_{31}} & 0 & 0 & 0 & 0 \\
t_1 e^{i\Phi_{31}} & 0 & 0 & 0 & 0 \\
0 & 0 & -r_2 e^{i\Phi_{42}} & 0 & 0 \\
0 & 0 & t_2 e^{i\Phi_{42}} & 0 & 0 \\
0 & 0 & 0 & 0 & -t_3 e^{i\Phi_{53}} \\
1 & 0 & 0 & 0 & -r_3 e^{i\Phi_{53}} \\
0 & 1 & 0 & 0 & 0 \\
0 & 0 & 1 & 0 & 0 \\
0 & -r_5 e^{i\Phi_{45}} & 0 & 1 & 0 \\
0 & t_5 e^{i\Phi_{45}} & 0 & 0 & 1
\end{pmatrix}, \tag{24}$$

$$\mathbf{x} = (O_1, O_1^*, O_2, O_2^*, O_3, O_3^*, O_4, O_4^*, O_5, O_5^*)^T\,, \tag{25}$$

and

$$\mathbf{b} = (t_1 I_1, r_1 I_1, 0, 0, 0, 0, r_4 I_4^*, t_4 I_4^*, 0, 0)^T\,. \tag{26}$$

Note that the amplitudes on the external links coincide with the amplitudes of the super-SP as $I_1 = I', I_4^* = I'^*, O_5 = O'$ and $O_2^* = O'^*$. Setting the incoming links of the super-SP according to $I' = 1, I'^* = 0$ one can deduce the transmission coefficient t' of the super-SP, since $O' = t'I' = t'1 = t'$. For the transmission coefficient of the super-SP this method yields the following expression [44]:

$$t' = \left| \frac{t_1 t_5 (r_2 r_3 r_4 e^{i\Phi_3} - 1) + t_2 t_4 e^{i(\Phi_1+\Phi_4)} (r_1 r_3 r_5 e^{-i\Phi_2} - 1) + t_3 (t_2 t_5 e^{i\Phi_1} + t_1 t_4 e^{i\Phi_4})}{(r_3 - r_2 r_4 e^{i\Phi_3})(r_3 - r_1 r_5 e^{i\Phi_2}) + (t_3 - t_4 t_5 e^{i\Phi_4})(t_3 - t_1 t_2 e^{i\Phi_1})} \right| . \tag{27}$$

Here Φ_j corresponds to the sum over the three phases forming a closed loop within the RG unit (see Fig. 16). Equation (27) is the RG transformation, which allows one to generate the distribution $P(t')$ of the transmission coefficients of super-SPs using the distribution $P(t)$ of the transmission coefficients of the original SPs. Since the transmission coefficients of the original SPs depend on the electron energy ε, the fact that delocalization occurs at $\varepsilon = 0$, implies that a certain distribution, $P_{\mathrm{c}}(t)$ — with $P_{\mathrm{c}}(t^2)$ being symmetric with respect to $t^2 = \frac{1}{2}$ — is the FP distribution of the RG transformation (27).

A systematic improvement of the RG structure by inclusion of more than five SPs into the basic RG unit [50–52] leads to similar results. In contrast, using a smaller RG unit [53] does not describe the critical properties of the QH transition with the same accuracy [54]. For the construction of a properly chosen RG unit two conflicting aspects have to be considered. (i) With the size of the RG unit also the accuracy of the RG approach increases since the RG unit can preserve more connectivity of the original network. (ii) As a consequence of larger RG units the computational effort for solving the scattering problem rises, especially in the case where an analytic solution, as Eq. (27), is not attained. Because of these reasons building an RG unit is an optimization problem depending mainly on the computational resources available.

With this scheme very large system sizes can be achieved conveniently using a few nodes only. This method yields a very accurate value for the critical exponent of $\nu = 2.39 \pm 0.01$ [54]. The idea of tunneling at SPs remains a useful concept even in the presence of correlations among the electrons [55] and may, for instance, be used in an effective description of highly correlated states, as in the FQHE (d'Ambrumenil et al. 2007, unpublished).

Another application of the real-space RG approach to the CC model, concerns the distribution functions P of two-point conductance G and the resistances R_{xx} and R_{xy}. Furthermore, closing the incoming and outgoing links of the RG unit and thus quantizing the allowed energies, one can make contact with previous studies of energy level statistics. A suitable scaling ansatz again allows the independent estimation of ν. These results are in good agreement with previous studies and validate the present RG approach [49].

A further application is concerned with the possible existence of the quantized Hall insulator. While it is established that plateau-plateau and insulator-plateau transitions exhibit the same critical behavior [56–66] the value of the Hall resistance R_{xy} in this insulating phase is still rather controversial [67]. Various experiments have found that R_{xy} remains very close to its quantized value h/e^2 even deep in the insulating regime when already $R_{xx} \gg h/e^2$ [57–60, 68]. This scenario has been dubbed the *quantized Hall insulator*. On the other hand, theoretical predictions based on quantum coherent models show that a diverging R_{xy} should be expected [53, 69]. Extending the RG approach to the calculation of suitable means for R_{xy} and R_{xx} the RG approach can in fact reconcile these findings by establishing that

the most-probable value of R_{xy} remains rather close to h/e^2 even for large R_{xx}, but then diverges with the predicted power-law for $R_{xx} > 20h/e^2$.

Last, the RG approach is also ideally placed to study the changes of the critical properties due to truly long-ranged,[4] so-called macroscopic inhomogeneities. Close to the transition the localization length ξ becomes sufficiently large. Then the long-ranged disorder can affect the character of the divergence of ξ. We note that in previous considerations inhomogeneities were incorporated into the theory through a spatial variation of the *local* resistivity [71–75], that is, "inhomogeneously *incoherent*". The CC model based RG approach is able to retain the full quantum coherence.

4 Hartree-Fock Approach to the IQHE

In order to investigate the nonequilibrium currents of interacting electrons one might suggest to use results from HF calculations as input data for the nonequilibrium network model of Sect. 3.2. In the following we will briefly outline the HF approach in the Landau basis and present results for the charge density (i.e., effective potential) of such interacting calculations that could, in a further step, serve as more realistic input data.

4.1 Derivation of the Hartree-Fock Equations

We consider an interacting 2DES in the (x, y)-plane subject to a perpendicular magnetic field, $\mathbf{B} = B\mathbf{e}_z$. The system can be described by a Hamiltonian of the form

$$H^{\sigma}_{\mathrm{2DES}} h^{\sigma} + V_{\mathrm{C}} \frac{(\mathbf{p} - e\mathbf{A})^2}{2m^*} + \frac{\sigma g^* \mu_{\mathrm{B}} B}{2} + V_{\mathrm{I}}(\mathbf{r}) + V_{\mathrm{C}}(\mathbf{r}, \mathbf{r}') \,, \tag{28}$$

where $\sigma = \pm 1$ is a spin degree of freedom, V_{I} is the smooth random potential (7) modeling the effect of the electron-impurity interaction, V_{C} represents the electron-electron interaction term and m^*, g^*, and μ_{B} are the effective electron mass, g-factor, and Bohr magneton, respectively [76]. The electron-electron interaction potential has the form

$$V_{\mathrm{C}}(\mathbf{r}, \mathbf{r}') \frac{\gamma e^2}{4\pi\epsilon\epsilon_0} \frac{1}{|\mathbf{r} - \mathbf{r}'|} \sum_{\mathbf{q}} V_{\mathrm{C}}(\mathbf{q}) \exp\left[i\mathbf{q} \cdot (\mathbf{r} - \mathbf{r}')\right] \,, \tag{29}$$

with

$$V_{\mathrm{C}}(\mathbf{q}) = \frac{\gamma e^2}{4\pi\epsilon\epsilon_0 l_{\mathrm{c}}} \frac{1}{N_\phi |\mathbf{q}| l_{\mathrm{c}}} \,. \tag{30}$$

The parameter, γ, will allow us to continually adjust the interaction strength; $\gamma = 1$ corresponds to the bare Coulomb interaction. The Hamiltonian is represented in matrix form using the periodic Landau states $|nk\rangle$ and we have

[4] Note that sometimes the term "long-ranged disorder" is also used for a disorder that has a finite correlation radius which is larger than the magnetic length [70]. This is different from the present situation.

$$\mathbf{H}^{\sigma}_{n,k;n',k'} = \langle nk|H^{\sigma}_{\mathrm{2DES}}|n'k'\rangle$$
$$= \left(n + \frac{1}{2} + \frac{\sigma g^*}{4}\frac{m^*}{m_\mathrm{e}}\right)\hbar\omega_\mathrm{c}\delta_{n,n'}\delta_{k,k'} + \mathbf{V}_{n,k;n',k'} + \mathbf{F}^{\sigma}_{n,k;n',k'} \ , \quad (31)$$

with the cyclotron energy $\hbar\omega_\mathrm{c} = \hbar eB/m^*$. The disorder matrix elements are given by $\mathbf{V}_{n,k;n',k'} = \sum_{\mathbf{q}} V_\mathrm{I}(\mathbf{q}) S_{n,k;n',k'}(\mathbf{q})$, where mixing of LLs is included. The explicit form of the plane wave matrix elements, $S_{n,k;n',k'}(\mathbf{q}) = \langle nk|\exp(i\mathbf{q}\cdot\mathbf{r})|n'k'\rangle$ and the Fock matrix $\mathbf{F}^{\sigma}_{n,k;n',k'}$ can be found in [30]. The total energy E_tot in terms of the above matrices is given as

$$E_\mathrm{tot} = \mathrm{Tr}\left(\mathbf{hD} + \frac{1}{2}\mathbf{FD}\right) = \frac{1}{2}\sum_{\sigma}\sum_{n,k;n',k'}\left(2\mathbf{h}^{\sigma}_{n,k;n',k'} + \mathbf{F}^{\sigma}_{n,k;n',k'}\right)\mathbf{D}^{\sigma}_{n',k';n,k} \ , \quad (32)$$

where the density matrix is $\mathbf{D}_{n,a;m,b} = \sum_\alpha f_\alpha C^{\alpha}_{n,a} C^{\alpha,*}_{m,b}$ with f_α the Fermi function and $C^{\alpha}_{n,a}$ the expansion coefficients for the Landau basis [30]. A variational minimization of $\langle\Psi|H_\mathrm{2DES}|\Psi\rangle$ with respect to the coefficients yields the Hartree-Fock-Roothaan equation [77]. However, convergence of the Roothaan algorithm is rather poor. In most cases it runs into an oscillating limit cycle [76]. This limit cycle can be avoided be minimizing a penalized energy functional

$$E'(\mathbf{D}_\mathrm{old}, \mathbf{D}_\mathrm{new}) = E(\mathbf{D}_\mathrm{old}, \mathbf{D}_\mathrm{new}) + b||\mathbf{D}_\mathrm{old} - \mathbf{D}_\mathrm{new}||^2 \ , \quad (33)$$

instead of the actual HF energy functional where "old" and "new" denote two consecutive states in the HF-self-consistency cycle. This, then, leads to the Level-Shifting algorithm (LSA) [78]. However, while LSA avoids limit cycles, it can and does lead to unphysical solutions. A further improvement is based on the Optimal-Damping algorithm (ODA) [79]. The iteration is carried out just as in the Roothaan algorithm, only that the new density matrix is a mixture of the old and the new density matrix, thas is,

$$\mathbf{D} = (1-\lambda)\mathbf{D}_\mathrm{old} + \lambda\mathbf{D}_\mathrm{new} \ , \quad (34)$$

with a damping parameter, λ, which is chosen optimally according to the direction of steepest descent in the total HF energy [76]. As it turns out, the performance also depends strongly on the interaction strength and the position of the Fermi level. For some filling factors and choices of parameters, we might find fast convergence with one of the algorithms described above. However, over the whole range of filling factors only a combination of ODA and LSA can guarantee convergence in any case.

4.2 Charge Density Distribution and Screening

We will now focus on the behavior of the electron density in the presence of electron-electron interactions. The spatial distribution of the total electronic density

$$n(\mathbf{r}) = \sum_{\sigma}\sum_{\alpha=1}^{M}\left|\psi^{\sigma}_{\alpha}(\mathbf{r})\right|^2 \quad (35)$$
$$= L^{-2}\sum_{\sigma}\sum_{n,k,n',k'}\sum_{\mathbf{q}}\mathbf{D}^{\sigma}_{n,k;n',k'} S_{n,k;n',k'}(\mathbf{q})\exp(-i\mathbf{qr}) \quad (36)$$

is readily calculated in our system. It details the disorder screening mechanism by providing direct insight into the interplay of disorder and interaction. Let us start at the QH transition. Figure 17(a) depicts the critical charge density at $\nu = 1/2$ for a noninteracting system in units of n_0. The contour lines show the impurity potential $V_{\mathrm{I}}(\mathbf{r})$ where the critical energy $V_{\mathrm{I}}(\mathbf{r}) = \epsilon_{\mathrm{F}}$ is highlighted by a thick line. The charge density evidently behaves according to the semi classical approximation [29] and follows the equipotential lines of $V_{\mathrm{I}}(\mathbf{r})$. Similarly, Figs. 18(a) and 19(a) show the noninteracting situation at $\nu = 0.1$ and 0.9, respectively. For the interacting case, however, we expect Thomas-Fermi screening theory to apply [80–83]. This approximation is appropriate for an impurity potential smooth on the scale of the magnetic length as well as a sufficient separation of the Landau bands, characterized by the condition $\hbar\omega_{\mathrm{c}}/l_{\mathrm{c}} > \sqrt{\langle|\nabla V_{\mathrm{I}}(\mathbf{r})|^2\rangle}$. The electrostatic potential of the charge density

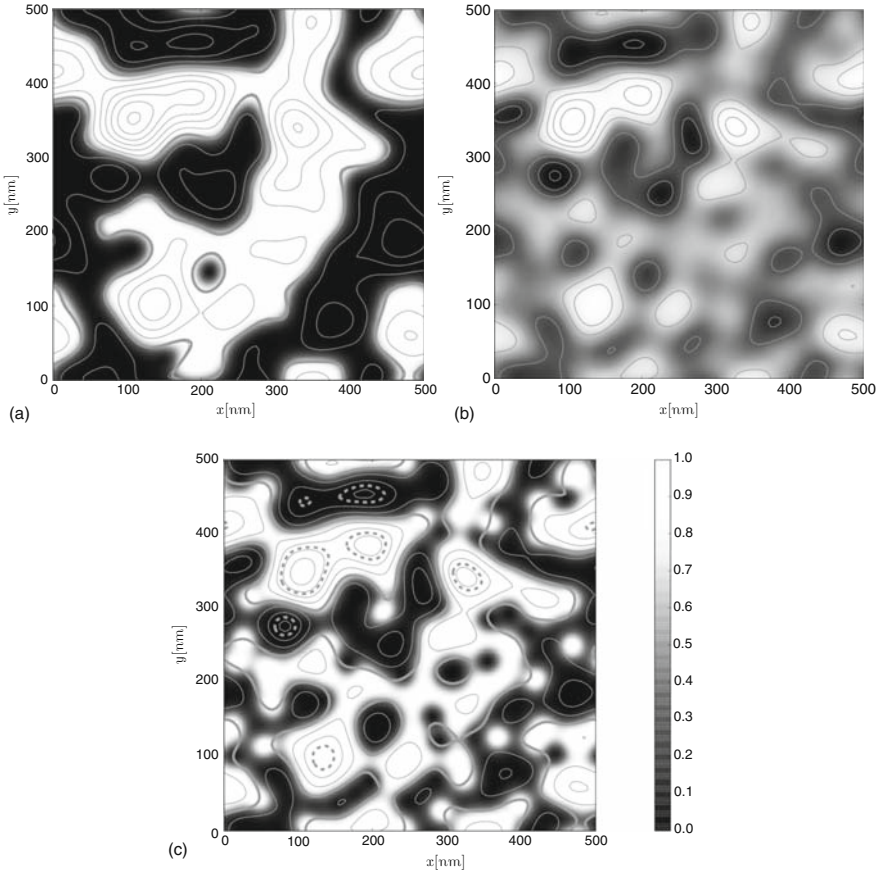

Fig. 17. Spatial distribution of electron density $n(\mathbf{r})/n_0$ at $B = 4\mathrm{T}$ and $\nu = 1/2$ as indicated by the grey scale for (**a**) $\gamma = 0$, (**b**) Hartree-interaction at $\gamma = 0.3$ and (**c**) full HF interaction with $\gamma = 0.3$. Solid contour lines show the equipotential lines of $V_{\mathrm{I}}(\mathbf{r})$ for (**a**) and the screened potential contours of (39) for (**b**) and (**c**). The thick solid lines corresponds to half-filling

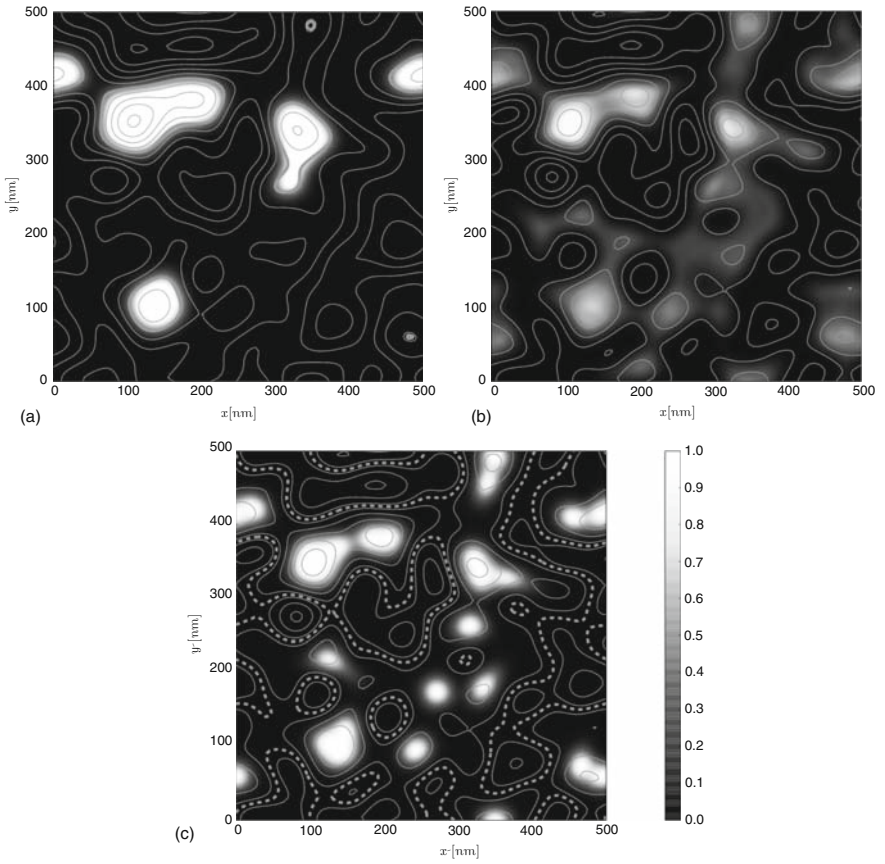

Fig. 18. Spatial distribution of electron density $n(\mathbf{r})/n_0$ at $B = 4$T and $\nu = 0.1$ as indicated by the grey scale for (**a**) $\gamma = 0$, (**b**) Hartree-interaction at $\gamma = 0.3$ and (**c**) full HF interaction with $\gamma = 0.3$. *Lines* and *grey scales* as in Fig. 17

$$\phi(\mathbf{r}) = \frac{e}{4\pi\epsilon\epsilon_0} \int d^2\mathbf{r}' \frac{n(\mathbf{r}') - \bar{n}}{|\mathbf{r}' - \mathbf{r}|} \tag{37}$$

and the impurity potential $V_{\mathrm{I}}(\mathbf{r})$ form a screened potential $V_{\mathrm{scr}}(\mathbf{r}) = V_{\mathrm{I}}(\mathbf{r}) + e\phi(\mathbf{r})$. Here, $\bar{n}$ accounts for the positive background. Since a flat screened potential is energetically most favorable, one expects to find $V_{\mathrm{scr}}(\mathbf{r})\epsilon_{\mathrm{F}}$ for the case of perfect screening. However, since fluctuations of the density, $\delta n(\mathbf{r}) = n(\mathbf{r}) - \bar{n}$, are restricted between an empty and a full LL, that is, $0 < \delta n(\mathbf{r}) < n_0$, the screening is not always perfect, but depends on the fluctuations in the impurity potential as well as on the filling factor [80–82]. The plane can be divided into fully electron or hole depleted insulating regions — where $n(\mathbf{r}) = 0$ or $n(\mathbf{r}) = n_0$, respectively — and metallic regions — where $n(\mathbf{r})$ lies in between. Depending on the filling factor, the extent of those regions varies. Close to the band edge, insulating regions dominate (see Figs. 18 and 19). Screening is highly nonlinear and transport virtually impossible. On the

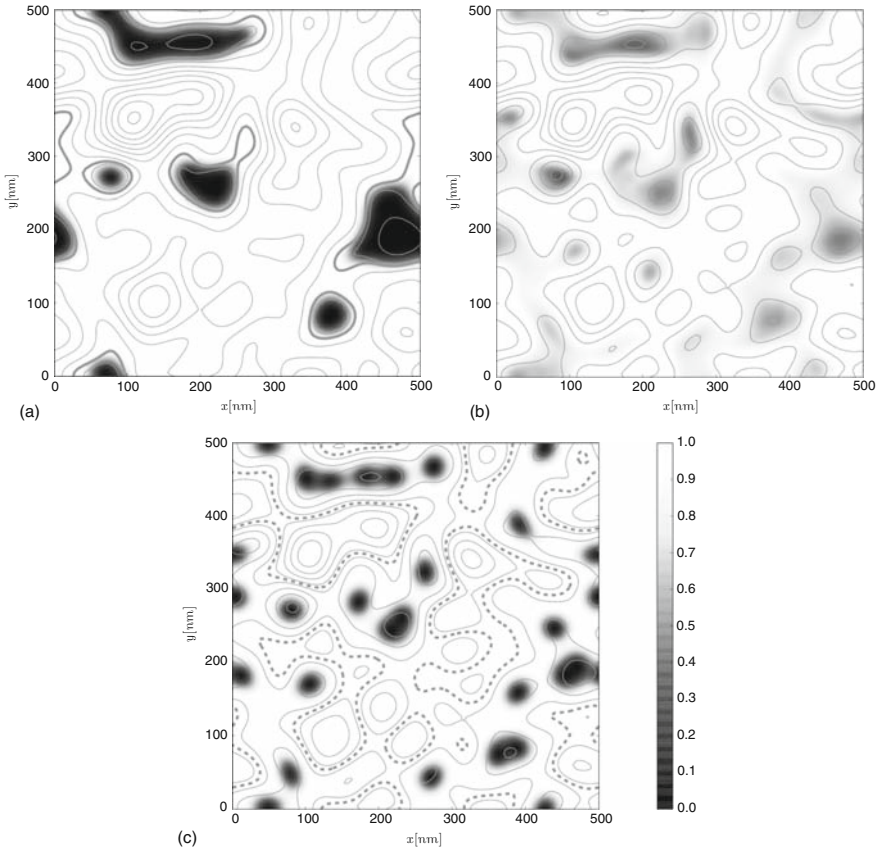

Fig. 19. Spatial distribution of electron density $n(\mathbf{r})/n_0$ at $B = 4$T and $\nu = 0.9$ as indicated by the grey scale for (**a**) $\gamma = 0$, (**b**) Hartree-interaction at $\gamma = 0.3$ and (**c**) full HF interaction with $\gamma = 0.3$. Lines and grey scales as in Fig. 17

other hand, if disorder is weak enough, there exists a finite range of filling factors in the centers of each band where metallic regions cover most of the sample, percolate and render the whole system metallic. The disorder is effectively screened and transport greatly enhanced. In that case, the charge density $n_{\rm scr}(\mathbf{r})$ can be obtained by Fourier transforming the screened potential. In 3D, this simply leads to the Laplace equation. For 2D, however, one obtains [84]

$$n_{\rm scr}(\mathbf{q}) = -\frac{2\epsilon\epsilon_0}{e^2}|\mathbf{q}|V_{\rm I}(\mathbf{q}) + \nu n_0 \delta_{q,0} \ , \tag{38}$$

where the $|\mathbf{q}| = 0$ term is "perfectly screened" by the positive background and thus does not contribute to the screening of the impurity potential. In other words, in our system only the fluctuations, $\delta n(\mathbf{r})$ are essential for screening. Hence, in 2D, a perfectly screening charge density would obey

$$n_{\rm scr}(\mathbf{r}) = -\frac{4\pi\epsilon\epsilon_0}{e^2}\int d^2\mathbf{r}'\frac{\Delta_{\rm 2D}V_{\rm I}(\mathbf{r}')}{|\mathbf{r}-\mathbf{r}'|} + \nu n_0 \ . \tag{39}$$

Clearly, the actual charge density is expected to deviate from $n_{\rm scr}(\mathbf{r})$ for several reasons. First, the fluctuations of $n(\mathbf{r})$ are restricted as discussed above. Second, (39) is valid for the Hartree case only. For comparison, in Figs. 17, 18, 19(b) we have depicted the charge density of a *Hartree*-calculation. The density displays purely classical behaviour and fits the contour lines, Eq. (39), perfectly. Taking the Fock contribution into account will introduce short wavelength fluctuations due to the tendency for crystallization. However, we still expect the charge density to follow (39) in the limit of $|\mathbf{q}| \to 0$. Figure 17(c) shows results for the charge density of interacting electrons at $\nu = 1/2$. Broken lines indicate the regions where $n_{\rm scr}(\mathbf{r})$ exceeds the range for $\delta n(\mathbf{r})$ either below or above, that is, areas that cannot be screened at all and, thus, exhibit insulating behavior. Otherwise, we find the charge density to follow $n_{\rm scr}(\mathbf{r})$ very closely. In this regime, the density is well described by (39) and the screening is very effective. Metallic regions dominate over insulating ones and transport is expected to be good. In contrast, if the filling factor is close to an integer value, the charge density cannot provide sufficient fluctuations in order to screen effectively. We have depicted this situation for $\nu = 0.1$ in Fig. 18(c) and for $\nu = 0.9$ in Fig. 19(c). In Figs. 18(c) and 19(c) we depict plots of $n(\mathbf{r})$ and $n_{\rm scr}(\mathbf{r})$ for the sample of Fig. 17, demonstrating the discussed effects again very clearly.

5 Conclusions

In Sect. 3, we have reviewed some of the most prominent network models for the explanation of the IQHE. These models are largely based on and most easily justified by single-particle wave function arguments as recalled in Sect. 2. Let us now comment how the HF results above modify these approaches. Clearly, the inclusion of the electronic many-body interactions, even at the Hartree level alone, changes the pattern and spatial distribution of the electronic wave functions. No longer the bare, but rather the screened disorder potential dictates the behavior of the wave functions. Nevertheless, we also find that the topology of the resulting 2D wave function in the HF approximation retains much of the character of the noninteracting state. The percolating, delocalized state is much the same as before. And even at the band edges, we see that the HF-localized states still localize roughly where the nointeracting states did. This is not true for the simple Hartree approximation, where states tend to be much more smeared. Thus, we see that while the inclusion of interaction at the HF level does alter some of the characteristics of the IQHE and in particular highlights the importance of screening effects (and the division into linear and nonlinear screening regions), it does at the same time support the basic justifications on the network models: states exist along contours of some disordered (but not necessarily bare) potential and the percolation across this effective potential describes the QH phenomenon.

These qualitative arguments can in principle be put on a firm quantitative basis by using the results of the microscopic HF calculation to extract for each SP in a

given (screened) disorder landscape the transmission and reflection coefficients as well as the connectivity network of the SPs. In order to do so, one could for example identify two states $\psi_\alpha^\sigma(1)$, $\psi_\beta^\sigma(2)$, separated by a SP at $\nu \lesssim 0.5$, and then compute their overlap $\langle\psi_\alpha^\sigma(1)|\psi_\beta^\sigma(2)\rangle$ restricted to the vicinity of the SP. In practice, however, such a numerical identification appears far from trivial, particularly if more than one LL is to be taken into account. As a first attempt to address this task one could follow the procedure as described in Sect. 3.4 in context with Fig. 9: One takes the density distribution from the HF calculation, as shown for example, in Fig. 17 and maps it on a sufficiently dense grid of the nonequilibrium network. As an initial step the nodes are handled as usual by applying Eq. (22), which can be easily transformed into a much more suitable form for this purpose [33]

$$P = \exp\left[-\Delta\nu L^2 \frac{eB}{h}\right] . \tag{40}$$

The exponent of Eq. (40) contains the typical size of the fluctuation period L, the filling factor of the LL relative to half-filling $\Delta\nu$ and the remaining part is the density of states of the LL. On this basis the results of Fig. 17 can be directly mapped on the network grid. Only for those nodes, which are sufficiently close to half-filling and thus get a P value close to 1, the above equation is replaced by the calculation of the overlap between the real states resulting from the HF calculation at the saddle. This overlap is expected to be a measure of the transmission coefficient of the node. Finally, the involved saddle is described by the value $P = R/T$, which is transferred back to the corresponding node of the grid. The final numerical solution procedure for the network in order to obtain the distribution of the excess current and the excitation voltage remains the same as already described. We believe this strategy to be a promising route to future research.

Acknowledgements

Free file hosting has been provided by CVSDude.org. Financial support by the Austrian National Science Foundation FWF project P19353-N16 for the nonequilibrium network model and by the Deutsche Forschungsgemeinschaft (SPP "Quanten-Hall-Systeme") for the renormalization group studies as well as the HF results. Numerical computations were performed in part on the UK National Grid.

References

1. K.v. Klitzing, G. Dorda, and M. Pepper, Phys. Rev. Lett. **45**, 494 (1980) 163
2. B. Jeckelmann and B. Jeanneret, Rep. Prog. Phys. **64**, 1603 (2001) 164
3. D.C. Tsui, H.L. Stormer, and A.C. Gossard, Phys. Rev. Lett. **48**, 1559 (1982) 164
4. R.B. Laughlin, Phys. Rev. B **23**, 5632 (1981) 164
5. R.B. Laughlin, Phys. Rev. Lett. **50**, 1395 (1983) 164

6. F.D.M. Haldane, Phys. Rev. Lett. **51**, 605 (1983) 164
7. B.I. Halperin, Phys. Rev. Lett. **52**, 2390 (1984) 164
8. R.E. Prange, Phys. Rev. B **23**, 4802 (1981) 164
9. T. Chakraborty and P. Pietiläinen, *The Quantum Hall effects* (Springer, Berlin, 1995) 164
10. M. Janssen, O. Viehweger, U. Fastenrath, and J. Hajdu, *Introduction to the Theory of the Integer Quantum Hall effect* (VCH, Weinheim, 1994) 164
11. A.M.M. Pruisken, Nucl. Phys. B **235**, 277 (1984) 164
12. D.J. Thouless, M. Kohmoto, M.P. Nightingale, and M. den Nijs, Phys. Rev. Lett. **49**, 405 (1982) 164
13. A.M. Chang. In: *The Quantum Hall Effect*, ed by R.E. Prange and S.M. Girvin (Springer, Berlin, 1987) 164
14. J.T. Chalker and P.D. Coddington, J. Phys.: Condens. Matter **21**, 2665 (1988) 164, 167, 168
15. P. Cain and R.A. Römer, EuroPhys. Lett. **66**, 104 (2004) 164
16. B. Kramer, T. Ohtsuki, and S. Kettemann, Phys. Rep. **417**, 211 (2005), ArXiv: cond-mat/0409625 164, 167, 168, 170
17. S. Ilani, J. Martin, E. Teitelbaum, J. Smet, D. Mahalu, V. Umansky, and A. Yacoby, Nature **427**, 328 (2004) 164
18. J. Martin, S. Ilani, B. Verdene, J. Smet, V. Umansky, D. Mahalu, D. Schuh, G. Abstreiter, and A. Yacoby, Science **305**, 980 (2004) 164
19. D.H. Cobden, C.H.W. Barnes, and C.J.B. Ford, Phys. Rev. Lett. **82**, 4695 (1999) 164
20. T. Machida, S. Ishizuka, S. Komiyama, K. Muraki, and Y. Hirayama, Phys. Rev. B **63**, 045318 (2001) 164
21. O.E. Dial, R.C. Ashoori, L.N. Pfeiffer, and K.W. West, Nature **448**, 176 (2007) 164
22. J.P. Eisenstein, L.N. Pfeiffer, and K.W. West, Phys. Rev. Lett. **68**, 674 (1992) 164
23. S.G. Semenchinskii, **41**, 605 (1985) 164
24. L. Zheng and H.A. Fertig, Phys. Rev. B **50**, 4984 (1994) 164
25. D.-H. Lee and Z. Wang, Phys. Rev. Lett. **76**, 4014 (1996) 164
26. S.-R.E. Yang, A.H. MacDonald, and B. Huckestein, Phys. Rev. Lett. **74**, 3229 (1995) 164
27. L.D. Landau and E.M. Lifshitz, *Quantum Mechanics* (Butterworth-Heinemann, Oxford, 1981) 165
28. T. Dittrich, P. Hänggi, G.-L. Ingold, B. Kramer, G. Schön, and W. Zwerger, *Quantum Transport and Dissipation* (Wiley-VCH, Berlin, 1998) 166
29. B. Huckestein, Rev. Mod. Phys. **67**, 357–396 (1995) 166, 173, 186
30. C. Sohrmann and R.A. Römer, New J. Phys. **9**, 97 (2007) 166, 185
31. M. Tsukada, J. Phys. Soc. Jpn. **41**, 1466 (1976) 167
32. J. Oswald and A. Homer, Physica E **11**, 310 (2001) 171, 173
33. J. Oswald and M. Oswald, J. Phys. Cond. Mat. **18**, R101 (2006) 171, 172, 190
34. J. Oswald, G. Span, and F. Kuchar, Phys. Rev. B **58**, 15401 (1998) 173
35. J. Oswald, Physica E **3**, 30 (1998) 173
36. B. Piot, D.K. Maude, M. Henini, Z.R. Wasilewski, K.J. Friedland, R. Hey, K.H. Ploog, A.I. Toropov, R. Airey, and G. Hill, Phys. Rev. B **72**, 245325 (2005) 173
37. J. Oswald, Int. J. Modern Phys. **B 21 (8–9)**, 1424 (2007) 173

38. E. Ahlswede, J. Weis, K. Van Klitzing, and K. Eberl, Physica E: Low-Dimensional Systems and Nanostructures **12 (1–4)**, 165 (2002) 178
39. J. Weis, Int. J. Modern Phys. **B 21 (8–9)**, 1297 (2007) 178
40. R. Mani, J. Phys. Soc. Japan **65 (6)**, 1751 (1996) 178, 180
41. M. Oswald, J. Oswald, and R. Mani, Phys. Rev. B **72 (3)**, 1 (2005) 179
42. J. Oswald and M. Oswald, Phys. Rev. B **74 (15)**, 153315 (2006) 179
43. D.P. Arovas, M. Janssen, and B. Shapiro, Phys. Rev. B **56**, 4751 (1997), ArXiv: cond-mat/9702146 181
44. A.G. Galstyan and M.E. Raikh, Phys. Rev. B **56**, 1422 (1997) 181, 182
45. J. Bernasconi, Phys. Rev. B **18**, 2185 (1978) 181
46. P.J. Reynolds, W. Klein, and H.E. Stanley, J. Phys. C **10**, L167 (1977) 181
47. D. Stauffer and A. Aharony, *Introduction to Percolation Theory* (Taylor and Francis, London, 1992) 181
48. P. Cain, R.A. Römer, M. Schreiber, and M.E. Raikh, Phys. Rev. B **64**, 235326 (2001), ArXiv: cond-mat/0104045 181
49. P. Cain, R.A. Römer, and M.E. Raikh, Phys. Rev. B **67**, 075307 (2003), ArXiv: cond-mat/0209356 181, 183
50. M. Janssen, R. Merkt, J. Meyer, and A. Weymer, Physica **256–258**, 65 (1998) 183
51. M. Janssen, R. Merkt, and A. Weymer, Ann. Phys. (Leipzig) **7**, 353 (1998) 183
52. A. Weymer and M. Janssen, Ann. Phys. (Leipzig) **7**, 159 (1998), ArXiv: cond-mat/9805063 183
53. U. Zülicke and E. Shimshoni, Phys. Rev. B **63**, 241301 (2001), ArXiv: cond-mat/0101443 183
54. P. Cain and R.A. Römer, Int. J. Mod. Phys. B **19**, 2085 (2005) 183
55. N.R. Cooper and J.T. Chalker, Phys. Rev. B **48**, 4530 (1993) 183
56. V. Goldman, J. Wang, B. Su, and M. Shayegan, Phys. Rev. Lett. **70**, 647 (1993) 183
57. M. Hilke, D. Shahar, S. Song, D. Tsui, Y. Xie, and D. Monroe, Nature **395**, 675 (1998) 183
58. D. de Lang, L. Ponomarenko, A. de Visser, C. Possanzini, S. Olsthoorn, and A. Pruisken, Physica E **12**, 666 (2002) 183
59. D. Shahar, D.C. Tsui, M. Shayegan, J.E. Cunningham, E. Shimshoni, and S.L. Sondhi, Solid State Commun. **102**, 817 (1997) 183
60. D. Shahar, D. Tsui, M. Shayegan, E. Shimshoni, and S. Sondhi, Science **274**, 1 (1996) 183
61. R. Hughes, J. Nicholls, J. Frost, E. Linfield, M. Pepper, C. Ford, D. Ritchie, G. Jones, E. Kogan, and M. Kaveh, J. Phys.: Condens. Matter **6**, 4763 (1994) 183
62. S. Murphy, J. Hicks, W. Liu, S. Chung, K. Goldammer, and M.B. Santos, Physica E **6**, 293 (2000) 183
63. W. Pan, D. Shahar, D.C. Tsui, H.P. Wei, and M. Razeghi, Phys. Rev. B **55**, 15431 (1997) 183
64. D. Shahar, D.C. Tsui, M. Shayegan, R.N. Bhatt, and J.E. Cunningham, Phys. Rev. Lett. **74**, 4511 (1995) 183
65. D. Shahar, D.C. Tsui, M. Shayegan, E. Shimshoni, and S.L. Sondhi, Phys. Rev. Lett. **79**, 479 (1997) 183

66. R.T.F. van Schaijk, A. de Visser, S.M. Olsthoorn, H.P. Wei, and A.M.M. Pruisken, Phys. Rev. Lett. **84**, 1567 (2000) 183
67. E. Shimshoni, Mod. Phys. Lett. B **18**, 923 (2004) 183
68. E. Peled, D. Shahar, Y. Chen, E. Diez, D.L. Sivco, and A.Y. Cho, (2003), cond-mat/0307423. 183
69. L.P. Pryadko and A. Auerbach, Phys. Rev. Lett. **82**, 1253 (1999) 183
70. F. Evers, A.D. Mirlin, D.G. Polyakov, and P. Wölfle, Phys. Rev. B **60**, 8951 (1999) 184
71. N.R. Cooper, B.I. Halperin, C.-K. Hu, and I.M. Ruzin, Phys. Rev. B **55**, 4551 (1997) 184
72. I.M. Ruzin, N.R. Cooper, and B.I. Halperin, Phys. Rev. B **53**, 1558 (1996) 184
73. E. Shimshoni, Phys. Rev. B **60**, 10691 (1999) 184
74. E. Shimshoni, A. Auerbach, and A. Kapitulnik, Phys. Rev. Lett. **80**, 3352 (1998) 184
75. S.H. Simon and B.I. Halperin, Phys. Rev. Lett. **73**, 3278 (1994) 184
76. C. Sohrmann, Ph.D. thesis, University of Warwick, 2007, in preperation. 184, 185
77. C.C.J. Roothaan, Rev. Mod. Phys. **23**, 69 (1951) 185
78. V.R. Saunders and I.H. Hillier, Int. J. Quantum Chem. **7**, 699 (1973) 185
79. E. Cancès and C.L. Bris, Int. J. Quantum Chem. **79**, 82 (2000) 185
80. A.L. Efros, J. Comput. System Sci. **65**, 1281 (1988) 186, 187
81. A.L. Efros, Solid State Commun. **67**, 1019 (1988) 186, 187
82. A.L. Efros, Solid State Commun. **70**, 253 (1989) 186, 187
83. A.L. Efros, Phys. Rev. B **45**, 11354 (1992) 186
84. U. Wulf, V. Gudmundsson, and R.R. Gerhardts, Phys. Rev. B **38**, 4218 (1988) 188

Percolative Quantum Transport in Manganites

P. Majumdar

Harish-Chandra Research Institute, Chhatnag Road, Jhusi, Allahabad 211 019, India

1 Introduction

Recent experiments on transition metal oxides, in particular the manganites [1–4], have brought the issue of 'percolative transport' center stage in correlated electron systems. On the one hand, there are spatial imaging experiments [5–8], using scanning tunnelling microscopy, magnetic force microscopy, etc., which suggest the coexistence of metallic and insulating regions on the nanoscale, on the other hand there are theoretical predictions [9] on phase separation (PS) and cluster coexistence near first order phase boundaries. This has led to the suggestion [6] that the unusual transport in these materials, including the 'colossal magnetoresistance' (CMR), arises from percolative conduction through a network of metallic and insulating domains. The volume fraction of the metallic regions, e.g., changes with temperature, applied field, etc., but it was hoped that classical percolation theory would provide a suitable framework for analysing the complex phenomena. Figure 1, from Uehara et al. [6], has been a defining image. The authors spatially resolved measurements on manganite thin films in the phase coexistence regime and suggested that the transport should be interpreted in terms of percolation of ferromagnetic metallic (FMM) clusters in an antiferromagnetic insulating (AF-I) background.

The attempts to fit transport results in the vicinity of insulator-metal transitions (IMT) in these materials to predictions of percolation theory have had mixed success. While there have been impressive fits to the transport data by using effective medium theory, there are several fundamental shortcomings of the standard percolation scenario when applied to the manganites. For example, (a) the resistivity changes much faster with concentration than predicted by percolation theory, and (b) the metal-insulator transitions are often *first order*, unlike typical percolation transitions that are second order. It seems that even if 'percolation theory' were to be a suitable starting point we would need a more sophisticated framework than *uncorrelated classical percolation*. In this review, our focus will be on the underlying microscopic theory,

Majumdar, P.: *Percolative Quantum Transport in Manganites*. Lect. Notes Phys. **762**, 195–226 (2009)
DOI 10.1007/978-3-540-85428-9_7

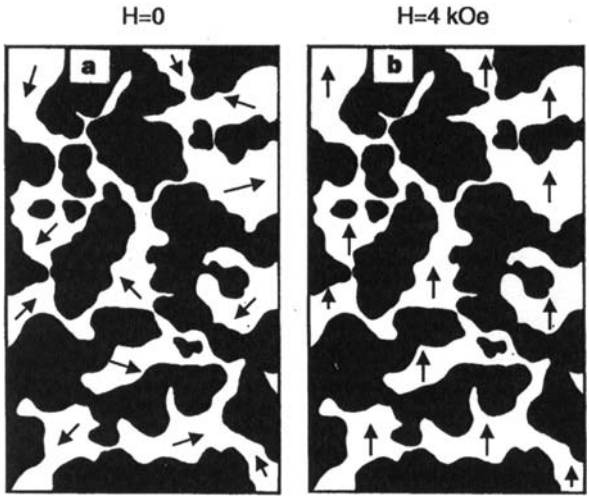

Fig. 1. Schematic illustration of sub-micrometer scale coexistence of charge ordered insulating (dark area) and ferromagnetic metallic (white area) domains, based on TEM measurements in $La_{1-x-y}Pr_yCa_xMnO_3$. The typical size of the domains is $0.5\,\mu m$. **(a)** At zero field the magnetisations of ferro domains are random. **(b)** All domains can be aligned by applying a field of order 4 KOe, allowing percolative conduction through the ferromagnetic metallic regions. From M. Uehara et al., Nature **399**, 560 (1999), with permission

its connection with quantum percolation, and the circumstances under which a classical percolation limit might emerge.

The review is organised as follows: In the next section I recapitulate a few standard results in quantum percolation. This is followed by (ii) a summary of some of the key transport and spatially resolved measurements in the manganites, and the relevant microscopic model. The section after (iii) describes cluster coexistence and percolative effects in a single-band model with magnetic phase competition. This is followed by (iv) the results on percolative phenomena in a more realistic two-band model, including the effect of electron-phonon interactions. The final section (v) attempts a connection between the microscopic results, quantum percolation, and phenomenological resistor network theory.

2 Standard Quantum Percolation

Quantum percolation [10, 11] is usually discussed as the quantum variant of classical percolation, i.e., with wave propagation and interference effects included. We would like to view quantum percolation, in the manganite context, as a limiting case of the general quantum disorder problem, defined below. As we will see in our discussion of microscopic models, this, rather than usual quantum percolation, is the more appropriate starting point.

2.1 The Disordered Quantum Problem

The general disorder problem for non interacting spinless electrons on a lattice has the form:

$$H = \sum_{\langle ij \rangle} t_{ij} c_i^\dagger c_j + \sum_i \epsilon_i c_i^\dagger c_i \tag{1}$$

c and $c^\dagger$ are fermionic annihilation and creation operators, respectively, and the model involves 'bond disorder' in the nearest neighbour hopping amplitude, t_{ij} and 'site disorder' in the ϵ_i. A complete description of the problem requires the probability distribution for these variables, $\mathcal{P}\{t_{ij}\}$ and $\mathcal{P}\{\epsilon_i\}$, where the angular brackets $\{..\}$ refer to the complete *bond or site configuration*.

In most cases, the problem is simplified by assuming *uncorrelated disorder*, where the distribution factorises into a product of the form

$$\mathcal{P}\{\epsilon\} = \Pi_i P(\epsilon_i), \tag{2}$$

where P is now a 'one point' distribution. In this case, the realisation of disorder can be generated by picking the random variable independently at each site (or bond) irrespective of its value in the neighbouring sites. Most model calculations are done using a Gaussian, binary or 'box' distribution $P(\epsilon_i)$, while the distribution for t_{ij} depends on the specific physical context. Often the entire probability distribution is not relevant and low-order moments, e.g., the mean $\bar{\epsilon} = \langle \epsilon_i \rangle = \int P(\epsilon) \epsilon d\epsilon$, the variance $\langle (\epsilon_i - \bar{\epsilon})^2 \rangle$, etc., are used to characterise the disorder.

Most of the theoretical effort in disorder studies has been on understanding transport and localisation in the case of uncorrelated disorder. One is usually interested in: (i) the mobility edge that separates spatially extended states from localised states, (ii) the localisation threshold, i.e., the disorder at which all states in the band become localised, and (iii) the critical behaviour of conductivity (σ), correlation length (ξ), etc., near the localisation transition.

Among the well-known results [12] are (i) the absence of a metallic phase in 1D and 2D in the presence of arbitrarily weak disorder, and (ii) the localisation of all eigenstates in the band in 3D when the disorder is comparable to the bandwidth.

Even *non-interacting* disordered electron systems may have unusual properties if the background 'disorder' distribution is non-trivially correlated. The standard percolation problem assumes an uncorrelated distribution, while in manganites the effective 'disorder' will turn out to be essentially correlated.

2.2 Quantum Percolation

The quantum percolation problem is a limiting case of the more general disorder problem defined above and involves an uncorrelated binary distribution for $P(\epsilon)$ or $P(t)$ as discussed below.

Site Percolation

Site percolation involves two kinds of sites, one with a low potential $\epsilon = 0$, say, and another with a large potential $\epsilon \to \infty$. A fraction p of the sites have potential $\epsilon = 0$ and a fraction $1 - p$ have potential $\epsilon \to \infty$. In the language of the distribution function

$$P(\epsilon) = p\delta(\epsilon) + (1 - p)\delta(\epsilon - V)_{V\to\infty} \tag{3}$$

and all the bonds in the problem are set to $t = 1$. The problem is, thus, characterised purely by the fraction p of low-energy sites. The threshold p at which these sites form a spanning cluster defines the classical site percolation threshold, p^s_{Cl}. That threshold is 0.593 for a 2D square lattice and 0.312 for a 3D simple cubic lattice [13]. Due to interference effects quantum transport requires a higher threshold p^s_Q. The threshold for localisation of all eigenstates is $p^s_Q \approx 0.44$ [11] for a 3D simple cubic lattice.

Bond Percolation

The bond percolation problem keeps all site potentials at the same value $\epsilon = 0$, say, but sets a fraction $1 - p$ of the hopping integrals to zero. The bond distribution function assumes the form

$$P(t) = p\delta(t - 1) + (1 - p)\delta(t). \tag{4}$$

Here, again classical bond percolation and conduction would occur at some threshold p^b_{Cl} and quantum transport at a higher value p^b_Q. The thresholds are $p^b_{Cl} = 0.500$ for a 2D square lattice and $p^b_{Cl} = 0.249$ for a 3D simple cubic lattice [13]. The corresponding $p^b_Q \approx 0.32$ [11] for a 3D simple cubic lattice. Both site and bond percolation in the classical limit involve a connected path through the 'valley', while the quantum case is complicated by additional interference and localisation effects. In 2D, e.g., neither the site nor the bond percolation model allow any extended electronic states.

Effective Medium Theory

What is the actual conductivity of a system after the spanning cluster forms? The answer to this requires the solution of a resistor network model [14] by utilising Kirchoffs laws. In the continuum limit this leads to 'effective medium theory' and, except close to the insulator-metal transition, one can use simple analytical approximations. Resistor network theory and effective medium approximations have been used to model the manganite data as we will see later.

3 Manganites: Phenomenology and Model

The manganites have a vast phenomenology involving several kinds of long range order, unusual magnetotransport and spatially inhomogeneous electronic states. These

have been ably reviewed [1–4] in the recent past. Since this volume focuses on percolative effects I highlight only those aspects of manganite phenomena that are associated with spatial clustering and percolative transport. Similarly, although there is finally a single model for the real material, simpler versions of it can usefully clarify aspects like phase competition, polaron formation, etc. In what follows we first review the phenomenology relevant for us, and then present the comprehensive model. Limiting cases of this are studied in the next two sections.

3.1 Phenomenology

Among the experiments relevant to percolative effects in the manganites are examples of remarkable spatial imagery, which indicate 'insulator-metal' coexistence on the nanoscale [5–8], and bulk data on magnetisation and transport [15, 16]. There are also noise measurements, etc., which seem to indicate a percolation transition [17].

We started with a suggestive image of phase segregation based on a TEM experiment. Figure 2 shows an explicit spatial map [8] of the 'local conductance' in a sample of $La_{1-x}Ca_xMnO_3$ at $x \sim 0.3$, just below the ferromagnetic transition, $T_C \sim 230\,K$, for different magnetic fields. The nature of a region, metallic or insulating, is decided by the slope of the local $I-V$ characteristic. The 'volume fraction'

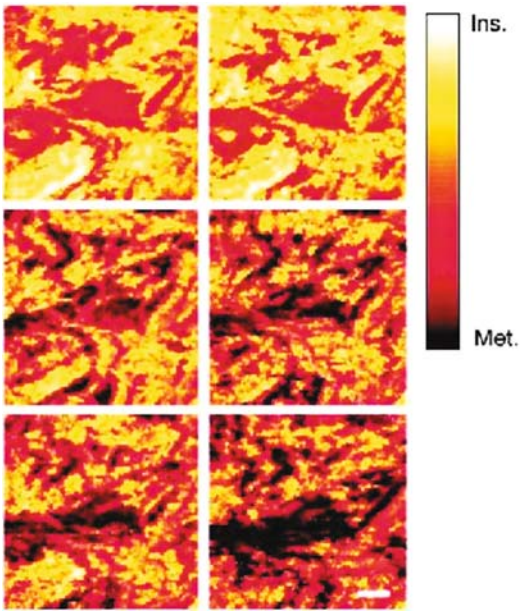

Fig. 2. A generic spectroscopic image $0.61\,\mu\mathrm{m} \times 0.61\,\mu\mathrm{m}$ of the local electronic structure of (La,Ca)MnO_3 for T just below T_C for magnetic fields $0,\ 0.03,\ 1,\ 3\ ,5$ and 9T (*left* to *right* and *top* to *bottom*). The light areas correspond to insulating regions and dark areas to metallic regions. The shade represents the slope of the local I-V spectrum. From M. Fath, et al., Science, **285**, 1540 (1999), with permission

of the (dark) 'metallic' regions grows with applied field and correlates with an increase in the *bulk conductance* of the sample. This example is mainly to provide a concrete instance of nanoscale coexistence in the manganites – with the caution that such explicit measurements are rare, and the large MR observed in manganite samples is not always associated with phase separation.

Let us now turn to a set of measurements that explicitly tried to analyse transport in phase separated manganites within a percolative framework.

Uehara et al. [6] made an attempt to interpret their magnetotransport data on $La_{1-x-y}Pr_yCa_xMnO_3$ in terms of percolation theory. These samples, at $x = 3/8$ and varying y, show spatial segregation in their TEM image. At $y = 0$ the system is primarily a ferromagnetic metal at low temperature, while increasing y increases the charge-ordered insulating (CO-I) character and the d.c resistivity. At low temperature the system shows a metal-insulator transition at $y = y_c \approx 0.41$. The TEM images suggested a spatial patchwork of FMM and CO-I domains at intermediate y, and the natural inference was that the conduction occurs when *spin polarised* FMM domains percolate. The aspect of 'spin polarisation' is necessary since, unlike standard metal-insulator composites, electron motion in manganites is intimately tied to the orientation of the background spins: antiparallel orientation of domain moments prevents electron transmission. Figure 3, from their paper [6], shows the (hysteretic) temperature dependence of the resistivity, $\rho(T, y)$, the magnetoresistance for various y in a field of 4kOe, and a log-log plot of the low T resistivity with respect to $y_c - y$.

How well does the result fit within the (classical) percolation framework? The lowest panel shows that at zero field, $h = 0$, the exponent p in $\rho \propto (y_c - y)^p$ turns out to be -6.9, far above the 3D percolation prediction of $p \approx -1.9$. Part of this discrepancy can be attributed to the requirement of 'domain polarisation' for transport, which goes beyond 'scalar' percolation and introduces an extra variable (the domain moment orientation) in the transport process. If the transport is measured in a moderate field, $h = 4$kOe in this case, the resistivity follows $\rho \propto (y_c - y)^{-2.6}$ – certainly closer to the standard value.

The same group did measurements [15] of the electrical conductivity (σ), thermal conductivity (κ) and thermopower (S) for these phase separated systems, and attempted a fit of the complete temperature dependent conductivity using a 'generalised effective medium' (GEM) theory. Figure 4 shows the raw data on the temperature dependence of the conductivity and the low field magnetisation (left panels) and the correlation of σ, κ and S, with the magnetisation at low temperature (right panels). The chemical control parameter is the Pr concentration (now called x instead of y).

The GEM formulation uses the conductivity of the metallic and insulating 'building blocks', $\sigma_M(T)$ and $\sigma_I(T)$ respectively, as inputs and predicts the conductivity of the composite as a whole. A 'fit' would indicate that a percolative scenario is valid for the system. The GEM equation has the form

$$(1-f)\left(\frac{\sigma_I^{1/t} - \sigma_E^{1/t}}{\sigma_I^{1/t} - A\sigma_E^{1/t}}\right) + f\left(\frac{\sigma_M^{1/t} - \sigma_E^{1/t}}{\sigma_M^{1/t} - A\sigma_E^{1/t}}\right) = 0, \tag{5}$$

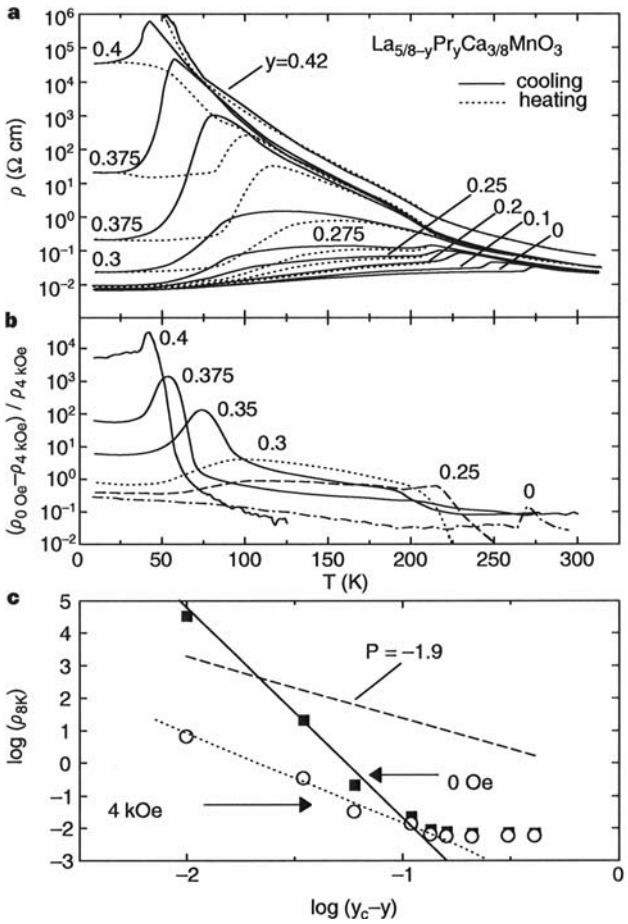

Fig. 3. Transport and magnetic properties of $La_{5/8-y}Pr_yCa_{3/8}MnO_3$ as a function of temperature and y. (**a**) T dependence of resistivity, cooling and heating runs. (**b**) Magnetoresistance of samples at $h = 4$kOe. (**c**) Log-log plot of resistivity versus $(y_c - y)$, with $y_c = 0.41$, zero and finite field. The slopes are mentioned in the text. Percolation theory predicts a smaller slope ~ -1.9 shown as a dashed line. From M. Uehara et al., Nature **399**, 560 (1999), with permission

where σ_E is the effective medium conductivity to be determined. $A = (1 - f_c)/f_c$, where f_c is the MIT threshold and f is the volume fraction of the metal. In this case it was assumed that $f(T, x)$ is proportional to the FMM volume fraction $M_x(T)/M_0(T)$, and that σ_I corresponds to the $x = 0.625$ material and σ_M to $x = 0$. Figure 5 shows the fit of the measured conductivity to the GEM expression and the complex temperature dependence is indeed well reproduced, but the best fit to the low temperature data occurs for $t \sim 4$, which is too large for standard percolation.

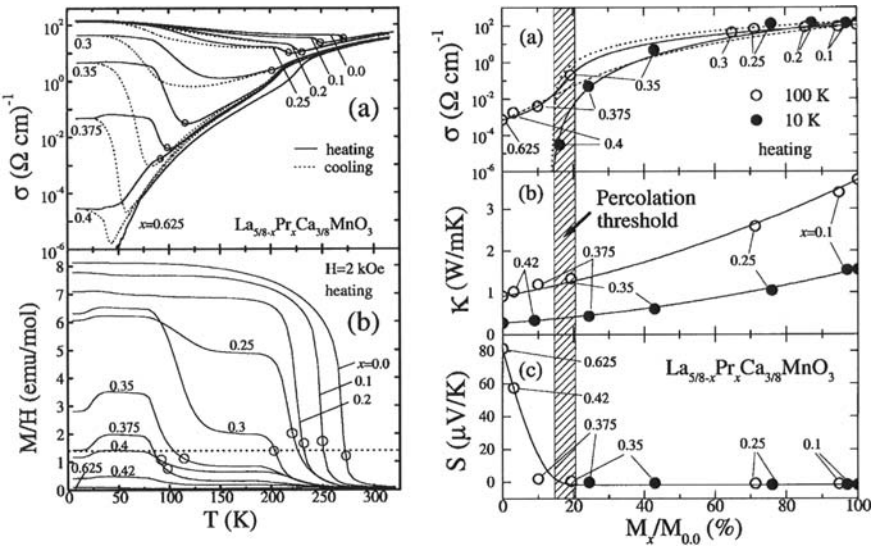

Fig. 4. Percolative features in transport in the $La_{5/8-x}Pr_xCa_{3/8}MnO_3$ family. *Left panels*: (**a**) Conductivity for heating and cooling, (**b**) m/h data on heating after zero field cooling. Right panels: Electrical conductivity, thermal conductivity and thermopower, respectively, in **(a)**, **(b)**, and **(c)**, at temperature 100K and 10K. The lines are various fits to the GEM equation (see text). From K.H. Kim et al., Phys. Rev. Lett. **84**, 2961 (2000), with permission

In the same spirit, experiments by Hardy et al. [16], Figure 6, study the manganite sample $Pr_{1-x}Ca_xMnO_3$ at $x = 0.37$ under various perturbations, use the measured magnetisation as a basic indicator of the 'metallic' phase fraction, and correlate it with the conductivity of the sample. The conductivity, when plotted against M, seems to follow a simple power law over four orders of magnitude:

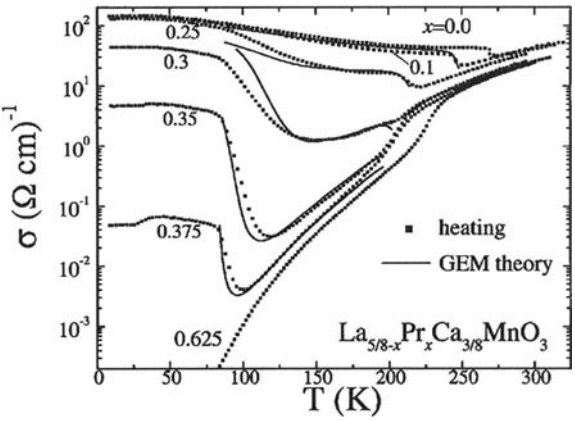

Fig. 5. Fit of the conductivity data to a generalised effective medium (GEM) result with $t = 2$ and $f_c = 0.17$. From K.H. Kim et al., Phys. Rev. Lett. **84**, 2961 (2000), with permission

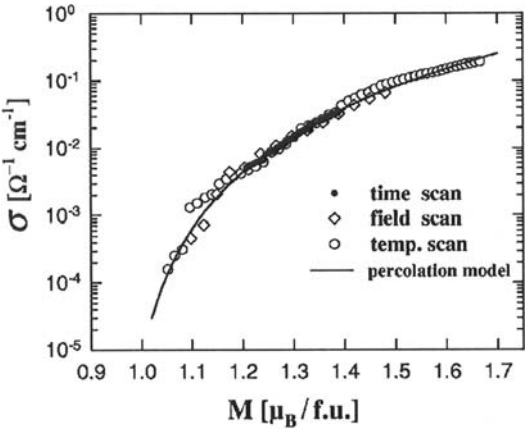

Fig. 6. Scaling of the conductivity with magnetisation for different variations in external conditions. The solid line is $\sigma \propto (M - M_c)^s$, where M_c is the critical value for percolation, and $s = 3.6$. From V. Hardy et al., Phys. Rev. **B 64**, 064402 (2001), with permission

$\sigma \sim (M - M_c)^{3.6}$. While the correlation is impressive the critical exponent is much larger than 2.

If these results suggest that transport in the manganites is necessarily tied to phase coexistence and percolation, albeit a non-standard form of percolation, careful experiments have revealed [18–20] that CMR can also arise without any PS (and associated percolative effects). We do not enter into that discussion right now and only highlight in Figure 7 the circumstance where cluster coexistence, percolative transport, and CMR are related. Systems where the disorder is large can show CMR without any spatial coexistence. The 'left' pathway is what we will explore in this review.

3.2 Microscopic Model

The manganites are remarkably complex in terms of the number of interactions at play [4, 21]. Thankfully, there is a consensus on the relevant degrees of freedom and the interactions between them. Let us write the most 'complete' model, highlight the physical effects at play and abstract simpler models that one can analyse with control.

The electronically active orbitals in the manganites arise from the twofold degenerate e_g level, which delocalise via hybridisation with oxygen $2p$ states. The comprehensive tight-binding model, neglecting oxygen orbitals, etc., is

$$H = \sum_{\langle ij\rangle\sigma}^{\alpha\beta} t_{ij}^{\alpha\beta} c_{i\alpha\sigma}^{\dagger} c_{j\beta\sigma} + \sum_i (\epsilon_i - \mu) n_i - J_H \sum_i \mathbf{S}_i . \hat{\sigma}_i + J_{AF} \sum_{\langle ij\rangle} \mathbf{S}_i . \mathbf{S}_j - \lambda \sum_i \mathbf{Q}_i . \hat{\tau}_i + H_{\mathrm{stiff}} + H_{\mathrm{ph-dyn}} + H_{\mathrm{Hubb}}. \quad (6)$$

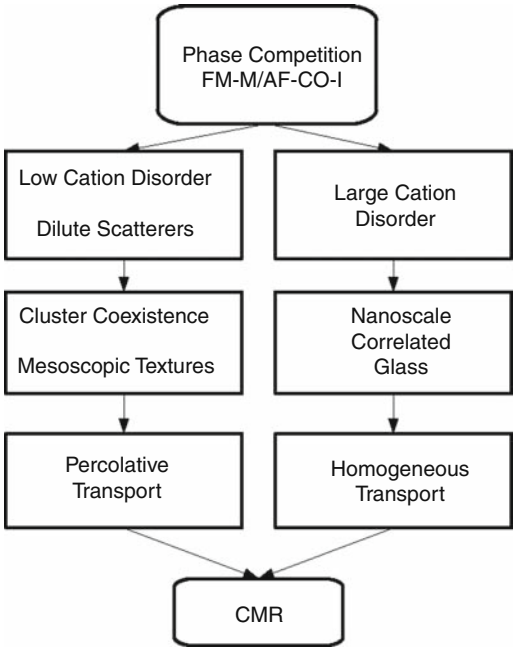

Fig. 7. Pathways to colossal magnetoresistance in the manganites. Experiments indicate that cluster coexistence and percolative effects are not essential for CMR effects to emerge. In special circumstances, however, there could be percolative effects (the left path) and it is these parameter regimes that we will study in this review

The $t_{ij}^{\alpha\beta}$ are hopping amplitudes between doubly degenerate Mn e_g levels at neighbouring sites, ϵ_i refers to substitutional disorder and μ is the chemical potential. J_H is the strong Hunds coupling between the e_g electrons and the $S = 3/2$ 'core spin' (t_{2g} electrons) and J_{AF} the antiferromagnetic superexchange between neighbouring Mn spins. The 'orbital moment', τ_i, of the e_g electrons is Jahn-Teller coupled to the octahedral distortion parameter $\mathbf{Q}_i$, through the electron-phonon coupling λ. $H_{\rm stiff}$ is the stiffness of the lattice. In its simplest form it is $\sim (K/2)\sum_i Q_i^2$, but in reality is of 'cooperative' character, i.e., involves phonon degrees of freedom in more than one octahedra. The phonons are quantum variables, with intrinsic dynamics arising from $H_{\rm ph-dyn} \sim P^2/(2M_Q)$, where P is the momentum and M_Q the mass of the relevant oscillator. Finally, the undoped state in the manganites, e.g., $LaMnO_3$, is a Mott insulator, arising (partly) from large on site 'inter-orbital' Hubbard repulsion, $H_{\rm Hubb} \sim U' \sum_{i,\alpha\neq\beta} n_{i\alpha} n_{i\beta}$.

The electron-phonon, electron-spin and Hubbard interactions are all large $\gg t$, where t is the typical hopping scale in the problem, and therefore beyond the range of perturbation theory. The detailed model, unfortunately, is far too complex for the present methods of many body theory, if it were to be handled in a realistic three dimensional situation. However, it is possible to simplify the model somewhat, recognising that (i) at large doping of the Mott insulator, e.g., $x \sim 0.3 - 0.4$, the Hubbard

interaction probably does not have a qualitative effect, (ii) the phonons are in the adiabatic regime, with typical frequency $\omega_{\rm ph} = \sqrt{K/M_Q} \ll t$ and, as a first approximation, we can explore the *adiabatic limit* $\omega_{\rm ph} = 0$, and (iii) the $S = 3/2$ may be approximated as a 'classical' spin.

This still leaves us with the problem of (disordered) electrons strongly coupled to (classical) phonon and spin degrees of freedom. The qualitative effects in such a system include (i) magnetic order, arising from J_H driven double exchange and J_{AF} driven AF superexchange, (ii) the possibility of polaron formation if the electron-phonon (EP) coupling is sufficiently large compared to the kinetic scale, and (iii) the phase competetion between different kinds of long range order.

These complexities, observed experimentally in the manganites, can be recovered by retaining double exchange, the AF superexchange and the Jahn-Teller interaction. Phonon dynamics $H_{\rm ph-dyn}$ or the Hubbard interaction $H_{\rm Hubb}$ are not essential for the qualitative effects. 'Percolative' transport is one among many effects that emerge in this model. It arises from cluster coexistence, which in turn originates from phase competition between a homogeneous ferromagnetic metal and an antiferromagnetic charge ordered insulator (AF-CO-I), as we have mentioned earlier.

Postponing a discussion of EP coupling related complications to a later section let us start with a simpler case that involves competition between a FMM and an AF-I in a one band model, without involving phonon or orbital variables. This will throw light on several key qualitative issues related to cluster coexistence and associated transport.

4 Percolative Effects in a One Band Model of Phase Competition

The coexistence of two phases with distinct electronic, magnetic and possibly structural properties is best conceived at $T = 0$ in a *clean system*. Think of electrons coupled to phonons, spins, etc. What kind of long-range order can arise in the ground state? For a specified chemical potential, μ, the ground state configuration of the spin and lattice variables, $\{X_i\}$ say, assumed classical, is determined by $\delta\mathcal{E}/\delta X_i = 0$, where $\mathcal{E}\{X_i;\mu\}$ is the energy of the system in the $\{X_i\}$ background. The minimum, $\mathcal{E}_{min}(\mu)$, usually occurs for a unique $\{X_i\}$ at each μ, and in this background the electron density $n(\mu)$ is also unique. However, in the presence of competing interactions, two *distinct* $\{X_i\}$ configurations could be degenerate minima of $\mathcal{E}$ at some μ. The corresponding $\mu = \mu_c$ marks a *first order phase boundary*, and the two 'end-point' densities, n_1 and n_2 bracket a region of coexistence. There is no homogeneous phase with density between n_1 and n_2. In this regime the system breaks up into two macroscopic domains, with density n_1 and n_2.

4.1 Scenario

The effect of disorder is to convert the regime of macroscopic phase separation to mesoscale or nanoscale cluster coexistence of the two phases. Cluster coexistence can lead to an insulator-metal transition (IMT) when the ferromagnetic 'metallic'

clusters percolate, generating a conducting pathway through the system. Conversely, with increasing temperature, the ferromagnetic clusters can fragment due to spin disorder, leading to a rapid rise in resistance due to disruption of the conducting backbone. An applied field can also have a remarkable effect in the poorly conducting low-temperature phase, if the system is near the critical density for the IMT. The magnetic field can polarise the large but 'uncorrelated' cluster moments, enhance inter cluster tunnelling in these half-metallic systems and enormously enhance the conductance. There is a fascinating variety of IMT's driven by varying density, temperature or magnetic field that can emerge in such a system.

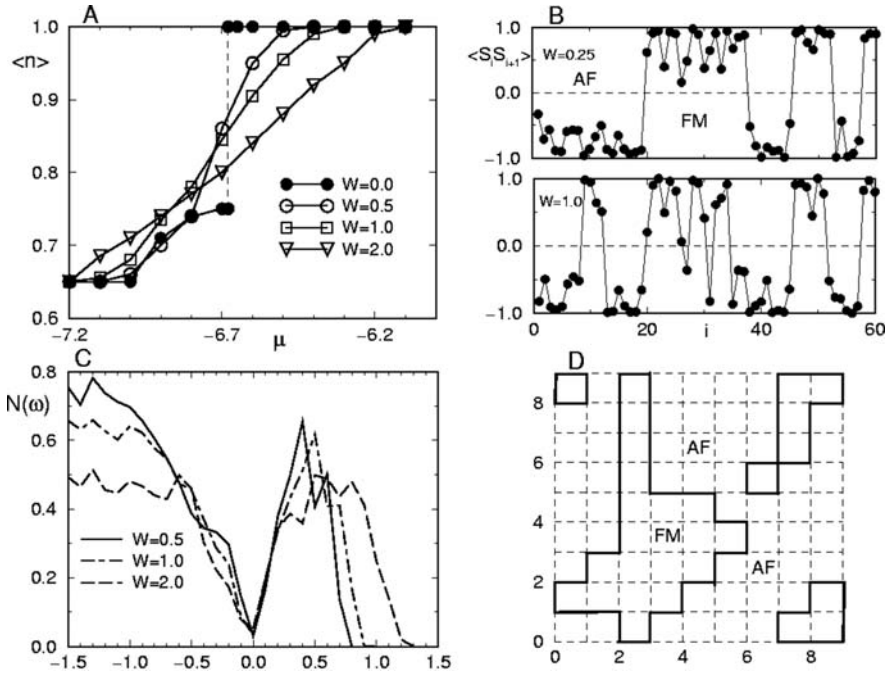

Fig. 8. An early result on cluster coexistence in the one orbital model from A. Moreo et al., Phys. Rev. Lett. **84**, 5568 (2000). The model uses *finite* J_H and $J_{AF} = 0$, but the central feature is still phase competition between FMM and AF-I. Monte Carlo (MC) simulation with on site disorder, J_H=8.0, and J_{AF}=0.0, in units of $t = 1$. (**A**) $\langle n \rangle$ vs μ for a L = 20 chain at T = 1/75 using 24,000 MC sweeps per $\{\phi_i\}$ set. The results are averages over ∼100 of $\{\phi_i\}$ configurations for the values of W shown; (**B**) Nearest-neighbours t_{2g}-spin correlations versus their location along a L = 60 chain with $\mu = -6.7$ and T = 1/75. Shown are results for one representative MC snapshot, W = 0.25 (*upper panel*) and W = 1.0 (*lower panel*). Other snapshots differ from this one only by small fluctuations. The FM-AF clusters remain pinned at the same locations as the simulation evolves; (**C**) Density of states at T=1/75, L = 20 and $\mu = -6.7$ showing the presence of a pseudo-gap. The average density is $\langle n \rangle \sim 0.87$; (**D**) Results of a representative MC snapshot for an 8×8 cluster, T = 1/50, $\mu = -6.2$ (*close to the critical value*), and W = 1.0. Regions with FM or AF nearest-neighbour t_{2g}-spin correlations are shown. Reproduced with permission

While this scenario is attractive and plausible, and provides a conceptual framework for analysing the transport data, first principles calculations on the underlying disordered interacting models are quite difficult. The 'real space' approach required in this inhomogeneous problem requires a Monte Carlo technique involving iterative diagonalisation of the system Hamiltonian. The computational cost scales as N^4, where N is the system size, and limits N to $\sim$ 100. Results of such studies (see Fig. 8 [9] for an early example) suggest the validity of the coexistence argument, in terms of the emerging spatial structures, but cannot quantify the effect of disorder on the cluster distribution. More seriously, given the large finite size gaps in small lattices, it is impossible to access the dc conductivity and analyse metal-insulator transitions.

We used the 'self consistent renormalisation' (SCR) method [22], developed by us, wherein the spin-fermion model is mapped on to a classical spin model with self consistently computed exchange. We first compare our results in detail with exact simulations on small lattices, and then present transport results and spatial features on large lattices. The large size allows us detailed access to the spatial correlations, the electronic density of states (DOS), the resistivity, and the full optical response. We also describe the evolution of these properties in response to a magnetic field, and the origin of colossal 'tunnelling magnetoresistance' (TMR) in the model.

4.2 Model and Method

The model we use is $H = H_{el} + H_{AF} + H_{mag}$ in 2D [23], with:

$$\begin{aligned} H_{el} &= \sum_{\langle ij\rangle,\sigma} t_{ij} c^{\dagger}_{i\sigma} c_{j\sigma} + \sum_i (\epsilon_i - \mu) n_i - J_H \sum_i \mathbf{S}_i.\sigma_i \\ H_{AF} &= J_{AF} \sum_{\langle ij\rangle} \mathbf{S}_i.\mathbf{S}_j \\ H_{mag} &= -h \sum_i S_{iz}. \end{aligned} \tag{7}$$

The hopping $t_{ij} = -t$ for nearest neighbours, and ϵ_i is a random on site potential uniformly distributed between $\pm\Delta/2$. We assume $J_H/t \to \infty$, and set the reference scale $t = 1$, For illustrative purpose we choose disorder $\Delta = 1.0$ and $J_{AF} = 0.05$. We vary μ as needed, use $|\mathbf{S}_i| = 1$, and measure all our energies, temperature, frequency, etc., in units of t.

At large J_H/t the electron spin at site $\mathbf{R}_i$ is 'slaved' to the orientation of $\mathbf{S}_i$. Since the electron 'hopping' process is spin conserving, a random magnetic background greatly impedes electron motion. Conversely, a ferromagnetic state aids electron propagation and minimises the energy of the system. This is the heart of double exchange ferromagnetism. Notice that this mechanism works only if there are electrons present and, crudely, becomes stronger with increasing electron density. On the other hand superexchange antiferromagnetism driven by J_{AF} works even in the absence of electrons. It is not hard to see that at fixed J_{AF} the system will make a transition from an anti-ferromagnetic state to a ferromagnet when the electron density is increased from $n = 0$. This change turns out to be *first order* and that is at the heart of our story.

Technically, the $J_H/t \to \infty$ limit leads to a spinless fermion problem with nearest neighbour hopping amplitude t_{eff}^{ij} dictated by $\mathbf{S}_i$ and $\mathbf{S}_j$, $t_{eff}^{ij}/t = \cos\frac{\theta_i}{2}\cos\frac{\theta_j}{2} + \sin\frac{\theta_i}{2}\sin\frac{\theta_j}{2}e^{-i\,(\phi_i-\phi_j)}$. θ_i and ϕ_i are the polar and azimuthal angles for the vector $\mathbf{S}_i$. 'Integrating out' the fermions using the SCR approximation leads to the following effective spin Hamiltonian:

$$H_{eff}\{\mathbf{S}_i\} = -(1/\beta)logTre^{-\beta(H_{el}+H_{AF})}$$
$$\approx -\sum_{\langle ij\rangle} D_{ij} f_{ij} + J_{AF}\sum_{\langle ij\rangle}\mathbf{S}_i.\mathbf{S}_j. \tag{8}$$

D_{ij} is determined self consistently as the average of $\hat{\Gamma}_{ij} = (e^{i\Phi_{ij}}\gamma_i^\dagger\gamma_j + h.c)$ over the assumed equilibrium distribution $\propto e^{-\beta H_{eff}\{\mathbf{S}_i\}}$. Φ is a phase factor related to $\tan^{-1}\frac{Im(t_{\rm eff})}{Re(t_{\rm eff})}$ and γ etc. represent spinless fermions in the large J_H model.

Although the D_{ij} enter as 'nearest neighbour' exchange, they arise from a solution of the *full quantum statistical problem in the disordered finite temperature system.* In the presence of competing interactions and quenched disorder, this leads to a set of strongly inhomogeneous, spatially correlated and temperature dependent 'exchange' D_{ij}. These exchange in turn determine the FM-AF clusters and the related percolation effects.

The principal results that are relevant for our discussion are as follows:

- The visual evidence of cluster coexistence, and the dependence of cluster size on temperature, disorder and electron density.
- A microscopic estimate of the resistivity, and its correlation with the spatial structures.
- The strong low field response in magnetisation and conductivity, due to alignment of 'cluster moments'.

Let us first show the benchmarks of our SCR method with respect to exact diagonalisation based calculation, and then move on to the actual results.

4.3 Benchmarks Against Exact Results

How well does our effective Hamiltonian capture the correct physics at coexistence? Since the parameter space is large, the checks are focused on $n = 0.1$ and $\Delta = 1.0$, tracking results across disorder realisations and with varying temperature.

Figure 9, left panels, compares the variation of carrier density with chemical potential obtained within the two schemes at low temperature. The discontinuity at $\Delta = 0$, between the undoped AF state and the ferromagnetic metal signifies a first order transition, and the instability of homogeneous phases for $0 < n < 0.25$. There is only a slight difference in the 'critical' μ at which the transition occurs, obtained within the two schemes. Disorder $\Delta = 1.0$ smears out the discontinuity (on these small lattices) and 'allows' stable mean densities between $n = [0, 0.25]$. The disorder averaged $n - \mu$ data is almost identical between ED-MC and $H_{\rm eff}$.

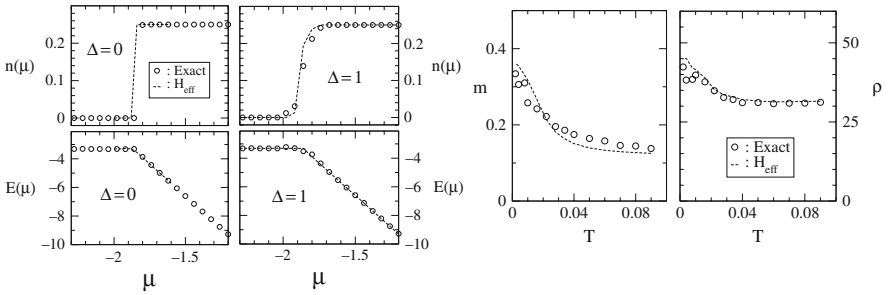

Fig. 9. Comparing thermodynamic and transport results between exact diagonalisation based Monte Carlo (ED-MC) and our SCR scheme on a 8×8 lattice. Symbols for ED-MC results and dashed lines for SCR

Now the transport, Fig. 9 extreme right. Our resistivity is the inverse of the (thermal and disorder averaged) optical conductivity $\sigma(\omega)$ at the scale of mean level spacing in the system. The 'resistivity' so computed is compared between ED-MC and H_{eff} in Fig. 9, right. We also show the associated magnetisation.

There are two features to note: (i) transport properties match reasonably between the two schemes, and (ii) the small size 'resistivity' *does not show the crucial turnaround feature* that would signify low-temperature metallicity (and shows up only on larger systems). It is crucial to break the size barrier and access transport at lower frequency.

The 'density field' that emerges is of course *not* homogeneous and involves coexisting regions of FMM and AFI. While the detailed cluster pattern and correlation length can only be studied by using $H_{\rm eff}$ on large lattices, notice the ability of $H_{\rm eff}$ to capture the *same spatially resolved patterns* as ED-MC for a specific realisation of $\{\epsilon_i\}$. In Fig. 10 we show the 'cluster pattern', as encoded in the nearest neighbour spin correlation, for both H_{eff} and ED-MC for two realisations of disorder. The first pair of rows belong to one realisation of $\{\epsilon_i\}$ and the next pair to another. Within a pair, the top row tracks the result with ED, the bottom row with H_{eff}. Temperature varies along the row, from $\sim 2T_c$ to $T = 0$ (left to right). As the results indicate both schemes lead to the same 'fingerprint' of the underlying disorder. The basic reason that H_{eff} reproduces such detailed features faithfully is that it actually solves the same Schrodinger equation as ED-MC, albeit fewer times, in the same disordered background.

4.4 Results at Zero Field

Having established the credibility of the SCR scheme in this context, let us look at the results obtained using this method on large lattices, $\sim 24 \times 24$ to 32×32.

At low-electron density, the competetion in the DE+SE model is between a $\{\pi, \pi\}$ AF phase and a ferromagnet. We set $J_{AF} = 0.05$ and scanned in μ to locate the μ_c for the first order boundary. The density changes from $n = 0$ to $n \sim 0.20$

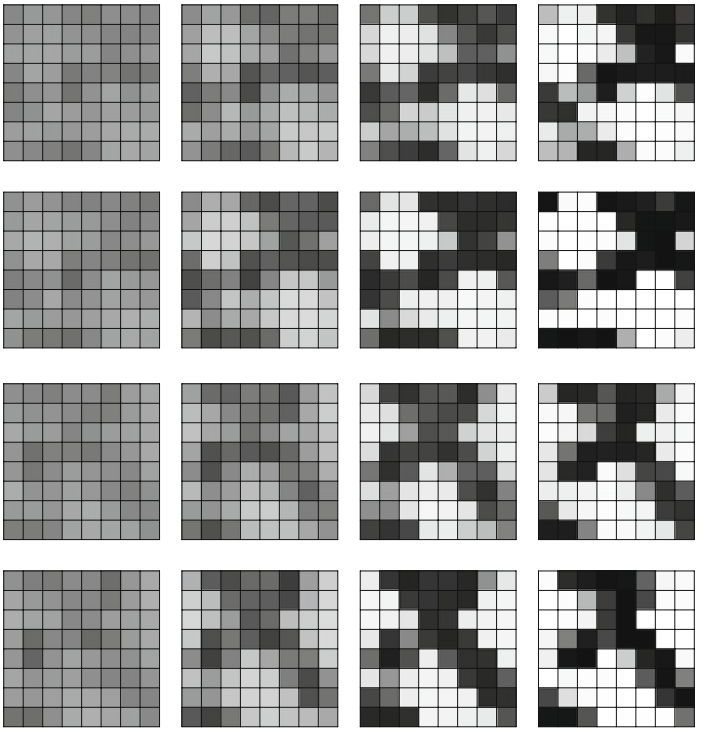

Fig. 10. Comparing cluster patterns in ED-MC with SCR results for two different realisations of disorder. Temperature values along a row are $T = 2T_c, 1.2T_c, 0.8T_c$ and $0.1T_c$

at the discontinuity. Moderate disorder smooths out the discontinuity in $n(\mu)$ converting it to a sharp crossover.

We probed the coexistence regime, $n \sim 0 - 0.2$, with varying electron density, temperature (T), and $\Delta = 0.2$ and $\Delta = 1.0$. All the results are obtained by cooling the system from the high T paramagnetic, approximately homogeneous, phase.

The two panels in Fig. 11 show the thermally averaged nearest-neighbour spin correlation. The mean density n in these figures vary from 0.06 to 0.15 from the top row to bottom the row in each panel, straddling the coexistence region, the disorder is $\Delta = 0.2$ (left panels) and $\Delta = 1.0$, (right panels), and the data is obtained in a cooling sequence. Along each row the temperature varies as $T = 2T_c, 1.2T_c, 0.8T_c$, and $0.1T_c$ for both panels, as one moves from left to right.

The figure provides direct visual evidence of 'clustering'. Note that the FMM clusters form in an attempt to minimise electronic kinetic energy – and are far from random as in standard percolation. At fixed density and temperature, the cluster pattern for stronger disorder ($\Delta = 1.0$) is more fragmented than for $\Delta = 0.2$. The contrast reduces with increasing T, as the spins in the AF regions fluctuate out of antiparallel alignment.The large density regions sustain a finite local magnetisation, whereas, the empty regions give rise to local AFM.

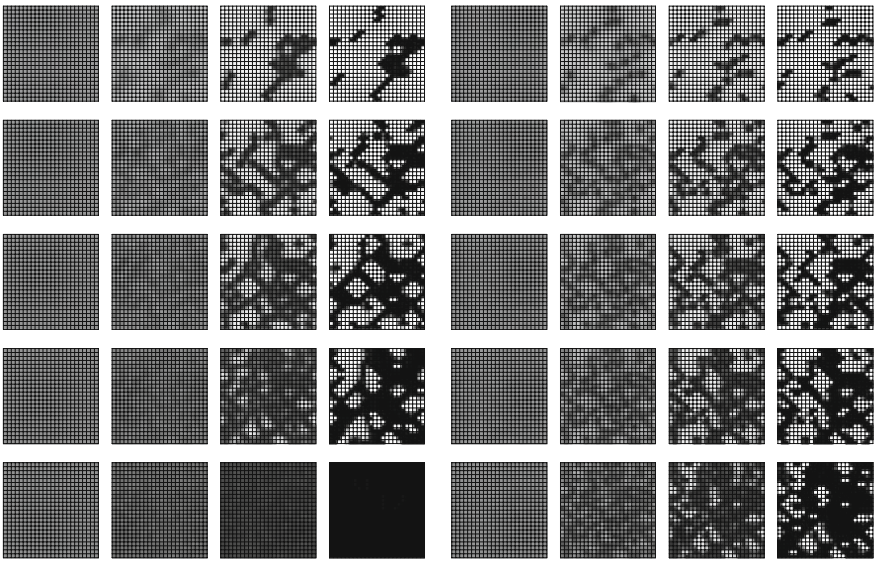

Fig. 11. Cluster pattern with varying density, temperature and disorder. Left Panel: weak disorder, $\Delta = 0.2$, Right Panel: strong disorder, $\Delta = 1.0$. Electron density $n = 0.06, 0.08, 0.10, 0.12$ and 0.15 from top to bottom. Temperatures $T = 2T_c, 1.2T_c, 0.8T_c$ and $0.1T_c$ from left to right in each panel

Figure 12 shows the typical size of FMM clusters [23], inferred from a Lorentzian fit to the magnetic structure factor, i.e., $S_{\mathbf{q}} \sim (q^2 + \xi^{-2})^{-1}$. The resulting correlation length depends on n, Δ and T, decreasing with increasing disorder and T, and increasing with increasing density. The main panels, (a) and (b), highlight the n dependence at different T and Δ, while the inset replots the same data to highlight the dependence on disorder. To completely understand the variation of cluster sizes with temperature, density and disorder one would have to solve the problem on even larger

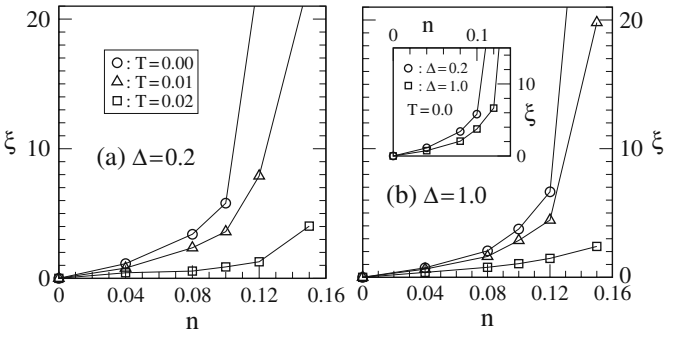

Fig. 12. Ferromagnetic correlation length inferred by fitting Lorentzians through the spin structure factor data

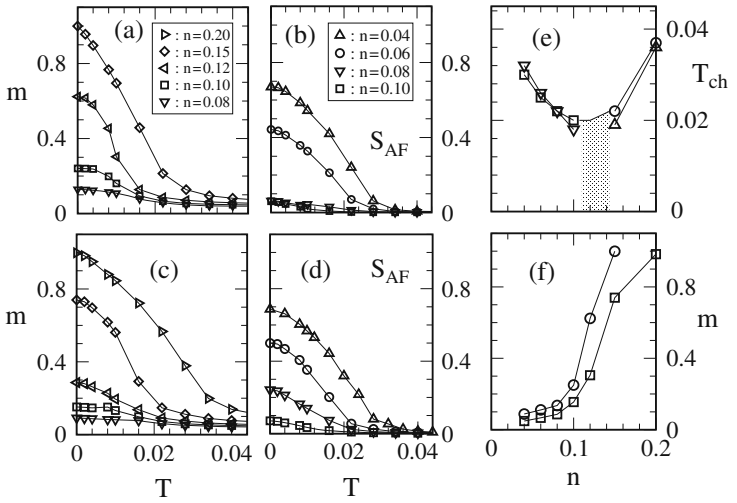

Fig. 13. Magnetisation, $m(T)$, and structure factor, $S_{\mathbf{q}}(T)$ at $\mathbf{q} = \{\pi, \pi\}$. Panel $(a) - (b)$: data for $\Delta = 0.2$, panel $(c) - (d)$: data for $\Delta = 1.0$. The legends are common to panels $(a) - (d)$. Panel (e): The characteristic temperature (see text), $T_{ch}(n, \Delta)$: triangle down: AF at $\Delta = 1.0$, square: AF at $\Delta = 0.2$, triangle up: FM at $\Delta = 1.0$, circles: FM at $\Delta = 0.2$. Panel (f): $m(T = 0)$ with varying n, circles: $\Delta = 0.2$, squares: $\Delta = 1.0$. System size: 24×24

lattices.The dependences, overall, are intuitive, and correlate well with the transport data that we discuss further on.

Figure 13 shows the magnetisation, $m(T)$, and the AF peak in the magnetic structure factor $S_{\mathbf{q}}$ at $\mathbf{q} = \{\pi, \pi\}$ to illustrate the evolution from the AF to the FM phase with increasing n. Panel (a)–(b) are at $\Delta = 0.2$ and panel (c)–(d) at $\Delta = 1.0$. The 'extremal' densities are either strongly AF or FM, while for $n \sim 0.08 - 0.12$ *both FM and AF reflections have finite weight*. Panel (e) tracks the 'characteristic temperature', $T_{ch}(n, \Delta)$, identified from the maximum in $\partial^2 O / \partial T^2$, where O is the appropriate order parameter (of the FM or AF phase). In the shaded region, $0.10 < n < 0.14$, it is difficult to resolve the T_{ch} accurately. Panel (f) shows the change in 'saturation magnetisation' $m(T = 0)$ with increasing n and changing disorder. The small moment regime, $m < 0.1$, for $n < 0.1$ is a 'ferro-insulator' phase, as we will discover from the transport data. In this regime the moments in different clusters are only weakly correlated. It would be very interesting to see the effect of a magnetic field on these weakly coupled FM regions. We will discuss these effects later in this section.

Figure 14 shows the low-energy density of states (DOS) for $n = 0.1$. Even at weak disorder, panel (a), there is a 'pseudogap' in the system averaged DOS, at the lowest temperature, $T \sim 0.01$. However, the pseudogap rapidly fills up with increasing T, and the DOS tends towards the universal profile of the spin disordered 2D DE model. At stronger disorder, panel (b), the 'dip' in the DOS at μ is deeper.

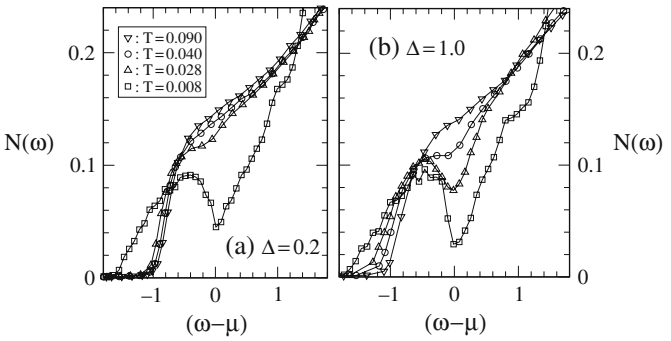

Fig. 14. Low-energy density of states, at $n = 0.10$. Panel (a): data at $\Delta = 0.2$, panel (b): data at $\Delta = 1.0$. The DOS is plotted with respect to $\omega - \mu(T)$, incorporating the T dependent shift in μ. Lorentzian broadening of δ functions to 0.03. Data averaged over 30 copies

Due to stronger pinning, the clusters and the gap feature, survives to higher T, and only for $T \gg T_{ch}$ tends to the asymptotic form.

Figure 15 shows resistivity, $\rho(T)$, with varying n and disorder. The comparison of panel (a), $\Delta = 0.2$, and panel (b), $\Delta = 1.0$, indicates that $\rho(T)$ for stronger disorder is systematically larger. The *trends*, however, are similar in the two cases and allows a tentative classification of the 'global' aspects of transport. At both $\Delta = 0.2$ and $\Delta = 1.0$ there is a critical density, $n_c(\Delta)$, below which $\rho(T = 0)$ diverges, indicating the absence of any connected 'conducting path'. The inset to panel (b) shows the trend in the $T = 0$ conductivity with increasing FM cluster area, a_{FM}. The following qualitative picture emerges for transport in the coexistence regime:

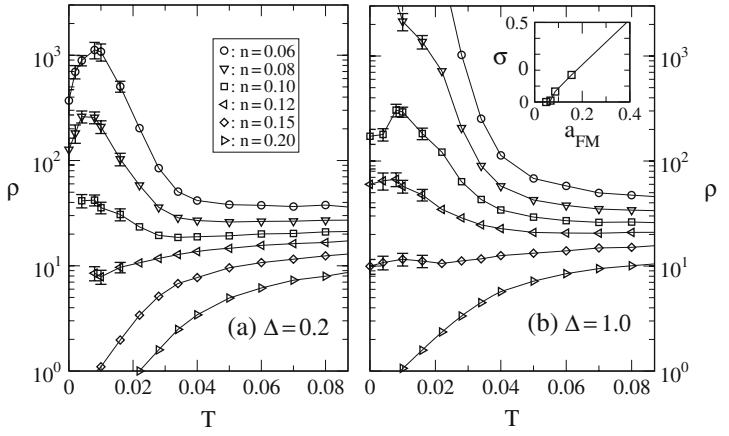

Fig. 15. Resistivity, $\rho(T)$, with varying n. Panel (a): $\Delta = 0.2$, panel (b): $\Delta = 1.0$. Results obtained on 'cooling'. System size 24×24, data obtained by inverting the 'mean conductivity'. Average over $20 - 50$ copies of $\{\epsilon_i\}$ (error bars comparable to symbol size, unless otherwise indicated). Results on size 32×32 are similar. Inset, panel (b): Normalised $T = 0$ conductivity, at $\Delta = 1$, -vs- FMM surface area

- At low T, and for $n > n_c(\Delta)$, there is, by definition, some connected 'metallic path' through the sample. It is reasonable to assume that at least in this connected region the spins are aligned due to DE. Since cluster dimension and electron wavelength are comparable in our system a large fraction of the resistance arises from the non-trivial geometry of the current path. This scattering is quantum mechanical, and the low T metallic phase corresponds to a *quantum percolative regime* for roughly $0.15 > n > 0.08$ at $\Delta = 1.0$.
- With increasing T, the resistance of the conducting network increases due to DE spin fluctuations and, till the network is disrupted, there is a regime $d\rho/dT > 0$. This 'metallic' behaviour occurs despite the very large residual resistivity. This is a regime of *weak magnetic scattering on the conducting network*. If $n \gg n_c$, e.g., $n = 0.20$ in Fig. 15(b), so that inhomogeneities are weak, $\rho(T)$ will smoothly increase to the $T \gg T_{ch}$ asymptotic value.
- With further increase in T, in the $n > n_c$ regime, the spin disorder can destroy some of the 'weak links', disrupting the conducting network and leading to a sharp increase in $\rho(T)$ see, e.g., $n = 0.1$ in Fig. 15(b). This correlates well with reduction in typical cluster size with increasing T, discussed in the next paragraph. Depending on n and the extent of disorder (and system size, in a simulation) there could be a rapid rise or a 'first order' metal-insulator transition (MIT). This is *spin disorder induced breakup of clusters driving a MIT.*
- Beyond this 'MIT' the conduction is through the 'insulating' regions, with isolated patches contributing to nominally activated transport, as visible in Fig. 15(b) for $n < 0.12$. For $T \gg T_{ch}$, as the structures disappear, Fig. 11, and the system becomes homogeneous, $\rho(T)$ is dominated by spin disorder scattering. This is a *diffusive regime with saturated spin disorder scattering*, visible for $T > 0.08$ at all densities.
- For $n < n_c$, the regime of low-density isolated clusters, $\rho(T)$ falls monotonically, and the response is typical of *low-density ferromagnetic polarons in a AF background.* This occurs for $n < 0.08$ at $\Delta = 1.0$, and at lower n at $\Delta = 0.20$.

The variation in the FMM cluster size, discussed earlier, is broadly consistent with the above description and strengthens the proposed transport scenario.

4.5 Effect of a Magnetic Field

The effect of a magnetic field [24] and temperature can be studied through a host of physical indicators, e.g., the density-density correlation function $D_{nn}(\mathbf{q})$, the spin-spin correlation function $D_{ss}(\mathbf{q})$, the density of states at Fermi level $N(\epsilon_F)$, the magnetisation $m(h,T)$ and, of course, the resistivity $\rho(h,T)$.

The pattern for the nearest neighbour spin correlation $f_2^s(\mathbf{R}_i) = \langle \mathbf{S}_i.\mathbf{S}_{1+\delta} \rangle$ is shown in Fig. 16 [24] for three temperatures and for three fields, $h = 0$, $h = 0.01$ (central column) and $h = 0.10$ (right column). The first row shows the high T paramagnetic phase, where f_2^s is small on all links since the thermal scale is much larger than both the exchange and field scales. It is only at $h = 0.10$ that we see signs of magnetisation. The contrast improves with cooling (left column) but the field

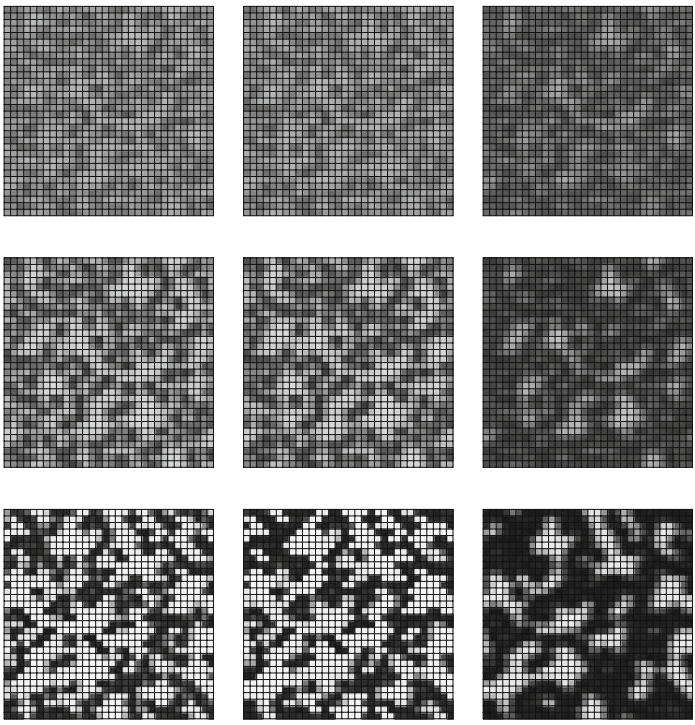

Fig. 16. Nearest neighbour spin correlation $f_2^s = \langle \mathbf{S}_i.\mathbf{S}_{1+\delta} \rangle$ at $n = 0.1$, $\Delta = 1.0$. System size 32×32. Field variation along the row: $h = 0.0, 0.01, 0.10$, and temperature, up the column, $T = 0.06, 0.03, 0.01$

response is similar at the lower temperatures as well, i.e., $h = 0$ and $h = 0.01$ are virtually indistinguishable.

For the $n = 0.1$ case at $\Delta = 1.0$, where the low T cluster pattern is rather fragmented, and the $h = 0$ magnetisation is rather low, < 0.1, the immediate effect of an applied field is to orient the 'cluster moments' parallel to the field. Since the clusters typically have > 10 spins coupled together even a weak field have a large effect on $m(h, T)$. Although this does not change the 'local electronic structure' and $N(\epsilon_F)$ is mostly unaffected, the parallel moments allow enhanced tunnelling between the FMM domains leading to large low-field MR. Since the cluster pattern does not change (at low fields) the correlation length associated with D_{nn} is unaffected. Overall, the main low-field effect at low T is alignment of the large 'cluster moments' in the direction of the field and a consequent increase in electron mobility.

At larger fields two other effects come into play. The FMM phase grows in volume, and residual spin disorder (due to finite temperature) within the domains gets suppressed. The system now behaves like a canonical 'clean' DE ferromagnet, with a large DOS at ϵ_F. The bulk magnetisation nears saturation.

While the cluster pattern is insensitive to a weak magnetic field, both the resistivity and the magnetisation respond dramatically, Fig. 17. There is essentially a 'two

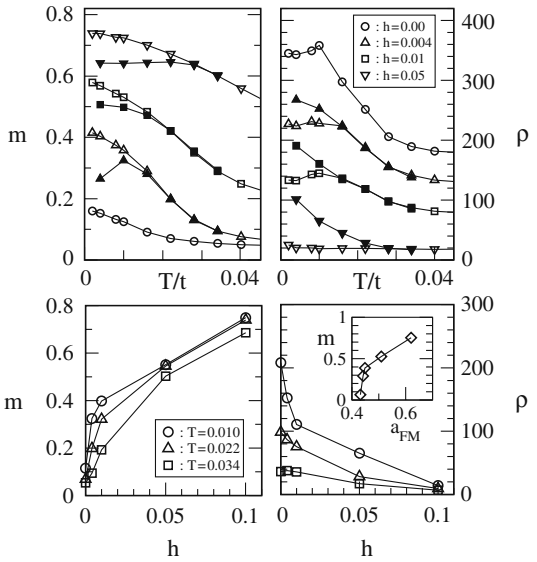

Fig. 17. Magnetism and magnetotransport at $(a), (b)$ constant magnetic fields and at $(c), (d)$ constant temperatures. The inset to (d) shows the variation of magnetisation with the total area of the ferromagnetic region. $\Delta = 1.0$ and $n = 0.1$

stage' response to an applied field (particularly at low temperature) in the coexistence regime. A weak field aligns the large 'cluster moments' parallel to the field, without significantly changing the FMM volume fraction. This enhances the tunnelling between FMM domains, which may have been supressed earlier due to random orientation of the cluster moments. The magnetisation rises sharply and there is an attendant sharp drop in resistivity. At a larger field, the FMM volume fraction itself increases and the transport phenomena can probably be described by a volume fraction dependent percolative effect.

These results on magnetotransport at phase coexistence share several generic features with the manganites [5–8], but there are key differences too. These are (i) the important regime of coexistence in manganites is between a FMM and an antiferromagnetic charge ordered insulator (AF-CO-I), and crucially involves the Jahn-Teller (JT) phonons. This requires enlarging our model. (ii) It is supposed that the FMM and CO-I regions are nominally of *equal density*, which is why such domains can survive over μm scale. Our clusters are 'charged' due to the density difference between FMM and AFI. In any real system, Coulomb effects would have to be considered in such a case.

Nevertheless, the single band model sheds light on several qualitative issues that arise in interpreting transport data and spatial structures on the manganites. A more quantitative comparison with manganite data requires inclusion of the lattice and orbital degrees of freedom. This is relevant also because the presence of strong electron-phonon coupling in the manganites makes the condition for cluster coexistence and percolation more restrictive.

5 Percolation in Two Band Models with Electron-Phonon Coupling

The changing balance between superexchange and double exchange, with increasing electron density, in the one band model leads to either an AF-I or a FMM. While other phases are possible, these two dominate. In the two band model, there are more exotic possibilities, and in particular close to electron density $n = 0.5$ the system goes into an orbital ordered AF state, the so called CE phase [25], with zigzag ferromagnetic chains coupled AF between them. The presence of electron phonon interaction leads to charge modulations in this phase [26], resulting in a CE-CO-OO state. The reason we enter into this discussion is because this CE phase, rather than a simple AF, is the main competitor of the FMM in the manganites. One component of the percolative pattern, when it occurs, is the CE-CO-OO-I phase, the other is the FMM. The other element that will emerge due to the electron-phonon coupling is the rather unusual effect of disorder – something not foreseen in the Imry-Ma [27] scenario.

5.1 Scenario

Much of the 'action' in the manganites is near $n = 0.5$, which also corresponds to hole doping $x = 1-n = 0.5$ of the parent Mott insulator. The CE phase lives at (and around) $n = 0.5$ in systems with low bandwidth, while the FMM lives at $n > 0.6$. There is a first order phase boundary between the CE-CO-OO-I and FMM, just as between AF-I and FMM in the one-band case. This is potentially the most promising regime for exploring phase separation and percolative transport in a 'composite' of metallic FM and insulating CE-CO-OO domains. Indeed, the experiments we cited early on were precisely in this regime. With that in mind our focus will be on identifying the circumstances (bandwidth, temperature, type of disorder) under which percolative effects emerge. In essence, we will explore the two pathways indicated earlier in Fig. 7.

5.2 Model and Method

The model below describes a two-band situation [28] with e_g electrons Hunds coupled to t_{2g} derived core spins, in a two-dimensional square lattice. The electrons are also coupled to Jahn-Teller phonons, while the core spins have an AF superexchange coupling between them. These ingredients are all necessary to obtain a CE-CO-OO phase. We include the effect of disorder through an on site potential.

$$H = \sum_{\langle ij\rangle\sigma}^{\alpha\beta} t^{ij}_{\alpha\beta} c^{\dagger}_{i\alpha\sigma} c_{j\beta\sigma} + \sum_i (\epsilon_i - \mu) n_i \; - J_H \sum_i \mathbf{S}_i . \boldsymbol{\sigma}_i + J_{AF} \sum_{\langle ij\rangle} \mathbf{S}_i . \mathbf{S}_j$$
$$- \lambda \sum_i \mathbf{Q}_i . \boldsymbol{\tau}_i + \frac{K}{2} \sum_i \mathbf{Q}_i^2 . \tag{9}$$

Here, c and $c^{\dagger}$ are annihilation and creation operators for e_g electrons and α, β are the two Mn-e_g orbitals $d_{x^2-y^2}$ and $d_{3z^2-r^2}$, labelled (a) and (b) in what follows. $t^{ij}_{\alpha\beta}$

are hopping amplitudes between nearest-neighbour sites with the symmetry dictated form: $t^x_{aa} = t^y_{aa} \equiv t$, $t^x_{bb} = t^y_{bb} \equiv t/3$, $t^x_{ab} = t^x_{ba} \equiv -t/\sqrt{3}$, $t^y_{ab} = t^y_{ba} \equiv t/\sqrt{3}$, where x and y are spatial directions

The e_g electron spin is $\sigma^\mu_i = \sum^{\alpha}_{\sigma\sigma'} c^\dagger_{i\alpha\sigma} \Gamma^\mu_{\sigma\sigma'} c_{i\alpha\sigma'}$, where the Γ's are Pauli matrices. It is coupled to the t_{2g} spin $\mathbf{S}_i$ via the Hund's coupling J_H, and we assume $J_H/t \gg 1$. λ is the coupling between the JT distortion $\mathbf{Q}_i = (Q_{ix}, Q_{iz})$ and the orbital pseudospin $\tau^\mu_i = \sum^{\alpha\beta}_{\sigma} c^\dagger_{i\alpha\sigma} \Gamma^\mu_{\alpha\beta} c_{i\beta\sigma}$, and K is the lattice stiffness. We set $t = 1$, $K = 1$, and treat the $\mathbf{Q}_i$ and $\mathbf{S}_i$ as classical variables. The chemical potential μ is adjusted so that the electron density remains $n = 1/2$, which is also $x = 1 - n = 1/2$.

We consider effectively a lattice of Mn ions and consider two kinds of disorder, since they seem to have rather distinct effects on the phase competition between FMM and CE-CO-OO-I. (i) The alloy disorder due to cationic substitution, introduced to control hole doping, is modelled as a random potential ϵ_i at the Mn site picked from the distribution $P_A(\epsilon_i) = \frac{1}{2}(\delta(\epsilon_i - \Delta) + \delta(\epsilon_i + \Delta))$. This is called A-site disorder in a perovskite ABO_3, and is homogeneous – in that every site has a potential. (ii) One can also substitute on the Mn site itself, the 'B site'. Such a situation is modelled via $P_B(\epsilon_i) = \eta\delta(\epsilon_i - V) + (1 - \eta)\delta(\epsilon_i)$, where η is the percent substitution and V the effective potential at the impurity site. For dilute B-type scatterers only a small fraction of sites have a potential, although that potential can be large.

For A-type disorder the mean value is $\bar{\epsilon}_i = 0$ and the variance is $\Delta^2_A = \langle(\epsilon_i - \bar{\epsilon}_i)^2\rangle = \Delta^2$, while for B-type disorder $\bar{\epsilon}_i = \eta V$ and $\Delta^2_B = \langle(\epsilon_i - \bar{\epsilon}_i)^2\rangle = V^2\eta(1 - \eta)$.

We use the 'travelling cluster approximation' (TCA) [29], developed by us, to solve this problem. It handles both strong coupling and disorder effects accurately and allows access to large system size.

5.3 Results

Let us start with the phases that emerge [28] for varying JT coupling and J_{AF} at $x = 0.5$, Fig.18 left panel, in the absence of disorder. We will also discuss how the ground state changes with x for a typical choice of λ and J_{AF}, shown in Fig. 18, right panel.

At low λ and low J_{AF} double exchange is the dominant interaction and kinetic energy optimisation leads to a homogeneous ferromagnetic state without any orbital or charge order (FM-OD-CD). This phase has a finite density of states at the Fermi level ϵ_F and is metallic. As J_{AF} is increased, keeping the JT coupling small, the character first changes to 'A-type' with peaks in the magnetic structure factor $S_{mag}(\mathbf{q})$ at $\mathbf{q} = \{0, \pi\}$ or $\{\pi, 0\}$, then an orbital ordered but uniform density CE phase, with simultaneous peaks at $\mathbf{q} = \{0, \pi\}, \{\pi, 0\}$, and $\{\pi/2, \pi/2\}$. At even larger J_{AF} the dominant correlations are 'G-type' with a peak at $\mathbf{q} = \{\pi, \pi\}$. By contrast, increasing λ at weak J_{AF} keeps the system ferromagnetic but leads to charge and orbital order (FM-CO-OO) for $\lambda > 1.6$. Our interest is in a *charge ordered* CE phase. Such

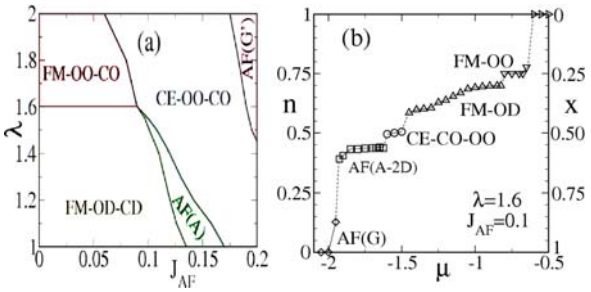

Fig. 18. (**a**) The ground state at $x = 0.5$ for varying J_{AF} and λ, in the absence of disorder. (**b**) The doping $(n = 1 - x)$ dependence of the ground state for varying chemical potential μ and typical electronic couplings, $\lambda = 1.6$ and $J_{AF} = 0.1$, near the FM-OD-CD & CE-CO-OO phase boundary. The phases in the vicinity of $x = 0.5$ are expected to show up in a cluster pattern on introducing disorder at $x = 0.5$

a state, with charge modulation $\sim 0.5 \pm 0.2$, say, shows up when both λ and J_{AF} are moderately large.

Since the effect of disorder might be to create cluster coexistence of phases *of different densities* that arise in the clean limit, Fig.18.(b) shows the phases and phase separation windows that occur at a typical coupling, $J_{AF} = 0.1$ and $\lambda = 1.6$. For these couplings the clean system is a CE-CO-OO phase at $x = 0.5$, a FMM for $x < 0.4$, and an A type AF for $x > 0.55$.

The naive expectation is that disorder would lead to cluster coexistence of AF-CO phases, that arise for $x \geq 0.5$, with the FMM phase at $x < 0.4$, Fig. 18(b). For weak A-type disorder we discover [28] that the long range charge and magnetic order is broken down to the nanoscale, with no signs of a percolative pattern of FMM clusters. The system is an insulating glass. The response to B-type disorder is more interesting, with a moderately large on site energy V on the B-impurities. We explored $V = 1,\ 2$ and 4 and $\eta = 2,\ 4$ and 8%. The response, as we vary the fraction of scatterers (η), is similar to A-type at weak Δ_B. However, before the peak at $\mathbf{q} = \{0, \pi\},\ \{\pi, 0\}$ vanishes we see the emergence of a ferromagnetic feature at wavevector $\mathbf{q} = \{0, 0\}$. There is a window at intermediate η where *B-type disorder leads to coexistence of FM and CO-OO-AF regions*. In terms of transport, intermediate A-type disorder strengthens the insulating character in $\rho(T)$, while B-type disorder of comparable variance leads to an insulator-metal transition on cooling, and a (poor) metallic state at low temperature [28].

The top row in Fig. 19 compares low temperature MC snapshots of the magnetic correlations at $\lambda = 1.6$, in the clean system (left), to that with $\Delta_A = 0.5$ (centre) and $\Delta_B = 0.56$. The respective panels in the middle row show the electron density $\langle n_i \rangle$ corresponding to the panels above. The panels at the bottom are the thermally averaged $S_{\rm mag}(\mathbf{q})$ in the three cases. In the clean limit, the magnetic correlations are CE, with a checkerboard density distribution, and simultaneous magnetic peaks at $\mathbf{q} = \{0, \pi\},\ \{\pi, 0\}$ and $\{\pi/2, \pi/2\}$. For A-type disorder there are stripelike magnetic correlations with small (atomic scale) FM clusters but no signature of phase

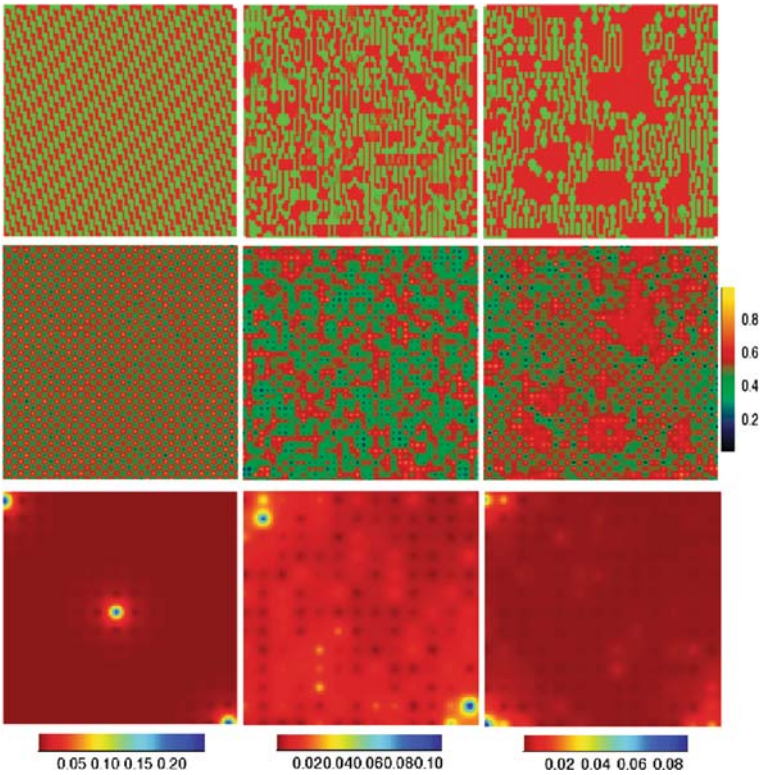

Fig. 19. MC snapshots and magnetic structure factor at low temperature, $T = 0.01$, size 40×40. Left row: $\lambda = 1.6$, non disordered, middle row, $\lambda = 1.6$, A-type disorder with $\Delta_{eff} = 0.5$, right row, $\lambda = 1.6$, B-type disorder with $V = 2$, $\eta = 8\%$, $\Delta_{eff} = 0.56$. Top panel shows the nearest neighbour magnetic correlation $\mathbf{S}_i.\mathbf{S}_{i+\delta}$, where $\delta = x$ or y. Middle panel shows the charge density $\langle n_i \rangle$ for the configuration above. Bottom panels shows the MC averaged $S_{mag}(\mathbf{q})$. In each panel $\mathbf{q} = \{0, 0\}$ at the bottom left corner, $\mathbf{q} = \{\pi, 0\}$ at the bottom right corner, etc.

coexistence. The density field is also inhomogeneous in the nanoscale, with only short range charge correlations, and $S_{\rm mag}(\mathbf{q})$ has weak peaks at $\mathbf{q} = \{0, \pi\}$ and $\{\pi, 0\}$ but no noticeable feature at $\mathbf{q} = \{0, 0\}$. B-type disorder, however, leads to FM *regions* coexisting with stripelike AF correlations. The density field shows a corresponding variation, being roughly homogeneous within the FM droplets (with local density $n \sim 0.6$), and a CO pattern away from the FM regions. $S_{mag}(\mathbf{q})$ now has peaks at $\mathbf{q} = \{0, \pi\}$, $\{\pi, 0\}$ *and* $\{0, 0\}$.

We can understand the difference between the impact of A-type and B-type disorder as follows. (1) The presence of A-type inhibits the coexistence of large FMM and AF-CO-OO clusters, despite the presence of a PS window in the clean problem, Fig. 18.(b), because (a) atomic scale potential fluctuations disallow CO coherence beyond a few lattice spacings, while (b) homogeneous FMM clusters are destabilised

by the disorder and become charge modulated. The result is a nanoscale correlated insulating glassy phase. (2) Dilute strongly repulsive scatterers act very differently: (a) they force an e_g^0 state at the impurity sites and generate an 'excess density' $0.5 \times \eta$ that has to be distributed among the remaining Mn sites, (b) the parent $x = 0.5$ CO phase cannot accommodate this excess charge homogeneously and the system prefers to phase separate into $x \sim 0.5$ AF-CO and $x \sim 0.4$ FM clusters, (c) unlike the A-type case, the FM clusters can survive and percolate since at low η there can be *large connected patches* without a B-type site. We have verified this explicitly for several impurity configurations. These observations are consistent with what has been long observed in the manganites [18–20, 30, 31], and stresses that while percolative effects do indeed occur in the manganites they do so only in systems with low ionic mismatch (like the La-Pr-Ca family). B-site substitution can be used as a 'trigger' in these situations.

6 Connection with Quantum Percolation and Resistor Networks

Although we finally have transport calculations for manganites based on microscopic theory, the system sizes are still modest, $\sim L = 40$, and can hardly access the mesoscale, let alone the 'bulk' limit. However, it seems meaningless to try and extend these microscopic calculations to ever larger scales. What one requires is an effective description at large scales whose parameters can be extracted from a microscopic theory of the kind we have discussed. This could be at two levels:

- Recreate the effective background 'disorder' (including spins, phonons, etc.) on large spatial scales and solve the quantum transport problem exactly in these non-trivial backgrounds. This in effect is the *correlated quantum percolation* framework that we had mentioned earlier. Notice that this scheme can be used even when there is no 'cluster coexistence' in the system.
- If cluster patterns emerge and have significantly large correlation length (compared to electron phase breaking length) then one should be able to use a *classical* percolation framework where the resistivity can be computed via effective medium theory. This seems to be appropriate for some of the experiments on La-Pr-Ca based systems but the critical exponents suggest that the cluster size distribution is non-trivial.

In the rest of the review, we briefly discuss the two issues above. The first aspect has not seen much discussion in the literature since it is hard to solve the microscopic problem. The second approach has been thoroughly explored by Dagotto and coworkers and I will only provide a summary of their key results.

6.1 Effective Quantum Percolation Models

What is the possible connection of the disordered interacting electron problems we described to the problem of quantum percolation? It is true that results from these

models yield spatial patterns reminiscent of percolation but we need a microscopic understanding to critically compare and exploit the similarity.

To recapitulate, quantum percolation is a limiting case of a disordered electron system of the form:

$$H = \sum_{\langle ij \rangle} t_{ij} c_i^\dagger c_j + \sum_i \epsilon_i c_i^\dagger c_i, \tag{10}$$

where the fraction of non-zero bonds and 'low-energy' sites are specified simply by fractions p_b and p_s, say.

Does this resemble the manganite problem in any way? Let us revisit the one band model, which is the simplest case involving FMM and AF-I phase competition and resulting cluster coexistence. In the $J_H/t \to \infty$ limit it assumes a form:

$$H = \sum_{\langle ij \rangle} t_{ij}^{eff}(\mathbf{S}_i, \mathbf{S}_j)\gamma_i^\dagger \gamma_j + \sum_i \epsilon_i \gamma_i^\dagger \gamma_i + J \sum_{\langle ij \rangle} \mathbf{S}_i.\mathbf{S}_j. \tag{11}$$

Here, the nearest neighbour hopping is $t_{ij}^{\text{eff}}/t = -(\cos\frac{\theta_i}{2}\cos\frac{\theta_j}{2} + \sin\frac{\theta_i}{2}\sin\frac{\theta_j}{2} e^{-i(\phi_i - \phi_j)})$ where θ_i and ϕ_i are polar and azimuthal angles of the spin $\mathbf{S}_i$. The random potential is just the 'bare' random potential.

This model does have some similarity to our 'disordered electron' model in that

1. It involves bond randomness in the t_{ij}^{eff}.
2. It involves site randomness in the ϵ_i.

The differences, however, are more significant:

1. The t_{ij}^{eff} are not $0/1$ as in the quantum percolation model but have a continuous distribution.
2. ϵ_i is a weak potential, and does not by itself create 'excluded' sites.
3. There are crucial correlations in the spatial distribution of the t_{ij}^{eff}, since they are related to background spin variables and the spin configuration is controlled by the Boltzmann distribution

$$\mathcal{P}\{\mathbf{S}\} \propto Tr_{\gamma,\gamma^\dagger} e^{-\beta H}. \tag{12}$$

For example the nearest neighbour (NN) spin-spin correlation, that primarily controls D_{ij} is decided by

$$\langle \mathbf{S}_i.\mathbf{S}_j \rangle = Z^{-1} \int \mathcal{D}\mathbf{S} Tr_{\gamma,\gamma^\dagger} \mathbf{S}_i.\mathbf{S}_j e^{-\beta H},$$

where Z is the partition function and it is obvious that NN exchange D_{ij} and D_{jk}, say, will be highly correlated due to the spin-spin correlations.

The spin-spin correlation is controlled by the Boltzmann weight that prefers connected clusters for FMM domains in order to minimise electronic kinetic energy. The bond correlations in the standard quantum percolation model, by contrast, are purely statistical in nature. As a consequence, such clusters have a fractal structure, while

the clusters that emerge from energy optimisation have smooth surfaces. To generate cluster patterns as in Fig. 11, e.g., one would need to use not only the 'one point' distribution for the $t_{ij}^{\rm eff}$ and ϵ_i but also short range correlations in the $t_{ij}^{\rm eff}$. That can be extracted either via some approximation on the full distribution above, or through parametrisation of the patterns obtained via MC.

6.2 Resistor Network Theory

Due to the difficulty in accessing transport properties from microscopic calculations, there have been attempts [32, 33] to construct a 'resistor network' theory, replacing the coexisting clusters by 'metallic' or 'insulating' resistors, and computing the overall resistance of the network. We have reviewed some attempts by experimenters to fit their data to the percolation/effective medium framework, and the mixed success. The critical exponents turn out to be too large, and first-order transitions cannot be obtained. We reproduce below some data reviewed by Burgy et al. [33], Fig. 20, highlighting these shortcomings.

The resistor network approach is somewhat unsatisfactory also because: (i) the 'resistance' of the network elements have to be inferred from experiments depending on the endpoint compositions in the coexistence regime, (ii) the quantum character of electron transmission between clusters is lost out in the Ohm-Kirchhoff formulation, and (iii) the sensitivity of intergrain transmission to core spin orientation (and the resulting low field MR) cannot be captured.

The failure of traditional percolation has led to the exploration of more evolved schemes for generating the cluster distribution. It is clear from Fig. 21(d), reproduced

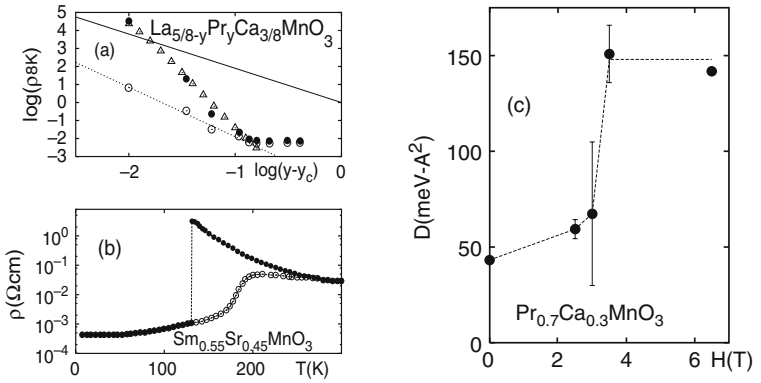

Fig. 20. Results illustrating the 'abrupt' character of the metal-insulator transition in some manganites (compositions indicated). (**a**) Dependence of residual ρ_{dc} on chemical substitution at 0 (●) and 4 kOe (○). The solid line represents the prediction of standard percolation, while the dotted one is a guide to the eye. The △ are results of a simulation using a broad distribution of bonds (α=0.857). (**b**) Resistivity versus T, at magnetic fields 0 (●) and 7 T (○). (**c**) Field dependence of the spin-wave stiffness at T=40 K. From Burgy et al., Phys. Rev. **B 67**, 014410 (2003), with permission

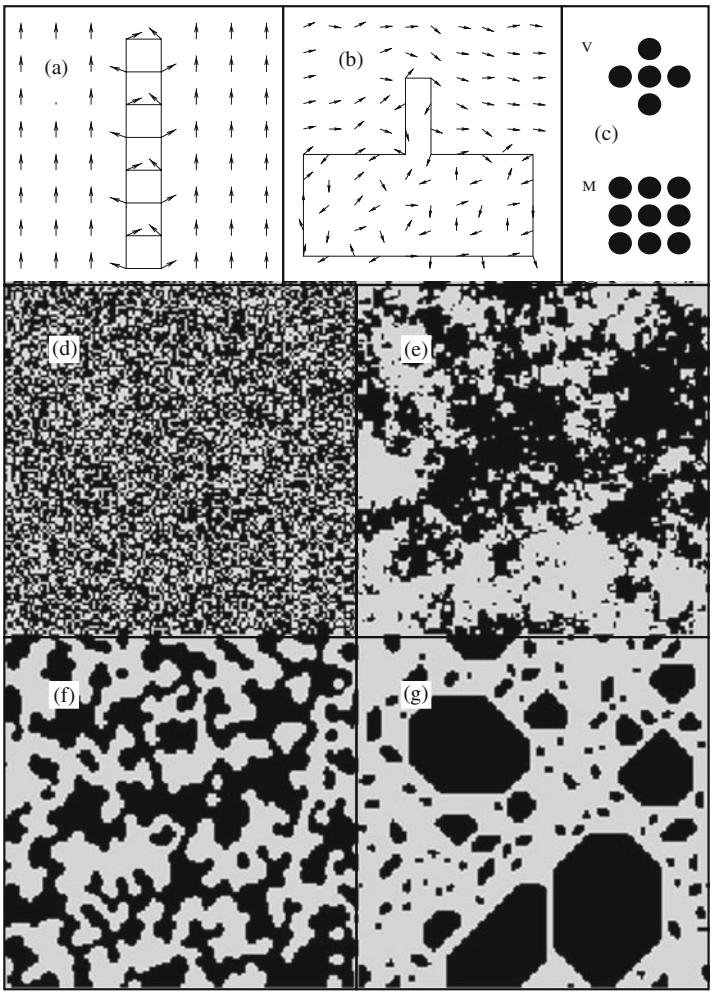

Fig. 21. (**a**) Typical snapshot of an 8×8 MC simulation of the one-orbital model (Hund coupling $J_{\rm H}$=∞, T=0.01t, t the hopping amplitude, and density 0.8). $J_{\rm AF}$ is 0 everywhere, but in the bonds of the ladder where they take the value 0.12t. The average spin-spin correlation in the ladder is –0.4 (effective "double-exchange" hopping 0.54), as opposed to –1.0 (effective hopping 0) when isolated from the FM region (effective hopping 1). (**b**) Similar to (a) but for density 0.5. Here $J_{\rm AF}$=0 is 0 in the upper portion minus the finger-like region. In the rest $J_{\rm AF}$=0.15t, favouring a flux state. The effective hopping in the flux region is 0.7, while in the finger it is as high as 0.9. (**c**) The different neighbourhoods in Vichniac's notation. (**d**) Typical configuration for standard percolation on a 128^2 lattice at (or just below) the critical density. (e) Same as (d) but for correlated disorder (γ=0.2). (f) Same as (d) but for the annealing rule (MGE5). (g) Same as (d) but for the nucleating rule (MGE4). The latter is particularly promising since a small increase in p leads to a fully saturated final state, in a first-order transition. From Burgy, *et al.*, Phys. Rev. B **67**, 014410 (2003), with permission

from [33] that the density distribution created in standard percolation models has no correpondence with the kind of structures that emerge in the experiments or microscopic theory. More complex schemes have been used to generate the clusters as Fig. 21(e)–(g) shows. These involve annealing/nucleating rules discussed in detail by the authors. When the resistivity is computed in these kind of backgrounds the results do show critical exponents quite different from standard percolation, and even a first-order transition. In the absence of microscopic understanding, however, such schemes remain ad hoc.

7 Conclusions

The manganites are a promising system for studying percolative transport in a correlated electron system. Not all of transport phenomena in the manganites involve 'percolation', there are regimes where interesting magnetotransport is seen without any obvious cluster coexistence. Nevertheless, there are situations, involving systems with low cation disorder, where cluster coexistence and percolative transport is evident. While this provides hope that a well established formalism can be employed to analyse the physics, standard percolation theory needs to be significantly expanded to address these phenomena. The complexity arises from the non-trivial character of the cluster distribution, dictated by the quantum physics of electron delocalisation. I hope this article provides an entry point to this fascinating field. It is obvious that the task of constructing effective percolation models faithful to the microscopic theory is far from over!

Acknowledgement

The numerical work at HRI was done using several Beowulf clusters. I acknowledge the contribution made by Sanjeev Kumar, Anamitra Mukherjee, and Kalpataru Pradhan to my understanding of manganite physics over the last several years.

References

1. Cheong and H.Y. Huang. In: *Colossal Magnetoresistive Oxides*, ed by Y. Tokura (Gordon and Breach, Amsterdam 2000) 195, 199
2. N. Mathur and P. B. Littlewood, Solid. State. Commun. **119**, 271 (2001) 195, 199
3. E. Dagotto, T. Hotta, and A. Moreo, Phys. Repts. **344**, 1 (2001) 195, 199
4. E. Dagotto, *Nanoscale Phase Separation and Colossal Magnetoresistance* (Springer, 2003) 195, 199, 203
5. L. Zhang, C. Israel, A. Biswas, R. L. Greene, and A. de Lozanne, Science, **298**, 805 (2002) 195, 199, 216
6. M. Uehara, S. Mori, C.H. Chen, and S.-W. Cheong, Nature, **399**, 560 (1999) 195, 199, 200

7. Ch. Renner, G. Aeppli, B.G. Kim, Y. Soh, and S.-W. Cheong, Nature, **416**, 518 (2002) 195, 199, 216
8. M. Fath, S. Freisem, A.A. Menovsky, Y. Tomioka, J. Aarts, and J.A. Mydosh, Science, **285**, 1540 (1999) 195, 199, 216
9. A. Moreo, M. Mayr, A. Feiguin, S. Yunoki, and E. Dagotto, Phys. Rev. Lett. **84**, 5568 (2000) 195, 207
10. Y. Meir, A. Aharony, and A. B. Harris, Phys. Rev. Lett. **56**, 976 (1986) 196
11. C. M. Soukoulis, Q. Li and G. S. Grest, Phys. Rev. **B 45**, 7724 (1992) 196, 198
12. P. A. Lee and T. V. Ramakrishnan, Rev. Mod. Phys. **57**, 287 (1985) 197
13. D. Stauffer and A. Aharony, *Introduction to Percolation Theory* (Taylor & Francis, London, 1991) 198
14. S. Kirkpatrick, Rev. Mod. Phys. **45**, 574 (1973) 198
15. K.H. Kim, M .Uehara, C. Hess, P.A. Sharma, and S-W. Cheong, Phys. Rev. Lett. **84**, 2961 (2000) 199, 200
16. V. Hardy. A. Wahl, and C. Martin, Phys. Rev. **B 64**, 064402 (2001) 199, 202
17. V. Podzorov, M. Uehara, M.E. Gershenson, T.Y. Koo, and S-W. Cheong, Phys. Rev. **B 61**, 3784 (2000) 199
18. D. Akahoshi, M. Uchida, Y. Tomioka, T. Arima, Y. Matsui, and Y. Tokura, Phys. Rev. Lett. **90**, 177203 (2003) 203, 221
19. R. Mathieu, D. Akahoshi, A. Asamitsu, Y. Tomioka, and Y. Tokura, Phys. Rev. Lett. **93**, 227202 (2004) 203, 221
20. Y. Tokura, Rep. Prog. Phys. **69**, 797 (2006) 203, 221
21. A.J. Millis, in *Colossal Magnetoresistive Oxides*, ed by Y. Tokura (Gordon and Breach, Amsterdam, 2000) 203
22. S. Kumar and P. Majumdar, Eur. Phys. J. B, **46**, 315 (2005) 207
23. S. Kumar and P. Majumdar, Phys. Rev. Lett. **92**, 126602 (2004) 207, 211
24. S. Kumar, C.S. Mohapatra, and P. Majumdar, Europhys. Lett. **71**, 804 (2005) 214
25. E. O. Wollan and W.C. Koehler, Phys. Rev. **100**, 545 (1955) 217
26. J. van den Brink, G. Khaliullin, and D. Khomskii, Phys. Rev. Lett. **83**, 5118 (1999) 217
27. Y. Imry and S-k. Ma, Phys. Rev. Lett. **35**, 1399 (1975) 217
28. K. Pradhan, A. Mukherjee, and P. Majumdar, Phys. Rev. Lett. **99**, 147206 (2007) 217, 218
29. S. Kumar and P. Majumdar, Eur. Phys. J. **B 50**, 571 (2006) 218
30. T. Kimura, Y. Tomioka, R. Kumai, Y. Okimoto, and Y. Tokura, Phys. Rev. Lett. **83**, 3940 (1999) 221
31. T. Kimura, R. Kumai, Y. Okimoto, and Y. Tomioka, Phys. Rev. **B 62**, 15021 (2000) 221
32. M. Mayr, A. Moreo, J. A. Verges, J. Arispe, A. Feiguin and E. Dagotto, Phys. Rev. Lett. **86**, 135 (2000) 223
33. J. Burgy, E. Dagotto and M. Mayr, Phys. Rev. **B 67**, 014410 (2003) 223, 225

Classical and Quantum Breakdown in Disordered Materials

D. Samanta[1], B.K. Chakrabarti[2] and P. Ray[3]

[1] Theoretical Condensed Matter Physics Division, Saha Institute of Nuclear Physics, 1/AF Bidhannagar, Kolkata 700064, India
debashis.samanta@saha.ac.in

[2] Theoretical Condensed Matter Physics Division and Centre for Applied Mathematics and Computational Science, Saha Institute of Nuclear Physics, 1/AF Bidhannagar, Kolkata 700064, India
bikask.chakrabarti@saha.ac.in

[3] The Institute of Mathematical Sciences, C.I.T. Campus, Taramani, Chennai 600113, India
ray@imsc.res.in

1 Introduction

It is our common household experience that when the voltage drop across a fuse exceeds a limit, the fuse burns out. A fuse is nothing but a conductor that conducts uniform current under an applied voltage up to a certain limit beyond it burns out and becomes non-conducting. This is called fuse failure. Similarly, in a dielectric breakdown, a dielectric starts to conduct electricity when the voltage drop across it attains certain threshold value. The above two phenomena are examples of breakdown process that is described broadly as the failure of a physical attribute when the perturbing force driving it goes beyond a limiting value. The most common example of the process is the breaking of a material at a high stress beyond its strength.

Naturally occurring solids are almost always inhomogeneous and have defects like vacancies, micro cracks or impurities. These defects are weak points across which stress fields or electric fields or current densities concentrate. Depending on the geometry of the defect, the concentrated field can be very high. If the field or density exceeds the material fatigue limit, failure nucleates locally around the defect and starts to propagate. The propagation can be arrested, or can spread to the entire system leading to the global failure of the system, depending on the field strength and the defect structure in the material. The failure of a material, thus, depends largely on the disorder present in it.

The simplest form of the weak points is substitutional disorder that can be realised by the inclusion of non-conducting material in a conducting material or vice versa. Since we are interested in the macroscopic properties of global failure, we consider failures at length scale larger than the regions in which the local failure appears (i.e. atomic distances). At this scale, the disordered fuse system can be modelled

Samanta, D. et al.: *Classical and Quantum Breakdown in Disordered Materials*. Lect. Notes Phys. **762**, 227–250 (2009)
DOI 10.1007/978-3-540-85428-9_8

by a lattice whose bonds are non-conducting with a certain probability $(1-p)$ and conducting otherwise.

For such models, one can apply the principles of percolation theory [47, 48]. Below the percolation threshold p_c (for $p < p_c$) the system is not connected globally by channels of conducting bonds and so non-conducting, whereas for $p > p_c$ the system is conducting (at least one continuous path exists across the system via the conducting bonds).

For $p > p_c$, when conducting channels span across the system and the system is conducting, one can ask what is the fuse current I_f required so that the system becomes non-conducting. At $I > I_f(p)$ not a single spanning path of conducting bonds exists. At $p = 1$, all the conducting bonds are present and $I_f(1)$ normalised by the sample size is simply the fuse threshold current for each of the conducting bonds. For $p < p_c$, the conducting bonds does not form a continuous path across the sample, and the sample is insulating. With increasing voltage V across the sample, one can get a continuous path through original conductors and broken dielectric for $V \geq V_b(p)$, where $V_b(p)$ is the dielectric breakdown voltage. At $p = 0$, all the non-conducting bonds are there in the system and $V_b(0)$ normalised by the system size is simply the breakdown threshold of each of the non-conducting bonds. On the other hand, as $p \to p_c$, both the dielectric breakdown voltage and fuse failure current tend to zero. The corresponding phase diagram is shown in Fig. (1).

In this article, we will review the basic ideas in breakdown problems in terms of the fuse failure and dielectric breakdown problems and then discuss how these ideas can be extended to the breakdown in quantum mechanical systems such as Anderson insulators. In disordered electronic systems above two dimensions, the electronic states below the mobility edge are all localised (the system with Fermi level within this range behaves as an insulator) and the states above the mobility edge are extended (the system turns to a conductor for Fermi level in this range). The Anderson transition from insulating to conducting phase across the mobility edge is well stud-

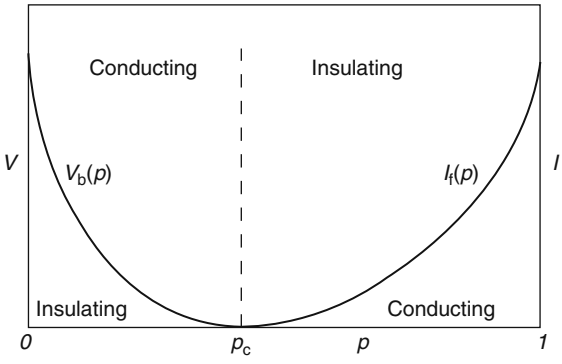

Fig. 1. Phase diagram of a mixture containing p fraction of conductors and $(1-p)$ fraction of insulators at random. On the left side, the sample is insulating for voltage V less than the breakdown voltage $V_b(p)$ and conducting otherwise. On the right side, the system is conducting for current I less than the fuse current $I_f(p)$ and insulating otherwise

ied [26]. We discuss here the possibility of a breakdown from insulating to conducting phase by applying strong electric field and compare the quantum breakdown with the classical dielectric or fuse breakdown in disordered materials.

2 Analysis of the Fuse Problem

2.1 Disordered Fuse Network

In a pure conductor placed between two electrodes with a potential difference, the field lines within the conductor are all parallel to each other and perpendicular to the electrode surfaces. In presence of a disorder in the form of an insulating region, the field lines get deformed around the defect. As a result in the vicinity of the defect current density increases to i_e from i, the current density value far away from the defect. So one can write

$$i_e = i(1 + k), \tag{1}$$

where k is the enhancement factor that depends on the geometry of the defect. As an example, k becomes l/b for an elliptic defect of semi-major axis l and semi-minor axis b [12]. For electrode surface area S total current I is

$$I = Si = \frac{Si_e}{1 + k}. \tag{2}$$

Failure occurs for the first time when i_e becomes equal to i_0 which is the fatigue limit of the sample material. The failure current is then

$$I_f = \frac{Si_0}{1 + k}. \tag{3}$$

Larger the enhancement factor k, smaller is the failure current I_f. For an example, if $l >> b$ for an elliptic defect, I_f may get reduced by a large extent. So the presence of defects in the material facilitates failure and the presence of sharper edges of defects make the system more vulnerable to failure. The failure makes the defect bigger and hence k larger. This means that the current density around the defect enhances further causing failure again. The process causes rapid failure of the whole sample. This means that external voltage for the global failure is the same as the voltage for the first local failure and a local failures once started leads to the failure of the entire sample. This type of failures are called *brittle failures*.

So far we have discussed the influence of a single defect of a regular size within the sample. Natural and engineering samples usually contain a large number of defects of irregular shapes and sizes at random. To get some quantitative estimate of the failure criteria in terms of defect parameters we idealise the solid to lattice model and use percolation theory for defects [18, 38, 39].

We start with a hypercubic lattice in $2d$ or $3d$ with all conducting bonds. The simplest defect can be introduced by removing one bond parallel to the direction of the current flow. In this case, failure current is calculated as

$$I_f = \frac{\pi}{4} L i_0 \tag{4}$$

in $2d$, where Li_0 is the fracture current of the lattice in absence of any defects and L is the linear size of the lattice. The enhancement factor is $4/\pi$ here. We introduce randomness in shape and size of the defect by removing $(1-p)$ fraction of the bonds randomly. It is no longer possible to determine the most vulnerable defect and to calculate the enhancement factor. We consider two limits: (1) dilute limit $(p \to 1)$ when the defect density is small and (2) near the critical point p_c, where the defect density is large and beyond which the lattice loses its connectivity.

Dilute Limit $(p \to 1)$

In this limit, there are only a few isolated defects (insulating bonds) in the sample. The current density around a defect is effectively independent of the presence of other defects. Under such considerations the most vulnerable of the defects will lead to the failure of the system. So our primary task is to identify the *most probable dangerous defect* (the weakest point that causes the largest concentration of the current density).

The ensemble of n successively removed bonds, far from boundaries [18, 19], in a plane perpendicular to the current flow, act as a dangerous defect. In $2d$, it is a linear defect and in $3d$ the defect has the shape of a disc. The current through the conducting bonds at the immediate neighbourhood of the defect is

$$i_e = i(1 + k_2 n) \quad (\text{in } 2d), \qquad i_e = i(1 + k_3 n^{\frac{1}{2}}) \quad (\text{in } 3d). \tag{5}$$

Here, i is current density through the bonds far away from the defect. Enhancement factor k contains $\sqrt{n}$ term because current is diverted by n defects to spread uniformly around the perimeter of the disc, which is proportional to $\sqrt{n}$. The probability of appearance of a defect of n successive insulating bonds is

$$P(n) \sim (1-p)^n L^d, \tag{6}$$

where L is the lattice size and d is the dimension of the lattice. L^d provides the number of places that the defects can occupy. The approach of $P(n) \approx 1$ gives the size of most probable dangerous defect:

$$n_c = -\frac{2}{\ln(1-p)} \ln L \quad (\text{in } 2d), \qquad n_c = -\frac{3}{\ln(1-p)} \ln L \quad (\text{in } 3d). \tag{7}$$

Combining (5) and (7) i_e becomes

$$\begin{aligned} i_e &= i\left[1 + k_2\left(-\frac{2\ \ln L}{\ln(1-p)}\right)\right] \quad (\text{in } 2d), \\ &= i\left[1 + k_3\left(-\frac{3\ \ln L}{\ln(1-p)}\right)^{\frac{1}{2}}\right] \quad (\text{in } 3d). \end{aligned} \tag{8}$$

Here, the total current is $iL^{(d-1)}$. Equating i_e with the threshold value i_0, the expression for the failure current becomes

$$I_f = \frac{i_0 L}{1 + 2k_2[\frac{\ln L}{\ln(1-p)}]} \quad (\text{in } 2d),$$
$$I_f = \frac{i_0 L^2}{1 + \sqrt{3}k_3[\frac{\ln L}{\ln(1-p)}]^{\frac{1}{2}}} \quad (\text{in } 3d). \tag{9}$$

From the equations it is clear that as $p \to 1$, I_f reduces to $i_0 L^{d-1}$, the value of the current in the lattice with all the bonds conducting. The slope of the $I_f(p)$ versus p curve at $p = 1$ is infinite (see Fig. 1). It is expected because even the presence of a single defect enhances the process of breakdown through cascade. The most important thing is the size dependence of I_f. For large enough L and p not very close to 1 (such that the absolute value of $\ln(1 - p)$ is not too large) the failure current per bond $i_f (= I_f/L^{d-1})$ decreases as $1/\ln L$ and $1/(\ln L)^{1/2}$ in $2d$ and $3d$, respectively.

Critical Behaviour ($p \to p_c$)

Near criticality ($p \to p_c$), the material is strongly disordered and can be described by *node-link-blob* picture [17, 43, 45] of percolation theory (see Fig. 2). Close to p_c the conducting part of the material extends over the sample to form percolating cluster, which is *self-similar* up to the length scale ξ_p, the percolation correlation length. The geometry of the cluster inside each cell appears same as that of the original cluster at smaller scale. This means that the infinite cluster may be divided into cells of size ξ_p. Each cell consists of backbone bonds (which takes part in current conduction) and numerous dangling bonds (bonds which do not take part in current conduction). Only backbone is important because it takes part in conductivity. The backbone is made of two kinds of bonds: multiply connected bonds that appear as blobs; and singly connected bonds (called *red* bonds) that appear as links. Distribution of current in the sample is solely determined by links; being singly connected, each link has to carry the full current inside a cell. Since at threshold (p_c) correlation length (ξ_p) spans the sample (large enough), it is reasonable to assume that the failure current approaches zero as $p \to p_c$.

To determine quantitatively the critical behaviour of the failure current I_f, we consider the voltage V applied across the node-link-blob network. Since V is distributed among L/ξ_p number of links (or cells) in series, the average voltage across each link is $V_L \sim \xi_p V$. The resistance of the sample R is related to average link resistance R_L through $R \sim \xi_p^{d-2} R_L$, since there are $L\xi_p^{-1}$ number of links in series in the length L of the sample and there are ξ_p^{-1} number of parallal such links. So the mean current in a link appears to be $i_L \sim \xi_p^{d-1} V/R$ through the relation $i_L = V_L/R_L$. V equals to failure or fuse voltage V_f when i_L reaches the maximum current which a link can stand. One can assume fuse voltage behaves as

$$V_f \sim (p - p_c)^{-t_f}. \tag{10}$$

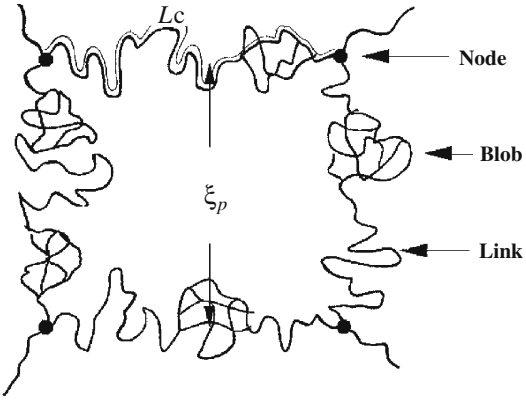

Fig. 2. A portion of the node-link-blob super lattice model near p_c. The distance between two nodes of the lattice is ξ_p, while chemical length of the tortuous link of the super lattice is L_c

Using the relation $\xi_p \sim (p - p_c)^{-\nu}$ and $R \sim (p - p_c)^{-t_c}$, t_f comes out as $t_f = t_c - (d-1)\nu$. From the relation $I_f = V_f/R$, we get

$$I_f \sim (p - p_c)^{(d-1)\nu}. \tag{11}$$

The values of the correlation length exponent ν are 1.33 in $d = 2$ and 0.88 in $d = 3$ and the values of the conductivity exponent t_c are 1.33 in $d = 2$ and 2 in $d = 3$ [47, 48]. So it is clear that the fuse voltage V_f attains finite value in $2d$ and diverges with the exponent 0.2 in $3d$, in contrary to the failure current which always approaches zero as $p \to p_c$.

Influence of the Sample Size

Size dependence of I_f is related to the notion of the most dangerous defect present in the sample. In the present context, the most dangerous defect is a 'cell' of the infinite cluster with length ξ_p in the direction parallel to the applied voltage and $l_{\max}$ in the perpendicular direction. The total probability of having a defect of size l is, $P = g(l)(L/\xi_p)^d$, where $g(l)$ is the probability density of defect cluster of linear size l. Percolation theory predicts [40, 47, 48] that

$$P \sim exp\left(-\frac{l}{\xi_p}\right)\left(\frac{L}{\xi_p}\right)^d. \tag{12}$$

$l_{\max}$ is obtained when $P \approx 1$ and

$$l_{\max} \sim \xi_p \ln L. \tag{13}$$

Now the current that flows through the side link of the defect is proportional to $(l_{\max})^{d-1} I$ and one obtains

$$I_f \sim \frac{(p-p_c)^{(d-1)\nu}}{(\ln L/\xi_p)^{(d-1)}}. \tag{14}$$

So this is the correction over equation (11) due to finite size of the sample. Bergman and Stroud [7] gave an idea about the competition between extreme statistics and percolation statistics. The extreme statistics (size dependence of the most probable defect and failure current) is expected to dominate for $\ln L > \xi_p$ (or, when Lifshitz scale is greater than the connectedness correlation length). The dominance of extreme statistics is expected for p far away from percolation threshold when the correlation length ξ_p is small.

Li and Duxbury [27] proposed the dependence of I_f on L through $(\ln L)^{-\psi_f}$. The approximate range of ψ_f is

$$\frac{1}{2(d-1)} < \psi_f < 1. \tag{15}$$

Considering the results of the dilute limit and in the critical region, the combined form of (9) and (11) is

$$I_f = I_0 \frac{\left[\frac{(p-p_c)}{(1-p_c)}\right]^{\phi_f}}{1 + K\left[-\frac{\ln(L/\xi_p)}{\ln(1-p)}\right]^{\psi_f}}. \tag{16}$$

The value of the different exponents (see Table 1) and the constant K depend on the dimension and on the type of percolation. From (9) and (14) one can see that the combined result is valid only for $2d$. The expression has three obvious features:

1. For $p = 1$, $I_f = I_0$, as expected.
2. Near $p = 1$, $(p - p_c)$ is almost constant and we get back the expression (9).
3. Near p_c, the denominator of (16) is of the order of unity and we recover the expresion (11) with $\phi_f = (d-1)\nu$.

Table 1. Theoretical estimates for the fuse failure exponent ϕ_f

Dimension	Lattice percolation	Continuum percolation
2	$\nu(= 4/3)$	$\nu + 1(= 7/3)$
3	$2\nu(\simeq 1.76)$	$2(\nu + 1)(\simeq 3.76)$

2.2 Distribution of the Failure Current Dilute Limit ($p \longrightarrow 1$)

In random fuse networks, the failure current I_f shows large sample to sample fluctuations. Since the failure current is determined by the weakest defect in the sample, the fluctuations in the failure currents do not come down with the system size. The average failure current is not a self-averaging quantity.

Distribution of the failure currents in a system of size L follows as (see Ref. [12])

$$F_L(I) = 1 - \exp\left[-A_d L^d \exp\left\{-dA \ln L \left(\frac{\frac{I_0}{I} - 1}{\frac{I_0}{I_f} - 1}\right)^{d-1}\right\}\right]. \tag{17}$$

The derivative of this cumulative failure probability distribution $F_L(I)$ with respect to current I provides the current I at which the system fails. Certainly, at most probable failure current the derivative becomes maximum. Here, I_0 is the failure current for pure sample. It may become obvious with a simple calculation that I_f appears to be the most probable failure current (as was assumed in calculation) only in the limit of large enough system size.

Though the current I can vary from zero to infinity, the form of $F_L(I)$ is meaningful only for I upto I_0. One should expect the value unity for $F_L(I)$ at $I = I_0$ and $I = \infty$, but it is true only for large system size. $F_L(I)$ suffers from size and defect concentration dependence through I_f (see equation 9).

The above expression is referred to as the Gumbel distribution [23]. Another well known one that is very often used in engineering is Weibull distribution

$$F_L(I) = 1 - \exp\left[-rL^d \left(\frac{I}{I_f}\right)^m\right]. \tag{18}$$

Here, m is a constant and for large m (say more than 5) I_f refers to most probable failure current.

At Critical Region ($p \to p_c$)

Near criticality the cumulative failure distribution function is

$$F_L(I) = 1 - \exp\left[-A'_d L^d \exp\left(-\frac{k'(p - p_c)^\nu}{I^{\frac{1}{d-1}}}\right)\right], \tag{19}$$

where A'_d and k' are two constants.

2.3 Continuum Model

One can extend the ideas of lattice percolation to continuum conducting medium. A material at the scale of the size of the defects can be looked upon as a continuous field with some defects as inclusions in the field. In continuum model of lattice percolation, insulating spherical holes (circular holes in $2d$) are punched at random as defects in a uniform conducting sample. The holes can overlap (*Swiss-cheese model*) and two non-overlapping neighbouring holes have a conducting region between them. These regions constitute conducting channels of cross-section δ. Somewhat similar to the breakdown problem discussed above, the transport properties of any such channel depend on the transport capacities (cross-section and

length) of the narrowest part (the weakest bond) of the channel. With some reasonable assumptions, one [24] can express the transport capacities of the weakest region in terms of percolation cluster statistics on the lattice (particularly in terms of the percolation correlation length ξ_p).

Both the discrete and continuum type are almost same in the dilute limit ($p \to 1$). So all the results derived earlier for discrete model are valid here. But near criticality an infinite percolation cluster, with the links of mean length ξ_p and of different cross-sectional width δ, is formed. The backbone [17, 43] of this cluster is represented by a super lattice (see Sect. 2.1) of tortuous singly connected links and blobs crossing at nodes at a separation

$$\xi_p \sim |p - p_c|^{-\nu}. \tag{20}$$

The chemical length between any two nodes is

$$L_c \sim |p - p_c|^{-\zeta}. \tag{21}$$

For singly connected bonds (or sites) on the percolating backbone, $\zeta = 1$ in all dimensions [24] except $d = 1$ [15, 47, 48]. There are $(L/\xi_p)^{d-1}$ number of parallel links exist between two electrodes, where L is the size of the sample. The current in a link is given by $i_L = (\xi_p/L)^{d-1} I$. The current density i in a channel of cross-section δ is given by

$$i \sim \frac{\xi_p^{d-1} I}{\delta^{d-1}} \tag{22}$$

The maximum current density is obtained for minimum cross-section δ_{min}, which is inversely proportional to the shortest chemical length L_c [4, 6, 24]. If i_0 is the threshold current density at which the material fails, then

$$i_0 \sim \xi_p^{d-1} L_c^{d-1} I_f \tag{23}$$

and we get,

$$I_f \sim (p - p_c)^{\nu+1} \quad (\text{in } 2d), \qquad I_f \sim (p - p_c)^{2(\nu+1)} \quad (\text{in } 3d). \tag{24}$$

Thus, the exponents for the failure current are higher than those of the discrete model.

Using $I_f = V_f/R$ and $R \sim |p - p_c|^{-\tilde{t}_c}$ with Eqs (20) and (21) the expression for fuse voltage becomes $V_f \sim |p - p_c|^{\tilde{t}_f}$ with $\tilde{t}_f$ equal to $(d-1)(\nu+1) - \tilde{t}_c$ [12]. $\tilde{t}_c$ is the conductivity exponent: $\tilde{t}_c \simeq 1.3$ and 2.5 in $2d$ and $3d$, respectively. Consequently, $\tilde{t}_f$ becomes approximately 1 and 1.3 in $2d$ and $3d$, respectively. Unlike discrete percolation where failure current at p_c attains a finite value in $2d$ and vanishes only in $3d$, in continuum percolation failure voltage always vanishes at p_c.

2.4 Electromigration

Electromigration is an example where we find the practical application of the concepts we have hitherto discussed. Miniaturisation of the circuits and gadgets have become the norm of the day. Very thin metallic films are used as interconnects among

the active parts of devices, resulting in large current densities through the metallic films. Having large enough momentum, the free electrons become able to displace metallic ions from their equilibrium positions. Thus, depending upon the material a net material transport occurs [51] through grain boundary diffusion, surface diffusion or lattice diffusion. This ionic displacement and the accumulated effect of material transport due to large current densities (more than 10^4 A/cm^2) are called *electromigration*. Over time such electromigration leads to void formation at the cathode and extrusion at the anode in thin film interconnects. Such void formation and hillock formation cause an open circuit and a short circuit to neighbouring connecting wires, respectively. The problem of material accumulation can be suppressed by the layers of other material around and above the interconnects. The problem of open circuit due to void formation has received much attention as the random failures of several interconnects finally lead to failure of the entire device.

Let a fraction $(1 - p)$ of the resistors he removed from random resistor network (say in 2d). A random walker starts its walk from one of the lateral sides (those without electrodes) of the network, and jumps from one cell to a nearest neighbour cell by crossing the bonds irrespective of occupied or unoccupied bonds, intending to reach the opposite side, with the constraint that it never visits a cell more than once. Let the whole path consists of n_0 occupied and n_1 unoccupied bonds. For a given configuration of missing resistors the minimum value of n_0 is the *shortest path*.The mean shortest path $< n_0 >$ (for theoretical study see Ref. [14, 49]) can be realised by considering the average over a large number of configurations. An electro migration induced failure of the network can be realised if the walker fuses the resistors as it crosses them. The criterion for a resistor to fuse is not a particular value of current (as in the fuse model), rather a particular value of threshold charge Q_0 that attains the resistor from the time of application of the constant current I_0 to the network (for details of the model see Ref. [10, 55]). If t_1 is the failure time of an arbitrary resistor of the network which is subjected to a constant current I_0, then the resistor must satisfy

$$\int_0^{t_1} I(t)dt = Q_0 \tag{25}$$

to fail.

So *shortest path* for a given impurity concentration is the path that corresponds to the smallest number of resistors to fuse. The problem is to study the variation of failure time of the whole network τ with p. For a network having an isolated defect of length n, τ is given by

$$\tau = (L - n)Q_0/I_0, \tag{26}$$

where LQ_0/I_0 is the τ value for the pure network. In pure limit the mean failure time $< \tau >$ is related to the longest probable defect with size n_c. This means that the bonds which fuse are also the bonds with largest current.

τ decreases as p decreases from pure limit, and approaches zero at p_c, since the number of bonds to be broken goes also to zero. The shortest path n_0, the failure current I_f, the number of broken bonds N_f and the failure time $< \tau >$, all these quantities tend to go to zero at p_c with the correlation length exponent ν.

2.5 Numerical Simulations of Random Fuse Network

The numerical simulation of failure of random fuse network in $2d$ was carried out by de Arcangelis et al. [16]. Here, one starts with a lattice, the bonds of which are conductors and present with a probability p. An increasing external voltage is applied across the lattice and the voltage V_f^1 when there is first local failure is recorded. The fused bond is removed and the voltage is raised till there is a second failure at V_f^2. The process is continued till the global failure at a voltage V_f^{fin} occurs. The variation of V_f^1 and V_f^{fin} with p are studied. V_f^1 decreases with decreasing p till $p \sim 0.7$ whereupon it attains minimum value and then it starts increasing again. V_f^{fin}, on the contrary, increases monotonically and behaves almost identically as V_f^1 for $|p - p_c| < 0.08$. Both approaches p_c with the diverging exponent 0.48. It seems that V_f^1 exhibits pseudodivergence in $2d$.

Duxbury et al. [19] performed similar type of simulations covering the whole range of p from 1 to $p_c = 0.5$. Their simulation results concerning I_f versus p graph fit well with the interpolation formula (16) with the exponent value $\phi_f = 1$, whereas the theoretically predicted value is 1.33. This may be due to the finite size effect (see Fig. 3).

They also demonstrated the finite value of V_f^1 at p_c by looking into the variation of I_f and the conductance near p_c. Following Eq. (9) they checked the linear dependence of L/I_f on $\ln L$ successfully for several values of p, varying L from 10 to 200 and determined $\psi_f = 1$ from their slopes. The slope increases as p approaches p_c. Instead of (17) they preferred

$$F_L(V) = 1 - exp\left[-AL^2 exp\left(-\frac{KL}{V}\right)\right] \tag{27}$$

as cumulative distribution function of failure voltage.

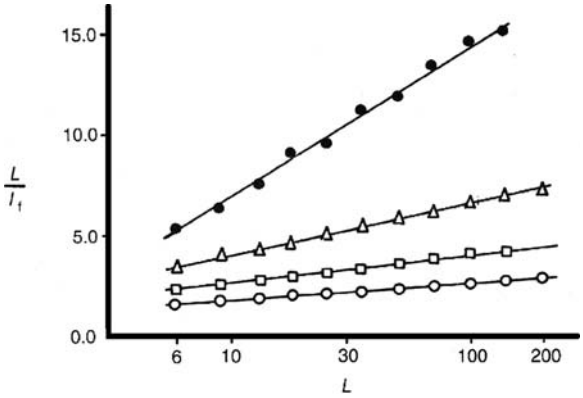

Fig. 3. L/I_f versus $\ln L$ expressing their linear dependence (after Duxbury et al. [19]). The curves from top to bottom correspond to initial impurity probability $p = 0.6, 0.7, 0.8$ and 0.9, respectively

Arcangelis et al. [16] and Duxbury et al. [19] determined the number of fused bonds N_f up to complete failure and they found that N_f goes to zero algebraically as $p \to p_c$ with an exponent seemingly equal to the correlation length exponent ν.

3 Dielectric Breakdown Problem

In dielectric breakdown problem the sample is insulating and conducting material acts as defects in the composite. The volume fraction (p) of the conducting material is less than the critical volume fraction (p_c) so that the system overall is not conducting. The dielectric portions can withstand electric field upto e_c, at and beyond which they become conducting (local breakdown). Global breakdown occurs when the conducting portions span the sample with the succession of local breakdown under the influence of an increasing external field.

In $2d$, the solution for dielectric problem can be obtained from the solution of fuse problem with the aid of *duality relation* [9, 35]. We follow Bowman and Stroud [9] and consider the case where p is smaller than p_c and the sample is macroscopically insulating. The equations for the induction vector $\mathbf{D}$ and the field $\mathbf{E}$ are

$$\begin{aligned} \bigtriangledown \cdot \mathbf{D} &= 0 \\ \bigtriangledown \times \mathbf{E} &= 0 \\ \mathbf{D}(r) &= \epsilon(r)\mathbf{E}(r), \end{aligned} \tag{28}$$

where $\epsilon(r)$ is local dielectric constant of the insulating portion and $\mathbf{E}$ is irrotational . With $\mathbf{E} = -\bigtriangledown \phi$ equations (28) yields

$$\frac{\partial}{\partial x}\left[\epsilon(r)\frac{\partial \phi}{\partial x}\right] + \frac{\partial}{\partial y}\left[\epsilon(r)\frac{\partial \phi}{\partial y}\right] = 0, \tag{29}$$

where ϕ is the scalar potential. Now consider the dual composite of the original, where insulator phase of the original is replaced by conducting phase and vice versa. The sample is macroscopically conducting and the relevant quantities are current density $\mathbf{i}$ and electric field $\bar{\mathbf{E}}$. These satisfy the equations

$$\begin{aligned} \bigtriangledown \cdot \mathbf{i} &= 0 \\ \bigtriangledown \times \bar{\mathbf{E}} &= 0 \\ \mathbf{i}(r) &= \sigma(r)\bar{\mathbf{E}}(r) \end{aligned} \tag{30}$$

Since $\mathbf{i}$ is divergence less, $\mathbf{i}$ can be expressed as a curl of a vector potential $\mathbf{V}$. $\mathbf{V}$ ($\mathbf{V} = V_z = \psi(x, y)$) is chosen in such a way, only z-component of $\mathbf{i}$ vanishes. Assuming local conductivity as $\sigma(r) = 1/\epsilon(r)$ equations (30) yields

$$\frac{\partial}{\partial x}\left[\epsilon(r)\frac{\partial \psi}{\partial x}\right] + \frac{\partial}{\partial y}\left[\epsilon(r)\frac{\partial \psi}{\partial y}\right] = 0. \tag{31}$$

Comparing (29) and (31), one has

$$\frac{\partial\psi}{\partial x} = \frac{\partial\phi}{\partial x}, \qquad \frac{\partial\psi}{\partial y} = \frac{\partial\phi}{\partial y}. \tag{32}$$

With all these, the components of current density **i** in dual composite become

$$i_x = \partial\psi/\partial y = E_y, \qquad i_y = -\partial\psi/\partial x = -E_x. \tag{33}$$

Thus, we see that the magnitude of the current density in the dual composite is equal to the magnitude of the electric field in the original one and the direction is rotated by 90°. It can also be shown that the field $\bar{\mathbf{E}}$ of the dual problem is equal to vector $\mathbf{D}$ of the dielectric problem and is rotated by 90°. Now the physical correspondence of the two pictures can be easily established [12, 41].

All the results of fuse problem can be utilised for obtaining the solution for dielectric problem. For example, the equations (16) and (19) can be used in a straight forward way on replacing I_0 and I_f by V_0 and V_b, respectively, and also $(1-p)$ by p.

3.1 Dielectric Breakdown Problem

As in the fuse problem, dielectric breakdown problem can be viewed on a discrete lattice with disorder in the framework of percolation theory. Basically, a lattice of insulating bonds is considered out of which p $(p < p_c)$ fraction of bonds are conducting at random. For this purpose resistor (capacitor) of different resistivity (capacitance) [8, 9] can be used. Resistors (capacitors) of smaller (higher) resistance (capacitance) are used for conducting bonds.

Dilute Limit ($p \longrightarrow 0$)

The problem is very similar to the fuse problem. The enhanced local field due to the presence of long defect (made of n number of larger valued capacitors (conducting bonds) perpendicular to the electrode, is (following Beale and Duxbury [5])

$$E_e = E(1 + kn), \tag{34}$$

where E is the externally applied field and k is the enhancement factor. It is valid for all dimensions. The probability to find a long defect made of n conducting bonds is

$$P(n) \sim p^n L^d. \tag{35}$$

The most probable defect size is

$$n_c = -\frac{d}{\ln p} \ln L. \tag{36}$$

The enhanced field near the insulating bond adjacent to the most probable defect is now

$$E_e = E\left[1 + K_d\left(-\frac{\ln L}{\ln p}\right)\right]. \tag{37}$$

When enhanced field E_e of any bond attains threshold value of dielectric breakdown, local breakdown takes place and the bond becomes conducting. So breakdown voltage becomes

$$V_b = \frac{E_0 L}{\left[1 + K_d \left(-\frac{\ln L}{\ln p}\right)\right]}, \tag{38}$$

where E_0 is the breakdown field without defect.

Close to Critical Point ($p \to p_c$)

In this limit, consider the conducting defects that are on the average the percolation correlation length ξ_p distance apart. Hence, average field is $V_1/\xi_p = V/L$, where V and V_1 are externally applied voltage and potential difference between any two conducting defects, respectively. The maximum attainable field is V_1/a, where a is the minimum available separation (bond length) between the defects in the network. When the local electric field V_1/a reaches the bond-threshold value e_c, breakdown occurs. Now the required average electric field for local breakdown is $E_b = (a/\xi_p)e_c$. Near p_c, ξ_p diverges as $\xi_p(p) \propto a(p - p_c)^{-\nu}$. So the critical behaviour of the average breakdown field as derived by Lobb *et al.* [28] appears as

$$E_b \sim (p_c - p)^{\nu}. \tag{39}$$

in all dimensions. This can also be derived [49] from the concept of minimum gap $g(p)$, as E_b can be considered as proportional (see Sect. 2.4) to $g(p)$ and $g(p)$ is proportional to ξ_p^{-1} (see relation 20), the result above follows. Since E_b is inversely proportional to the linear dimension of the most vulnerable defect and the typical size of the defect or conducting clusters diverges at p_c, E_b approaches zero in this limit.

Influence of Sample Size

We consider a critical defect that is a pair of longitudinal very closely spaced clusters of conducting material (almost linear in shape) of the order of size l situated one after one, parallel to the direction of the applied field E in a L^d lattice. The field between these two clusters enhanced by a factor l time E. Far from p_c these clusters appear with the probability $(1/\xi_p)\exp(-l/\xi_p)$. Thus, the most dangerous defect (the largest cluster) is of the order of $l_{\max} \sim \xi_p \ln(L^d)$. The first breakdown field E_b^1 (field needed to break the first bond) scales as $1/l_{\max}$ in a finite but large system [5]. Since, in this particular case breakdown field for the sample is same as for the first breakdown, E_b becomes

$$E_b \sim \frac{(p_c - p)^{\nu}}{\ln L}. \tag{40}$$

This approximate expression for the average breakdown field was derived by Beale and Duxbury [5].

Larger sample has higher chance of having a larger vulnerable defect. So larger sample requires smaller electric field for breakdown and E_b becomes zero in the limit $L \to \infty$. Breakdown path is always on the average perpendicular to the electrode. So the above result is independent of dimension.

Due to the dominating behaviour of $(p_c - p)^\nu$ over $\ln L$, breakdown field tends to zero as p approaches p_c. Very near to p_c Chakrabarti and Benguigui ([12] p. 66) proposed a scaling relation as

$$E_b \sim \frac{(p_c - p)^\nu}{\ln(L/\xi_p)}. \tag{41}$$

According to Bergman and Stroud [7], E_b may become size independent very close to p_c, and a cross-over from extreme statistics to percolation dominated statistics may be there.

Summary

A general formula may be inferred for dielectric breakdown field as follows:

$$E_b = E_0 \frac{[(p_c - p)/p_c]^{\phi_b}}{1 + K\left[\frac{\ln(L/\xi_p)}{-\ln p}\right]}, \tag{42}$$

with the exponent ϕ_b (=ν for lattice percolation) dependent on the dimension and on the type of percolation. For the theoretically estimated value for ϕ_b (see Table 2).

Table 2. Theoretical estimates for the dielectric breakdown exponent ϕ_b

Dimension	Lattice percolation	Continuum percolation
2	$\nu(= 4/3)$	$\nu + 1(= 7/3)$
3	$\nu(\simeq 0.88)$	$\nu + 1(\simeq 1.88)$

3.2 Distribution of Breakdown Field

Distribution function $F_L(E)$ in dielectric breakdown is defined as the probability of breakdown of a dielectric system of size L in an external electric field E. Usually, Weibull distribution [52, 53]

$$F_L(E) = 1 - \exp(-rL^d E^m) \tag{43}$$

is used to fit the distribution function of breakdown and failure problems. Here r and m are constants. Duxbury and his co-workers [5, 18–20] argued that the distribution function for dielectric (and electrical) breakdown is given by Gumbell distribution:

$$F_L(E) = 1 - \exp\left[-AL^d \exp\left(-\frac{K}{E}\right)\right]. \tag{44}$$

It can be derived [5] from a simple scaling argument based on percolation cluster statistics [21, 25, 46]. It is valid for $L >> \xi_p$ or in dilute limit. The two expression (43) and (44) are qualitatively same if the Weibull exponent m is large. Although second one provides better fit to numerical simulation [5]. Sornette [44] argued that the expression (44) is not appropriate in continuum system having percolation type of disorder, rather, Weibull-like distribution is valid there.

3.3 Continuum Model

The model consists of dielectric material with the spherical (circular in $2d$) conducting inclusions as defects with randomly positioned centres having the possibility to overlap. We assume breakdown field E_b is proportional to the width δ. For breakdown ξ_p^{-1} numbers of link elements to be broken. With the same logic as in Sect. 2.3, $E_b \sim \delta_{\min}\xi_p^{-1} \sim L_c^{-1}\xi_p^{-1}$ or

$$E_b \sim (p_c - p)^{\nu+1} \tag{45}$$

very near to p_c [13, 28]. So continuum system is weaker than the discrete one. This is because the conductivities of the conducting channels increases as $p \to p_c$, whereas, conductivity of the bonds in discrete model is independent of p.

3.4 Shortest Path

The concept of shortest path is already mentioned in Sect. 2.4 in the context of electromigration. Just as before, we consider a walker starting to walk from one electrode with jump from one site to another and reaches the opposite electrode after executing a self-avoiding walk. The aim of the walker is to create a percolating conducting path by transforming a insulating bond to conducting bond when it jumps between two conducting sites separated by the insulating bond. n_0 denotes the total number of insulating bonds that are to be transformed into conducting bonds during walk across the sample. After completion of the walk, the sample experiences a continuous conducting path between the electrodes and in this way dielectric breakdown comes into existence.

The shortest path for a given configuration is defined as the path with the smallest n_0.The normalised smallest path is given by $g(p) =< n_0 > /L$, where $< n_0 >$ is obtained by considering the average of n_0 over a large number of configurations. Some authors call $g(p)$ by minimum gap.

The behaviour of $g(p)$ has been studied [20, 49] extensively in $2d$ and $3d$ for regular and directed percolation scenario. As p increases from zero to p_c, the minimum gap $g(p)$ decreases from unity to zero with the correlation length exponent ν.

3.5 Numerical Simulations in Dielectric Breakdown

Stochastic Models

In these models, stochastic growth processes are considered which mimic the dielectric breakdown processes. For example, Sawada et al. [42] considered a random growth process where growth takes place in two ways: tips of the pattern grow with a probability p_0 and new tips (branching) appear with probability p_n (here, $p_n < p_0$). In their simulation, the pattern appears as fractal and fractal dimension can be tuned by the parameter $R\ (= p_o/p_n)$. However, results of such a simplification do not satisfy experimental results of dielectric breakdown [37].

To mimic the dielectric discharge pattern in gasses Niemeyer et al. [36] suggested a stochastic model where the breakdown pattern generated in turn determines the local electric field and the growth probability. The model could reproduce the fractal properties of dielectric breakdown process by numerical simulations. In this model, the breakdown pattern starts growing from the centre of a lattice with insulating bonds. One electrode is placed at the centre and other one is placed at a long distance on the circumference of a circle. In one step, only one interface bond (and a point) among all the nearest neighbours of the pattern breaks down, depending upon the growth probability p and becomes the member of the pattern. The newly added bond becomes a conductor and the newly added site is shorted to the voltage of the central electrode. The growth starts from the centre and grows radially outwards. The growth probability p depends on the local field (potential), which in turn is controlled by the breakdown pattern via the relation

$$p(i,j \to i\prime, j\prime) = \frac{(V_{i\prime,j\prime})^{\eta}}{\sum (V_{i\prime,j\prime})^{\eta}}, \tag{46}$$

where the indices i, j and $i\prime, j\prime$ represent the discrete lattice coordinates. The electric potential V is defined for all sites of the lattice by the discrete Laplace equation

$$V_{i,j} = \frac{1}{4}(V_{i+1,j} + V_{i-1,j} + V_{i,j+1} + V_{i,j-1}) \tag{47}$$

with the boundary condition $V = 0$ for each point of the discharge pattern and $V = 1$ outside the external circle. η describes the relation between local field and growth probability. The fractal structure of the pattern has been seen to obey

$$N(r) \sim r^{d_f}, \tag{48}$$

where $N(r)$ is the total number of discharge points inside a circle of radius r and d_f is the Hausdorff dimensions. In $2d$ one has $d_f \simeq 2, 1.89 \pm 0.01, 1.75 \pm 0.02, 1.6$ for $\eta = 0, 0.05, 1, 2$, respectively. The structure tends to be more linear with larger η. The observed value of d for $\eta = 1$ is in good agreement with the experimental result $(\simeq 1.7)$ (Niemeyer and Pinnekamp [37]) and the resulting figure is very similar to Lichtenberg figure.

The same pattern for $\eta = 1$ has been produced surprisingly by a different growth model: diffusion-limited aggregation model (DLA) of Witten and Sadner [54] (For review see Meakin [31]). Niemeyer et al. neither justifies the appearance of η nor provides any theoretical explanation regarding explicit rule for breakdown. Many models (for details see Ref. [41]) have been proposed but a model that fully describes dielectric breakdown in solids is still lacking.

Deterministic Models

Contrary to Niemeyer et al. [36], Takayasu [50] introduced deterministic approach to produce dendritic fractal pattern (as is found in lightning) by considering *a priori* spatial fluctuation on bond resistances ($r_i = \theta r;\ \theta \in [0, 1]$) and the non-linear irreversible characteristics of the resistance: once the potential difference across a resistance r_i attain a pre-assigned threshold voltage v_c, r_i reduces to δr_i (δ is a small positive quantity) and its resistivity then never changes. This is the breakdown of a resistor in this model. Breakdown of a resistor induces successive breakdown of other resistors leading to the formation of percolation cluster of broken resistors. The pattern appears to be anisotropically fractal with the dimension $d_f = 1.58 \pm 0.12$ in $2d$. Due to anisotropy this d_f is less than the fractal dimension 1.89 of a percolating network in $2d$.

Family et al. [22] made the stochastic model of Niemeyer et al. [36] deterministic by attaching randomly a breakdown coefficient θ ($\theta \in [0, 1]$) to each insulating bond. There are two versions of this model: In one model, at each time step an interface bond ij with the largest θV_{ij}^{η} breaks down, whereas in the other model an interface bond breaks down with a probability $\theta V_{ij}^{\eta}/p_{\max}$, where η is an adjustable constant and $p_{\max}$ is the largest value of θV_{ij}^{η} among all the interface bonds. The patterns appear as tuneable (varying η) fractal. In the first model, stringy highly anisotropic (with branches) pattern with fractal dimension of about 1.2 appears in $2d$, whereas in the second one pattern is strikingly lacking in anisotropy. The shape of the pattern is similar to those found in Niemeyer et al. [36] except the fractal dimension of 1.70 ± 0.05 (for $\eta = 1$) in $2d$. The results for d_f appear same to that for DLA on a square lattice [30] and to that for the same model in a homogeneous medium (here, cross and square-shaped patterns appear) [22].

Direct simulations of dielectric breakdown from various groups confirmed the theoretical consideration for size and impurity dependence of breakdown voltages quite successfully. In these simulations, a discrete lattice of insulating bonds is considered with p fraction of bonds as conductors. Each insulator breaks down to conductor at a threshold value of voltage drop v_c. A macroscopic voltage is applied and the voltage distribution throughout the lattice is computed by solving Laplace equation (47). The insulator with largest voltage drop (at or above v_c) is converted to a conductor (incidence of first local breakdown). The voltage distribution is then recalculated, the second local breakdown is identified and the process continues. If at any step the applied voltage is not large enough to cause breakdown of any insulator, it is increased gradually. The simulation continues till a sample spanning cluster of conductors appears. The applied voltage V_b at which global breakdown occurs divided

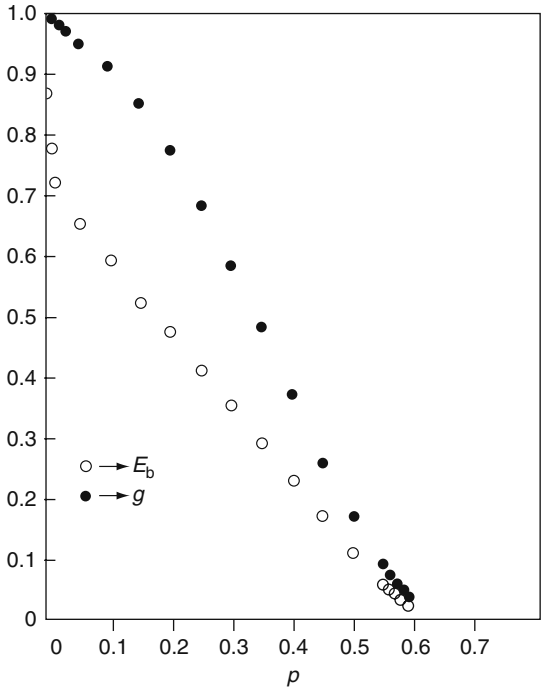

Fig. 4. The variation of first breakdown field E_b and the minimum gap $g(p)$ with initial impurity probability p, (after Manna and Chakrabarti [29]). The two quantities behave same very near to the percolation threshold p_c, whereas far from p_c they behave differently

by the sample size L is identified as breakdown field E_b. It has been experienced that the breakdown field E_b is same as the field E_b^1 required for the occurrence of first local breakdown.

Manna and Chakrabarti [29] determined the p dependence of both E_b^1 and $g(p)$ for the entire range of p below p_c. They found (see Fig. 4) that both E_b^1 and $g(p)$ go to zero at p_c with the exponent of value almost equal to 1. They argued that the exponent is actually ν and the smallness of the value is due to the smallness of the lattice size ($L = 25$, where exact p_c is not reachable). Bowman and Stroud [9] found that E_b^1 vanishes at p_c with an exponent equal to 1.1 ± 0.2 in $2d$ and 0.7 ± 0.2 in $3d$ for both site and bond problems. These are consistent with the correlation length exponent (ν) values of $4/3$ and 0.88 in $2d$ and $3d$, respectively.

Beale and Duxbury [5] proposed a relation for first (local) breakdown field as

$$E_b^1 \sim \frac{1}{A(p) + B(p) \ln L}. \tag{49}$$

Near p_c, they found $A(p)$ and $B(p)$ vary like $(p_c - p)^{-\nu}$ (in the lattice of size $L = 50, 70, 100$) as is expected from (40). From the plot of $\ln\{B(p) \ln(p)\}$ versus $-\ln(p_c - p)$ their data shows $\nu = 1.46 \pm 0.22$, which is in good agreement with

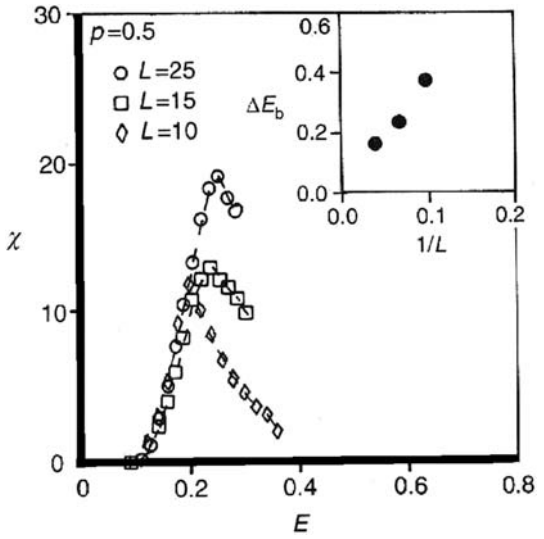

Fig. 5. The plot of dielectric breakdown susceptibility versus applied voltage for several sample sizes (after Acharyya and Chakrabarti [1]). The inset shows that the difference of the maximum susceptibility field and the minimum sample-spanning cluster field decreases with increasing sample size

exact value $4/3$ in $2d$. Their data fits well to the Gumbel double exponential form (44) for cumulative failure distribution. Manna and Chakrabarti [29] and Beale and Duxbury [5] found the exponent ϕ_b of Eq. (42) to be about 1.0 and 1.2, respectively.

Acharyya and Chakrabarti [2] found that starting with a concentration p ($p < p_c$) of the conductors, the rate at which the insulating bonds breaks down to conductors as the electric field is raised in a dielectric breakdown diverges at breakdown voltage V_b.

This indicates that global breakdown process is highly correlated very near to V_b. They defined a new quantity named as breakdown susceptibility χ ($= dn/dV$). Here, $n(V)$ is the average number of broken bonds at an external voltage V ($< V_b$) for a fixed value of p. It is obvious that for a sufficient voltage V, $n(V)$ saturates to L^d. χ exhibits a maxima at $V_b^{\rm eff}$ which is different from $V_b^{\rm fin}$, where $V_b^{\rm fin}$ is the voltage required to create the last member of the sample-spanning conducting cluster. $V_b^{\rm eff}$ approaches $V_b^{\rm fin}$ with increasing sample size L. It seems that χ is a divergent quantity for infinite sample (see Fig. 5). So there exists a possibility to predict V_b^{fin} without going to the complete breakdown point of the sample. Statistics of the growing clusters up to V_b (minimum external voltage required to have the global connection across the sample via the conducting sites) in $2d$ site percolation was studied by Acharyya et al. [3]. V_b is identified not only as the point of global breakdown but also the point of divergence of the rate of the various statistical quantities such as

total number of conducting sites, the average size of the conducting cluster and the number of such clusters.

4 Zener Breakdown in Anderson Insulators

From the microscopic point of view, current conduction requires the mobility of the electrons across the material and for composites of metals and dielectrics or insulators this means that there must be percolating paths of conducting material in the system (as long as electron is considered a classical particle). If p denotes the concentration of the conducting material in the composite and p_c the percolation threshold, then from our previous discussion we know that the conductivity will go to zero at p_c as $|p - p_c|^{t_c}$ [47, 48]. For p below p_c, the composite ceases to be conducting and the classical breakdown voltage needed to make the system conducting goes as $|p - p_c|^{\phi_b}$ (see Sect. 3.1).

Studies on Anderson transition (see Ref. [26] for example) show that electron as a quantum particle cannot diffuse even through the geometrically percolating path due to the coherent back scattering (of the wave function) from the random geometry of the cluster in a dimension less than three. Since all the states on any percolating lattice gets localised (exponentially) electrons do not diffuse through the disordered (percolating) lattice.

In a three dimensional disordered systems, there exist a mobility edge (a sharp energy level in conduction band) ϵ_c below which all the states are localised and above which all the states are extended. Insulting or conducting phase appears depending upon the position of Fermi level ϵ_f below or above the mobility edge ϵ_c. The (Anderson) transition from the insulating phase $(\epsilon_f < \epsilon_c)$ to metallic phase $(\epsilon_f > \epsilon_c)$ (where the electrons are quantum mechanically percolating that is their wave functions extend all over) across the mobility edge in a percolating disordered solid, has already been well studied [26]. In metallic phase, the conductivity increases as $|\epsilon_f - \epsilon_c|^{t_q}; t_q \neq t_c$.

In the case of a classical non-percolating $(p < p_c)$ system, an application of an external electric field E_b forces the system to undergo breakdown following the relation $E_b \sim |p_c - p|^{\nu}$ (see Sect. 3.1). In analogy with the above classical dielectric breakdown problem, one can think of a problem of quantum dielectric breakdown (possibility of the appearance of a conducting path) in Anderson insulating ($\epsilon_f < \epsilon_c$ or quantum mechanically non-percolating) phase with an application of strong electric field. This may be thought as a kind of complementary problem of the Zener breakdown in insulator.

In an insulator, states are localised exponentially within the atomic distance a and effective band width w is in general larger than a. There exists a possibility of tunnelling of the states across the band gap if the energy gained by an electron in travelling an atomic distance a in an electric field E is larger or equal to the band gap $\triangle\epsilon_b$ (or when $eEa \geq \triangle\epsilon_b$). Here e denotes the electronic charge and the band gap is the separation between conduction and valance band. In Zener breakdown, bands get effectively tilted in strong electric field E in the direction of the field, reducing

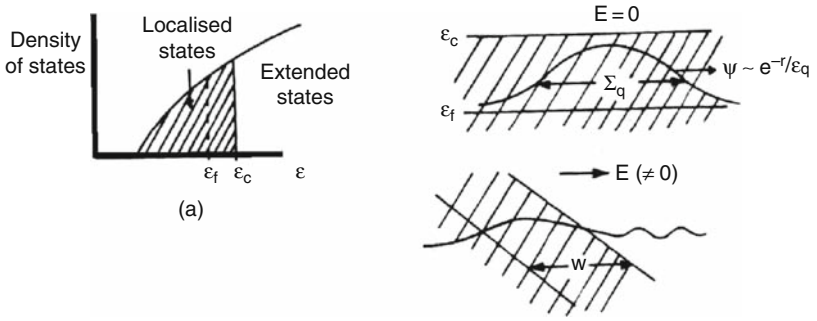

Fig. 6. Schematic density of states for Anderson insulators ($d > 2$) shown in (**a**), where the Fermi label ϵ_f is below the mobility edge ϵ_c (metallic phase for $\epsilon_f > \epsilon_c$). For strong electric field E, the band of (localized) states get tilted and tunnelling occurs when the effective width $w(= |\triangle\epsilon_m|/eE)$ of the mobility gap $\triangle\epsilon_m$, is less than or equal to the localization length ξ_q

the band gap effectively from $\triangle\epsilon_b$ to eEa. If the effective width of the reduced band gap ($w = \triangle\epsilon_b/eE$) becomes of the order of atomic distance a interband tunnelling takes place for $w \leq a$ and the insulation breaks down. So the Zener breakdown field E_b scales linearly with the band gap: $E_b = \triangle\epsilon_b/ea$.

Similar kind of breakdown of insulation can occur in the case of Anderson insulators with an application of strong electric field E in more than two dimension. States are localised (exponentially) with in the localisation length ξ_q, where ξ_q varies as $\xi_q \sim |\triangle\epsilon_m|^{-\nu_q}$. Here $\triangle\epsilon_m$ is the mobility gap; $\triangle\epsilon_m \equiv \epsilon_c - \epsilon_f$. One can now easily think of a possibility of tunnelling across the mobility gap, if the energy gained by an electron in travelling a distance ξ_q in field E is of the order of the mobility gap $\triangle\epsilon_m$ (or when $eE\xi_q \geq \triangle\epsilon_m$). Thus, in contrary to the standard Zener breakdown in semiconductors, here breakdown field E_b scales almost quadratically with mobility gap as [11]

$$E_b = \frac{\triangle\epsilon_m}{e\xi_q} \simeq |\triangle\epsilon_m|^{T_q};\ T_q = 1 + \nu_q \tag{50}$$

($\nu_q \sim 0.9$ [26, 32–34], giving $T_q \sim 1.9$ in $3d$).

The tunnelling probability $g(E)$ decreases exponentially with the width of the effective barrier as $g(E) \sim exp(-w/\xi_q) \sim exp(-\triangle\epsilon_m/eE\xi_q) \sim exp(-|\triangle\epsilon_m|^{T_q}/E)$. The cumulative failure probability of Gumbel form (same as for fracture [18–20]) for a sample of size L under field E is given by [11]

$$\begin{aligned} F_L(E) &\sim 1 - exp[-L^d g(E)] \\ &\sim 1 - exp\left[-L^d exp\left(-\frac{|\triangle\epsilon_m|^{T_q}}{E}\right)\right]. \end{aligned} \tag{51}$$

This gives

$$E_b \sim \frac{|\triangle\epsilon_m|^{T_q}}{\ln L}, \tag{52}$$

as the size dependence of the typical breakdown field for and above which $F_L(E)$ is significant.

5 Conclusions

We have discussed the classical failure of the fuse system, the dielectric breakdown and the quantum breakdown in the Anderson insulators. We have discussed how the extreme value statistics and the resulting Gumbel distribution arises in breakdown and failure processes, especially when the disorder concentration is low. At high concentration of disorder near the percolation threshold, we have discussed how the cross-over might take place from extreme value to percolation statistics. We discussed the system size dependence that arises at the distribution of the failure current at low disorder regime. Finally, the extension of Zener breakdown phenomenon for band insulators to the disorder-induced Anderson insulators have been discussed in Sect. 4.

References

1. M. Acharyya and B.K. Chakrabarti, Phys. Rev. E **53** 140 (1996) 246
2. M. Acharyya and B.K. Chakrabarti, Physica A **224** 254 (1996) 246
3. M. Acharyya, P. Ray, and B.K. Chakrabarti, Physica A **224** 287 (1996) 246
4. C. Baudet, E. Charlaix, E. Clement, E. Guyon, F.P. Hulin, and C. Leroy. In: *Scaling Phenomena in Disordered Systems*, eds R. Pynn and A. Skjeltorp, p. 399 (Plenum; New York, 1985) 235
5. P.D. Beale and P.M. Duxbury, Phys. Rev. B **37** 2785 (1988) 239, 240, 241, 242, 245, 246
6. L. Benguigui, Phys. Rev. B **34** 8176 (1986) 235
7. D.J. Bergman and D. Stroud. In: *Sol. State Phys.* **46** eds H. Ehrenreich and D. Turnbull, p. 147 (Academic Press, New York, 1992) 233, 241
8. D.R. Bowman and D. Stroud, Bull. Am. Phys. Soc. **30** 563 (1985) 239
9. D.R. Bowman and D. Stroud, Phys. Rev. B **40** 4641 (1989) 238, 239, 245
10. R.M. Bradley and K. Wu, Phys. Rev. E **50** R631 (1994) 236
11. B.K. Chakrabarti. In: *Non-Linearity and Breakdown in Soft Condensed Matter* eds K.K. Bardhan, B.K. Chakrabarti, and A. Hansen, p. 71 (Springer-Verlag, Heidelberg, 1994) 248
12. B.K. Chakrabarti and L.G. Benguigui. In: *Statistical Physics of Fracture and Breakdown Disordered Systems* (Oxford Uninversity Press, Oxford 1997) 229, 234, 235, 239
13. B.K. Chakrabarti, A.K. Roy, and S.S. Manna, J. Phys. C **21** L65 (1988) 242
14. J.T. Chayes, L. Chayes, and R. Durret, J. Stat. Phys. **45** 933 (1986) 236
15. A. Coniglio, J. Phys. A: Math. Gen. **15** 3829 (1982) 235
16. L. de Arcengelis, S. Redner, and A. Conilgo, Phys. Rev. B **31** 4725 (1985) 237, 238
17. P.G. de Gennes, J. Physique Lett. **52** L1 (1976) 231, 235
18. P.M. Duxbury, P.D. Beale, and P.L. Leath, Phys. Rev. Lett. **57** 1052 (1986) 229, 230, 241
19. P.M. Duxbury, P.D. Beale, and P.L. Leath, Phys. Rev. B **36** 367 (1987) 230, 237, 238, 241
20. P.M. Duxbury and P.L. Leath, J. Phys. A **20** L411 (1987) 241, 242, 248

21. J.W. Essam, Rep. Prog. **43** 833 (1980) 242
22. F. Family, Y.C. Zhang, and T. Vicsek, J. Phys. A **19** L733 (1986) 244
23. E.J. Gumbel. In: *Statistics of Extremes* (Columbia University Press, New York, 1958) 234
24. B.I. Halperin, S. Feng, and P. Sen, Phys. Rev. Lett. **54** 2391 (1985) 235
25. K. Kunz and B. Souillard, Phys. Rev. Lett. **40** 133 (1978) 242
26. P. Lee and T.V. Ramakrishnan, Rev. Mod. Phys. **57** 287 (1985) 229, 247, 248
27. Y.S. Li and P.M. Duxbury, Phys. Rev. B **36** 5411 (1987) 233
28. C.J. Lobb, P.M. Hui, and D. Stroud, Phys. Rev. B **36** 1956 (1987) 240, 242
29. S.S Manna and B.K. Chakrabarti, Phys. Rev. B **36** 4078 (1987) 245, 246
30. P. Meakin, J. Phys. A: Math. Gen. **18** L661 (1985) 244
31. P. Meakin. In: *Fractals, Scaling and Growth far from Equilibrium* (Cambridge University Press, Cambridge, 1998) 244
32. Y. Meir, A. Aharony, and A.B. Harris, Euro. Phys. Lett. **10** 275 (1989) 248
33. Y. Shapir, A. Aharony, and A.B. Harris, Phys. Rev. Lett. **56** 976 (1986); 248
34. B. Shapiro. In: *Percolation Structure and Processes*, eds G. Deutscher, R. Zallen, and J. Adler, p. 367 (Hilger, Bristol, 1983) 248
35. K.S. Mendelson, J. Appl. Phys. **46** 917, 4740 (1975) 238
36. L. Niemeyer, L. Pietronero, and H.J. Wiesmann, Phys. Rev. Lett. **52** 1033 (1984) 243, 244
37. L. Niemeyer and F. Pinnekamp. In: *Gaseous Dielectrics III*, ed L.G. Christophorou, p. 379 (New York, Pergamon, 1982) 243
38. P. Ray and B. K. Chakrabarti, J. Phys. **C18** L185 (1985) 229
39. P. Ray and B. K. Chakrabarti, Solid State Commun. **53** 477 (1985) 229
40. M. Sahimi, *Application of Percolation Theory* (Taylor and Francis, London, 1994) 232
41. M. Sahimi, *Heterogeneous Materials II: Nonlinear and Breakdown Properties and Atomistic Modeling*, p. 207 (Springer, 2002) 239, 244
42. Y. Sawada, S. Ohta, M. Yamazaki, and H. Honjo, Phys. Rev. A **26** 3997 (1982) 243
43. A. Skal and Shklovskii, Sov. Phys.-Semicond. **8** 1029 (1975) 231, 235
44. D. Sornette, J. Physique **49** 889 (1988) 242
45. H.E. Stanley, J. Phys. A: Math. and Gen. **10** L211 (1977) 231
46. D. Stauffer, Phys. Rep. **54** 1 (1979) 242
47. D. Stauffer and A. Aharony, *Introduction to Percolation Theory* (Taylor and Francis, London, 1992) 228, 232, 235, 247
48. D. Stauffer. In: *Quantum and Semi-classical Percolation and Breakdown in Disordered Solids* (Springer, Heidelberg, 2009) 228, 232, 235, 247
49. R.B. Stinchcombe, P.M. Duxbury, and P.K. Shukla, J. Phys. A: Mathematical and General **19** 3903 (1986) 236, 240, 242
50. H. Takayasu, Phys. Rev. Lett. **54** 1099 (1985) 244
51. K.N. Tu, J. Appl. Phys. **94** 5451 (2003) 236
52. W. Weibull, *Fatigue Testing and Analysis of Results* (Pergamon, New York, 1961) 241
53. S.M. Weiderhorn, Ann. Rev. Mater. Sci. **14** 373 (1984) 241
54. T.A. Witten and L.M. Sander, Phys. Rev. Lett. **47** 1400 (1981) 244
55. K. Wu and R.M. Bradley, Phys. Rev. B **50** 12468 (1994) 236

Nonequilibrium Quantum Breakdown in a Strongly Correlated Electron System

T. Oka and H. Aoki

Department of Physics, University of Tokyo, Hongo, Tokyo 113-0033, Japan
oka@cms.phys.s.u-tokyo.ac.jp, aoki@cms.phys.s.u-tokyo.ac.jp

1 Introduction

During the past decades, there has been an increasing fascination and surprises with diverse *quantum many-body effects*. With the magical touch of interaction a simple electron system may assume insulating, metallic, magnetic or superconducting states according as the control parameters are changed. Strongly correlated electron systems, as exemplified by the high-Tc superconductors and their host materials realized in transition-metal oxides, as well as by organic metals, have provided us with an ideal playground, where various crystal structures with band-filling control and band-width control etc., provide the richness in the phase diagram [1].

On the other hand, there is a long history of interests in *nonequilibrium phase transitions*. Statistical mechanically, there is an intriguing problem of how we can generally define the notion of a 'phase' in nonequilibrium systems, but we can still discuss individual systems in specified nonequilibrium conditions to extract more general viewpoints. Now, if we combine the above two ingredients, namely if we consider *strongly correlated electron systems in nonequilibrium*, we plunge into an even more fascinating physics (Fig. 1). In fact, recent years have witnessed an upsurge of interests in nonequilibrium states in many-body systems with drastic changes in the electronic states in strong dc electric fields, in intense laser fields, etc.

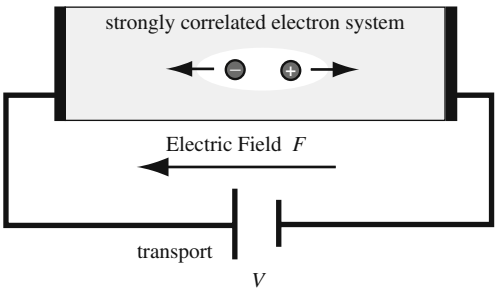

Fig. 1. Non-linear transport and optical response

Oka, T., Aoki, H.: *Nonequilibrium Quantum Breakdown in a Strongly Correlated Electron System*. Lect. Notes Phys. **762**, 251–285 (2009)
DOI 10.1007/978-3-540-85428-9_9

Developments in fabrication techniques such as realization of clean thin films with electrodes attached have triggered several groundbreaking experiments, for example, nonlinear transport measurements in thin films [2–7], in layered systems [8] and observations of clean metallic states in heterostructures [9]. Nonlinear phenomena in correlated electron systems now begin to attract interests in a wide range of researchers. One obvious area of application is future-generation electronic devices, where a high sensitivity of a system near a phase boundary to external conditions may lead to drastic functionalities [2]. However, even more attractive is its relevance to fundamental physics, especially, to nonequilibrium statistical physics, where we can observe the behavior of various phase transitions taking place under nonequilibrium conditions.

The purpose of the present article is to discuss the nonequilibrium metal-insulator transition in strongly correlated electron systems [10–13], which is known, for equilibrium systems, as Mott's transition. Before going into detail, we first give a brief introduction of the transition, and discuss how quantum breakdown through nonadiabatic transitions in nonequilibrium becomes relevant in nonlinear transports.

The model we study is the single-band Hubbard model, which is the simplest possible one that captures many essential properties of correlated electron physics. The Hamiltonian reads

$$H_0 = -t_{\rm hop} \sum_{\langle i,j\rangle\sigma} \left(c^\dagger_{i\sigma} c_{j\sigma} + \text{h.c.} \right) + U \sum_i n_{i\uparrow} n_{i\downarrow}, \tag{1}$$

where $c_{i\sigma}$ annihilates an electron on-site i with spin σ, $n_{i\sigma} = c^\dagger_{i\sigma} c_{i\sigma}$ the number operator, U the strength of the on-site Coulomb repulsion, and $t_{\rm hop}$ the hopping integral. The filling $n = \dfrac{1}{L} \sum_{i=1}^{L} \langle n_{i\uparrow} + n_{i\downarrow} \rangle$, with L the number of sites, is an important parameter, which changes the groundstate property drastically.

When the band is half-filled with one electron per site on average ($n = 1$), each electron tends to be localized on a separate lattice site and the spin tends to be antiferromagnetically correlated. When U/t is large enough, the groundstate is insulating, which is called Mott's insulator (Fig. 2(a)), and the groundstate is separated from the charge excited states with a many-body energy gap – Mott gap. When we inject

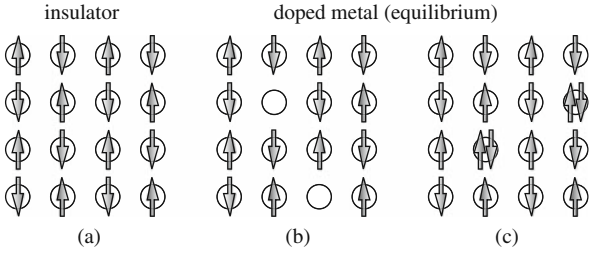

Fig. 2. Metal-insulator transition in equilibrium due to doping: (**a**) A Mott insulator realized at half filling. (**b**) A hole-doped metallic state. (**c**) An electron-doped metallic state

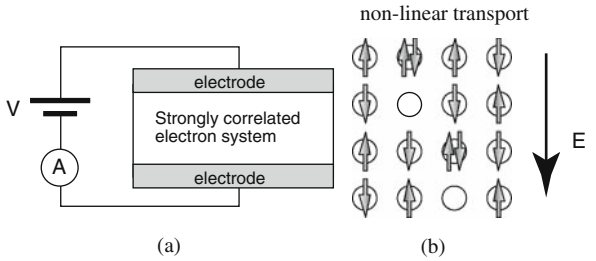

Fig. 3. (**a**) Schematic experimental configuration. (**b**) Carriers (doublons and holes) created by an external electric field

carriers (usually with a chemical doping by adding or replacing to other elements) to increase (electron doping) or decrease (hole doping) the filling from unity, the Mott gap collapses for large enough doping, and the system becomes metallic. This is the metal-insulator transition or the Mott transition, which is widely observed in strongly correlated materials. In these materials, a state occupied simultaneously by up and down spin electrons—which we call a doublon—and holes carry the current. After the discovery of the high-temperature superconductivity in cuprates, carrier-doped Mott insulators have been subject to a huge number of experimental and theoretical studies.

Now, let us consider what will happen if we attach a set of electrodes to a strongly correlated sample, and apply a large bias voltage across the electrodes (Fig. 3 (a)). Although the setup may seem simple enough, there is a profound physics involved.

In regions near the electrodes (or near the interface in the case of heterojunctions between a strongly correlated and ordinary materials), a "band bending" similar to doped semiconductors can take place and lead to an interface Mott transition when the filling becomes one [14]. The width of the insulating layer changes as the applied bias is changed, which dominates the behavior of the nonlinear transport (i.e. the I-V characteristics). The result (with DMRG + Hartree potential) for the band-bending effects in this case can be understood if we assume a *local equilibrium* for the relation between the density of electrons and the potential. The local properties are determined by the Hartree potential governed by Poisson's equation, which in turn determines the local chemical potential and controls the metal-insulator transition.

Even more interesting, however, is the case where we no longer have local equilibrium. Specifically, a *quantum many-body breakdown of a Mott's insulator* takes place when the applied electric field is large enough and creates doublons and holes in the Mott insulating groundstate (Fig. 3(b)) [11–13].

The creation mechanism is a many-body analogue of the "Zener breakdown" , well-known in semiconductor physics [15]. Namely, while we cannot use the notion of the electronic band structure for correlated electron systems, we can envisage the carrier-creation process as a tunneling across a kind of barrier. As displayed in Fig. 4, production of carriers occurs through tunneling between the Mott insulating ground state and excited states with doublons and holes. If we denote the distance between a doublon and a hole by $l_{\rm dh}$, the energy profile as a function of $l_{\rm dh}$ roughly reads

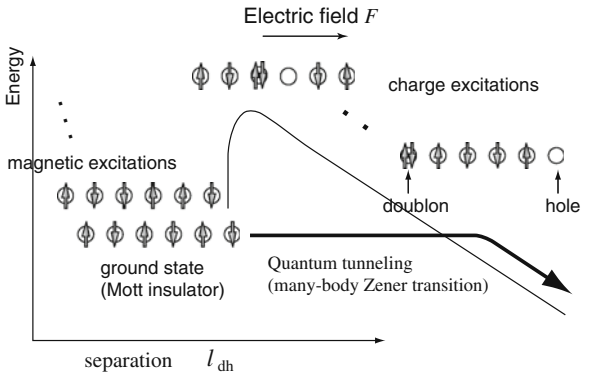

Fig. 4. Dielectric breakdown of a Mott insulator in a strong electric field due to many-body Landau-Zener transition: The ground state and excited states with charge excitations are separated by an energy barrier, and quantum tunneling among many-body states takes place when the electric field is strong enough

$$\Delta E \sim U - l_{\rm dh} F, \tag{2}$$

where F is the strength of the electric field. The profile curve reaches the energy before the creation of the doublon-hole pair for the separation at which

$$\Delta E \sim U - \bar{l}_{\rm dh} F = 0, \tag{3}$$

to which the tunneling becomes possible. There is a threshold field strength for this process to occur. This is because larger quantum fluctuations are required to have a larger separation between doublon and hole in the Mott insulator.

In other words, the overlaps of many-body wave function of the ground state and excited states decrease rapidly for large $l_{\rm dh}$. We can formulate this with the Landau-Zener picture in the time-dependent gauge for the external electric field, for which, as we shall show below [12] (50), the threshold field strength is given by

$$F_{\rm th} = \frac{\Delta_{\rm c}(U)^2}{8 t_{\rm hop}}, \tag{4}$$

where $\Delta_{\rm c}(U)$ is the charge gap (i.e. the Mott gap), and the tunneling rate per length is given by

$$\Gamma(F)/L = -\frac{2F}{h} a \ln\left[1 - p(F)\right], \tag{5}$$

where $p(F) = e^{-\pi \frac{F_{\rm th}}{F}}$ is the tunneling probability and a a non-universal constant depending on the detail of the system. The tunneling rate $\Gamma(F)/L$, being related to the production rate of carriers, is directly related to physical properties in the bulk if the interface effect is neglected. Indeed, such a nonlinearity in the I-V characteristics has been observed in real materials, most prominently in a one-dimensional copper oxide [16].

Another interesting consequence of (3) is that it gives the "critical separation" of the doublon-hole excitation $\bar{l}_{\rm dh} = U/F_{\rm th}$. This has to do with the convex shape of the energy profile against $l_{\rm dh}$ (Fig. 4), which is reminiscent of the energy profile for the standard nucleation theory that treats the critical size of a stable-phase droplet to grow without being crushed, although the physics involved is quite different. In the present case, when the field is greater than the threshold, the *electric-field induced metallic state*, where doublon-hole pairs continue to be created, becomes the stable phase.

The first goal of this article is to derive the relations presented above and study the creation mechanism of carriers (this part is the extended argument of our papers [12, 13]). We need to treat the process quantum mechanically and in a many-body formulation. In doing so, we present a renewed and unified interpretation of the Zener transition of insulators . The key quantity is the effective Lagrangian of quantum dynamics (see Sect. 2.2 for a detailed introduction) which is defined by [12]

$$\mathcal{L}(F) = -\frac{i}{L^d} \lim_{t\to\infty} \frac{1}{t} \ln \Xi(t), \tag{6}$$

where $\Xi(t)$ is the ground state-to-ground state transition amplitude and L^d is the volume of the d dimensional system and L the linear size. There is a deep relation between the theories of dielectric breakdown in condensed matter and a branch in quantum field theory known as nonlinear quantum electrodynamics (QED) (Table 1). The effective Lagrangian defined above coincides with the Heisenberg-Euler effective Lagrangian for nonadiabatic evolution [12, 17]. The effective Lagrangian have been used to study the Schwinger mechanism of electron-positron pair production from the QED vacuum in strong electric fields [18]. In fact, we show that the Schwinger mechanism and the Zener tunneling are equivalent, where the effective action coincides if we consider the breakdown of simple Dirac type band insulators. Furthermore, the effective action gives the nonadiabatic extension of the Berry phase theory of polarization.

Table 1. Relation between the theory of dielectric breakdown in condensed matter and nonlinear QED from the point of view of the effective Lagrangian

	Dielectric breakdown in cond. matter	Non-linear QED
Mechanism	Zener breakdown [13]	Schwinger mechanism [18]
Excitation	Electron (doublon)-hole pair	Electron-positron pair
Effect of interaction	Many-body Landau-Zener	back reaction
Nonlinear polarization	Cross correlation (ME effect)	photon-photon interaction
	Nonadiabatic Berry phase theory [12]	–

In the latter part of the chapter we shall discuss the effect of annihilation of doublon-hole pairs (Fig. 5). In a one-dimensional system, a doublon and a hole

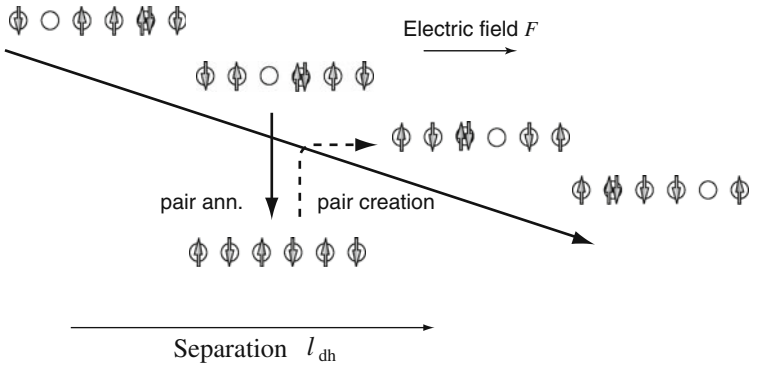

Fig. 5. Annihilation processes for carriers in a correlated electron system

cannot pass each other without being pair-annihilated even as virtual processes. Since the ground state is locally stable, the many-body state tends to remain in the ground state, but there should be a finite probability for the state to "branch into" excited states through many paths in the many-body energy space. Thus, the long-time behavior of the wave function involves numerous scattering processes in the energy space, where, as we shall see, the phase interference plays a key role. We can indeed regard the phase before the dielectric breakdown takes place as a dynamical localization in the many-body energy space, which reduces the tunneling rate and makes the groundstate survive [10, 11]. A statistical mechanical treatment helps in understanding this, and we briefly discuss it in terms of the quantum walk.

A brief comment on the numerical methods used in the article. In order to understand the nonequilibrium processes, we need to integrate the time-dependent, many-body Schrödinger equation to look at the evolution of the many-body wave function in, say, the Hubbard model in strong electric fields. This is a formidable task, for which no analytically exact treatment is known, therefore we rely on several numerical methods, which include the exact diagonalization and the time-dependent density matrix renormalization group method (td-DMRG; The version of td-DMRG we adopt is the one proposed by White and Feiguin [19]).

2 Nonadiabatic Evolution and Pair Creation of Carriers

2.1 Electric Fields and Gauge Transformation

When we describe a system in finite electric fields, we can choose from two gauges. One is the case where we have a slanted electrostatic potential, with the gauge field $A^{\mu} = (Fx, 0)$ for a one-dimensional system with $F = eE$ being the electric field, while the other represents the electric field via a time-dependent vector potential, $A^{\mu} = (0, -Ft)$.

In the first gauge, the tilted potential enters in the Hamiltonian as

$$H(F) = H_0 + F\hat{X}, \quad \hat{X} = \sum_j j n_j, \tag{7}$$

where $\hat{X}$ is the position operator [20] and H_0 the original Hamiltonian. This gauge is *in*compatible with systems that have periodic boundary conditions. The Hamiltonian $H(F)$ in fact becomes an unbounded operator in an infinite system, since one can lower the energy indefinitely by moving an electron to $j \to -\infty$.

In the other gauge, which we call the time-dependent gauge, the hopping term of the Hamiltonian becomes time-dependent as

$$H(\phi(t)) = -t_{\text{hop}} \sum_{i\sigma} \left(e^{i\frac{2\pi}{L}\phi(t)} c^{\dagger}_{i+1\sigma} c_{i\sigma} + \text{h.c} \right) + \hat{V}, \tag{8}$$

where $\Phi(t)$ represents a time-dependent Aharonov-Bohm(AB) flux,

$$\phi(t) \equiv \Phi(t)/\Phi_0 = FLt/h. \tag{9}$$

Physically, this gauge amounts to considering a periodic system (a ring) and a magnetic flux piercing the ring, where the time-dependent flux induces electric fields by Faraday's law (Fig. 6). For a higher-dimensional system, the ring becomes a (generalised) torus. The time-dependent gauge is suited for periodic systems since it is compatible with the lattice translation symmetry. The electric current operator is obtained by differentiating the Hamiltonian by A^1 as

$$J(\phi) = -\frac{dH(\phi)}{dA^1} = -it_{\text{hop}} \sum_{i\sigma} \left(e^{i\frac{2\pi}{L}\phi} c^{\dagger}_{i+1\sigma} c_{i\sigma} - e^{-i\frac{2\pi}{L}\phi} c^{\dagger}_{-i\sigma} c_{i+1\sigma} \right). \tag{10}$$

There exists an important operator relation among H, J and $\hat{X}$,

$$J(\phi) = \frac{i}{\hbar} \left[H(\phi), \hat{X} \right], \tag{11}$$

which comes from Heisenberg's equation of motion for the current operator, $J(\phi) = \frac{d}{dt}\hat{X}$.

We can relate the two gauges with a twist operator [21] defined by

$$g(\phi) = e^{-i\frac{2\pi}{L}\phi\hat{X}}, \tag{12}$$

and the two Hamiltonians are related by a gauge transformation generated by the twist operator, that is,

$$H(F) = g^{\dagger}(\phi(t))H(\phi(t))g(\phi(t)) - ig^{\dagger}(\phi(t))\partial_t g(\phi(t)). \tag{13}$$

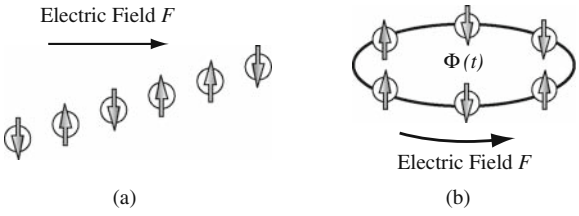

Fig. 6. (**a**) Time-independent gauge. (**b**) Time-dependent gauge

2.2 Heisenberg-Euler Effective Lagrangian

We first discuss the nonadiabatic evolution of electron wave functions in insulators (either one-body or many-body) in strong electric fields. Let us consider an insulator at $T = 0$ and $F = 0$, which is described by the ground state wave function $|\Psi_0\rangle$. We then switch on the electric fields at $t = 0$ to study the quantum mechanical evolution of the system. We limit our discussions to coherent dynamics and ignore the effect of dissipation due to heat bath degrees of freedom as well as boundary effects near the electrodes.

A key quantity to study the nonadiabatic evolution and quantum tunneling in strong electric fields is the (condensed-matter counterpart to the) effective Lagrangian introduced for QED by Heisenberg and Euler [17]. In the time-independent gauge, the electrons are described by the solution of the Schrödinger equation,

$$|\Psi(t)\rangle = e^{-itH(F)}|\Psi_0\rangle, \tag{14}$$

where we have put $\hbar = 1$. The overlap of the solution with the ground state for $F = 0$ – groundstate-to-groundstate transition amplitude – should contain the information on the tunneling processes, so we define

$$\Xi(t) = \langle\Psi_0|e^{-itH(F)}|\Psi_0\rangle e^{itE_0}, \tag{15}$$

where we have factored out the trivial dynamical phase of the ground state, $E_0 = \langle\Psi|H(F = 0)|\Psi\rangle$. In the case of the time-dependent gauge, we need to be careful, since the ground state is ϕ dependent. If we denote $|0;\phi\rangle$ as the instantaneous groundstate of $H(\phi)$ and its energy as $E_0(\phi)$, the groundstate-to-groundstate transition amplitude becomes

$$\Xi(\tau) = \langle 0;\phi(\tau)|\hat{T}e^{-\frac{i}{\hbar}\int_0^\tau H(\phi(s))ds}|0;\phi(0)\rangle e^{\frac{i}{\hbar}\int_0^\tau E_0(\phi(s))ds}, \tag{16}$$

where $\hat{T}$ stands for the time ordering, and $E_0(\phi) = \langle 0;\phi(\tau)|H(\phi)|0;\phi\rangle$ the dynamical phase of the ground state.

We define [12] the effective Lagrangian by

$$\mathcal{L}(F) = -\frac{i}{L^d}\lim_{t\to\infty}\frac{1}{t}\ln\Xi(t), \tag{17}$$

where L^d is the volume of the d dimensional system with a linear dimension of L. We can also regard the Lagrangian as the exponent of the asymptotic behavior of the amplitude, $\Xi(\tau) \sim e^{i\tau L^d\mathcal{L}(F)}$. When the electric field is large enough, the groundstate becomes unstable with the quantum tunneling to excited states activated. The tunneling rate is described by the imaginary part of the effective Lagrangian,

$$\Gamma(F)/L^d \equiv 2\mathrm{Im}\ \mathcal{L}(F), \tag{18}$$

which gives the rate of the exponential decay of the vacuum (groundstate). In the quantum field theory, the decay rate of an unstable vacuum has been discussed by

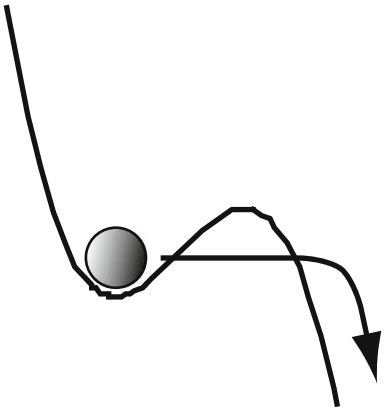

Fig. 7. The original problem studied by Callan and Coleman in which quantum tunneling from an unstable vacuum is considered [22]

Callan and Coleman, where the tunneling takes place when the potential is suddenly changed by an external field [22] (Fig. 7).

As we shall see later in several models, in the theory of dielectric breakdown, the tunneling corresponds to creation of charge carriers. In band insulators the carriers are electrons and holes, while in Mott insulators they are doublons and holes. If we neglect boundary effects and assume that all the carriers are absorbed by electrodes, we can conclude that the tunneling rate is proportional to the leakage current, that is,

$$J_{\text{leak}} \propto \Gamma(F)/L^d. \tag{19}$$

Indeed, this is the original picture of Zener when he calculated the leakage current in a simple band insulator (Fig. 8). Zener has studied the dielectric breakdown in a simple one-dimensional insulator, using the time-independent gauge [23] as well as the time-dependent gauge [15]. In the former, he has calculated the tunneling probability of Bloch functions in constant electric fields to obtain the tunneling rate. In,

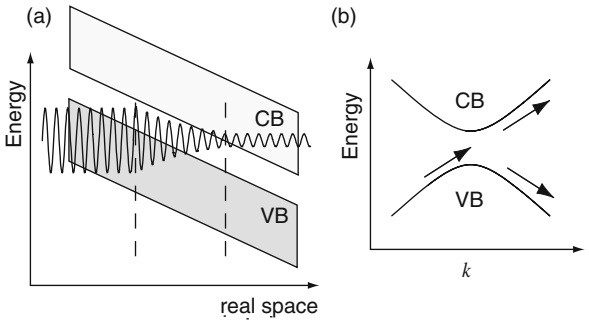

Fig. 8. Two models of the dielectric breakdown studied by Zener. (**a**) Time-independent gauge. (**b**) Time-dependent gauge

the time-dependent gauge, he has described the problem as a system with a time dependent Hamiltonian represented by a two-by-two matrix to study the tunneling near the level anti-crossing, which is now known as the Landau-Zener transition [15, 24].

The reason why we have called $\mathcal{L}(F)$ the effective Lagrangian is that it coincides with the Heisenberg-Euler effective Lagrangian in QED [17]. They have studied the dynamics and nonlinear responses of the QED vacuum in strong electric fields by calculating the effective Lagrangian (for a review, see e.g. [25]). By integrating out high-energy degrees of freedom (polarization processes due to electron-positron creation/annihilation) they arrived at an effective description of the low-energy degrees of freedom, namely the quantum correction, originating from the fluctuation of the QED vacuum, to the Maxwell theory of electromagnetism. Indeed, if we apply our formalism to band insulators with Dirac-type (mass-gapped) dispersions, the effective Lagrangian coincides with the Heisenberg-Euler Lagrangian with some modifications coming from the Brillouin zone structure of the Bloch waves as will be shown in the next section. The correspondence between the two phenomena is straightforward: The ground state of the insulator translates to the QED vacuum, charge excitations to the electron-positron pairs. The tunneling rate also has its QED counterpart, namely, the vacuum decay rate due to the Schwinger mechanism – creation of electron-positron pairs in strong electric fields [18].

Related Theories

We conclude this section with comments on the relation of the effective Lagrangian approach to earlier theoretical frameworks.

Berry's phase theory of polarization:

In the Berry's phase theory of polarization [26–29], the ground state expectation value of the twist operator $e^{-i\frac{2\pi}{L}\hat{X}}$, which shifts the phase of electron wave functions on-site j by $-\frac{2\pi}{L}j$ [27], plays a crucial role. It was revealed that the real part of a quantity

$$w = \frac{-i}{2\pi}\ln\langle 0|e^{-i\frac{2\pi}{L}\hat{X}}|0\rangle \tag{20}$$

gives the linear-response electric polarization, $P_{\rm el} = -{\rm Re}w$ [20], while its imaginary part gives a criterion for metal-insulator transition, that is $D = 4\pi{\rm Im}w$ is finite in insulators and divergent in metals [29]. The present effective action is regarded as a non-adiabatic (finite electric field) extension of w. To give a more accurate argument, recall that the effective Lagrangian can be expressed as

$$\mathcal{L}(F) \sim \frac{-i\hbar}{\tau L}\ln\left(\langle 0|e^{-\frac{i}{\hbar}\tau(H+F\hat{X})}|0\rangle e^{\frac{i}{\hbar}\tau E_0}\right) \tag{21}$$

for $d = 1$. Let us set $\tau = h/LF$ and consider the small F limit. For insulators we can replace H with the groundstate energy E_0 to have $\mathcal{L}(F) \sim wF$ in the linear-response regime. Thus, the real part of Heisenberg-Euler's expression [17] for the nonlinear polarization $P_{\rm HE}(F) = -\partial\mathcal{L}(F)/\partial F$ naturally reduces to the Berry's phase formula $P_{\rm el}$ in the $F \to 0$ limit (cf. (26) below). Its imaginary part, which is

related to the decay rate as $\mathrm{Im}P_{\mathrm{HE}}(F) = -\frac{\hbar}{2}\frac{\partial\Gamma(F)/L}{\partial F}$, reduces to $-D/4\pi$ and gives the criterion for the transition, originally proposed for the zero field case.

Non-Hermitian quantum mechanics

The dielectric breakdown of Mott insulators was also studied in the framework of non-Hermitian quantum mechanics [30, 31]. Fukui and Kawakami studied a non-Hermitian Hubbard model in which the leftward and rightward hopping integral are assumed to be unequal [30]. The non-Hermiticity is assumed to represent the coupling of the system with a "dissipative environment". With the Bethe ansatz solution they have observed the gap between the ground state and the first excited state to close when the hopping asymmetry is large enough. It seems that the remaining question is to relate this result with measurable quantities.

2.3 Zener Breakdown of Band Insulators Revisited – Nonadiabatic Geometric Phase and the Schwinger Mechanism

Before examining the dielectric breakdown of correlated electron systems, let us first discuss the dielectric breakdown of band insulators in an electric field $\mathbf{F}$ within the effective-mass picture. This will turn out to be heuristic, since we can obtain an analytic expression for the effective Lagrangian that can be readily applied to general band insulators.

For simplicity, we take a pair of hyperbolic bands $\varepsilon_{\pm}(\mathbf{k}) = \pm\sqrt{V^2 + v^2k^2}$ (considered here in d spatial dimensions), where $2V$ is the band gap, $-(+)$ denote the valence (conduction) band, and v the asymptotic slope of the dispersion.

We first obtain the groundstate-to-groundstate transition amplitude with the time-dependent gauge in the periodic boundary condition. There, a time-dependent AB-flux in units of the flux quantum, $\phi(\tau) = FL\tau/h$ (with the electronic charge $e = 1$ and L being the system size), is introduced to induce an electric field F, which makes the Hamiltonian time dependent as

$$H(\phi(\tau)) = \sum_{\mathbf{k},\alpha=\pm} \varepsilon_\alpha \left(\mathbf{k} + \frac{2\pi}{L}\phi(\tau)\mathbf{e}_{\parallel}\right) c_\alpha^\dagger(\mathbf{k}) c_\alpha(\mathbf{k}). \tag{22}$$

Here $\mathbf{e}_{\parallel}$ is the unit vector parallel to $\mathbf{F}$, and $c_\alpha^\dagger(\mathbf{k})$ the creation operator with spin indices dropped. The groundstate-to-groundstate transition amplitude is as given in (16) and, as before, the quantum dynamics is defined from the asymptotic behavior, $\Xi(\tau) \sim e^{\frac{i}{\hbar}\tau L^d \mathcal{L}(F)}$.

The dynamics of the one-body model can be solved analytically (Fig. 9(b)), since we can cut the dispersion in d spatial dimensions into slices, each of which reduces to Landau-Zener's two band model in 1D [15, 24]. Namely, if we decompose the k vector as $(\mathbf{k}_\perp, k_\parallel)$, where $\mathbf{k}_\perp$ ($k_\parallel$) is the component perpendicular (parallel) to $\mathbf{F}$, where each slice for a given $\mathbf{k}_\perp$ is a copy of Landau-Zener's model with a gap $\Delta_{\mathrm{band}}(\mathbf{k}) \equiv 2\sqrt{V^2 + v^2k_\perp^2}$. The Landau-Zener transition takes place around the level anti-crossing for which $k_\parallel + \frac{2\pi}{L}\phi(\tau)$ moves across the Brillouin zone(BZ) in a time interval $\delta\tau = h/F$. The process can be expressed as a scattering and the

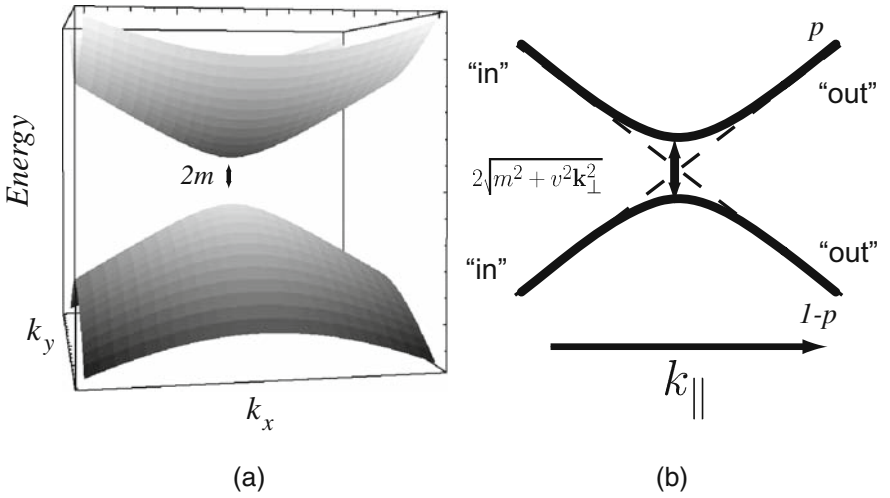

Fig. 9. (**a**) Energy levels of a Dirac band in 2D. (**b**) A one-dimensional slice of the higher dimensional Dirac band in which carriers (doublons and holes) are created by an external electric field in the $k_\parallel$ direction

Bogolubov coefficients between the "in" and "out" states (see Fig. 9) is given by the solution to the two band problem, that is,

$$\begin{aligned} c_+^\dagger(\mathbf{k}) &\to \sqrt{1-p(\mathbf{k})}e^{-i\chi(\mathbf{k})}c_+^\dagger(\mathbf{k}) + \sqrt{p(\mathbf{k})}c_-^\dagger(\mathbf{k}), \\ c_-^\dagger(\mathbf{k}) &\to -\sqrt{p(\mathbf{k})}c_+^\dagger(\mathbf{k}) + \sqrt{1-p(\mathbf{k})}e^{i\chi(\mathbf{k})}c_-^\dagger(\mathbf{k}). \end{aligned} \tag{23}$$

Here the tunneling probability for each $\mathbf{k}$ is given by the Landau-Zener(LZ) formula [15, 24],

$$p(\mathbf{k}) = \exp\left[-\pi\frac{(\Delta_{\rm band}(\mathbf{k})/2)^2}{vF}\right]. \tag{24}$$

On the other hand, the phase $\chi(\mathbf{k}) = -\theta(\mathbf{k}) + \gamma(\mathbf{k})$ appearing in the Bogolubov coefficients consists of the trivial dynamical phase, $\hbar\theta(\mathbf{k}) = \int_0^{\delta\tau}\varepsilon_+(\mathbf{k}+\frac{2\pi}{L}\phi(s)\mathbf{e}_\parallel)ds$, and the Stokes phase [15, 32],

$$\gamma(\mathbf{k}) = \frac{1}{2}{\rm Im}\int_0^\infty ds\frac{e^{-i(\Delta_{\rm band}(\mathbf{k})/2)^2 s}}{s}\left[\cot(vFs) - \frac{1}{vFs}\right]. \tag{25}$$

The Stokes phase, a non-adiabatic extension of Berry's geometric phase [33], depends not only on the topology of the path but, unlike the adiabatic counterpart, also on the field strength F [34]. In terms of the fermion operators the ground state is obtained by filling the lower band $|0;\phi\rangle = \prod_{\mathbf{k}} c_-^\dagger(\mathbf{k} - \frac{2\pi}{L}\phi\mathbf{e}_\parallel)|{\rm vac}\rangle$, where $|{\rm vac}\rangle$ is the fermion vacuum with $c_\pm(\mathbf{k})|{\rm vac}\rangle = 0$. If we assume that excited charges are absorbed by electrodes we obtain from Eqs. (16) and (23)

$$\begin{aligned} {\rm Re}\ \mathcal{L}(F) &= -F\int_{\rm BZ}\frac{d\mathbf{k}}{(2\pi)^d}\frac{\gamma(\mathbf{k})}{2\pi}, \\ {\rm Im}\ \mathcal{L}(F) &= -F\int_{\rm BZ}\frac{d\mathbf{k}}{(2\pi)^d}\frac{1}{4\pi}\ln\left[1-p(\mathbf{k})\right], \end{aligned} \tag{26}$$

where the dynamical phase θ cancels the factor $e^{\frac{i}{\hbar}\int_0^\tau E_0(\phi(s))ds}$ in (16).

Integration over $\mathbf{k}$ in (26) leads to the ground state decay rate per volume for a d-dimensional hyperbolic band,

$$\Gamma(F)/L^d = \frac{F}{(2\pi)^{d-1}h}\left(\frac{F}{v}\right)^{(d-1)/2} \times \sum_{n=1}^{\infty} \frac{1}{n^{(d+1)/2}} e^{-\pi n \frac{V^2}{vF}} \left[\mathrm{erf}\left(\sqrt{\frac{nv\pi^3}{F}}\right)\right]^{d-1}. \tag{27}$$

The threshold for the tunneling is governed by the most nonlinear (actually essentially singular) factor in the above formula, namely, $e^{-\pi n \frac{V^2}{vF}}$, so that the threshold electric field is given by

$$F_{\mathrm{th}} = \frac{V^2}{v}. \tag{28}$$

Although an analytic integration in (26) is possible for a Dirac band (= hyperbolic valence and conduction bands), the expression is valid for general band dispersions. In Fig. 10, the leakage current divided by the field strength, which is proportional to $\Gamma(F)/FL^d$, is plotted for the spatial dimension $d = 1, 2, 3$. The F-dependence is essentially

$$J_{\mathrm{leakage}} \propto F^{(d+1)/2} e^{-\pi \frac{F_{\mathrm{th}}}{F}}, \tag{29}$$

which has a threshold behavior as shown in the inset of the figure. Above the threshold, two regimes exist. In the medium field regime, the current scales as $j_{\mathrm{leakage}} \sim F^{(d+1)/2}$, where the power depends on d. However, when the field strength is even stronger, the error function appearing in (27), which is due to the lattice structure (with the $\mathbf{k}$ integral restricted to the BZ), starts to take an asymptote ($\mathrm{erf}(x) \sim (2/\sqrt{\pi})x$). Then various factors (including a power of F) cancel with each other, and the leakage current in the $F \to \infty$ limit approaches a *universal* function,

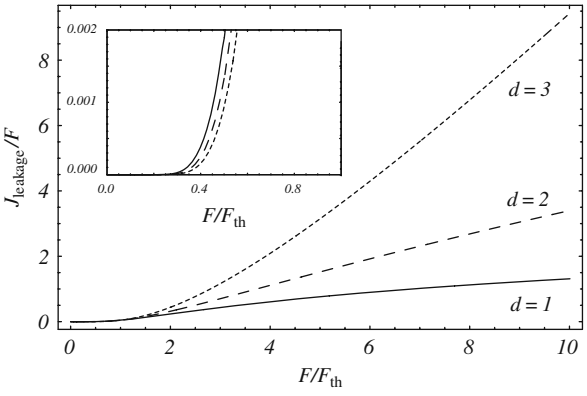

Fig. 10. The dependence of the conductivity on the electric field in the non-linear regime for band insulators with spatial dimension $d = 1, 2, 3$. The inset zooms in the threshold region

$$J_{\text{leakage}} \propto \Gamma(F)/L^d \to -\frac{F}{h} \ln\left[1 - \exp\left(-\pi \frac{F_{\text{th}}}{F}\right)\right], \tag{30}$$

where the d dependence disappears up to a trivial d-dependent numerical factor. This prediction on the non-linear transport can be checked experimentally including low-dimensional systems such as carbon nanotubes ($d = 1$). Graphene ($d = 2$) is also interesting, but this system has a massless Dirac dispersion, so that a special treatment is required.

Comparison to Heisenberg-Euler-Schwinger's results in nonlinear QED

Let us have a closer look at the decay of the QHE vacuum. In 1936, Heisenberg and Euler studied Dirac particles in strong electric fields, and discussed nonlinear optical responses of the QED vacuum – vacuum polarization – in terms of an effective Lagrangian [17]. Later, Schwinger refined their approach and calculated the vacuum decay rate [18].[1] Up to the one-loop level, Schwinger calculated the vacuum-to-vacuum transition amplitude using the proper time regularization method to obtain

$$\Delta\mathcal{L}^{\text{QED}}(F) = \frac{1}{8\pi^2} \int_0^\infty \frac{ds}{s^2} \left[F \cot(Fs) - \frac{1}{s}\right] e^{-ism_e^2} \tag{31}$$

for (3+1)-dimensional QED, where m_e is the electron mass. The integrand has a pole in the complex domain and has an imaginary part, which gives

$$\Gamma(F)^{\text{QED}}/L^d = \frac{\alpha F^2}{2\pi^2} \sum_{n=1}^{\infty} \frac{1}{n^2} \exp\left(-\frac{n\pi m_e^2}{|F|}\right), \tag{32}$$

the famous Schwinger's formula for the electron-positron pair creation rate [18], where $\alpha = 1/137$ is the fine-structure constant.

Thus, the expression for the QED effective Lagrangian, (31), coincides with the Stokes phase for the nonadiabatic Landau-Zener tunneling, except for a difference in the momentum integral. As we have mentioned above, an important difference in lattice systems is that the momentum integral is limited to the Brilliouin zone, and the decay-rate acquires an extra factor (compare (27) with (32)). This modification changes the strong field limit of the leakage current that leads to the universal expression (30). Another important difference, which is quantitative, appears in the threshold voltage: The threshold for band insulators $E_{\text{th}}^{\text{band}} = F_{\text{th}}^{\text{band}}/e = V^2/vae$ (a: lattice constant) is many orders smaller than the threshold for the QED instability $E^{\text{QED}} = \frac{m_e^2 c^3}{\hbar} \sim 10^{16}$ V/cm. For example, if we have an insulator with parameters $a = 10^{-7}$cm, $v = 2t_{\text{hop}} = 1$eV, $V = 1$eV, then the threshold becomes as small as $E_{\text{th}}^{\text{band}} = 10^7$V/cm.

Heisenberg and Euler's original aim was to discuss nonlinear optical properties of the vacuum in terms of $\Delta\mathcal{L}$. In fact, they calculated the effective Lagrangian in the presence of both electric and magnetic fields [17], and obtained

[1] For references on the effective-action approach of nonlinear electrodynamics, see [25, 35].

$$\Delta\mathcal{L}^{\rm QED}(F) = C\frac{\mathbf{E}^2-\mathbf{B}^2}{2} + \frac{2\alpha^2}{45m_e^4}\left[(\mathbf{E}^2-\mathbf{B}^2)^2 + 7(\mathbf{E}\cdot\mathbf{B})^2\right] + \ldots, \quad (33)$$

where C is a diverging constant that we drop after renormalization. The electric polarization can be obtained from the real part of the effective action via

$$\Delta P(F) = \frac{\partial}{\partial F}\Delta\mathcal{L}(F). \quad (34)$$

If we plug in (33), the nonlinear polarization of Dirac particles becomes

$$\Delta P = \frac{2\alpha^2}{45m_e^4}\left(-4B^2E + 14B_\parallel^2 E + 4E^3\right) + \ldots, \quad (35)$$

$$= \sum_{n=1}^{\infty} P^{(n)}(\mathbf{B})E^n, \quad (36)$$

where $B_\parallel$ is the component of $\mathbf{B}$ parallel to $\mathbf{E}$, and $P^{(n)}(\mathbf{B})$ the $n-$th order nonlinear polarization. Thus, we can examine nonlinear polarizations and cross correlations (a combined effect of $\mathbf{E},\mathbf{B}$) with the effective Lagrangian, as touched upon in Table 1.

2.4 Dielectric Breakdown in a Mott Insulator – Many-Body Landau-Zener Transition and a Nonequilibrium Phase Diagram

Before applying the effective Lagrangian approach to the dielectric breakdown of Mott insulators, we need to examine the excitation spectra, which is displayed in Fig. 11. There we plot, for the half-filling, the many-body energy levels of the Hamiltonian,

$$H(\phi(t)) = -t_{\rm hop}\sum_{i\sigma}\left(e^{i\frac{2\pi}{L}\phi(t)}c^\dagger_{i+1\sigma}c_{i\sigma} + \text{h.c.}\right) + U\sum_i n_{i\uparrow}n_{i\downarrow} + V\sum_i(-1)^i n_i. \quad (37)$$

Here U is the Hubbard repulsion, V a staggered potential to introduce valence and conduction bands, so that $U = V = 0$ corresponds to a noninteracting system in a free space, $U = 0,\ V \neq 0$ a band insulator, and a large U and $V = 0$ a Mott insulator. In the figure, we have only plotted charge excitations (where the charge rapidities are excited in the language of Bethe-ansatz solution). As can been seen, levels cross in the free model while in the band and the Mott insulators an energy gap separates the ground state from excited states. The gap is $2V$ for the band insulator. The Hubbard Hamiltonian Eq. (37) with $U \neq 0,\ V = 0$ is also exactly solvable in 1D. Woynarovich used the Bethe-ansatz method [36, 37] to study the ground state as well as the excited states (see also [38–40]). The two solid lines in Mott insulator's spectrum correspond to the ground state and the charge-excited state with one pair of complex charge rapidities, quantum numbers appearing in the Bethe-ansatz solution.

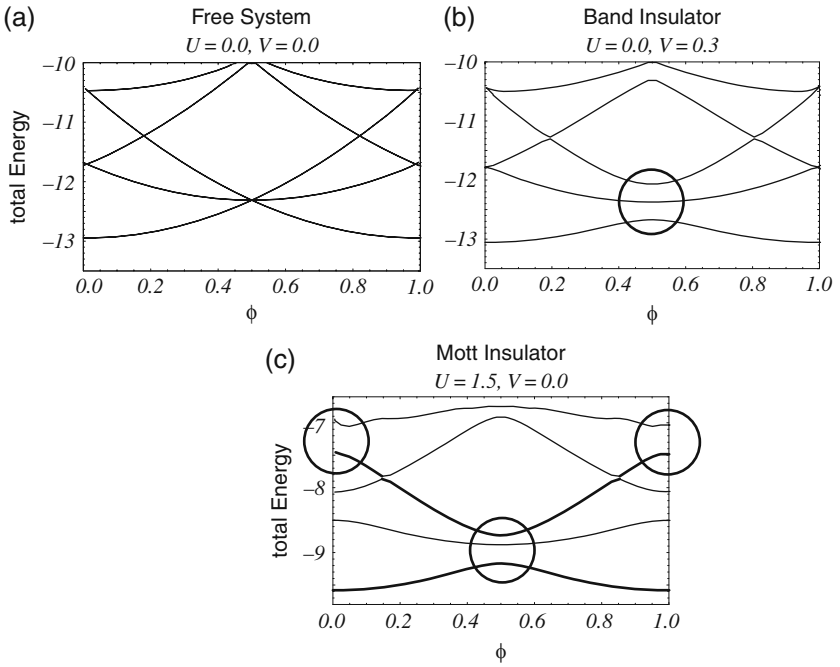

Fig. 11. Adiabatic spectrum $E_n(\phi)$ for a finite system ($L = 10$ here) obtained by the Lanczos method. We plot low-lying excitations in the half-filled subspace $N_\uparrow = N_\downarrow = L/2$. (**a**) a non-interacting system in a free space, (**b**) a band insulator ($U/t_{\rm hop} = 0, V/t_{\rm hop} = 0.3$), and (**c**) a Mott insulator ($U/t_{\rm hop} = 1.5, V/t_{\rm hop} = 0$). The circles indicate avoided level crossings

The energy gap $\Delta E(U)$ between these states are known to converge to the Mott gap $\Delta_{\rm Mott}(U)$ in the limit of infinite system,

$$\Delta E(U) \to \Delta_{\rm c}(U). \tag{38}$$

An important feature in the spectrum of the Mott insulator is that level repulsion occurs at many places over the excited states. The repulsion comes from Umklapp electron-electron scattering, that is a scattering process in which the momentum sum changes by reciprocal lattice vectors. In band insulators level, repulsions obviously come from one-body scattering as we have seen above.

Why have we first looked at the adiabatic spectrum? There is an important relation between the adiabatic energy and the current expectation value. From the Hellmann-Feynman theorem, 'that is', $\dfrac{dE}{d\lambda} = \dfrac{\langle\Psi|\partial H/\partial\lambda|\Psi\rangle}{\langle\Psi|\Psi\rangle}$ for $H(\lambda)|\Psi(\lambda)\rangle = E(\lambda)|\Psi(\lambda)\rangle$, we obtain

$$\begin{aligned} J_n(\phi) &= \langle n;\phi|J(\phi)|n;\phi\rangle \\ &= \left(\frac{L}{2\pi}\right)\frac{\partial E_n(\phi)}{\partial\phi}\,, \end{aligned} \tag{39}$$

which is valid for all ϕ. If we expand it around $\phi = 0$, we get

$$J_n(\phi) = J_n(0) + \left(\frac{L}{2\pi}\right) \frac{\partial^2 E_n(0)}{\partial \phi^2} \phi + O(\phi^2). \tag{40}$$

Using $\phi = FLt/h$ and defining the transport coefficients $\mathcal{D}_n$ by $J_n(\phi) = J_n(0) + \mathcal{D}_n F t + O(F^2)$, we obtain

$$\mathcal{D}_n(L) = \left(\frac{L}{2\pi}\right)^2 \frac{\partial^2 E_n(0)}{\partial \phi^2}. \tag{41}$$

When we focus on a dissipation less adiabatic transport at $T = 0$, the total current thus reads

$$\langle J(t) \rangle = \mathcal{D}_0(L) F t, \tag{42}$$

which is determined by the Drude weight (charge stiffness) $\mathcal{D}_0(L)$. As we can see in Fig. 11, even for insulators ((b) and (c)), the Drude weight $\mathcal{D}_0(L)$ of a finite system is not necessarily zero. If we remember *Kohn's criterion* [41] for metal-insulator transitions, stated as

$$\lim_{L\to\infty} \mathcal{D}_0(L) = \begin{cases} 0 & \text{insulator,} \\ \text{finite} & \text{perfect metal,} \end{cases} \tag{43}$$

we can see that we must go to the limit of infinite systems to distinguish metals from insulators. Indeed, the problem of taking the infinite-size limit is that also occurs in the study of dielectric breakdown in Mott insulators as we shall see later.

Short-Time Behavior – An Exact Diagonalization Result

Since the time evolution of many-body systems cannot be treated analytically, we employ numerical methods to time-integrate in two steps—for short-time behavior and long-time behavior. For the short-time evolution in dielectric breakdown of Mott insulators we exactly diagonalize the time-dependent Schrödinger equation as follows: First we start from the ground state of $H(\phi = 0)$ at time $t = 0$. The wave function evolves with the phase that increases as

$$\phi(t) = 0 \to FLt/h. \tag{44}$$

Here $F = eaE$ is the field strength, L the length of the chain. We numerically solve the time-dependent Schrödinger equation,

$$i\frac{d}{dt}|\Psi(t)\rangle = H(\phi(t))|\Psi(t)\rangle. \tag{45}$$

We choose the initial state to be the ground state $|0\rangle$ of $H(0)$, which is obtained here by the Lanczos method. The time integration of the state vector, which, being a many-body state, has a huge dimension, requires a reliable algorithm. So we adopt here the Cranck-Nicholson method that guarantees the unitary time evolution, where the time evolution is put into a form,

$$|\Psi(t+\Delta t)\rangle = e^{-i\int_t^{t+\Delta t} H(t)\, dt}\, |\Psi(t)\rangle \simeq \frac{1 - i\Delta t/2 H(t+\Delta t/2)}{1 + i\Delta t/2 H(t+\Delta t/2)}\, |\Psi(t)\rangle, \tag{46}$$

which is unitary by definition. Here, the time step is taken to be small enough ($dt = 1.0 \times 10^{-2}$ with the time in units of $\hbar/t$ hereafter) to ensure convergence for $L \leq 10$, for which the dimension of the Hamiltonian is $\sim 10^4$. We have concentrated on the total $S^z = 0$ subspace with $N_\uparrow = N_\downarrow = L/2$.

Evolution of the total current

We first plot in Fig. 12(b) the result for the expectation value of the current density averaged over the sites, $J = -\frac{it}{L}\sum_{i,\sigma}\left(e^{i\frac{2\pi}{L}\phi(t)}\, c^\dagger_{i+1\sigma}c_{i\sigma} - \text{h.c.}\right)$. The behavior of $J(t)$ for a fixed value of the electric field F is seen to fall upon three regimes when U is varied: A perfect metallic behavior ($J(t) \propto t$) when the electrons are free ($U/W = 0$), an insulating behavior ($J(t) = 0$) when the interaction is strong enough ($U/W \gg 1$), and an intermediate regime of U/W where J is finite with some oscillations for finite systems. In contrast, a non-half-filled system in non-equilibrium ($F \neq 0$) has a time evolution that is distinct from the ground-state behavior (Fig. 12(d)). The difference has its root in the spectral property as will be discussed later.

If we look at the behavior over several periods ($0 < \phi < 10$) for a fixed value of U/W for the half-filled (Fig. 12(c)) and for a non-half-filled case (Fig. 12(d)), the result may be summarized as follows:

(i) Small F regime (Mott insulator preserved at half filling)
A drastic difference between the half-filled and doped systems appears for small F. When half-filled, $J(t)$ in the limit of $F \to 0$ smoothly approaches a periodic saw-tooth behavior with periodicity $\phi = 1$, which is the AB-oscillation of the ground-state current.

(ii) Moderate F regime (metal)
In this regime, the current in the half-filled case is nonzero and shows oscillatory behaviors (seen typically in data for $LF = 0.008$ in Fig. 12(c)).

(iii) Large F regime (perfect metal)
When the electric field F becomes large enough, the system behaves as a kind of metal. The current $J(t)$ exhibits a long-period ($\Delta\Phi = \Phi_0 L$) oscillation, which is the Bloch oscillation, a hallmark of a metal.

The averaged current,

$$\langle J \rangle = \frac{1}{T}\int_0^T \langle J(t)\rangle dt, \tag{47}$$

integrated over a quarter of the Bloch period (with $\phi(T) = \frac{L}{4}$) is plotted against F in Fig. 13 for various values of U. We can see that $\langle J \rangle$ becomes nonzero rather abruptly at the metallization as F is increased, where the threshold electric field increases and the F- dependence becomes weaker when we increase U/t. Just after the metallization some oscillation (in the F- dependence this time) is seen for finite systems.

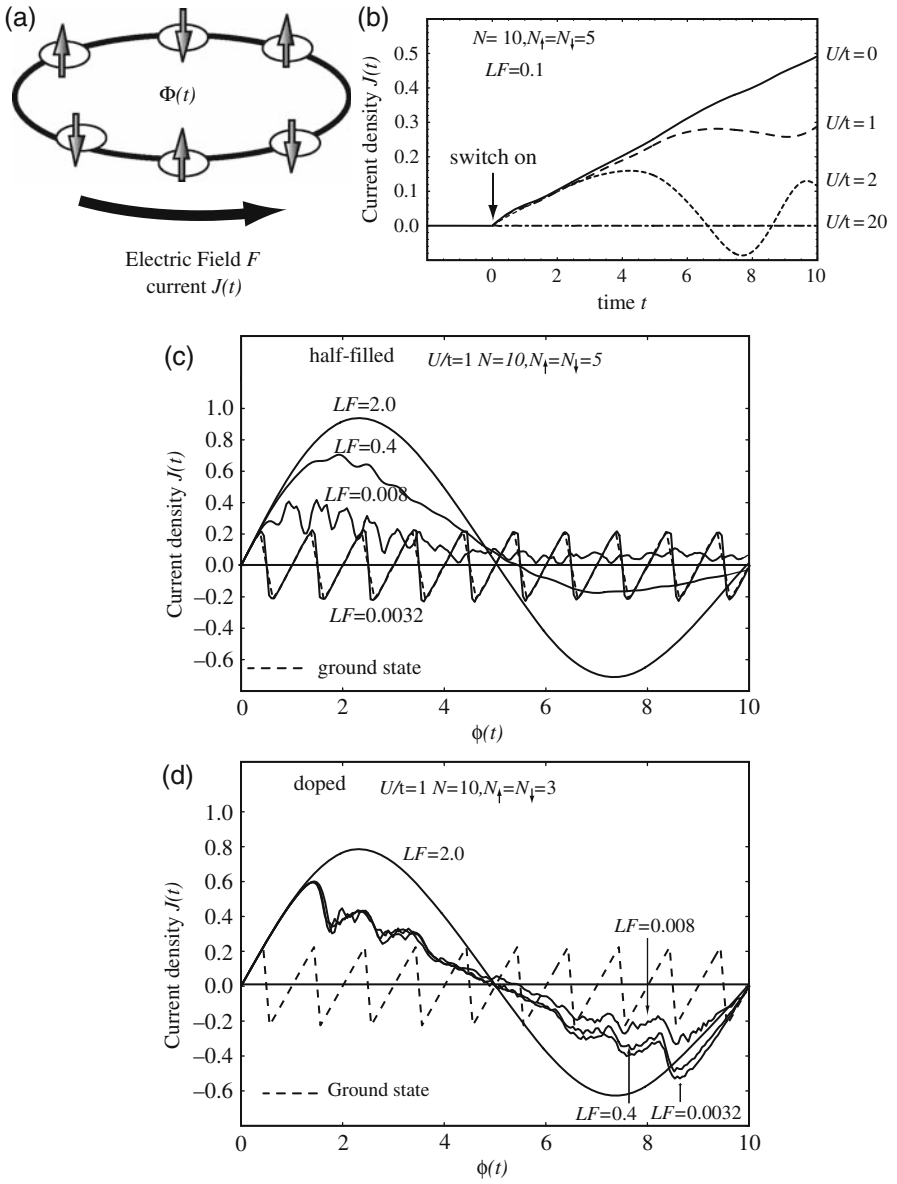

Fig. 12. (**a**) The sample geometry, where an AB flux, $\phi(t) = LFt$, increasing linearly with time induces an electric force through Faraday's law. (**b**) Time evolution of the current, $J(t)$, for a half-filled, 10-site Hubbard model for various strengths of the Hubbard repulsion, $0 \leq U/W \leq 5$ ($W = 4t_{\rm hop}$ is the noninteracting band width) for a fixed electric field $F = 1/10L$. Time is measured in units of $\tau_t \equiv \hbar/t_{\rm hop}$, LF in $t_{\rm hop}$, and $J(t)$ in $1/\tau_t$. The range of the time in this panel is restricted to a range of the AB-flux $0 \leq \phi \leq 1$. (**c**) A wider plot of the current for various values of F with a fixed $U/W = 0.25$, again for the half-filled case. Here the horizontal axis is ϕ. (**d**) A plot similar to (c) for a non-half-filled case ($N_\uparrow = N_\downarrow = 3 < L/2 = 5$)

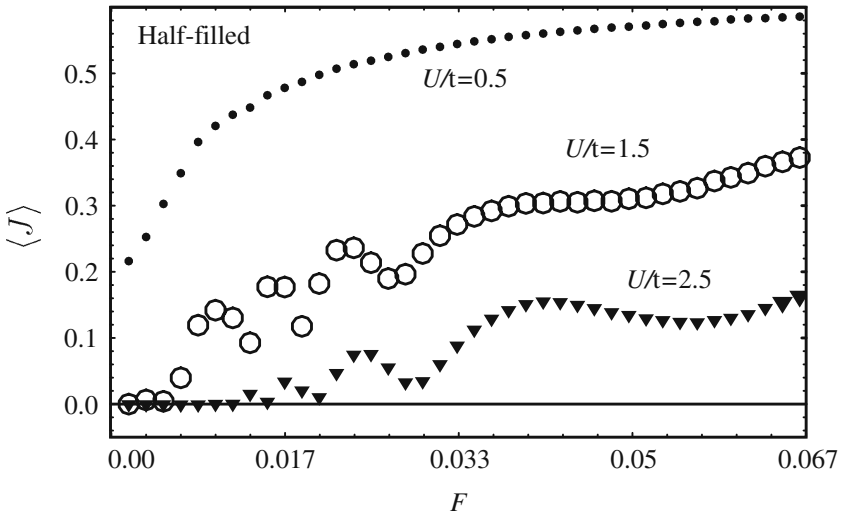

Fig. 13. Dependence of the averaged current $\langle J(t)\rangle$ on F for various values of U/t for the half-filled Hubbard model with $L = 6$

Evolution of the survival probability

In order to calculate the decay rate introduced above, we compute the temporal evolution of the ground-state survival probability,

$$P_0(t) = |\langle 0;\phi(s)|\hat{T}e^{-\frac{i}{\hbar}\int_0^t H(\phi(s))ds}|0;0\rangle|^2, \tag{48}$$

where $|0;\phi\rangle$ denotes the ground state of $H(\phi)$. The survival probability is related to the decay rate of the ground state by $P_0(t) = e^{-\Gamma t}$.

The short-time feature in the survival probability is expected to be described by the single Landau-Zener transition between the ground state and the lowest excited

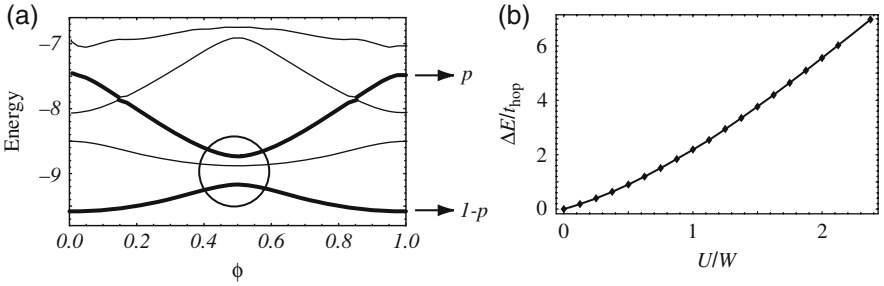

Fig. 14. (**a**) Spectrum of the half-filled Hubbard model $H(\phi)$ for $0 \leq \phi \leq 1$. *B*old lines represent the ground state and the first state among the tunneling-allowed excited states, respectively. (**b**) U/W-dependence of the Mott gap ΔE, encircled in (a). $W = 4t_{\rm hop}$ is the non-interacting band width, and system size is $L = 10$ and $U/t_{\rm hop} = 1.5$

state, displayed by the two bold lines in the figure,[2] that takes place around $\phi = \frac{1}{2}$ (Fig. 14(a)). If we concentrate on the two levels, the time evolution operator at $t = \Delta t$ ($\Delta t = \frac{h}{FL}$ is defined as the time when $\phi(\Delta t) = 1$ is reached) is approximated by a 2×2 matrix,

$$U_{\rm 2level}(t = \Delta t) = \begin{pmatrix} \sqrt{1-p}e^{-i\chi} & -\sqrt{p} \\ \sqrt{p} & \sqrt{1-p}e^{i\chi} \end{pmatrix}, \tag{49}$$

where the tunneling probability p is given by the Landau-Zener formula [15, 24, 42],

$$p = \exp\left(-\pi \frac{F_{\rm th}^{\rm LZ}}{F}\right), \quad F_{\rm th}^{\rm LZ} = \frac{\left[\Delta_c(U)/2\right]^2}{v}. \tag{50}$$

Here, $\Delta_c(U)$ is the excitation gap (Fig. 14(b)), $v = 2t_{\rm hop}$, and χ the sum of dynamical and Stokes phases.

In order to verify (50), we can numerically calculate the survival probability $P_0(t)$ from $t = 0$ to $t = \Delta t$ for various U and F (Fig. 15). After determining the tunneling probability from $p = 1 - P_0(\Delta t)$, we plot it against the diabaticity parameter $\frac{\left(\Delta_c(U)/2\right)^2}{vF}$. The data points (Fig. 15(b)) for various values of U fall around a common line, which is just the prediction of the Landau-Zener formula. The agreement is better for smaller values of U where we can treat the Umklapp term as a perturbation.

Long-Time Behavior—A Time-Dependent DMRG Result

The conclusion obtained in the previous section with the exact diagonalization is that the short-time behavior after the electric field is switched on is dominated by the single Landau-Zener transition between the ground state and the first excited state. However, several important questions remain, for example,

Will the first transition remain finite in the infinite-size limit? Indeed, Kohn's criterion (43) asserts that the ϕ dependence of the ground-state energy of a Mott insulator should vanish for $L \to \infty$. This implies that the adiabatic flow (Fig. 11(c)) should become flat in this limit, which may seem to indicate that the transition will be washed out. However, this contradicts with the expression for the threshold $F_{\rm Zener} = \frac{\left[\Delta_c(U)/2\right]^2}{v}$ (50), which remains finite in the $L \to \infty$ limit. Since this expression is obtained in a small system and in the small U limit, there is a possibility that this breaks down. Surprisingly, we shall show that this expression survives in large systems even when U is not small (Fig. 18).

The effect of pair annihilation After the first transition, we expect the system to undergo further transitions to higher-energy levels. This process, however, should be couterbalanced by other processes, the *pair annihilation* of doublons and holes. These processes, which do not conserve the total momentum in general,

[2] In Fig. 14(a), three states appear in the circle. However, transition from the ground-state to the middle state is forbidden by symmetry.

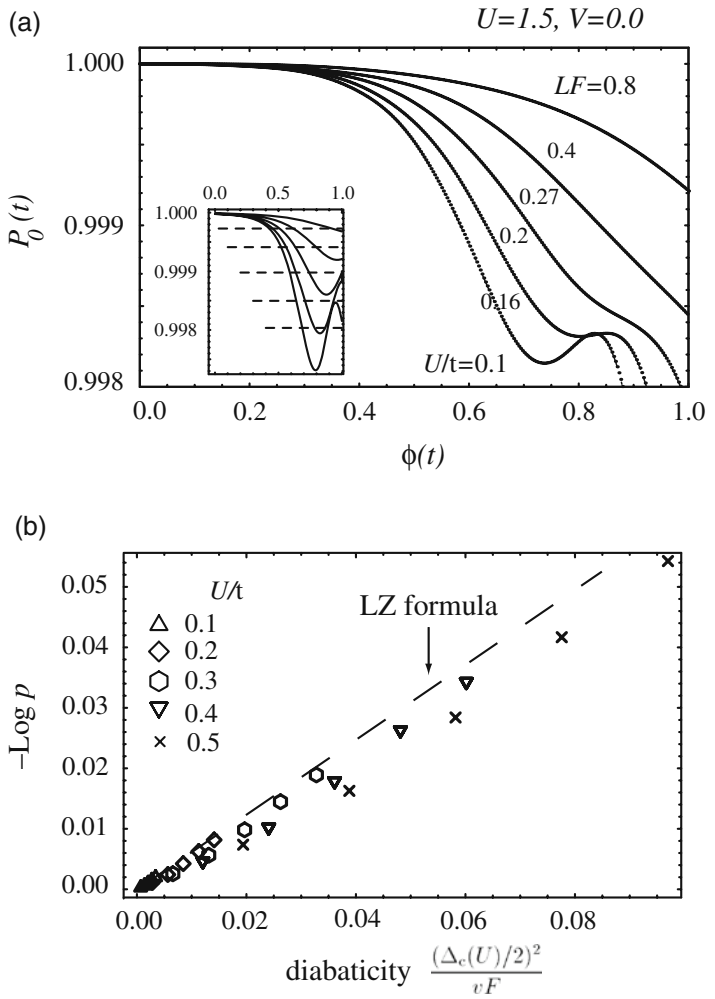

Fig. 15. (**a**) Short-time temporal evolution of the survival probability $P_0(t)$ in the half-filled Hubbard model ($L = 10, N_\uparrow = N_\downarrow = 5$) for various values of F with $U/t = 0.1$. The inset shows the solutions of the LZS equation with its asymptotic values indicated as dashed horizontal lines. (**b**) The transition probability p, with $P(t = \Delta t) = 1 - p$, plotted against the diabaticity parameter. The dashed line is the prediction of the Landau-Zener formula

are caused by the Umklapp scattering. Thus, the pair creation (= Landau-Zener transitions to high-energy states) tends to be offset by pair annihilation, which implies that the decay rate of the ground state may become smaller compared to the single Landau-Zener transition case.[3]

[3] A similar problem has been studied from a general point of view by Wilkinson and Morgan [44].

These questions have motivated us to study the dielectric breakdown in the half-filled Hubbard model for longer time periods, which is accomplished by the time-dependent density matrix renormalization group method. A version of the real-time DMRG was first introduced by Cazalilla and Marston with a truncated DMRG Hilbert space and a renormalized Hamiltonian [43]. Precision of their method degrades rapidly in the long-time limit, since an update of the Hilbert space is lacking. Recently, Vidal proposed an improved method for simulating time-dependent phenomena in one-dimensional lattice systems employing the Trotter-Suzuki decomposition [45, 46]. White and Feiguin [19] as well as other groups [47] modified this idea and combined it with the finite-size DMRG algorithm.

If we denote the DMRG wave function as

$$|\Psi\rangle = \sum_{l\alpha_j\alpha_{j+1}r} \psi_{l\alpha_j\alpha_{j+1}r}|l\rangle|\alpha_j\rangle|\alpha_{j+1}\rangle|r\rangle, \tag{51}$$

where $|l\rangle$, $|r\rangle$ is the basis of the truncated Hilbert space with dimension m and $|\alpha_j\rangle$, $|\alpha_{j+1}\rangle$ are the two sites that bridge the left and right blocks in the DMRG procedure. By employing the Trotter-Suzuki decomposition,

$$e^{-idtH} \simeq e^{-idtH_1/2}e^{-idtH_2/2}\dots e^{-idtH_2/2}e^{-idtH_1/2}, \tag{52}$$

we can apply the time-evolution operator $e^{-idtH_j/2}$ to the j-th wave function as

$$\left(e^{-idtH_j/2}\psi\right)_{l\alpha_j\alpha_{j+1}r} = \sum_{\alpha'_j\alpha'_{j+1}} \left(e^{-idtH_j/2}\right)_{\alpha_j\alpha_{j+1};\alpha'_j\alpha'_{j+1}} \psi_{l\alpha'_j\alpha'_{j+1}r}. \tag{53}$$

After applying $e^{-idtH_j/2}$, we diagonalize the density matrix and move to the next link just as in the usual finite-size algorithm. One cycle of this procedure results in an evolution of time by dt, and we can repeat it as many times as we wish. Compared with the version by Cazalilla-Marston [43], this algorithm has a higher precision and we can simulate non-equilibrium excited states efficiently [47], although one drawback of the t-dependent DMRG is that we can only treat systems with open boundary conditions.

Here we study transient behaviors of the one-dimensional Hubbard model with open-boundary condition. We use the time-independent gauge, for which the Hamiltonian is

$$H(F) = -t_{\rm hop}\sum_{j,\sigma}\left(c^\dagger_{j+1\sigma}c_{j\sigma} + \text{h.c.}\right) + U\sum_j n_{j\uparrow}n_{j\downarrow} + F\hat{X}, \tag{54}$$

where $\hat{X} = \sum_j jn_j$ is the position operator representing the tilted potential. As in the previous section, we start the time evolution from the $F = 0$ ground state $|0\rangle$ obtained by the usual finite-size DMRG. The wave function in this gauge is simply

$$|\Psi(t)\rangle = e^{-itH(F)}|0\rangle, \tag{55}$$

which is obtained with the t-dependent DMRG.

Evolution of the charge density

We first discuss the temporal evolution of the charge density, $n_j(t) = \langle \Psi(t)|n_j|\Psi(t)\rangle$, after the electric field is switched on at $t = 0$. At half-filling, the initial distribution is $n_j(t) = 1$. After the application of the electric field, a charge density wave (CDW) pattern is formed when the electric field is not too strong (Fig. 16(a)). This state is stationary and the density profile do not change any further. The pattern is formed because the boundary condition breaks the translational symmetry, where the amplitude of the pattern corresponds to the polarization $\Delta P(F)$ induced by the field. When the electric field becomes stronger, charge transfers start to occur, with charge accumulation and charge depletion being formed around the edges in an open-boundary chain (Fig. 16). This is a sign that the ground state collapses due to quantum tunneling.

The decay rate of the ground state

The groundstate-to-groundstate transition amplitude is, in the time-independent gauge,

$$\Xi(t) = \langle 0|e^{-\frac{i}{\hbar}\tau\left(H+F\hat{X}\right)}|0\rangle e^{\frac{i}{\hbar}tE_0}, \tag{56}$$

where we denote the ground state of H as $|0\rangle$ and its energy as E_0. Figure 17(a) shows the temporal evolution of the ground-state survival probability $|\Xi(t)|^2$ for a

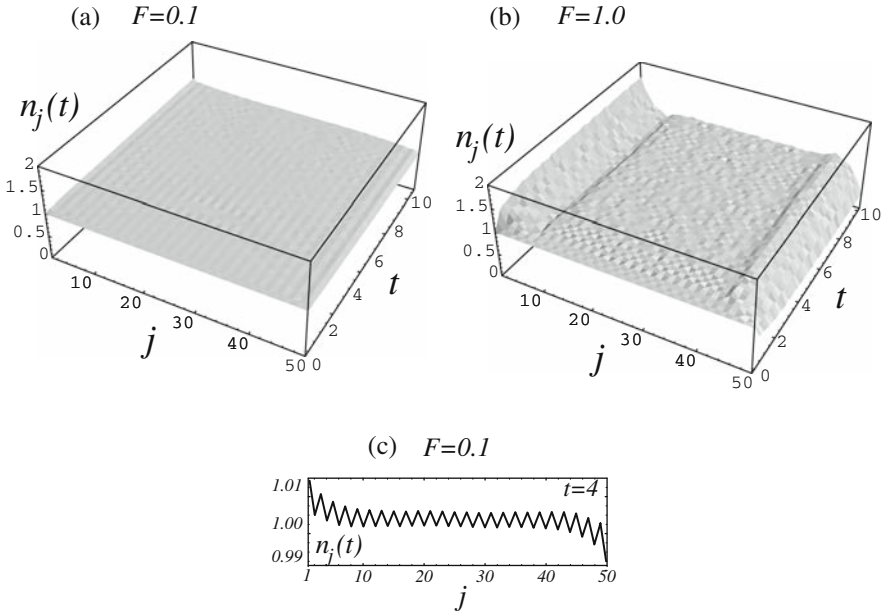

Fig. 16. Temporal evolution of the charge density $n_j(t)$ in the half-filled Hubbard model with $m = 150, L = 50, dt = 0.02$ for $F = 0.1$ (**a**) and $F = 1.0$ (**b**). (**c**) depicts a cross section of (a) for $t = 4$

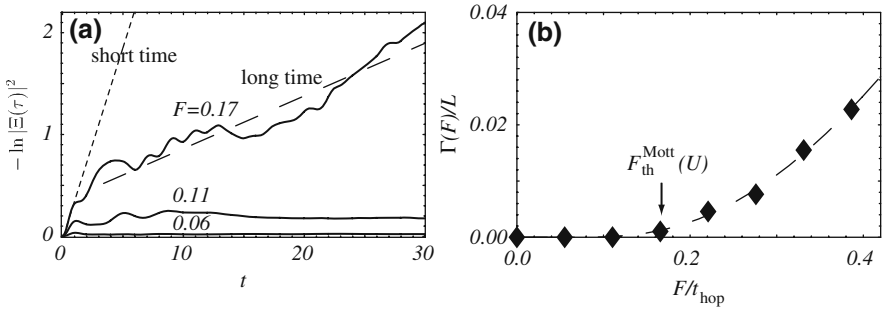

Fig. 17. (a) Temporal evolution of the ground-state survival probability $|\Xi(t)|^2$ after the electric field F is switched on at $t = 0$ in the 1D half-filled Hubbard model with $U/t_{\rm hop} = 3.5$, obtained with the time-dependent DMRG for $L = 50$ with the size of the DMRG Hilbert space $m = 150$ and the time step $dt = 0.02$. The dashed line represents $-\ln|\Xi(t)|^2 = \Gamma(F)t + c$ for $F/t_{\rm hop} = 0.17$, while the dotted line delineates the initial slope (the short-time behavior). (b) The decay rate versus F in the half-filled Hubbard model. Dashed curve is a fit to (57), where $F_{\rm th}^{\rm Mott}(U)$ is the threshold

system with $U/t_{\rm hop} = 3.5$. As time evolves, the slope of $-\ln|\Xi(t)|^2$ ($\propto$ the decay rate) decreases after an initial stage, which implies a suppression of the tunneling from the short-time behavior. This should indicate that charge excitations are initially produced due to the Landau-Zener tunneling from the ground state to the first excited states, but that scattering among the excited states become important as the population of the excitations grows. In other words, pair annihilation of carriers becomes important and acts to suppress the tunneling rate. We have determined $\Gamma(F)$ from the long-time behavior with a fitting $-\ln|\Xi(t)|^2 = \Gamma(F)t + \text{const}$.

The decay rate per length $\Gamma(F)/L$ is plotted in Fig. 17(b), where we have varied the system size ($L = 30, 50$) to check the convergence. $\Gamma(F)/L$ is seen to remain vanishingly small until the field strength exceeds a threshold. To characterize the threshold $F_{\rm th}(U)$ for the breakdown we can evoke the form obtained above for the one-body system. The formula (in (27) for $d = 1$ with the error function ignored and the factor of 2 recovered for the spin degeneracy),

$$\Gamma(F)/L = -\frac{2F}{h}a(U)\ln\left[1 - \exp\left(-\pi\frac{F_{\rm th}^{\rm Mott}(U)}{F}\right)\right], \tag{57}$$

is originally derived for one-body problem, and an obvious interest here is whether the formula can be applicable if we replace the one-body $F_{\rm th}^{\rm band}$ with the many-body $F_{\rm th}^{\rm Mott}(U)$. In the above we have added a factor $a(U)$, a parameter representing the suppression of the quantum tunneling. The dashed line in Fig. 17(b) is the fitting to the formula for $U/t_{\rm hop} = 3.5$, where we can see that the fitting, including the essentially singular form in F, is surprisingly good, given a small number of fitting parameters. The value of $a(U)$ turns out to be close to but smaller than unity (taking between 0.77 to 0.55 as U/t is increased from 2.5 to 5.0).

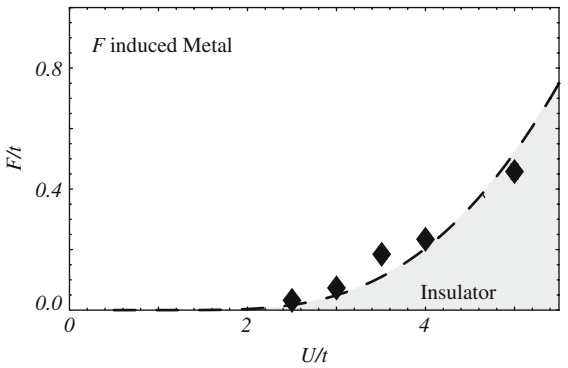

Fig. 18. The dielectric-breakdown phase diagram on the (U, F) plane for the one-dimensional Hubbard model. The symbols are the threshold $F_{\rm th}^{\rm Mott}(U)$ obtained by fitting the decay rate $\Gamma(F)/L$ to (57)), while the dashed line is the prediction $F = F_{\rm th}^{\rm LZ}(U)$ of the Landau-Zener formula (58)

If we perform this for various values of U we can construct a "nonequilibrium (dielectric-breakdown) phase diagram", as displayed in Fig. 18, which plots the U dependence of $F_{\rm th}^{\rm Mott}$. The dashed line is the prediction of the Landau-Zener formula [13],

$$F_{\rm th}^{\rm LZ}(U) = \frac{[\Delta_{\rm c}(U)/2]^2}{v}. \tag{58}$$

For the size of the Mott (charge) gap we use the Bethe-ansatz result, [48]

$$\Delta_{\rm c}(U) = \frac{8t_{\rm hop}}{U}\int_1^\infty \frac{\sqrt{y^2-1}}{\sinh(2\pi y t_{\rm hop}/U)}dy, \tag{59}$$

with $v/t_{\rm hop} = 2$. As can be seen, the DMRG result and the Landau-Zener result agrees surprisingly well.

2.5 Long-Time Behavior and a Mapping to a Quantum Random Walk

Since many levels should be involved in the above pair creation/annihilation processes, next thing we want to have is a statistical mechanical setup for the time evolution of the Mott insulator. The problem at hand is a closed quantum system in external driving forces (e.g., electric fields), which are represented by a time varying parameter $\phi(t)$ of the Hamiltonian. We want to discuss the asymptotic solution of the time-dependent Schrödinger equation

$$i\hbar\frac{d}{dt}|\Psi(t)\rangle = H(\phi(t))|\Psi(t)\rangle. \tag{60}$$

We introduce $|n;\phi\rangle$ as the set of eigenstates of the time-dependent Hamiltonian $H(\phi)$, and denote the energy eigenvalue as $E_n(\phi)$, that is $H(\phi)|n;\phi\rangle = E_n(\phi)|n;\phi\rangle$

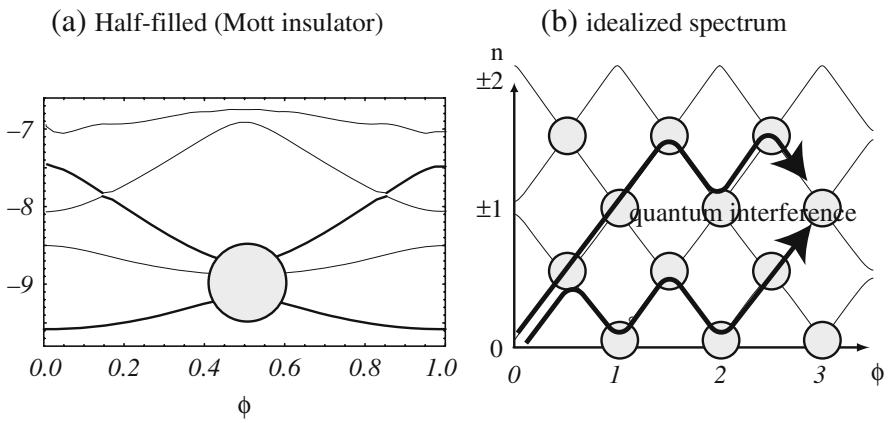

Fig. 19. (**a**) The spectrum of the half-filled Hubbard model. The circle corresponds to Landau-Zener transition between the two energy levels which can be expressed by a 2×2 unitary matrix (65). (**b**) Idealized energy levels where level anticrossings are expressed by circles. Quantum interference takes place, when contributions from different paths are considered

(Fig. 19). Since $|n;\phi\rangle$ forms a complete orthonormal basis, the wave function $|\Psi(t)\rangle$ can be expanded as

$$|\Psi(t)\rangle = \sum_n \psi(n,t) e^{-\frac{i}{\hbar}\int_0^t E_n(s)ds} |n;\phi(t)\rangle \tag{61}$$

with coefficients $\psi(n,t) = \langle n;\phi(t)|\hat{T}e^{-i\int_0^t H(\phi(s))ds}|0;0\rangle / e^{-\frac{i}{\hbar}\int_0^t E_n(s)ds}$. Note that we have removed the contribution from the dynamical phase $\int_0^t E_n(s)ds/\hbar$ in the definition of $\psi(n,t)$. Although the evolution depends on the detail of the system ($H(\phi)$), we can deduce some *universal* features that depend only on the feature of the energy levels, that is distribution of level repulsion in the spectrum.

Each energy level is subject to the Landau-Zener tunneling to neighboring levels in a time period $\Delta t/2$, and is most conveniently expressed in terms of the transfer matrix representation [10, 49]. To this end, we denote the pairs as

$$\Psi(n,\tau) = \begin{pmatrix} \psi_L(n,\tau) \\ \psi_R(n,\tau)) \end{pmatrix}, \tag{62}$$

and the time evolution "rule" (shown in Fig. 20) can be expressed as

$$\Psi(n,\tau+1) = P_{n+1}\Psi(n+1,\tau) + Q_{n-1}\Psi(n-1,\tau), \tag{63}$$

where P_n (Q_n) is the upper (lower) half of a 2×2 unitary matrix,

$$U_n = \begin{pmatrix} a_n & b_n \\ c_n & d_n \end{pmatrix}, \quad P_n = \begin{pmatrix} a_n & b_n \\ 0 & 0 \end{pmatrix}, \quad Q_n = \begin{pmatrix} 0 & 0 \\ c_n & d_n \end{pmatrix}. \tag{64}$$

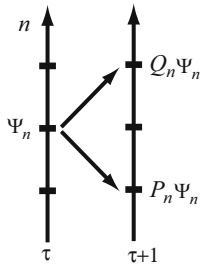

Fig. 20. Application of Q_n and P_n in the quantum random walk

The diagonal elements of U_n represent the Landau-Zener transition from the n-th level to $(n-1)$ or $(n+1)$-th level, where the explicit form is

$$U_n = \begin{pmatrix} \sqrt{p_n}e^{i\beta_n} & \sqrt{1-p_n}e^{i\gamma_n} \\ -\sqrt{1-p_n}e^{-i\gamma_n} & \sqrt{p_n}e^{-i\beta_n} \end{pmatrix}. \tag{65}$$

Here the Landau-Zener tunneling probability p_n depends on the ratio of the Zener threshold field F^n_{Zener} and the electric field F as

$$p_n = \exp\left(-\pi \frac{F^n_{\text{Zener}}}{F}\right), \tag{66}$$

where F^n_{Zener} generically depends on n.

If we regard $\Psi(n,\tau) = \begin{pmatrix} \psi_L(n,\tau) \\ \psi_R(n,\tau) \end{pmatrix}$ as a "qubit" on "site" n, Eq. (63) defines an evolution of a *one-dimensional quantum walk* with a reflecting boundary at $n = 0$ corresponding to the ground-state (Fig. 19(c)). A quantum walk is a quantum counterpart of the classical random walk. Models with essentially equivalent ideas have appeared in various fields: to name a few, quantum transport and dissipation [13, 50], quantum Hall effect [51], optics [52, 53] and recently in quantum information [54–65]. In the field of quantum information (see e.g. [66]), introduced by Aharonov, Ambainis, Kempe and Vazirani in 2001 [67], the quantum walk is arousing interest in the hope of revealing new features in the quantum algorithms (for reviews see [54, 56, 61]). Researches stem into many directions, for example, the effect of absorbing boundary conditions [55, 57, 64], higher-dimensional systems [57, 64, 68], localization in systems with internal degrees of freedom [69], and many powerful analytical techniques are being developed.

An important feature of the quantum walk, as opposed to the classical walk, is that different transition paths interfere with each other quantum mechanically. We in fact find that the quantum interference leads to a *dynamical localization*, an analog of Anderson's localization taking place in the energy space rather than in the position space. In our previous work [7], we have employed the PRQS method, a technique to treat quantum walks, to perform the path integral, and obtained the exact asymptotic distributions of the wave function for a simplified model. The resultant states can be categorized into three types, depending on the strength of

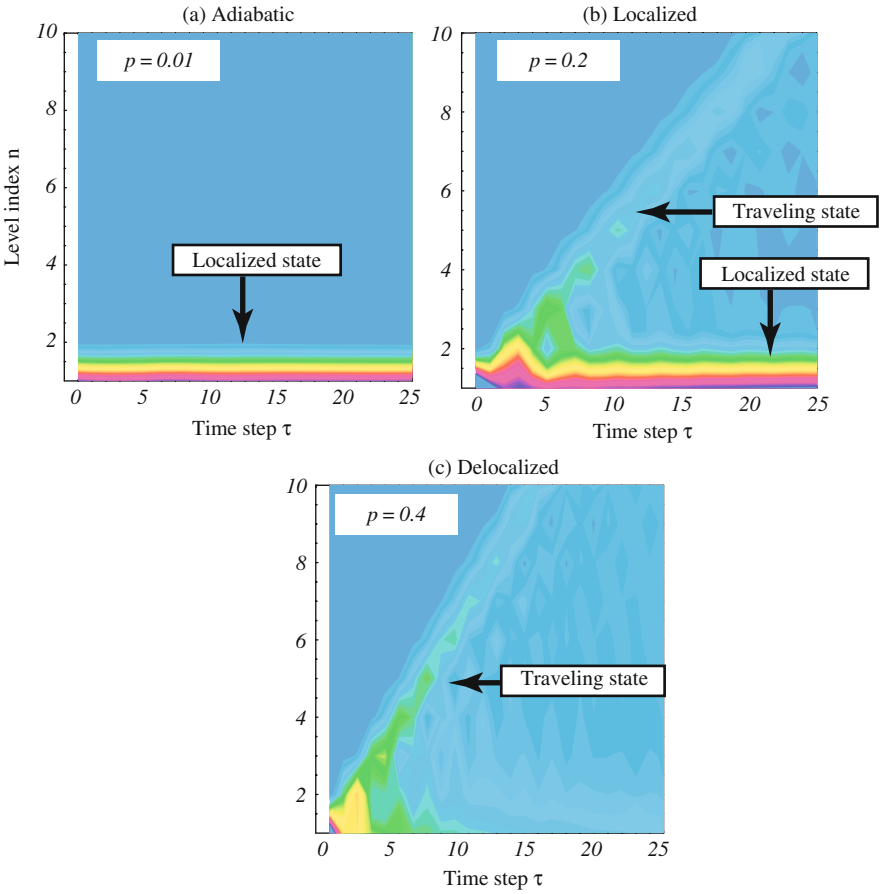

Fig. 21. The time evolution of the distributions of wave function amplitude $\rho(n,t) = |\psi(n,t)|^2$ in energy space. The vertical axis n is the index of the energy levels. (**a**) For small tunneling, the distribution is localized at the ground state. (**b**) For intermediate tunneling, a localized state remains, while the amplitude starts to bifurcate into excited states of the wave function is excited. (**c**) When the tunneling is larger than the threshold, the localized state disappears

the electric field, as schematically plotted in Fig. 21. (A) is an adiabatic evolution that takes place in weak driving forces (electric fields). The dominant part of the distribution $\rho(n,t)$ against energy is a delta function localized around the ground-state. When the driving force become stronger, quantum tunneling broadens the delta function, as plotted in (B). The shape of the peak is maintained by a balance between tunneling and dynamical localization. (C) is the case where the driving force overwhelms the effect of dynamical localization, and the system is driven rapidly into the excited states. This, in our view, corresponds to the dielectric breakdown.

2.6 Experimental Implications

Now we discuss experimental implication of the many-body Landau-Zener transition mechanism. In fact, there are several mechanisms that may lead to breakdown of insulators. For example, Fröhlich's electric avalanche mechanism may take place, in which a small number of excited electrons act as a seed and become accelerated by the electric field until they cooperatively destroy the insulator. We can distinguish Landau-Zener transition from the avalanche mechanism through the temperature dependence and from interface effects by changing the size of the sample. Another important effect is the band bending near an interface of the Mott insulator and electrodes. For a thin sample, this may lead to injection of carriers, and results in the interface Mott transition [14].

Dielectric breakdown of one-dimensional Mott insulators was experimentally studied by Taguchi et al., who obtained the $J-E$ characteristics (Fig. 22) of Sr_2CuO_3 and $SrCuO_2$ samples [16], which are both quasi-1D, strongly correlated electron systems. Experiments were done by placing small single crystals in circuits as shown in Fig. 22(a), and the voltage drop V was measured while the current density J was fixed. Depending on the strength of the electric field F, transport properties change drastically, as summarized in the following.

In weak electric fields, the $J-E$ characteristics shows an Ohmic behavior at finite temperatures. When the electric field exceeds a threshold value, the current shows a dramatic increase. Such drastic changes cannot be explained by perturbation in F, and we must consider non-perturbative effects, that is a behavior essentially singular in F like $J \sim$ function of $\exp(-F_{\rm th}/F)$, which is a typical tunneling effect with threshold $F_{\rm th}$. The temperature dependence (Fig. 23) of the threshold can be fit well by $F_{\rm th}(T)/F_{\rm th}(0) \sim \exp(-T/T_0)$. This excludes the avalanche mechanism, for which an activation type temperature dependence ($F_{\rm th}^{\rm avalanche}(T)/F_{\rm th}(0) \sim \exp(T_0/T)$) is expected.

One indication that the breakdown is indeed quantum in nature is that the threshold extrapolates to a finite value for $T \to 0$. From the extrapolation (Fig. 23(a)), we obtain a threshold,

$$F_{\rm th}^{\rm exp} \sim 10^6 - 10^7 \ (\text{eV/cm}), \tag{67}$$

for Sr_2CuO_3 and $SrCuO_2$. The Landau-Zener result (intended for $T = 0$) of the threshold (50) is

$$F_{\rm th}^{\rm LZ}(U) = \frac{[\Delta_{\rm c}(U)/2]^2}{v} \sim (1\text{eV})^2/(10^{-7}\text{eV/cm}) \sim 10^6 \ (\text{eV/cm}) \tag{68}$$

is comparable with the experimental result.

Interestingly, the decay rate $\Gamma(U)$ we have introduced theoretically can be measured experimentally [16]. This is done by studying the transient behavior of the current after the electric field is switched on at $t = 0$. At first the current density is zero, and then becomes non-zero after a certain delay time $t = \tau(F)$ (Fig. 23(b), lower inset). The authors in [16] have introduced a phenomenological percolation model to relate the delay time with the production rate $P(F)$ of the conductive domains (see [16]). In this model, conductive domains are envisaged to grow in the

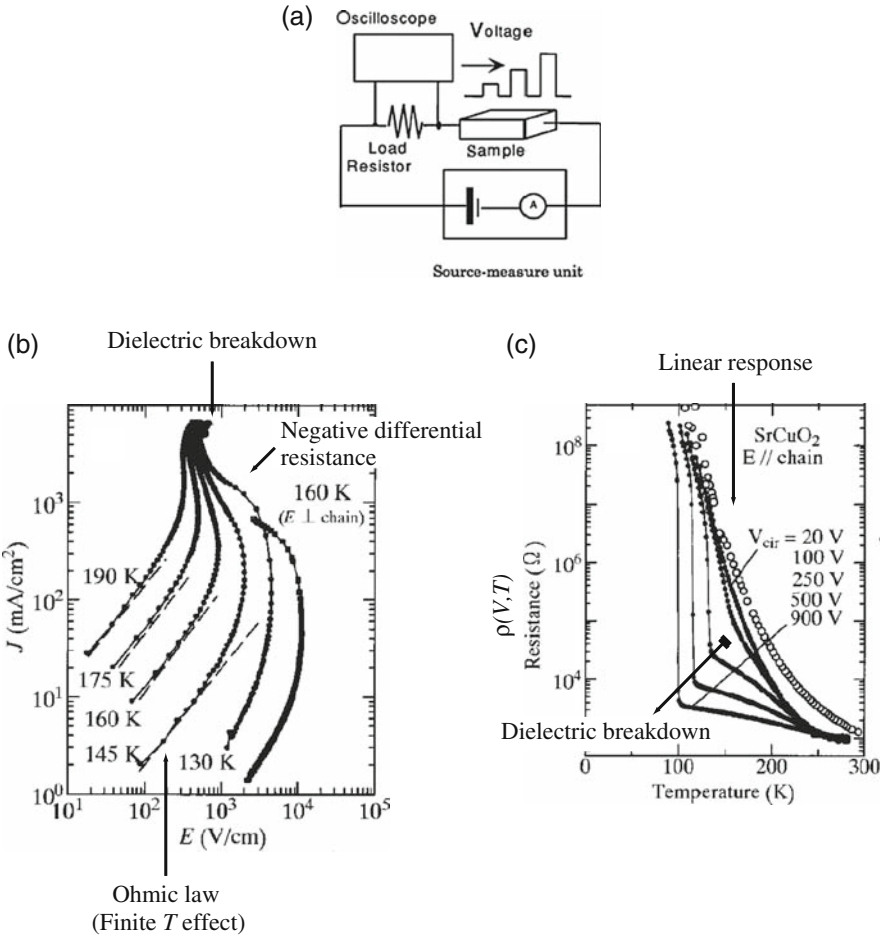

Fig. 22. (**a**) A schematic measurement circuit. (**b**) $J - E$ characteristics of a $SrCuO_2$ sample. (**c**) Temperature dependence of the resistance for various applied voltages. After Taguchi et al. [16]

sample, and the current density is assumed to become finite when the left and right electrodes are connected by these domains (Fig. 23(c)). This leads to a relation,

$$P(F) = -\left(F\frac{d\tau}{dF}\right)^{-1}. \tag{69}$$

The experimental result for the production rate in Fig. 23(b) is obtained in this way.

The nature and the microscopic origin of the "conductive domain" are not clear, but if we interpret them to be domains with a high density of charge excitations produced by the Landau-Zener transition, the vacuum decay rate per volume $\Gamma(F)/L^d$

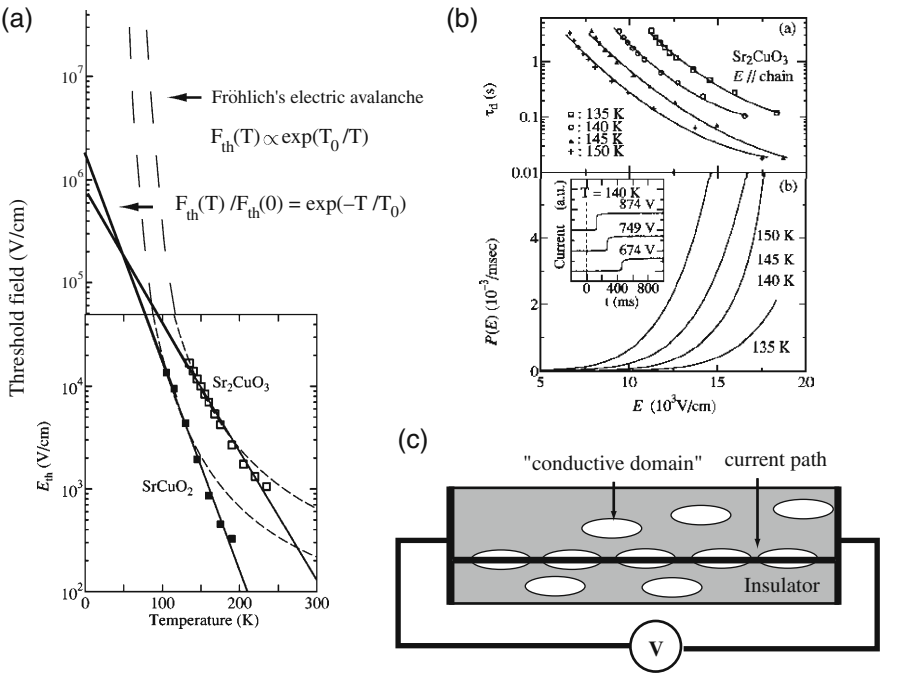

Fig. 23. An experimental result for the temperature dependence of the threshold electric field $F_{\rm th}(T)$ for the dielectric breakdown (adopted from Taguchi et al. [16]). Dashed lines correspond to a fitting to $\exp(T_0/T)$ predicted by Fröhlich's electron avalanche. Solid lines correspond to a fitting to $\exp(-T/T_0)$. (b) The electric-field dependence of the delay time $\tau_{\rm d}$ for Sr_2CuO_3. (c) The production rate of "conductive domains". The inset exemplifies the temporal evolution of the current at various applied voltages. Adopted from Taguchi et al. [16]

characterizes quantum tunneling from the ground state to excited states. With the identification we expect that the decay rate and the production rate are identical, that is,

$$P(F) \sim \Gamma(F). \tag{70}$$

This identification is encouraged by the field dependence of $P(F)$ (lower panel of Fig. 23(b)), which is close to the expected form,

$$\Gamma/L \sim -\frac{2F}{h} a(U) \ln\left[1 - \exp\left(-\pi \frac{F_{\rm th}^{\rm Mott}}{F}\right)\right], \tag{71}$$

of the decay rate.

In this experiment a scaling study—a systematic change of the size of the sample—was also performed to confirm that the nonlinear effect occurs in the bulk. From these observations, we conclude that the experiment by Taguchi et al. [16] can be explained by the many-body Landau-Zener tunneling mechanism. However, to

be more confident, we need to know the temperature dependence of the threshold theoretically, which is still a challenging task in the present many-body system.

2.7 Conclusion

In this chapter, we have explained how dielectric breakdown of Mott insulators can be explained from the non-equilibrium behaviors of charge carriers, especially from their creation and annihilation processes. Both processes are the result of many-body Landau-Zener non-adiabatic tunneling transition between many-body energy levels, where charge creation processes are counterbalanced by annihilation processes. From numerical result we have obtained a nonequilibrium (dielectric-breakdown) phase diagram. If the coherence of the dynamics is preserved at sufficiently low temperatures, a quantum interference, as modeled by a quantum walk in energy space, may lead to dynamical localization, which saturates the creation process and leads to a nonequilibrium stable state. The decay rate $\Gamma(F)$ that we have discussed is a measurable quantity: it is the production rate observed by Taguchi *et al.* [16] in copper oxides. The experimental result is consistent with our prediction $\Gamma(F) \sim \frac{F}{2\pi} \ln(1-p)$ when an extrapolation to zero temperature is made. It is an interesting future topic to understand the properties of the nonequilibrium stable state in more detail.

An important open question is how the energy dissipation processes take place in non-equilibrium situations. Here we have stressed that the many-body processes act effectively as a source of dissipation through scattering, but an explicit incorporation of heat-bath effects, electrode effects, etc, is left to a future problem.

Acknowledgement

We wish to thank Rytaro Arita and Norio Konno for the collaboration in the workes described here and for illuminating discussions. We also indebted to Yshai Avishai and Paul Wiegmann for illuminating discussions. TO acknowledges Masaaki Nakamura, Kazuma Nakamura, Shuichi Murakami, and Naoto Nagaosa for helpful comments.

References

1. M. Imada, A. Fujimori, and Y. Tokura, Rev. Mod. Phys. **70**, 1039 (1998). 251
2. A. Asamitsu, Y. Tomioka, H. Kuwahara, and Y. Tokura, Nature **388**, 50 (1997). 252
3. A. Baikalov, Y.Q. Wang, B. Shen, B. Lorenz, S. Tsui, Y.Y. Sun, Y.Y. Xue, and C.W. Chu, Appl. Phys. Lett. **83**, 957 (2003). 252
4. A. Sawa, T. Fujii, M. Kawasaki, and Y. Tokura, Appl. Phys. Lett., **85**, 4073 (2004). 252
5. H. Oshima, K. Miyano, Y. Konishi, M. Kawasaki, and Y. Tokura, Appl. Phys. Lett. **75**, 1473 (1999). 252

6. S.Q. Liu, N.J. Wu, and A. Ignatiev, Appl. Phys. Lett. **76**, 2749 (2000). 252
7. V. Ponnambalam, S. Parashar, A.R. Raju, and C.N.R. Rao, Appl. Phys. Lett. **74**, 206 (1999). 252, 278
8. K. Inagaki, I. Terasaki, H. Mori, T. Mori, J. Phys. Soc. Jpn **73**, 3364 (2004). 252
9. A. Ohtomo and H.Y. Hwang, Nature, **427**, 423 (2004). 252
10. T. Oka N. Konno R. Arita, and H. Aoki, Phys. Rev. Lett. **94**, 100602 (2005). 252, 256, 277
11. T. Oka R. Arita, and H. Aoki, Physica B. **759**, 359–361 (2005). 252, 253, 256
12. T. Oka and H. Aoki, Phys. Rev. Lett. **95**, 137601 (2005). 252, 253, 254, 255, 258
13. T. Oka, R. Arita, and H. Aoki Phys. Rev. Lett. **91**, 66406 (2003). 252, 253, 255, 276, 278
14. T. Oka and N. Nagaosa, Phys. Rev. Lett. **95**, 266403 (2005). 253, 280
15. C. Zener, Proc. R. Soc. London Ser. A **137**, 696 (1932). 253, 259, 260, 261, 262, 271
16. Y. Taguchi, T. Matsumoto, and Y. Tokura, Phys. Rev. B **62**, 7015 (2000). 254, 280, 281, 282
17. W. Heisenberg and H. Euler, Z. Physik **98**, 714 (1936). 255, 258, 260, 264
18. J. Schwinger, Phys. Rev. **82**, 664 (1951). 255, 260, 264
19. S.R. White and A.E. Feiguin, Phys. Rev. Lett. **93**, 076401 (2004). 256, 273
20. R. Resta, Phys. Rev. Lett. **80**, 1800 (1998). 257, 260
21. J.E. Avron and J.Nemirovsky, Phys. Rev. Lett. **68**, 2212 (1992). 257
22. C.G. Callan Jr. and S. Coleman, Phys. Rev. D **16**, 1762 (1977). 259
23. C. Zener, Proc. R. Soc. London **145**, 523 (1934). 259
24. L.D. Landau, Phys. Z. Sowjetunion **2**, 46 (1932). 260, 261, 262, 271
25. W. Dittrich and H. Gies, Probing the Quantum Vacuum (Springer-Verlag, Berlin, 2000). 260, 264
26. R.D. King-Smith and D. Vanderbilt, Phys. Rev. B **47**, R1651 (1993). 260
27. M. Nakamura and J. Voit, Phys. Rev. B **65**, 153110 (2002). 260
28. R. Resta, Ferroelectrics **136**, 51 (1992). 260
29. R. Resta and S. Sorella, Phys. Rev. Lett. **82**, 370 (1999). 260
30. T. Fukui and N. Kawakami, Phys. Rev. B **58**, 1651 (1998). 261
31. Y. Nakamura and N. Hatano, J. Phys. Soc. Jpn. **75**, 104001 (2006). 261
32. Y. Kayanuma, Phys. Rev. B **47**, 9940 (1993). 262
33. M.V. Berry, Proc. R. Soc. Lond. A **392**, 45 (1984). 262
34. Y. Kayanuma, Phys. Rev. A **55**, R2495 (1997). 262
35. C. Itzykson and J-B. Zuber, Quantum Field Theory (McGraw-Hill, Inc., 1980). 264
36. F. Woynarovich, J. Phys. C, **15**, 85 (1982). 265
37. F. Woynarovich, J. Phys. C, **15**, 97 (1982). 265
38. R. Arita, K. Kusakabe, K. Kuroki, and H. Aoki, J. Phys. Soc. Jpn. **66**, 2086 (1997). 265
39. K. Kusakabe and H. Aoki, J. Phys. Soc. Jpn. **65**, 2772 (1996). 265
40. B. Sutherland, Phys. Rev. Lett. **74**, 816 (1995). 265
41. W. Kohn, Phys. Rev. A **133**, 171 (1963). 267
42. E.C.G. Stuckelberg, Helv. Phys. Acta **5**, 369 (1932). 271
43. M.A. Cazalilla and J.B. Marston, Phys. Rev. Lett. **88**, 256403 (2002). 273
44. M. Wilkinson and M.A. Morgan, Phys. Rev. A **61**, 062104 (2000). 272
45. G. Vidal, Phys. Rev. Lett. **91**, 147902 (2003). 273
46. G. Vidal, Phys. Rev. Lett. **93**, 040502 (2004). 273

47. A.J. Daley, C. Kollath, U. Schollwoeck, and G.Vidal, J. Stat. Mech.: Theor. Exp. P04005 (2004). 273
48. E.H. Lieb, and F.Y. Wu, Phys. Rev. Lett **21**, 192 (1968). 276
49. H. Nakamura, J. Chem. Phys. **87**, 4031 (1987). 277
50. G. Blatter and D.A. Browne, Phys. Rev. B **37**, 3856 (1988). 278
51. J.T. Chalker and P.D. Coddington, J. Phys. C **21**, 2665 (1988). 278
52. A. Wöjcik T. Luczak P. Kurzynski A. Grudka and M. Bednarska, Phys. Rev. Lett. **93**, 180601 (2004). 278
53. D. Bouwmeester, I. Marzoli, G. P. Karman, W. Schleich, and J. P. Woerdman, Phys. Rev. A **61**, 013410 (2000). 278
54. A. Ambainis, Int. J. Quantum Information **1**, 507 (2003). 278
55. E. Bach, S. Coppersmith, M.P. Goldschen, R. Joynt, and J. Watrous, J. Of Computer and System Sci. **69**, 562 (2004). 278
56. J. Kempe, Contemporary Physics **44**, 307 (2003). 278
57. T. Yamasaki H. Kobayashi, and H. Imai, Phys. Rev. A **65**, 032310 (2003). 278
58. N. Konno, Quantum Information and Computation **2**, 578 (2002). 278
59. N. Konno, Quantum Information Processing **1**, 345 (2002). 278
60. N. Konno, J. Math. Soc. Jpn. **57**, 1179 (2005). 278
61. B. Tregenna, W. Flanagan, W. Maile, and V. Kendon, New J. Phys. **5**, 83.1 (2003). 278
62. T. Namiki, N. Konno, and T. Soshi, Interdisciplinary Information Sci., **10**, 11 (2004). 278
63. A. Nayak and A. Vishwanath, quant-ph/0010117 (2000). 278
64. N. Konno, T. Namiki, T. Soshi, and A. Sudbury, J. Phys. A: Math. Gen. **36**, 241 (2003). 278
65. T.D. Mackay, S.D. Bartlett, L.T. Stephanson, and B.C. Sanders, J. Phys. A: Math. Gen. **35**, 2745 (2002). 278
66. M.A. Nielsen and I.L. Chuang, *Quantum Computation and Quantum Information* (Cambridge University Press, 2000). 278
67. D. Aharonov, A. Ambainis, J. Kempe, and U.V. Vazirani, Proceedings of the 33rd Annual ACM Symposium on Thoery of Computing **50** (2001). 278
68. N. Inui, Y. Konishi, and N. Konno, Phys. Rev. A, 052323 (2004). 278
69. N. Inui and N. Konno, Physica A **353**, 133 (2005). 278

Percolation in Quantum Computation and Communication

K. Kieling[1,2,3] and J. Eisert[1,2]

[1] QOLS, Blackett Laboratory, Imperial College London, Prince Consort Road, London SW7 2BW, UK
[2] Institute for Mathematical Sciences, Imperial College London, Prince's Gate, London SW7 2PG, UK
[3] konrad.kieling05@imperial.ac.uk

1 Introduction

1.1 Percolation Theory

Percolation theory is concerned with the behaviour of connected clusters in a random graph. Originally developed to mathematically describe random media, it has over the years matured to a field of research in its own right. At its core is the notion of a percolation threshold: Say, on a cubic two-dimensional lattice $\mathbb{Z}^2$ neighbouring vertices are connected by an edge with probability p, the distributions being identical for all edges and independent. We say then that this edge is 'open'. Clearly, when $p = 0$, all vertices are unconnected to each other. If we now increase the probability p starting from zero, more and more vertices will be connected. For small values of p, this will typically lead to isolated, non-crossing, small clusters of connected vertices. With increasing probability, the size of the clusters will also increase. The key observation now is that there exists a *critical percolation threshold* $p_2^{(c)}$ that marks the arrival of an infinite crossing cluster. For $p < p_2^{(c)}$, all open clusters are finite, whereas for $p > p_2^{(c)}$ there exists almost certainly an open-infinite cluster. This behaviour of having a connected open-crossing cluster in a finite subset of $\mathbb{Z}^2$ can also be impressively documented by simple numerical simulations. Since the early work on fluid flow in a porous stone giving rise to the first simple percolation model [21], percolation theory has found numerous applications in a quite impressive portfolio of diverse fields, besides being a mathematical discipline in its own right [16]. This includes the study of disordered many body systems in classical and quantum physics of instances of fluid dynamics and fire propagation, of reliability of processes or of many aspects of statistical mechanics.

When it comes to applying percolation theory to physical systems, this article forms an exception in this book. This chapter is concerned with the *connection between percolation theory on the one hand and quantum information processing on*

Kieling, K., Eisert, J.: *Percolation in Quantum Computation and Communication*. Lect. Notes Phys. **762**, 287–319 (2009)
DOI 10.1007/978-3-540-85428-9_10

the other hand. We are facing a percolation-type situation somewhat similar to the one encountered in the study of disordered systems.

- However, in the context of quantum information processing, the *randomness* we encounter is not the one of classical probabilistic parameters in a model, but rather originates from the statistical character of quantum theory under measurements as such.
- Also, it is not the aim to model physical systems in their unknown properties, but rather think of *engineered quantum systems* that have been prepared in a very specific state for a very specific purpose. In this sense, the emphasis is less on *a posteriori* description of properties of systems or materials that are already there. Instead, to explore what state preparation and what communication protocols are possible, when limited to probabilistic processes in quantum information applications.

This chapter forms an instance of a 'review' on the link between percolation theory and quantum information theory, as a topic that is presently receiving notable attention. We will see that this link is a quite natural one, where percolation in several ramifications enters as a concept to overcome limitations imposed by probabilistic processes that occur in measurement processes. Yet, whereas this link has been mentioned a number of times in the literature, so far, only four research articles flesh out this link in detail [1, 9, 28, 34]. This chapter can, hence, be seen as (i) a short review on the material that is known and published at present, as (ii) a presentation of a long and more detailed version of the short proof presented by the same authors in [28], and, most importantly, as an (iii) invitation to the subject. Readers familiar with elements of quantum information theory may wish to skip to Sect. 2.

1.2 Quantum Computation and Communication

Quantum information processing takes the idea seriously that when storing or processing information, it matters whether the underlying physical system follows classical or quantum laws. In classical information theory, one is used to the fact that it hardly makes sense to think of the physical carrier of information, as one can transform the information stored in one form to another carrier in a lossless fashion anyway. This abstraction from the physical carrier is challenged when one thinks of *single quantum systems* forming the elementary processing units. Indeed, the task of transforming the 'information stored in a quantum system' into classical information and back is impossible. Quantum information processing is, however, not so much concerned with limitations due to quantum effects, but rather thinks of new applications in computing and communication when the carriers of information are single quantum systems.

A *quantum computer* [14, 32] is such an envisioned device: One thinks of having an array of quantum systems – spins, say, referred to as *qubits*. This system, associated with a Hilbert space $\mathcal{H} = (\mathbb{C}^2)^{\otimes n}$, is initially prepared in a known, preferably pure quantum state described by a state vector $|\psi\rangle$. Then one manipulates the state by means of unitary time evolution or by means of measurements. Acknowledging that

not any unitary dynamics is accessible on a quantum many-body system, in the *circuit model*, this step of computation is broken down to *quantum gates* [14, 32]. One, hence, implements a sequence of unitary gates that have trivial support on all sites except single sites – giving rise to *single qubit gates* – and pairs of sites – *two-qubit gates*. The state vector after the unitary time evolution is then

$$|\psi\rangle = \prod_j U_j |\psi\rangle. \tag{1}$$

This is followed by local individual measurements on the spins. The measurement outcomes at the end then deliver (typically statistical) data, from which the outcome of the computation can be estimated. The important point is that because the quantum system follow the laws of quantum mechanics and can be prepared in a superposition exploring an exponentially large Hilbert space, some problems could be solved with significantly less effort on this envisioned device than on any classical computer. In fact, they could be solved with polynomial effort in case of some problems such as factoring that are believed to be computationally hard classically.

Yet, the circuit model is only one out of the several models for quantum computation. In the computational model having center stage in this chapter, one abandons the need for unitary control via quantum gates, and performs only local measurements on an entangled quantum state of many constituents. This is the model of the *one-way computer* [8, 23, 37]. The entanglement present in the initial resource then facilitates the efficient simulation of any other computation that had unitary gates available. Needless to say, in any such approach, the core question is how to actually prepare this initial resource state, an instance of a *cluster* or *graph state* [23, 24]. It is in this preparation – and in the way to overcome the intrinsically probabilistic character of quantum measurements – that percolation ideas will be important in the first part of this chapter. It will turn out that by making use of percolation ideas some of the key obstacles in some physical architectures to realize quantum computation can be weakened. In particular, in optical approaches, we will see that percolation ideas facilitate the preparation of such states with little dependence of preparation steps on earlier measurement outcomes – an experimentally very difficult prescription in this context. Percolation will, hence, help us to think of what is known as linear optical quantum computation [9, 28, 29, 47].

The second part of this chapter is dedicated to a related but different question. This is taken from *quantum communication* and *key distribution*: Several applications in quantum information processing, most importantly, quantum key distribution for the secure transmission of classical data, but also instances of the envisioned distributed quantum computing, rely on the availability of almost maximally entangled states shared between spatially separated laboratories. If one has several such stations on the way, each communicating and exchanging quantum particles with a number of neighbours, one arrives at the idea of a *quantum network*. In Sect. 3 we will review the use of percolation ideas to establish maximally entangled pairs for quantum communication between arbitrary stations, based on the published work [1, 34]. Here, the main point will be that classical percolation ideas can be employed to meet the aim of sharing entanglement between arbitrary vertices of a graph: Instead, appropriate

quantum measurements allow to outperform the situation of classical edge percolation. In this sense, one encounters a notion of *entanglement percolation*. In fact, such entanglement percolation can drastically outperform strategies based on standard edge percolation.

2 Percolation and Quantum Computing

2.1 General Concepts

We now turn to the preparation of cluster or more generally graph states as resource state for measurement-based quantum computation. This measurement-based model is a desirable route to quantum computation in a number of architectures. This is not the least due to the very clear distinction between the preparation of entanglement, and the consumption thereof by means of measurements, abandoning the need for unitary gates. Percolation ideas play the crucial role here when thinking of errors, of dealing with probabilistic gates building up the states and, most importantly, of coping with the daunting feed-forwards (dependence of later action on earlier measurement outcomes).

It will be necessary – before we establish the percolation argument – to introduce a number of concepts that will be used later on. A *graph state* [24, 41, 43] is a quantum state described by an undirected graph $G = (V, E)$, with V being the set of vertices, and E the set of edges. The vertices are embodied by physical systems, so single spins or qubits. The edges represent interactions. More specifically, a *graph state* is the simultaneous eigenstate to the set of *stabilizers*

$$K_G^{(a)} = \sigma_x^{(a)} \bigotimes_{b:\mathrm{dist}(a,b)=1} \sigma_z^{(b)} \tag{2}$$

for all $a \in V$ with eigenvalue 1, that is,

$$K_G^{(a)} |\psi_G\rangle = |\psi_G\rangle \qquad \forall a \in V. \tag{3}$$

Here, $\mathrm{dist}(x, y)$ is the graph-theoretical distance [5] between vertices x and y on G, that is, $\mathrm{dist}(x, y) = 1$ for neighbouring vertices. Here and in the following, $\sigma_{x,y,z}^{(b)}$ denotes a Pauli operator with support on the Hilbert space of the physical system labelled b.

Equivalently, this state can be thought of as having each qubit prepared in the state vector $|+\rangle = (|0\rangle + |1\rangle)/\sqrt{2}$ and applying an interaction leading to a *phase gate* or *controlled-Z*-gate

$$U_z = |0,0\rangle\langle 0,0| + |0,1\rangle\langle 0,1| + |1,0\rangle\langle 1,0| - |1,1\rangle\langle 1,1| \tag{4}$$

to neighbouring vertices $a, b \in G$, so to vertices that are connected by an edge $(a, b) \in E$. Because these gates are diagonal in the computational basis, they commute, and hence the order in which they are applied does not influence the final state.

Such a graph state may be defined for any graph. Most important for our purposes are lattices where $V \subset \mathbb{Z}^2$, so finite cubic lattices in two dimensions. Such a graph state of a cubic lattice is called a *cluster state* [8]. It has been shown that local measurements on single constituents of such a cluster state are just as powerful as the gate model for quantum computation, and it can, hence, efficiently simulate any other quantum computer [37, 38]. That is, for a given finite computation there exists a finite graph with $V \subset \mathbb{Z}^2$ such that the computation can be simulated by a sequence of suitable single-qubit local measurements on the cluster state. The usual mapping from a circuit model to a cluster state allows to label one dimension as time that comes in handy because only time slices of a cluster actually have to exist at a given point during the computation. We will also frequently encounter finite subsets of the hexagonal lattice which, is a computation resource in the same sense. Note that *a priori* the lattice does not correspond to any spatial lattice – what determines the quantum state are solely the adjacencies on the graph.

When preparing cluster states, there are two main types of errors where percolation comes into play:

- One can think of the above lattice structure emerging from a *physical lattice*. This may be an *optical lattice* generated by standing wave laser light, where atoms are located at individual lattice sites [31].[4] By means of interactions or controlled collisions, implementing (2) or (4), respectively, a cluster state can in principle be prepared in such systems. Yet, Mott hole defects, where sites are left unoccupied in a random fashion, lead to defects. This is a situation where ideas of *site percolation* can overcome the problem of having non-unit filling factors.
- Using other types of quantum systems, cluster states have to be prepared sequentially, by means of explicitly employing gates to pairs of constituents. This should not be confused with the absence of gates when doing the actual computation via measurements – the gates used during state preparation are independent of the actual algorithm to perform. The most resource-efficient and, hence, most feasible ideas of doing quantum computation with *linear optical systems* or with *atoms in optical cavities* (see, e.g. [30] and references therein) rely on exactly such a sequential build-up of the cluster state. Here, one starts from elementary building blocks, like entangled photon pairs. From these building blocks the full cluster or graph state can be prepared by means of a sequential application of controlled-Z gates. During the course of this process, in principle, gates between any pair of qubits are allowed, which one is actually applied at a given step depends on a chosen prescription which, in turn, depends on outcomes of earlier gate applications. The lattice structure is imposed by the sequence of gates, so every state described by an undirected graph without degenerate edges can be generated.

[4] We leave issues that are under significant consideration in the literature such as the question of locally addressing single sites in measurements aside and focus on the preparation of the cluster state.

This being the most promising approach to think of optical quantum computing, it seems important to address two major challenges that have to be overcome in such an approach:[5].

1. The applied gates necessarily operate in a probabilistic fashion.[6] Indeed, the probability of success of such gates is typically quite small [13, 40]. Hence, when sequentially preparing a cluster state, needless to say, the very order in which the states are sent through the entangling gates plays a crucial role [20, 26, 27]. Especially, the success probability of the fusion gates, $p_{\mathrm{success}} = 1/2$, will be of central interest as this is already the optimal probability for such a gate in linear optics [11, 20]. A naive approach of trying to grow an $n \times n$ cluster state by using such gates will fail. However, this obstacle can in principle be overcome: One can show, using combinatorical methods and ideas of convex optimization, that there exist methods to achieve an optimal scaling of $O(n^2)$ invocations of quantum gates (and number of qubits), despite the gates operating probabilistically [20].
2. Unfortunately, this – and actually any such – procedure leads to a great deal of conditional dynamics: Depending on the outcomes of earlier fusion operations, one has to decide which pair of states will be used in the next step. This, however, turns out to be a significant challenge in actual experimental realizations, as it requires active switching including coherent interaction between any pair of modes in the setup, while unused modes are stored in quantum memories, thus, clearly rendering it a very difficult prescription.

To lessen this daunting requirement, percolation ideas can come into play: One could think of a static setup, that is, an underlying structure is imposed onto the resources and only applications of entangling gates between nearest neighbours are allowed. The probabilistic nature of quantum gates is the source of randomness; we now face a problem of *edge percolation*. How exactly this will work and how to find bounds to the scaling of the resource requirements to prepare two-dimensional cluster states even if the probability of an edge being open is smaller than the critical percolation threshold for a two-dimensional cubic lattice $p < p_2^{(\mathrm{c})}$, will be the subject of the next section [28]. The latter property – which is responsible for some technicalities – is important, as the probability of success of the fusion gate happens to be $p_{\mathrm{success}} = 1/2$, which is identical with the critical percolation threshold $p_2^{(\mathrm{c})} = 1/2$. Hence, ways have to be found to achieve percolation even using such gates.

[5] Again, we will focus on the intrinsic problems of such an idea. From a physical perspective, the development of heralded sources with high efficiency and mode quality, as well as detectors with high-detector efficiency are major obstacles, a significant research effort is dedicated to.

[6] This is a consequence of gates being in turn implemented by means of measurements. All non-linearities in *fully linear optical systems* have to be effectively realized by means of measurements, and this randomness is, hence, the intrinsic randomness in measurements in quantum mechanics. Gates such as the *fusion gates* [10, 35] act in effect as the desired controlled-Z gate, albeit in a probabilistic fashion. In approaches based on *atoms in optical cavities, coupled via light* similar issues occur.

By further developing these ideas, one can ask whether there is a *phase transition* in edge percolation with respect to quantum computing applications: One thinks of a cubic lattice as in 2, with edges being open in case a gate was successful. If $p > p_2^{(c)}$, one can extract a resource almost certainly that allows for universal quantum computing. Below the threshold $p < p_2^{(c)}$, one can show that one can almost certainly simulate the evolution of the quantum system on a classical computer. Hence, this regime is not only useful for quantum computation, but also classically efficiently tractable.[7] In this sense, there is a phase transition in the computational potency of the resource depending on the probability of an edge being open.

In these different flavours, we will encounter percolation ideas in the context of quantum computing. To be brief, we concentrate on the latter two aspects, putting an emphasis on bond percolation (so all p will be bond probabilities unless stated otherwise). We note, however, that the problem of site percolation can be treated similarly.

2.2 Resource State Preparation in Measurement-Based Computing

Renormalization

The goal of this section will be to show how to generate a cluster state of a given size with probabilistic entangling gates (succeeding with probability p) almost certainly with the help of bond percolation. The lattice will be divided into blocks, which will be reduced later to single qubits, thus 'renormalizing' the lattice. Whenever a block contains a crossing open cluster that connects the block's four faces (in the first two dimensions), we will refer to this crossing cluster as a renormalized qubit. If the crossing clusters of two neighbouring blocks actually touch each other (i.e. there exists an open path between two vertices of the first and the second renormalized qubits that lies completely within the union of the two respective blocks, and they are connected by open bonds), then the reduction of the blocks to single qubits will yield a 'renormalized bond' between these qubits. How this reduction actually works is the scope of the following sections. Now, we are looking for the probability $P_p(\mathfrak{U}(L,k))$ of the event $\mathfrak{U}(L,k)$ to occur. $\mathfrak{U}(L,k)$ denotes the event that the renormalied square lattice of size $L \times L$ with hyper cubic blocks of size $k^{\times d}$ is fully occupied and connected. Given a dependence of the block size on the lattice size, $k(L)$, we will use the abbreviation $P_p(L) = P_p(\mathfrak{U}(L,k(L)))$.

The result is more precisely phrased as follows:

Theorem 1 (Resource consumption). *Let $p > p_d^{(c)}$, $d \geq 2$ being the dimension of a hyper cubic lattice. Then for any $\mu > 0$, the probability $P_p(L)$ of having an $L \times L$ renormalized cubic lattice fulfils*

[7] A similar situation has been observed in Ref. [19], where a *Kitaev's toric code state* is not a universal resource, but can be classically efficiently simulated [7]. If one modifies the state very little by means of local phases, one cannot keep track of measurements classically in an efficient fashion. But in fact, it can be shown that the state would serve as a universal resource for quantum computation [18, 19].

$$\lim_{L\to\infty} P_p(L) = 1, \tag{5}$$

with an overall resource consumption of $R(L) = O(L^{2+\mu})$.

Here, $p_d^{(\mathrm{c})}$ denotes the percolation threshold of the d-dimensional hyper cubic lattice. R is used to refer to the number of initial resources, so that the constituents are placed on each lattice site with the ability of 'growing' connections to their neighbours in a probabilistic manner. Note, that the dimension d can always be chosen such that the gates at hand ($p > 0$) operate in a regime that allows for percolation ($p > p_d^{(\mathrm{c})}$).

Proof. ($d \geq 3$) In the case of dimensions $d > 2$, so different from $d = 2$, crossing paths in different directions do not necessarily intersect. This approach is often, nevertheless, favourable due to the higher critical percolation threshold in higher dimensions. Let us fix $L \in \mathbb{N}$ and take

$$U = [1, 2kL]^{\times 2} \times [1, 2k]^{\times d-2} \subset \mathbb{Z}^d \tag{6}$$

for some $k \in \mathbb{N}$. This slab can be divided into L^2 disjoint hypercubes with an edge length of $2k$. With $A_y(k)$, $y = (y_1, y_2) \in [2, 2L]^{\times 2}$ we denote the $(2k)^{\times d}$ hypercube starting at $(y_1 - 2)k + 1, (y_2 - 2)k + 1, \ldots, 1)$. For $y = 2x$,

$$x \in M = [1, L]^{\times 2}, \tag{7}$$

these hyper cubes $A_y(k)$ are the disjoint blocks, and M plays the role of the renormalized square lattice.

Furthermore, we will use the overlap between adjacent blocks in the first direction,

$$B_y(k) = A_y(k) \cap A_{(y_1+1,y_2)}(k) \tag{8}$$

for $y_1 = 2, \ldots, 2L - 1$, and the union of disjoint neighbouring blocks in the second direction, $C_z(k) = A_z(k) \cap A_{(z_1,z_2+2)}(k)$, $z_2 = 2, 4, \ldots, 2(L - 1)$.

On these blocks we will define a series of *events* as follows:

- $\mathfrak{A}_y(k)$: There exists an open crossing cluster in $A_y(k)$ in the first dimension, so an open path containing open vertices a and b with $a_1 = (y_1-2)k+1$, $b_1 = y_1 k$. For $p > p_d^{(\mathrm{c})}$ there exists a constant $g > 0$, only dependent on p, such that [16]

$$P_p(\mathfrak{A}_y(k)) \geq 1 - \exp(-gk^2). \tag{9}$$

- $\mathfrak{B}_y(k)$: The number of open left-to-right crossing clusters in $B_y(k)$ (see Fig. 1) does not exceed 1. It is shown in [2] that for $p > p_d^{(\mathrm{c})}$ there exist constants $a, c > 0$, only dependent on p, such that the probability of $\mathfrak{B}_y(k)$ occurring satisfies

$$P_p(\mathfrak{B}_y(k)) \geq 1 - (2k)^{2d} a \exp(-ck). \tag{10}$$

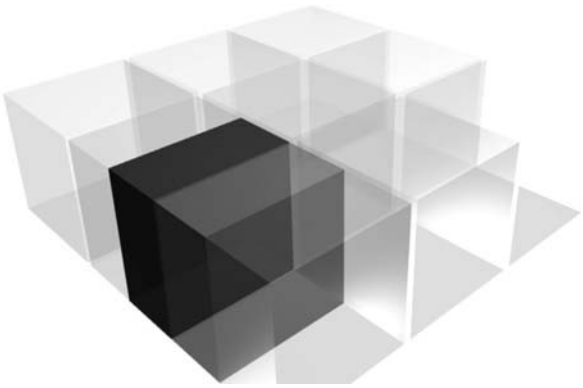

Fig. 1. The blocks A_y for $y = 2x$. The two highlighted regions constitute the block $A_{(3,2)}$, and the darkest one is an overlap with a neighbouring block, so $B_{(3,2)}$

- $\mathfrak{D}_y(k)$: We can now make use of the two events defined before. Let $\mathfrak{D}_z(k)$, $z_1 = 3, 5, \ldots, 2L-1$, $z_2 = 2, 4, \ldots, 2L$, be the events in which there exists an open left-to-right crossing cluster in both blocks, at $(z_1 - 1, z_2)$ and at $(z_1 + 1, z_2)$, and these two clusters are actually connected (see Fig. 2). That means, there exists an open left-to-right crossing cluster in $A_{(z_1-1,z_2)}(k) \cup A_{(z_1+1,z_2)}$. The events $\mathfrak{A}_y(k)$ and $\mathfrak{B}_y(k)$ are *increasing events*[8]. This allows for application of

  Lemma 1 (FKG inequality). *Let $\mathfrak{X}$ and $\mathfrak{Y}$ be increasing events. Then*

  $$P_p(\mathfrak{X} \cap \mathfrak{Y}) \geq P_p(\mathfrak{X}) P(\mathfrak{Y}). \tag{11}$$

  This results in an upper bound for $P_p(\mathfrak{D}_y(k))$, with

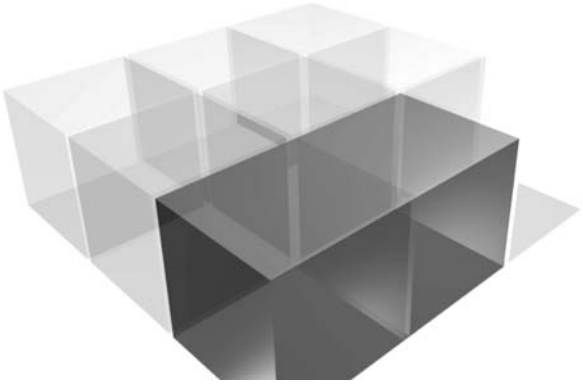

Fig. 2. Again, the blocks A_y for $y = 2x$ are shown and the highlighted region is the intersection $C_{(2,2)}$

[8] Let $\chi(\mathfrak{A}_p)$ denote the characteristic function of the event $\mathfrak{A}$ for an elementary probability p. An increasing event $\mathfrak{A}$ is one that satisfies $|\chi(\mathfrak{A}_p)| \leq |\chi(\mathfrak{A}_{p'})|$ if $p \leq p'$.

$$\mathfrak{D}_y(k) = \left(\bigcap_{a=0,\pm 1} \mathfrak{A}_{(y_1+a,y_2)}(k) \right) \cap \mathfrak{B}_{(y_1-1,y_2)}(k) \cap \mathfrak{B}_{(y_1,y_2)}. \tag{12}$$

- $\mathfrak{E}_z(k)$: The next event we need is the one that 'connects' two blocks in the second dimension. Let $\mathfrak{E}_z(k)$ be the event that there exist at most one open left-to-right crossing cluster in $C_z(k)$. In order to apply the arguments of [2], we extend the blocks in the last $d-2$ dimensions by another $2k$. The probability of $\mathfrak{E}_z(k)$ occurring is bounded by

$$P_p(\mathfrak{E}_z(k)) \geq 1 - (4k)^{2d} a \exp(-2ck). \tag{13}$$

- The last event, $\mathfrak{F}_z(k)$, we will define here is that of having an open left-to-right crossing clusters in both, $A_{(z_1,z_2)}(k)$ and $A_{(z_1,z_2+2)}(k)$, but at most one in $A_{(z_1,z_2)}(k) \cup A_{(z_1,z_2+2)}(k)$. That means, again, that there is actually one left-to-right crossing cluster in $C_z(k)$, but it connects the left and right faces of $A_{(z_1,z_2)}(k)$ and $A_{(z_1,z_2+2)}(k)$ simultaneously. Again, by using the FKG inequality we can construct an upper bound to the probability of occurrence of $\mathfrak{F}_z(k) = \mathfrak{A}_{(z_1,z_2)}(k) \cap \mathfrak{A}_{(z_1,z_2+2)}(k) \cap \mathfrak{C}_z(k)$.

Having all these events at our disposal, the goal of realizing a fully renormalized lattice can be formulated quite easily: we are looking for a simultaneous occurrence of $\mathfrak{D}_z(k)$ and $\mathfrak{F}_z(k)$ for a suitable set of $z = (z_1, z_2)$'s, so

$$\mathfrak{U}(L,k) = \left(\bigcap_{\substack{z_1=3,5,\ldots,2L-1 \\ z_2=2,4,\ldots,2L}} \mathfrak{D}_z(k) \right) \cap \left(\bigcap_{\substack{z_1=2,4,\ldots,2L \\ z_2=2,4,\ldots,2(L-1)}} \mathfrak{F}_z(k) \right). \tag{14}$$

By subsequent application of the FKG inequality we can express an upper bound to the probability of $\mathfrak{U}(L,k)$ occurring in terms of the probabilities of the former events:

$$\begin{aligned} P_p(\mathfrak{U}(L,k)) \geq & \prod_{\substack{y_1=2,3,\ldots,2L \\ y_2=2,4,\ldots,2L}} P_p(\mathfrak{A}_y(k)) \prod_{\substack{y_1=2,3,\ldots,2L-1 \\ y_2=2,4,\ldots,2L}} P_p(\mathfrak{B}_y(k)) \times \\ & \prod_{\substack{y_1=2,4,\ldots,2L \\ y_2=2,4,\ldots,2(L-1)}} P_p(\mathfrak{E}_y(k)) \\ \geq & (1-\exp(-gk^2))^{2L^2-L} \times \\ & \left((1-(2k)^{2d} a \exp(-ck))^2 (1-(4k)^{2d} a \exp(-c2k))\right)^{L(L-1)}. \end{aligned} \tag{15}$$

Now, we will have to find the block-size scaling $k(L)$ such that this probability is approaching unity for large L. Moreover, we are looking for a 'good' scaling, in the sense that the overall resource scaling $L^2 k(L)^d$ does not differ too much from the optimal $O(L^2)$. In order to invert (15), so to find the best $k(L)$ consistent with this approach, we, however, still need to relax the problem to some extent. By using the slowest increasing term in (15) we can bound the expression from above: there exists an integer k_0 such that

$$P_p(\mathfrak{U}(L,k)) \geq (1-(2k)^{2d} a \exp(-ck))^{5L^2} \tag{16}$$

for all $k \geq k_0$. Let us now use the ansatz $k = \lceil L^\varepsilon \rceil$, for some $\varepsilon > 0$.

For any $x \in \mathbb{N}$ there exists a $L_0 \in \mathbb{N}$ such that for all $L \geq L_0$

$$1 - A(2L^\varepsilon)^{2d} \exp(-cL^\varepsilon) \geq 1 - 1/(xL^2). \tag{17}$$

Further,

$$\lim_{L\to\infty} \left(1 - 1/(xL^2)\right)^{5L^2} = \mathrm{e}^{-5/x} \tag{18}$$

and for every $\epsilon > 0$ we can find an x such that $1 - \mathrm{e}^{-5/x} < 1 - \epsilon$.

Therefore, the chosen dependence of k on L is sufficient to achieve a success probability within a chosen ϵ around 1, getting arbitrary close in the limit of large L:

$$\lim_{L\to\infty} P_p(\mathfrak{U}(L,k(L))) = 1. \tag{19}$$

Combining this with the number of blocks used, L^2, this induces a resource scaling of $R(L) = O(L^{2+d\varepsilon})$.

($d = 2$) In the two-dimensional case the connection between paths in the two directions is, of course, not an issue – whenever a block A_y is crossed in both directions, these two crossing paths necessarily intersect. The events needed in this case are the following:

- $\mathfrak{G}_{\mathrm{i},\mathfrak{r}}$: The rectangle $C_{i,r} = \cup_{y,y_r=i} A_y$ is crossed in the r-th dimension. Here, $C_{i,r}$ is the i-th row or i-th column in case of $r = 1$ or $r = 2$, respectively. The probability for such an event to happen satisfies [16]

$$P_p(\mathfrak{G}_{\mathrm{i},\mathfrak{r}}) \geq 1 - skL \exp(-tk), \tag{20}$$

with $s, t > 0$.

Again, the $\mathfrak{G}_{i,r}$ are increasing events, so the probability of simultaneous crossing in all rows and columns,

$$\mathfrak{U} = \bigcap_{\substack{i=1,\ldots,L \\ r=1,2}} \mathfrak{G}_{i,r} \tag{21}$$

satisfies

$$P_p(\mathfrak{U})(L,k) \geq (1 - skL \exp(-tk))^{2L}. \tag{22}$$

Now, the choice of $k = \lceil L^\varepsilon \rceil$ can be used again, together with the last steps for the case $d > 2$. Thus, in the two-dimensional case a resource scaling of $R(L) = O(L^{2+d\varepsilon})$ holds as well.

Although the proof was explicitly stated in terms of bond percolation, a reasoning along these lines will hold as well for site percolation or mixed site/bond percolation, as long as the probabilities in question are above the respective threshold.

Path Identification

For the cluster state to be of any use in quantum computing, the number of resources required to simulate a given quantum circuit has to depend efficiently (i.e. polynomially) on the size of the circuit. As the size L of the cluster state required to implement a given circuit has a polynomial dependence on the circuit's size [37], Theorem 1 already provides a suitable scaling in the number of qubits required.

Still, the amount of time and classical memory required to implement a given computation has to obey a well-tempered scaling as well. The 'quantum part' (i.e. the number of subsequent measurements in the preparation- and in the computing stage) only requires $O(1)$ of time for preparation of the initial pieces, a single step for all the simultaneous entangling operations, and the measurements to reduce the cluster to the renormalized one and perform the computation. Many of them can be performed in parallel, but an upper bound is given by $R(L)$.

The classical amount of memory, of course, starts with $R(L)$ to store all gate outcomes (and therefore the percolated graph). In the following, the scaling of classical resources will be analysed [9].

Crossing clusters

For identification of the crossing clusters within the blocks, cluster finding algorithms such as the Hoshen-Kopelman-algorithm [25] can be employed. Out of the box this would require $O(k^{d-1})$ of classical memory and $O(kL^2)$ time steps. If there exist more than one crossing cluster (which is as of (13) highly improbable), only a single one (e.g. the one with the largest surface) will be chosen for the subsequent procedure.

Connecting the blocks

A 'mid-qubit' which is a member of a crossing cluster near the centre of the block will be chosen ($R(L)$ time-steps) in every block. Let us define an open path on $G = (V, E)$ between $a_1, a_{n+1} \in V$ by $\mathcal{P}(a_1, a_{n+1}) = \{(a_1, a_2), (a_2, a_3), \ldots, (a_n, a_{n+1})\}$ with $(a_i, a_i + 1) \in E$, $i = 1, \ldots, n$, and its length by $|\mathcal{P}(a_1, a_{n+1})| = n$. Because we are using undirected graphs, $(a, b) = (b, a)$ and there is a corresponding path from b to a for each path from a to b. Open paths between the mid-qubits of all pairs of neighbouring blocks are identified using a breadth-first-search (BFS) algorithm [42] ($R(L)$ time and memory complexity).

To prevent loops from being present in the paths in the first place, the following procedure is employed:

1. Using BFS on the crossing clusters starting from the mid-qubits and constrained to the respective block, each site is labelled with the length of the shortest path to the mid-qubit in this block. By going in the direction of decreasing length, the shortest path $\mathcal{P}(s, m(x))$ to a block's x mid-qubit $m(x)$ can be found within its block, starting from any site s.

[9] More details and a MatLab implementation of the relevant parts can be found in the supplementary material of [28] at http://www.imperial.ac.uk/quantuminformation.

2. The facing boundaries of all pairs of neighbouring blocks (x_1, x_2) are searched for the pair of sites (s_1, s_2), one in each block, with the least sum of their distances $|\mathcal{P}(s_1, m_1)| + |\mathcal{P}(s_2, m_2)|$ from their respective mid-qubits m_1 and m_2, and the bond (s_1, s_2) being open.
3. With the composite path $\mathcal{P}(m_1, s_1) \cup (s_1, s_2) \cup \mathcal{P}(s_2, m_2)$ a loop-free connection between m_1 and m_2 is found. Although paths from the mid-qubits to different neighbours might have sub-paths in common, there will be no loops inside a block due to starting always with the same site and the same algorithm for all paths to the boundaries in a given block.

Reduction to a Renormalised Lattice

Instead of the whole square lattice which would require to identify cross-like junctions within the blocks, the procedure will renormalize to a hexagonal lattice where only T-junctions are required. Of course it will be embedded in the square lattice geometry in the obvious way. A square lattice would involve crosses the construction of which is not clear when T-junctions have been found and local measurements are used for reduction. There is, however, an easy way to turn the whole lattice into a square one by using local measurements afterwards [44].

The procedure to cut out parts of the cluster, or yanking paths straight, involves single qubit measurements of the Pauli operators σ_y and σ_z. Let us briefly summarize the effective action of these operations when applied to a qubit constituting a vertex $a \in V$ of a graph state $|\psi_G\rangle$ with $G = (V, E)$ [24]. The neighbourhood of a vertex a will be denoted by $N_a = \{b : \mathrm{dist}(a, b) = 1\}$, the sub graph of G induced by $A \subset V$ is $G[A] = (A, \{(a, b) \in E : a, b \in A\})$ and the complement of a graph G with respect to the set of all possible edges by $G^c = (V, \{(a, b) : a, b \in V\} \setminus E)$. The measurement rules now read

- σ_y measurements perform local complementations: $G' = (G[V \setminus \{a\}] \setminus G[N_a]) \cup G[N_a]^c$. So, it swaps all possible edges in its immediate neighbourhood.
- A σ_z 'cuts' the vertex a. The graph representing the resulting state is $G' = G[V \setminus \{a\}]$.

The resulting graphs G' actually are only obtained after applying some local unitaries to the neighbours of a, which depend on the measurement outcomes, to the remaining qubits. However, one can also store the effective unitary to apply to each remaining qubit (a memory requirement of $O(1)$ per qubit) and adjust the measurement basis of the subsequent measurements. Because each qubit will be measured out by the end of the computation, it is sufficient to use the second approach to the compensation of random measurement results.

The first application is to isolate the paths and eliminate the spare sites and dangling ends towards the mid-qubits. This is achieved by cutting out all unneeded sites by measuring their qubits in the σ_z basis.

Now, one is left with a hexagonal lattice where each edge possibly consists of a long path and each site might consist of a triangular structure in the worst case (depending on the type of lattice used, also the wanted single-qubit sites are possible).

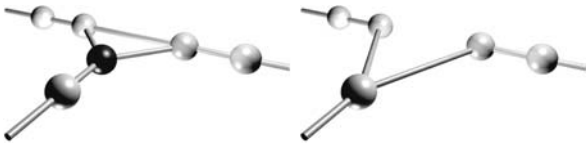

Fig. 3. Effect of a σ_y measurement on a triangular junction of a cluster. If the three arms are, as shown, not immediately connected outside the triangle, a σ_y measurement on the dark qubit has the effect of destroying the triangle in favour of a T-shaped junction. Due to symmetry, any of the three qubits in the triangle could have been chosen

The triangles can be destroyed by suitable σ_y-measurements, as shown in Fig. 3. After that, only single-qubit junctions are left, the paths between which can be shrinked by subsequent application of σ_y-measurements to a single edge.

Summing up all these contributions we realize that both – the amount of classical memory and the number of time-steps – are bounded by $R(L)$ as well.

It should be pointed out that one obstacle in one-way quantum computation is to keep the whole state in memory. Having fixed the algorithm in advance, the required state size is known and therefore also the block size for a fixed allowed error rate. Therefore, to grow individual blocks and reduce them to single qubits, only the neighbouring blocks have to exist. This especially allows for growing the reduced lattice in the time direction while the computation moves on, requiring only $O(L^{1+\mu})$ qubits to be kept in memory.

Decreasing the Vertex Degree

Choosing the appropriate lattice

To actually utilize the protocols based on percolation theory the initial resources (i.e. the stars sitting on the lattice sites) should be as small as possible. As it is more difficult to prepare larger states (this is the problem to be solved in the first place), the lattice with the lowest vertex degree for which $p_{\mathrm{success}} > p^{(\mathrm{c})}$ is still fulfilled will be favourable.

Again, results known in percolation theory, but also specifics of the physical implementation can be used to decrease the vertex degree of the initial states. First, using star resources, one would have to look for the lattice with the smallest vertex degree that is still suitable for the bond probabilities at hand. It is not necessary to stay in two dimensions, as the blocking procedure can use high-dimensional lattices and renormalize them to two-dimensional square lattices.

For example, in the case mentioned above, $p_{\mathrm{success}} = 1/2$, the smallest vertex degree compatible with p is 4, realized by the diamond lattice with $p_{\diamond}^{(\mathrm{c})} \approx 0.389$. That translates into five-qubit initial states. To see, that the procedure still works for lattices different from cubic, see the results of numerical simulations on the diamond lattice in Fig. 4.

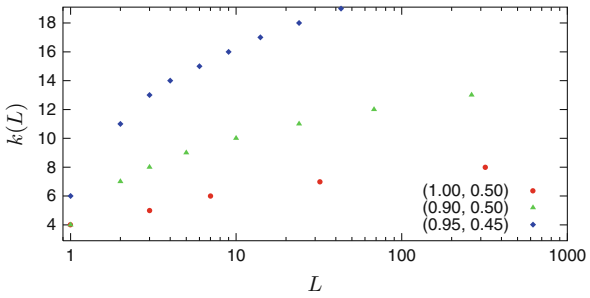

Fig. 4. Results of Monte Carlo simulations to determine the scaling behaviour of the renormalization procedure on the diamond lattice. The dependence of the diamond lattice's block size $k \times k \times k$ on the size $L \times L$ of the renormalized square lattice is shown for three different sets of site- and bond probabilities $(p_{\mathrm{s}}, p_{\mathrm{b}})$. The threshold for the probability of $\mathfrak{U}$ occurring was chosen to be $1/2$. 10^5 blocks of each size were created and used to randomly populate each lattice size 10^3 times

Covering lattice

If the entangling operations at hand have the property that one of the qubits survives (such as the probabilistic parity check 'fusion' [10] in linear optics), the following property of bond-percolation can further reduce the size of the initial pieces. So far, the sites of the lattice are occupied by single qubits, the bonds are given by edges in the underlying entanglement graph. If one qubit is left by the entangling operation we will not think of this one as being a site itself, but rather belonging to the bond between its neighbouring site.

Having such a graph state (which exact lattice type does not matter), we can measure the central qubit a of the initial stars (the dark one in Fig. 5) in the σ_y-basis. Given the specific structure we have at hand, this operation actually performs a transformation from the lattice type we had before to its covering lattice: now think of the qubits that were sitting on the bonds as proper sites. The old sites have disappeared (they have been measured out) and the new ones are connected to all the new sites that were in the same neighbourhood of an old site (local complementation).

Intuitively, the covering lattice has the same connectivity properties as the original lattice before. Paths through a star between two arms are existent iff the star was present and the two entangling operations involving these arms were successful. The same holds on the covering lattice. This property is reflected by the equation $p^{(c)}_{G,\mathrm{b}} = p^{(c)}_{G_{\mathrm{c}},\mathrm{s}}$, so bond percolation on the original lattice induces site percolation on the covering one.

As the local complementation inside the stars commute with the entanglement operation between them, the central qubit might be neglected from the very start (see Fig. 5). So, one further qubit can be saved by starting with the fully connected graph state (locally equivalent to the GHZ state) that has one qubit less than the corresponding star. In case of the diamond lattice, with four-qubit GHZ states (tetrahedral states), the pyrochlore lattice can be built.

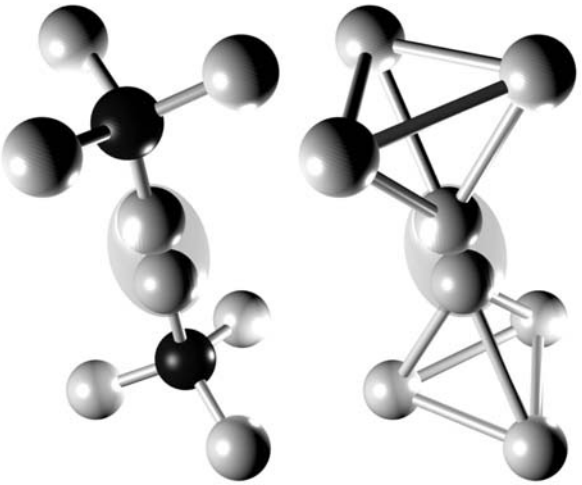

Fig. 5. Pairs of initial resources for the diamond lattice and its covering one, the pyrochlore lattice. A probabilistic entangling gate is applied between pairs of qubits of all neighbouring initial states. The central qubit (*dark*), is measured out in the σ_y-basis, resulting in the transformation from diamond to pyrochlore lattice

Further methods to reduce the amount of conditional dynamics in linear optical quantum computing

Surely, if the scheme requires quite large initial stars, they can be prepared with the same tools probabilistically, starting from smaller stars. For a fair assessment, however, the constraints that led to the percolation scheme in the first place have to be imposed here as well. That is, the restriction to a static setup. Whether composite stars can be used in a static layout now depends on how the entangling gates work in detail, that is, what the failure outcomes are. This is of interest due to the fact that in general a failure in the star preparation step would require back-up steps that do not allow for subsequent application of further entangling gates without re-routing. A type of gates with suitable properties is the one that acts as a σ_z-measurement on both qubits on failure. For example, parity check based gates in linear optics offer this feature.

That this feature might actually bring some benefit is shown by the following example (see Fig. 6). Two instances of such an entangling gate are applied to a pair of five-qubit stars, one to a pair of arms and one to the central qubits. On success of one of the 'arm' fusion gates, the two stars are connected by a two-edge chain. The middle qubit of this chain (dark) will be measured out in the σ_x-basis, leaving the two centres merged in a redundantly encoded qubit, being the centre of a star with six arms. A second application of such a gate on the two qubits of the new centre will always succeed due to the entanglement already existing between them.

If, however, the first gate operation failed, the two arms the gate was acting on will be cut of as a consequence of the σ_z failure outcome. The σ_x measurement

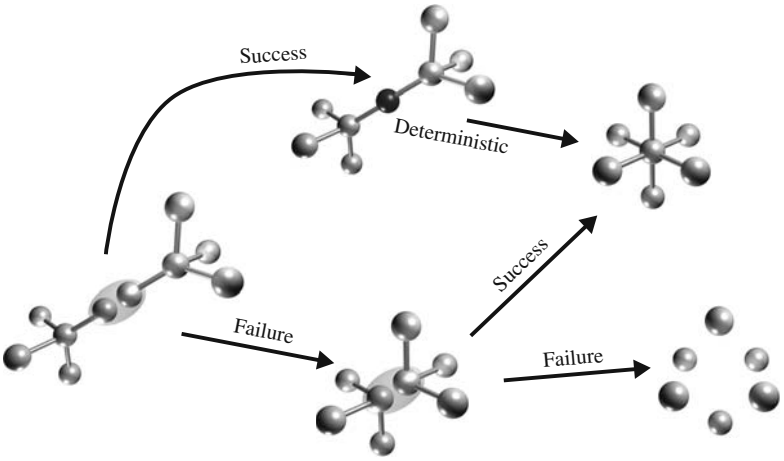

Fig. 6. A pair of five-qubit stars (stars with four arms and one central qubit) can be used to create a single seven-qubit star with a probability of $p_{\mathrm{success}} = 1 - (1 - p_{\mathrm{gate}})^2$. With $p_{\mathrm{failure}} = (1 - p_{\mathrm{gate}})^2$ the six arm qubits are separated from each other

now acts on one part of a product state, leaving the other part – the two stars – unchanged. Now, a second try is possible by application of the entangling operation to the centre qubits. The success outcome will be the same as above, on failure the centres will be cut off, leaving the six qubits in the product state vector $|+\rangle^{\otimes 6}$. The failure outcome is the result of two consecutive failures of these entangling gates, so $p_{\mathrm{success}} = 1 - (1 - p_{\mathrm{gate}})^2$, which is $p_{\mathrm{success}} = 3/4$ in the case of the linear optics gate mentioned earlier.

All these operations do not need any classical post-processing or re-routing, therefore, this scheme is suitable to be used in the procedures introduced above. Because the centre qubits are simply cut off when a failure occurs, this procedure and the bond percolation involving the arms are completely independent. So, both processes together can be modelled as a mixed site/bond percolation with the site probability being $p_{\mathrm{s}} = p_{\mathrm{success}}$.

As long as the bond probability and the initial state preparation (site-) probability are above the percolation threshold of the respective lattice, this scheme might be useful to further reduce the size of the initial star shaped quantum states.

2.3 Phase Transitions in the Computational Power

A related yet complementary motivation to look at percolation theory in the context of quantum computing is the question whether a universal resource state can be prepared in principle. Surely, above the percolation threshold a universal resource for quantum computing can be extracted from a percolating lattice in an efficient manner, as has been described in the previous section. This approach, in turn, will fail almost surely below the threshold. Indeed, it has been shown in [9] that for $p < p^{(\mathrm{c})}$ the statistics of all possible measurements (so all possible quantum computations)

on the state represented by the resulting graph can almost certainly be efficiently simulated on a classical computer. This effect can indeed be seen as a phase transition in computational power of the resource state described by the lattice (caused by the phase transition of the mean cluster size). Assuming that BQP≠BPP[10], this phase transition distinguishes between states that can be used for universal quantum computing and those which cannot (see also [19]).

This phase transition can be made precise under the assumption that a certain quantity – the entanglement width – provides a handle on the computational universality of a family of states, by using it as an order parameter and investigating its properties in the sub- and supercritical regime. The entanglement width E_{wd} is a measure of entanglement, introduced in [44]. It can be used to characterize the amount of entanglement – somehow the degree of 'non-classicality' – contained in a quantum system. We refer to [44] for its definition and properties. For $d = 2$, it can be seen that the amount of entanglement contained in the states described by the lattice jumps from a logarithmic to a linear scaling in L at the percolation threshold.

Supercritical

Above the respective percolation threshold of a particular lattice of size $L^{2+\mu}$ with $\mu > 0$, an $L \times L$ square lattice can be extracted efficiently, as shown in Sect. 2.2. In [9] an alternative algorithm is proposed, which achieves $\mu = 0$ for $d = 2$.

Theorem 2 (Supercritical states). *Let $p > p_2^{(\mathrm{c})}$. With probability*

$$\lim_{L\to\infty} P_p(L) = 1, \tag{23}$$

and an overall resource consumption of $O(L^2)$ an $L \times L$ cluster – a resource for universal quantum computing – can be generated from a square lattice.

In this approach, in contrast to the renormalization algorithm described in Sect. 2.2, the block size of the renormalized lattice is not held fixed [9], resulting in an improved scaling of the resource consumption in case of the two-dimensional square lattice.

Again, this approach can be used to grow the cluster state while computation moves on. With a fixed width new layers can be added on top, allowing for subsequent identification of new horizontal paths (and their connections to the underlying lattice). So it is not required to keep the whole lattice in memory, rather only a set of qubits of size $O(L)$.

A natural substructure of a percolating $n \times n$ lattice is already provided by the fact that there exist at least $m = O(n)$ vertex-disjoint crossing paths (which shall be event $\mathfrak{G}_m(n)$) in either dimension almost certainly in the limit of large n.

[10] This means that quantum computers are actually more powerful than classical computers. Although this feature is assumed to be highly plausible, the strict separation of the complexity classes remains unproven today, not unlike the situation for P≠NP.

Consider the event of having at least one left-to-right crossing path in a two-dimensional $n \times n$ block, which happens with probability

$$P_p(\mathfrak{A}(n)) \geq 1 - \exp(-g(p)n^2), \tag{24}$$

$g(p) > 0$ (9). When this event is still happening when changing the state r arbitrary edges on the lattice, there have to be at least $r + 1$ vertex-disjoint left-to-right crossings in this block. With $r = \beta(p)n$ an inequality from [16] allows us to write

$$P_p(\mathfrak{G}_{\beta(p)n}(n)) \geq 1 - \left(\frac{p}{p - p_2^{(c)}}\right)^{\beta(p)n} \mathrm{e}^{-ng(p)}. \tag{25}$$

In the limit of $n \to \infty$ this probability approaches unity, if

$$g(p) - \beta(p) \log\left(\frac{p}{p - p_2^{(c)}}\right) > 0, \tag{26}$$

which can always be achieved by suitable choice of β for a given p. Therefore, in the limit of large m, there are almost certainly m vertex-disjoint open left-to-right crossing paths in a square lattice of side length $n = m/\beta(p)$. In other words, the number of these crossings scales as $O(n)$.

Algorithm

The challenge now is to identify $O(L)$ suitable paths such that the reduction to a fully populated regular lattice with the tools of Sect. 2.2 is possible. In [9] a very detailed description of an algorithm achieving this goal can be found, some of the steps of which are illustrated in Fig. 7. The important stages are the following:

1. *Path identification*: An algorithm from maze solving, the *right-hand wall follower*, which can identify the right-most path along a wall (which will be the surface of

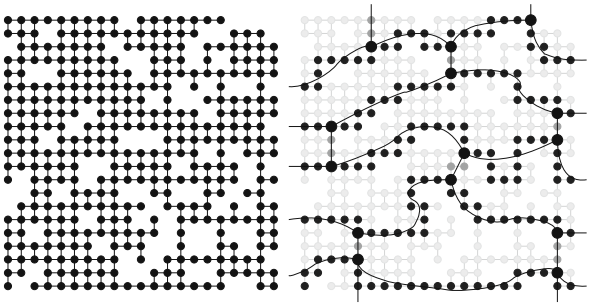

Fig. 7. Illustration of the algorithm to extract an $L \times L$ lattice with only constant overhead per site. The left picture shows the initial percolated lattice. At the right, the identified paths after alternating bridge decomposition and error correction, as well as the final graph after the quantum measurements are shown

the graph or the previous path), is used. By applying it consecutively it finds a maximum set of non-intersecting crossing open paths in either direction.
Vertical paths are found by using every third path that result from the right-hand wall follower. For horizontal paths, the *2-local* version of this algorithm is used, which means that a graph distance on the underlying lattice to the previous path of at least 3 is ensured.
These gaps between neighbouring paths ensure that the reduction can be performed in the end. A distance of 1 between neighbouring horizontal paths is surely not enough when it comes to the shortening of intermediate parts by means of σ_y measurements. Having one qubit in between turns out to be not enough, where intersections with vertical paths occur.

2. *Alternating bridge decomposition*: While fixing paths in the horizontal direction, the vertical ones are cut into segments between neighbouring horizontal paths (*bridge decomposition*). By only using every other of these segments (alternating bridge decomposition), a hexagonal structure is imposed, simplifying the reduction stage as before, while still giving rise to a universal resource state. Due to the choice of using every third vertical path, the graph has essentially the same topology as a hexagonal lattice, up to local errors at the crossings. For an in-depth analysis we refer to [9]. The bridge decomposition further assures a simple topology of the crossing points, because multiple crossings and common parts of horizontal and vertical paths are cut out.
3. *Correction of local errors*: All that is left at this stage is a hexagonal structure where the bonds consist of paths the vertices of which have vertex degree 2, and the sites consist of a couple of vertices with degree not necessarily 3. More specifically, they contain vertices of degree ≥ 3 on the horizontal paths (the *abutments*) and one vertex per crossing of degree ≥ 2 at the beginning (or end, respectively) of a vertical path. By appropriately removing the vertices in the middle of the abutments from the graph, the crossings are reduced to single vertices of degree 3 (a T-shaped junction), thus allowing for reduction of the lattice by local Pauli measurements.

After this classical identification process is done, the graph is reduced to a hexagonal lattice using local measurements as in Sect. 2.2.

Entanglement width

An $L \times L$ cluster state has an entanglement width of $E_{\mathrm{w}d} = O(L)$. Due to the fact that the entanglement width does not increase during one-way computation (which also is what is effectively done to extract the cluster from the percolated lattice in all known proposals, see also Sect. 2.2), the extracted cluster can be used to derive a lower bound to this entanglement width,

$$E_{\mathrm{w}d}(p > p^{(\mathrm{c})}) \geq O(L). \tag{27}$$

This bound holds for any regular lattice with $d \geq 2$ above its respective percolation threshold.

Subcritical

Below the percolation threshold the following behaviour is observed:

Theorem 3 (Subcritical states). *For $p < p_2^{(c)}$, the corresponding quantum states can be simulated efficiently on a classical computer.*

The idea behind the proof is that the entanglement width is bounded by the entanglement width of the largest connected component [9]. Below the percolation threshold, this is of size $O(d \log L)$ [3], therefore bounding

$$E_{wd} \leq O(\log L). \tag{28}$$

Making use of [3], it is shown that this bound holds for $2 \leq d \leq 6$. Further, the logarithmic scaling of the size of the largest connected component results in the computational space to be of size $\mathrm{poly}(L)$, so efficiently simulatable by classical means.

3 Quantum Repeater Networks for Quantum Communication

3.1 General Concepts

Another quite natural application of percolation ideas in the context of quantum information processing is to find ways of designing quantum networks for quantum communication. This is now an application no longer related to quantum computation, but to quantum communication and quantum key distribution. Here, the concept of a network emerges quite naturally, and it seems meaningful to ask to what extent percolation ideas can help here.

The setting we will discuss in this section – reviewing the content of [1, 22, 34] – is slightly different from the previous ones: We will no longer make strict use of classical percolation ideas to identify threshold behaviour in the possibility of preparing some quantum states. Instead, but in a closely related fashion, we will ask to what extent one can modify quantum measurement schemes to realize percolation-like settings which outperform standard-bond percolation when naive measurement patterns are used. It will, hence, be not be sufficient to look at classical properties of quantum states as before, but we will have to consider the quantum states as such.

The idea of *quantum communication* or, more specifically, of *quantum key distribution* plays a seminal role in quantum information science. Indeed, whenever two laboratories share quantum systems in highly entangled states, by appropriate measurements and classical post-processing, a *secret key* can be extracted from the measurement data. This key can then be used for the secure transmission of classical data. For a review on this idea, which has led to numerous experimental implementations, and based on which commercial devices are available, see, for example [15]. For 'sufficiently entangled' states one can indeed show that the resulting key distribution is unconditionally secure, in the sense that the security proof does not rely on

unproven assumptions on the hardness of certain mathematical problems. Instead, it is merely assumed that an eventual eavesdropper could have access to any technological device, but is constraint by the laws of quantum theory as such in his or her possible action.

The functioning of such ideas, however, relies on the availability of sufficiently pure and entangled quantum states. If – in a sense – too much noise is in the system, which is the situation encountered in the distribution of entangled state through noisy channels over large distances, then the key will no longer necessarily be secure. In such a situation, ideas of *quantum state distillation* or of *quantum repeaters* offer a solution. This amounts to a fragmentation of the whole transmission line to a sequence of *repeater stations*, or, more generally, to a network of repeater stations. And here, needless to say, is where percolation ideas come in.

We will start by describing the setting of [1]. Consider some lattice, the vertices of which are identified with repeater stations, or laboratories in which one can perform quantum operations. Between such vertices, non-maximally entangled states can be created. Once two vertices share entangled quantum systems, we will say that they are connected by a *'quantum edge'*. Following this entanglement distribution process, only 'local' operations constrained to the qubits of a repeater station are possible, coordinated by classical communication. This is the setting of *local operations with classical communication* (LOCC), which is the standard paradigm when considering distributed quantum systems. Based on such operations, purification protocols [6, 46] can transform a single pair or a chain of two pairs into a maximally entangled pair, the equivalent to an open bond. This process is intrinsically probabilistic, which represents the bond probability. The probability of success of such a protocol (and with it the bond probability) depends not only on the amount of entanglement that is available in the very beginning but also on the distillation strategy employed. Therefore, we cannot assign unique bond probabilities to a lattice with quantum bonds.

3.2 Classical Entanglement Percolation

We will now compare two different settings, following [1, 34]. The first approach is to make use of natural physical measurements, where each of the quantum edges is purified separately. This then leads to a familiar edge percolation problem: A quantum edge corresponds to sharing a non-maximally entangled state with a state vector of the form

$$|\varphi\rangle = {\lambda_1}^{1/2}|0,0\rangle + {\lambda_2}^{1/2}|1,1\rangle. \tag{29}$$

λ_1 and λ_2 are the *Schmidt coefficients* satisfying $\lambda_1 + \lambda_2 = 1$, assuming that $\lambda_1 \geq \lambda_2$. For simplicity, all non-maximally entangled states are taken to be pure. It is known that there exist local quantum operations assisted by classical communication (LOCC) that transform $|\varphi\rangle$ into a maximally entangled pair with state vector $2^{-1/2}(|0,0\rangle + |1,1\rangle)$, with a probability of success of

$$p_1 = \min(1, 2(1-\lambda_1)). \tag{30}$$

This probability of success will be referred to as *singlet conversion probability* (SCP) of a single quantum edge. In general, having a LOCC conversion protocol means that there exist operators $M_A^{(k)}, M_B^{(k)}$ satisfying $\sum_k (M_A^{(k)})^\dagger M_A^{(k)} \leq \mathbb{1}$ and $\sum_k (M_B^{(k)})^\dagger M_B^{(k)} \leq \mathbb{1}$ which can be implemented with LOCC such that

$$(M_A^{(k)} \otimes M_B^{(k)})|\varphi\rangle = (p^{(k)})^{1/2}(|0,0\rangle + |1,1\rangle)2^{-1/2}, \tag{31}$$

$p_1 = \sum_k p^{(k)}$. In this case, the filtering is quite simple: we merely need to consider a single successful outcome, $k = 1$, and take $M_A^{(1)} = (\lambda_2/\lambda_1)^{1/2}|0\rangle\langle 0| + |1\rangle\langle 1|$ and $M_B^{(2)} = \mathbb{1}$. As can be readily verified, this leads to a maximally entangled state with the above probability of success. This filtering process is called *Procrustean method* [4].

Once one has a maximally entangled pair, we encounter the situation as before, and we say the corresponding edge is open, in the sense of usual edge percolation, and as being used throughout this chapter. If the protocol fails, one is led to an unentangled state, and the edge is closed. Hence, λ_1 governs the percolation behaviour and defines the edge probability. If one is above the percolation threshold of the respective lattice, a connected path can be identified almost certainly between any two vertices A and B of the lattice. Let $\mathfrak{c}(A, B)$ denote the event that A and B are connected by maximally entangled bonds. Then,

$$\lim_{\mathrm{dist}(A,B)\to\infty} P(\mathfrak{c}(A, B)) > 0 \tag{32}$$

if and only if $p_1 > p^{(c)}$. Physically, this means that A and B share a perfect quantum channel through which the state of a single qubit can be sent in a lossless fashion. This setting which is the natural analogue of edge percolation will be called *classical entanglement percolation (CEP)*.

3.3 Quantum Percolation Strategies

The quantum character of the involved states ('quantum edges'), however, allows for some improvement. The main observation is that for quantum systems, one does not necessarily have to perform the above measurements, leading individually to open or closed edges, but can resort to appropriate local collective operations. If the task is to achieve a perfect quantum channel between any two vertices A and B in a lattice, then we have achieved this when having a maximally entangled pair of qubits between A and B at our disposal. This process should succeed in the best possible fashion. The aim, hence, is to maximize the SCP, so the probability to achieve a maximally entangled pair between two vertices A and B, but not necessarily exploiting the above CEP.

To exemplify the mechanism, let us first consider a one-dimensional chain with three vertices, A, B, and C, such that A and B, and B and C share a state with state vector $|\varphi\rangle$ each (they are connected by a quantum edge). This is a quantum repeater situation. Then, clearly, applying the above filtering corresponding to CEP twice, one succeeds with a probability p_1^2.

But, since vertex B holds two quantum systems, one can also do a collective local operation. The SCP asks for the optimal probability $p = \sum_k p^{(k)}$ such that

$$(M_A^{(k)} \otimes M_{B_1,B_2}^{(k)} \otimes M_C^{(k)})|\varphi\rangle_{A,B_1}|\varphi\rangle_{B_2,C} = (p^{(k)}/2)^{1/2} \times (|0,0\rangle_{A,C} + |1,1\rangle_{A,C})|0,0\rangle_{B_1,B_2}. \tag{33}$$

Clearly, $p \geq p_1^2$, as the protocol in (33) includes the prescription of CEP where one tries to purify the entanglement between A and B_1 and B_2 and C individually.

We can also easily obtain an upper bound to the probability of success: The class of protocols defined in (33) is included in the one of (31) in the case when A, B_1, and B_2 are treated as a single system. Doing such collective operations (instead of only in B_1 and B_2) can only improve the probability of success, hence, this upper, bound.

Somewhat surprisingly, it can be shown that this bound can indeed be achieved [6, 46]. In B_1 and B_2 one performs a joint measurement $k = 1, \ldots, 4$ with

$$M_{B_1,B_2}^{(k)} = |\psi^{(k)}\rangle_{B_1,B_2}\langle\psi^{(k)}|_{B_1,B_2}, \tag{34}$$

where

$$|\psi^{(1)}\rangle = (|0,0\rangle + |1,1\rangle)2^{-1/2}, \ |\psi^{(2)}\rangle = (|0,0\rangle - |1,1\rangle)2^{-1/2}, \tag{35}$$

$$|\psi^{(3)}\rangle = (|0,1\rangle + |1,0\rangle)2^{-1/2}, \ |\psi^{(4)}\rangle = (|0,1\rangle - |1,0\rangle)2^{-1/2}. \tag{36}$$

Two of the outcome probabilities of this four-outcome measurement are equal to $p_{\max} = (\lambda_1^2 + \lambda_2^2)/2$, whereas the two further outcome probabilities are given by $p_{\min} = \lambda_1\lambda_2$. This local filtering is in fact nothing but a collective *'Bell'-measurement* in the $\sigma_z\sigma_z$-basis. This procedure reaches the above upper bound, and hence,

$$p = p_1. \tag{37}$$

This scheme, simple as it is, already shows that with collective operations, one can improve the involved probabilities, from p_1^2 to p_1. Note that here the SCP is taken as a figure of merit, whereas other figures of merit, like the average final entanglement quantified in terms of an entanglement measure, can also be meaningful quantifiers of success of the scheme [34]. Also, the same protocol is optimal in case one has two different pure states in the Schmidt basis at hand.

3.4 Absence of Improvement for One-Dimensional Systems

A first natural instance where this process can be applied is the case of one-dimensional systems. In this case, it turns out, there is no improvement possible [22, 34]. The improvement that is possible for two quantum edges does not persist in the asymptotic limit of a quantum chain, and an exponential decay of the SCP with the distance between two vertices of the chain cannot be avoided [1]. Moreover, the only way of having unit SCP is to have a chain of maximally entangled pairs in the first place. The argument to show this makes use of the entanglement measure

of the *concurrence* of a two-qubit state. For a state vector $|\varphi\rangle = \sum_{j,k} T_{j,k}|j,k\rangle$ its concurrence is found to be $C(\varphi) = 2|\det(T)|$, in terms of the 2×2-matrix T. In the situation of having a one-dimensional chain of repeaters involving $N+1$ quantum edges and hence $N+w$ vertices, involving N correlated measurements, one then finds that the maximum average concurrence of the first and the last qubit in the chain is given by

$$C = \sup_{\mathcal{M}} \sum_{r_1,\ldots,r_N} 2 \left| \det \left(|\varphi_1\rangle\langle\varphi_1| M_1^{(r_1)} |\varphi_2\rangle\langle\varphi_2| \ldots M_N^{(r_N)} |\varphi_{N+1}\rangle\langle\varphi_{N+1}| \right) \right| . \tag{38}$$

In this expression, $\mathcal{M}$ stands for all measurements, whereas the $M_i^{(r_i)}$ are 2×2 matrices specifying the r_i-th outcome at site i, corresponding to the state vector $|\mu_i\rangle = \sum_{j,k} (M_i^{(r_i)})_{j,k} |j,k\rangle$ of this specific measurement outcome. From this expression demonstrating the exponential decay of the concurrence with the distance between two vertices in a one-dimensional chain, one can also derive the exponential decay of the SCP. Hence, while for two repeaters one can find a better probability of success, this does not lead to a different asymptotic performance of this type of quantum percolation strategy.

For other lattices, different from simple one-dimensional chains, one can improve the situation, however, compared to classical entanglement percolation, as we will discuss in the subsequent subsection. In this way, a lattice having some quantum edges can be transformed into a different lattice with maximally entangled pairs being randomly distributed, whereas the distribution will depend on the strategy employed (e.g. CEP or collective operations). This approach can outperform methods relying solely on classical probabilities and equivalences between these lattices (e.g., covering, matching, or dual lattices). This is an effect which is caused by the quantum nature of the bonds.

3.5 Examples of Quantum Percolation Strategies

Hexagonal lattice

An example to highlight the difference to a purely classical approach is the following: One starts from the situation where neighbours on a hexagonal lattice share two specimens of the same state. This situation is very natural in the quantum case. One simply has to distribute a state of the same kind twice. The aim is to establish a connected open path between arbitrary vertices (taken from a triangular sub lattice).

Theorem 4 (Singlet conversion probability in the hexagonal lattice). *Consider a hexagonal lattice, where nearest neighbours share* $|\varphi\rangle^{\otimes 2}$ *with* $|\varphi\rangle = {\lambda_1}^{1/2}|0,0\rangle + {\lambda_2}^{1/2}|1,1\rangle$. *Then, if* $\lambda_1 > (1/2 + \sin(\pi/18))^{1/2}$ *but* $1 - \lambda_1 > \sin(\pi/18)$, *CEP does not lead to edge percolation, whereas joint measurements result in an infinite connected cluster.*

We start by describing the situation for CEP. Each pair of neighbours shares $|\varphi\rangle^{\otimes 2}$, so the optimal SCP of transforming these two copies into a maximally entangled state (an open edge) is $p_1 = 2(1-\lambda_1^2)$, where the λ_1^2 originates from the fact

that we have two specimens at hand. It is easy to see that with the above choice for λ_1 one arrives at an edge probability of

$$2(1-\lambda_1^2) < 1 - 2\sin(\pi/18) = p_{\hexagon}^{(\mathrm{c})} \approx 0.6527. \tag{39}$$

Hence, with this strategy one falls below the percolation threshold of the hexagonal lattice.

We now turn to a strategy exploiting the more potential of the quantum setting. We resolve every second site as shown in Fig. 8. Now, as described in the caption of Fig. 8, one performs the protocol of (33), leading to a triangular lattice. The edge probability in this new triangular lattice is given by

$$2\lambda_2 = 2(1-\lambda_1) > 2\sin(\pi/18) = p_{\triangle}^{(\mathrm{c})} \approx 0.3473 \tag{40}$$

with the above choice for λ_1. Hence, we are now above the percolation threshold for the triangular lattice, and one can proceed as usual to demonstrate that an infinite cluster emerges. Therefore, bond percolation processes with quantum bonds are related to each other in a different way than those with classical bonds. More specifically, it is possible to find a parameter regime for which the hexagonal lattice does not percolate, but can be transformed into a percolating triangular lattice, if quantum operations are allowed for.

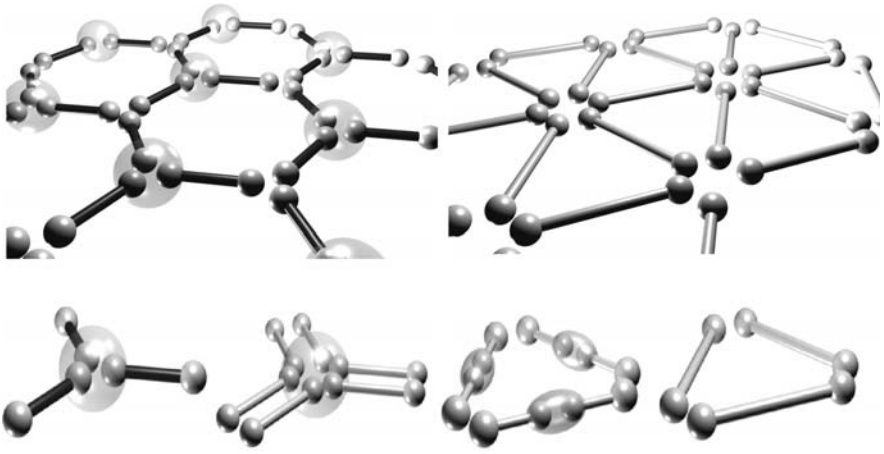

Fig. 8. *Top row*: A hexagonal and a triangular lattice. Each dark bond is constituted by two entangled pairs (here shown as light bonds). Every second vertex is highlighted. The bottom row shows how the transformation works: Pairs of qubits are taken from the highlighted vertices. Onto the respective pairs of edges, the protocol of (33) is applied, succeeding with probability p. Using this quantum operation, the lattice is transformed from a hexagonal lattice to a new triangular lattice (for cluster states this actually corresponds to performing a σ_y-measurement on the highlighted sites). On this new triangular lattice, an edge is open if the protocol of (33) has been successful

Equally interesting is the proposal to use the optimal singlet conversion strategy to transform a square lattice into two independent square lattices of doubled size, for which the bond probability is larger than in the original lattice.

Square lattice

Another striking example of what can happen in quantum percolation is a nested protocol of distillation steps. This has been proposed in [34], which develops the ideas of [1] in more detail. Here, a set of non-maximally entangled pairs will be used which cannot be transformed into maximally entangled ones deterministically by employing the process mentioned above, so $p_1 < 1$.

Consider the situation of Fig. 9. Initially, arranged in a square, one has four identical pairs in a state with state vector $|\varphi\rangle$. Then one can perform local operations to the marked subsystems, as Bell-measurements in the $\sigma_x\sigma_z$-basis (Fig. 9a). The original states $|\varphi\rangle$ have Schmidt coefficients $\{\lambda_1, \lambda_2\}$, the new state with state vector $|\varphi'\rangle$ will have Schmidt coefficients, the smaller of which is given by

$$\lambda_2' = (1 - (1 - (4\lambda_1\lambda_2)^2)^{1/2})/2. \tag{41}$$

Given the four original input states, by applying this local filtering twice, two such output states will be left. By using a further local operation (Fig. 9b) – an instance of a distillation protocol – a final state vector $|\varphi''\rangle$ can be achieved (Fig. 9c), which is more entangled than $|\varphi'\rangle$. The largest Schmidt coefficient of this final state is given by $\lambda_1'' = \max\{1/2, (\lambda_1')^2\}$ [33, 34]. This state is maximally entangled iff both Schmidt coefficients are equal, so iff $\lambda_1'' = 1/2$. The range in which that can be achieved is

$$1/2 \leq \lambda_1 \leq \lambda_1^* = \frac{1}{2}\left(1 + (1 - (2(\sqrt{2} - 1))^{1/2})^{1/2}\right) \approx 0.65. \tag{42}$$

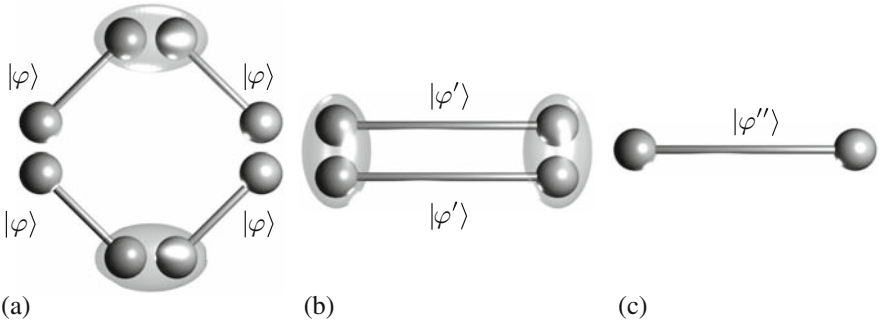

Fig. 9. Transformation of a square lattice (**a**) to another square lattice (**c**) by means of a pair of (**a**) two-partite measurements and (**b**) an entanglement distillation on the resulting state. Starting with a square lattice where each bond consists of $|\varphi\rangle^{\otimes 2}$ (similar to Fig. 8), this process generates a square lattices with $\sqrt{2}$ times the lattice constant

Hence, certain non-maximally entangled 'quantum edges' (with CEP probability smaller than one) can be deterministically transformed into maximally entangled bonds, so edges that are open with unit probability.

Note that each of the above steps involving local operations can be achieved deterministically, resorting to LOCC operations. In each case, the measurement outcome on each vertex has to be available to the other vertices to do the appropriate corrections and to render the scheme deterministic. Such an idea can be used to transform a square lattice, in which vertices share 'quantum edges' with nonunit CEP bond probability in form of non-maximally entangled states into a square lattice with unit edge probability.

Theorem 5 (Singlet conversion in the square lattice). *A square lattice where nearest neighbours share* $|\varphi\rangle^{\otimes 2}$ *can be transformed into a square lattice, the edges of which being fully occupied by maximally entangled pairs, using collective measurements at the individual sites, given that* $\lambda_1 < \lambda_1^*$.

One could say that the protocol transforms a square lattice with

$$1 \geq p_1 \geq 2\lambda_2^* \approx .70 \tag{43}$$

into a square lattice with $p_1 = 1$. Again, and more clearly so, this is a transformation between different bond percolation processes that crosses the critical threshold in a way that is not possible in percolation with classical edges.

Square lattice II

To consider yet another effect, we will have a second look at the square lattice[34]. As mentioned in Sect. 3.3, a joint measurement can be applied to a two-pair chain such that the SCP of the new bond equals the original bonds' SCP on average. Let us apply this operation at every other site of a square lattice as indicated in Fig. 10, thereby replacing it with two disjoint square lattices with double the lattice constant.

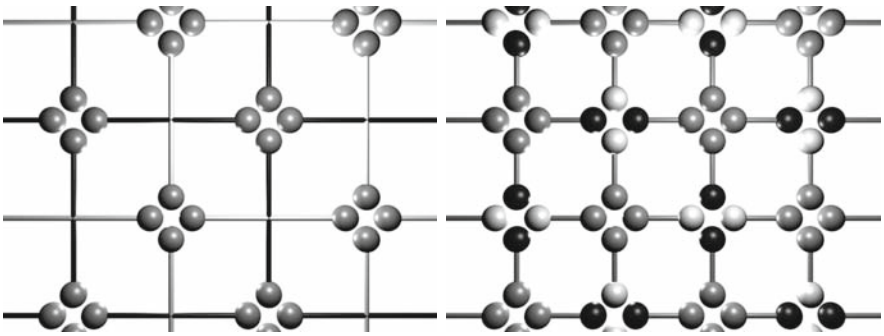

Fig. 10. Transformation of a square lattice into two disjoint ones by means of two qubit measurements. *Left*: At every other lattice site two operations are carried out, affecting the dark and light qubits, respectively. *Right*: The resulting lattice consists of two disjoint square lattices

Neighbouring sites in the resulting graph sit on different lattices. We pick two pairs of neighbours, $a = (A, A')$ and $b = (B, B')$ and ask for the probability of finding at least one open path between these two sets of sites, so the event $\mathfrak{H} = a \leftrightarrow b$. On the doubled lattices this accounts to the event of having at most one path out of $A \leftrightarrow B$ and $A' \leftrightarrow B'$. In the limit of large separation of a and b, the probability amounts to

$$P'_p(\mathfrak{H}) = \theta^2(p)(2 - \theta^2(p)), \tag{44}$$

where $\theta(p)$ is the percolation probability, so the probability of a given site to belong to an infinite spanning path.

In contrast, on the original lattice this quantity asymptotically fulfils

$$P_p(\mathfrak{H}) \leq \theta^2(p)(2 - P_p(A \leftrightarrow A'))^2. \tag{45}$$

In [34] a Monte Carlo simulation to find the quantity $P_p(A \leftrightarrow A')$ for $p \searrow p_2^{(c)}$ is carried out, yielding $2 - P_p(A \leftrightarrow A') \approx 1.313$ in comparison to $(2 - \vartheta^2(p_2^{(c)}))^{1/2} = \sqrt{2}$. So, a doubling of the lattice spacing using joint quantum operations can be advantageous when it comes to the connection of pairs of sites. It is conjectured [34] that this property holds for all p. Further, examples along similar lines are also presented in [34].

4 Summary and Open Problems

4.1 Open Problems

To elaborate the aforementioned invitation to this topic, we list some open problems that arose from the work so far. Concerning issues of 'classical percolation for cluster state preparation' this includes the following list of problems:

- In dimensions $d \geq 3$ crossing paths in different directions do not imply a crossing of these paths. Further, development could aim at finding an algorithm similar to the one in Sect. 2.3. These would be able to identify structures that are topologically equivalent to universal computing resource states in a percolated lattice at higher dimension, thus allowing this tool to be used for resource state production for arbitrary gate probabilities with resources amounting to $O(L^2)$.
- While it appears from numerical results that a constant overhead per site cannot be achieved with static renormalization, its optimal scaling is not evident. According to Fig. 4, this is at most logarithmic, rather than polynomial as the bound in Theorem 1 suggests.
- Further, an investigation towards the required initial resource size would help implement these protocols in the future. After all, small highly entangled quantum states have to be produced in the very beginning, the smaller the better. There will be a tradeoff between the possible gate probabilities and the number of initial qubits needed, the exact behaviour of which might be interesting. It includes optimization over possible local linear optical operations that do not require global re-routing.

- All ideas presented in this chapter presume ideal states, optical elements or quantum gates. This, however, will of course never be achieved in any implementation. The general problem of quantum error correction needs to be revisited in the framework of percolation, as there might arise new ways for error correction of special classes of errors (for first ideas see [28]).
- As has been shown in [18], there are a number of resource states very different from the cluster states that form universal resources for quantum computing. Dictated by the underlying physical architecture, there might be states that are more suitable than cluster states, exploiting the specific strengths of the respective architecture. However, if probabilistic processes are involved (like PEPS projections with linear optics), it is not obvious how to generalize the percolation scheme to other states.
  Information flow through these states is in general not ruled as easily as with single qubit Pauli measurements. Suitable applications of SWAP gates might help in using percolated versions of these resources for computing, though not giving a solution for distillation of hole-free states as such (as may be needed as resource for error correction).

Complementing these questions on the tightness of the given bounds, there are a number of open questions relating to the idea of entanglement percolation:

- The aim of Sect. 3 was to look at the problem of entangled state distribution with the tool of percolation. One, relatively vague, open problem is to find applications of this idea in a context different from entanglement distribution as such.
- One step in this direction could be to combine the idea of entanglement percolation with ones of quantum computation in the first part of this book chapter. Clearly, entanglement percolation could also help to further reduce the required resources in a renormalized lattice, albeit requiring more difficult collective measurements on the way, the probabilistic nature of which might lead to some tradeoff.
- Within restricted classes of percolation settings (such as restrictions to the geometry or the possible local operations), it seems important to identify the optimal entanglement percolation strategy.
- It is still far from clear how to fully incorporate mixed states in this setting, which seems important when considering lossy quantum channels.

4.2 Summary

Even though the first ideas to incorporate quantum information with percolation theory were only proposed very recently [1, 28], it seems clear that open problems in quantum state preparation and quantum communication can indeed benefit from results known in percolation theory. Since randomness is intrinsic in quantum mechanics, one often has to overcome the probabilistic nature of quantum operations. As we have discussed, a context in which this most naturally occurs is in quantum computation using lattice system. Here static lattices with a non-unit probability of the existence for bonds and sites occur naturally in cluster state preparation, where

the random nature is due to probabilistic quantum gates, or due to Mott defects in the preparation. Ideas of percolation – specifically questions of when crossing clusters exist – led to methods of renormalization that effectively remove this probabilistic aspect from quantum state preparation. Along similar lines, it seems realistic to expect related instances where percolation ideas help to overcome the intrinsic randomness of quantum mechanical state manipulation.

A key challenge will be, needless to say, to take mixed quantum states fully into account, and to see in quantitative terms to what extent renormalization ideas can be combined with methods of fault tolerance, error correcting codes or protection strategies in state preparation for the use of quantum computation [12, 36, 39, 45]. A step into this direction has been taken in [28].

We have also seen that when taking the quantum nature of the states seriously, one can often outperform strategies based on simple measurements and invoking notions of edge percolation. Such an approach seems particularly suitable for realizations in quantum networks for quantum communication and key distribution, but could equally well also be applied to the above context of quantum computation. New phenomena emerge when appropriate collective operations are allowed for, giving rise to an interesting interplay between questions of entanglement theory on the one hand and percolation theory on the other hand.

On a related but different note, ideas of percolation seem also to provide powerful tools in a slightly different context, namely to study correlation and entanglement properties of quantum many-body systems from the perspective of quantum information. Notably, the scaling of the entanglement entropy in the Ising model can be assessed by invoking concepts of classical percolation [17]. The question of relating percolation ideas to problems in quantum information science is at its infancy, but one should expect more applications to come.

Acknowledgments

We warmly thank T. Rudolph for numerous fruitful and fun discussions on the subject of the connection between percolation theory and quantum information theory, who is also coauthor of the joint publication [28]. We also thank T. Acin, D.E. Browne, W. Dür, A. Miyake, and T.J. Osborne for correspondence on percolation ideas in the quantum information context. This work has been supported by Microsoft Research through the European PhD Programme, the EPSRC, the EU (QAP), and the EURYI award scheme.

References

1. A. Acín, J.I. Cirac, and M. Lewenstein, Nat. Phys. **3**, 256 (2007) 288, 289, 307, 308, 310
2. M. Aizenman, Nuclear Phys. B **485**, 551 (1997) 294, 296
3. M. Z. Bazant, Phys. Rev. E **62**, 1660–1669 (2000) 307

4. C. Bennett, H. Bernstein, S. Popescu, and B. Schumacher, Phys. Rev. A **53**, 2046 (1996) 309
5. J.A. Bondy and U.S.R. Murty, *Graph Theory with Applications* (Macmillan, 1976) 290
6. S. Bose, V. Vedral, and P. L. Knight, Phys. Rev. A, **60**, 194 (1999) 308, 310
7. S. Bravyi and R. Raussendorf, Phys. Rev. A, **76**, 022304 (2007) 293
8. H.J. Briegel and R. Raussendorf, Phys. Rev. Lett., **86**, 910 (2001) 289, 291
9. D.E. Browne, M.B. Elliott, S.T. Flammia, S.T. Merkel, A. Miyake, and A. Short. Phase transition of Computational Power in the Resource States for One-Way Quantum Computation *arXiv:0709.1729* (2007) 288, 289, 303, 304, 305, 306, 307
10. D.E. Browne and T. Rudolph, Phys. Rev. Lett. **95**, 010501 (2005) 292, 301
11. J. Calsamiglia and N. Lütkenhaus, Appl. Phys. *B*, **72**, 67 (2001) 292
12. C. Dawson, H. Haselgrove, and M. Nielsen, Phys. Rev. Lett. **96**, 020501 (2006) 317
13. J. Eisert, Phys. Rev. Lett. **95**, 040502 (2005) 292
14. J. Eisert and M.M. Wolf, *Quantum computing, in Handbook of innovative computing*, Chapter 8, 253 (Springer, New York, 2004) 288, 289
15. N. Gisin, G. Ribordy, W. Tittel, and H. Zbinden, Rev. Mod. Phys. **74**, 145 (2002) 307
16. G. Grimmett, *Percolation*, 2nd edition. (Springer, 1999) 287, 294, 297, 305
17. G. Grimmett, T.J. Osborne, and P. Scudo. *Entanglement in the Quantum Ising Model*. (2007) 317
18. D. Gross and J. Eisert, Phys. Rev. Lett., **98**, 220503 (2007) 293, 316
19. D. Gross, J. Eisert, N. Schuch, and D. Perez-Garcia, Phys. Rev. A, **76**, 052315 (2007) 293, 304
20. D. Gross, K. Kieling, and J. Eisert, Phys. Rev. A, **74**, 042343 (2006) 292
21. J.M. Hammersley and W. Morton, J. Royal Stat. Soc. (B) **16**, 23 (1954) 287
22. L. Hardy and D.D. Song, Phys. Rev. A **62**, 052315 (2000) 307, 310
23. M. Hein, W. Dür, J. Eisert, R. Raussendorf, M. V. den Nest, and H.-J. Briegel, Entanglement in graph states and its applications. *quant-ph/0602096*, 2006. 289
24. M. Hein, J. Eisert, and H. J. Briegel, Phys. Rev. A **69**, 062311 (2004) 289, 290, 299
25. J. Hoshen and R. Kopelman, *Phys. Rev. B*, **14**, 3438 (1976) 298
26. K. Kieling, D. Gross, and J. Eisert, J. Opt. Soc. Am. B **24**(2), 184 (2006) 292
27. K. Kieling, D. Gross, and J. Eisert, *New J. Phys.* **9**, 200 (2007) 292
28. K. Kieling, T. Rudolph, and J. Eisert, Phys. Rev. Lett. **99**, 130501 (2007) 288, 289, 292, 298
29. E. Knill, R. Laflamme, and G. Milburn. *Nature* **409**, 46 (2001) 289
30. Y.L. Lim, S. Barrett, A. Beige, P. Kok, and L. Kwek *Phys. Rev.* A **73**, 012304 (2006) 291
31. O. Mandel, M. Greiner, A. Widera, T. Rom, T.W. Hänsch, and I. Bloch. *Nature* **425**, 937 (2003) 291
32. M.A. Nielsen and I. Chuang, *Quantum Computation and Quantum Information* (Cambridge University Press, 2000) 288, 289
33. M.A. Nielsen and G. Vidal, Quantum Information and Computation **1**, 76 (2001) 313
34. S. Perseguers, J.I. Cirac, A. Acin, M. Lewenstein, and J. Wehr, *Entanglement Distribution in Pure State Quantum Networks* (2007) 288, 289, 307, 308, 310, 313, 314, 315
35. T.B. Pittman, B.C. Jacobs, and J.D. Franson, Phys. Rev. A **64**, 062311 (2001) 292
36. J. Preskill, *Fault-Tolerant Quantum Computation*, *quant-ph/9712048* (1997) 317

37. R. Raussendorf and H.-J. Briegel, Phys. Rev. Lett. **86**, 5188 (2001) 289, 291, 298
38. R. Raussendorf, D.E. Browne, and H. Briegel, Phys. Rev. A **68**, 022312 (2003) 291
39. R. Raussendorf and J. Harrington, Phys. Rev. Lett. **98**, 190504 (2007) 317
40. S. Scheel and N. Lütkenhaus, New J. Phys. **6**, 51 (2004) 292
41. D. Schlingemann and R.F. Werner. Phys. Rev. A **65**, 012308 (2002) 290
42. R. Sedgewick, *Algorithms* (Addison-Wesley, 1983) 298
43. M. van den Nest, J. Dehaene, and B.D. Moor. Phys. Rev. A **69**, 022316 (2004) 290
44. M. van den Nest, A. Miyake, W. Dür, and H.J. Briegel, Phys. Rev. Lett. **97**, 150504 (2006) 299, 304
45. M. Varnava, D. Browne, and T. Rudolph, Phys. Rev. Lett. **97**, 120501 (2006) 317
46. G. Vidal, Phys. Rev. Lett. **83**, 1046 (1999) 308, 310
47. P. Walther, K. Resch, T. Rudolph, E. Schenck, H. Weinfurter, V. Vedral, M. Aspelmeyer, and A. Zeilinger. Nature **434**, 169 (2006) 289

Index

abutment, 306
Aharonov-Bohm phase, 182
Anderson localization, 83, 141, 278
Anderson model, 87, 88, 109, 139
  magnetic field, 88
Anderson transition, 84, 85, 88, 228, 247
ant, 14

Bell-measurement, *see* mesurement, Bell-
Berry phase, 260
  non-adiabatic, theory of, 255
  theory of polarization, 255
Bethe lattice, 3
biased diffusion, 16
binary alloy model, 144
bipartite, 110, 117, 119
Boltzmann's relaxation time approximation, *see* Debye relaxation
  failure of, *see* non-Debye relaxation
bond percolation, 1, 31
  tunneling enhanced, 27
breadth-first-search, 298
breakdown dynamics (reversible) in RRTN
  breakthrough or first passage time, 67, 74
  breakthrough *vs.* relaxation time, 76
breakdown field
  breakdown exponent, 44
  dynamical critical point, 44
breakdown susceptibility, 246
bridge decomposition, 306
brittle failure, 229
busbar contact, 114

Cayley tree, 3
Chalker-Coddington, 168
Chebyshev expansion, 151
chemical length, 232, 235
classical entanglement percolation, *see* percolation, entanglement, classical
classical percolation, 31, 164
cluster, 1
  crossing, 293, 298, 304
cluster state, *see* state, cluster
collective excitations, 164
colossal magneto-resistance
  CMR effect, 154
  in manganites, 195, 203, 204
compressibility, 164
concurrence, 311
conditional dynamics, *see* feed-forward
conductance, 110, 164
conductivity, 8
  tensor, 163
continuous time random walk, 60
  scale-invariance of (response) shape, 60
correlated electron system, 195
  insulating glassy phase, 221
  manganites, 225
  nonlinear phenomena, 252
  spin-spin interaction, 222
correlation length, 7, 231, 233, 235
Coulomb interaction, 55, 56, 139, 184, 252, *see* correlated electron system
critical energy, 169
critical exponent, 164, 166
cubic lattice, *see* lattice, cubic
current conservation, 35, 57, 168, 169

global, 62, 64
lattice Kirchhoff's dynamics, 63, 74
local, 62, 64
cyclotron energy, 185

Daboul ansatz, 115, 121
Debye relaxation, 59
degenerate Landau functions, 165
delocalization transition, 100
density matrix, 185
density matrix renormalization group
DMRG, 273
finite-size DMRG, 273
real-time DMRG, 273
time dependent DMRG, 256
diamond lattice, *see* lattice, diamond
dielectric breakdown, 238, 239, 249
field, 66, 245
half-filled Hubbard model, 273
quantum version, 247, 249
reversible, in semi-classical RRTN, 65–73
voltage, 66, 228
diffusion, 14
diffusion-vibration analogy, 111
disorder, quantum problem, 165, 196, *see* Anderson model
distribution function
Gumbel, 234, 237, 241, 246, 249
Weibull, 234, 241
doublon-hole excitation, 254, 255
field induced/driven metal, 255
Landau-Zener tunneling, 275
tunneling threshold field, 254
ductile failure, 74
in the RRTN, 74, 76
dynamic criticality, 22
dynamic random resistor network, 28
DRRN, 42, 44, 67
dynamical localization, 278, 279, 283

early stage power-law dynamics
blinking times of fluorescence in single CdSe quantum dots, 60
Ca^{2+} channels in living cells, 61
cellular automata models of earthquakes, 62
dielectric relaxation experiment, 60
earthquakes, 62
grain-size growth by gelation, sintering etc., 61
hole transport in PVK, Si-MOS, 60
in the RRTN, 63–65
photocurrent in a-semiconductors, 60
rebinding of ligands of iron in dissociated heme-proteins, 60
simulation of diffusion limited aggregate (DLA) growth, 61
earthquake dynamics
two power-laws
aftershocks, Omori law, 62
foreshocks, 62
electromigration, 236
energy level repulsion
interacting: Mott insulator, 266
single particle:band insulator, 266
energy level statistics, 183
entanglement, 289, 302, 308
distillation, 313
purification, 308, 310
width, 304, 306
entanglement percolation, *see* percolation, entanglement
equipotential lines, 166, 167, 182
excitation potential, 170, 172, 177
exponent
chemical length, 235
conductivity in continuum model, 235
conductivity in discrete model, 232
conductivity in the RRTN, 34
correlation length, 232, 236, 240, 242, 245
maximal RRTN, 32, 33
dielectric breakdown field in continuum model, 242
dielectric breakdown field in discrete model, 240, 241, 245, 246
dielectric breakdown field in RRTN model, 70–73
fuse failure current in continuum model, 233, 235
fuse failure current in discrete model, 232, 233, 237
fuse failure voltage in continuum model, 235
fuse failure voltage in discrete model, 232, 237
minimum gap, 67, 240

number of broken bonds upto global fuse failure, 238
size dependence of fuse failure current, 233, 237
extended states, 131

feed-forward, 290, 292, 302, 303, 315
Fermi level, 173
filling factor, 165
finite size scaling, 98, 100, 121
in RRTN, near p_{ct}, 33–34
FKG inequality, 295, 296
Flory, 1
FQHE, 164
fractal, 9
fractal dimension
maximal RRTN, 34
fractional charge, 164
fragmentation of the spectrum, 150
free energy, 6
fuse failure, 227
current, 228, 231, 233, 234

gate, 289
controlled-Z, 290–292
fusion, 292, 301, 302
probabilisitc, 290
probabilistic, 292, 293, 301, 302, 317
SWAP, 316
Gaussian wave packet, 125
Gaussian-type impurities, 166
gelation, 1, 18
GHZ state, *see* state, GHZ
graph, 290
graph state, *see* state, graph
graphene, 154

Hall bar, 163, 175
Hall conductivity, 163
Hartree-Fock, 164
Hausdorff dimension, 243
hexagonal lattice, *see* lattice, hexagonal
high magnetic field regime, 171
high-field limit, 166
high-precision determination of the fine-structure constant, 163
Hoshen-Kopelman method, 4
Hoshen-Kopelman-algorithm, 298
Hubbard interactions
adiabatic limit, 205
Hubbard model, single-band, 252

ideal chain, 111
incipient, 11
incipient infinite cluster, 34
incompressible stripe, 178
infinite cluster, 11
international reference resistance, 163
inverse participation ratio, 113
IQHE, 163
Ising, 5

joint measurement, *see* measurement, joint

Kosterlitz-Thouless transition, 125, 132
KPM, 139

Landau level, 164, 165
Landau-Zener formula, 276
Landau-Zener model, two-band, 261
Landau-Zener transition, 260, 261, 270, 271, 277, 278
Laplace equation, 243, 244
lattice, 291, 308
covering, 301
cubic, 291–297
diamond, 300–302
hexagonal, 291, 299, 306, 311–313
optical, 291
pyrochlore, 301, 302
square, 293, 297, 299, 304, 313–315
triangular, 312
LDOS, 139
Leath method, 4
Lifshitz scale, 233
linear optics, 289, 291, 301, 302, 315
local distribution approach, 137
local measurement, *see* measurement, local
localization length, 56, 125, 166, 170
localized states, 110, 131
localized-to-delocalized transition, 105, 109
LOCC, 308, 314
log-periodic, 16
longitudinal conductivity, 163

magnetic field, 163
magnetic length, 165
magnetisation, 6

Markov process, 111
MatLab, 298
mean cluster size, 7
mean DOS, 139
measurement, 288, 292, 307
  Bell-, 310, 313
  joint, 310, 311, 314
  local, 289, 291, 299, 302, 306, 312, 316
measurement-based quantum computer, *see* quantum computer, measurement based
minimum gap, 240, 242, 245
minimum gap path, 67, 69
minimum metallic conductivity, 84
mobility edge, 87, 247
Monte Carlo, 301
  in RRTN, 33
MOSFET, 22, 163
Mott metal-insulator transition, 253, 280
Mott/charge gap, 254, 266, 276
  metallic doping, 253
  Mott insulator, 204, 252
    quantum breakdown, 253

negative compressibility, 164
network-type models, 164
node-link-blob model, 231
non-adiabatic transition, 252
non-adiabatic tunneling, 264
  Landau-Zener transition, 283
non-Debye relaxation, 26, 59, 64
non-equilibrium currents, 170, 172
non-equilibrium network, 181
non-equilibrium phase transition, 251
  metal-insulator transition, 252
non-self-averaging property of RRTN, 43
nonlinear ac response
  in the RRTN/CRC model, 46–55
    intermediate frequency, 51
    low frequency insulator, 53
    low frequency metal, 52
nonlinear dc response, 21
  2D electron gas, MOSFET, 22
  C-black-polymer composites, 24
  carbon-black loaded rubbers, 23
  DNA molecules, 23
  granular superconductors, 22
  in the RRTN, 35–46
  intramolecular junction SWNT, 23
  metal-insulator composites, e.g. Ag-KCl, 25
  mobility of a polymer, 23
  movement of foam in porous rocks, 23
  oil/water microemulsions, 25
  viscosity of a Bingham fluid, 23
  ZnO varistors, 23, 43
nonlinear response
  optical properties, 264
  polarization, 260
  QED vacuum, 260

Omori law
  earthquake, aftershock dynamics, 62
one parameter scaling theory, 84
  vs. quantum percolation, 100
one-way quantum computer, *see* quantum computer, measurement-based
optical cavities, 291
optical lattice, *see* lattice, optical

participation ratio, 118
Pauli measurement, *see* measurement, Pauli
percolation
  bond, 31, 293, 312
    semi-classical, or semi-quantum, 24, 27
  bond correlated, 34
  entanglement, 290, 309–316
    classical, 308–309
  quantum, 88, 90, 197
    (statistically) correlated disorder, 221
    one band model, 205
    two band model, 217
  site, 291
  site/bond, 303
percolation probability, 7
persistent currents, 170
phase transition, 303
  non-equilibrium, 252
point-to-point contact, 114
Potts, 5
purification, *see* entanglement purification
pyrochlore lattice, *see* lattice, pyrochlore

quantization, 163
quantized Hall insulator, 183
quantum algorithms, 278
quantum bond percolation model, 198
quantum breakdown, 252

relation to nonlinear QED, 255
quantum communication, 289, 307
quantum computer, 288
measurement-based, 289, 290, 293–307
quantum electrodynamics, QED
nonlinear theory, 255
quantum information, 278
quantum interference, 277, 278, 283
quantum mechanical self-interference, 168
quantum mechanical tunneling, 168
quantum percolation, *see* percolation, entanglement
quantum random walk, 256, 276, 278
quantum site percolation model, 144, 198
qubit, 288, 293

radius of gyration, 7
random graphs, 3
random network models, 170
random resistor cum tunneling-bond network
RRTN, 28
random resistor cum tunnelling-bond network
RRTN, 28, 78
random resistor network
RRN, 28, 39, 154
re-routing, *see* feed-forward
real-space RG approach, 13, 33, 181
recursion method
scalar version, 90
slice version, 90
vector version, 92
renormalization, 12, 32, 293–300
repeater, 307
resistivity tensor, 163
resonant reflection, 117
resonant transmission, 117
resource consumption, 292, 293, 298, 304, 315
resource overhead, *see* resource consumption
resource scaling, *see* resource consumption
RRTN
effective medium approximation, 29
maximal, 28, 29, 32–34, 39

saddle point, 168, 172
scaling laws, 7
scattering matrix, 172
Schmidt coefficients, 308
shortest path, 236, 242
singlet conversion probability, 309, 311, 314
site percolation, 1
spanning, 2
spin, 184
square lattice, *see* lattice, square
stabilizer, 290
state
cluster, 290–291
GHZ, 301
graph, 290–291
mixed, 316
toric code, 293
Stokes phase, 262
non-adiabatic Berry phase, 262
stretched exponential, 112
strongly correlated electron system, 251, 252, 280
in non-equilibrium, 251
susceptibility, 6
swiss-cheese model, 234

temperature, 5
Thomas-Fermi screening, 164, 186
threshold, 2
dielectric breakdown voltage, 66, 228, 244
fuse current, 228, 231
Landau-Zener, 276
Landau-Zener tunneling, 254
percolation, 27, 228, 247, 249
QED instability, 264
site percolation, 144
tunneling enhanced percolation, 27
tight binding hamiltonian, 110
comprehensive for manganites, 203
time evolution, 151
toric code state, *see* state, toric code
transfer matrix, 169
transmission coefficient, 116, 127
triangular lattice, *see* lattice, triangular
typical DOS, 139

universal scaling, 109
universality, 8
universality class, 24, 100
maximal RRTN *vs.* RRN, 34, 72
quantum percolation *vs.* Anderson model, 100, 105

variable range hopping, VRH, 55, 86
  Efros-Shklovskii type, 55
  Mott type, 55, 86
  RRTN results, 56–59
  with super-localized states, 56
vertex degree, 300
vulcanisation, 1

wall follower, 305

Zener breakdown, 247–249, 253, 255, 259, 261
  quantum version, 247, 248